

Doctoral Thesis

Be Stars in Binary Systems

Danilo Ferreira da Rocha

Rio de Janeiro - RJ
August 22, 2025.

Ministry of Science, Technology, Innovations and Communications
National Observatory
Postgraduate Program in Astronomy

Doctoral Thesis

Be Stars in Binary Systems

Danilo Ferreira da Rocha

Thesis submitted to the Faculty of the Postgraduate Program in Astronomy of the National Observatory, as part of the requirements necessary to obtain the Degree of Doctor in Astronomy.

Advisor: Prof. Dr. Marcelo Emilio

Rio de Janeiro - RJ
August 22, 2025.

...to my parents, for their love, support and inspiration throughout my journey.

"*For what it's worth: it's never too late or, in my case, too early to be whoever you want to be. There's no time limit, start whenever you want. You can change or stay the same, there are no rules to this thing. We can make the best or the worst of it. I hope you make the best of it. And I hope you see things that startle you. I hope you feel things you never felt before. I hope you meet people with a different point of view. I hope you live a life you're proud of. If you find that you're not, I hope you have the strength to start all over again.*"
- Benjamin Button's letter to his daughter.

"Lift up your eyes and look to the heavens. Who created all these?"
Isaías 40:26

Se as coisas são inatingíveis... ora!
Não é motivo para não querê-las...
Que tristes os caminhos, se não fora
A presença distante das estrelas!
- Mario Quintana
Espelho Mágico, 1951.

Acknowledgments

- I thank God for the air I breathe, the water that calms me, and the stars that inspire me to dream.
- To my parents, for their education, values, and the example they set throughout my life.
- To my family and friends, for their constant support, meaningful conversations, and moments of joy.
- To my advisor, Prof. Marcelo Emilio, for his guidance, patience, valuable advice, and availability throughout this important period of my studies.
- To all the professors who contributed to my academic formation.
- To the friends I met and shared experiences with during my graduate studies.
- To the Observatório Nacional, for its support and institutional resources.
- To the Coordenação de Aperfeiçoamento de Pessoal de Nível Superior (CAPES), and Fundação Carlos Chagas Filho de Amparo à Pesquisa do Estado do Rio de Janeiro (FAPERJ) for financial support.

Thanks.

Be Stars in Binary Systems

Danilo Ferreira da Rocha

Submitted to the Postgraduate Program in Astronomy of the National Observatory in **Day** of **Month** of **Year**, as a partial requirement for delivery of the title of Doctor in Astronomy.

Abstract

Be stars are fast-rotating B-type stars that display Balmer emission lines, especially Hα, produced in circumstellar decretion disks. In this thesis, we studied the role of binarity in these objects, aiming to determine their stellar and orbital parameters and to assess how companions affect disk dynamics, angular momentum, and variability. While rotation and non-radial pulsations are relevant, observational evidence shows that binary interaction is crucial for the Be phenomenon. To investigate this, we combined TESS photometry, BeSS/OPD/SOAR spectroscopy, and Gaia DR3 astrometry, applying frequency analysis, spectral modeling, and orbital solutions with Wilson–Devinney and MCMC methods. From our main sample list of 158 targets, we refined to 50 confirmed Be binaries, only two of which are eclipsing, while excluding non-Be binaries, non-binaries, and poorly observed systems. We found that the Be stars rotate at a large fraction of their critical velocity, with an average value of $v \sin i / v_{\rm crit} \approx 0.30 - 0.85$. The frequency analysis of TESS light curves revealed 3 dominant periodicities per target on average, and we identified harmonics up to the 5th order in one system. The Be stars exhibit relatively high effective temperatures and radii typical of main-sequence stars. A highlight of my work is the system V1371 Tau, which we modeled as a hierarchical triple. For this system, we determined an eccentric inner orbit with $P_{\rm orb} \sim 34$ days and $e \sim 0.27$, and we detected a third body that significantly affects the dynamics. The system consists of a detached eclipsing B-type binary (B1V + B0V) orbited by a classical Be star (B0Ve). Photometric analysis reveals dominant low-frequency signals near 0.24–0.26 c/d, alongside higher-frequency signals attributed to non-radial pulsations of the Be star. Its projected rotation ($v \sin i \approx 250\,{\rm km\,s^{-1}}$) corresponds to a critical rotation fraction between 0.44 and 0.76, substantially faster than the inner components ($v \sin i \sim 160$–$200\,{\rm km\,s^{-1}}$). This study emphasizes the complexity of systems with Be stars and provides a basis for future research on their formation, evolution, and dynamics.

Keywords: Be stars; Binary Systems; Stellar Characterization; Stellar evolution.

Estrelas Be em Sistemas Binários

Danilo Ferreira da Rocha

Submetida ao Programa de Pós-graduação em Astronomia do Observatório Nacional em **Dia** de **Mês** de **Ano**, como requisito parcial para a obtenção do título de Doutor em Astronomia.

Resumo

Estrelas Be são estrelas do tipo B de rotação rápida que exibem linhas de emissão de Balmer, especialmente Hα, produzidas em discos de decreção circumestelar. Nesta tese, investigamos o papel da binariedade nesses objetos, com o objetivo de determinar seus parâmetros estelares e orbitais e avaliar como companheiras influenciam a dinâmica do disco, o momento angular e a variabilidade. Embora a rotação e pulsações não-radiais sejam relevantes, evidências observacionais mostram que a interação binária é crucial para o fenômeno Be. Para investigar isso, combinamos fotometria do TESS, espectroscopia BeSS/OPD/SOAR e astrometria Gaia DR3, aplicando análise de frequências, modelagem espectral e soluções orbitais utilizando os métodos Wilson–Devinney e MCMC. A partir da lista principal de 158 alvos, refinamos para 50 binárias Be confirmadas, das quais apenas duas são eclipsantes, excluindo binárias não-Be, sistemas não binários e alvos com dados insuficientes. Verificamos que as estrelas Be apresentam rotação próxima de uma fração significativa de sua velocidade crítica, com valores médios entre $v \sin i / v_{\rm crit} \approx 0,30 - 0,85$. A análise de frequência das curvas de luz do TESS revelou em média três periodicidades dominantes por alvo, sendo que em um sistema identificamos harmônicos até a quinta ordem. As estrelas Be exibem temperaturas efetivas relativamente altas e raios típicos de estrelas da sequência principal. Um destaque do meu trabalho é o sistema V1371 Tau, modelado como um triplo hierárquico. Neste sistema, determinamos uma órbita interna excêntrica com $\rm P_{orb} \sim$ 34,dias e $e \sim 0,27$, além de detectar um terceiro corpo que influencia significativamente a dinâmica. O sistema consiste em uma binária B-type eclipsante destacada (B1V + B0V) orbitada por uma estrela Be clássica (B0Ve). A análise fotométrica revelou sinais dominantes de baixa frequência próximos de 0,24–0,26 c/d, além de sinais de alta frequência atribuídos a pulsações não-radiais da estrela Be. Sua rotação projetada ($v \sin i \approx 250\,\rm km\,s^{-1}$) corresponde a uma fração de rotação crítica entre 0,44 e 0,76, significativamente mais rápida que os componentes internos ($v \sin i \sim$ 160–200 $\rm km\,s^{-1}$). Este estudo enfatiza a complexidade de sistemas contendo estrelas Be e fornece uma base sólida para pesquisas futuras sobre sua formação, evolução e dinâmica.

Palavras chaves: Estrelas; Sistemas Binários; Caracterização Estelar; Evolução Estelar.

List of Figures

2.1 Cartoon of the phenomenon of astronomical parallax . . . 13
2.2 Cartoon of the phenomenon of astronomical parallax . . . 14
2.3 Standard Hertzsprung-Russell Diagram . . . 15
2.4 Illustration of Stellar Evolution . . . 19
2.5 Schematic diagram of the a standard Be star. . . . 21
2.6 Be star Dschubba (δ sco): Spectral overview . . . 22
2.7 Raw KELT light curve for BK-052 . . . 23
2.8 Stellar Rotation Scheme. . . . 25
2.9 Distribution of projected rotation velocity values as a function of spectral type. 26
2.10 Artist's impression of waves of different frequencies propagating through the inner layers of a red giant star. . . . 28
2.11 Snapshot of the radial component of the l = 3 octupole modes . . . 29
2.12 The frequency of modes versus their degree l for a solar model. . . . 30

3.1 Orbit diagram of an Binary Stars . . . 34
3.2 Visual Binary Stars Scheme. . . . 39
3.3 Astrometric Binary Stars Scheme. . . . 40
3.4 Spectroscopy Binary Stars Scheme. . . . 42
3.5 Eclipsing Binary Stars Scheme. . . . 44
3.6 Gravitational potential of a binary system . . . 47
3.7 Classification of binary systems according to Roche surfaces . . . 49
3.8 Tidal Locking Configuration. . . . 51
3.9 Configuration of Be Stars in Binary Systems. . . . 52

4.1 Aperture mask used for extracting the target flux . . . 68
4.2 Light curve of TIC 124407255 observed by TESS in flux at BTJD (BJD-2,457,000). 68

5.1 Targets sample in aitoff projection . . . 83

5.2 Photometric modeling for eclipsing system TIC 51288359 classified as containing a Be star. . . . 85
5.3 Distribution of the three main frequencies by target . . . 87
5.4 Distribution of frequencies by group . . . 87
5.5 Histogram of the harmonic orders identified among the Be binary systems . . . 89
5.6 Correlation between Be Stars parameters . . . 92
5.7 Distribution of $v \sin i / v_{\rm crit}$ for the Be binary sample . . . 94
5.8 Color-color Hertzsprung Russell diagram . . . 95
5.9 Aperture mask used for extracting the V1371 Tau flux . . . 97
5.10 Light curve of V1371 Tau observed by TESS . . . 97
5.11 Comparison between the best-fit TLUSTY spectral model of V1371 Tau and the observed Goodman spectrum . . . 100
5.12 The dynamical spectra of V1371 Tau and a corner plot illustrating dimensional posterior distributions . . . 101
5.13 Light curve and radial velocity of eclipsing binary in orbital phase of The V1371 Tau . . . 103
5.14 Corner plot showing the posterior distributions for the free parameters derived from the WDC models fitted to the V1371 Tau. . . . 104
5.15 Hα analysis of data from BeSS, Goodman and HERMES . . . 108
5.16 Hertzsprung-Russell diagram of V1371 Tau . . . 110
5.17 TESS light curve of V1371 Tau and residuals analyses . . . 111

List of Tables

2.1 Main ranges of the UBV photometric system. 8
2.2 Morgan–Keenan (MK) stellar classification for main sequence (class V) stars. . 9

4.1 The complete catalog of targets analyzed in this study. Systems classified as Be binaries are marked with †. 59
4.2 Summary of spectroscopic observations of V1371 Tau. 71
4.3 Summary of binary system parameters derivable with the Wilson–Devinney code, depending on the available observations. 74

5.1 Summary of the main results of the sample of eclipsing binary systems with Be stars. 85
5.2 Targets grouped by the type of Hα EW variability. 90
5.3 Resume of parameters for the eclipsing binary in V1371 Tau. 105

Summary

Acknowledgments vii
Abstract ix
Resumo xi
List of Figures xiii
List of Tables xiv

1 Introduction **1**

2 The Stars **5**
2.1 Fundamental Properties of Stars 5
2.1.1 Stellar Structure and Evolution 14
2.2 Classical Be Stars 18
2.2.1 Spectroscopic characteristics 22
2.2.2 Stellar Rotation 23
2.3 Stellar Seismology 27
2.3.1 The Pulsation Mechanism 31
2.3.2 The Rotation Effect 31

3 Binary Systems **33**
3.1 Orbital Motion 34
3.1.1 Movement without Eccentricity 35
3.1.2 Orbital Motion with Eccentricity 37
3.2 Observation Method 39
3.2.1 Visual and Astrometric Binary 39
3.2.2 Spectroscopic 40
3.2.3 Eclipsing Binary 43
3.3 Separation and the Roche Lobe 47
3.4 Rotation and Tidal Effect 49

3.5 Be Stars in Binary Systems . . . 51
3.5.1 Impact of Binarity on the Observed Rotational Velocity Distribution of Be Stars . . . 54

4 Objectives, Data and Methodology **57**
4.1 Objectives . . . 57
4.2 Sample and Selection Criteria . . . 58
4.3 Gaia Astrometric Data . . . 64
4.4 Photometry . . . 65
4.4.1 TESS . . . 66
4.5 Spectroscopy . . . 69
4.5.1 BeSS . . . 69
4.5.2 HERMES and SOAR observations of V1371 Tau . . . 70
4.6 Determination of Stellar Parameters . . . 71
4.6.1 Linear Ephemeris and Orbital Characteristics . . . 71
4.6.2 Wilson–Devinney code . . . 72
4.6.3 Characterization of Be Stars . . . 77

5 Results and Discussion **81**
5.1 Be Binary Systems Sample Analysis . . . 81
5.1.1 Confirmation of Classical Be Stars in Binary Systems . . . 81
5.1.2 Characterization of Binary Systems . . . 83
5.1.3 Characterization of Be Stars . . . 86
5.1.4 Stellar Evolution Study . . . 94
5.2 The Triple System V1371 Tau . . . 96
5.2.1 Ephemeris and Eccentric Orbit Identification . . . 97
5.2.2 Spectral Temperature and Rotational Broadening . . . 98
5.2.3 Radial Velocity Scheme . . . 99
5.2.4 Binary Modelling Scheme . . . 101
5.2.5 The Third Body and its Be Nature . . . 104
5.2.6 Evolutionary Status . . . 107
5.2.7 Frequency Analysis . . . 109
5.2.8 Orbital Dynamics . . . 111

6 Conclusions and Perspectives **113**

A Mathematical Descriptions **119**
A.1 Calculation of the True Anomaly in Radial Velocity Analysis . . . 119
A.2 Some detailed analysis of V1371 Tau . . . 120

B Sample List of the Proposals Approved in TESS General Investigator program 125

C Individual Sample Description 129

C.1 TIC 10176636 . . . 130
C.2 TIC 103994174 . . . 131
C.3 TIC 11411724 . . . 132
C.4 TIC 115091314 . . . 133
C.5 TIC 117501818 . . . 134
C.6 TIC 118842700 . . . 135
C.7 TIC 124219174 . . . 136
C.8 TIC 124407255 . . . 137
C.9 TIC 125755072 . . . 138
C.10 TIC 126756648 . . . 139
C.11 TIC 12725034 . . . 140
C.12 TIC 127493611 . . . 141
C.13 TIC 128116539 . . . 142
C.14 TIC 136027289 . . . 143
C.15 TIC 136704900 . . . 144
C.16 TIC 140006471 . . . 145
C.17 TIC 140031673 . . . 146
C.18 TIC 140214221 . . . 147
C.19 TIC 14200511 . . . 148
C.20 TIC 144028101 . . . 149
C.21 TIC 146036695 . . . 150
C.22 TIC 14709809 . . . 151
C.23 TIC 148917425 . . . 152
C.24 TIC 151300497 . . . 153
C.25 TIC 151546818 . . . 154
C.26 TIC 152859121 . . . 155
C.27 TIC 153880067 . . . 156
C.28 TIC 154355871 . . . 157
C.29 TIC 155030422 . . . 158
C.30 TIC 155573117 . . . 159
C.31 TIC 157420220 . . . 160
C.32 TIC 159117671 . . . 161
C.33 TIC 16887256 . . . 162
C.34 TIC 171895762 . . . 163
C.35 TIC 174008063 . . . 164
C.36 TIC 174664153 . . . 165

C.37 TIC 175523591 166
C.38 TIC 181627638 167
C.39 TIC 186598770 168
C.40 TIC 187683138 169
C.41 TIC 19704573 170
C.42 TIC 200410503 171
C.43 TIC 201373582 172
C.44 TIC 202788979 173
C.45 TIC 203468988 174
C.46 TIC 203500116 175
C.47 TIC 204191276 176
C.48 TIC 209330890 177
C.49 TIC 213153401 178
C.50 TIC 217667184 179
C.51 TIC 228199255 180
C.52 TIC 230981971 181
C.53 TIC 231430254 182
C.54 TIC 232166879 183
C.55 TIC 23459321 184
C.56 TIC 237532447 185
C.57 TIC 237840594 186
C.58 TIC 238771552 187
C.59 TIC 239103320 188
C.60 TIC 239408899 189
C.61 TIC 239880242 190
C.62 TIC 239968973 191
C.63 TIC 240003393 192
C.64 TIC 240258004 193
C.65 TIC 240285395 194
C.66 TIC 240757326 195
C.67 TIC 243647020 196
C.68 TIC 24824031 197
C.69 TIC 250936039 198
C.70 TIC 252414037 199
C.71 TIC 252500679 200
C.72 TIC 252670277 201
C.73 TIC 253212775 202
C.74 TIC 253380837 203
C.75 TIC 25692574 204

C.76 TIC 258704817 . . . 205
C.77 TIC 259463816 . . . 206
C.78 TIC 261993378 . . . 207
C.79 TIC 262169297 . . . 208
C.80 TIC 26432264 . . . 209
C.81 TIC 264459943 . . . 210
C.82 TIC 264631173 . . . 211
C.83 TIC 265911941 . . . 212
C.84 TIC 266498398 . . . 213
C.85 TIC 27043894 . . . 214
C.86 TIC 27141005 . . . 215
C.87 TIC 271959772 . . . 216
C.88 TIC 279192753 . . . 217
C.89 TIC 281047621 . . . 218
C.90 TIC 281717549 . . . 219
C.91 TIC 283206453 . . . 220
C.92 TIC 28569279 . . . 221
C.93 TIC 285937814 . . . 222
C.94 TIC 2940839 . . . 223
C.95 TIC 294355648 . . . 224
C.96 TIC 29628522 . . . 225
C.97 TIC 296969980 . . . 226
C.98 TIC 304114338 . . . 227
C.99 TIC 30562668 . . . 228
C.100 TIC 310852121 . . . 229
C.101 TIC 311282109 . . . 230
C.102 TIC 312730071 . . . 231
C.103 TIC 317958778 . . . 232
C.104 TIC 322060937 . . . 233
C.105 TIC 322104948 . . . 234
C.106 TIC 323348984 . . . 235
C.107 TIC 324252945 . . . 236
C.108 TIC 324820890 . . . 237
C.109 TIC 326247844 . . . 238
C.110 TIC 326999260 . . . 239
C.111 TIC 32882261 . . . 240
C.112 TIC 329947655 . . . 241
C.113 TIC 331811163 . . . 242
C.114 TIC 333670784 . . . 243

C.115 TIC 33993533 244
C.116 TIC 343908909 245
C.117 TIC 354462452 246
C.118 TIC 354770601 247
C.119 TIC 355653322 248
C.120 TIC 356239023 249
C.121 TIC 358499972 250
C.122 TIC 364398342 251
C.123 TIC 364921141 252
C.124 TIC 368237682 253
C.125 TIC 368799545 254
C.126 TIC 370042412 255
C.127 TIC 370259865 256
C.128TIC 377900979 257
C.129 TIC 377967736 258
C.130 TIC 385509348 259
C.131 TIC 387813185 260
C.132 TIC 394728064 261
C.133 TIC 399626383 262
C.134 TIC 402978131 263
C.135 TIC 404619905 264
C.136 TIC 405216722 265
C.137 TIC 410193513 266
C.138 TIC 410627159 267
C.139 TIC 411577031 268
C.140 TIC 412724758 269
C.141 TIC 4154938 270
C.142 TIC 42360166 271
C.143 TIC 424566072 272
C.144 TIC 425224332 273
C.145 TIC 427396133 274
C.146 TIC 429843636 275
C.147 TIC 429863539 276
C.148 TIC 431116093 277
C.149 TIC 434893323 278
C.150 TIC 441027987 279
C.151 TIC 442240473 280
C.152 TIC 444325059 281
C.153 TIC 455463415 282

C.154 TIC 460532958 283
C.155 TIC 46247269 284
C.156 TIC 51288359 285
C.157 TIC 709917565 286
C.158 TIC 90296023 287

References **289**

1 Introduction

Classical Be stars represent a distinct and complex subclass of B-type stars characterized by the presence of one or more Balmer emission lines in their spectra, particularly Hα. These emissions originate from a geometrically thin, gaseous, circumstellar disk formed through episodic mass ejection from the central star, which typically rotates at a substantial fraction of its critical velocity (Porter and Rivinius, 2003a). While the mechanisms behind disk formation are still not fully understood, rapid rotation, non-radial pulsations, magnetic fields, and, notably, binarity have all been proposed as contributing factors.

Mounting observational evidence suggests that stellar binarity plays a fundamental role in shaping the structure and evolution of Be stars. Binary interactions can influence the angular momentum budget of the primary star, potentially inducing or enhancing the Be phenomenon through angular momentum transfer during close encounters or Roche lobe overflow episodes (Sana et al., 2012; Rivinius et al., 2013). The binary nature of Be stars may also affect the morphology and longevity of their disks, the variability of emission line profiles, and even the observed photometric behavior, including long-term modulations and outbursts.

From a galactic perspective, binary and multiple systems are ubiquitous, with more than half of all massive stars believed to form in such systems (e.g., Abt, 1984; Duchêne and Kraus, 2013; Sana, 2014; Moe and Di Stefano, 2017a). With interactions such as mass transfer and mergers significantly affecting their evolution (Paczyński, 1967; Langer, 2012; de Mink et al., 2014). Observational characterization of post-interaction systems is therefore crucial to constrain binary evolution models, which still involve many uncertainties (Marchant et al., 2024). Identifying products of binary interaction remains challenging, and various observational criteria have been proposed, such as chemical abundances, magnetic fields, apparent ages, and rotation rates (Schneider et al., 2019; Shenar et al., 2023). Models predict that stripped donors should rotate slowly, whereas mass gainers become fast rotators (Packet, 1981; Sen et al., 2023).

In this context, OBe stars (i.e., non-supergiant OB stars with emission lines) become particularly relevant. Their decretion disks are sustained by near-critical rotation, suggesting a binary origin for many of them (Pols et al., 1991; Wang et al., 2020). Population synthesis models show

that binary channels could account for the high observed fraction of OBe stars, provided that most interactions proceed through stable mass transfer without merger (Hastings et al., 2021). Be stars, therefore, do not evolve in isolation. Interactions with stellar companions—whether through tidal forces, wind accretion, or disk truncation—have profound consequences for the physical and evolutionary properties of these objects. However, single-star models also predict fast rotation via internal angular momentum transport or initial conditions (Ekström et al., 2012a). Thus, multiplicity properties of OBe stars are key to discriminating between scenarios. If predominantly post-interaction products, stripped or compact companions should be common; if not, many could still be in pre-interaction systems (Wang et al., 2024).

Challenges include the faintness of companions, small radial velocity amplitudes, and the transient nature of the Be phenomenon (Townsend et al., 2004). In some cases, the originally OBe star no longer exhibits emission, as in NGC 1850 BH1 (El-Badry and Burdge, 2022). Additionally, the OBe class encompasses objects with diverse evolutionary paths (Rivinius et al., 2013), and it remains uncertain whether the most massive O-type stars can form decretion disks (Vink et al., 2009). The Small Magellanic Cloud (SMC), with its low metallicity ($Z \sim 0.2Z_{\odot}$), offers a privileged environment to study these stars, with a high observed OBe fraction and large BeXRB population (Antoniou and Zezas, 2016; Schootemeijer et al., 2022). Studies in such environments are crucial to disentangle the effects of binarity and rotation on stellar evolution across different galactic conditions. Recent studies, such as Labadie-Bartz et al. (2017), have highlighted complex variability patterns in Be stars that may be attributable to binary modulation or disk-companion interactions. Another recent work within the BLOeM survey has shown that only $\approx$ 18% $\pm$ 4% of Oe/Be stars in the Small Magellanic Cloud host detectable spectroscopic companions, significantly lower than the fraction observed in normal OB stars, underscoring that multiplicity properties of Be stars differ fundamentally, even at low metallicity (Bodensteiner, J. et al., 2025).

This thesis is dedicated to the study of Be stars in binary systems, aiming to provide a comprehensive characterization of their fundamental and orbital parameters through a multi-technique observational approach. The research draws upon high-precision time-series photometry from the Transiting Exoplanet Survey Satellite (TESS), enabling the detection of periodic and quasi-periodic variability, as well as the application of time-domain analysis techniques such as Lomb-Scargle periodograms. These photometric data are complemented by spectroscopic observations from the Be Star Spectra (BeSS) database (Neiner et al., 2011) and dedicated campaigns at the Southern Astrophysical Research Telescope (SOAR), which allow for line profile analysis and the monitoring of disk variability via Hα emission.

In addition, the use of astrometric data from the Gaia Data Release 3 (Collaboration, 2021) provides robust estimates for stellar distances, proper motions, and absolute magnitudes, which are essential for inferring radii and luminosities. Stellar parameters such as effective temperature and projected rotational velocity ($v \sin i$) are derived from spectroscopic modeling, while orbital solutions are obtained through the Wilson–Devinney code in combination with

the MCMC-based `emcee` sampler (Foreman-Mackey et al., 2013). This integrated methodology allows for the identification and modeling of eclipsing and non-eclipsing binary systems, including potential triple configurations such as V1371 Tau.

By analyzing a carefully selected sample of Be stars in binary systems, this work aims to: (i) identify and confirm binary companions through photometric and spectroscopic variability; (ii) determine stellar and orbital parameters with high precision; and (iii) explore correlations between binarity and the observed Be phenomenon. The findings are expected to contribute to our understanding of angular momentum evolution, disk dynamics, and the broader role of binary evolution in shaping the Be star population.

In this context, this manuscript is divided as follows: chapters 2 and 3 present the theoretical foundation of our work, defining and presenting the characteristics of Be stars and binary systems. In chapter 4, we describe the objectives, methods of photometric and spectroscopic data collection, the reduction techniques employed and the methodology used in order to achieve our objectives. Chapter 5 presents the results and the in-depth analysis of binary systems with Be stars, using current techniques to derive precise orbital and physical parameters, discussing their implications for the broader context of stellar systems and their evolution. In chapter 6 finally, we summarize our findings, in addition to pointing out future work with possible developments arising from this manuscript, new paths for understanding the role of classical Be stars in complex stellar systems and their contribution to the galactic ecosystem.

2 The Stars

A star is a self-luminous astronomical object made of gas, which shines due to radiation and maintains its spheroidal shape due to the hydrodynamic relationship between the internal forces of pressure, caused by nuclear fusion, and the external force of gravity. The study of its properties and characteristics is done based on the variation of its apparent brightness, allowing us today to determine its mass, age, temperature, chemical composition (metallicity) and distance. The main source of support and hydrodynamic equilibrium of a star occurs due to the thermonuclear fusion of hydrogen atoms into helium atoms in its interior through the CNO cycle, which is its longest phase of evolution and is determined by the total mass it has when the nuclear fusion processes begin. Stars play a unique role in the maintenance and evolution of the universe, reionizing the interstellar medium with heavy elements such as carbon, nitrogen and oxygen, fundamental elements in the formation and evolution of other celestial bodies, such as comets, asteroids and planetary systems. Furthermore, many stars are born in pairs or multiple systems, and are gravitationally linked by a common center of mass, with this characteristic of multiplicity being a determining factor in the evolution of the stars that make up such systems (Sana et al., 2012). Furthermore, stars can form larger groups, with a well-defined gravitational structure, known as clusters or even galaxies, depending on the number of stars belonging to this group, such as our galaxy called the Milky Way.

2.1. Fundamental Properties of Stars

Luminosity and Flux

Luminosity is the total amount of energy a body, such as a star, radiates each second across all wavelengths of the electromagnetic spectrum. This parameter is the most important physical quantity in the study of stellar astrophysics, as its variations can reveal physical processes occurring both on the surface and in the interior of stars. Furthermore, this quantity is independent of the distance between the luminous object and the observer, that is, it is intrinsic and unique

to each star. The luminosity (L) of a star is expressed from the following equation:

$$L = 4\pi k_B R^2 T^4 , \tag{2.1}$$

where R is the mean surface radius of the star, T is the temperature in its photosphere, that is, in its outer layers, and σ is the Stefan-Boltzmann constant, which is $1.38065 \times 10^{-23}\,J{\cdot}K^{-1}$.

Unfortunately, we are not able to measure luminosity directly, with the exception of the Sun's brightness. This is done by measuring the stellar radius and surface temperature using an independent method, or by measuring the energy that reaches the observer after traveling a distance (d) between the star and the observer. We call this trace of luminosity flux (or luminous flux, apparent flux and brightness). The flux is then the observer's measure of the star's energy, per unit of time, per unit of area*, and is given by the following relation:

$$F(d) = \frac{L}{4\pi d^2} . \tag{2.2}$$

Magnitude, Color and Temperature

Another physical quantity is also used to measure the apparent flux observed from stars, called Magnitude. Developed by the Greek astronomer Hipparchus around 150 BC, the magnitude originated from a scale of 1 to 6, where the value 1 indicated the group of brightest stars observed with the naked eye on a night with good observational conditions, and 6 the group of less bright stars in those same observational conditions. Two factors helped maintain and widely use this scale. It was observed that the human eye reacted to brightness on a logarithmic scale, corroborating the improvements in the theory of stellar magnitude made by the English astronomer Norman R. Pogson (1829-1891), who realized that the ratio of the luminous flux that reaches the observer, between two stars of magnitudes equal to 1 and 5, according to the Hipparchus system, was exactly 100 times. Thus, any body that shone in the sky, whether by its own light or not, would be covered by the new scale, and we would no longer have the integer limits defined by Hipparchus, with magnitudes between 1 and 6. Pogson presented the following relationship between magnitude and flux:

$$m_1 - m_2 = -2.5 \log \frac{F_1}{F_2} , \tag{2.3}$$

where m_1 is the apparent magnitude of object 1, m_2 is the apparent magnitude of object 2, both measured with filters that allow observation in a predefined region of the electromagnetic spectrum. By default, the apparent magnitude and flux of the star Vega are used as the standard. It is worth noting that even considering the Weber-Fechner Law and Stevens Potential Law in these studies, what we have most concretely is that stars with a difference in apparent magnitude equal to 1 correspond to a factor of $100^{1/5}$ for the flux ratios.

* We consider this to be the surface area of a sphere with a radius equal to the distance between the star and the observer.

We also have other variations for this concept of magnitude, namely: (i) Absolute Magnitude (e.g. M), (ii) Intrinsic Magnitude and (iii) Bolometric Magnitude.

- (i) Absolute Magnitude: Defined as the apparent magnitude of a star at a fixed distance of 10 parsecs.

- (ii) Intrinsic Magnitude: Represented by the index 0 (e.g. M_0), it corresponds to the value of the absolute magnitude, if there were no red scattering of light on its path to the observer.

- (iii) Bolometric Magnitude: Magnitude with the flux observed across the entire wavelength. It is determined using the bolometric magnitude and the luminosity of the Sun through the following equation:

$$M^{bol} - M_{\odot}^{bol} = -2.5 \log \frac{\mathrm{L}^{bol}}{\mathrm{L}_{\odot}^{bol}} \,. \tag{2.4}$$

  It can also be obtained as a relation of the absolute magnitude, given a bolometric correction (CB), we have:

$$M^{bol} = M_{\lambda} + CB_{\lambda} \,. \tag{2.5}$$

One of the scientific revolutions occurred due to the study of radiation emitted by a black body, where some relationships were observed between temperature and energy emitted at a given wavelength of the electromagnetic spectrum. Then came the Stephan-Boltzmann Law and Wien's Law, precursors of Planck's Law for black body radiation, which among their functions allow the estimation of the temperature of stars, being defined as follows, respectively:

$$\mathrm{k_B T_{eff}^4} \equiv \int_0^{\infty} \mathrm{F}_{\nu} \, d\nu = \mathrm{F(d)} \,, \tag{2.6}$$

and

$$\lambda_{\mathrm{max}} \mathrm{T_{eff}} = 2,898 \cdot 10^7 \,, \tag{2.7}$$

where k_B is the Boltzmann constant, λ_{max} is the wavelength corresponding to the maximum radiation, and $\mathrm{T_{eff}}$ is the emission temperature at the surface of the star (effective temperature) (Smalley, 2005). Observing these equations, we can initially conclude that cooler stars have a wavelength with maximum intensity at low frequencies (more towards the red of the spectrum), and hotter stars tend to have wavelengths with greater intensity at high frequencies (in the blue region of the spectrum).

Obtaining spectra of stars is a challenging task, which requires state-of-the-art equipment and people capable of assembling the best configuration for each observational objective. The equipment available today does not have the technological capacity to obtain high-resolution

spectra at different wavelengths at the same time. Therefore, we perform spectroscopic observations with the aid of filters in specific regions of the spectrum, in order to obtain the best possible resolution and understand the physical phenomena presented in that particular spectral region. Today, there are dozens of photometric systems. In the visible spectrum region, the most widely used filters are those of the Johnson-Morgan photometric system (UBV System), created in 1953. In the other regions of the spectrum, the photometric bands have small differences in relation to the central wavelength of the filter ($\bar{\lambda}$). Below we summarize the main filters used in some telescopes with the $\bar{\lambda}$ point of each one.

Table 2.1: Main ranges of the UBV photometric system.

Filter Letter	$\bar{\lambda}$	**Description**
U	3700 Å	Ultraviolet Region
B	4400 Å	Blue Region
V	5500 Å	Visual Region
R	6400 Å	Red Region
I	8000 Å	Infrared Region

With flux (or magnitude) measurements at different wavelengths, we can estimate the star's temperature through its color index (IC), defined as:

$$IC = m_1 - m_2\,, \tag{2.8}$$

which applied to Eq. 2.3, becomes,

$$IC = -2.5 \log \frac{F_1}{F_2}\,, \tag{2.9}$$

with the indices 1 and 2 representing 2 different filters, and can also be represented by the letter indicating their respective filter. The star Vega, for example, has (U-B)=(B-V)=0 and temperature ~10 000 K. Especially for stars with temperatures between 9 500 K < T_{eff} < 30 000 K, a relation between the color index [u-b] corrected for reddening and the effective temperature. This correction of the color index and the relation that computes the temperature are presented below:

$$[u-b] = (u-b) - 1,53(b-y)\,, \tag{2.10}$$

$$\Theta = \frac{5040K}{T_{eff}} = 0,1692 + 0,2828[u-b] - 0,0195[u-b]^2. \tag{2.11}$$

It is worth noting that this is not the best way to determine the surface temperature of a star, because in addition to the radiation that interacts with the interstellar medium throughout its journey to the observer, several physical-chemical phenomena that occur in the stellar atmosphere interfere with the accurate determination of such a measurement, such as: Rotation, flattening, pulsation, tidal force when we have interacting systems, among others. Thus, as will be discussed later, the best way to determine the temperature of a star is through spectral mod-

eling, which allows us to include other variables in the generation of the theoretical model, in addition to determining the temperature, such as surface gravity and stellar abundance.

With this information, it is possible to develop a stellar classification, in order to group stars with similar characteristics based on their spectra, and consequently on their temperatures, given that a certain stellar group is in the same evolutionary phase, having similar characteristics such as chemical composition and rotation velocity.

The first widely accepted classification was developed around 1910, called the Harvard classification, which, in a simplified way, was based directly on stellar grouping based on effective temperature ranges. However, it was noted that there was a need to subdivide these classes by also taking into account luminosity, which is directly related to the evolutionary phase of the star, giving rise to the system known as the Morgan–Keenan (MK) classification, which is the most modern classification used today. In it, each star receives a spectral class, based on the Harvard classification and with nomenclature based on the Roman alphabet, and a luminosity classification index, following the Roman numerals from I to VII (1 to 7). A summary of this classification with its characteristics and estimated values for class V stars is presented in Table 2.2.

Table 2.2: Morgan–Keenan (MK) stellar classification for main sequence (class V) stars.

Type	**Color**	T_{eff} **(K)**	**Mass ($M_\odot$)**	**Radius ($R_\odot$)**	**Luminosity ($L_\odot$)**
O	Blue	$\geq$ 30,000	$\geq$ 16	$\geq$ 6.6	$\geq$ 30,000
B	Blueish	10,000 - 30,000	2.1 - 16	1.8–6.6	25–30,000
A	White	7,500 - 10,000	1.4 - 2.1	1.4–1.8	5–25
F	Yellowish	6,000 - 7,500	1.04 - 1.4	1.15–1.4	1.5–5
G	Yellow	5,200 - 6,000	0.8 - 1.04	0.96–1.15	0.6–1.5
K	Orange	3,700 - 5,200	0.45 - 0.8	0.7–0.96	0.08–0.6
M	Red	2,400 - 3,700	0.08 - 0.45	$\leq$ 0.7	$\leq$ 0.08

Stellar Mass and Surface Gravity

When it comes to physical parameters, stellar mass stands out in relation to other parameters such as radius, temperature and rotation, when it comes to the behavior and evolution of this star. All phenomena that occur and will occur with the star are directly related to the amount of mass that this star managed to attract gravitationally, until the moment in which its core reached a temperature sufficient to initiate thermonuclear reactions[†], which we call the initial mass. We measure stellar mass based on the mass of the Sun ($M_\odot$), and this can vary throughout its life and evolution, and can be lost through mechanisms such as stellar wind and pulsations, or be added through gravitational accretion from a companion star, whether in a simple binary system or a multiple system.

We can classify stars based on their initial mass, which is directly related to their possible type of evolution, as will be expanded upon in the next topic. In simple terms, we divide

[†] Approximate temperature of 8 million kelvins.

stars into three mass groups: (i) low-mass stars, which are those with less than $0.8\,M_\odot$, (ii) intermediate-mass stars, which have masses between $0.8\,M_\odot$ and $8.0\,M_\odot$, (iii) and high-mass stars, which have masses equal to or greater than $8.0\,M_\odot$. Interestingly, high-mass stars are considered rare in the universe; for every high-mass star, there are approximately 300 intermediate-mass stars in the universe.

The most accurate and direct way to determine stellar mass is through the study of binary systems, given Newton's law of gravitation and Kepler's third law. However, there is an empirical way to estimate the mass of stars, and this is due to a proportional relationship between stellar mass and luminosity. The stellar mass usually varies between $0.08\,M_\odot$ and $100\,M_\odot$, while the luminosity varies between $10^{-4}\,L_\odot$ and $10^{+6}\,L_\odot$, thus, the average relationship between the luminosity and all masses is $L \propto M^3$.

With this mass measurement, together with the stellar radius measurement, we can calculate the surface gravity of the star, which is equivalent to the photospheric pressure of the stellar atmosphere, and is given by the following expression:

$$g = g_\odot \frac{M}{R^2}\,, \tag{2.12}$$

or, in logarithmic form, it is expressed by:

$$\log g = \log M - 2\log R + 4,437^{\ddagger}\,. \tag{2.13}$$

Limb Darkening and Gravity Darkening

Two other important concepts are *Limb Darkening* and Gravity Darkening. Limb Darkening is the decay of brightness from the center to the edge of the star and occurs mainly due to the spheroidal shape of stars, allowing the study of theoretical models for this darkening gradient (Milne, 1921). Work using limb darkening has been done to determine the temperature and structure of the solar surface. The calculation of this parameter is based on the ratio of brightness at the center of the star, $I(0)$, and the intensity of the brightness, $I(\psi)$, which will be a function of the angle of incidence with the stellar atmosphere ψ, seen in the direction θ from a point P outside the atmosphere, but centered on the star. The brightness gradient is often expressed as a linear, quadratic or logarithmic decay function, with its most convenient form being a cosine function, given as follows:

$$\frac{I(\psi)}{I(0)} = \sum_{k=0}^{N} a_k \, cos^k \psi\,, \tag{2.14}$$

with a_k being a constant of the dimming function, dependent, among other parameters, on the wavelength at which the brightness intensity I is observed.

Gravity Dimming, on the other hand, is a result of the flattening[§] of the poles due to high

‡ $\log g_\odot$=4.4374±0.0005 (Gray 1992).

§ We can define stellar flattening through the following equation $f = \frac{(r_e - r_p)}{r_e}$.

stellar rotation, and/or due to the tidal effect caused by the gravitational attraction of interacting stars, such as binary systems, causing an increase in the surface gravity of the star at the poles, and consequently the elevation of temperature and pressure in these regions, a stellar mechanism necessary to maintain the hydrostatic equilibrium of these stars. In this way, the equator of the star appears to be "darkened by gravity" while the poles appear to be "illuminated by gravity".

The quantitative study of this phenomenon is based on the concept that the gravitational force ($\vec{F}_g$) is related to the gravitational potential (ϕ_g) in the following way:

$$\vec{F}_g = -\vec{\nabla}\phi_g \,. \tag{2.15}$$

Due to rotation, the star loses its spherical shape, becoming oblate and the total force of the system is increased by a centripetal force, and therefore, the Laplacian of the total potential must be related to the mass distribution that rotates according to Poisson's equation given as follows:

$$\vec{\nabla}^2\phi = 4\pi G\rho - 2\omega^2 \,, \tag{2.16}$$

with ρ being the (average?) stellar density.

Using this result together with the general equation of hydrodynamic equilibrium, we arrive at an expression that relates the radiative energy transport flux to the gravitational equipotential surface just below the stellar surface, given by:

$$\mathcal{F} = f(\phi_0)\,\nabla\phi_0 = f_0\,\vec{g} \,. \tag{2.17}$$

In this expression, we observe that the flux is proportional to effective gravity, that is, gravity minus centrifugal acceleration (see Eq. 2.16), so that the stellar surface near the equator will be "darker", since effective gravity is small, and consequently will have a reduced flux, calling this phenomenon Gravitational Darkening. This result can also be expressed in scalar form according to Von Zeipel (1924)'s Law, Eq. 2.18, which in a simplified way shows that the surface temperature of a star with a radioactive envelope varies with latitude due to rotation, having its highest value at the poles.

$$\mathcal{F} \propto g \Longrightarrow \mathrm{T_{ef}} \propto \mathrm{g}^{1/4} \,. \tag{2.18}$$

Lucy (1967) attempted to generalize Von Zeipel's Law, $\mathrm{T_{ef}} \propto \mathrm{g}^{\beta}$, by calibrating the exponent β in their relation. She inferred the value of β=0.08 for Sun-like stars with convective envelopes.

Distance and Extinction

Although it is not a stellar parameter, a large parenthesis is appropriate here to discuss the distance to the stars, a fundamental measurement for determining the physical parameters of stars and thus studying their evolution. The relationship between luminosity and flux (see Eq.

2.2) depends on the distance between the observer and what is observed, and these, together with the effective temperature, are of fundamental importance for evaluating the position of the star in the HR diagram. Therefore, a complete understanding of stellar evolution is linked to the precise measurement of the distance to the stars.

Astronomical distances use a specific convention of units of magnitude, which in terms of kilometers (km), are related as follows:

$$1\,\text{pc} = 30,856,775,814,913.67\,\text{km};$$

$$1\,\text{AU} = 149,597,870.70\,\text{km};$$

$$1\,\text{al} = 9,460,730,472,580.80\,\text{km},$$

where AU is the astronomical unit, pc is the distance in parsecs, and the light-year is represented by al.

Among the methods for determining distances, we highlight the measurement by trigonometric parallax and distance module.

The trigonometric parallax method, see Fig. 2.1, is very effective for objects not so far from Earth (<2.0 pc) and is based on the parallax effect, which is the difference in the apparent position of an object in relation to a background, as seen by observers in different locations. We use heliocentric parallax, which consists of two observations of the star spaced approximately six months apart, so that we have right angles between the Earth, the Sun and the observed object. We then determine the parallax angle (p), which from the trigonometric definition of the tangent[¶], gives us the distance (d_p) to the star, through the following equation,

$$\mathrm{d}_p \simeq \frac{206,265}{p}\,\text{AU} = \frac{1}{p}\,\text{pc}\,. \tag{2.19}$$

On the other hand, combining Eq. 2.4 and Eq. 2.5, results in a way to obtain the absolute magnitude of a star, given by:

$$M_\lambda = M_\odot^{bol} - BC_\lambda - 2,5\,\log\left(\frac{\mathrm{L}}{\mathrm{L}_\odot}\right). \tag{2.20}$$

We combine this result with Eq. 2.2 and Eq. 2.3 to obtain the following relation:

$$m_\lambda - M_\lambda = 5\log_{10}\mathrm{d} - 5 = 5\log\left(\frac{\mathrm{d}}{10\,\text{pc}}\right). \tag{2.21}$$

The method called distance modulus is based on the difference between m_λ and M_λ of the star of interest, with the distance d being given in parsecs. A diagram of this distance measurement can be seen in Figure 2.2, as well as a representation of the definition of luminosity and flux.

¶ For small angles, it is common to approximate tan p to p, which is given in arcseconds.

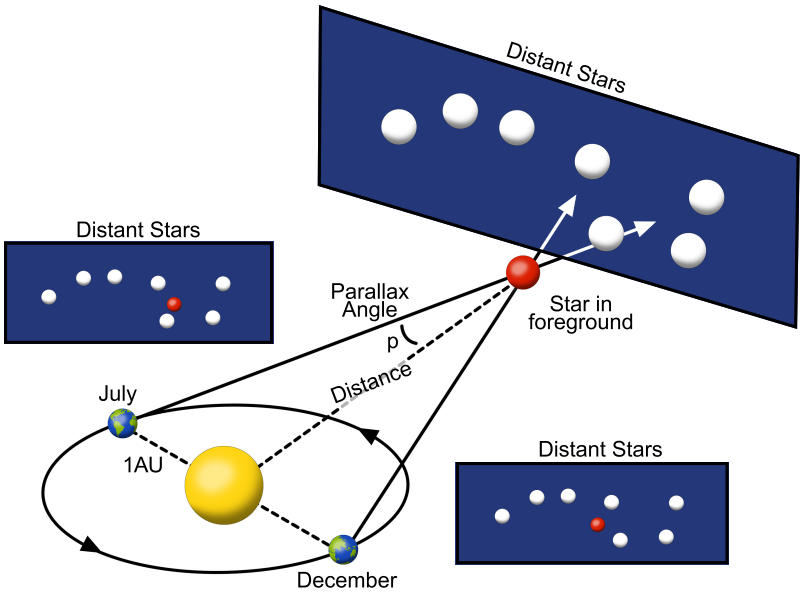

Figure 2.1: Cartoon of the phenomenon of astronomical parallax. In this figure, d is the distance between the object (O) and the observer, p is the parallax angle and 2r the distance from the earth between the two measurements of the object.

However, the light coming from the stars encounters grains of dust and gas in the interstellar medium (van de Hulst, 1946) on its way to the observer, which cause absorption and scattering of the light, and its quantity is subtracted from the radiation emitted by the star, thus causing the so-called extinction. In this phenomenon, part of the wavelength in the blue range emitted is extinguished by these grains, causing reddening. Cardelli et al. (1989); Damineli et al. (2016) explains that the ratio between the wavelength of the emitted light (λ) and the grain size (d_g) directly influences the extinction, so that all photons are scattered or absorbed for $\lambda << d_g$, and for $\lambda > d_g$, a fraction of photons escapes the scattering.

Thus, Eq. 2.21 must undergo a small adjustment, taking the following form,

$$m_\lambda = M_\lambda + 5.\log\frac{\mathrm{d}}{10\,\mathrm{pc}} + A_v\,, \tag{2.22}$$

where A_v is the extinction amount, in magnitudes. To determine it, we need to find the reddening value, which is related to the difference between the apparent color and the true color of the star. Usually expressed in terms of the color index $(B-V)$, also in magnitude, as

$$E(B-V) = (B-V) - (B-V)_0\,, \tag{2.23}$$

where $(B-V)_0$ is the intrinsic color of the object, determined theoretically. And so, we can define the amount of extinction using the following equation

$$A_v = R_v \times E(B-V)\,, \tag{2.24}$$

where R_v is the ratio between total and selective extinction, with its value varying between 3

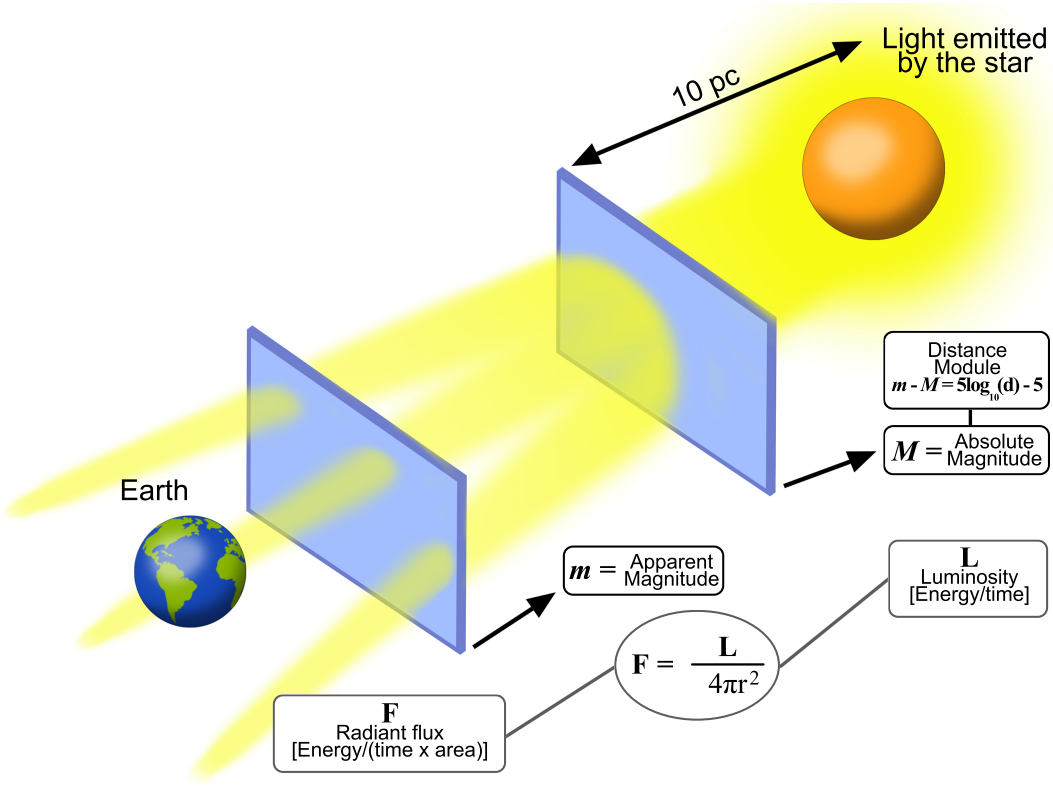

Figure 2.2: Cartoon of the phenomenon of astronomical parallax. In this figure, d is the distance between the object (O) and the observer, p is the parallax angle and 2r the distance from the earth between the two measurements of the object.

and 5.

Reddening prevents observations in the optical band ($UBVRI$ bands) from showing the full extent of the SP of a given star cluster. The use of the near infrared (JHK bands) mitigates this effect, as it is less sensitive to interstellar reddening, but at the cost of a small variation in magnitudes between photometric bands, for the spectral distribution of energy of hot stars.

2.1.1. Stellar Structure and Evolution

Once the stellar parameters are known, it is possible to study the phases of stellar evolution by analyzing the relationship between the temperature and luminosity of stars with different characteristics. This study is done with the aid of the HR diagram (Hertzsprung-Russell diagram), which was independently developed by the engineer and amateur astronomer, Ejnar Hertzsprung (Hertzsprung, 1908), and by the astronomer, Henry Norris Russell (Russell, 1914), the HR diagram is the main astronomical tool for studying stellar evolution. Fig. 2.3 presents a standard HR diagram with the average position of stars relative to their type and spectral classification.

The relationship between effective temperature and luminosity, as well as the nomenclatures presented in the HR diagram, can be observed naturally, when analyzing and reorganizing the stellar luminosity relationship, Eq. 2.1, we have an equation that allows us to analyze the

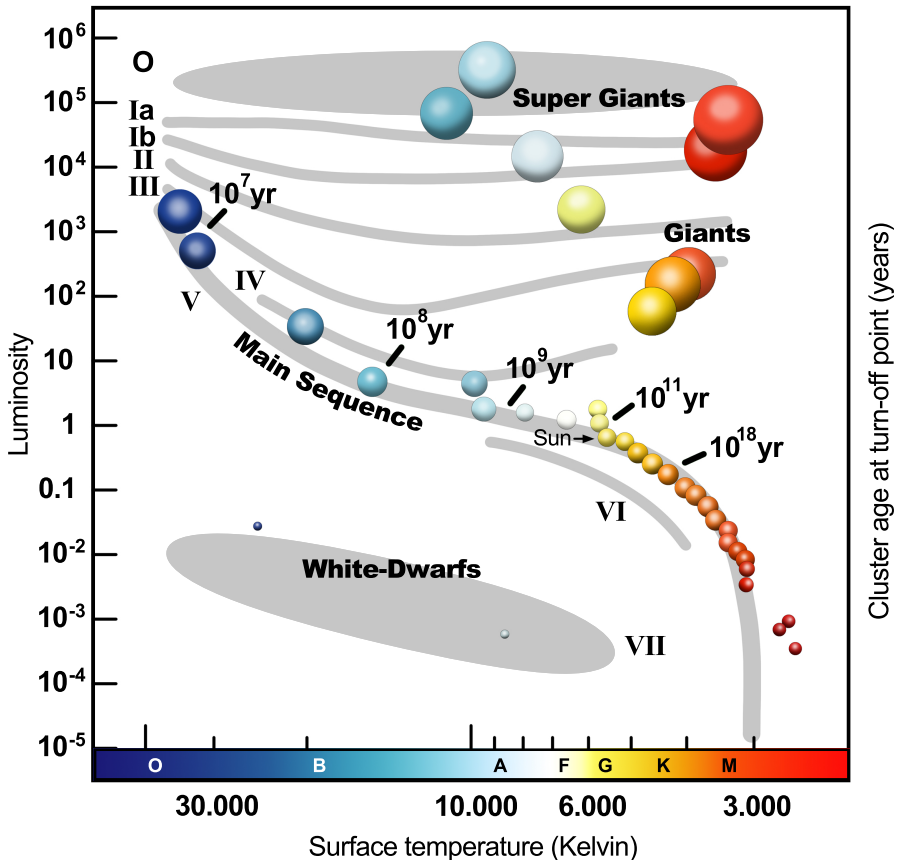

Figure 2.3: Hertzsprung-Russell Diagram for observational data from the Hipparcos catalogue. Cluster age depending on the location of the *Turn off* point in the HR diagram.

variation of the stellar radius, described as follows:

$$R = \frac{1}{T_{eff}^2}\sqrt{\frac{L}{4\pi k_B}}\,. \tag{2.25}$$

This equation tells us that the effective temperature and luminosity can only vary directly in relation to each other, that is, for a constant R, when the effective temperature undergoes a variation, the luminosity must have a variation of the same proportion for this equality to remain constant. We observe that approximately most of the stars are in a diagonal band sequenced in the HR diagram, the so-called Main Sequence (SP), which increases in temperature and luminosity from right to left, from the least massive M-type stars to the most massive O-type stars; this band is called the main sequence.

In addition, it is possible to use the HR diagram to estimate the age of a given group of stars. To do this, considering that a local group of stars were born at approximately the same time and have the same chemical characteristics, we consider the exit point of the SP, called *Turn off* (see Fig. 2.3), to estimate the age of this stellar group.

It is worth noting that the evolutionary state and age of a stellar group is also directly related to the distance measurement, since the luminosity is directly related to this parameter (see Eq. 2.2), a greater or lesser distance measurement implies a variation in the position of this ob-

ject on the y-axis of the HR diagram, causing uncertainty in the evolutionary pattern of the target star, due to the difference between the calculated mass and the initial mass of the evolutionary model traces, as well shown in Fig. 10 of the work by Aghakhanloo et al. (2020).

The structure and evolution of stars depend on their physical properties. Stars have a variety of parameters and physical-chemical characteristics of stars, which result in luminosity variability and unique spectra, with emission and absorption lines characteristic for each type of star. Classified by temperature/luminosity and mass, these characteristics help us understand how stars form and what happens in their phases of evolution.

The most widely accepted theory for the beginning of the universe was the great expansion, the Big Bang, from a singularity called the "primordial atom" (Munitz and Payne-Gaposchkin, 1957), and was proposed by the priest and cosmologist Georges Lemaître. The Cosmological Principle is based on the idea that the Universe is homogeneous and isotropic, expanding and cooling for approximately 14 billion years and forming all the objects we know, and those yet to be discovered.

In this event, which gave rise to what we know as time and space, the equivalent mass of the primordial universe was spread into subatomic particles, such as quarks, mesons and neutrinos, forming, approximately 10^{-7} seconds into the universe's lifetime, the lightest atoms ever known, such as hydrogen and helium. The first stars, called primordial stars, emerged 10^8 years after their birth. They were responsible for the first reionization of the interstellar medium, disseminating heavy elements such as oxygen and carbon.

In this context, Stellar Astrophysics has made a fundamental contribution to understanding the formation of the universe through the study of stellar evolution. Understanding star formation and the possible evolutionary paths of a star has proven to be of fundamental importance in tracing and searching for clues as to how the universe began and how it is evolving.

Star formation begins in large regions of dust and gas in the interstellar medium, known as nebulae, or "stellar nurseries", consisting basically of light elements such as hydrogen and helium. Initially, these elements clump together due to the gravitational interaction to which they are mutually subject, forming small regions of dense gas with higher temperatures, giving rise to protostar. At this stage, the core of this gas does not yet undergo nuclear fusion, with a constant accretion of matter through interstellar dust disks and an increase in the temperature of the gas. At this point, the force of gravity dominates the dynamics of the protostar, until the moment when the core of the gas reaches a temperature of approximately 8 million Kelvins, starting to generate thermonuclear reactions in its interior, transforming hydrogen into helium, and entering a period of hydrodynamic equilibrium, where the gravitational force and the internal pressure generated by the nuclear reactions are equivalent, beginning the initial phase of the star.

The first stage of a star's evolution lasts approximately 90% of its total existence, and is the period of dynamic equilibrium and stability of the star, appearing in the SP of the HR diagram (class V). During this period, the star is fusing hydrogen into helium through *proton-proton*

chain reactions, generating enough energy to remain stable and not collapse due to gravitational force. During this period, the physical description that governs the stellar structure is based on some differential equations, which are:

$$\frac{\partial \mathrm{P}(\mathrm{m},\mathrm{t})}{\partial \mathrm{m}} = -\frac{\mathrm{Gm}}{4\pi \mathrm{r}(\mathrm{m},\mathrm{t})^4} - \frac{1}{4\pi \mathrm{r}(\mathrm{m},\mathrm{t})^2}\frac{\partial^2 \mathrm{r}(\mathrm{m},\mathrm{t})}{\partial \mathrm{t}^2}\,, \tag{2.26}$$

$$\frac{\partial \mathrm{r}(\mathrm{m},\mathrm{t})}{\partial \mathrm{m}} = \frac{1}{4\pi \mathrm{r}(\mathrm{m},\mathrm{t})^2 \rho(\mathrm{m},\mathrm{t})}\,, \tag{2.27}$$

$$\frac{\partial \mathrm{L}(\mathrm{m},\mathrm{t})}{\partial \mathrm{m}} = \epsilon_n(\mathrm{m},\mathrm{t}) - \epsilon_\nu(\mathrm{m},\mathrm{t}) + \epsilon_{\mathrm{grav}}(\mathrm{m},\mathrm{t})\,, \tag{2.28}$$

$$\frac{\partial \mathrm{T}(\mathrm{m},\mathrm{t})}{\partial \mathrm{m}} = \frac{\mathrm{GmT}(\mathrm{m},\mathrm{t})}{4\pi \mathrm{r}(\mathrm{m},\mathrm{t})^4 \mathrm{P}(\mathrm{m},\mathrm{t})}\,, \tag{2.29}$$

$$\frac{\partial \mathrm{X}_i(\mathrm{m},\mathrm{t})}{\partial \mathrm{m}} = \frac{\mathrm{m}_i}{\rho(m)}\left[\sum_j \mathrm{r}_{ji}(\mathrm{m}) - \sum_j \mathrm{r}_{ik}(\mathrm{m})\right] \mathrm{com}\ i = 1, ..., I\,. \tag{2.30}$$

These equations deal with the variation of physical quantities present in the study of stellar physics, namely: pressure P(m), radius r(m), density ρ(m), luminosity L(m), temperature T(m) and mass fraction X_i(m) of ions of type i inside the star as a function of the independent mass coordinate m, where m=0 has the center of the star as the reference and m=M for the reference on the stellar surface at a given time t.

We can point out some important characteristics of these equations. We have in equation 2.26 the classical hydrostatic equilibrium relationship between pressure and gravity when we ignore the second term on the right-hand side of the equation, so that if at any moment this equality is not true, the star's gas will be accelerated towards the stellar core or towards the external environment, and the stellar structure will be undone. The description of the distribution of mass inside the star is presented in Eq. 2.27, the so-called mass continuity equation. Furthermore, while Eq. 2.28 represents the conservation of energy, the equation 2.29 indicates the transport of energy that occurs inside the star under conditions of hydrostatic equilibrium. Finally, the last differential equation (i.e., Eq. 2.30) contains the reaction rate variables r_{ji}(m) indicating the number of reactions per unit mass (and unit time) that generated ion i, while r_{ik}(m) gives the loss of ion i to k by various chemical reactions, which excluding mixing processes, deals with the net nuclear reaction within the star for an ion i with mass m_i (Kippenhahn et al., 1990).

The end of this SP phase begins when helium is transformed into heavier elements, which are the fusions called stellar nucleosynthesis, destabilizing the equations presented above. From this moment on, its next stages are influenced mainly by its initial mass, that is, the total mass acquired at the moment of the final transition from protostar to star. The only factor that can override the orders of the known evolutionary stages are the cases of stars in binary or multiple systems, since their evolutionary stages will depend on the effects caused by the presence of one or more companions, such as the tidal effect and the exchange of matter.

Stars between 0.08 $M_\odot$ and 0.80 $M_\odot$ are the longest-lived, and can spend trillions of years in the SP phase. In some cases, stars of this type with more mass lose their outermost layers, leaving only a dense helium core. Stars with masses between 0.80 $M_\odot$ and 8.00 $M_\odot$ are able to fuse heavier chemical elements in their interior. In this process, the star increases in size, becoming a red giant, entering the AGB stage (the asymptotic branch of the giants in the HR diagram). In the next stage, these stars lose their outer layers of matter, becoming a planetary nebula, with a dense core surrounded by a ring of ionized gas and dust. Finally, after a period of fading of this ring, what remains in its final stage is a dense core of degenerate matter composed of helium, carbon, nitrogen and oxygen, with a mass similar to that of the Sun and a radius approximately the same as that of the Earth, which we call a white dwarf.

Now entering the high-mass stars, the stars between approximately 8.00 $M_\odot$ and 20.00 $M_\odot$ have a similar evolution to the previous ones, however, after their growth and passage through the branch now called super giants, these have their matter collapsed in on themselves due to the gravitational force generating a large explosion called a Supernova. The result of a supernova is the reionization of the interstellar medium with chemical elements heavier than even iron, leaving a dense core called a Neutron star. Finally, after their expansion, stars with masses greater than ~20 $M_\odot$ explode as a supernova collapsing continuously (**cite oppenheimer**) in an astronomical event little known to date, leaving an extremely dense object, capable of gravitationally attracting even light, the so-called black holes - see the recent review by Rosen et al. (2020).

A detailed and illustrative summary of stellar evolution for objects of different initial masses can be seen in Figure 2.4.

2.2. Classical Be Stars

Classical Be stars (or simply Be stars) are variable, luminous, blue-white dwarf stars of spectral type B, with a surface temperature between 10,000 K and 30,000 K. The main characteristics of these stars are: rapid rotation, which can be comparable to the critical speed of stellar rotation, presence of a Keplerian circumstellar disk[‖] of "decretion", created due to the mass ejected non-radiatively by the rotation and/or because of non-radial pulsations (NRP), which consequently generate hydrogen emission profiles in the Balmer lines of their spectrum (Rivinius et al., 2013), such emission being represented by the index "e" which is added to the spectral classification of the star. Its first observation was made by Secchi (1866), an Italian Catholic priest and director of the Observatory of the Roman College, who, when evaluating the spectrum in the visible region of the star γ Cassiopeiae, noticed that the Hβ line was in emission, unlike other stars he had already observed.

... "Je ne pourrais différer davantage à vous signaler une particularité curieuse de l'étoile γ Cassiopée, unique jusqu'à présent. Celle-ci est que pendant que la grande

[‖] Equatorial.

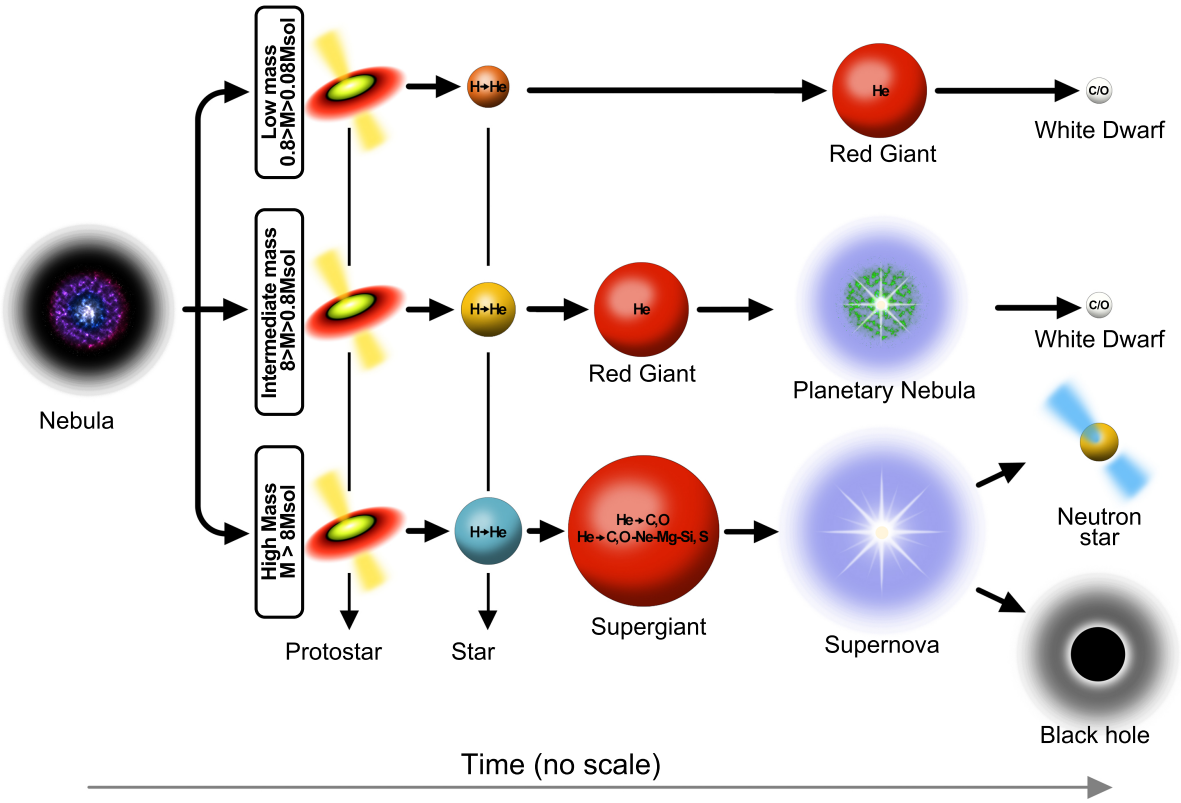

Figure 2.4: Illustration of stellar evolution for objects of different initial masses.

> *majorité des étoiles blanches montre la raie f très-nette et large, et comme α Lyre, Sirius etc., γ Cassiopée a à sa place une ligne lumineuse très-belle et bien plus brilhante que tout le reste du spectre." ...*
>
> Translation:
> *... "I could not delay any longer in pointing out to you a curious peculiarity of the star γ Cassiopeia, unique to date. This is that while the great majority of white stars present a very clear and broad f line, and like α Lyra, Sirius, etc., γ Cassiopeia has in its place a very beautiful luminous line, much brighter than any other in the spectrum." ...*

Since then, emission lines in the visible spectrum have become a new element in the analysis of stellar spectra, highlighting them given the new possibility of study, characterization and understanding of what causes such emissions. A great example is the Mount Wilson Observatory catalog of stars with emission lines, published in four parts by Merrill and Burwell (1933, 1943, 1949, 1950).

From this discovery, the need arose to define this type of star that presented emission lines based on its own nature, from other stars or astronomical objects that also presented such a phenomenon, but due to factors external to the object. Struve (1931) carried out an extensive analysis of emission lines in the spectra of a set of stars, verifying that this phenomenon is observed in all spectral types, presenting mainly emission in the Balmer lines of Hydrogen. In particular, for B-type stars, these emissions are divided into two groups: a) a single centralized emission line that is opposite to what would be the absorption line, or b) two symmetrically spaced emission lines within what would be the central wavelength of the line. Furthermore,

the variability in the intensity of these emission lines indicates that the emitting body is not stable, possibly having changes in its shape.

At the 1922 general assembly of the International Astronomical Union (IAU) in Rome, the term *Be star* was introduced to the community, which, despite this knowledge about emission lines, classified numerous astronomical objects, such as supergiant stars and young planetary nebulae, as Be stars (Slettebak, 2012). Merrill (1929) was an enthusiast in the study of these stars. In addition to the extensive classification and study of emission lines, the scientist pointed out that a possible nature of Be stars would be due to pulsations in their atmosphere:

> ... *"The immediate outcome of this investigation is an example of what a stellar atmosphere can do, [...] Or there may be a special, temporary type of pulsation with pronounced effects in an unusually extensive chromosphere."*

Jaschek et al. (1981) suggested a first definition of what a Be star is, which was later refined by Collins (1987) as: *"Non-supergiant stars of spectral type B, whose spectrum has or had at some point in its life, one or more Balmer lines in emission"*. However, this definition did not prove to be adequate because objects with similar characteristics continued to be classified as Be stars, namely: *Herbig Ae/Be* stars[**], symbiotic stars with the B[e] phenomenon[††], and stars in interacting binary systems, where one of the components is a star of spectral type B.

More recently, a definition was proposed based on the characteristic phenomena of this group of stars, which included late spectral type O stars (Negueruela et al., 2004) and early spectral type A stars (Tutukov and Fedorova, 2007). Martayan et al. (2010b) then proposed the following definition:

> *"This is a star with innate or acquired very fast rotation, which combined to other mechanism such as non-radial pulsations beating leads to episodic matter ejections creating a decretion disk or envelope."*

However, despite being a more restrictive definition, this is still not ideal because its applicability depends on more concrete and reliable studies about the physical properties of these stars. A schematic diagram of the Be star model can be seen in figure 2.5.

Be stars represent about ~15% of the total number of B-type stars in the Milky Way (Rivinius et al., 2013), reaching 34% if we consider only B1 and B2-type stars (Zorec and Briot, 1997; Porter and Rivinius, 2003b). Furthermore, it is worth noting that Be stars are transient, that is, this is a phenomenon that causes a B-type star to become Be when it ejects material equatorially, producing the emission observed in the spectrum in the hydrogen lines, so that this B-Be cycle is transient and presents some variations in luminosity, as reported and follows a sequence shown by De Wit et al. (2006).

Only in the last few decades has its study become an important field of research, due to its peculiarity within the B star branch, and its relevance within the study of the characterization

** Newly formed stars that are in the pre-main sequence, and have a primordial disk formed by both gas and dust.

†† They present a circumstellar accretion disk formed by gas and dust and forbidden lines in their spectrum.

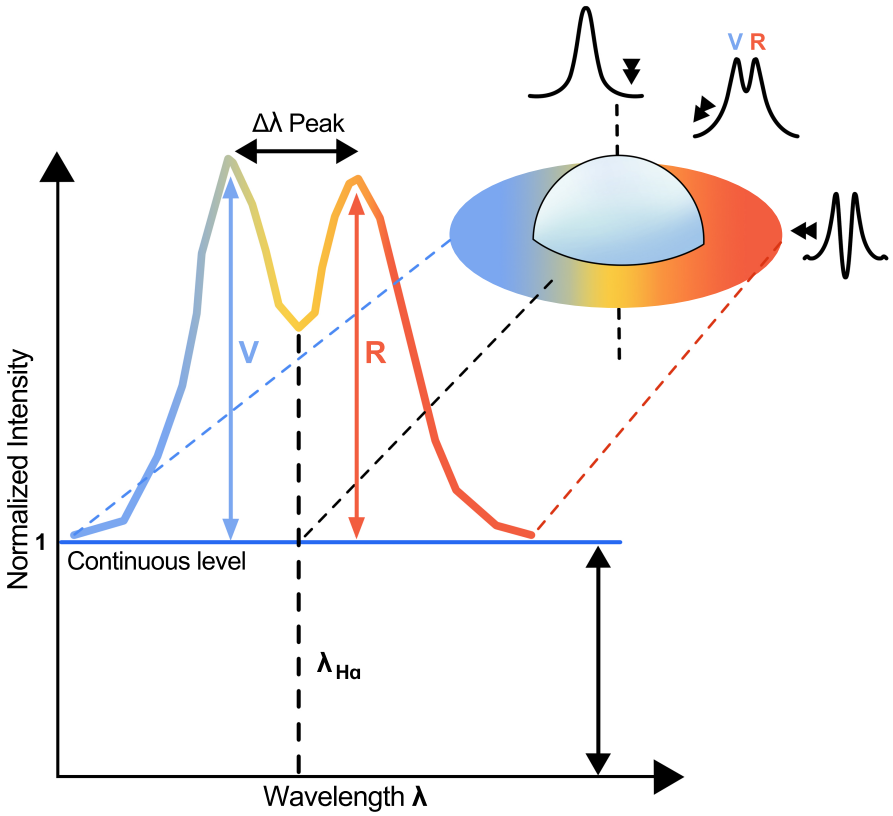

Figure 2.5: Schematic diagram of the a standard Be star.

and evolution of stars due to the effects of their rapid rotation on the evolutionary trajectories of more massive stars.

Zorec and Briot (1997) suggests three hypotheses for the emergence of this phenomenon: 1) Innate stellar characteristics of the star originating since its formation; 2) an effect of stellar evolution causing an acceleration in its rotation (Schild and Romanishin, 1976); or 3) due to the involvement of this star in a binary system. Thus, a reliable understanding of the Be phenomenon requires the precise and reliable determination of the physical parameters of these stars, such as initial mass, evolutionary stage, rotation and metallicity (Martayan et al., 2010a). Questions about the physics and chemistry of Be stars remain unanswered to this day, and since this is a group of stars that are predominantly in the main sequence, these answers may fill gaps that exist today in general studies of the structure and evolution of stars. Some examples of these questions are: Do they actually acquire rapid rotation? How? Why do they have characteristics of pulsating stars and how do they do it? How does rapid rotation influence internal processes, such as angular momentum transport and chemical mixing? How are matter and angular momentum ejected in sufficiently large quantities? How does this ejected matter organize itself around the star in a geometrically thin and Keplerian disk? Why do some stars undergo fission while others eject matter equatorially?

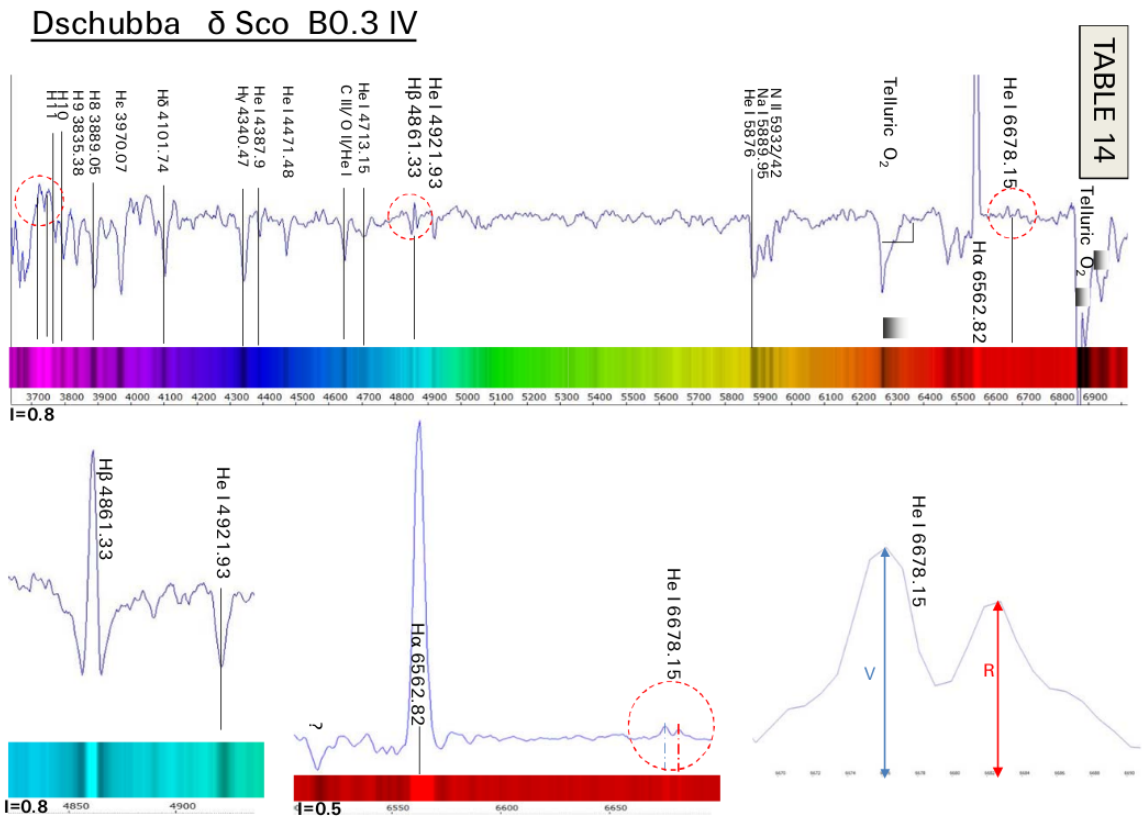

Figure 2.6: Be star Dschubba (δ sco): Spectral overview (200L grid) and higher resolution profiles (900L grid) around the Hα and Hβ lines, plus a zoomed-in detail of the neutral helium double peak at λ6678. Source: Harrison (2011)

2.2.1. Spectroscopic characteristics

Because it is a type of star with a predominance of the B spectral type, the spectra of Be stars are characterized by absorption lines of Neutral Helium throughout the spectrum, with the presence of weakly ionized Helium visible only in the hot B0 subclass, and spectral lines of individually ionized metals of OII, SiII and MgII. In addition, the spectra of B-type stars present weak Fraunhofer K lines of Ca II, unlike the lines of the Balmer series of Hydrogen, which are significantly stronger.

Specifically dealing with Be stars, as already mentioned, the suffix *e* is added due to the Hydrogen emission lines found in these stars, characteristic of the presence of a Keplerian circumstellar gas disk. For double-peaked emissions (see Fig. 2.5 and 2.6), the intensities of V and R[‡‡], as well as the distance between the two peaks, provide information about the apparent "current" state of the disk (Harrison, 2011). When V/R = 1 we have symmetric profiles indicating axis-symmetric disks, while such an inequality would indicate a non-symmetric disk configuration and/or radial motions. An example with observational data for a Be star can be seen in Figure 2.7.

The Be phenomenon is also accompanied by strong lines in X-ray and infrared. In infrared, the free-free emission of the ionized gas of the disk generates the observed excess, where in the

‡‡ Where V is the blue-shifted peak and R is the red-shifted peak.

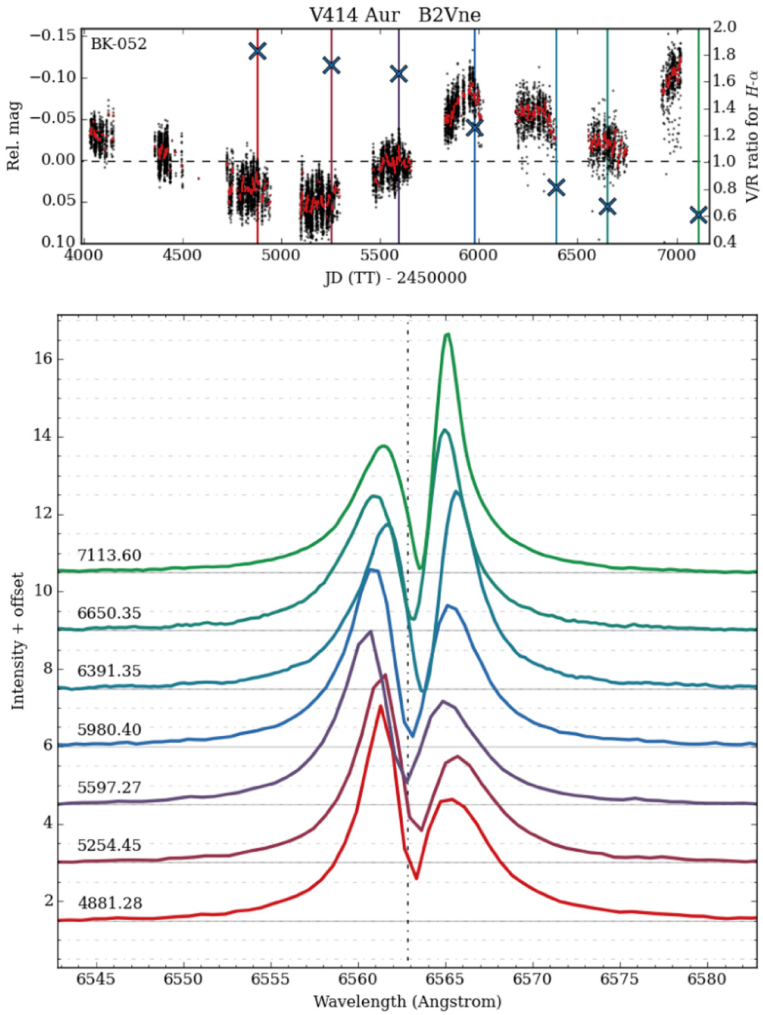

Figure 2.7: Top: Raw KELT light curve for BK-052 (HD 33232 = V414 Aur; B2Vne). The seven colored vertical lines correspond to the dates of the spectroscopic observations, and the blue Xs show how the V/R ratio at the Hα emission peaks is changing over time, as determined from existing BeSS spectra for this target. Bottom: The Hα line profiles collected from the BeSS, increasing in time from bottom to top, show a gradual change in the V/R ratio over the ~6 years of spectroscopic observation. Retrieved from (Labadie-Bartz et al., 2017).

SED (from the English *"Spectral Energy Distribution"*) we will have a contribution from the stellar continuum and a continuum from the disk. In X-ray, the Be star is usually found brighter than a single B-type star, possibly as a result of the ejection of matter. For Be stars in binary or multiple systems, the X-ray radiation is even more intense due to tidal interaction and/or a possible exchange of matter, which can occur mainly during the orbital periastron moment, when the companion star can cross the disk of the Be star causing great disturbance.

2.2.2. Stellar Rotation

The Sun was the first scientific laboratory for several stellar phenomena, including rotation, which had its first idealizations with the advent of telescopes that allowed astronomers such as Galileo Galilei, Johannes Fabricius, Thomas Harriot and Christopher Scheiner to study dark spots observed on the Sun. Between the years 1853-1861, Richard Carrington and Gustav

Spörer were able to determine that the Sun's rotation period varies with latitude, resulting in the equation developed by the French astronomer Hervé Faye (1814-1902),

$$\Omega(^\circ/dia) = 14^\circ 37 - 3^\circ 10 \sin^2 \delta \,. \tag{2.31}$$

Using formal mathematics, the study of stellar rotation starts from the total potential equation,

$$\phi = \phi_g + \frac{1}{2}\omega^2 a^2 \tag{2.32}$$

where a is the distance from the center of the star to the edge from the z axis, that is, at the pole $a = 0$ while at the equator $a = r$. Thus, the local gravity will be given by:

$$\vec{g} = -\nabla\phi = -\frac{GM}{r}\,\hat{r} + \omega^2 a\,\hat{a}\,. \tag{2.33}$$

When gravity is zero, we will then have a maximum rotation speed where the star's structure breaks, given by

$$\omega_c = \left(\frac{GM}{r_e^3}\right)^{1/2} ou\, v_c = \left(\frac{GM}{r_e}\right)^{1/2}, \tag{2.34}$$

where r_e is the equatorial radius. If the stellar rotation approaches this value, the star projects outwards towards the equator until it becomes an oblate spheroid.

Rotation plays an important role in the structure of stars, specifically by inducing mixing through rotation within their interiors, altering their properties and chemical abundance, in addition to generating/modifying the stellar magnetic field (Maeder and Meynet, 2000). Along with the different metallicity regimes, rotation represents a major source of uncertainty in theoretical models of stellar evolution, especially when estimating the masses and ages of high-mass stars (e.g. Aerts (2021); Serenelli et al. (2021)).

There are two methods for measuring rotation speed. The most widely used method is the indirect measurement of rotation speed from the broadening of spectral lines. The faster the star rotates, the wider some specific lines in the spectrum become, allowing us to measure the projected rotation speed of the star, that is, the rotation measured by the observer in relation to the tilt of the star's real rotation axis, as shown in the diagram shown in Fig. 2.8. The measurement made through this broadening is $v_e \sin i$, making it necessary to measure the tilt of the rotation axis to reach the desired final result.

With its phenomenon observed in all evolutionary phases of stars, the effects of stellar rotation play a role that can no longer be ignored in studies of Stellar Astrophysics. Scientific works indicate that in the case of main sequence stars, cooler stars (F0-M9) have low (Herbig and Spalding Jr, 1955) rotation, increasing as the spectral type increases, having a peak of projected rotation speed for hot B-type stars (see Figure 2.9).

The other method is more precise but more difficult to determine. It involves measuring the radius and period of stellar rotation and, using the classical equation of uniform circular motion,

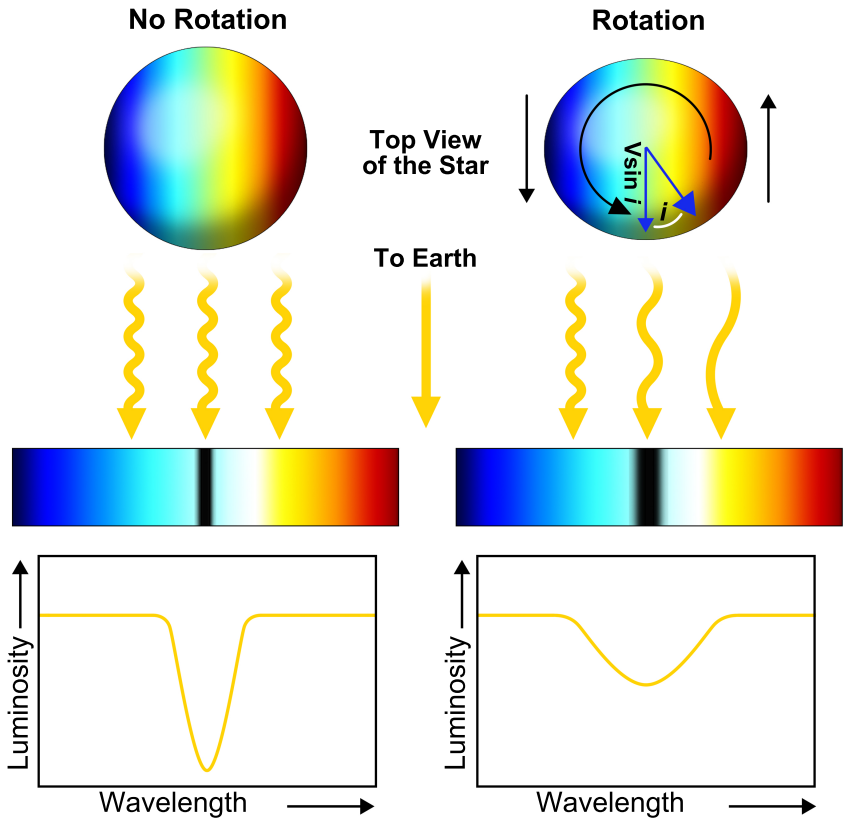

Figure 2.8: Stellar Rotation Scheme.

arriving at the measurement of the stellar rotation speed. The rotation period can be measured from photometric modulation, which is possible due to starspots characteristic of cool stars and non-radial pulsations in the g mode characteristic of hotter stars.

In this scenario, we highlight the Be stars that have a rotation speed much higher than the average of B-type stars, or of any other spectral type. Struve (1931) suggests that this is a prerequisite for the presence of emission lines observed in their spectra, but it is still unknown what happens to the structure of these stars due to their high angular momentum, making them dangerous and unstable. One of the possible results of this structural instability would be the flattening of the star and the ejection of gas at the stellar equator, making the star *"similar in appearance to the planet Saturn"*. The author also adds that inclinations of the gas ring close to 90° result in two bright lines in the spectrum superimposed on what would be the normal hydrogen absorption line. If we have a perfect inclination of $i = 0°$, we observe a single emission line. The Keplerian disk also becomes a reason for the particular study of these stars, and can answer important questions about the physical-chemical structure of Be stars.

For Be stars, it is estimated that their rotation speed is 1.5 or 2 times greater than that of simple B-type stars, with their rotation rate ($\Omega = \omega/\omega_c$) of the order of 0.80±0.10 (Zorec and Briot, 1997; Zorec, 2004). Furthermore, Townsend et al. (2004) suggests that the possibility that Be stars rotate close to their critical velocities should be left open, since the measurement of $v_e \sin i$ is systematically underestimated, given that the physical mechanisms that structure

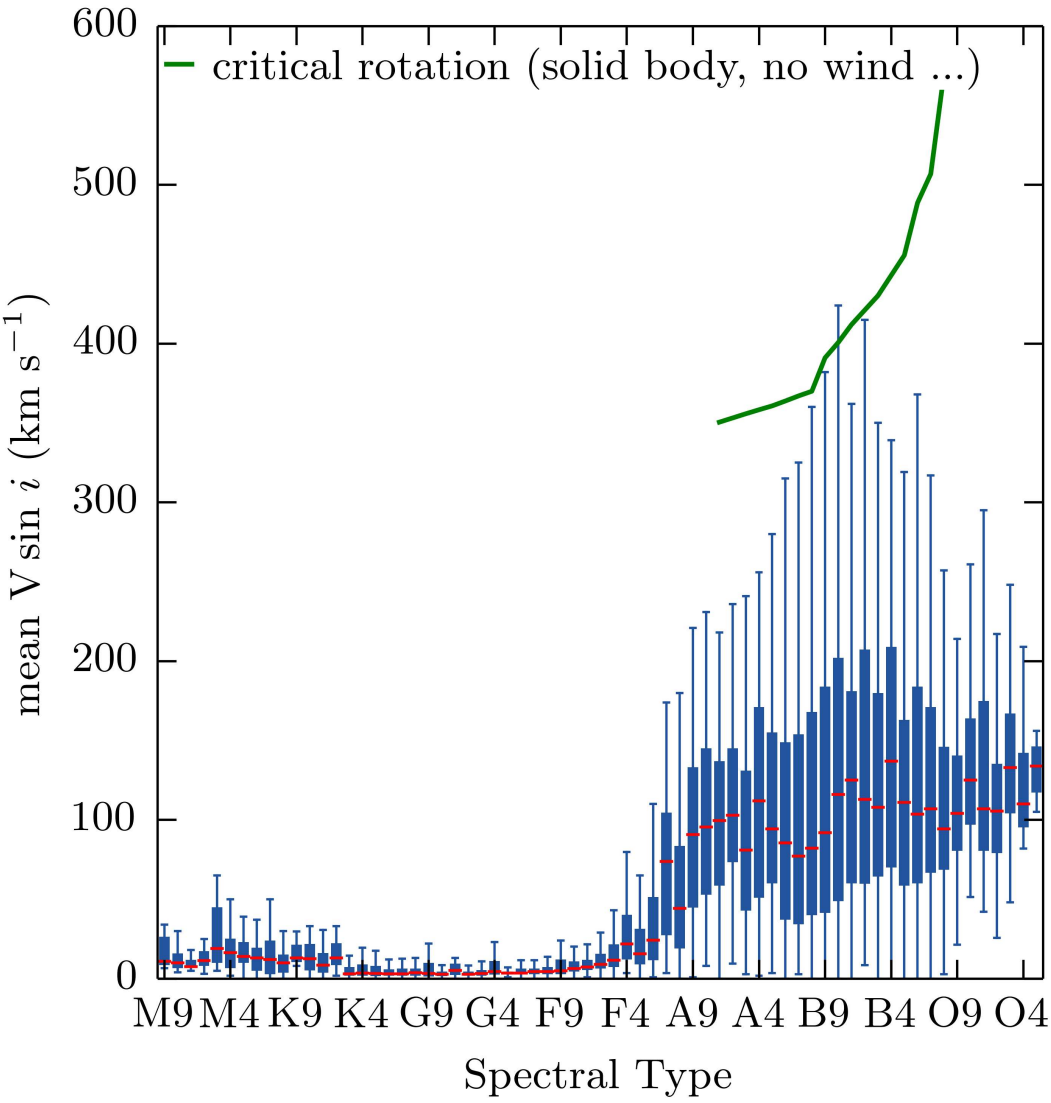

Figure 2.9: Distribution of projected rotation velocity values as a function of spectral type. Two distinct populations of stars can be observed: one towards the hotter region (stars between spectral types O-A), for which high rotation is effectively observed; on the other hand, towards the colder region (stars between spectral types F-M) essentially stars with low rotation are observed. The rotation values were extracted from the work of Glebocki and Gnacinski (2005), and include 39,351 stars from 166 open and globular clusters (Modify - taken from https://aa.oma.be/stellar_rotation).

Be stars are still unknown, such as gravity darkening at the equator and the formation of the circumstellar equatorial disk, so that such a rotation rate can reach 0.95, a result later corroborated by Cranmer (2005).

2.3. Stellar Seismology

Stars are not completely stable and immobile. In addition to rotation, it is possible to observe regions of expansion and contraction in the stellar photosphere, generating waves that travel through the interior of the star, resonating and generating vibration modes specific to each star, like a fingerprint. Stellar Seismology seeks to understand the internal structure and dynamics of stars from these oscillations that exhibit nodes and anti-nodes and are described by spherical harmonics observed on their surface.

The physics behind such pulsations requires that there be a force that acts to restore the disturbed stellar equilibrium. In stars, we then have two main modes of oscillation: i) pressure wave oscillation (acoustic) and ii) gravity wave oscillations (internal for B-Type star), classified respectively as p modes and g modes of vibration, due to the nature of their restoring forces, pressure and gravity. The oscillation modes also assume individual configurations on the stellar surface in the latitude and longitude directions, defined by three numbers: radial order, harmonic degree (number of surface nodes), and azimuthal order, represented respectively by the letters n, l and m[§§]. Figure 2.10 shows a schematic view of the pressure and gravity waves propagating in the stellar interior.

The simplest possible geometry of stellar oscillations is related to radial symmetry (l=0), which is successful in many cases. However, radial oscillations are only some of the many possible oscillations of a star, with other modes being called Non-Radial Oscillation (or Non-Radial Pulsation). In particular, non-radial modes occur when n≥1, being called dipole mode when l=1, quadrupole mode for l=2 and octopole mode for l=3. Figure 2.11 shows some configurations of pulsation modes.

Small amplitude oscillations of a spherical object, such as a star, can be described in terms of the sphere's radius r, co-latitude θ, and longitude ϕ. The displacement equations of motion for a sphere symmetric in the directions r, θ, and ϕ are given by

$$\xi_r(r,\theta,\phi,t) = a(r)Y_l^m(\theta,\phi)e^{-i2\pi\nu t} \tag{2.35}$$

$$\xi_\theta(r,\theta,\phi,t) = b(r)\frac{\partial Y_l^m(\theta,\phi)}{\partial\theta}e^{-i2\pi\nu t} \tag{2.36}$$

$$\xi_\phi(r,\theta,\phi,t) = \frac{b(r)}{sen\,\theta}\frac{\partial Y_l^m(\theta,\phi)}{\partial\theta}e^{-i2\pi\nu t} \tag{2.37}$$

[§§] The degree of each order can vary as follows: n = 0, 1, 2, ...; l = 0, 1, 2, ...; and m = -l, ..., l.

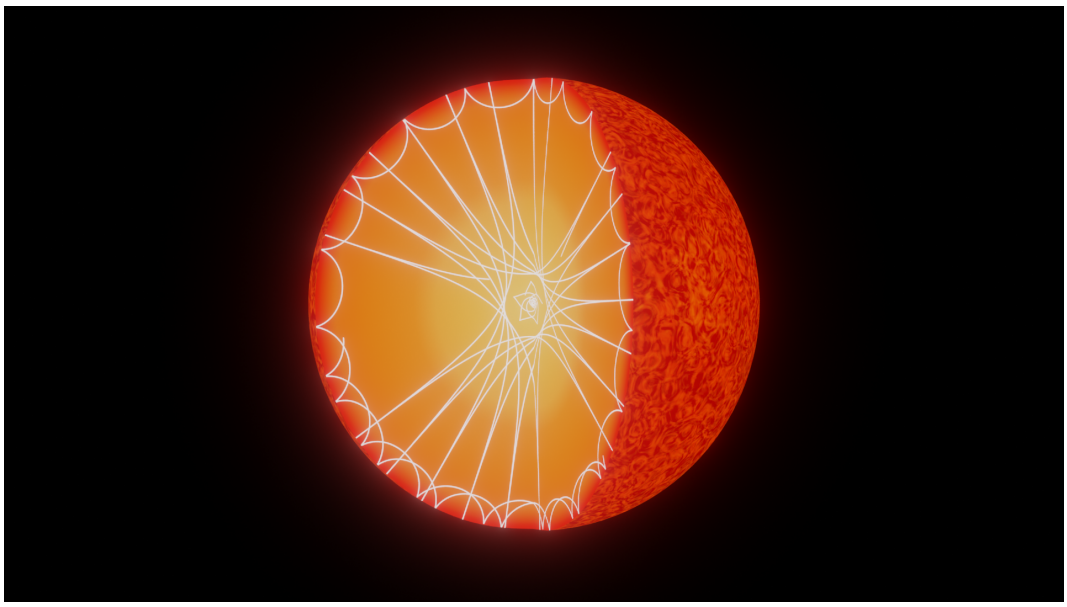

Figure 2.10: Artist's impression of waves of different frequencies propagating through the inner layers of a red giant star. Sound (or pressure) waves spend most of their time in the outermost layer of the star and are detectable at the surface. Gravity waves pass through the radiative zone and contain information about the core. In red giants, these two types of waves are coupled and the resulting waves transmit information from all layers, revealing valuable information about the innermost layers.

with $Y_l^m(\theta, \phi)$ being the spherical harmonics given by

$$Y_l^m(\theta, \phi) = (-1)^m \sqrt{\frac{(2l+1)(l-m)!}{4\pi(l+m)!}} P_l^m(cos\,\theta) e^{im\phi}, \tag{2.38}$$

where P_l^m is a Legendre polynomial.

But why do stars pulsate? From the conservation of energy we know that with each pulsation cycle the star should lose energy, but we observe that the pulsation cycles repeat themselves, suggesting that there is an internal force that feeds such pulsation and its damping for the entire stellar mass. The main idea is that when a layer contracts it gains heat, generating the pulsation damped by the layers that lost heat. Such layers will then function as a heat engine, transforming thermal energy into mechanical energy, a driving phenomenon known as the heat engine mechanism. In some types of stars that pulsate, such as Cepheids, opacity is the cause of the triggering of these oscillations, which occur mostly in the fundamental radial mode and is known as the k mechanism. Finally, it is important to emphasize that given the nature of their atmosphere, we have a greater ease in identifying a particular pulsation mode. For stars with predominantly radioactive outer layers, we can more easily find the frequencies of p-mode waves, while for stars with predominantly radioactive energy transfer in their outer layers, we find the frequencies of g-mode oscillations. An exception to this is the Sun, because due to its proximity to the Earth, we are able to study it very precisely, determining all the frequencies and modes of oscillation (see Fig. 2.12).

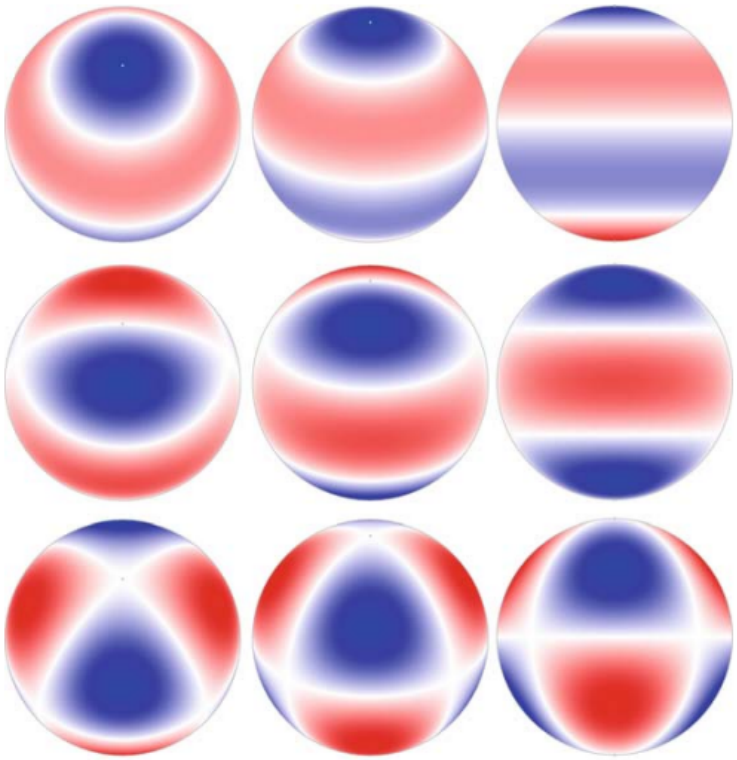

Figure 2.11: Snapshot of the radial component of the l = 3 octupole modes. The columns show the modes from different viewing angles; the left column is for a pulsation pole tilt of 30°, the middle column is for 60°, and the right column is for 90°. The white bands represent the positions of the surface nodes; red and blue represent sections of the star that are moving inward (outward) and/or heating (cooling) at a given time, and vice versa. The top row shows the axisymmetric octupole mode (l = 3, m = 0) where the nodes lie at latitudes ±51° and 0°. The second row shows the tesseral (meaning $0 < |m| < l$) l = 3, m = ±1 mode with two nodes that are lines of latitude and one that is a line of longitude. The third row is the tesseral mode l = 3, m = ±2, and the bottom row shows the sectoral mode (i.e., l = |m|) with l = 3, m = ±3. Importantly, rotation distinguishes the sign of m, as discussed in Section 1.4.3 (Aerts et al., 2010).

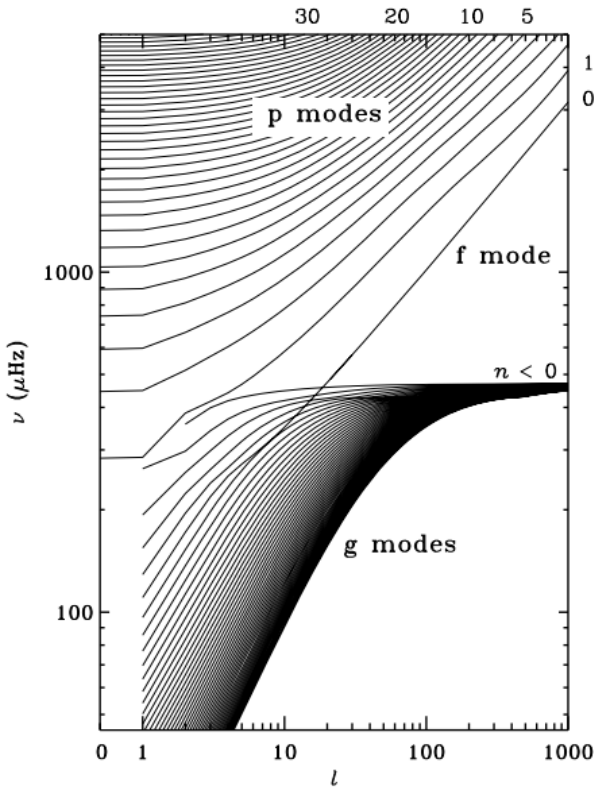

Figure 2.12: The frequency of modes versus their degree l for a solar model. For g modes, the frequency decreases with higher harmonics, but increases with n if we use the convention that n is negative for g modes. The frequency still increases with degree l for g modes, just as it does for p modes. Note that although solid lines are shown for clarity, the individual modes are discrete points, corresponding to the integer l, which are not shown here (Aerts et al., 2010).

2.3.1. The Pulsation Mechanism

Non-radial pulsations occur when different regions of the stellar surface oscillate in an uncoordinated manner, with some parts expanding while others contract. As already mentioned, these pulsations can be of two main types, and behave as follows for B-type stars:

- g (gravity-dominant) mode: Governed by gravity restoring forces, occurs in deeper regions of the star and has longer periods.
- p (pressure-dominant) mode: Controlled by gas pressure and predominant in the outer layers, with shorter periods.

In Be stars, these pulsations transport angular momentum to the upper layers of the stellar atmosphere, facilitating the ejection of mass into the disk.

The theory proposed by Cranmer (2009) suggests that non-radial pulsations can become resonant waves in the star's atmosphere, amplifying until they become shocks. These shocks transfer energy and angular momentum to material in the photosphere, helping to propel matter away from the star.

Although the rapid rotation of Be stars is a key factor in the formation of decretional disks, stellar pulsations play a crucial role in mass ejection by providing the necessary angular momentum. The combination of non-radial pulsations and amplification of acoustic waves may explain why some Be stars are able to form disks even when rotating below the critical speed.

This is a field still under study, and future observations and hydrodynamic modeling may help to better understand the connection between pulsations and disk formation in Be stars.

2.3.2. The Rotation Effect

So far we have considered pulsations in stars with spherical symmetry. However, stars have their own rotation movement, which in extreme cases, such as Be stars and stars in binary systems, generate an asymmetry in their shape, resulting in a degeneracy in the characteristic pulsation frequencies.

Assuming a constant angular velocity (Ω), the coordinates of a point on the sphere that rotates at an instant t will be:

$$(r', \theta', \phi') = (r, \theta, \phi - \Omega t)\,. \tag{2.39}$$

Similarly, given an observed inertial frame the frequency varies uniformly according to the following relation:

$$\omega_m = \omega_0 + m\Omega\,. \tag{2.40}$$

This description would be more complete if we added the Coriolis force, but this force is considerably small, making the previous equation a good approximation of the real result.

Due to the oblateness of the star caused by rotation, the effective gravity at a point on the surface is given by:

$$g_{\text{eff}} = g - \Omega^2 R\, cos\theta\,, \tag{2.41}$$

where θ is the stellar latitude (0° at the equator and 90° at the poles), which leads to the result of Eq. 2.18.

Such pulsation (with episodes of eruptions) and rotation characteristics are characteristic of Be stars, the main object of study of this work, and therefore, photometric variability is of crucial importance in the study of these stars, as it plays the role of intermediary between the energy emitted by the star and what is observed here on Earth.

In this way, rotation profoundly affects the pulsation modes, altering their frequencies and the way the waves propagate inside the star. Due to centrifugal force, a rapidly rotating star becomes flattened at the poles and expanded at the equator (oblation effect). This flattening results in:

- Variation of surface gravity: Greater at the poles and lower at the equator.
- Higher temperature at the poles and lower at the equator (von Zeipel effect).
- Altered oscillation frequencies, as the internal structure of the star changes due to rotation.

Rotation leads to the splitting of the pulsation modes, an effect known as the Coriolis effect, which occurs when: i) The oscillations are affected by the differential rotation of the star. ii) The propagation of the waves inside the star is altered, changing the observed frequencies. iii) Degenerate pulsation modes split into multiple distinct frequencies, depending on the rotation rate.

The combination of fast rotation and pulsations in Be stars can explain several observational phenomena, such as:

- Periodic spectral variations, associated with g-modal pulsations affected by rotation.
- Interaction between pulsations and mass ejection, helping to form decretional disks.
- Transitions between Be and non-Be phases, depending on the intensity and distribution of pulsation modes.

3 Binary Systems

Most stars in the Galaxy are not born isolated, but rather as part of binary or multiple systems. Stellar multiplicity is now considered a natural product of the star formation process, influenced by gravitational instabilities, fragmentation of molecular clouds and interaction with the stellar environment (Tobin et al., 2016). Studying binary systems is therefore fundamental to understanding the formation, evolution and ultimate fate of stars.

The fraction of stars in multiple systems strongly depends on the stellar mass. In their extensive review, Duchêne and Kraus (2013) showed that the multiplicity increases monotonically with the mass of the primary star: while about 20–30% of M dwarfs have detectable binary companions, this fraction exceeds 70% for B-type stars and reaches over 80% for O stars. Furthermore, the distribution of orbital parameters, such as separation, mass ratio, and eccentricity, also varies with stellar mass, suggesting differences in the formation mechanisms and subsequent dynamical interactions.

The impact of binary companions on stellar evolution is especially pronounced among massive stars. The work of Sana et al. (2012), based on high-resolution spectroscopy of a large set of O stars in young clusters of the Milky Way, revealed that more than 70% of O stars interact with a binary companion during their evolution. This result was obtained through the VLT-FLAMES Tarantula Survey project and reinforces the idea that the evolution of massive stars cannot be properly understood without considering binary interactions. Such interactions include mass transfer, common envelope, stellar mergers and spin-up, which have direct implications for the formation of neutron stars, black holes and gravitational wave sources.

These systems also present high rates of close binarity, with periods shorter than 10 days in about 30% of cases (Sana et al., 2012). The high number of interacting binaries challenges standard stellar evolution models and requires approaches that include detailed binary scenarios for the prediction of transient events, such as core-collapse supernovae, kilonovae and mergers of compact objects.

Duchêne and Kraus (2013) also highlight the role of the density of the star formation environment in the evolution of multiplicity. In regions of dense star formation, dynamical interac-

tions can lead to the dissolution of large systems or to the formation of more stable hierarchical systems. This implies that the multiplicity observed in the field is, in part, a legacy of the dynamical history of stellar clusters and associations.

In addition, observational advances have allowed the characterization of multiple systems with increasing resolution. Techniques such as high-resolution spectroscopy, optical interferometry and radio interferometry (such as ALMA and VLTI), as well as precision astrometric data from the Gaia satellite, have revealed new populations of binaries and enabled the precise modeling of their orbital parameters and masses.

The study of binary systems goes beyond the characterization of individual stars: it is crucial to understand the chemical enrichment of the galaxy, the distribution of rotation velocities, the presence of circumstellar disks and the origin of exotic objects such as Be stars, X-ray binaries and pairs of coalescing black holes.

3.1. Orbital Motion

Given that we are dealing with two bodies that rotate around a center of mass, as proven by observations, the geometry of their movement must obey the Law of Universal Gravitation and Kepler's Laws, so that the bodies attract each other with forces that vary with the square of the distance between them, of the same magnitude but in opposite directions. Thus, to understand the geometry of these systems, we define an ellipse as the geometric locus of points on a plane whose distances to two fixed points (focus) of this plane have a constant sum, these points being separated by 2ae, where a is the semi-major axis and e the eccentricity (see Fig. 3.1).

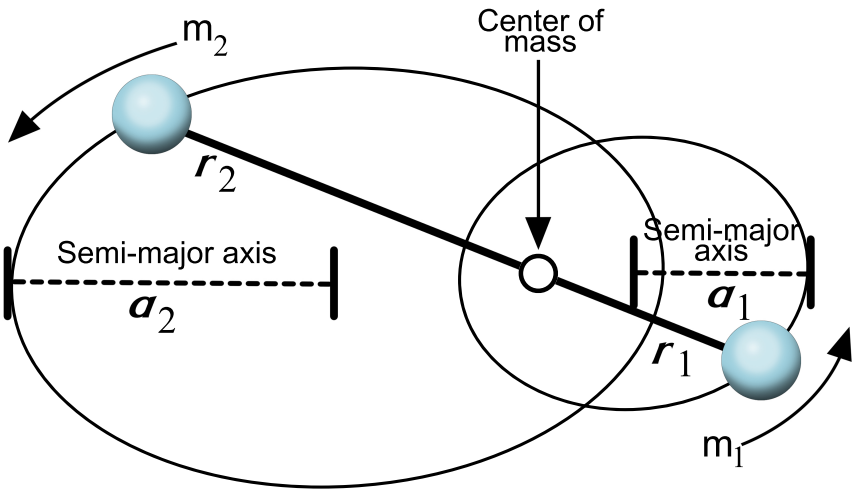

Figure 3.1: Geometric Orbit diagram of an Binary Stars.

By definition of ellipse, we can define the following relation for r and r_1:

$$r + r_1 \equiv 2a\,. \tag{3.1}$$

Now by the law of cosines, we have that:

$$r_1^2 = r^2 + (2ae)^2 + 2r(2ae)\cos\theta\,, \tag{3.2}$$

thus, applying Eq. 3.1 to Eq. 3.2, we can define r as the separation between a point on the orbit and one of the foci:

$$r = \frac{a(1-e^2)}{(1+e\cos\theta)}\,. \tag{3.3}$$

If $e = 0$, the ellipse is a circle, and if $0 < e < 1$, the ellipse is elongated.

3.1.1. Movement without Eccentricity

We analyze now the specific case of a binary system without eccentricity, where the orbits are circular. This type of system is fundamental for astrophysics, since it allows precise measurements of stellar masses and orbital properties.

In a binary system with stars of masses M_1 and M_2, their positions in an inertial reference frame are $\mathbf{r}_1$ and $\mathbf{r}_2$. The center of mass (CM) of the system is given by:

$$\mathbf{r}_{CM} = \frac{M_1\mathbf{r}_1 + M_2\mathbf{r}_2}{M_1 + M_2}. \tag{3.4}$$

In the CM reference, we have:

$$M_1\mathbf{r}_1 + M_2\mathbf{r}_2 = 0. \tag{3.5}$$

This leads to the relationship between the radii of the orbits:

$$\frac{r_1}{r_2} = \frac{M_2}{M_1}. \tag{3.6}$$

The total separation between the stars is $r = r_1 + r_2$, so that:

$$r_1 = \frac{M_2}{M_1 + M_2}r, \quad r_2 = \frac{M_1}{M_1 + M_2}r. \tag{3.7}$$

The gravitational force between stars is determined by the Law of Universal Gravitation:

$$F = \frac{GM_1M_2}{r^2}\,, \tag{3.8}$$

where G is the gravitational constant ($6.674\times10^{-11}\ m^3\,kg^{-1}\,s^{-2}$).

This force acts as the centripetal force needed to maintain the circular motion of the stars:

$$\mathrm{M_1}\frac{\mathrm{v_1^2}}{\mathrm{r_1}} = \frac{\mathrm{GM_1M_2}}{\mathrm{r^2}}, \quad \mathrm{M_2}\frac{\mathrm{v_2^2}}{\mathrm{r_2}} = \frac{\mathrm{GM_1M_2}}{\mathrm{r^2}}. \tag{3.9}$$

Using $v_1 = \Omega r_1$ and $v_2 = \Omega r_2$, we obtain the angular frequency of the system:

$$\Omega = \sqrt{\frac{G(\mathrm{M_1} + \mathrm{M_2})}{r^3}}. \tag{3.10}$$

The orbital velocities of stars are:

$$v_1 = \frac{\mathrm{M_2}}{\mathrm{M_1} + \mathrm{M_2}}\sqrt{\frac{G(\mathrm{M_1} + \mathrm{M_2})}{r}}, \quad v_2 = \frac{\mathrm{M_1}}{\mathrm{M_1} + \mathrm{M_2}}\sqrt{\frac{G(\mathrm{M_1} + \mathrm{M_2})}{r}}. \tag{3.11}$$

The relationship between the orbital period P and the radius of the orbit is determined by Kepler's Third Law:

$$\mathrm{P} = 2\pi\sqrt{\frac{r^3}{G(\mathrm{M_1} + \mathrm{M_2})}}. \tag{3.12}$$

The positions of stars over time can be expressed as:

$$x_1 = r_1\, cos(\Omega \mathrm{t}), \quad \mathrm{y_1} = \mathrm{r_1}\sin(\Omega \mathrm{t}), \tag{3.13}$$

$$x_2 = -r_2\, cos(\Omega \mathrm{t}), \quad \mathrm{y_2} = -\mathrm{r_2}\sin(\Omega \mathrm{t}). \tag{3.14}$$

In astronomical observations, the radial velocity of stars can be measured via the Doppler effect. The radial velocities of stars are given by:

$$v_{r,1} = K_1\, sin(\Omega \mathrm{t}), \quad \mathrm{v_{r,2}} = -\mathrm{K_2}\sin(\Omega \mathrm{t}), \tag{3.15}$$

where the amplitudes are:

$$K_1 = \frac{\mathrm{M_2}}{\mathrm{M_1} + \mathrm{M_2}}\frac{2\pi r}{\mathrm{P}}, \quad K_2 = \frac{\mathrm{M_1}}{\mathrm{M_1} + \mathrm{M_2}}\frac{2\pi r}{P}. \tag{3.16}$$

It's worth noting that in a binary system, orbital velocity is the actual velocity of a star as it moves around the system's center of mass. However, what we observe from Earth is radial velocity, which is the projection of orbital velocity along the line of sight, and will be discussed in more detail in the next section. Orbital velocity cannot be measured directly; only radial velocity can be measured through the Doppler shift of the spectral lines. It varies with time according to the orbital motion and depends on the inclination and orbital parameters of the system.

3.1.2. Orbital Motion with Eccentricity

We consider a binary system composed of two stars of masses m_1 and m_2 orbiting a common center of mass C. The relation between the distances of the stars and the center of mass is given by:

$$r_1 = \frac{m_2}{m_1 + m_2} \cdot r \tag{3.17}$$

and

$$r_2 = \frac{m_1}{m_1 + m_2} \cdot r \tag{3.18}$$

where r_1 and r_2 are the distances of the stars m_1 and m_2 from the center of mass C, and r is the total distance between the two stars.

The eccentricity (e) of an elliptical orbit describes the degree of "flattening" of the orbit. When $e = 0$, the orbit is circular. The general equation for the distance $r(\theta)$ between the two stars, where θ is the true anomaly*, is given by:

$$r(\theta) = \frac{a(1 - e^2)}{1 + e\, cos(\theta)}\,. \tag{3.19}$$

The true anomaly is related to the eccentric anomaly E by a trigonometric relation, and the eccentric anomaly E is related to time by Kepler's equation.

The *eccentric anomaly* E is an auxiliary variable used to describe the position of a star in an elliptical orbit. The relation between E and ν is given by:

$$tan\left(\frac{\nu}{2}\right) = \sqrt{\frac{1 + e}{1 - e}}\, tan\left(\frac{E}{2}\right)\,. \tag{3.20}$$

Kepler's equation relates the eccentric anomaly E to the mean anomaly M:

$$M = E - e\, sin(E)\,, \tag{3.21}$$

where M is the *mean anomaly*, which is proportional to time. Kepler's equation does not have a simple analytical solution, but it can be solved numerically using, for example, the Newton-Raphson method.

The orbital speed of stars m_1 and m_2 varies along the orbit. The formula for the speed of m_1 in terms of the distance $r(\nu)$ and the mass of m_2 is given by:

$$v_1 = \sqrt{\frac{Gm_2}{r(1 - e^2)}}\,. \tag{3.22}$$

* The true anomaly, denoted θ, is the angle between the direction of the periastron and the current position of an orbiting body, measured from the focus of the elliptical orbit. It describes the body's position along its orbit at a given time.

Similarly, the velocity v_2 of m_2 is given by:

$$v_2 = \sqrt{\frac{Gm_1}{r(1-e^2)}}\,. \tag{3.23}$$

These expressions indicate that the speed of the stars is not constant. The highest speed occurs at periastron, where the stars are closest, and the lowest speed occurs at apastron, when they are farthest apart.

The total energy E of a binary system with eccentricity is the sum of the kinetic energy and the gravitational potential energy. The potential energy (U) is given by:

$$U = -\frac{Gm_1m_2}{r}\,, \tag{3.24}$$

where r is the distance between the two stars. The *kinetic energy* K of the system is given by:

$$K = \frac{1}{2}m_1v_1^2 + \frac{1}{2}m_2v_2^2\,. \tag{3.25}$$

Therefore, the total energy of the binary system is the sum of these two energies:

$$E = K + U = -\frac{Gm_1m_2}{2a(1-e^2)}\,. \tag{3.26}$$

The total energy is negative, indicating that the stars are gravitationally bound.

The equations of motion for each star can be derived from *Newton's second law*. For star m_1, the acceleration $\vec{a}_1$ is given by:

$$\vec{a}_1 = -\frac{Gm_2}{r^2}\hat{r}\,, \tag{3.27}$$

where $\vec{a}_1$ is the acceleration of m_1 and $\hat{r}$ is the unit vector in the direction of r. Similarly, the acceleration of m_2 is:

$$\vec{a}_2 = -\frac{Gm_1}{r^2}\hat{r}\,. \tag{3.28}$$

These equations describe the gravitational interaction between the stars. The acceleration is always directed toward the center of mass of the system, and the magnitude of the acceleration depends on the distance r.

Eccentricity has important effects on the orbital evolution of the binary system. If the eccentricity is not zero, the orbits of both bodies are not circular, but elliptical. This implies that the distance between the two stars varies along the orbit, which causes a variation in the velocity of each star. In binary systems with high eccentricity, orbital precession effects may occur. Precession occurs when the periastron point (the point of closest approach between the stars) moves along the orbit over time. This phenomenon can be caused by gravitational interactions with other bodies or by the emission of gravitational radiation.

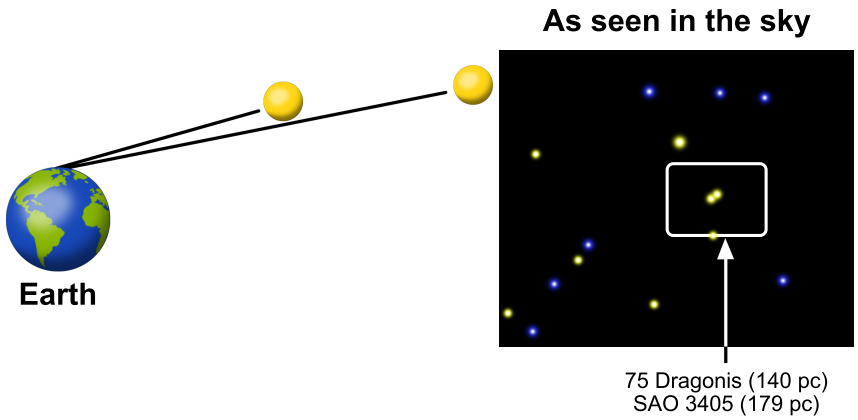

Figure 3.2: Visual Binary Stars Scheme.

3.2. Observation Method

3.2.1. Visual and Astrometric Binary

A visual binary (Fig. 3.2) is a system in which the two stars can be resolved separately through an optical telescope. This means that the angular separation between the components is large enough for them to be seen as two distinct points of light. The angular separation can usually be measured in arcseconds.

The orbital period of these systems ranges from years to centuries, depending on the actual separation between the stars, so that their orbital motion can be monitored over time, allowing the determination of their orbital parameters. Continuous observation of the orbit of a visual binary allows the application of Kepler's laws, especially Kepler's third law, which relates the orbital period, as shown in Eq. 3.12. The orbit projected onto the sky follows an apparent ellipse, and the orbital elements can be adjusted based on observations over time.

An astrometric binary (Fig. 3.3) is a system in which only one of the stars is directly visible, but the presence of the second component is inferred by perturbations in its position in the sky.

In this way, only the primary star can be observed. The presence of the companion is inferred due to small periodic oscillations in the motion of the visible star, caused by its motion around the center of mass of the system. Using astrometric and spectroscopic measurements, it is possible to estimate the mass of the invisible companion.

The position of an astrometric binary star can be modeled by considering the reflection of the motion of the primary star around the center of mass. The observed angular displacement (α) due to this motion is given by:

$$\alpha = \frac{a_1}{d}, \tag{3.29}$$

where α is the observed angular displacement (in arcseconds), a_1 is the actual distance of the primary star from the center of mass (in AU), and d is the distance of the system from Earth (in parsecs).

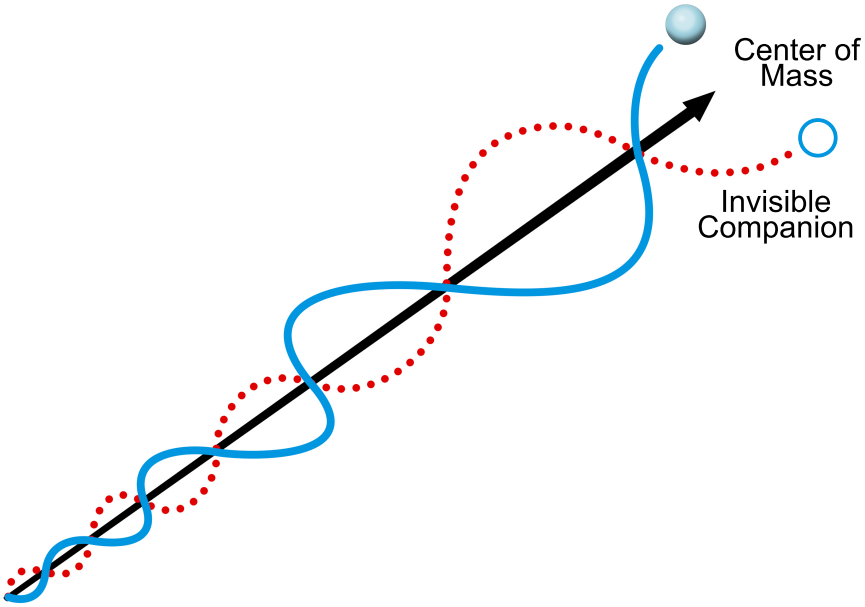

Figure 3.3: Astrometric Binary Stars Scheme.

The position of the star varies periodically, and this effect can be detected with high-precision telescopes, such as Gaia, which measure astrometric variations on the scale of microarcseconds.

If the mass of the primary star and the observed orbit are known, the mass of the unseen companion can be estimated by the relation:

$$M_2 = \frac{M_1 a_1}{a_2}, \tag{3.30}$$

where a_2 is the distance of the companion from the center of mass. This equation comes from the definition of the center of mass.

3.2.2. Spectroscopic

A spectroscopic binary system is a binary star system in which the two stars cannot be resolved individually, but their presence is detected through variations in the spectrum of the light emitted by the system. These variations occur due to the Doppler effect in the spectral lines, caused by the orbital motion of the stars around their common center of mass.

The Doppler effect describes the change in the frequency of light due to the relative motion between the source and the observer. If a star is moving toward the observer, its spectral lines are shifted to the blue (blueshift); if it is moving away, they are shifted to the red (redshift). The variation in the radial velocity (v_r) of the star in a binary system follows the relativistic Doppler equation for small velocities (v«c):

$$\lambda_{obs} = \lambda_0 \left(1 + \frac{v_r}{c}\right), \tag{3.31}$$

or, in terms of radial velocity:

$$v_{\mathrm{r}} = \mathrm{c}\left(\frac{\lambda_{\mathrm{obs}} - \lambda_0}{\lambda_0}\right), \tag{3.32}$$

where: λ_{obs} is the observed wavelength, λ_0 is the resting wavelength of the spectral line, and c is the speed of light ($\sim 3.0 \times 10^5$ km/s),

The periodicity of this spectral shift indicates that the star is in orbital motion, suggesting the presence of a binary system.

If the orbit is circular, the radial velocity varies sinusoidally with time according to the equation:

$$v_{\mathrm{r}}(t) = \gamma + \mathrm{K}\cos(\nu \mathrm{t} + \phi), \tag{3.33}$$

where γ is the systemic velocity, K is the half-amplitude of the radial velocity, $\nu = 2\pi/\mathrm{P}$ is the angular frequency of the orbit, and ϕ is the initial phase, which is increased by π depending on which component of the binary system the equation is referring to.

If the orbit is eccentric, the radial velocity is given by:

$$v_{\mathrm{r}}(t) = \gamma + \mathrm{K}[\cos(\omega + \theta) + \mathrm{e}\cos\omega], \tag{3.34}$$

where e is the eccentricity of the orbit, θ is the true anomaly, which depends on time, and ω is the argument of periastron. Details on the calculation of θ can be found in Appendix A.

A one-line spectroscopic binary (SB1) occurs when only one of the stars in the system has detectable spectral lines. This happens when the other star is much fainter or does not contribute significantly to the spectrum. Its characteristics are:

- Only the primary star exhibits variations in its spectral lines due to the Doppler effect.
- The secondary may be much less luminous, have a spectrum that overlaps with that of the primary, or emit radiation at a different wavelength (for example, a white dwarf or a black hole).
- Only the mass function can be determined, which provides a lower limit on the mass of the secondary.

The fundamental equation for determining masses in spectroscopic binary systems is the mass function, which depends on the inclination i of the system with respect to the line of sight and is given by:

$$f(\mathrm{M}) = \frac{\mathrm{M}_2 \sin^3 \mathrm{i}}{(\mathrm{M}_1 + \mathrm{M}_2)^2} = \frac{\mathrm{PK}_1^3}{2\pi \mathrm{G}}, \tag{3.35}$$

where K_1 is the half-amplitude of the radial velocity curve of the primary star.

A two-line spectroscopic binary (SB2) occurs when both stars are bright enough to have their spectral lines detected and exhibit periodic variations in the Doppler effect. Its characteristics are:

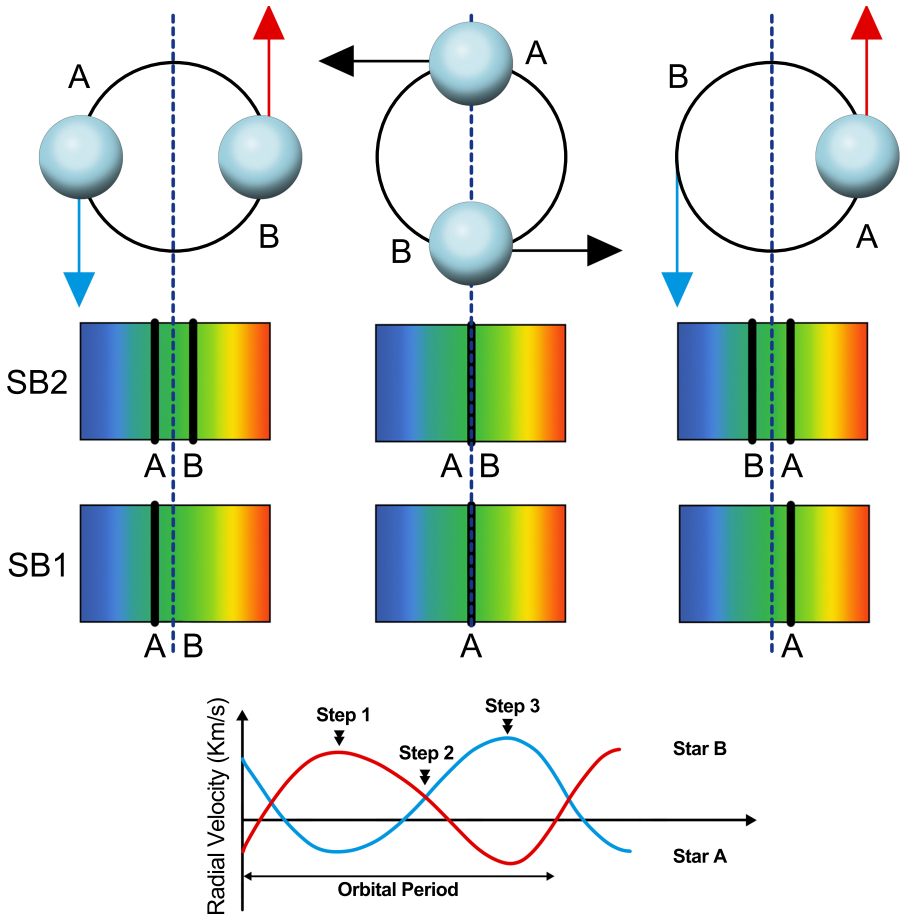

Figure 3.4: Spectroscopy Binary Stars Scheme.

- The two stars have comparable luminosity and temperature, allowing their spectral lines to be visible.
- In the spectrum, we see the two series of spectral lines moving in opposite directions over time.
- The mass ratio can be determined directly from the radial velocities.

The Fig. 3.4 shows a diagram of the movement of stars in the binary system, and its equivalent spectral effect of displacement of spectral lines. If both components of the system are spectroscopically detected, we can measure K_1 and K_2, which allows us to determine the mass ratio (q):

$$q = \frac{M_1}{M_2} = \frac{K_2}{K_1}\,. \tag{3.36}$$

Heliocentric Radial Velocity Correction

The radial velocity of an astronomical object is the component of its velocity along the observer's line of sight. Because the Earth moves around the Sun, radial velocity measurements made from a ground-based telescope are influenced by the Earth's motion. To obtain an ac-

curate radial velocity, it is necessary to apply the heliocentric correction, which removes the effects of the Earth's orbital motion.

The heliocentric correction adjusts the observed radial velocity ($v_{\rm obs}$) to a radial velocity referenced to the center of the Sun ($v_{\rm helio}$):

$$v_{\rm helio} = v_{\rm obs} + v_{\rm corr}\,, \tag{3.37}$$

where $v_{\rm corr}$ is the heliocentric correction, which depends on the position of the Earth in its orbit and the direction of the observed object.

The heliocentric correction can in turn be expressed as:

$$v_{\rm corr} = \vec{\rm V}_{\rm earth} \cdot \hat{\rm r}\,, \tag{3.38}$$

where $\vec{\rm V}_{\rm earth}$ is the speed of the Earth around the Sun, and $\hat{\rm r}$ is the unit vector pointing towards the observed object.

The speed of the Earth in its orbit varies throughout the year, with a maximum value of approximately 30 km/s. Depending on the position of the object and the time of observation, the correction can be positive (if the Earth is moving towards the object) or negative (if the Earth is moving away from the object).

To calculate the heliocentric correction, we need the following information:

- Equatorial coordinates of the object (α,δ);
- Date and time of observation (to determine the Earth's position in orbit);
- Earth's orbital speed (~30 km/s);
- Location of the observer on Earth (altitude and latitude of the telescope).

Many astronomical software programs, such as IRAF, RVSAO and Python libraries (Astropy), can calculate this correction automatically, or extract it from the internal information of the spectroscopy files.

The heliocentric correction is essential for accurate measurements of radial velocities, especially in studies such as: Measurement of velocities in binary stars, Detection of exoplanets by variation of radial velocity, Studies of galactic dynamics and red shift in distant galaxies. For extragalactic objects, the heliocentric correction can be replaced by the correction for the cosmic microwave background (CMB) reference frame, which takes into account the motion of the Sun relative to the universe on a large scale.

3.2.3. Eclipsing Binary

According to *The Astronomical Almanac*, the phenomenon of an eclipse is described as an astronomical event that occurs when a celestial body is temporarily obscured, totally or partially,

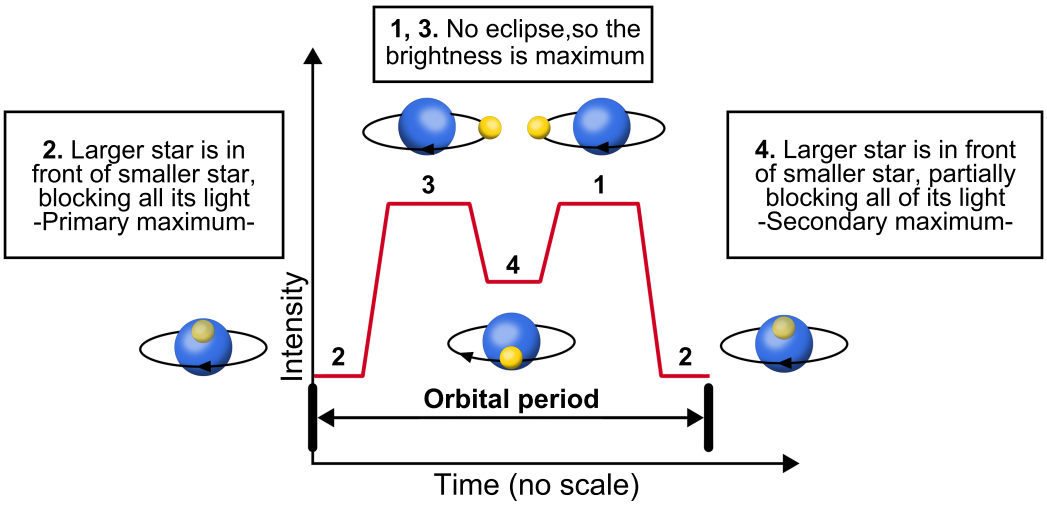

Figure 3.5: Eclipsing Binary Stars Scheme.

by another body or by its shadow. An eclipsing binary system is a pair of stars that orbit around a common center of mass and whose orbital plane is close to the observer's line of sight. This results in periodic eclipses, where one star obscures the other, causing predictable variations in the total brightness of the system.

Fig. 3.5 shows a diagram of the movement of stars in the binary system, and its equivalent photometric effect, generating cyclical eclipses.

Eclipsing binary systems are fundamental tools for astrophysics because they allow the direct determination of fundamental parameters of stars. Among their main applications, the following stand out:

- Accurate determination of stellar masses and radii: Essential for testing stellar evolution models.
- Calculation of luminosities and temperatures: By combining the light curves and spectra, we can determine parameters such as temperature and chemical composition of the stars.
- Detection of exoplanets and neutron stars: Small variations in light curves and radial velocities can reveal compact objects hidden in the system.

For a binary system to produce observable eclipses, the inclination i of its orbit with respect to the line of sight must satisfy the following condition:

$$cos\,\mathrm{i} \leq \frac{\mathrm{R}_1 + \mathrm{R}_2}{\mathrm{a}}, \tag{3.39}$$

where: R_1 and R_2 are the radii of the stars, a is the semi-major axis of the orbit, and i is the inclination of the system ($\mathrm{i} = 90°$ corresponds to an exact alignment). This means that the smaller the separation between the stars and the larger their radii, the greater the probability of eclipses occurring.

The light curve of an eclipsing binary system shows periodic variations in the total brightness of the system due to eclipses. The shape of the light curve depends on the relative sizes of the stars, their temperatures, and the geometry of the orbit.

The intensity of the total luminous flux is given by:

$$F(t) = F_1 + F_2 - \Delta F_{eclipse}\,, \tag{3.40}$$

where: F_1 and F_2 are the fluxes of the primary and secondary stars, respectively, $\Delta F_{eclipse}$ is the reduction of the total flux during an eclipse. Furthermore, we define the types of eclipses as follows:

1. Primary eclipse: occurs when the less luminous star passes in front of the brighter one. The brightness of the system drops significantly.

2. Secondary eclipse: occurs when the brightest star obscures the secondary one. The drop in brightness is smaller because the eclipsed star is less luminous.

The depth of eclipses depends on the luminosity of the stars and is described as follows:

$$\frac{\Delta F_{primario}}{F} = \frac{L_2}{L_1 + L_2}\,, \tag{3.41}$$

and

$$\frac{\Delta F_{secundario}}{F} = \frac{L_1}{L_1 + L_2}\,, \tag{3.42}$$

where $L_1 + L_2$ are the luminosities of the stars. If the stars have very different temperatures, the secondary eclipse may be difficult to detect.

The characterization of orbital eccentricity in eclipsing binary systems or transiting exoplanet systems can, under certain conditions, be achieved through analysis of the photometric light curve alone. Although precise determination of orbital parameters typically requires the combination of photometric and spectroscopic data, it is possible to obtain reliable estimates of parameters such as the eccentricity (e) and argument of periastron (ω) directly from features observed in the light curve.

One of the most direct approaches involves analyzing the phase offset between the primary and secondary eclipses. In a perfectly circular orbit, the secondary eclipse is expected to occur at orbital phase $\phi = 0.5$. However, in eccentric orbits, the timing of the secondary eclipse is displaced due to orbital velocity variations and the geometry of the system. This time shift can be used to estimate the quantity $ecos\omega$ through the following expression:

$$\Delta\phi = \frac{(t_{sec} - t_{prim})}{P} - 0.5 = \frac{ecos\omega}{\pi}\,, \tag{3.43}$$

where t_{prim} and t_{sec} represent the central times of the primary and secondary eclipses, respectively, and P is the orbital period of the system. The quantity $\Delta\phi$ represents the phase shift of the

secondary eclipse relative to its expected position in a circular orbit. This expression assumes a Keplerian orbit and sufficiently narrow eclipses such that the central times can be measured precisely.

Additionally, orbital eccentricity affects the durations of eclipses or transits, since the orbital velocity varies along the orbit, being higher near periastron and lower near apastron. The ratio of the durations of the primary ($T_{\rm prim}$) and secondary ($T_{\rm sec}$) eclipses can provide an estimate of $e \sin \omega$. An approximate relation, valid under favorable geometric conditions and for moderately eccentric orbits, is given by:

$$\frac{T_{\rm prim}}{T_{\rm sec}} \approx \frac{1 + e \sin \omega}{1 - e \sin \omega}. \tag{3.44}$$

This relation reflects the asymmetry in eclipse durations resulting from differences in orbital speed at the points where the eclipses occur, modulated by the orientation of the periastron. While this approximation simplifies the dynamics, it offers a useful complement to the phase-based estimate. By combining Equations (1) and (2), it is possible to solve for both e and ω, at least approximately, using only photometric data.

These relations were originally discussed in detail in the context of binary systems by Kopal (1959a), and they remain widely employed in modern analyses of light curves, especially as initial estimates for more detailed photometric modeling.

Eclipsing binary systems that are also spectroscopic binaries allow us to determine the masses and radii of the stars with great accuracy. Combining the light curve with the radial velocity curve provides the necessary information. If the inclination i can be estimated independently, as is the case for an eclipsing binary, we can determine the true masses for an SB2 system by relating Eqs. 3.35 and 3.36, resulting in the following equations:

$$\mathrm{M_1} = \frac{\mathrm{f(M)}}{\sin^3 \mathrm{i}} \left(1 + \frac{\mathrm{K_1}}{\mathrm{K_2}}\right)^2 , \tag{3.45}$$

and

$$\mathrm{M_2} = \frac{\mathrm{f(M)}}{\sin^3 \mathrm{i}} \left(1 + \frac{\mathrm{K_2}}{\mathrm{K_1}}\right)^2 . \tag{3.46}$$

Finally, from the light curve, the eclipse duration provides information about the radii of the stars as follows:

$$\frac{\mathrm{R_1} + \mathrm{R_2}}{\mathrm{a}} = \frac{\Delta t}{\mathrm{P}} , \tag{3.47}$$

where: Δt is the duration of the eclipse, and P is the orbital period. If we know the inclination i of the system, we can calculate the absolute radii of the stars:

$$\mathrm{R_1} = \mathrm{a} \frac{\mathrm{R_1'}}{\sin \mathrm{i}} , \tag{3.48}$$

and

$$R_2 = a\frac{R_2'}{\sin i}, \tag{3.49}$$

where R_1' R_2' are the relative radii obtained from the light curve.

3.3. Separation and the Roche Lobe

The geometry, separation and relative luminosity of the components of the binary system will determine the classification and the best method to be used to characterize these stars. The classification of these stars in double systems is divided into: optical double, visual binary stars, astrometric binary stars, spectroscopic binary stars and eclipsing binary stars.

There is also an exclusive classification for binary systems, based on the dynamics of forces between their components. The classification then arises due to the principle of equipotential surfaces. The most influential forces of the system are: (i) the gravitational force that arises due to the mass of the bodies in the system, and (ii) the centrifugal force, which opposes the gravitational force and is caused by the rotation of the bodies. We then have the Roche surfaces Paczynski (1971), which are regions that have the same energy per unit area, and the Lagrange points, places where the resulting force cancels out.

Figure 3.6: Gravitational potential of a binary system. L_1, L_2 and L_3 are the Lagrange points. The transfer of matter between the components occurs through the internal Lagrange point L_1.

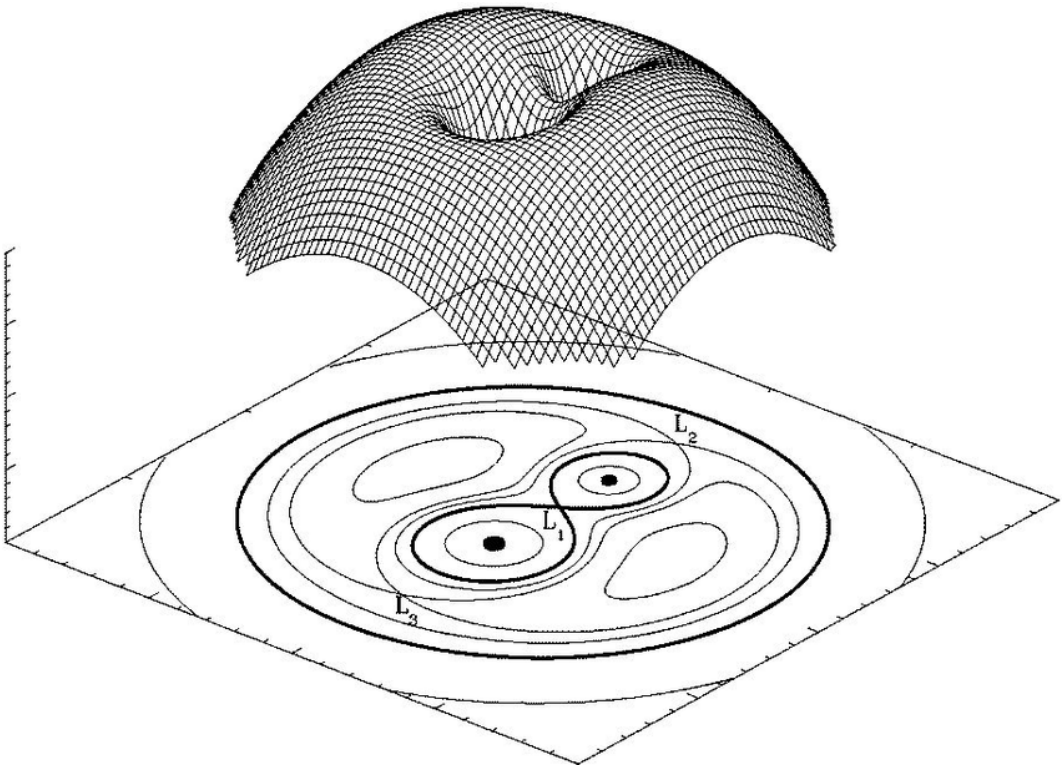

Source: (Martinez et al., 2008).

To define the potentials of this surface, we have to determine the potential energy of the two masses, which rotate around a center of mass. We then have two contributions, one gravita-

tional (U_g), due to the masses, and one centrifugal (U_c), due to the rotation speed. These two contributions are represented mathematically by:

$$U_g = -G\frac{\mathrm{Mm}}{a}\,, \tag{3.50}$$

and

$$U_c = -\frac{1}{2}\mathrm{mw^2r^2}\,, \tag{3.51}$$

where m is the mass of any test body in space, w is the angular velocity, and r is the distance from the center of mass of the system to the body m. The gravitational potential (Φ) tested at any point $P(x, y, z)$ will correspond to the sum of the gravitational and rotational contributions, so we have the following equation for the effective gravitational potential,

$$\Phi = -G\left(\frac{\mathrm{M_1}}{\mathrm{r_1}} + \frac{\mathrm{M_2}}{\mathrm{r_2}}\right) - \frac{1}{2}w^2\left[\left(x - \frac{\mathrm{m_2}}{\mathrm{m_1 + m_2}}\right)^2 + y^2\right]\,, \tag{3.52}$$

where,

$$\mathrm{r_1} = (\mathrm{x^2 + y^2 + z^2})^{(1/2)}\,, \tag{3.53}$$

$$\mathrm{r_2} = [(\mathrm{x - 1})^2 + \mathrm{y^2 + z^2}]^{(1/2)}\,, \tag{3.54}$$

with $\mathrm{r_1}$ being the distance from star 1 to P, and $\mathrm{r_2}$ the distance from star 2 to point P. The angular frequency w can be derived using Kepler's third law,

$$w^2 = \left(\frac{2\pi}{\mathrm{P_{orb}}}\right)^2 = \frac{G\,(\mathrm{M_1 + M_2})}{\mathrm{a^3}}\,, \tag{3.55}$$

where P_{orb} is the orbital period of the system, and a is the separation between the stars. Taking a≡1, defining the normalized potential Φ_n = -2Φ/G($\mathrm{M_1 + M_2}$), and the mass ratio, then,

$$\Phi_n = \frac{2}{(1 + \mathrm{q})\mathrm{r_1}} + \frac{2\mathrm{q}}{(1 + \mathrm{q})\mathrm{r_2}} + \left(x - \frac{\mathrm{q}}{1 + \mathrm{q}}\right)^2 + y^2\,. \tag{3.56}$$

The internal Lagrange point $\mathrm{L_1}$, through which mass transfer can occur, is obtained by solving:

$$\nabla\Phi_n = 0\,, \tag{3.57}$$

on the axis of connection between the two stars. Another important parameter is the Roche lobe radius $\mathrm{R_L}$, where a useful approximation in terms of the orbital separation a is given by Eggleton's empirical formula (Eggleton, 1983):

$$\frac{\mathrm{R_L}}{\mathrm{a}} = \frac{0.49\mathrm{q}^{2/3}}{0.6\mathrm{q}^{2/3} + \ln(1 + \mathrm{q}^{1/3})}\,. \tag{3.58}$$

From these results, the potentials can be derived for any point (x, y, z), as shown in Fig. 3.6,

around two masses, allowing the construction of Roche equipotential surfaces (Hilditch, 2001).

These results allow us to classify binary systems as follows:

Detached Binary System: A detached binary is a system where both stars remain within their Roche lobes, interacting gravitationally but without significant mass transfer, so each evolves almost independently. They have long orbital periods, which can reach tens to hundreds of years. See a geometric representation in Fig. 3.7.

Semi-detached Binary System: A semi-detached binary occurs when one star expands to fill its Roche lobe, potentially allowing mass transfer through the inner Lagrangian point L1; these systems typically have short orbital periods, and eclipsing binaries show light curves with both eclipses and ellipsoidal variations due to the deformed star.

Contact Binary System: A contact binary is a system in which both stars have expanded to share a common envelope of mass, confined by a dumbbell-shaped equipotential surface; these systems have short orbital periods, and eclipsing binaries display light curves with eclipses and characteristic "m"-shaped variations due to the deformations of both stars (see Fig. 3.7).

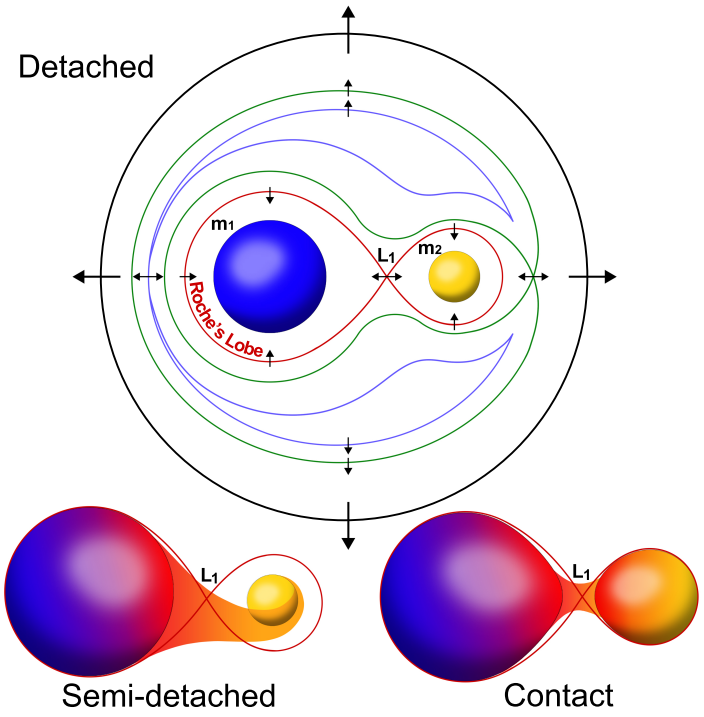

Figure 3.7: Classification of binary systems according to Roche surfaces. From the upper left system to the lower right: Detached system; semi-separated system; and Contact System.

3.4. Rotation and Tidal Effect

In binary star systems, tide interactions play a crucial role in the orbital evolution and rotation of stars. Tidal interactions result from the gravitational force between the stars, which causes deformations of the stars and an exchange of angular momentum between the orbit and the

stars. These effects can lead to the synchronization of the rotations of the stars with the orbital period and to the circularization of the orbits. This thesis explores the main tidal effects and their implications, focusing on the rotation of stars and orbital evolution.

The angular momentum L of a star is given by:

$$L = I\mathrm{w}\,, \tag{3.59}$$

where I is the moment of inertia of the star. For a star with mass M and radius R, the moment of inertia I can be expressed as:

$$I = \frac{2}{5}\mathrm{MR}^2\,. \tag{3.60}$$

The rotation of the star can be modified by the tidal interaction with the other star in the binary system. The temporal variation of the angular momentum is given by:

$$\frac{dL}{d\mathrm{t}} = -\frac{1}{2}k\left(\frac{\mathrm{MR}^2}{\mathrm{a}^6}\right)\left(1-e^2\right)^{3/2}\,, \tag{3.61}$$

where a is the semi-major axis of the orbit, e is the orbital eccentricity, and k is a factor that depends on the internal structure of the star ($k \approx 0.1$ for massive stars). This term describes the dissipation of angular momentum due to the tidal interaction, which tends to slow the rotation of the star until its angular velocity synchronizes with the orbital motion (Tassoul, 1987).

The tidal forces in binary systems result from the gravitational differences that one star exerts on the other. The differential tidal force $\mathrm{F_{tide}}$ can be approximated by:

$$\mathrm{F_{tide}} \approx \frac{2\mathrm{GM_2R_1}}{\mathrm{a}^3}\,, \tag{3.62}$$

where $\mathrm{M_2}$ is the mass of the companion star, $\mathrm{R_1}$ is the radius of the affected star, and a is the orbital separation. The energy dissipation due to tidal forces tends to circularize the orbit and synchronize the stellar rotation with the orbit. The rate of change of the orbital eccentricity e due to the tide is given by:

$$\frac{de}{d\mathrm{t}} = -\frac{e}{\tau_{\mathrm{tide}}}\,, \tag{3.63}$$

where τ_{tide} is the time scale of tidal dissipation. Studies such as the one by Landin et al. (2009) have investigated the combined effects of tidal and rotation distortions on the equilibrium configuration of low-mass pre-main sequence stars, highlighting how these distortions affect the internal structure and stellar evolution.

One of the most notable effects of tidal interaction is the circularization of the binary orbit. The eccentricity e of the orbit decreases over time due to the dissipation of energy in the tidal. The rate of change of the semi-major axis is given by:

$$\frac{d\mathrm{a}}{d\mathrm{t}} = -\frac{63}{4}\frac{G^3\mathrm{M_1M_2(M_1+M_2)}}{\mathrm{a}^6}\left(1-e^2\right)^{15/2}\,, \tag{3.64}$$

where M_1 and M_2 are the masses of the stars and G is the gravitational constant. The dissipation of energy in the tides causes the orbit to become more circular with time, especially in close binary systems (Zahn, 1977).

In addition to circularization of the orbit, the dissipation of the tides also affects the eccentricity e. The rate of change of the eccentricity is given by the equation:

$$\frac{de}{dt} = -\frac{304}{15}\frac{G^3 M_1 M_2 (M_1 + M_2)}{a^6 e}\left(1 - e^2\right)^{13/2} . \tag{3.65}$$

The equation shows how the eccentricity decreases over time due to energy dissipation, leading to an increasingly circular orbit (Hut, 1981).

When a binary system is subject to tidal interactions, the stars tend to synchronize their rotations with the orbital period. The orbital period and the rotation period of the star P_{rot} are related by the synchronization condition (Goldreich and Nicholson, 1989):

$$P_{rot} = P = \frac{2\pi}{w_{orbital}} . \tag{3.66}$$

When the star reaches synchronization, its rotation aligns with the orbital motion, which implies that the sides of the star that face the other star in the system do not show any variation in rotation. In massive binary systems, this can lead to a "tidal locking" configuration (see Fig. 3.8), where the rotation of the star is synchronous with the orbit, as observed in systems like that of Li et al. (2020).

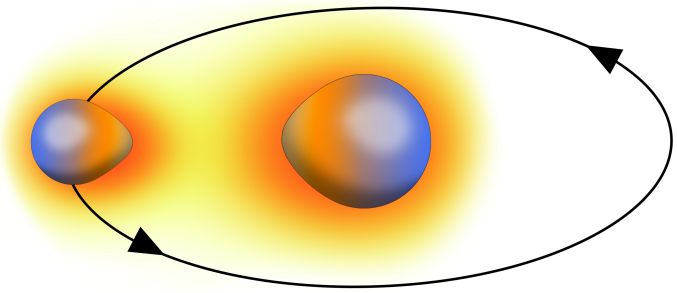

Figure 3.8: Tidal Locking Configuration.

3.5. Be Stars in Binary Systems

Given the availability of an extensive multi-epoch spectroscopic dataset, it is appropriate to investigate the presence of radial velocity variations in the stellar spectral lines. As established for massive stars in general (Sana et al., 2012; Mahy et al., 2013), a substantial fraction of Be stars, exceeding 30%,are confirmed or suspected members of binary systems (Oudmaijer and Parr, 2010). In Be stars, binarity can be diagnosed not only through classical methods such as

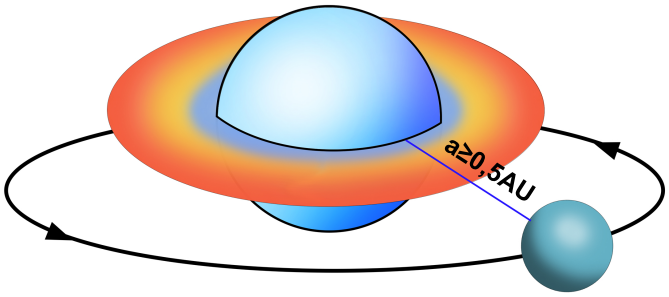

Figure 3.9: Configuration of Be Stars in Binary Systems.

high-angular-resolution imaging, photometric variability, and RV shifts, but also through phase-locked modulation of circumstellar disk features, which may reflect dynamical interactions with a companion (e.g., Bjorkman et al., 2002a). A cartoon of the orbital configuration of a Be star in a binary system can be seen in Figure 3.9.

Be stars can form by two main mechanisms. In some cases, they are born with high rotation rates due to the initial conditions of the collapse of the molecular cloud (Zorec and Briot, 1997; Rivinius et al., 2013). In these situations, the formation of the disk of matter around the star is natural and the evolution follows patterns typical of massive stars, but strongly influenced by the high rotation speed. Another widely accepted formation pathway is from mass transfer in binary systems (Pols et al., 1991; De Mink et al., 2013). In this scenario, an originally more massive star transfers part of its mass to its companion during its expansion phase to a giant or supergiant, accelerating its rotation and thus forming a Be star. Observations of Be stars with compact companions, such as white dwarfs, neutron stars or black holes, strongly support this hypothesis. Binary interactions play a crucial role in the evolution of these systems. When the companion is a main sequence star or a giant, tidal forces can disturb the disk of the Be star, causing brightness variations and disk oscillations (Okazaki and Negueruela, 2001a; Panoglou et al., 2016). In systems with neutron stars, the so-called Be/X-ray systems (BeXRBs) are formed, in which the neutron star in generally eccentric orbits captures material from the disk during orbital approach, generating intense bursts of X-ray emission (Reig, 2011). These emissions can be periodic or explosive, depending on the interaction of the material with the neutron star's magnetic field. In Be+ white dwarf systems, moderate accretion of matter can produce brightness variations and, occasionally, nova explosions (Mennickent et al., 2012).

The final evolution of binary Be systems is diverse. The Be star may become a supergiant and explode as a supernova, forming a compact object, or, in cases of stellar merger, result in a rejuvenated blue star (De Mink et al., 2014). In other situations, the system may stabilize as a high-mass binary containing a compact star and a rapidly rotating Be star. Over time, the Be star may dissipate its disk, returning to the normal B star state before evolving into gravitational collapse.

Thus, Be stars in binary systems represent natural laboratories for the study of extreme astrophysical processes, such as rapid rotation, disk formation and dissipation, mass transfer

and high-energy emission. Observational advances at multiple wavelengths, especially in X-rays and radio, have allowed new discoveries and driven this field of research, essential for understanding the evolution of massive stars.

In addition to the traditional formation and interaction scenarios, several recent studies have deepened our understanding of the circumstellar disks of Be stars. These disks are modeled as viscous decretion disks (Lee et al., 1991; Carciofi et al., 2011), in which the material ejected by the star is redistributed under the action of viscosity, resulting in dense and flattened structures detectable in different bands of the electromagnetic spectrum. Interferometric observations, such as those performed by the VLTI and the CHARA Array, have confirmed the presence of flattened and Keplerian disks around several Be stars, in addition to evidencing the gravitational flattening of the stars themselves due to their high rotation (Meilland et al., 2012).

In his work on the frequency and characteristics of Be stars, Zorec and Briot (1997) included in his sample single and binary stars that presented "*Hα in emission*" or "*shell spectrum*", emphasizing that the binary systems used had periods greater than 0.1 years, and therefore the tidal force would not impede the high rotation of the Be star (Abt and Cardona, 1984)[†] In fact, with the exception of systems with eccentricity, this long period facilitates non-synchronous rotation and does not effectively interfere with the formation of its equatorial disk. Zorec et al. (2016) conducted a study on the rotational velocities of 233 Be stars and found a symmetric distribution of velocity ratios spanning from 0.30 to 0.95, indicating most Be stars are rapid but rarely at critical speeds.

Another fundamental aspect is the role of non-radial pulsations (NRPs) in the dynamics of these systems. High-precision photometric observations by missions such as BRITE and TESS have revealed pulsation modes that are likely associated with mass ejection episodes (Baade et al., 2018). The interaction between fast rotation and pulsation modes may be one of the triggers for the formation and maintenance of circumstellar disks.

The frequency of Be stars also appears to be related to the metallicity of the environment. In regions of low metallicity, such as the Magellanic Clouds, a higher incidence of Be stars is observed compared to the Milky Way (Martayan et al., 2007). This is consistent with the fact that stellar winds are less efficient in low-metallicity stars, allowing them to maintain a high rotation throughout their lives.

Finally, in star clusters, some Be stars are identified as "blue stragglers", appearing to be younger than the rest of the population. This rejuvenation is often attributed to mergers or mass transfer in binary systems (McSwain and Gies, 2005), which further reinforces the role of binary interactions in the formation and evolution of Be stars.

Thus, the study of Be stars, in their multiple contexts, isolated, in binary or hierarchical systems, provides a privileged window to understand not only the evolution of massive stars, but also the formation of extreme phenomena such as pulsars, black holes and gravitational

[†] The separation of 0.5 to 10^4 AU is also pointed out by Abt and Cardona (1984) as characteristic of a weak tidal interaction.

wave sources.

3.5.1. Impact of Binarity on the Observed Rotational Velocity Distribution of Be Stars

A precise analysis of the rotational velocities of Be stars in binary systems requires careful consideration of the effects introduced by the presence of a companion on spectroscopic observations. As discussed by Zorec et al. (2016), the light from the companion star can significantly alter the spectral line profiles of the Be star, potentially leading to an overestimation of $v \sin i$ if this influence is not properly accounted for. This effect arises because the companion's spectral contribution may dilute or broaden the lines of the primary star, as well as cause line blending in systems where the components have significant radial velocity differences.

To mitigate these effects, it is essential to accurately identify which stars in the sample are confirmed or candidate binaries. Segregating the sample into single and binary stars allows for the differentiated treatment required for each case.

A robust approach to quantify and correct the impact of binarity on the observed rotational velocity distribution involves the application of statistical deconvolution methods. Following Zorec et al. (2016), the observed distribution $\Psi(v)$ can be modeled as the convolution of the true distribution $\Phi(v)$ with a spreading function $f(v)$, which represents the companion's effect, weighted by the binary fraction $f_{\rm bin}$:

$$\Psi(v) = f_{\rm bin} \int_0^v \Phi(u) f(v-u)\, du + (1 - f_{\rm bin})\Phi(v)\,, \tag{3.67}$$

here, $f_{\rm bin}$ corresponds to the estimated fraction of the population composed of binary systems, which can range between 0.7 and 1.0 depending on the sample and detection sensitivity. The function $f(v)$ encapsulates how the companion's contribution modifies the measured velocity profile.

To recover the intrinsic distribution $\Phi(v)$, Zorec et al. (2016) employ the iterative Lucy-Richardson deconvolution algorithm, which is particularly suitable for inverse problems of this kind, especially when dealing with noisy and incomplete data. After several iterations, this method separates the binary contribution from the observed distribution, revealing the true distribution of normalized rotational velocities V/V_c.

Moreover, additional astrophysical effects such as gravity darkening and macroturbulence impact the spectral line profiles used to estimate $v \sin i$, potentially biasing the measurements (Townsend et al., 2004; Zorec et al., 2016). Therefore, corrections accounting for these phenomena are incorporated to refine the velocity estimations.

Importantly, binarity can also contaminate spectral lines and affect the inferred rotational velocities. The approach by Zorec et al. (2016) integrates corrections for binarity effects, ensuring that the derived velocity distribution reflects the true rotation of the Be stars rather than

orbital or contamination artifacts.

The determination of the true equatorial rotational velocity v of Be stars from the observed projected velocity $v \sin i$ requires careful consideration of the inclination angle i, which is generally unknown for individual stars. In large stellar samples, it is customary to assume a random orientation of rotational axes, implying that the distribution of $\sin i$ is uniform between 0 and 1 (Chandrasekhar, 1950). This geometric assumption allows a statistical treatment to infer the underlying distribution of v from the observed $v \sin i$ distribution.

4 Objectives, Data and Methodology

4.1. Objectives

The main objective of this project is to investigate Be-type stars in binary systems, aiming to evaluate their fundamental stellar and orbital parameters, characterize Be stars in these systems and study the influence on the dynamics and evolution of the sample.

The specific objectives of this work are outlined as follows:

- To collect and analyze photometric and spectroscopic data from ground- and space-based facilities (TESS, Gaia, SOAR, BeSS) to detect variability, emission lines, and other features for characterizing Be stars and their binary companions.

- To systematically classify the target list by (i) confirming the binary nature of each system, excluding single stars and higher-order multiples, based on photometric and/or spectroscopic evidence, and (ii) identifying classical Be star components through characteristic spectral features such as Balmer and He I emission lines, ensuring the sample contains only binary systems with at least one Be star for further characterization.

- To develop and apply binary modeling algorithms to estimate physical and orbital parameters, using light curve and radial velocity modeling codes with Bayesian inference techniques such as Markov Chain Monte Carlo (MCMC) simulations. Short MCMC chains will be used for computational efficiency, providing robust estimates of masses, radii, orbital inclinations, and separations. This was done for TIC 74386000.

- To analyse rotational velocities, helium emission lines, and non-radial pulsations of the Be component in one analyzed system. Line profile analysis and spectral fitting are used to measure projected rotational velocity and identify prominent Balmer emission lines (e.g., Hα, Hβ), typical of circumstellar disks in Be stars. These spectral properties help probe the internal structure, mass-loss mechanisms, and angular momentum distribution.

- To identify and study periodic variations in the light curves and spectral lines of the systems using time-series analysis techniques such as Fourier analysis and prewhitening. The goal is to detect signals from orbital motion, non-radial pulsations, and rotational modulation, enabling the selection of targets with significant and coherent variability for detailed modeling.

- To interpret the derived parameters in the context of stellar evolution and the role of Be stars in binary systems by comparing results with theoretical models. The analysis will explore how the presence of a Be star influences the system's evolution and assess whether binarity contributes to the Be phenomenon, particularly regarding mass transfer history, disk formation, and pulsation behavior.

4.2. Sample and Selection Criteria

The selection of binary systems containing Be stars requires a careful approach based on the combination of spectroscopic, photometric, and astrometric data from specialized literature. With the aim of constructing a representative sample of Galactic Be stars in binary systems, we performed an extensive review of previous studies, incorporating results from observational investigations and detailed modeling published over the past decades.

Initially, we considered classical systems with robust Be star identification, such as η Centauri (TIC 128116539), studied by Janot-Pacheco et al. (1991a) and later characterized by Levenhagen et al. (2003b), Levenhagen and Leister (2006a), and Levenhagen et al. (2024b). These works provided fundamental parameters (effective temperature, $\log g$, projected rotational velocity, stellar mass), in addition to the presence of non-radial pulsations. Similarly, HD 72067 (TIC 140006471) was included based on the works of De Araujo and de Freitas Pacheco (1990b), Nichols and Slavin (2004a), and its binary classification by van den Bos (1929), with recent confirmation by Souza et al. (2020) using speckle interferometry.

To identify stellar or substellar companions associated with Be stars, we employed results from Kervella et al. (2019), who used high-precision astrometry applicable to objects such as HD 201522 (TIC 136027289) and HD 71510 (TIC 140031673). The latter also had fundamental parameters determined by Kochanek (2022b) and Solar et al. (2022b). Based on these and other works, we considered systems such as TIC 140214221 and TIC 146036695, where multiple values of projected rotational velocities and temperatures were reported by different authors (Sigut and Ghafourian, 2023b; Levenhagen et al., 2024b; Solar et al., 2022b), emphasizing the importance of multi-source analysis for confirming Be characteristics and binary status.

The inclusion of systems with known orbital parameters was guided by Klement et al. (2024a), who analyzed HD 194335 (TIC 14200511), a B2IIIe system with an orbital period of 63.1 days, complemented by mass determinations from Wang et al. (2023a). We also included HD 135734 (TIC 144028101), classified as a binary system composed of B7V and B8Ve

stars by Zwintz et al. (2024a), with detailed stellar parameters provided by Levenhagen et al. (2024b).

We also considered the works of Labadie-Bartz et al. (2017); Desnoux and Buil (2005), who used high-cadence photometry and spectroscopy to identify variability and binarity in Be stars, contributing key information for target selection. These authors notably emphasized the importance of periodic variability as an indicator of stellar companions. Additionally, we included the recent results of Shi et al. (2023b), who analyzed a large set of Be binary systems with a focus on interactions between the star and its disk, offering critical constraints on their dynamical properties.

Finally, the sample was enriched with historically known systems such as RY Gem (TIC 14709809), an eclipsing binary system composed of an A0V star and a K0IV subgiant, as described by Plavec and Dobias (1987a) and further characterized by Malkov (2020a). Altogether, the resulting sample represents a collection of Galactic Be stars in binary systems candidates, supported by multidisciplinary data and multiple reliable sources. This dataset provides a solid foundation for future analyses on the influence of binarity on the evolution and observable properties of Be stars.

Photometric variability is also an important tool, especially when modulated coherently with orbital time scales. Effects such as eclipses, ellipsoidal modulation, and reflection can indicate the presence of a companion, as discussed by Rivinius et al. (2013) and Koubský et al. (2006). Modulation in emission lines, especially in Balmer lines, is another relevant sign. Systematic variations in line profiles, such as V/R variability, may reflect perturbations in the disk caused by a nearby companion. Works by Okazaki and Negueruela (2001b) and Hummel and Vrancken (2000) highlight these effects in binary systems.

In systems with sufficiently large angular separations, the companion can be directly identified using optical interferometry or adaptive optics imaging. Observations with instruments like VLTI and CHARA have enabled such detections, as reported by Mourard et al. (2015) and Wheelwright et al. (2012).

Full details of each target are presented in the Ap C. The complete catalog obtained following the criteria described above is presented in table 4.1.

Table 4.1: The complete catalog of targets analyzed in this study. Systems classified as Be binaries are marked with †.

TIC ID	Common Name	RA (deg)	Dec (deg)	T-mag	S-Type
10176636	HD 57539	110.39	-5.90	6.68	B3IV
103994174	HD 189847	300.24	31.23	6.96	B7V
11411724	HD 37903	85.41	-2.26	7.66	B3IV
115091314†	HD 168135	274.71	-12.45	7.70	B8IV/V
117501818	HD 15113	36.89	48.23	7.57	B9
118842700†	HD 167128	274.28	-56.02	5.32	B3IIIe

TIC ID	Common Name	RA (deg)	Dec (deg)	T-mag	S-Type
124219174†	HD 179405	288.17	-6.46	8.61	B2Vnne
124407255	V747 Mon	104.29	-8.54	8.16	B5Vne?
125755072	Alcyone	56.87	24.11	2.94	-
126756648†	HD 201036	316.58	28.41	9.00	B6/8V
12725034†	HR 5953	239.55	-14.28	2.38	B0.3IV
127493611†	HR 3034	111.79	8.29	4.43	B1IVe
128116539†	HR 5440	207.40	-42.47	0.90	B2Ve
136027289	HD 201522	317.12	47.26	7.98	B5V
136704900†	HD 201836	317.63	47.69	6.53	B6IV
140006471†	HD 72067	127.28	-44.16	6.01	B2/3V
140031673	HIP 41296	126.38	-51.73	5.39	B3IV
140214221	HR 1956	84.80	4.12	2.65	B9Ve
14200511†	HR 7807	305.93	37.48	6.12	B2IIIe
144028101†	HR 5683	207.40	-42.47	4.74	B8Ve
146036695†	HD 68980	123.37	-35.90	5.15	B1V
14709809†	HD 58713	111.85	15.66	8.43	A0V:e+K0II
148917425†	kap Dra	188.37	69.79	4.02	B6IIIpe
151300497	HD 155806	258.83	-33.55	5.82	O7,5V((f))z(e)
151546818	HD 174513	282.79	-7.80	8.30	B2n(e)
152859121†	hr 6175	249.29	-10.57	1.50	O9.2IVnn
153880067†	HD 215227	340.74	44.72	8.57	B1,5-B2III
154355871†	HD 216200	342.59	41.95	5.79	B4+F9III
155030422	omi And	345.48	42.33	3.75	B6IV/V_sh
155573117†	CD-27 5181	123.52	-28.32	10.62	Be
157420220†	HD 142926	238.88	42.57	5.82	B9pe
159117671	HD 112028	192.31	83.41	5.31	A1IIIp shell
16887256†	HD 138749	233.23	31.36	5.52	B6Vnne
171895762	HR 6304	255.45	-58.96	6.16	B2IVne
174008063	HD 60606	113.46	-36.34	5.52	B2Vne
174664153	HD 61925	114.99	-37.58	6.04	B3IV(e)
175523591	HD 63215	116.54	-37.93	6.00	B6Vnne
181627638	HD 179343	288.01	2.62	6.82	B7/8(e)_sh
186598770	HD 18552	45.05	38.13	6.12	B7IVe
187683138	HD 33656	78.38	38.11	9.29	Be
19704573†	Zeta Tauri	84.41	21.14	4.62	B2 IIIpe
200410503	HD 159845	264.48	-24.97	7.79	B3III
201373582†	HR 2170	84.91	-34.07	5.85	B5Ve
202788979	HIP 2382	7.60	60.17	9.23	B6III

TIC ID	Common Name	RA (deg)	Dec (deg)	T-mag	S-Type
203468988	HD 161004	266.06	-27.46	8.49	B8V
203500116	HIP 91591	280.19	-7.97	9.57	B8V
204191276†	HD 148184	246.76	-18.46	3.88	B2Vne
209330890†	V1448 Aql	288.76	9.81	7.83	Be
213153401†	HD 154538	257.13	-49.47	8.48	B3V
217667184†	HR 6451	260.82	-47.47	5.34	B1V
228199255	hip 93292	285.02	3.32	8.47	B8
230981971†	alf Eri	257.16	-25.56	1.32	B4V(e)
231430254†	HD 159032	263.31	-19.38	9.27	B9IV
232166879	HD 41288	91.06	0.61	8.78	B5V
23459321†	HD 55606	108.39	-2.08	8.94	B0,5Vnnpe
237532447	HD 50087	102.92	0.33	9.05	B8/9III
237840594†	HD 51893	104.81	4.45	9.08	B9V
238771552	HD 6343	16.47	65.97	7.92	B5Vn:e
239103320	HD 37266	84.77	37.98	7.45	Be
239408899†	hip 105741	321.26	44.45	8.22	B1,5V:nnep
239880242	HD 42529	93.17	32.97	8.20	B9V
239968973	HD 254168	94.23	34.24	9.39	Be
240003393	HD 43681	94.75	34.23	9.03	Be
240258004†	HD 204722	322.31	44.34	7.47	B1,5IV:np
240285395	V2163 Cyg	322.50	45.49	6.93	Be
240757326	HR 193	11.18	48.28	4.42	B5IIIe
243647020	HR 5193	193.66	-59.15	2.18	B2Vnpe
24824031	HR 2358	97.21	-7.03	5.49	B3V:nne
250936039	HD 232214	8.30	51.67	7.59	B8e
252414037	HR 1622	67.28	-13.05	5.41	B3Ve
252500679	HR 8731	344.27	48.68	5.22	B4IIIpe
252670277†	HD 218393	346.78	50.19	6.47	B2IIIe+KOII
253212775†	CD-55 4911	195.40	-56.09	9.15	Be
253380837	HD 113573	196.39	-56.85	8.75	B3/5V
25692574	HD 221188	352.40	48.38	8.20	A0
258704817	HD 129954	222.19	-66.59	6.06	B2,5
259463816†	HR 1273	62.17	47.71	3.94	B3Ve
261993378	HR 4897	182.09	-50.72	4.78	B3Vne
262169297†	HD 33357	77.93	42.17	8.77	B1Vne
26432264	HD 18231	44.31	46.02	6.58	B8
264459943	HD 35439	81.19	1.85	4.75	B1Vn
264631173	HD 36012	82.20	2.16	7.44	B2Vne

TIC ID	Common Name	RA (deg)	Dec (deg)	T-mag	S-Type
265911941†	HD 212571	336.32	1.38	4.61	B1III-IVe
266498398	HD 25348	61.09	53.33	8.02	B1Vnnpe
27043894	HD 23478	56.67	32.29	6.91	B3IV
27141005†	HR 1660	76.54	58.97	5.59	B2Ve
271959772†	HD 186485	295.71	42.65	8.53	B9Vne
279192753	HD 628	2.69	58.02	10.46	Be
281047621	HR 1934	76.98	21.70	4.57	B3Ve
281717549	HD 49787	102.48	-5.51	7.60	B1V:ep
283206453	HD 51193	104.08	-3.81	8.22	B1V:nn
28569279	Sheliak	282.52	33.36	6.88	B6-8II
285937814	HR 1087	54.12	48.19	4.24	B5Ve
2940839	HD 35652	81.97	34.78	8.14	B3Vnne
294355648	HR 2198	91.77	-34.31	5.09	B5Vn
29628522†	HD 45871	97.16	-32.37	6.09	B3Ve
296969980	tet Cir	224.18	-62.78	6.45	B2IV/V
304114338	V1931 Cyg	315.30	46.16	5.62	B1Ve
30562668	HD 76838	134.28	-43.26	5.99	B2IV
310852121	HR 8773	345.97	3.82	4.70	B6Ve
311282109	HD 37838	86.08	52.70	8.09	B8
312730071	HD 40254	89.76	31.03	9.37	Be
317958778	HD 209409	330.83	-2.16	4.77	B5V
322060937	V433 Cep	324.24	68.19	8.17	B3V
322104948	HD 306989	175.78	-60.73	10.35	B1.5IIIn
323348984	HD 37330	84.47	0.97	7.53	B5III
324252945	HD 121195	208.97	-61.50	8.99	B8IV(n)
324820890	HIP 108738	330.41	50.17	9.15	Be
326247844	HIP 109113	331.53	49.90	9.61	B1,5V:nne
326999260†	HD 217675	345.48	42.33	7.76	B6IIIpe
32882261	HD 174886	283.31	-10.22	7.55	B3Vne
329947655	HD 187399	297.17	29.40	4.58	B8IIIe
331811163	HD 224559	359.69	46.41	6.94	B4Ven
333670784	HR 4621	158.01	-61.69	2.76	B2Vne
33993533	HR 2249	93.01	16.13	6.04	B2/B3Ve
343908909	HD 186637	296.27	16.29	8.04	B9
354462452	HR 7318	289.43	23.03	5.52	B1IIIn
354770601	HD 54786	107.40	-16.10	9.16	B1/2I(b)
355653322	HR 9076	359.98	-65.58	4.57	B8V
356239023	HD 162732	267.51	48.39	6.05	B6Ve

TIC ID	Common Name	RA (deg)	Dec (deg)	T-mag	S-Type
358499972	HD 39018	87.63	18.03	7.77	B9
364398342	HD 66194	119.71	-60.82	5.93	B2IVn(e)p(Si)
364921141	BD+50 3189	311.29	51.21	9.10	B0,5IV
368237682	MWC 1085	358.05	67.17	9.53	B3:e
368799545	HD 2789	8.01	67.16	7.10	B3Vne
370042412	7 Vul	292.34	20.28	6.45	B5Vn
370259865	QT Ser	277.77	4.63	7.56	B5
377900979†	BD+61 2408	348.87	62.08	8.89	B0IIIpe
377967736	BD+63 1955	348.87	64.27	7.19	B5V
385509348	Electra 17	56.22	24.11	3.85	B6 III
387813185†	HD 200775	315.40	68.16	6.77	B2Ve
394728064	HD 93237	160.46	-79.78	6.01	B5III
399626383†	RX Cas	46.94	67.58	7.68	(B5)+K1III
402978131	HD 5679	15.58	81.88	6.80	G2III:+B8/9
404619905	HR 6712	270.07	4.37	4.93	B2Ve
405216722	HD 60993	114.18	-13.06	9.03	B2II
410193513†	HD 276247	65.07	42.31	9.04	-
410627159	HR 5941	229.63	-47.88	4.83	B5IIIp_sh
411577031	HR 8375	328.88	65.32	5.94	B2Ve
412724758†	HR 6510	262.96	-49.88	8.50	B2Vne
4154938†	HIP 25066	80.49	-2.96	7.13	B3III/IV
42360166	HR 7708	302.36	36.84	5.23	B2.5Ve
424566072	HD 17520	42.81	60.39	7.88	O8V+O9:Ve
425224332	HR 2845	108.70	-26.77	2.99	B8Ve
427396133	HD 37115	83.98	-5.63	7.46	B7Ve
429843636	Trum 37 1513	323.09	59.57	7.58	B5
429863539	HD 43703	94.66	23.01	8.17	B1IVp(e)
431116093	HD 212044	335.09	51.86	7.12	B2ek
434893323	HD 218066	346.01	63.40	7.23	B1,5Vn
441027987†	HR 8260	324.27	-19.47	4.70	B3V
442240473†	HD 84511	145.98	-55.05	8.38	Bp shell
444325059	HD 223924	358.40	56.82	8.14	B1,5V
455463415	HD 135160	229.15	-60.90	6.01	B1/2Vn
460532958	HR 4140	117.02	-25.94	3.32	B4Vne
46247269	LR Gem	93.81	22.30	8.56	Variable
51288359†	HD 151083	251.96	-51.77	8.78	B2Vn
709917565	HD 45725	97.20	-7.03	4.69	B4Veshell

TIC ID	Common Name	RA (deg)	Dec (deg)	T-mag	S-Type
90296023	HD 72754	128.10	-49.60	6.66	B2IIpshe

4.3. Gaia Astrometric Data

The primary goal of the Gaia mission is to perform precise astrometric measurements to create a three-dimensional map of the Milky Way. Gaia measures stellar positions, parallaxes, proper motions, and radial velocities with extreme precision, achieving errors below 10 microarcseconds for the brightest stars (Collaboration, 2021). These high-precision data allow for a comprehensive understanding of stellar dynamics, the structure of the galaxy, and the distribution and evolution of its stellar populations. They are also crucial for investigating complex stellar phenomena such as binary systems, star formation, and overall galacTIC dynamics.

Gaia DR3 (et al., 2023) has proven to be a significant resource for the study of binary star systems. Its precise astrometric measurements enable the detection of small orbital motions even in systems with small angular separations. In addition, the radial velocity measurements, obtained with remarkable precision, are critical for characterizing the orbits of binary stars and determining the masses of their components (Evans, 2021; Gontcharov, 2022). These capabilities allow the identification of new binary systems, including short-period binaries that often exhibit complex dynamical interactions difficult to detect with traditional observational methods.

Moreover, Gaia's ability to measure periodic variations in radial velocities and positional shifts enables the detection of both spectroscopic binaries, where orbital motion induces line shifts, and astrometric binaries, where the orbital motion produces detectable changes in stellar positions (Brown, 2018). For Be stars, combining Gaia astrometric data with spectroscopic observations allows the determination of orbital parameters and provides insights into how companion stars influence the formation and evolution of Be circumstellar disks. Gaia also facilitates the study of long-period binaries, which are often challenging to observe with conventional techniques, thereby expanding our knowledge of more distant Be binary systems, including their ages, metallicities, and locations within the galaxy (Kervella et al., 2019).

Evolutionary Study

The 3DNHtool* is an online platform developed by the Institute for Astronomy and Astrophysics at the University of Tübingen. It is designed to support the analysis of hot stars and compact stellar objects, integrating theoretical stellar atmosphere models and interstellar medium (ISM) data. A key component of the tool is its 3D interstellar extinction map, which allows users to estimate the visual extinction (A_V) along a given line of sight as a function of distance and sky position.

* http://astro.uni-tuebingen.de/nh3d/nhtool

The NHtool provides a user-friendly interface to access a 3D model of interstellar extinction based on observational data from Gaia, 2MASS, and other large-scale photometric surveys. Users can input equatorial (RA, Dec) or GalacTIC (l, b) coordinates, along with a desired distance in parsecs, to retrieve the estimated extinction to that point in the Galaxy. The extinction values are computed from tomographic models of dust distribution in the Milky Way, such as those by Green et al. (2019), which rely on Bayesian inference techniques and stellar photometry. By correcting for A_V, users can recover the intrinsic properties of stellar spectra and compare them accurately with syntheTIC models.

The combination of astrometric and photometric data from the Gaia mission with 3D interstellar extinction maps enables the construction of accurate, reddening-corrected Hertzsprung-Russell diagrams in the form of color-color plots.

To achieve this, extinction values are estimated for each target using its sky position and distance, obtained from Gaia's parallax. The NHtool provides this information by querying 3D dust maps based on multi-survey data (e.g., Green et al. 2019). The estimated extinction can then be used to correct observed Gaia colors, such as $G_{BP} - G_{RP}$ or $G - G_{RP}$, by applying standard extinction laws (e.g., Cardelli et al. 1989).

A typical procedure includes:

1. Selecting a sample of stars from *Gaia* DR2/DR3 with reliable parallaxes and photometry.
2. Obtaining the 3D extinction A_V for each star using the NHtool or a comparable model.
3. Calculating the color excess using extinction coefficients, such as:

$$E(G_{BP} - G_{RP}) = k \cdot A_V, \tag{4.1}$$

   where k is the color-specific coefficient derived from the extinction curve.

4. Correcting the colors to their intrinsic values:

$$(G_{BP} - G_{RP})_0 = (G_{BP} - G_{RP})_{\text{obs}} - E(G_{BP} - G_{RP}). \tag{4.2}$$

5. Plotting the corrected values to obtain an HR diagram free from reddening effects.

This method is especially useful in regions near the GalacTIC plane, where extinction varies significantly with distance and direction. Reddening-corrected color–color diagrams allow clearer identification of stellar populations and more reliable comparison with theoretical isochrones.

4.4. Photometry

Photometric monitoring is a powerful tool to investigate variability in Be stars, which often display complex and multi-scale brightness changes arising from their circumstellar disks, stellar

pulsations, and binarity (Rivinius et al., 2013; Labadie-Bartz et al., 2017). The analysis of light curves, particularly those obtained from high-cadence space missions, enables the detection of periodic and quasi-periodic signals that can be interpreted in terms of physical mechanisms such as non-radial pulsations, disk oscillations, and orbital modulation.

Be stars are known to exhibit several types of photometric variability. Short-term variability (typically on timescales of hours to days) is commonly attributed to stellar pulsations, often non-radial g-modes, as shown by space photometry from missions like CoRoT, Kepler, and TESS (Labadie-Bartz, 2018; Baade, 2016). Medium- and long-term variability can arise from changes in the circumstellar disk (e.g., growth or dissipation events), which cause secular trends or outbursts in brightness.

In binary systems, photometric light curves can also reveal eclipses, ellipsoidal modulations, or reflection effects that trace the orbital configuration and interaction between the components (Koubský et al., 2006; Panoglou, 2018). Phase-folded light curves can be used to determine orbital periods and constrain the geometry of the systems. Additionally, periodic dips or brightness modulations can signal the presence of a companion or the precession of a non-axisymmetric disk structure.

The availability of long-term, high-precision photometry from surveys like ASAS-SN, OGLE, and TESS has revolutionized the time-domain study of Be stars, allowing researchers to build statistical samples, perform period analysis using tools such as the Lomb-Scargle periodogram (Scargle, 1982; Zechmeister and Kürster, 2009) or Fourier transforms, and correlate photometric variability with spectroscopic indicators (Labadie-Bartz et al., 2017; Jayasinghe, 2020).

Therefore, photometry and light curve analysis are indispensable for diagnosing variability mechanisms in Be stars and for identifying and characterizing Be binaries.

4.4.1. TESS

The Transiting Exoplanet Survey Satellite (TESS) was designed primarily to discover exoplanets by detecting their transits across bright nearby stars (Ricker, 2015). However, the mission's all-sky coverage and continuous, high-cadence photometry of millions of stars have significantly benefited time-domain stellar astrophysics. With a variable cadence (later extended to 20 seconds for selected targets), TESS enables the precise monitoring of stellar brightness variations, making it a powerful tool for detecting binary systems and investigating stellar pulsations, rotation, and disk variability.

Launched in 2018 by NASA, its mission has since broadened to encompass a wide range of time-domain astrophysical phenomena, including the variability of pulsating stars, classical Be stars, and binary systems (Southworth and Bowman, 2022; Ramsay et al., 2022; Burssens et al., 2020). With uninterrupted, high-cadence observations and no atmospheric interference, TESS offers a uniquely powerful dataset for the study of stellar variability.

TESS has enabled the detection and characterization of a large number of eclipsing and non-

eclipsing binary systems, thanks to its high photometric precision (Prša, 2022). The mission allows the identification of subtle periodic brightness variations caused by eclipses, ellipsoidal modulation, and reflection effects in close binaries, which are crucial for determining orbital parameters, stellar radii, and inclinations.

Using the TESS Input Catalog (TIC) and resources such as the TESS Eclipsing Binary Catalog (TEBC), researchers can analyze thousands of light curves to discover new binaries or study known systems in unprecedented detail. When combined with spectroscopic follow-up from Gaia or ground-based facilities, TESS photometry enables accurate mass and radius determinations of binary components (Southworth and Bowman, 2022). Continuous high-cadence monitoring also allows the detection of short-period pulsations and long-term disk-related variability in Be stars (Labadie-Bartz et al., 2017).

TESS has revealed multi-periodic variability in many Be stars, including non-radial pulsations, disk oscillations, and episodic outbursts. These observations provide insights into disk formation and maintenance mechanisms, such as angular momentum transport and mass ejection processes (Rivinius et al., 2013). The combination of TESS photometry with interferometric and spectroscopic data helps constrain the geometry and dynamics of Be star disks, particularly in binary systems where companion interactions can drive disk truncation and precession (Okazaki and Negueruela, 2001b). Although initially designed for exoplanet searches, TESS has become a transformative tool for stellar astrophysics, expanding our understanding of stellar variability, binary interactions, and the dynamics of circumstellar disks in rapidly rotating stars.

In this work, TESS photometric data were used to investigate a sample of classical Be stars in binary systems, as part of a larger effort to characterize their light variations and dynamical properties. Each target was observed in one or more sectors, with cadence modes (usually 475 or 158 seconds) depending on the mission configuration during the respective observational windows.

The extraction of light curves from the TESS Full-Frame Images (FFIs) was performed using the `TESScut` tool (Brasseur et al., 2019), which allows for the download of cutouts centered on the coordinates of each star. For each object, a Target Pixel File (TPF) was defined by selecting a square region (typically 20×20 pixels) around its position, ensuring inclusion of the target flux while minimizing contamination from nearby sources.

Subsequently, light curves were generated using the `Lightkurve` Python package (Collaboration et al., 2018). Aperture masks were automatically defined for each TPF by applying a threshold criterion, commonly set at 3σ above the median background level, to select pixels most representative of the target's flux. Background subtraction was carried out using surrounding pixels to remove residual sky.

This approach yielded normalized light curves that trace the intrinsic variability of the Be star sample with high precision. The same procedure was systematically applied to all targets in the catalog to ensure methodological consistency. Figures 4.1 and 4.2 illustrate an example of the TPF aperture mask and resulting light curves (in BTJD time format), respectively. A

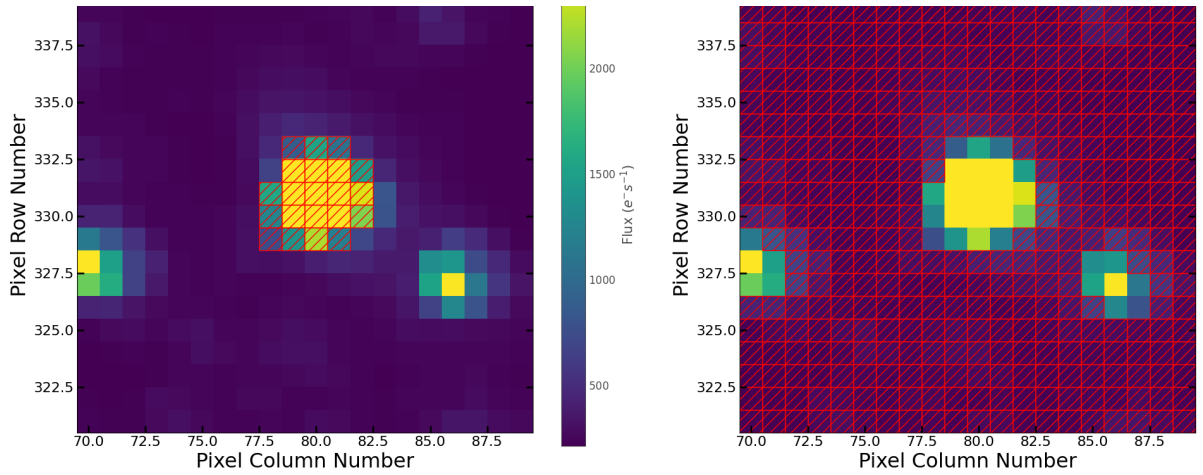

Figure 4.1: The figure shows the aperture mask used for extracting the target flux (left panel) and the background flux (right panel) for TIC 124407255.

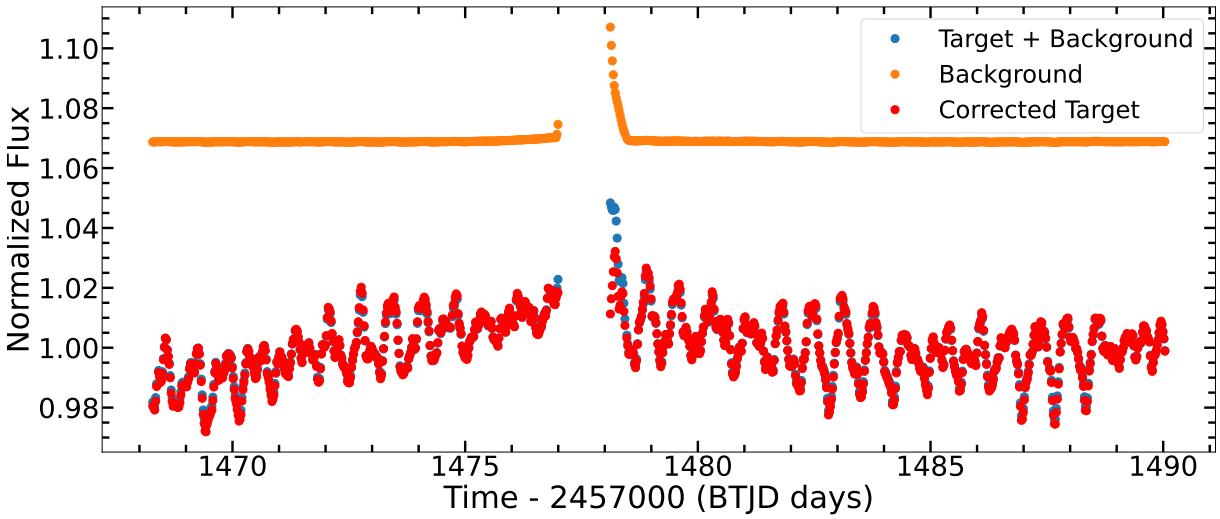

Figure 4.2: Light curve of TIC 124407255 observed by TESS in flux at BTJD (BJD-2,457,000).

systematic gap of approximately one day was present in the observations. This interval, along with the approximate duration of each sector's observation period (~30 days), was removed from the analysis to avoid introducing artificial signals in the time-series data.

Within the scope of the TESS General Investigator (GI) program, our team has had proposals approved in Cycle 5, 6 and 7[†], demonstrating the scientific relevance of our work, allowing some targets to be observed at a higher cadence, every 120 s or 20 s.

The Cycle 6 of the TESS program, starting in October 2023 and covering sectors 70 to 83, underwent a competitive selection process with over 100 proposals submitted across stellar astrophysics, exoplanets, and other fields. Our project was approved to collect high-quality photometric data, enabling detailed studies of Be stars in binary systems. The Cycle 7, which began in October 2024 and is scheduled through September 2025, covering sectors 84 to 96, also approved our project, extending the monitoring and temporal sampling of the targets. This

[†] https://heasarc.gsfc.nasa.gov/docs/tess/approved-programs.html

continuity allows for longer time series, essential for the analysis of periodic and transient variability. Additionally, we already have approved a proposal for Cycle 8 of the TESS program. With the continuation of the program, we expect to further deepen the study of the physics of Be stars in binary systems using advanced photometric and spectroscopic modeling techniques.

These approved projects are part of a continuous effort to exploit TESS data, complemented by ground- and space-based observations, consolidating a robust basis for the physical and dynamical characterization of the studied systems. The list of approved targets in the projects can be seen in the Ap. B.

4.5. Spectroscopy

Spectroscopic monitoring is essential for studying Be stars, particularly to identify binarity and probe circumstellar disk dynamics. High-resolution, multi-epoch spectroscopy allows the measurement of radial velocity (RV) variations, although disk emission can complicate these measurements. RV curves from absorption or less disk-affected lines (e.g., He,i, metallic lines) can reveal orbital motion and enable the determination of orbital parameters and companion masses. Spectroscopy is also crucial for deriving fundamental stellar parameters, such as spectral type, effective temperature, and projected rotational velocity.

Spectral line profile variability, including V/R ratio changes and phase-dependent features such as shell profiles or moving subpeaks, provides additional insight into disk structure and interactions with companions, especially in eccentric binaries.

Modern spectroscopic surveys using instruments like FEROS, HARPS, and telescopes at OPD and SOAR have greatly expanded time-resolved datasets for Be stars. These data are crucial for long-term RV monitoring, multi-wavelength modeling, and the determination of stellar parameters, making spectroscopy a cornerstone for identifying binarity and understanding the interplay between the star, disk, and companion in Be systems.

4.5.1. BeSS

The Be Star Spectra Database (BeSS), initiated in 2007, addresses this need by compiling and making available thousands of spectra of Be stars collected from both professional observatories and an active network of skilled amateur astronomers (Neiner et al., 2011; Neiner, 2018). BeSS contains spectra for over 2,000 Be stars, primarily focused on the Hα region, with spectral resolution typically ranging from $R \sim 1000$ to $R \sim 20000$. The database includes metadata such as observing conditions, instrument specifications, and cross-identifications with catalogs like SIMBAD and Gaia DR3.

The BeSS web interface allows users to search for spectra by object name, coordinates, date range, or specific spectral features. Most of the data are publicly available and regularly updated, which facilitates comparative studies and rapid follow-up of transient phenomena.

The BeSS database plays a critical role in several areas of Be star research:

- Disk Variability: By compiling multi-epoch Hα profiles, BeSS enables the tracking of disk build-up and dissipation cycles, as well as the detection of V/R variability linked to global disk oscillations (Rivinius et al., 2013).
- Binarity Detection: Long-term radial velocity variations or periodic changes in line profiles, identifiable in BeSS data, can signal the presence of binary companions. These signatures are essential for identifying Be binaries and constraining their orbital parameters (Klement, 2015).
- Transient Events: BeSS provides real-time spectroscopic alerts and light curve data that support time-domain studies and the rapid follow-up of outbursts or shell events (Baade, 2016).
- Amateur-Professional Collaboration: The synergy between amateur and professional observers extends observational coverage and enhances the temporal sampling of targets, which is crucial for dynamic systems like Be stars (Neiner, 2018).

The BeSS catalog is a powerful tool for studying the temporal evolution of Be stars and diagnosing binarity in emission-line B stars. Its comprehensive and collaborative nature makes it particularly well-suited for multi-epoch analyses and for complementing large-scale photometric surveys and spectroscopic missions such as Gaia and TESS. In the context of Be star binaries, BeSS remains an indispensable resource for spectroscopic diagnostics across timescales.

All targets were queried in the BeSS database, which provides spectra obtained with a variety of instruments and specifications. The dataset includes observations with different spectral resolutions and wavelength coverages. Details of the spectra used for each target, including instrument, resolution, and observing conditions, are presented in Appendix C.

4.5.2. HERMES and SOAR observations of V1371 Tau

Our investigation boasts extensive spectral coverage of V1371 Tau, mainly the visible (~0.40 - 0.90 μm) regions. All observation dates were converted to Barycentric TESS Julian Dates to maintain consistency throughout the analysis. A summary of spectroscopic observations is presented in Table 4.2.

High-resolution spectroscopic observations were obtained using the HERMES spectrograph, a fibre-fed instrument on the 1.2m Mercator telescope at La Palma Observatory. This spectrograph offers a resolving power of R~85,000 and covers the wavelength range of ~4000-9000 Å. We utilized 12 epochs of HERMES-reduced data collected between November 2020 and November 2023. Each epoch comprised a spectrum with an exposure time of 386 seconds. These observations were utilized to create the radial velocity curve of the eclipsing binary components of V1371 Tau.

Table 4.2: Summary of spectroscopic observations of V1371 Tau.

Date	Source (qty.)	t_{exp} (sec.)	R ($\lambda/\Delta\lambda$)
2020/11/18 to 2023/11/19	HERMES (12)	386	85,000
2023/02/11 and 2023/11/25	Goodman/SOAR (2)	180	1,400–14,000
2009/02/21 to 2024/09/10	BeSS Database (22)	Var.	3,400-18,000

Notes: Dates are given in YYYY/MM/DD format.

To classify the spectral types of the V1371 Tau system, we utilized data from the Goodman Spectrograph (Clemens et al., 2004; Crain et al., 2004) mounted on the 4.1m SOAR telescope. Two observations were made with a spectral resolution ranging from R=1,400-14,000, the Goodman data was reduced using *The Goodman Pipeline*, a Python-based software for producing wavelength-calibrated, science-ready, one-dimensional spectra. We used the Python tool `HANDY` for normalization theses spectrum.

4.6. Determination of Stellar Parameters

4.6.1. Linear Ephemeris and Orbital Characteristics

Using photometric data from the TESS mission, we accurately determined the ephemeris of the inner eclipsing binary system under analysis. To avoid ambiguity, we define the primary component as the star being eclipsed during the deepest minimum in the light curve, which corresponds to orbital phase zero.

To estimate the orbital period, we modeled two consecutive primary eclipses using a pair of Gaussian functions. The parameters of these Gaussians were inferred using the Markov Chain Monte Carlo method, implemented via the `emcee` package in Python (Foreman-Mackey et al., 2013). From the mid-times of these primary eclipses, we derived a linear ephemeris, using the mid-time of the first eclipse as the reference epoch. The time difference between the two eclipses yields the orbital period of the system. The linear ephemeris can be written as:

$$T(\mathrm{BTJD}) = T_0 + P \times E\,, \tag{4.3}$$

where T_0 is the reference mid-time of the primary eclipse, P is the orbital period, E is the orbital cycle number, and BTJD (BJD - 2,457,000) is the time format adopted by TESS. The results were also validated through a rapid frequency analysis with the Lomb-Scargle.

The orbital period of a binary system can be determined from both photometric and spectroscopic data. Radial velocity curves, which trace the periodic Doppler shifts of spectral lines,

allow the orbital period to be derived by fitting Keplerian or sinusoidal models to high-resolution time-series spectra. The interval between successive maxima or minima in the radial velocity directly corresponds to the orbital period, and consistency with periods obtained from the light curve provides strong confirmation of the orbital solution. Analysis of the light curve alone also yields key orbital characteristics. The time between consecutive primary eclipses gives the orbital period, while the depth and duration of eclipses inform the flux ratio, relative temperatures, and apparent sizes of the stars. The presence and shape of eclipses indicate a high orbital inclination, close to 90°, with partial or total eclipses providing further constraints on this inclination.

In systems with eccentric orbits, the light curve can reveal asymmetries in the spacing between primary and secondary eclipses. For a circular orbit, the secondary eclipse is expected to occur exactly at phase 0.5, any significant deviation from this phase indicates eccentricity. A quick estimate of the eccentricity e can be made using the approximate formula:

$$e\,cos\omega \approx \frac{\pi}{2}\,(\phi_s - 0.5)\ , \tag{4.4}$$

where ϕ_s is the phase of the secondary eclipse and ω is the argument of periastron. This relation assumes moderate eccentricity and well-defined eclipses and is commonly referenced in studies of eclipsing binaries, as discussed by Kopal (1959b) and later by Sterne (1940).

For example, if the secondary eclipse occurs at phase $\phi_s = 0.35$, applying the formula yields:

$$ecos\omega \approx \frac{\pi}{2}(0.35 - 0.5) = \frac{\pi}{2} \times (-0.15) \approx -0.2356\,. \tag{4.5}$$

This negative value indicates that periastron occurs before inferior conjunction. Although the equation only provides $e\,cos\omega$, it already suggests an eccentricity of at least $e \gtrsim 0.24$, depending on the value of ω. With an estimated value for ω, or assuming typical values (e.g., $\omega \sim 90°$ for largely displaced eclipses), one can obtain an initial estimate of e.

4.6.2. Wilson–Devinney code

A special edition celebrating the 50th anniversary (completed in 2021) of the most referenced binary system modeling code in the literature was published in 2022 by Kallrath (2022). It provides a historical and scientific review of the astrophysical capabilities of the algorithm known as the Wilson–Devinney (WD) Code, named after researchers Robert Wilson and Edward J. Devinney, who published their first paper on binary system modeling in 1971 (Wilson and Devinney, 1971).

The WD code is a widely used computational tool for modeling eclipsing binary systems, allowing the analysis of light curves and, optionally, radial velocity curves. It enables the determination of fundamental stellar parameters, such as masses, radii, effective temperatures, orbital inclination, eccentricity, mass ratio, and Roche lobe filling, based on photometric and

spectroscopic data.

The code accounts for key physical effects in binaries, including tidal distortion, reflection, eclipses, and synchronous rotation, allowing modeling of detached, semi-detached, and contact systems. Users provide initial estimates of orbital and stellar parameters, light curves, and radial velocities, and the code iteratively adjusts the model to fit observations using techniques like least squares minimization.

Modern interfaces like PHOEBE, based on the WD code, provide user-friendly, graphical tools for real-time visualization of stellar geometry, light and RV curves, and tidal distortion, facilitating accurate modeling of complex binary systems for both researchers and students.

In short, the Wilson–Devinney Code is one of the most powerful and consolidated tools for studying stars in binary systems. It allows obtaining detailed physical parameters, analyzing the interaction between the system's components, and modeling light curves with a high level of precision, being essential for research into stellar evolution, orbital dynamics, and multiple star physics.

Here's a simplified version of the Wilson–Devinney modes:

- Mode -1: For X-ray binaries; only one star (usually a compact object) is visible.
- Mode 0: General mode; no restrictions. Can be used for any system.
- Mode 1: Overcontact binaries (super-contact); both stars share a common envelope with equal surface potentials.
- Mode 2: Detached binaries; both stars are inside their Roche lobes (no mass transfer).
- Mode 3: Contact binaries; both stars fill their Roche lobes and share a common envelope.
- Mode 4: Semi-detached system where the primary star fills its Roche lobe.
- Mode 5: Semi-detached system where the secondary star fills its Roche lobe.

In table 4.3, the main physical parameters that can be determined for binary systems using the WD code are summarized, depending on the type of observation available: photometry, spectroscopy, or a combination of both.

Table 4.3: Summary of binary system parameters derivable with the Wilson–Devinney code, depending on the available observations.

Parameter	**Photometry Only**	**Spectroscopy Only**	**Photometry + Spectroscopy**
Orbital period (P)	✓	✓	✓
Time of periastron (T_0) or eclipse (T_{min})	✓	✓	✓
Eccentricity (e)	✓(if detectable)	✓	✓
Argument of periastron (ω)	✓(with high precision data)	✓	✓
Inclination (i)	✓	—	✓
Mass ratio ($q = M_2/M_1$)	—	✓(for double-lined binaries)	✓
Semi-major axis (a)	—	✓(from RV amplitude)	✓
Systemic velocity (γ)	—	✓	✓
Component temperatures (T_1, T_2)	✓(estimated)	—	✓
Stellar radii (R_1, R_2)	✓(relative to a)	—	✓
Stellar masses (M_1, M_2)	—	✓(if i is known)	✓
Luminosity ratio (L_2/L_1)	✓	—	✓
Third light (L_3)	✓(if present)	—	✓
Reflection effects	✓	—	✓
Gravity darkening coefficients	✓	—	✓

The version of the WD code used in this work is the 2015 release, which incorporates several improvements over previous versions, including native support for multiple photometric filters, such as the TESS band, which is included in our analysis.

We opted to use the LC module of the WD code to generate syntheTIC light and radial velocity curves based on an initial set of physical and orbital parameters for eclipsing binary systems. This approach allows us to avoid relying on the internal minimization algorithm of the DC (Differential Corrections) module, which is less flexible. Instead, we couple the LC module with a more robust and externally implemented optimization method.

To generate syntheTIC models, the LC program requires several initial parameters, such as: (i) the configuration of the eclipsing binary system, (ii) the effective temperatures of both components, (iii) the mass ratio, (iv) the orbital inclination, (v) the eccentricity, (vi) the distance to the system, (vii) the surface potentials, and (viii) the limb-darkening coefficients for both stars.

Based on general spectral classification, we assume that the components of the system share physical properties consistent with B-type stars. Given this, it is reasonable to adopt radiative atmospheres for all components. Consequently, the gravity darkening exponents ($g_a = g_b$) and bolometric albedos ($A_a = A_b$) were fixed to the standard values for hot stars, namely 1.00 and 0.50, respectively (Claret and Bloemen, 2011). For the treatment of limb darkening, we adopted the square-root law in the WD code, as recommended by Van Hamme (1993).

Using this information, the LC program produces syntheTIC light and radial velocity curves that are then compared with the observed data. Since the initial model is unlikely to fit the data perfectly, we apply a statistical method to evaluate and optimize the fit.

For this purpose, we adopt the MCMC method, a stochasTIC sampling technique widely used to explore the posterior probability distributions of model parameters. Initially, we implemented the Metropolis–Hastings version of MCMC using CL Script, a native language in the IRAF environment, integrated with the WD code executable within IRAF. Given the growing adoption of the `Python` programming language in the astrophysics community, we migrated the execution of the WD code to a Python-based environment. This enabled us to integrate the WD code with the `emcee` package Foreman-Mackey et al. (2013), developed at the Massachusetts Institute of Technology (MIT). Written in Python, `emcee` is a robust and modular implementation of MCMC sampling that has become widely used and regularly updated in astrophysics research.

Our Python implementation interfaces directly with the original WD code written in `Fortran`[‡], ensuring computational efficiency for the most demanding calculations. The posterior probability distributions are computed using `emcee`, and their visualizations are generated with the Python package `Corner`, which provides multidimensional projections of the sampled parameters.

During execution, the output files from the WD code, containing light curves in various

[‡] Fortran is a compiled, high-performance language suitable for intensive numerical computations.

filters (including the TESS band) and radial velocity curves, are processed in Python. The `emcee` package then generates chains of models with different combinations of parameters, systematically exploring the solution space.

The selection of the best-fit model is based on the minimization of a chi-square merit function, defined as:

$$\chi^2 = \sum_{i=1}^{N} \frac{(O_i - E_i)^2}{\sigma_i^2}\,, \tag{4.6}$$

where O_i represents the observed data, E_i the model prediction, σ_i the associated uncertainty, and N the number of data points. The χ^2 function gives more weight to points with lower observational uncertainties, and the model with the lowest χ^2 is considered the best fit to the observed light and radial velocity curves of the binary system W36.

The `emcee` sampler operates based on the likelihood function, which quantifies the probability that a given model reproduces the observed data, assuming that the observational errors are independent and Gaussian. The log-likelihood function used is given by:

$$\ln l(y|x,\sigma,f) = -\frac{1}{2}\sum_{n}\left[\frac{(y_n - x_n)^2}{s_n^2} + \ln(2\pi s_n^2)\right], \tag{4.7}$$

where:

$$s_n^2 = \sigma_n^2 + x_n^2 f^2\,, \tag{4.8}$$

in which y_n is the observed data point (such as photometric flux or radial velocities), x_n is the model prediction, σ_n is the observational uncertainty, and f is a free parameter accounting for additional model uncertainties.

Thus, by maximizing the likelihood function (or equivalently minimizing the χ^2), we determine the most probable model, i.e., the statistically best fit among all those explored.

For the light curve of the eclipsing binary systems under study, we consider the free parameters to be the mass ratio q, inclination i, gravitational potentials Ω_1 and Ω_2, and the temperature of the secondary component T_2. The log-likelihood function used to compare the syntheTIC model predictions to the observed data can be expressed as:

$$\begin{aligned}\ln l(y_n|x_n(\mathrm{q},\mathrm{i},\Omega_1,\Omega_2,\mathrm{T}_2)) = -\frac{1}{2}\sum_{\mathrm{n}=1}^{\mathrm{N}}\Bigg[&\frac{(y_n - x_n(\mathrm{q},\mathrm{i},\Omega_1,\Omega_2,\mathrm{T}_2))^2}{\sigma_n^2 + f^2 x_n(\mathrm{q},\mathrm{i},\Omega_1,\Omega_2,\mathrm{T}_2)^2} \\ &+ \ln\left(2\pi\left[\sigma_n^2 + f^2 x_n(\mathrm{q},\mathrm{i},\Omega_1,\Omega_2,\mathrm{T}_2)^2\right]\right)\Bigg],\end{aligned} \tag{4.9}$$

where $x_n(\mathrm{q},\mathrm{i},\Omega_1,\Omega_2,\mathrm{T}_2)$ are the model predictions for each observation n, and N is the total number of observations. This likelihood function forms the basis for parameter estimation methods such as MCMC, allowing us to explore the parameter space and find the best-fitting model to the observed data. It is important to emphasize that, in light curve modeling, the mass ratio parameter, although included as a variable in the probability analysis, is not a reliable

indicator for determining stellar masses on its own. While the mass ratio does influence the morphology of the light curve, its true physical value is fundamentally constrained by the radial velocity curve. Therefore, accurate determination of the mass ratio requires spectroscopic measurements, as photometry alone cannot resolve the mass degeneracy inherent in light curve fitting.

4.6.3. Characterization of Be Stars

We will analyze the light curves and the residuals of the modelled light curves from eclipsing binaries in order to investigate possible signatures of stellar pulsations or rotational modulation. For this analysis, we applied Lomb-Scargle periodograms in combination with the iterative prewhitening method described by Degroote et al. (2009), aiming to extract statistically significant periodicities from the light curve residuals.

The prewhitening technique operates by successively identifying and fitting dominant frequencies using a non-linear least-squares procedure. At each step, the current and previously identified frequencies are jointly fitted to the original light curve, following the methodology outlined in Burssens et al. (2019). This iterative process continues until the signal-to-noise ratio (S/N) of the next peak falls below the adopted threshold (S/N<4), ensuring that only statistically meaningful frequencies are retained.

The analysis of photometric variability in classical Be stars based on TESS observations did by Labadie-Bartz et al. (2022) reveals a remarkable richness in periodic behavior across the population. Nearly all Be stars show significant variability, with timescales ranging from tens of minutes to several days. A prominent feature among these stars is the presence of multiple periodic signals, particularly in the frequency range between approximately 0.5 and 4 d^{-1}. These signals often manifest as distinct groups of closely spaced frequencies, commonly referred to as frequency groups, which are detected in about 87% of the sample.

In particular, early-type Be stars that undergo brightening episodes, typically associated with mass-ejection events, show strong connections with these frequency groups. Among the 18% of the total sample (or 31% of early-type Be stars) exhibiting such outbursts, all present at least one frequency group, and 83% display a temporary enhancement in the amplitude of at least one group during these events.

The overall frequency behavior observed in the TESS sample of 430 Be stars can be classified into several distinct groups (Labadie-Bartz et al., 2022):

- Intermediate-frequency groups (0.5–4 d^{-1}): Found in nearly all Be stars, often as multiple closely spaced frequencies. This is the most common type of variability, present in 87% of the stars.

- Long-term trends (timescales >0.5 d^{-1}): Dominant in about 34% of the sample, these modulations may arise from large-scale disk structures or rotational effects.

- StochasTIC low-frequency signals: Observed in roughly 25% of the stars, often lacking coherent periodicity and displaying variable intensity.

- High-frequency signals ($6 < f < 15\,d^{-1}$): Present in approximately 15% of the sample, these are most likely associated with p-mode pulsations.

- Very high-frequency signals ($f > 15\,d^{-1}$): Detected in rare cases (~3%), extending beyond the classical p-mode regime and potentially linked to unexplored physical processes.

These results provide a detailed statistical view of the variability patterns in Be stars and serve as a foundation for selecting targets with coherent periodic behavior suitable for further asteroseismic and disk-evolution modeling efforts.

Building upon the comprehensive variability classification of classical Be stars provided by Labadie-Bartz et al. (2022), our study seeks to further refine the understanding of photometric behavior by focusing specifically on Be stars in binary systems. In addition to characterizing the presence and structure of frequency groups, long-term trends, stochasTIC signatures, and pulsational regimes, already identified in the broader TESS sample, we propose a systemaTIC separation of the frequency content into groups components based on their physical origin and spectral frequency characteristics.

These are categorized into the following groups:

- Intermediate-frequency groups: Frequencies in the range of 0.5 to $4\,d^{-1}$, often appearing as multiple coherent signals or frequency groups. These are typically associated with non-radial pulsations and dominate the variability spectrum of many Be stars. In binary systems, identifying these components is crucial for understanding the internal structure and potential mode coupling due to tidal interactions.

- High-frequency signals: Frequencies above approximately $4\,d^{-1}$, frequently accompanied by harmonic characteristics or beat patterns. These signals are interpreted as rotational modulation,, possibly due to surface inhomogeneities, magneTIC spots, or large-scale disk asymmetries. The separation from pulsational signatures in this frequency regime is non-trivial and requires detailed prewhitening and phase analysis.

- Long-term trends: Low-frequency signals below $0.5\,d^{-1}$, often quasi-periodic or transient in nature. These components may reflect the dynamical response of the circumstellar disk to outbursts or cyclic mass-loss processes. Their characterization is essential for connecting photometric behavior with disk-feeding episodes in Be stars, particularly under the influence of binarity.

By explicitly classifying the observed frequency content into these categories, our methodology enables a clearer interpretation of the variability mechanisms at play in Be binary systems.

It also provides a robust framework for comparing isolated Be stars with those in binaries and evaluating the influence of companions on pulsation, rotation, and circumstellar activity.

In the context of stellar pulsations, mode coupling refers to the interaction between different oscillation modes within a star, resulting in energy transfer, frequency mixing, or the generation of new oscillatory components. This phenomenon is especially relevant in rapidly rotating stars like Be stars, where rotation, binarity, and circumstellar environments introduce significant nonlinearities into the system.

Several types of coupling mechanisms may affect the observed frequency spectrum of Be stars:

- Nonlinear Mode Coupling: Intrinsic pulsation modes interact nonlinearly, producing combination frequencies of the form

$$f_{\text{new}} = f_1 \pm f_2, \tag{4.10}$$

  where f_1 and f_2 are parent frequencies. These are not independent modes, but products of mode interactions. Common in δ Scuti and SPB stars, and also suspected in Be stars (Dziembowski, 1982).

- Pulsation–Rotation Coupling: Rapid rotation alters pulsation frequencies via Coriolis and centrifugal forces, causing rotational splitting and shifts in observed frequencies. This can lead to multiplets and apparent harmonics (Kurtz et al., 2015).

- Pulsation–Disk Interaction: In Be stars, pulsations can modulate mass loss and interact with the circumstellar disk, potentially producing periodic variability, harmonics, or long-term trends (Rivinius et al., 2013).

- Binary-Induced Coupling: In binary systems, tidal forces and stellar deformation can perturb pulsations, leading to harmonics, subharmonics, or resonant modes tied to the orbital frequency.

The identification of coupled frequencies, particularly harmonics and combination terms, provides key insights into the internal and external dynamics of Be stars. Mode coupling may indicate:

- Nonlinear behavior in the pulsation regime;

- The influence of rapid rotation on mode geometry;

- The modulation of mass-loss events feeding the circumstellar disk;

- Resonant interactions in binary systems.

Analysis and Identification of Harmonic Orders in the Principal Frequencies

To understand the spectral structure of the frequencies extracted from the light curves, a detailed analysis was performed to identify the presence of harmonics among the principal components. The identification of harmonics is essential to distinguish true pulsation modes from integer multiples of fundamental frequencies, thereby avoiding misinterpretations in the study of stellar variability.

Consider a set of N principal frequencies f_i, with $i = 1, 2, \ldots, N$, obtained from Fourier analysis. For each pair of frequencies f_i and f_j (with $i \neq j$), the ratio is calculated as

$$R_{ij} = \frac{f_i}{f_j}\,. \tag{4.11}$$

If this ratio is close to an integer n, that is, it satisfies the condition

$$|R_{ij} - n| < \varepsilon\,, \tag{4.12}$$

where ε is a tolerance parameter that allows small deviations due to noise or resolution limits (in this case, $\varepsilon = 0.02$), then f_i is considered a harmonic of order n of the base frequency f_j.

The integer n is determined by rounding

$$n = \text{round}(R_{ij})\,, \tag{4.13}$$

with the additional restriction $n > 1$, since multiples of order 1 indicate identical frequencies rather than harmonics. Thus, each frequency can be classified as harmonic or non-harmonic based on the existence of a frequency f_j satisfying the above relation. The algorithm selects, for each frequency, the smallest harmonic order detected, ensuring the identification of the most probable and physically meaningful harmonic. Furthermore, an upper limit on the harmonic order was established, $n \leq 10$, because harmonics of an order greater than 10 are uncommon and often indicate artifacts or spurious components. Frequencies with harmonic orders above this threshold are excluded from graphical and quantitative analyses.

In summary, the harmonic detection methodology, formalized by the relation

$$\text{harmonic if} \quad \min_{j \neq i} \left| \frac{f_i}{f_j} - n \right| < \varepsilon, \quad n \in \mathbb{Z}^+, \quad 1 < n \leq 10\,, \tag{4.14}$$

allows for robust identification of integer relations between frequencies, facilitating the classification and interpretation of the physical processes governing the observed variability in the studied objects.

5 Results and Discussion

After the photometric and spectroscopic data reduction, it was necessary to establish a systematic sequence of analyses to achieve the main goals of this work: the characterization of Be stars in binary systems, carried out following the methodology described in Chapter 4. These goals include the determination of the physical and orbital parameters of the systems, the frequency analysis of light curves, and the subsequent interpretation of these results within the broader context of the Be star population. These steps are detailed below, along with their corresponding results.

5.1. Be Binary Systems Sample Analysis

5.1.1. Confirmation of Classical Be Stars in Binary Systems

To perform a systematic classification of the target list, a multi-step methodology was adopted to ensure the reliability and scientific robustness of the final sample. The primary objective was twofold: (i) to confirm the binary nature of each system, excluding single stars and higher-order multiples, and (ii) to verify the presence of a classical Be star component through spectroscopic signatures.

Initially, a thorough literature review was conducted to gather prior knowledge about each target system. This included cross-referencing existing catalogs and published studies to identify which objects had already been reported as binary systems and/or classified as Be stars. This step was crucial for establishing a foundational understanding of the nature of each target and for guiding the subsequent analyses.

Following this, a visual inspection and analysis of the available light curves were performed in order to detect photometric variability indicative of binarity, such as eclipses, ellipsoidal modulation, or periodic outbursts. In parallel, spectroscopic data, when available, were examined to identify radial velocity variations or composite line profiles that might suggest the presence of two stellar components. These observational diagnostics provided independent confirmation of

binarity and helped to exclude systems that did not meet the required criteria.

To assess whether each binary system contained a classical Be star, spectroscopic analysis focused on the identification of emission lines typically associated with these stars. Particular attention was given to the presence of Balmer lines in emission, especially Hα, as well as potential HeI emission features. For this purpose, the BeSS catalog was used as a key reference.

By combining insights from the literature, photometric light curve analysis, and spectroscopic diagnostics, including the consultation of the BeSS catalog, this comprehensive approach ensured that the final sample consisted exclusively of binary systems containing at least one classical Be star. Such a refined selection is essential for the subsequent stages of the study, which aim to perform a detailed physical characterization of these systems and their evolutionary contexts. From the master list of 158 targets, we were able to confirm that:

- 50 systems were classified as Be binaries, among which 02 exhibit eclipsing behavior.
- 66 systems are binary systems without a Be star component, often showing signs of contact or mass transfer, which may imitate the characteristics of Be binaries and thus represent false positives.
- 37 systems were identified as non-binaries, consisting either of single stars or higher-order multiple systems, and were excluded from the target sample.
- 05 systems lack sufficient observational data (photometric and/or spectroscopic) to allow a reliable preliminary classification at this stage.

The light curve and spectrum of the entire sample are summarized individually in Ap. C, and the systems classified as Be binaries were previously highlighted in table 4.1. In addition to these, we draw special attention to the V1371 Tau system. Despite being formally a hierarchical triple system, its configuration allows the components to be interpreted as two interacting binary pairs, which aligns with the criteria adopted in this study.

To analyze the angular distribution of Be stars in binary systems compiled in the catalog of this thesis, a `Aitoff` projection was employed and can be seen in Fig. 5.1. Prasow-Émond et al. (2024) use a similar procedure to display the position of the 14 observed x-ray binary targets onto the sky. It also indicates the distance from the observer (in kpc) and, if known, the nature of the system's compact object. This projection is widely used in astronomy to represent data distributed across the entire celestial sphere, offering a continuous two-dimensional visualization of equatorial coordinates (right ascension and declination). It is particularly useful for identifying global distribution patterns and possible structural asymmetries. The `Aitoff` projection is advantageous in this context because it allows for the complete representation of the sky while minimizing distortions, making it suitable for interpreting large-scale stellar distributions and its use is well-established in the literature.

The corresponding figure in this work shows the sky distribution of Be stars in binary systems from the compiled catalog. The stars appear to be approximately uniformly distributed

across the celestial sphere, with no significant clustering in specific regions. The observed spatial homogeneity in the distribution of sources suggests that the catalog is not significantly affected by spatial selection effects, such as clustering due to targeted observations or survey coverage gaps. This uniformity supports the notion that the sample provides a statistically robust basis for subsequent analyses, minimizing systematic biases associated with sky position. Furthermore, it implies that the selected systems constitute a representative subset of the intrinsic population of such binaries, at least within the sensitivity thresholds, spatial resolution, and completeness limits inherent to the observational surveys utilized.

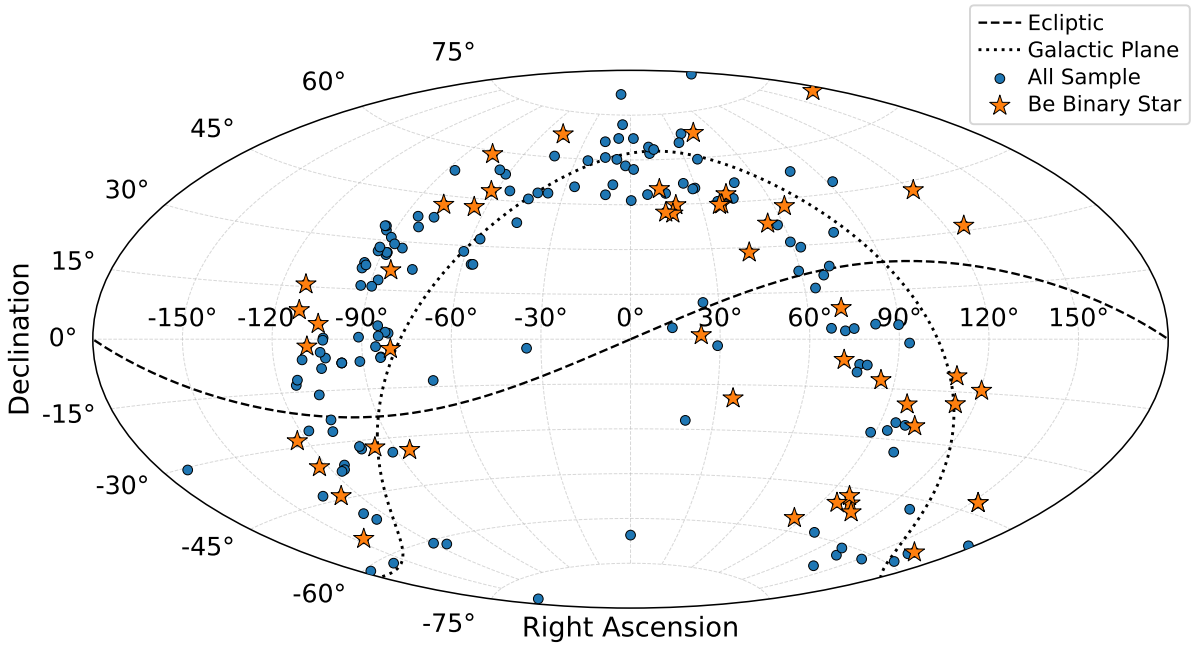

Figure 5.1: Sky distribution of the target sample using the Aitoff projection, with emphasis on Be stars in binary systems.

5.1.2. Characterization of Binary Systems

In this study, we compiled and analyzed the fundamental physical and orbital parameters of a sample of Be stars that are part of confirmed Be binary systems. The primary stellar parameters, including effective temperature (T_{eff}), surface gravity ($\log g$), projected rotational velocity ($v \sin i$), mass (M), and radius (R). The data used in this study were gathered from a wide range of peer-reviewed scientific articles available in the literature, encompassing observational and modeling results from multiple surveys and follow-up studies. In addition to general stellar properties, we also extracted all available parameters from eclipsing binary systems with WD code. These parameters, whenever present in the source works, were compiled systematically and homogenized for subsequent analysis. A more detailed description of the parameters retrieved and the methods employed for their incorporation and refinement is provided in the following sections.

For binary systems where it was not possible to collect or determine physical parameters directly from the literature, either due to the absence of dedicated studies or incomplete observational data, we adopted estimated values based on empirical calibrations. Specifically, we used the intrinsic stellar parameters tabulated in the work of Eker et al. (2020), selecting the appropriate values based on the reported spectral type of each system. In this work, they used a sample of 206 detachable, double, and double-spectral-line eclipsing binary systems with main-sequence components and accurate parallaxes from Gaia DR2 to empirically derive bolometric correction coefficients for stars with temperatures between 3 100 and 36 000 K. This approach provided consistent estimates of effective temperature, luminosity, and bolometric corrections, ensuring the inclusion of these systems in the statistical analysis while maintaining physical plausibility within the expected parameter space for main-sequence stars.

These parameters provide critical insights into the evolutionary stage of the Be stars, the effects of binarity on their physical properties, and potential interactions between components in each system. The values were selected based on spectroscopic, photometric, interferometric, and astrometric studies, prioritizing works that offered detailed and model-consistent measurements.

Eclipsing Binary Systems

For systems identified as eclipsing binaries, a more detailed analysis was conducted using the WD code, which allows for the modeling of light curve to extract precise orbital parameters and the eclipsing signal for study the Be star light variability. This approach enabled us to derive more accurate estimates for parameters such as inclination, ratio of stellar radii, eccentricity and periastron argument, taking into account the geometry and interaction between the binary components. The WD code was applied specifically to eclipsing systems where sufficient observational data (photometric time series) were available, ensuring robust modeling and minimizing degeneracies in the parameter space.

After analyzing the morphology of each light curve, binary systems that have been classified as eclipsing and containing a Be star are: TIC 51288359 and TIC 410193513. These systems were modeled using the methodology described in Section 4.6.2 (see the fitting figures presented in Figure 5.2) and the parameters are summarized in table 5.1. Thus, the modeling residual can be used in frequency analysis to identify the characteristics of Be stars in these systems.

Among approximately 50 known Be binary systems in our list, only two are observed as eclipsing binaries. It is worth noting that due to its short orbital period, the Be nature of the TIC 51288359 system remains open. This rarity can be primarily explained by geometric and observational factors, but their detection remains challenging due to several additional factors. The circumstellar disk contributes significantly to the total system luminosity and produces strong line emission (e.g., Hα), while intrinsic continuum variations can distort or mask shallow eclipses. Many Be companions are compact objects or low-mass stars, resulting in undetectable

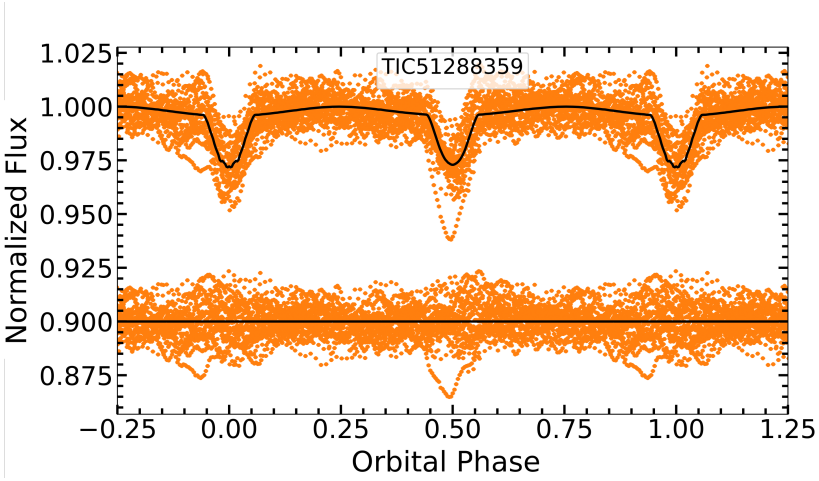

Figure 5.2: Photometric modeling results for eclipsing binary system TIC 51288359 classified as containing a Be star. The figure shows the observed TESS light curves (orange points), the best-fit model curves (black lines), and the residuals for each system. The fit was obtained using the Wilson–Devinney code and MCMC optimization, as described in Section 4.6.2.

Table 5.1: Summary of the main results of the sample of eclipsing binary systems with Be stars.

Parameters	TIC 51288359	TIC 410193513
Fixed Parameters		
P_{orb} (d)	1.799	13.198
E_0 (BTJD)	2363.4398	1822.5493
T_1 (K)	19 984±1 500	13 032±1 500
Adjusted Parameters		
q	0.02±0.01	0.99±0.07
i (°)	68.33±0.50	82.40±0.70
ϕ_1	2.45±0.03	3.90±0.12
ϕ_2	1.79±0.07	5.49±0.43
T_2 (K)	17 950±4 000	11 980±1 600

primary eclipses or very shallow secondary ones. Even in systems with comparable-mass companions, interactions with the disk can further obscure eclipses. Observational biases also play a role, as most Be catalogs were compiled from spectroscopy focused on emission lines rather than high-precision photometry. Only with long-duration, high-precision missions such as Kepler and TESS has it become possible to detect subtle eclipses and reveal previously unknown eclipsing Be binaries.

5.1.3. Characterization of Be Stars

Frequencies Analyses and Classifying

The analysis of the light curves revealed a diverse set of intrinsic periodic signals in several Be binary systems. After carefully removing orbital contributions, such as eclipses, ellipsoidal modulations, and other effects, like TESS observation sector period, we identified variability components consistent with Intermediate-frequency groups, Long-term trends, Stochastic low-frequency signals and High-frequency signals, such frequency groups can be associated with non-radial pulsations, rotational modulation, and mass-ejection-related phenomena.

The three most likely characteristic frequencies detected, extracted by the iterative prewhitening technique combined with Lomb-Scargle periodograms, are presented in Fig. 5.3 as a histogram, as well as a zoom plot to better observe the region with the greatest frequency bias. From the main frequency of each target, a concentration is observed predominantly in the range of 0.5 to 4.0 d^{-1} (see Figure 5.4), consistent with the typical frequency groups reported in larger samples of Be stars by Labadie-Bartz et al. (2022). No very high frequency signals ($f > 10\,d^{-1}$) were detected. In multiple systems, we observed clusters of frequencies close to each other - beat frequency - suggesting possible effects of modal coupling or tidal modulation.

Additionally, some systems show low-frequency signals ($< 0.5\,d^{-1}$), possibly attributed to instrumental, environmental or physical signals, and may interfere with the analysis of short-term variability (such as pulsations or rotations). These signals are often transient and, in some cases, coincide with temporary enhancements in the amplitude of pulsation frequency groups, indicating a potential link between photometric variability and disk feeding events. Rotational modulation was also identified in certain systems, typically appearing as harmonic structures or beating patterns in frequencies below 2.0 d^{-1}.

In a few systems, we also identified high-frequency signals in the range of 4 to 10 d^{-1}, which are likely associated with p-mode pulsations. Although less common in Be stars, the presence of such high-frequency variability, particularly in early-type components, may provide valuable constraints on the internal structure and excitation mechanisms influenced by rotation and binarity. These cases highlight the importance of extending asteroseismic analyses beyond traditional frequency domains, especially in complex systems where multiple variability processes coexist.

The results of the prewhitening procedure are summarized together the figures presents in

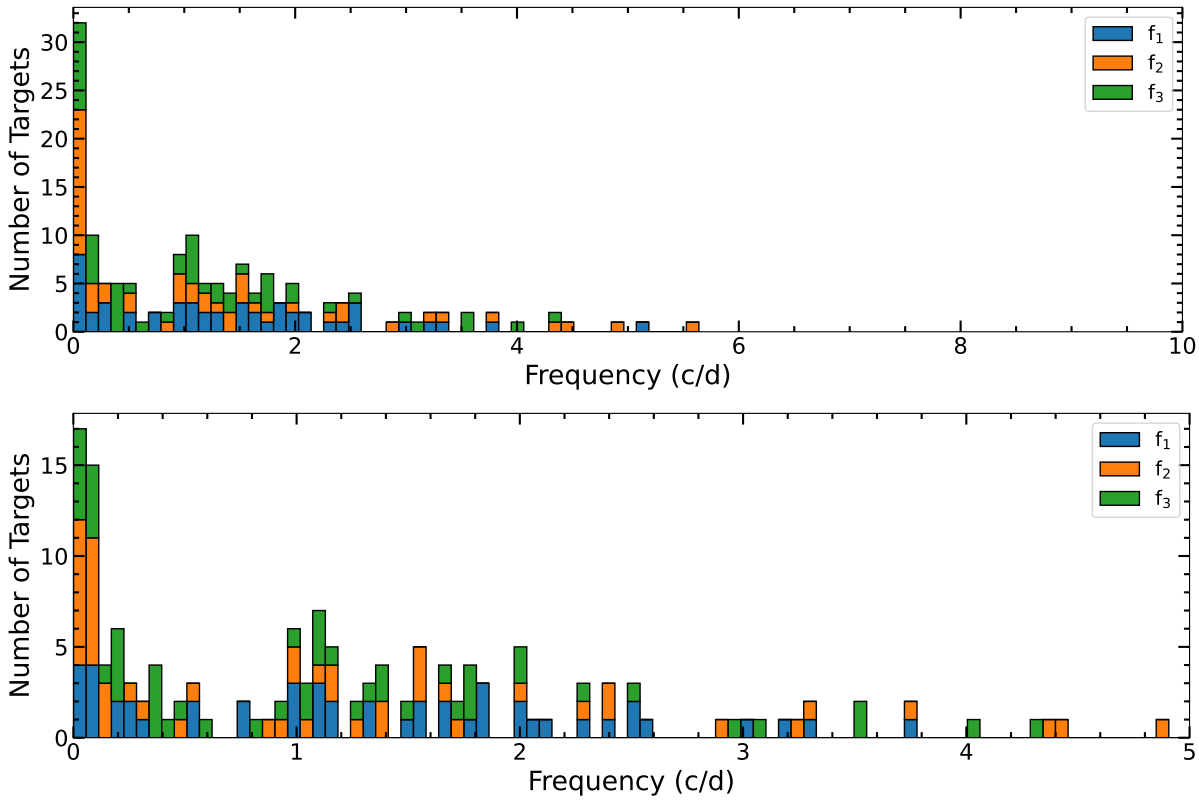

Figure 5.3: Distribution of the three main highest dominant frequencies by target. Stacked histogram showing the distribution of the first, second, and third dominant frequencies identified for each star. The x-axis shows the frequency in cycles per day (c/d), and the y-axis indicates the total number of frequencies in each bin. Multiple frequencies per star are considered, revealing the typical frequency ranges.

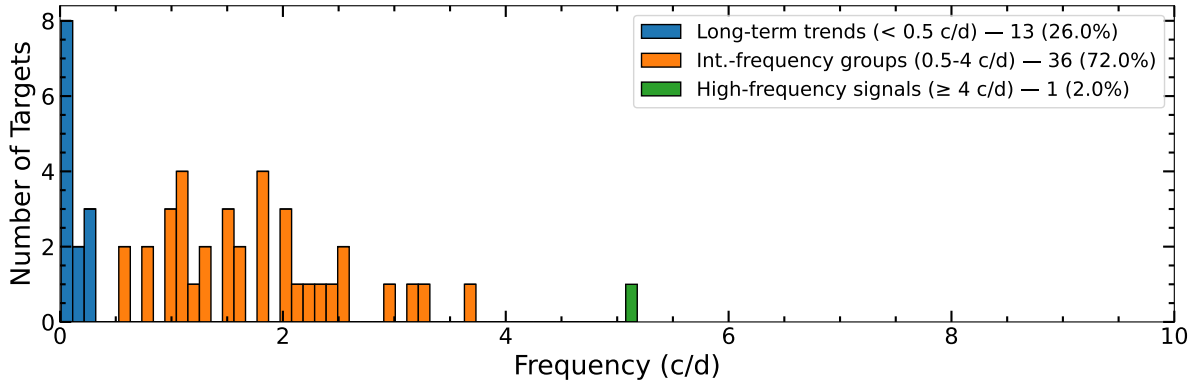

Figure 5.4: Distribution of dominant frequencies by variability group. Stacked histogram showing the distribution of dominant frequencies associated with three types of stellar variability: Long-term trends (blue, 13 targets), Int.-frequency groups (orange, 36 targets), and High-frequency signals (green, 1 targets).

Ap. C, that displays the resulting Lomb-Scargle periodogram of the light curve of Be Binary Sample, illustrating the dominant periodicities present in the light curves.

To enhance the clarity of the frequency content, we removed an excess flux contribution located around the primary and secondary eclipses from some systems. This residual excess arises due to limitations in the modeling process using `emcee`, a Markov Chain Monte Carlo sampler. The optimizer exhibits reduced performance when fitting light curves with sharp features such as deep, narrow eclipses. These discontinuities introduce steep gradients in the likelihood surface, which can hinder the convergence of the MCMC walkers and affect the precision of the fit in those regions. Despite this localized excess, its presence does not compromise the reliability of our frequency analysis, as it is confined to specific orbital phases and does not overlap with the regions where the intrinsic variability is most prominent.

Among the analyzed targets tree frequencies, only four cases showed frequencies that met the criteria for harmonic identification within the allowed range. The findings are summarized as follows:

- Harmonic of order $n = 2$, indicating a likely nonlinear modulation of a dominant periodic signal, potentially associated with rotational modulation or radial pulsation.
- Third-order harmonic ($n = 3$), which may suggest nonlinear coupling or the presence of high-overtone pulsation modes.
- Sixth-order harmonic ($n = 6$), possibly linked to geometrical disk precession, binary orbital effects, or complex resonance structures.
- Eighth-order harmonic ($n = 8$), an unusual but not implausible case in Be stars with circumstellar asymmetries or long-term modulations.

In each case, the fundamental frequency associated with the harmonic was also identified, and the harmonic order was confirmed as the lowest possible within the defined tolerance. Figure 5.5 a presents a histogram that summarizes the result of harmonic identification.

In contrast, approximately 80 individual frequencies were classified as non-harmonic. These frequencies exhibited no integer relationships to others within the specified tolerance range, suggesting that the dominant variability mechanisms in these stars are not predominantly harmonic in nature. This is consistent with the picture drawn by previous studies (e.g., Rivinius et al., 2013; Baade et al., 2018; Klement, 2019), in which the light curves of Be stars, particularly those in binaries, are shaped by multiple coexisting processes:

- Non-radial pulsations in gravity or pressure modes,
- Stochastic variability from circumstellar environments,
- Episodic mass ejections and disk oscillations,

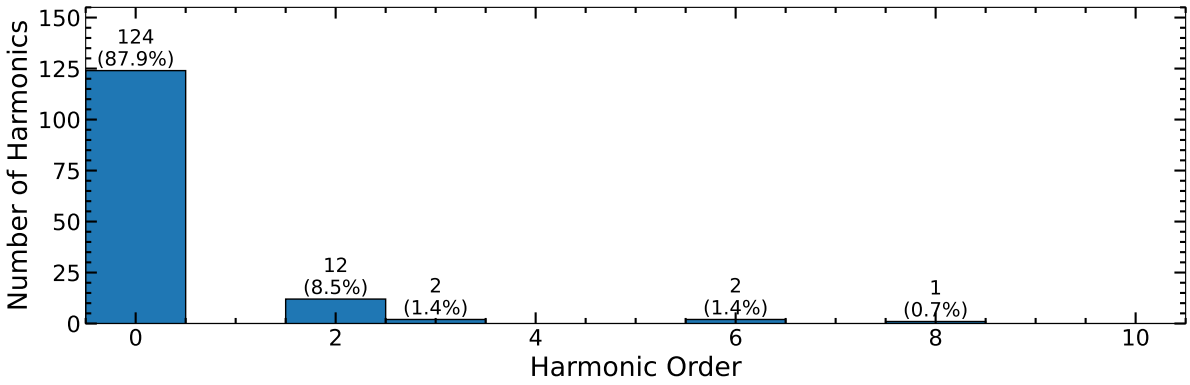

Figure 5.5: Histogram of the harmonic orders identified among the extracted frequencies from the Be star binary systems analyzed. The bars represent the number of targets exhibiting a given harmonic order, with the absolute count and corresponding percentage annotated above each bin.

- Binary-induced modulations, such as tidal interactions or orbital precession.

The low incidence of harmonic structures among the detected frequencies suggests that nonlinear periodic modulations are not the dominant mechanism in the observed light curves of these Be binaries. Nevertheless, the few identified harmonics offer valuable insight into potential coupling mechanisms and periodic structures within the systems.

The diversity of harmonic orders, ranging from $n = 2$ to $n = 8$, reflects the complex dynamical environment surrounding Be stars in binary systems. These findings reinforce the idea that the photometric variability in such systems is governed by a rich interplay between stellar pulsations, circumstellar dynamics, and binary interactions, rather than by simple harmonic oscillators.

Future investigations combining photometry with high-resolution spectroscopy and time-resolved interferometry may help disentangle the contributions of each physical process to the observed variability, enhancing our understanding of the underlying stellar and circumstellar physics.

Spectral Analysis - Hα equivalent width

The spectral variability of the Hα equivalent width (EW) was analyzed for a sample of Be stars in binary systems. The visual classification of the variability was based on criteria reported in the literature, considering the stability, linear trends, periodic modulation, and irregular behavior of the EW over time. Based on these criteria, the targets (see Table 5.2) were grouped into four main categories.

Stars with constant EW Hα exhibit minimal variation, suggesting stable circumstellar disks with little influence from a binary companion or a low-inclination geometry that reduces observable variability. Systems with small EW variations exhibit low-amplitude fluctuations or gradual trends, likely caused by slight changes in disk density or weak interactions with a com-

Table 5.2: Targets grouped by the type of Hα EW variability.

Category	**Targets (TIC ID)**
Constant EW	TIC 115091314, TIC 117501818, TIC 12725034, TIC 127493611, TIC 128116539, TIC 140214221, TIC 144028101, TIC 151546818, TIC 153880067, TIC 181627638, TIC 186598770, TIC 252670277, TIC 259463816, TIC 264459943, TIC 264631173, TIC 27141005, TIC 285937814, TIC 317958778, TIC 329947655, TIC 343908909, TIC 368799545, TIC 425224332
Small EW variations	TIC 118842700, TIC 125755072, TIC 171895762, TIC 174664153, TIC 175523591, TIC 19704573, TIC 26498398, TIC 296969980, TIC 310852121, TIC 323348984, TIC 32882261, TIC 333670784, TIC 33993533, TIC 364398342, TIC 410627159, TIC 427396133, TIC 431116093, TIC 434893323
Significant aperiodic EW variations	TIC 124219174, TIC 136704900, TIC 140006471, TIC 14200511, TIC 146036695, TIC 14709809, TIC 174008063, TIC 201373582, TIC 204191276, TIC 217667184, TIC 239408899, TIC 239880242, TIC 240757326, TIC 243647020, TIC 252500679, TIC 258704817, TIC 281047621, TIC 283206453, TIC 28569279, TIC 29628522, TIC 304114338, TIC 326247844, TIC 356239023, TIC 370259865, TIC 387813185, TIC 441027987, TIC 460532958, TIC 709917565
Significant periodic EW variations	TIC 148917425, TIC 240258004, TIC 252414037, TIC 253212775, TIC 265911941, TIC 42360166

panion; eclipses can also partially affect the observed emission. Stars with significant aperiodic EW variations exhibit irregular, high-amplitude changes associated with disk formation and dissipation, strong or erratic binary interactions, or intrinsic disk instabilities, sometimes intensified by eclipses. Finally, a subset of stars exhibit periodic EW variations, showing coherent modulation over time due to regular perturbations from short-period or eccentric companions.

Several targets in the initial sample have either no available spectra or an insufficient number of observations, preventing any robust classification regarding their EW variability.

Physical and Orbital Parameters Analysis

In order to investigate the distribution and the relationships among fundamental stellar parameters of Be stars in our sample, we constructed a multivariate correlation matrix using the Python library. This matrix, present in Fig. 5.6, enables the visualization of both the marginal distributions of individual variables (on the diagonal) and the pairwise relationships between them (in the lower triangle), while providing linear regression fits and statistical annotations for each scatter plot. The resulting figure allows a comprehensive assessment of how stellar properties

interrelate, particularly when distinguishing between apparently single stars and stars in confirmed or candidate binary systems.

The variables considered in the analysis include the following:

- Effective temperature (T_{eff}, in K);
- Surface gravity ($\log g$, in dex);
- Projected rotational velocity ($v \sin i$, in km s^{-1});
- Stellar mass (M, in $M_\odot$);
- Stellar radius (R, in $R_\odot$);
- Dominant photometric frequency (f_1, in cycles per day).

Each data point corresponds to an individual system. The sample is color-coded by the classification made previously: blue circles represent all binary sample, while orange stars indicate confirmed binaries with a Be star. The diagonal panels show histograms with kernel density estimates (KDEs), providing insight into the distribution of each variable across the sample. In each off-diagonal panel, a linear regression line is fit to all available binaries with a Be star. This approach enables an initial identification of correlations or lack thereof among the considered parameters.

The analysis reveals several significant trends and patterns among the fundamental parameters. The most notable relationships are discussed below.

- Effective Temperature vs. Stellar Mass: A strong positive correlation exists between stellar mass and effective temperature, in agreement with theoretical predictions. More massive stars have higher core pressures and temperatures, resulting in hotter surfaces. The linear fit shows a steep slope with low scatter, indicating a tight relationship. Binary stars generally follow this trend, though some exhibit slightly higher masses at a given temperature, possibly due to unresolved photometric blending or mass transfer in interacting systems.
- Stellar Mass vs. Radius: The mass–radius diagram shows a clear, roughly linear correlation, consistent with main-sequence models where stellar radius increases with mass in the Be-star range (3–20 $M_\odot$). While some scatter exists, the regression captures the overall trend well. A subset of stars, mostly binaries, appears slightly inflated, likely due to rotation or tidal interactions affecting their structure.
- Effective Temperature vs. Surface Gravity: An inverse correlation is observed between T_{eff} and $\log g$, with greater scatter than in mass–temperature or mass–radius relations. This trend is physically consistent, as stars expanding along or off the main sequence experience decreasing surface gravity. Hotter, more massive stars may thus exhibit lower

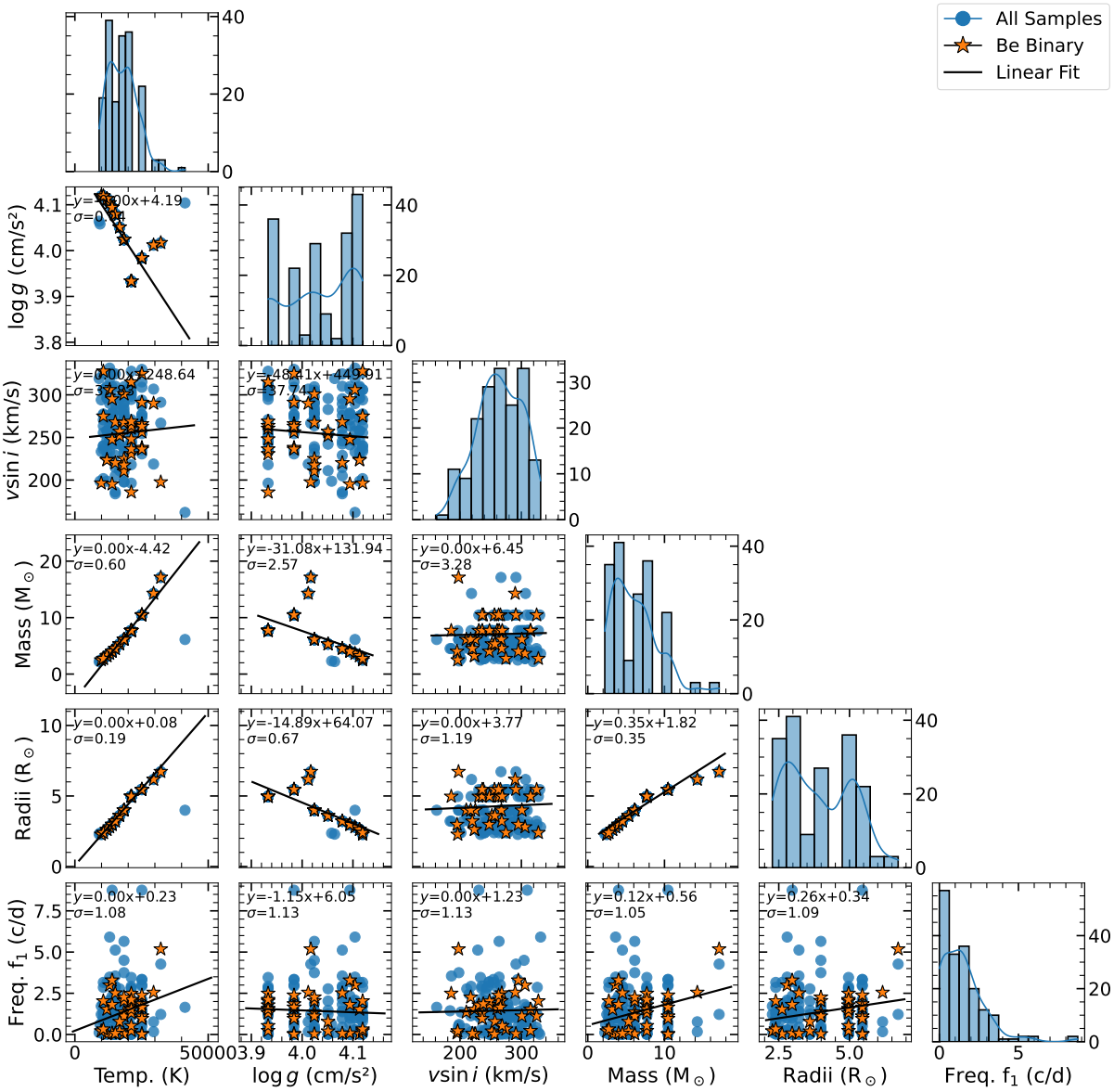

Figure 5.6: Scatter plot showing the correlation between physical and orbital parameters of the stellar sample. The full sample is represented by blue circles, while candidate Be binary systems are highlighted with orange stars. The plot explores possible trends among parameters such as orbital period, eccentricity, effective temperature ($T_{\rm eff}$), surface gravity ($\log g$), projected rotational velocity ($v \sin i$), mass, radius, and luminosity. A linear fit (black dashed line) is included to quantify the correlations, with the standard deviation of residuals (σ) indicated in the legend. These diagrams help identify distinct evolutionary regimes and characteristic signatures of Be systems.

$\log g$, particularly if evolved, while projection effects and inclination-dependent uncertainties in spectroscopic $\log g$ measurements contribute to the observed dispersion.

- Rotational Velocity vs. Mass, Radius, and Temperature: Relations between $v \sin i$ and parameters such as $T_{\rm eff}$, M, and R show substantial scatter and weak correlations. This is expected, as $v \sin i$ depends on both the intrinsic equatorial velocity and the inclination angle relative to the line of sight. Even stars with similar physical properties can display a wide range of $v \sin i$, and although Be stars rotate near their critical velocities, inclination effects complicate the extraction of meaningful correlations without detailed geometric modeling.

- Dominant Frequency (f_1) vs. Stellar Parameters: Relations involving the dominant photometric frequency f_1 exhibit weak trends and significant scatter, reflecting the complex and potentially non-linear dependence of variability on stellar parameters. In Be stars, variability arises from pulsations, rotational modulation, or disk-related phenomena, so observed frequencies do not correlate straightforwardly with mass, temperature, or radius. A detailed classification of variability types and identification of pulsation modes may be needed to reveal underlying patterns.

The inclusion of linear regression fits in each panel provides a useful first-order approximation of the trends between variables. Although many stellar parameter relationships follow power-law or non-linear behavior in theory (e.g., $L \propto M^{\alpha}$, $T_{\rm eff} \propto M^{\beta}$), linear fits over restricted domains can still provide valuable insight into empirical tendencies within a sample of limited parameter space. The lower σ values indicate tighter, more reliable correlations (e.g., M vs. R, M vs. $T_{\rm eff}$), while higher values reflect larger intrinsic scatter or the influence of unmodeled variables (e.g., $v \sin i$ vs. M or f_1 vs. $T_{\rm eff}$).

The distribution of the projected rotational fractions is shown in Figure 5.7: the observed $v \sin i / v_{\rm crit}$ values span 0.28–0.70, with a mean of ≈ 0.47. Given that our targets are viewed at intermediate inclinations ($i \in [40^\circ, 70^\circ]$), we de-projected the velocities. This correction increases the ratios by factors between $1/\sin 70^\circ \approx 1.06$ and $1/\sin 40^\circ \approx 1.56$, shifting the distribution from 0.28–0.70 to roughly 0.30–0.85 (with a small tail approaching the critical limit; values formally exceeding unity are capped at $v/v_{\rm crit} = 1$). For a uniform prior in i over $[40^\circ, 70^\circ]$, the mean rises to ~ 0.60. If our sample is preferentially oriented toward the lower end of this interval (e.g. $i \approx 40^\circ$), the mean reaches ~ 0.70. In either case, the bulk of the distribution moves to $v/v_{\rm crit} \gtrsim 0.70$, becoming consistent with the peak at 0.30–0.95 reported for single Be stars by Zorec et al. (2016). The adopted inclination range is justified by the fact that most of our binaries are not eclipsing, which excludes configurations close to $i \sim 90^\circ$, while very low inclinations are unlikely due to the clear spectroscopic signatures of rapid rotation. Thus, once inclination is accounted for, the apparent discrepancy from the raw $v \sin i$ values largely disappears, indicating that the rotational properties of Be stars in binaries are comparable to those of single Be stars.

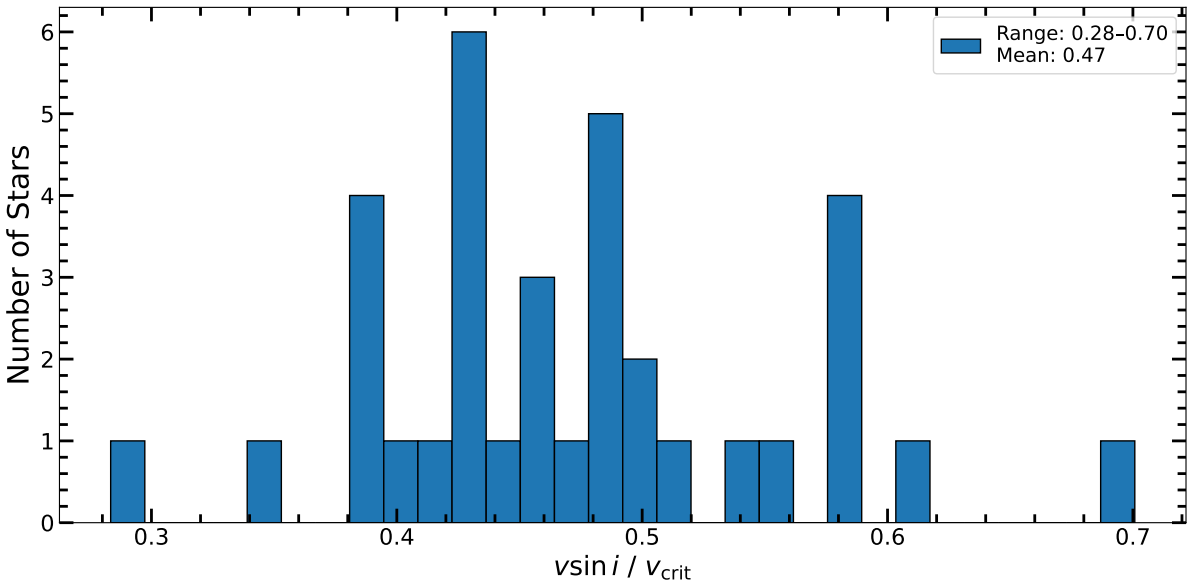

Figure 5.7: Distribution of the ratio $v \sin i \,/\, v_{\mathrm{crit}}$ for a sample of Be stars in binary systems. The ratio was computed using observational data of stellar mass, radius, and projected rotational velocity, with the critical velocity.

Our results indicate that Be stars in binaries exhibit a wide range of rotational velocities, suggests that while some stars rotate near moderate fractions of their critical velocity, others approach much higher rotation rates, reflecting the diversity in binary configurations, evolutionary stages, and past interactions. The presence of a companion may influence the angular momentum distribution in the stellar envelope, but it does not necessarily prevent the star from reaching high rotation.

The observed range of rotation fractions has implications for disk formation and stability. Since rapid rotation provides centrifugal support that facilitates mass ejection from the stellar surface, stars with lower fractions of critical velocity may require additional mechanisms—such as non-radial pulsations or magnetic activity—to efficiently feed the circumstellar disk. Overall, the data highlight that Be stars in binaries can maintain substantial rotation, with the wide range of observed values reflecting the complex interplay between rotation, binarity, and disk dynamics.

5.1.4. Stellar Evolution Study

To investigate whether Be stars in binary systems display distinct photometric properties compared to the broader population of B-type stars, we constructed a reddening-corrected color–color Hertzsprung–Russell (HR) diagram using data from the *Gaia* DR3 catalog. Our sample comprises confirmed and candidate Be stars in spectroscopic or astrometric binary systems.

Following the methodology of Zari et al. (2018), we corrected for interstellar extinction using a 3D dust map. For each star, we retrieved the visual extinction along its line of sight at its estimated distance, obtained via Gaia parallax. The extinction values were queried using the

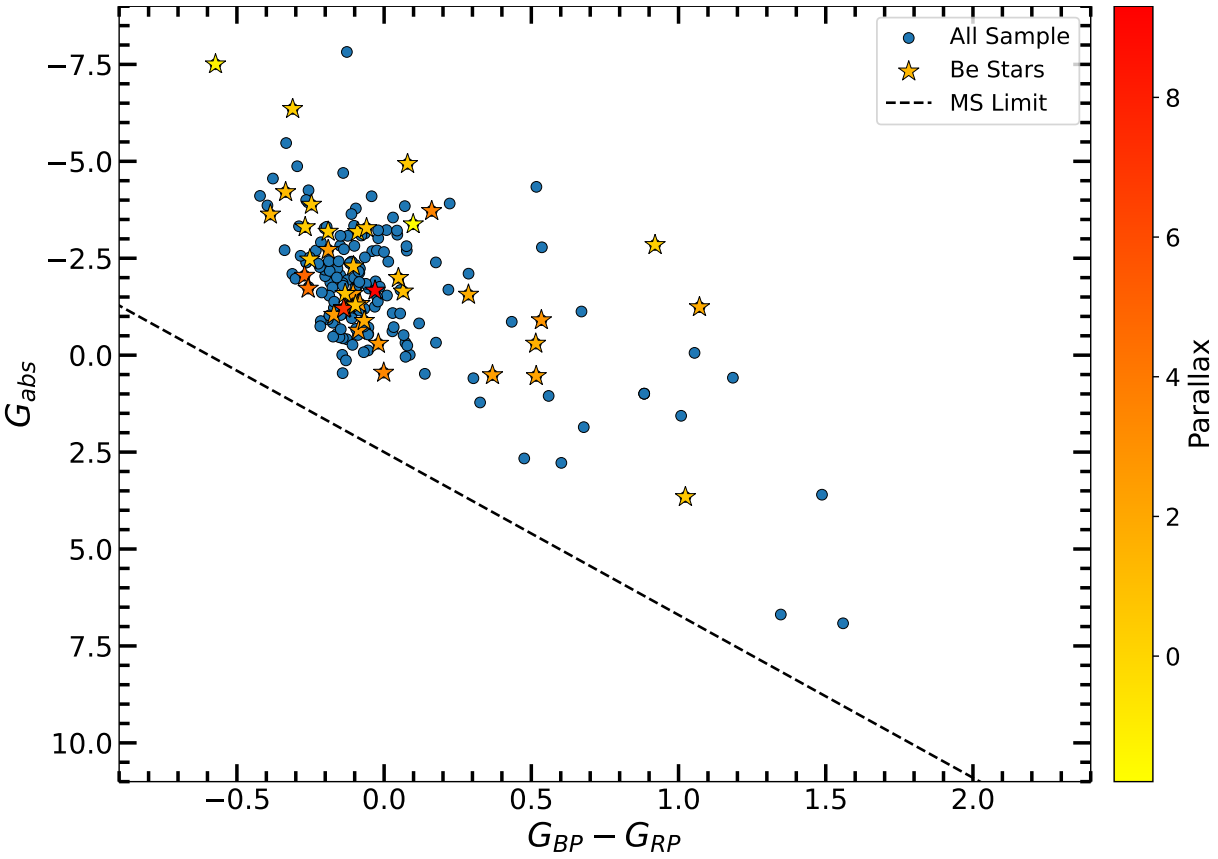

Figure 5.8: Reddening-corrected color–color Hertzsprung–Russell diagram of confirmed and candidate Be stars in spectroscopic or astrometric binary systems, based on Gaia DR3 photometry. Interstellar extinction was corrected using 3D dust maps accessed via the 3DNHtool, with extinction coefficients from Cardelli et al. (1989). The intrinsic colors were used to investigate potential photometric differences between Be stars in binaries and the broader population of B-type stars.

3DNHtool, which provides access to 3D extinction models based on Gaia and complementary surveys. Color corrections were applied to the Gaia photometric bands using standard extinction coefficients derived from the Cardelli et al. (1989) law. Corrected intrinsic colors, were then used to plot a color-color diagram, which can be seen in the figure 5.8.

Upon comparison with a control sample of normal B-type stars (non-emission, non-binary), we found that Be stars in binary systems are broadly distributed within the same color space. No clear segregation or concentration was observed that could uniquely identify the Be binary population in the corrected HR diagram. This suggests that, from a photometric perspective, Be stars in binaries do not significantly deviate in color-color space from the general B-star population, reinforcing the idea that the Be phenomenon is more strongly tied to circumstellar and rotational effects than to intrinsic photometric differences.

5.2. The Triple System V1371 Tau

Hierarchical multiples systems, especially with triple stars, become increasingly common with higher stellar masses, with their frequency rising from roughly ~10% among low-mass stars to nearly ~50% among B-type stars (Duchêne and Kraus, 2013; Moe and Di Stefano, 2017b; Maíz Apellániz, J. et al., 2019). However, despite their prevalence, the evolution of such systems still needs to be better understood due to the need for systematic studies. Notable examples include α Cen, the nearest triple star system (Tokovinin, 2014), and ν Gem, a hierarchical triple system where one component is a classical Be star (Klement et al., 2021; Gardner et al., 2020). These systems provide critical case studies for understanding the dynamics and evolution of complex stellar configurations, following pioneering work by Fekel Jr (1981).

In this context, we focus on V1371 Tau* (TIC 74386000, HD 36665), a multiple star system comprising an inner eclipsing binary (EB) orbited by a classical Be star (Rivinius et al., 2025a). Since it is a hierarchical system, the components will be identified as an external pair of binary system A + B, with A = a + b representing the eclipsing internal binary. This system is located within the supernova remnant (SNR) S147 (also known as Shajn 147 or Simeis 147) in a region rich with B-type stars (Minkowski, 1958). S147, known for its intricate filamentary structure spanning over 3 degrees of the sky (Dickel and McKinley, 1969), is centered in the Taurus constellation. It represents a unique stage in stellar evolution, believed to have originated from a double supernova event (Gvaramadze, 2006). However, the exact age of S147 remains a topic of debate. At the same time, Silk and Wallerstein (1973) suggested an age of 9×10^4 years based on the high-velocity gas detected in the ultraviolet spectrum of V1371 Tau, but at this age the SNR should already be very close to disappearing, since this estimate exceeds the typical age range of 10^4 to 10^5 years for evolved SNRs (Ferrand and Safi-Harb, 2012) and contradicts the 30 kyrs age inferred by Kramer et al. (2003) from the pulsar PSR J0538 + 2817's motion within the remnant.

Hierarchical triple systems with Be stars as the outer components are rare. Understanding the role of gravitational interactions and mass transfer in these systems can provide critical insights into such stars' formation and evolutionary processes. Borkovits et al. (2025) investigated 221 hierarchical triple systems candidates by combining Kepler and TESS data to analyze eclipse timing variations and uncover signs of precession and dynamical interactions. Among the systems studied, there is no mention of any Be-type stars. Examples, such as ν Gem (Klement et al., 2021), HR 2309, and possibly 141 Tau, stand out due to their unusual configuration, where the Be star occupies the outer position but is not the dominant source of light†. Investigating such systems is crucial for exploring evolutionary pathways that may lead to the forming of Be stars in multiple systems.

TESS observed this target in two distinct periods: ~76.5 days in 2021 (spanning Sectors

* Coord. (J2000): R.A. = 05h34m39.10s, Dec. = +28°03′03.78″

† For a discussion of such systems, see Rivinius et al. (2025a)

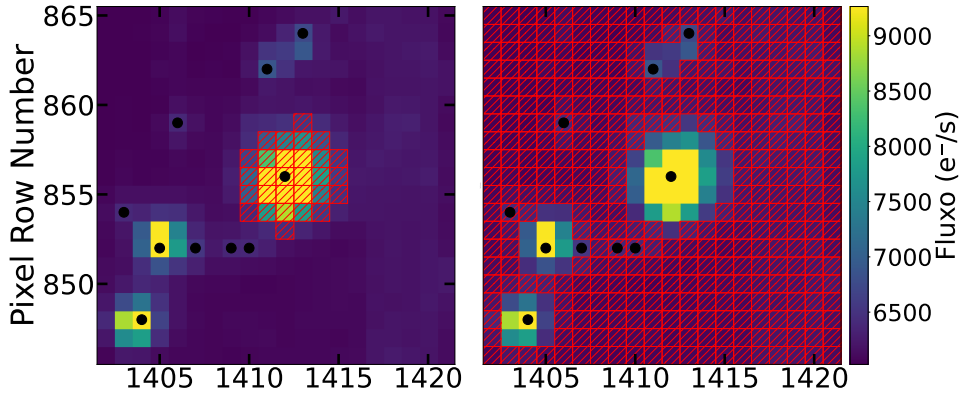

Figure 5.9: The figure shows the aperture masks used to extract the flux of V1371 Tau (left panel) and the background flux (right panel), as observed by *TESS* in Sector 43. Black dots indicate field sources from the *Gaia* catalog with magnitude $G \leq 15$.

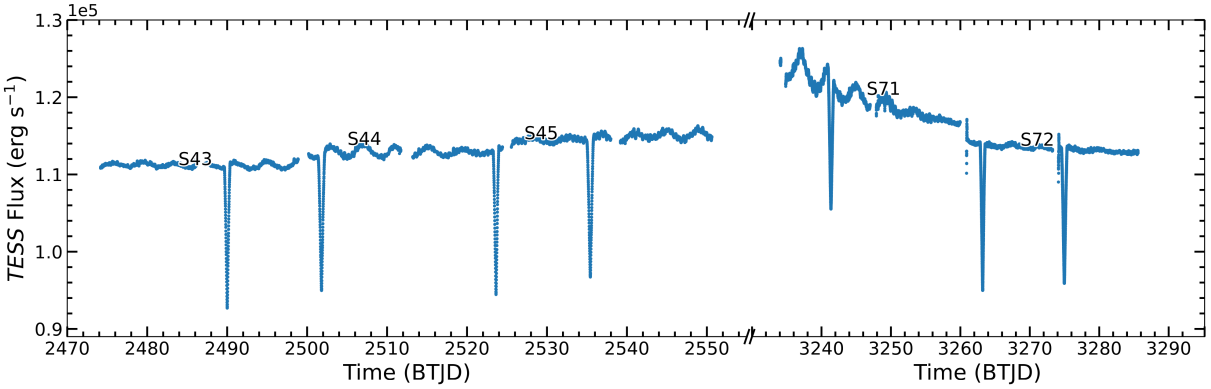

Figure 5.10: Light curve of V1371 Tau observed by TESS in flux at BTJD.

43-45) and ~51.5 days in 2023 (Sectors 71-72). The observations were conducted with exposure times of 475 seconds in 2021 and 158 seconds in 2023, yielding a substantial dataset for our analysis. The light curves were extracted from these Full-Frame Images (FFIs) using the `Lightkurve` package in Python (Collaboration et al., 2018).

Figure 4.1 displays the application of the aperture mask and background subtraction, presenting the TPF alongside the selected aperture mask used for flux extraction. Additionally, black points indicating field sources from the *Gaia* catalog with magnitudes $G < 15$ are overlaid to demonstrate that the target's flux is free from contamination by nearby objects of similar brightness. Figure 5.10 shows the resulting light curve of V1371 Tau as observed by TESS over the relevant sectors, with flux plotted as a function of BTJD, the time format adopted by TESS.

5.2.1. Ephemeris and Eccentric Orbit Identification

Using photometric data from TESS, we were able to accurately determine the ephemeris of the inner eclipsing binary system of V1371 Tau. To eliminate any doubt, we consider that the primary component of the inner binary system is the star that is being eclipsed at the moment of greatest depth shown in the light curve, that is, at orbital phase zero. We employed two Gaussians to model the primary consecutive eclipses. We estimated their parameters using the

MCMC technique implemented in the Python package `emcee` (Foreman-Mackey et al., 2013). Based on the mid-times of two consecutive primary eclipses, we derived a linear ephemeris with the initial epoch being the mid-time of the first eclipse. Subtracting the mid-time of the second eclipse yielded an orbital period of 33.62089 days. The linear ephemeris is expressed as:

$$T(\mathrm{BTJD}) = 2,490.00686 + 33.62089 \times E\,, \tag{5.1}$$

Upon phasing the light curve according to the derived ephemeris, we discovered that the secondary eclipse did not occur at phase 0.50 but closer to phase 0.35. This significant deviation from the expected phase in an EB system with a circular orbit confirms the presence of eccentricity. The observed secondary eclipse phase also suggests a periastron argument greater than $\pi/2$ radians. Performing a preliminary analysis of the light curve, we found a measurement of 0.268 for the eccentricity, a measurement that corroborates the result of 0.26 obtained by Rivinius et al. (2025a), and 150° for the periastron argument.

5.2.2. Spectral Temperature and Rotational Broadening

Previous studies have classified V1371 Tau with varying spectral types: B1Ve (Silk and Wallerstein, 1973; Sallmen and Welsh, 2004), B1±0.5V (Dinçel et al., 2015), and B0ne (Merrill and Burwell, 1943). More recently, Rivinius et al. (2025a) pointed out that the spectrum of V1371 Tau appears to be that of a star of type B1IIIe. These results highlight the need for a more rigorous and consistent analysis, now taking into account mainly the fact that we have a combined spectrum of three stars. The best technique to perform such an analysis is spectral disentanglement, but given the limited number and resolving power of spectra available, the most reliable approach is spectral comparison with related theoretical models to obtain greater precision in determining the characteristics of the stars. This approach allowed us to infer at the same time the atmospheric parameters of the three components of the system, including temperature, surface gravity ($\log g$) and projected rotational velocity ($v \sin i$) (Hadrava, 1995; Shenar et al., 2020). With this approach, in addition to obtaining the parameters of the inner eclipsing system, we will infer a result for the outer star of V1371 Tau.

The presence of HeI λ 4471Å closely aligned with MgII λ 4481Å confirms the B-type nature of all the stars composing V1371 Tau. Furthermore, its spectrum shows no characteristics of a cool B-type or early O-type star. We employ a synthetic spectrum that is the sum of three pre-computed synthetic energy distributions from TLUSTYBSTAR2006 (Lanz and Hubeny, 2007) with temperatures ranging from 18,000 to 30,000 K (with 1,000 K steps), $\log g$ between 3.50 and 4.50 km s^{-2} (with 0.25 km s^{-2} steps) and $v \sin i$ between 20 and 200 km s^{-1} (with 10 km s^{-2} steps), fitting it with the available spectrum from the χ^2 method. We accessed the pre-computed models generated with `SYNSPEC` (Hubeny and Lanz, 2011) for spectral modelling. Solar abundances, a micro-turbulence velocity of 2 km s^{-1} and macro-turbulence of 25 km s^{-1} were assumed in all models (Simón-Díaz and Herrero, 2014). The error associated in measurements

was calculated from the lowest χ^2 within the 1σ confidence interval. This is equivalent to approximately 3000 K for temperature, 0.25 dex for log g and 40 km s^{-2} for $v \sin i$.

Considering that the inner eclipsing system produces a greater variation in the wavelength shift, two Gaussians were previously adjusted and their central wavelengths were set as the center of the theoretical models of the blueshift star and the redshift star. The outer component, in turn, because of a smaller disturbance in the wavelength shift, had its model centered at the laboratory wavelength. The Goodman spectrum, obtained at 2,986.5401 BTJD and with an orbital phase of ~0.77, was used in this analysis because of its higher-SNR spectrum ideal for fitting the line profiles. In this case, the primary component of the eclipsing system appears redshifted, while the secondary component appears blueshifted.

The model with the lowest χ^2 and that reproduced the HeI line with the best accuracy is represented in Fig. 5.11, and resulted in the following values for each component of the system: $T_a = 25{,}000$ K, log $g_a = 4.50$ km s^{-2}, $v_a \sin i = 160$ km s^{-1}; $T_b = 28{,}000$ K, log $g_b = 4.50$ km s^{-2}, $v_b \sin i = 200$ km s^{-1}; $T_B = 28{,}000$ K, log $g_B = 4.50$ km s^{-2}, $v_B \sin i = 200$ km s^{-1}. These results reproduce the spectral type of B1 for the a star, B0 for the b component and B0 for the B outer star, based on Böhm-Vitense (1981) and Eker et al. (2020).

Having observed a large rotational broadening of the spectrum of V1371 Tau that was not fully fitted by the sum of the theoretical models (see Fig. 5.11), and which is possibly originating from its Be component, such a measurement was quantified by means of a second approach. This corroborative determination of $v \sin i$ was obtained by measuring the equivalent width of HeI λ 4471 Å, yielding a value of 250±40 km s^{-1}. This independent approach is in line with the value of $v \sin i$ inferred through the spectroscopic fitting of the external Be component, and will be the value adopted as the one referring to it, given that this should be the largest contribution to the spectral broadening and that our model is limited to a Rotational Broadening of 200 km s^{-1}.

Stellar luminosities are a key parameter for our subsequent analyses. Based on the derived atmospheric parameters, we estimate the luminosities using the following relation from (Gray, 2005):

$$\log\left(\frac{L}{L_\odot}\right) = 4\log\left(\frac{T_{eff}}{T_\odot}\right) - \log\left(\frac{g}{g_\odot}\right) + \log\left(\frac{M}{M_\odot}\right), \tag{5.2}$$

where, assuming $M = 14\,M_\odot$ for all stars, $T_\odot = 5{,}777$ K, and $\log g_\odot = 4.437$ (cgs), we have:

- Star a: $\log(L/L_\odot) \approx 3.63$
- Stars b, B: $\log(L/L_\odot) \approx 3.82$

5.2.3. Radial Velocity Scheme

The orbit of V1371 Tau has never been previously constrained. In the spectra with emission from the Hα, we observe absorption lines that repeat in some lines associated with HeI. They

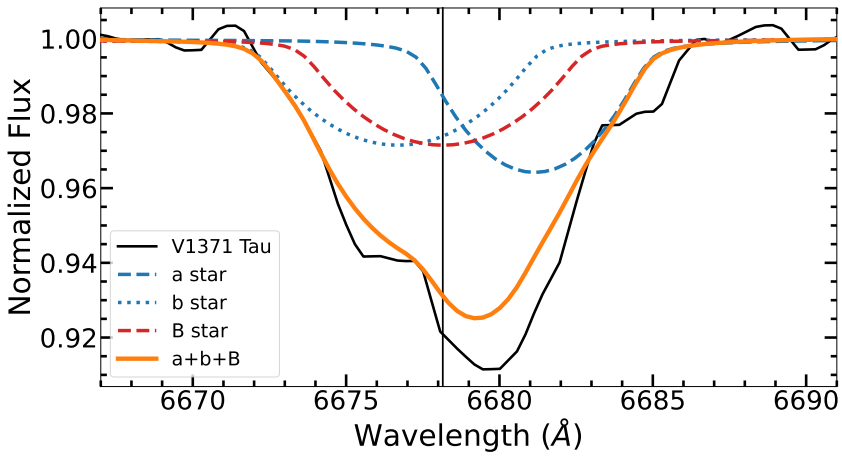

Figure 5.11: Comparison between the sum (orange solid line) of the best-fit TLUSTY spectral models for each component of V1371 Tau (non-solid lines) and the observed Goodman spectrum (black solid line) obtained on 2023/02/11. The laboratory wavelength of the HeI line, λ 6678.152 Å, is indicated by the vertical black line.

present a cyclic variation with a period of ~33 days, similar to the orbital period obtained in the light curve; therefore, such a variation is associated with the inner eclipsing binary system and is not associated with the Be star. We then find a new indication that V1371 Tau is a triple system since the emission lines in Hα and some HeI lines, referring to the Be star, do not exhibit orbital motion with the same period as the inner eclipsing binary. It is also worth noting that the HeI emission lines have a much larger peak separation than the $v \sin i$ of either star in the inner EB.

We independently derive it here following a radial velocity measurement technique from Gaussian fitting and Doppler calculation, finding that it is a double-lined spectroscopic binary system. We followed a similar procedure presented in (Shenar et al., 2022; Rocha et al., 2022). In short, gaussian profiles were fitted to the HERMES data for the HeI λ 4921.931 Å and in particular for the HeI λ 6678.152 Å absorption and emission lines. Furthermore, we added our spectral analysis of the B component obtained in Sec. 5.2.2 to the model, obtaining now a three-component fitting approach to take into account the third-body contribution, which even being a stationary or slowly varying component, can influence the shape and depth of the combined line profiles, affecting both the line intensity and potentially biasing the RV measurements. As can be seen, the variation in the wavelength of the emission lines (which we associate with the outer component) is irrelevant. Its explained by its orbital period on a scale of years. Its presence does not generate systematic errors in the measurement of the radial velocity of the eclipsing binary system. We adjusted the absorption line profiles by fixing the depth and FWHM of each component throughout all epochs. To identify the lines of the primary and secondary components, we used the fact that we do not have spectra in orbital phases smaller than 0.13 or larger than 0.82, and the radial velocity lines should cross around orbital phase 0.35. Heliocentric correction was applied to the measurement scale of all RV. The `emcee` code was used to search for the best solution of the models and sample the parameter space to obtain their respective

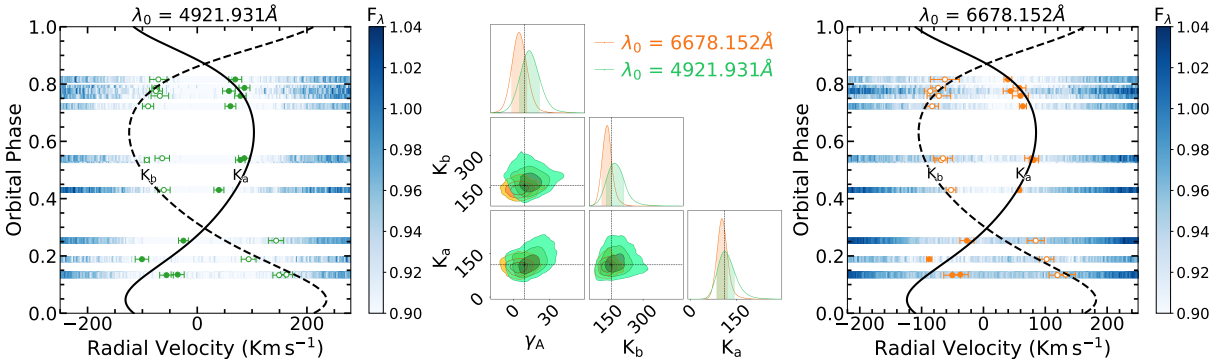

Figure 5.12: Left and Right Panel: The dynamical spectra of the HeI λ4921.931 Å and HeI λ6678.152 Å in V1371 Tau, phased with the system's orbital period of P = 33.6209 d. Colour-scales indicate the continuum-normalised flux F_λ. The orange and green dots are the observed points with their respective error bars, and the black solid line shows the radial-velocity curve model of the system.; Middle Panel: A corner plot generated using the `emcee` sampler illustrating one- and two-dimensional posterior distributions of free parameters derived from the Eq. 3.34 model fitted to the V1371 Tau inner binary radial velocity points for HeI λ4921.931 Å and HeI λ6678.152 Å lines.

uncertainties. The best value of the central wavelength of each Gaussian was used to calculate RV from the Doppler effect and its respective errors.

We performed simulations with for RVs measured using the Eq. 3.34, and tested it with the help of `emcee`, fixing the eccentricity and periastron argument with the previous light curve analysis and result. The best fit obtained are shown in Figure 5.12. To avoid including error in our next procedure, we decided to use the RV coming from the best fit, that is, the RV coming from HeI λ 6678.152 Å line. The average of the derived orbital elements (with 68% confidence interval) agrees well with the expectations, the systemic velocity being: $\gamma_A = 3.24^{+5.75}_{-5.42}$ km s^{-1} and finally the half-amplitudes of the velocity: $K_a = 101.22^{15.97}_{-13.48}$ km s^{-1} and $K_b = 139.73^{21.67}_{-19.55}$ km s^{-1}.

5.2.4. Binary Modelling Scheme

We adopt a light curve modelling approach similar to those described in Almeida et al. (2015), Rocha et al. (2022) and Sec 4.6.2 to characterize the eclipsing binary V1371 Tau. To optimize the search for the light and RV curve that best aligns with our observational data, we utilize the Python package `emcee`, employing a MCMC ensemble sampler for a statistical comparison between synthetic and observational data.

In the TESS light curve, the eclipse depth for the primary star is ~17%, while for the secondary star it is ~16% of the normalized flux., including the constant contamination from the third component flux. As discussed in Section 5.2.2, the third star contributes roughly 33% of the total system light, which leads to a dilution of the apparent eclipse depth. To find the true eclipse depth of the eclipsing stars alone, we remove the flux contribution of the third compo-

nent from the light curve. The corrected eclipse depth ($D_{\text{corrected}}$) is given by:

$$D_{\text{corrected}} = 1 - \frac{F_{\text{ecl}} - F_3}{F_{\text{total}} - F_3}, \tag{5.3}$$

where: F_{total} = 1.00 (flux out of eclipse), F_{ecl} = 0.83 (flux during primary eclipse), F_3 = 0.33 (flux from third component). After applying this correction, the true primary eclipse depth increases from ~17% to ~25%, indicating that the actual flux variation caused by the eclipsing pair is substantially deeper than initially measured.

For both the WDC and the `emcee`, the input comprises the light curve derived from TESS data and RV from HERMES data, ensuring that its point sampling comprehensively covers the entire orbital phase of the system. The prior parameters, deduced in the preceding section, serve as initial inputs, except inclination and gravitational potentials. These parameters are obtained exclusively through the analysis of the light curve. Establishing the initial epoch and orbital period according to Eq. 5.1, we derive their initial values to serve as priors for the subsequent `emcee` optimization process. Since the system has non-zero eccentricity and periastron argument, the initial time computed by the WDC occurs at the point of minimum separation of the system components, which is slightly different from the time calculated using the primary eclipse of the observed data. Thus, a previous analysis using the WDC was performed, defining the value of -0.067 for an orbital phase shift of the light curve.

Usually, the approximate similarity in primary and secondary eclipse depths suggests comparable temperatures for both stars. However, this does not apply to all cases, considering systems with non-zero eccentricity and inclination different from 90°, which is the case for V1371 Tau. We fixed the effective temperature of the primary component and used the previous value of the secondary component (T_b) determined in sec. 5.2.2 as an initial value. Finally, as in the RV analysis, we fixed the eccentricity and the periastron argument to avoid large variations in the shape of the EB orbit. In the eclipsing binaries, a crucial parameter is the mass ratio ($q_A = M_b/M_a = K_a/K_b$), typically derived from the radial velocity amplitudes, and in our case resulting in a mass ratio: q_A = 0.72. As this measurement was deferred to the previous section, we let it free in modelling the light and RV curve with WDC to obtain the other parameters with greater precision and confidence.

The spectrum does not present any characteristics different from a B star of early subtype and therefore we expect that not only the stars of the inner pair, but the third component also has parameters corresponding to a hot B-type star, so due to the B-type component's spectral type, both stars are assumed to possess radiative atmospheres. Consequently, gravity-dimming exponents ($g_a = g_b$) and albedos ($A_a = A_b$) were fixed to standard hot star values of 1.00 and 0.50, respectively (Claret and Bloemen, 2011). We adopted the square root limb darkening law in the WDC as recommended by Van Hamme (1993). We used the normalized light curve of the sectors observed in 2021 to isolate the system parameters determination of the sporadic phenomenon of brightness decay observed in the most recent sectors. Based on the observed

morphology of the light curve, characterized by two plateaus and well-defined deep eclipses, we configured the Wilson-Devinney code in mode 2 (detached) to avoid restrictions on Roche lobe filling. Subsequently, we used `emcee` to generate a sample of 100,000 models and infer the best values and associated error bars for the following parameters: (i) Separation (a_A); (ii) mass ratio (q_{ba}). (iii) orbital inclination (i_A); (iv) gravitational potentials of the primary (Ω_a) and secondary components (Ω_b); (v) effective temperature of the secondary component (T_b).

In special, we have two independent measurements for T_b. Using Bayes' Theorem and assuming that each measurement has a Gaussian distribution, we perform the Bayesian fusion of normal distributions in order to obtain a single measurement for T_b, resulting in the combined value of 27,997 K with an uncertainty of ±2,286 K.

Figure 5.13 showcases the best-fitting model for the light curve and radial velocity exclusively of the eclipsing pair, below a scaled diagram that illustrates the relative sizes of the stars and the orbital motion, and the Fig. 5.14 illustrates one-dimensional and two-dimensional posterior distributions of free parameters generated using `emcee`. Table 5.3 summarizes the orbital and physical final values and their uncertainties, obtained by averaging and considering the 1-σ range directly adjusted.

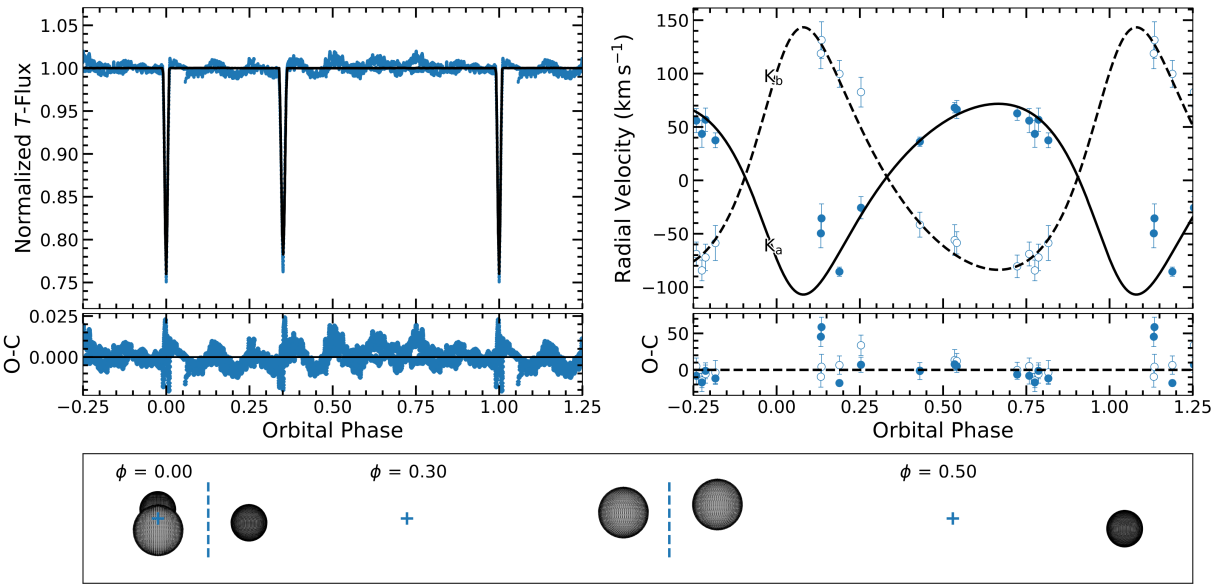

Figure 5.13: Top panel: Light curve and radial velocity of eclipsing binary in orbital phase of The V1371 Tau. The light contribution of the third component was removed from the normalized T-flux. The blue dots are the observed data, and the solid black line is the best-fit model generated by WDC.; Bottom panel: Unscaled 3D models of the eclipsing system in V1371 Tau in three distinct orbital phases, showing the relative positions of the stars and the system's center of mass (marked by a blue cross).

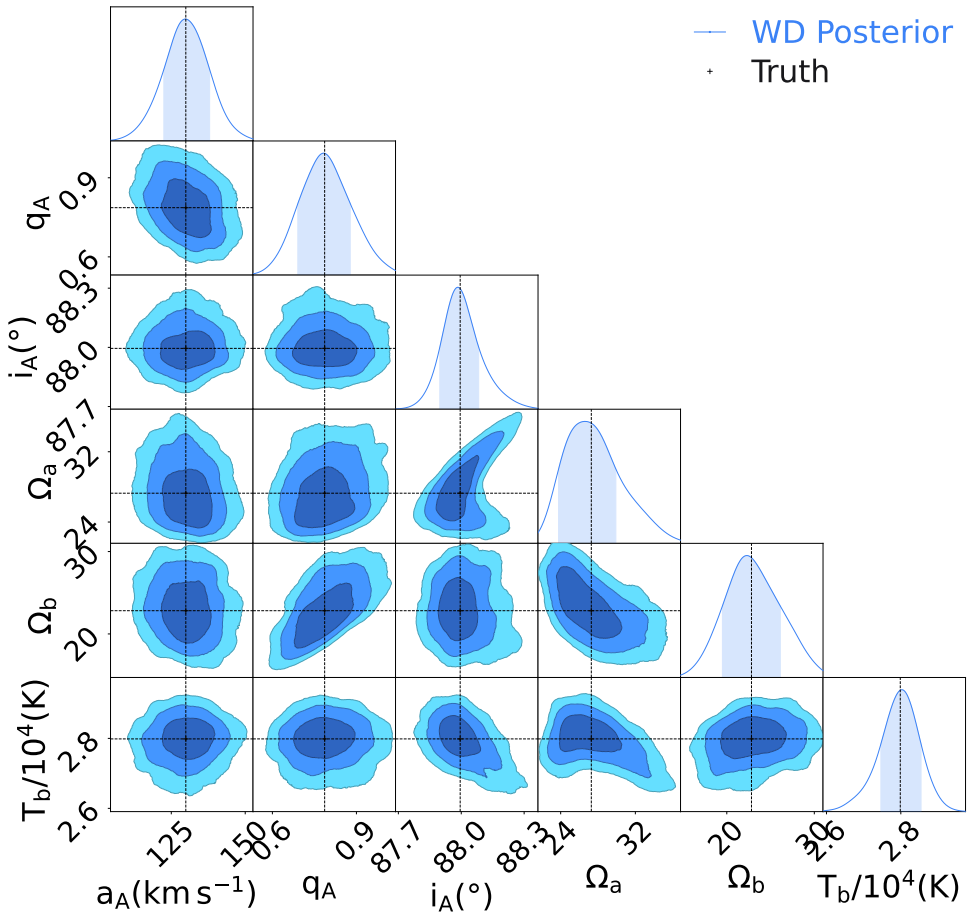

Figure 5.14: Corner plot generated using the `emcee` sampler, showing the one- and two-dimensional posterior distributions of 100,000 iterations for the free parameters derived from the WDC models fitted to the V1371 Tau. The plot represents the probability density of each parameter, with higher point density and denser contours indicating regions of greater probability within the overall posterior distribution. The shaded colour regions correspond to 68%, 95%, and 99% confidence intervals.

5.2.5. The Third Body and its Be Nature

Previous distance estimates for V1371 Tau ranged from 0.87 kpc (Mendoza and Eugenio, 1958) to 0.90 kpc (Gvaramadze, 2006). Leveraging the high-precision astrometry data from Gaia DR3, we have a significantly more precise distance of 1.20±0.03 kpc with high reliability due to the Renormalized Unit Weight Error (RUWE) value ≤ 1.4. This result aligns well with the recent distance estimation (~1.30±0.1 Kpc) for the nearby runaway star HD 37424 by Dinçel et al. (2015). Based on their analysis, we adopt a total V-band extinction of A_v=1.74 mag for V1371 Tau, further supporting the proximity between these objects. This refined distance estimate forms the crucial basis for calculating the absolute parameters of the Be component of V1371 Tau, such as separation, orbital period and mass.

In Sec. 5.2.3 we have already shown that Hα emissions do not present a variation equivalent to a period of ~33 days, a new factor that corroborates with the interferometric measurement of 5 *mas* (Rivinius et al., 2025a). For the purposes of this study, we consider a circular orbit for the

Table 5.3: Resume of parameters for the eclipsing binary in V1371 Tau.

Parameters	Inner Pair	
	a	b
Orbit Period (d)	$33.62090^{\dagger}$	
Time prim. ecl. (BTJD)	$2{,}490.00686^{\dagger}$	
Eccentricity	$0.268^{\dagger}$	
Long. of periastron (°)	$150^{\dagger}$	
Syst. velocity (km s^{-1})	$3.24^{+5.75}_{-5.42}$	
RV amplitude (km s^{-1})	$101.22^{15.97}_{-13.48}$	$139.73^{21.67}_{-19.55}$
Mass Ratio	0.78 ± 0.08	
Inclination (°)	$87.99^{+0.10}_{-0.07}$	
Surface potential	$27.28^{+3.38}_{-2.61}$	$22.82^{+3.47}_{-2.78}$
Orbital ph. shift	$-0.067^{\dagger}$	
Eff. temperature (K)	$25{,}000\pm3{,}000^{\dagger}$	$27{,}997\pm2{,}286$
Semi-major axis (R$_\odot$)	$128.90^{+7.30}_{-7.10}$	
Stellar mass (M$_\odot$)	13.98 ± 3.10	10.81 ± 2.01
Stellar radii (R$_\odot$)	4.93 ± 0.62	4.81 ± 0.57
Surface gravity (cm s^{-2})	4.21 ± 0.11	4.13 ± 4.11
Luminosity (log L/L$_\odot$)	3.93 ± 0.12	4.11 ± 0.11

Notes: †Parameters fixed in all procedures and analyses.

system A+B, and therefore, with the distance to V1371 Tau we determine the separation of the center of mass of the system from the third body, resulting in the measurement of ~1.300 R$_\odot$. For the orbital period of the third body, we use Kepler's third law assuming a mass of ~14 M$_\odot$ based on the measurement of its spectroscopic temperature, which resulted in an orbital period of ~2.50 years. We consider the average radius of ~6.20 R$_\odot$ referent to a standard B0-star, and determine the luminosity of log L/L$_\odot$=4.32 for the B component of V1371 Tau. It is also important to mention that in a system that has not undergone any form of interaction (between A and B), nothing favors a circular orbit, and these are just rough guesses with little confidence and huge margins of error.

It is worth mentioning that if we take the average of the dates with equivalent width of Hα less than zero in 2012 and 2013, and subtract it from the average of the negative EW dates in 2023, we get a period of ~11 years. However, looking at the higher cadence Hα data (in 2022/2023), we see variations on the time scale of months. Outside this time range, the data are too sparse to draw firm conclusions. However, the V/R ratio is approximately always constant and around one (see Figure 5.15), so there is no physical mechanism and no evidence that the disk is perturbed by, for example, tidal forces from some other star.

V1371 Tau appears to be similar to the triple system ν Gem, with the advantage that the inner binary system is eclipsing. V1371 Tau was initially categorized as a Be star by Merrill and Burwell (1943) due to its conspicuous hydrogen lines. To gain a comprehensive understanding of its Be nature, we conducted an in-depth examination of its historical Hα emission patterns using archival data. Employing data from the BeSS catalog, the Goodman and HERMES spec-

trograph spanning the years 2009 to 2024, we discerned noteworthy Hα emissions in 2012, 2013, and most recently, at 2023 (depicted in Fig. 5.15). This intermittent Hα emission pattern conforms to the distinctive mass ejection events characteristic of Be stars. Analysing the orbital phases of the inner binary with the observed Hα emissions, we found that these emissions do not occur due to a transfer of matter caused by the approach of their eclipsing binary companions, which occurs around the inferior conjunction phase of ~0.35. This indicates the true classical Be nature of the system, since this emission is caused by the formation of a Keplerian disk by the third body and that, considering the dilution of the flux from the triple system, the Hα behavior of the Be component in this system appears typical of an early-type Be star and, it behaves like a single Be star due to its large separation from the center of mass of the inner system, ~6 AU, which is greater than 0.5 AU, as proposed by Abt and Cardona (1984).

Although simultaneous TESS and Hα data are not available for 2021, the consistently positive Hα equivalent widths throughout the TESS observing period suggest that there was no major circumstellar disc present, nor significant mass accretion or decretion activity at that time. However, the TESS light curve shows long-term variations, which may be related to disc growth (during sectors 43/44/45) and dissipation (during sectors 71/72). In addition to the eclipses of the inner binary, the light curve also exhibits clear short-term variability outside eclipses. These signals are likely due to stellar pulsations, which may originate from one or more components of the system. Given that all Be stars are known to be pulsators, it is reasonable to attribute at least part of this variability to NRPs from the Be star.

Fortunately, we have extensive spectral coverage from 2023 and recent TESS observations from sectors 71 and 72. The analysis of the Hα equivalent width reveals a period of intense variability and circumstellar activity in early 2023, likely associated with the erratic formation or growth of the Be star's disk. This may have included outbursts that caused an increase in the system's flux, followed by a decay observed at the beginning of sector 71, possibly due to the gradual dissipation of the disk. This scenario is supported by the 2024 spectral observations, which no longer show Hα emission. We cannot rule out the possibility of accretion of material from the SNR by the stars in the system. However, it is unlikely that this would cause a significant variation in the system, especially in the size of the Be star, since the system is on the edge of SNR S147, a place where the dust and gas from the original supernova have practically disappeared into the interstellar medium.

The Be star is not coplanar with the inner eclipsing binary. Nevertheless, some quantitative conclusions can be drawn. The measured $v \sin i$ of the Be star is approximately 250 km s^{-1} (see Sec. 5.2.2). Assuming a range of possible inclination angles for the Be star between 30° and 70°, and adopting the measured $v \sin i$, we can estimate the corresponding equatorial rotation velocity $v_{\rm rot} = v \sin i / \sin i$. This results in $v_{\rm rot} \sim$ 290–500 km s^{-1} across this inclination range. Using the previously estimated stellar radius and mass, we calculated a critical velocity of

$v_{\rm crit} \sim 656\,{\rm km\,s^{-1}}$. This yields a rough estimate of the critical rotation fraction:

$$\Omega/\Omega_{\rm crit} \approx \frac{v_{\rm rot}}{v_{\rm crit}} \sim 0.44\text{–}0.76\,. \tag{5.4}$$

The Be star's $v \sin i$ is significantly higher than that of the components of the inner eclipsing binary, which likely have inclinations close to 90° and thus $v \sin i \approx v_{\rm rot}$. Therefore, we can confidently state that the Be star is rotating much faster than either component of the eclipsing pair. Moreover, the Be star's projected rotational velocity is consistent with typical values found in large Be star samples, especially if we consider the average value of $\Omega/\Omega_{\rm crit}$=0.60 (e.g., Zorec et al., 2016).

This wide range reflects the strong dependence on the unknown inclination angle and projected rotational velocity. Although uncertain, this estimate indicates that the Be star is likely rotating at a substantial fraction of its critical velocity, consistent with expectations for Be stars. A more precise determination of $\Omega/\Omega_{\rm crit}$ will require spectral disentangling and modeling of the circumstellar disk to constrain both the inclination and the intrinsic stellar parameters more reliably.

The combination of the object's physical and orbital characteristics determined so far, together with the spectral classification of its brightest stars, reveal an intriguing puzzle in determining the configuration of this system. Rivinius et al. (2025a) suggests the presence of a third component in the system with a separation of 5 *mas* (measurement obtained with GRAVITY Interferometry). In our analysis, we found other evidences that reinforces that this system is composed of three stars, the outer one being the classical Be star, like: i) the fact that the Hα emission lines do not present a variation in wavelength consistent with the orbital period of the inner binary system, ii) show no sign of shell absorption, which would be expected from a Be star viewed at very high inclination angles (which is the case for the eclipsing pair), iii) The helium emission appears at velocities well outside the photospheric absorption lines of the two eclipsing stars, and iv) They show no asymmetric variation, which would be expected from a close eccentric binary, if one of them were a Be star.

Having a third body in a gravitational stellar system, the dynamical stability will depend on new parameters, no less than eleven, that are necessary to define its orbit and stability, such as those already known in single and binary stars (e.g., eccentricity), mainly separation, inclination, and the argument of the periastron of the stars in the inner and outer orbits. We will now briefly analyses the evolution based on the data and parameters obtained so far, using theoretical models of evolution.

5.2.6. Evolutionary Status

The separation of the inner binary system suggests no continuous mass transfer, despite its eccentricity. As discussed in the previous section, the presence of Hα emission lines, even outside periastron (Fig. 5.15) indicates the Be nature of the system's third component.

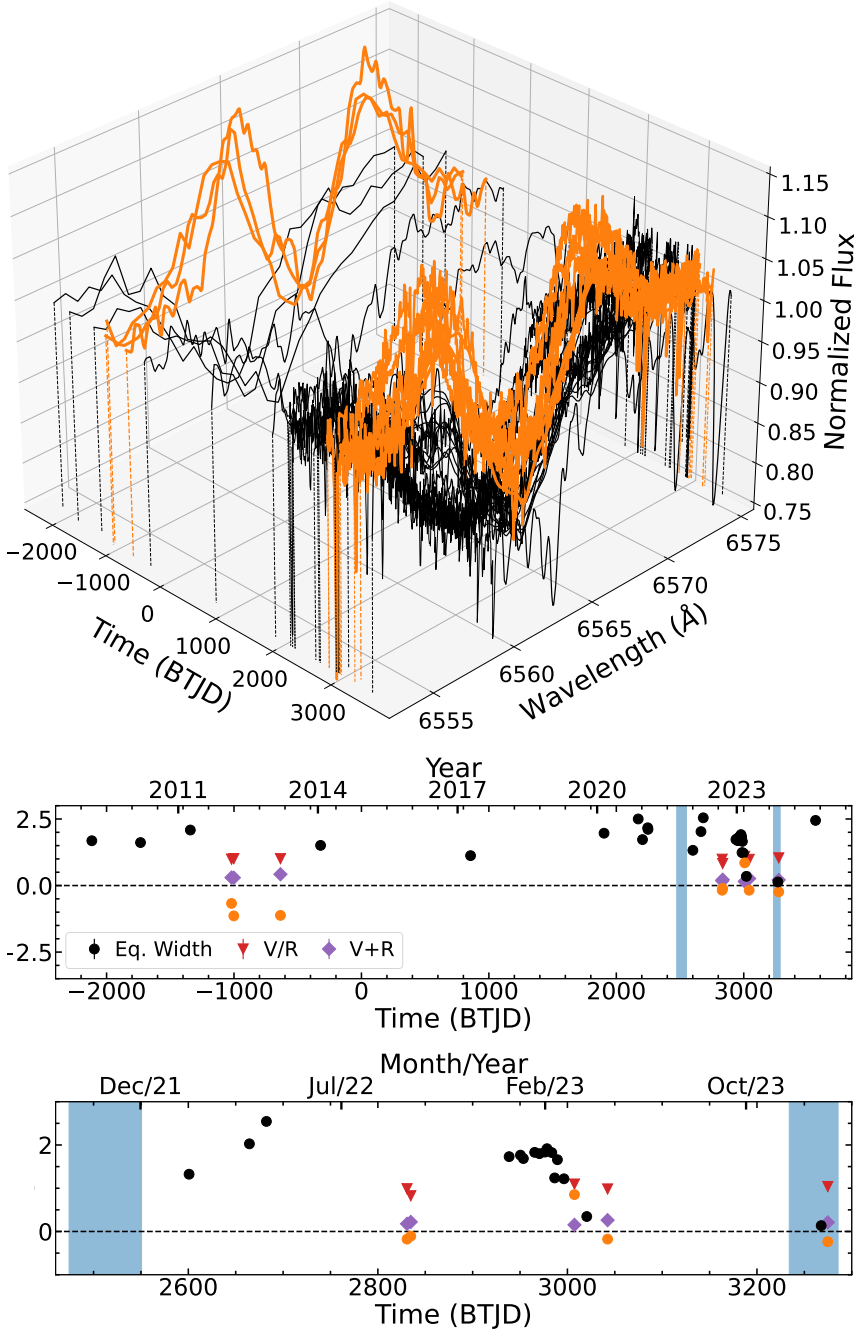

Figure 5.15: Hα analysis of data from BeSS, Goodman and HERMES. Top Panel: Normalized Hα emission lines from spectroscopic observations of V1371 Tau between 2009 and 2024; Mid and Bottom Panel: EW (dot), V/R (inverted triangle) and V+R (Rhombus) of Hα. Orange dots indicate the EW of observations with Hα emission. The blue band indicates the period of TESS photometric observations.

The Fig. 5.16 shows the Hertzsprung–Russell Diagram (HRD) that was constructed to evaluate the evolutionary state of V1371 Tau. The evolutionary and isochronous tracks are of Ekström et al. (2012b) for solar abundances and with rotation ($V/V_{\rm crit} = 0.40$), and were compared with the parameters derived from the component stars of the triple system, represented in the figure by blue stars. To complement our study, we also present the instability domains of SPB and β Cepheid stars defined by Miglio et al. (2007).

The spectrum of V1371 Tau gives us no indication of the presence of a star with a subclassification other than the main sequence, whether it is rich in hydrogen or helium. We can observe that the masses of the components are close with the theoretical trajectories, with the exception of the secondary component of the inner system. Considering the mass and radius measurements of this component and its position in the HRD, and taking into account the margins of error, we consider this as a massive and over-luminous star of the main sequence, as well as other objects already found in the literature (Rocha et al., 2022). This superluminosity characteristic may be linked to its rotation, since component b rotates faster than a, as if it had undergone a process of mass loss, altering its evolutionary stage, consequently making it more luminous than normal. Another fact is that this system is immersed in the supernova remnant S147, making the subclassification of this object a challenge given its possible influence on the brightness of the components due to reddening, which should be investigated further. Furthermore, the evolutionary models are based on single-star evolution, which introduces limitations when applied to systems with multiple stellar components. This result is also known in the literature due to the persistent discrepancy between the evolutionary and dynamical masses (Herrero et al., 1992; de Mink et al., 2009).

If we analyses the evolutionary status of this star disregarding that it is a main sequence star, we have the possibility that it is a post-EHB (Extended Horizontal Branch), becoming in the future a "luminous" sdOB star, which is unlikely due to the mass and radius measurements, and the fact that it is within the β Cepheid instability region. In any case, the key to unveiling the evolutionary status of this system lies in spectral disentangling, which enables more robust and independent determinations of the atmospheric parameters of the individual components of V1371 Tau.

The isochronous features that pass close to the main sequence components, we infer a common age of ~10 Myrs for the stars of V1371 Tau, making these stars one of the youngest known.

5.2.7. Frequency Analysis

To conduct a frequency analysis of the photometric data of V1371 Tau, it was necessary to isolate the intrinsic variability of the stellar atmosphere by removing the modulation caused by the eclipses. This was achieved by incorporating the constant flux contribution from the third component into the synthetic light curve of the inner eclipsing binary, and subsequently subtracting the resulting model from the observed light curve. For this analysis, we considered

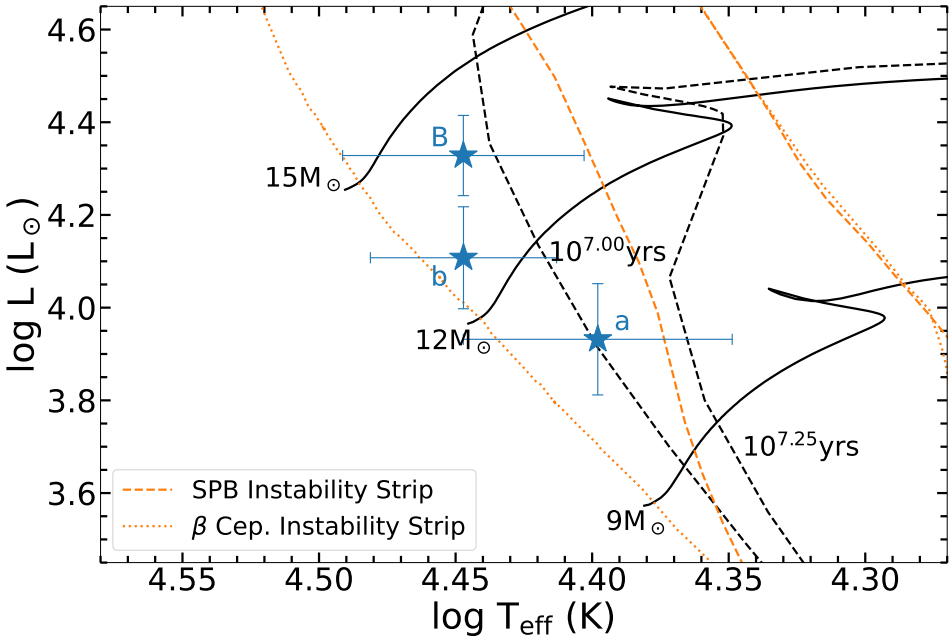

Figure 5.16: Hertzsprung-Russell diagram of V1371 Tau based on solar-metallicity models from Ekström et al. (2012b) with $V/V_{crit} = 0.4$. Solid black lines indicate evolutionary tracks for different stellar masses, while dotted black lines represent isochrones of various ages. The system's components are marked as blue stars.

that approximately two-thirds of the total system flux originates from subsystem A, while the remaining one-third is attributed to component B, as estimated in Section 5.2.2.

We analysed the residual light curve using Lomb-Scargle periodograms and the iterative prewhitening method to identify characteristic frequencies, aiming to infer pulsation modes and the rotation period. The Fig. 5.17 shows the Lomb-Scargle periodogram and the residual wavelet analysis of the light curve of V1371 Tau, with the eclipse excess removed to enhance the visualization of the residuals. This excess flux arises due to limitations in the fitting process with `emcee`, whose optimization does not work well when dealing with light curves with abrupt features, such as narrow eclipses. These features introduce steep gradients in the likelihood surface, making it difficult for the walkers to converge efficiently in parameter space. Despite this, the excess does not affect the physical, orbital or frequency analyses.

This analysis identifies two primary frequencies: $f_1 = 0.24\,\mathrm{d}^{-1}$ and $f_2 = 0.26\,\mathrm{d}^{-1}$ (see Fig. 5.17), which lead to a beat frequency of $f_{2-1} = 0.02\,\mathrm{d}^{-1}$. A similar phenomenon was reported by Emilio et al. (2010) in their photometric study of Be star CoRoT-ID 102761769. However, based on the TESS photometric data, this beat frequency corresponds to a beat envelope with period of the approximately 50 days. The stellar origin of these frequencies remains uncertain, but we cannot rule out the possibility that they originate from the star Be. After removing these low-frequency sinusoidal signals, we detect a high-frequency signal at $6.87\,\mathrm{d}^{-1}$. This frequency is characteristic of NRPs and may be associated with the Be star; however, since all components could be pulsators and have similar brightness, this identification remains uncertain.

The analysis revealed insufficient frequencies in the range required to apply the Takata

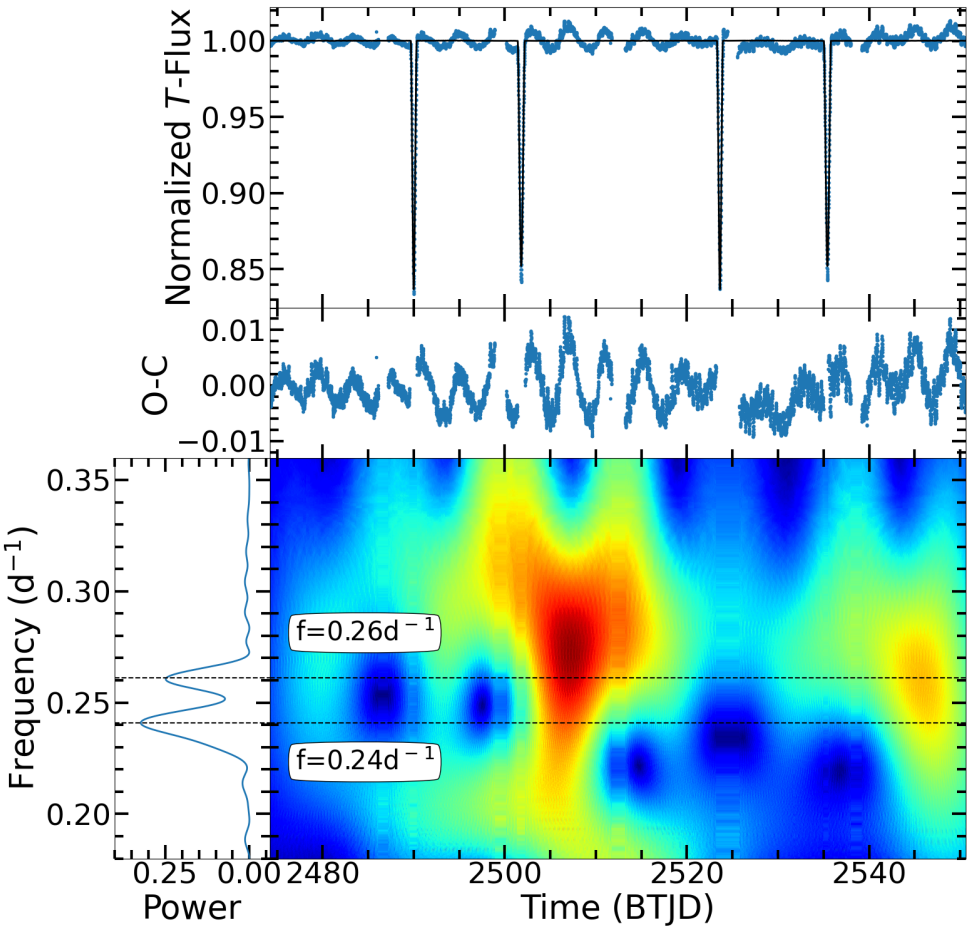

Figure 5.17: Top panel: Normalized TESS photometric light curve of V1371 Tau from sectors 43, 44, and 45. Middle panel: Residuals obtained after subtracting the scaled model of the eclipsing binary. Bottom panel: Frequency analysis of the residual light curve of V1371 Tau using the Lomb-Scargle periodogram (left) and the continuous wavelet transform (right).

method (Takata et al., 2020), which depends on detecting a clear pattern of progressively spaced sectoral modes. This lack of sufficient and distinct frequency patterns in the data prevents us from confidently linking the detected frequencies to specific physical mechanisms, such as stellar rotation or g-mode NRPs, to any of the stars within the system.

5.2.8. Orbital Dynamics

This system, initially studied with KELT ground-based photometry in 2017, revealed much more complexity when revisited with high-precision TESS data. While ~0.15 mag eclipses should have been detectable in KELT (given its design for exoplanet transits), they were not clearly identified, likely due to intrinsic variability from the Be star's disk and evolving orbital geometry (Labadie-Bartz et al., 2017).

TESS observations show that the timing of the eclipses varies across sectors, and no single period aligns both primary and secondary eclipses consistently—strongly suggesting apsidal motion in the inner binary. Moreover, the eclipses are noticeably shallower in the KELT data compared to TESS, even though the stellar components' physical properties should be un-

changed. This points to a variation in orbital inclination, possibly driven by Kozai-Lidov cycles (Naoz, 2016) induced by the outer Be star.

Photometric variability seen in KELT outside of eclipses is consistent with density changes in the Be disk at moderate inclination, typical for classical Be stars. These trends further support the scenario of an active and evolving circumstellar environment.

The system's formation history raises two possibilities:

1. The Be star may have evolved as an isolated rapid rotator, without past binary interactions.

2. Alternatively, it may have undergone mass transfer from a now-undetectable companion (e.g., a faint sdOB star), which would imply a previous binary phase.

However, current mass estimates are insufficient to favor either scenario, and no short-period luminous companion is detected. Further spectroscopic and interferometric observations are essential to determine the Be star's mass, inclination, and potential unseen companions.

6 Conclusions and Perspectives

This work presents a significant contribution to the understanding of Be stars in binary systems, a class of objects that challenges classical models of stellar evolution due to their extreme rotation, circumstellar disks, and photometric and spectroscopic variability. The methodology adopted in this thesis was multidisciplinary and based on high-quality observational data, combining astrometry (Gaia DR3), high-precision photometry, spectroscopy, and robust modeling using the Wilson–Devinney code and Bayesian inference techniques via `emcee`.

The analysis involved a sample of binary systems containing at least one Be star, selected with rigorous criteria based on visual inspection, spectral identification and orbital parameters. This manuscript reveals a considerable diversity of binary configurations involving Be stars, ranging from short-period systems to wide-orbit candidates. This supports the idea that binarity plays multiple roles in the emergence and maintenance of the Be phenomenon—from spin-up mechanisms through angular momentum transfer to gravitational interactions that trigger mass ejections or modulate circumstellar disk structures.

A systematic and rigorous methodology was adopted to confirm both the binary nature and the presence of classical Be stars in the initial list of 158 targets. The process involved three main steps: (i) an extensive literature review, (ii) photometric light curve analysis, and (iii) spectroscopic inspection, with special attention to typical Be star signatures such as Hα and HeI emission lines.

As a result, 50 systems were confirmed to host classical Be stars in binary configurations, including 2 exhibiting eclipsing behavior. An additional 66 systems were classified as binaries without a Be component, often showing signs of mass transfer or contact, which can mimic the characteristics of Be binaries. Furthermore, 37 systems were excluded due to lack of evidence for binarity, and 05 could not be reliably classified due to insufficient observational data.

The angular distribution of these confirmed Be binary systems was analyzed using the Aitoff projection, which revealed an approximately uniform distribution across the celestial sphere, with no significant clustering. This spatial homogeneity suggests that the sample is not significantly affected by selection biases such as survey coverage gaps or targeted observations,

thereby reinforcing its statistical robustness.

The frequency analysis of the Be binary systems presented in this work reveals a complex and heterogeneous pattern of stellar variability. After carefully removing orbital signatures, including eclipses, ellipsoidal modulations, and sector-dependent systematics, the residual light curves exhibit a dominant concentration of frequencies in the range of 0.5 to 4.0 d^{-1}. This frequency regime is typically associated with non-radial gravity-mode pulsations and rotational modulation, in agreement with previous studies of Be stars in both single and binary systems (e.g., Rivinius et al., 2013; Labadie-Bartz et al., 2022).

A small subset of systems exhibited higher frequency components (4–10 d^{-1}), which may correspond to pressure-mode (p-mode) pulsations. Although less common, such features are particularly intriguing in early-type Be stars, as they may reflect internal excitation mechanisms modulated by fast rotation or tidal interactions. Additionally, several systems displayed low-frequency signals (<0.5 d^{-1}), which may originate from instrumental effects, disk-related variability, or large-scale structural changes such as precession or episodic mass ejections.

Notably, the presence of beat patterns and frequency clustering in multiple systems suggests modal interaction or amplitude modulation, potentially influenced by binarity. The application of an iterative prewhitening technique combined with Lomb-Scargle periodograms enabled the extraction of the three most dominant frequencies per star, as summarized in Appendix C and visualized in Figures 5.3 and 5.4. The systematic classification of these frequency components enabled us to disentangle the intrinsic stellar variability from binary-induced modulations, providing a clearer picture of the physical mechanisms at play.

Despite the diversity of frequency content, only four targets showed evidence of harmonic structures, with orders ranging from $n = 2$ to $n = 8$, indicating that nonlinear, periodic modulations are not the prevailing mechanism in most cases. The low incidence of harmonics and the dominance of non-harmonic variability align with the current understanding that Be stars, especially those in binaries, are governed by a superposition of processes: non-radial pulsations, rotational modulation, circumstellar disk oscillations, stochastic activity, and binary-induced effects. The identification of high-order harmonics in a few systems, however, opens the door to targeted studies of specific coupling mechanisms, including resonance, disk asymmetries, or periodic mass-loss episodes.

Furthermore, the modeling of light curves for eclipsing systems allowed the subtraction of residual flux excess near eclipses, a byproduct of MCMC convergence challenges in fitting sharp features, ensuring that intrinsic stellar variability was preserved for frequency analysis. These residuals, although localized in orbital phase, did not impact the detection of pulsational or rotational signals.

Spectroscopic analysis of Be binaries shows that Hα equivalent width, a proxy for disk activity, displays diverse variability patterns influenced by both intrinsic processes and binary interactions. Four categories were identified: constant, small, significant aperiodic, and significant periodic changes. Constant or small variations indicate relatively stable disks, sometimes

affected by eclipses, while aperiodic variations suggest unstable environments linked to mass ejection or irregular interactions. Periodic modulation, though less common, points to phase-dependent binary effects, especially in short-period or eccentric systems. These results highlight the strong role of binarity in shaping disk dynamics and provide a framework for future follow-up studies.

Our multivariate correlation analysis of fundamental stellar parameters for Be stars in binary systems highlights several significant empirical trends consistent with theoretical stellar evolution models. In particular, effective temperature and stellar mass show a strong positive correlation, reflecting the well-understood relationship that more massive stars possess higher core and surface temperatures. Similarly, stellar mass correlates tightly with radius, confirming the expected mass-radius scaling for main-sequence stars in the 3–20 $M_{\odot}$ range typical of Be stars. An inverse trend between $T_{\rm eff}$ and surface gravity is observed, albeit with increased scatter due to evolutionary effects and observational uncertainties. Parameters related to stellar rotation, such as projected rotational velocity, exhibit weak or no clear correlation with mass, radius, or temperature, likely due to inclination effects and the intrinsic variability of rotational velocities in the sample. Furthermore, the dominant photometric frequency displays no straightforward dependence on these fundamental properties, indicating that the observed variability arises from complex mechanisms including pulsations, rotational modulation, and circumstellar disk phenomena.

Additionally, the rotational velocity distribution of Be stars in binaries, quantified by the ratio $v \sin i / v_{\rm crit}$ shows values ranging from 0.30 to 0.85 with an average near 0.47, whereas single Be stars typically cluster between 0.30 and 0.95 (Zorec et al., 2016). Theoretical studies support the possibility that Be phenomena can occur below the classical critical velocity limit when accounting for gravity darkening and stellar deformation effects. Our results therefore imply that Be stars in binary systems may achieve the conditions necessary for circumstellar disk formation at sub-critical rotations, potentially relying on additional processes like non-radial pulsations or magnetic fields to drive disk ejection. Overall, these findings emphasize the complex interplay between stellar structure, rotation, and binarity in shaping the observed properties and evolutionary pathways of classical Be stars.

Special attention was given to the V1371 Tau system. We present a detailed study of the hierarchical system V1371 Tau, located at 1.20±0.10,kpc, using TESS photometry and multi-epoch spectroscopy. The system consists of a close eclipsing B-type binary (B1V + B0V) orbited by a classical Be star (B0Ve). Identification of the outer Be component was confirmed via Hα variability and previous interferometric detection (Rivinius et al., 2025a).

Modeling the inner binary's spectra and light curves provided atmospheric and orbital parameters, including a mass ratio q_A=0.78, eccentricity ~0.27, component masses of 13.98 and 10.81 $M_{\odot}$, and radii of 4.92 and 4.81 $R_{\odot}$. The outer Be star likely follows a semi-major axis of ~1,300 R⊙, with a period of ~2.5 yrs and a rotation of 44–76% of its critical velocity. The HR diagram indicates all components are young massive main-sequence stars, with an age

of ∼10 Myrs. Future work includes spectral monitoring to determine individual temperatures, $\log g$, $v \sin i$, and outer orbit parameters, along with interferometric and X-ray observations. These efforts will enhance the understanding of Be-star disks, binary interactions, and the evolution of hierarchical massive systems.

In light of the results and the challenges identified, the following directions are proposed for future studies:

To enhance the robustness of our results and assess environmental effects on Be star evolution, we plan to extend our sample to binaries in different Galactic regions and in the Magellanic Clouds, where metallicity and star formation conditions vary. We will also include related subtypes (e.g., B[e] stars and transitional objects) to probe possible common evolutionary channels. This effort will be supported by large-scale photometric surveys such as OGLE and by upcoming high-precision PLATO data, enabling variability studies and binarity detection across diverse stellar populations.

Continued multi-wavelength monitoring of the Be binary sample is essential to improve parameter accuracy and trace variability linked to stellar activity and binary interactions. We plan to obtain new high-resolution optical spectra with the Coudé spectrograph at OPD/LNA for line profile analysis, radial velocity monitoring, and disk variability studies. Complementary near-infrared spectra from instruments such as TripleSpec at SOAR will provide constraints on disk structure, temperature, and density, as well as detect binarity signatures less evident in the optical. The joint use of optical and infrared diagnostics will allow a more complete characterization of Be disks across different orbital phases and viewing geometries.

Since the physical parameters of our sample were initially compiled from heterogeneous literature sources, the next step will be to derive them directly through individual spectral modeling of each binary component. This will provide more robust and homogeneous results, strengthening the reliability of our conclusions. In parallel, high-angular-resolution interferometry will be key to resolving Be-star disks in binaries and tracing their morphological changes across orbital phases. Such data will allow us to detect tidal truncation, warping, or precession, and to compare the disk orientation with the orbital plane. This comparison is crucial to assess alignment or misalignment, offering new insights into angular momentum transfer, binary evolution, and disk feeding processes.

Hydrodynamical simulations will be essential to investigate how companions affect the formation, evolution, and stability of Be-star disks. By modeling mass transfer, tidal forces, and angular momentum exchange, especially in eccentric binaries, it will be possible to test scenarios of disk truncation, warping, and spiral density wave formation. These models can also account for observed photometric and spectroscopic variability and provide predictions for upcoming high-resolution observations.

The parameters derived from our Be binary sample will provide key inputs for population synthesis models, allowing us to test evolutionary channels such as mass transfer, mergers, or tidal spin-up. By incorporating constraints like mass ratios, orbital periods, eccentricities, and

rotation into codes such as BSE, BPASS, or StarTrack, we can compare theoretical predictions with observed Be populations in different environments. This will help quantify the role of binary evolution in Be-star formation and assess whether these stars arise mainly from isolated evolution or binary interactions.

Building on the Gaia results, we will model the evolutionary histories of Be binaries with the MESA code. These simulations include rotation, mass transfer, angular momentum loss, and envelope inflation, allowing us to reconstruct evolutionary pathways, estimate disk formation and spin-up timescales, and evaluate the impact of binary interactions on Be lifetimes. Combined with our observations, this will provide a robust framework to interpret the diversity of Be star properties in the context of binary evolution.

Finally, we will focus on eclipsing and SB2 systems, where multiwavelength eclipses and combined photometry–spectroscopy enable detailed studies of disk structure, dynamics, and binary interactions, providing key insights into the formation and maintenance of Be circumstellar disks.

We also highlight stars with extensive long-term monitoring of Hα EW variations, which reveal cyclic patterns linked to disk dynamics, formation and dissipation cycles, and possible modulation by stellar rotation or pulsations. Such well-sampled datasets enable detailed investigation of disk stability, feeding processes, and the influence of a companion. Time-series analysis, including Fourier transforms and prewhitening, will be applied to detect periodicities and trends, with results integrated into photometric and interferometric data for a comprehensive system characterization.

Objects such as the triple system V1371 Tau will receive special attention through high-resolution spectroscopy, multi-filter precision photometry, interferometric disk mapping, and detailed numerical modeling. This in-depth study will clarify the physical mechanisms driving variability, evolution, and disk structure in Be binaries, while providing fundamental orbital and stellar parameters to improve our understanding of the broader population.

Final Remarks

This thesis presents a modern and technically refined synthesis of the complex nature of Be stars in binary and multiple systems. By integrating orbital and spectral modeling with high-quality observational data, it lays a solid foundation for understanding the physics of these stars in dynamic environments. Moreover, it opens promising avenues for future research in a field that still holds many mysteries regarding the conditions that give rise to the fascinating, and not yet fully understood, Be phenomenon.

A Mathematical Descriptions

A.1. Calculation of the True Anomaly in Radial Velocity Analysis

The calculation of the true anomaly (θ) for an elliptical orbit can be described in detail as follows.

Mean Anomaly M

The mean anomaly is defined as a linear function of time since periastron passage:

$$M(t) = n(t - T_0) = \frac{2\pi}{P}(t - T_0)\,, \tag{A.1}$$

where $n = 2\pi/P$ is the mean motion, P is the orbital period, and T_0 is the time of periastron passage. The mean anomaly grows linearly with time and is independent of the orbit's eccentricity.

The eccentric anomaly is obtained by solving Kepler's equation:

$$M = E - e\sin E\,, \tag{A.2}$$

which is transcendental and usually requires a numerical solution. Common methods include Newton-Raphson or bisection.

Newton-Raphson Iteration:

$$E_{i+1} = E_i - \frac{E_i - e\sin E_i - M}{1 - ecosE_i}\,. \tag{A.3}$$

Typical initial guesses are:

$$E_0 = M \quad \text{for } e < 0.8, \quad E_0 = \pi \quad \text{for } e \geq 0.8\,. \tag{A.4}$$

Convergence is achieved when $|E_{i+1} - E_i| < 10^{-8}$.

Low-Eccentricity Approximation: For $e \ll 1$, Kepler's equation can be expanded as:

$$E \approx M + e\sin M + \frac{e^2}{2}\sin 2M + \frac{e^3}{8}(3\sin 3M - \sin M) + \ldots\,. \tag{A.5}$$

This approximation is accurate for $e \lesssim 0.1$ and avoids iterative solutions.

True Anomaly θ

Once E is known, the true anomaly is calculated as:

$$\tan\frac{\theta}{2} = \sqrt{\frac{1+e}{1-e}}\,\tan\frac{E}{2}\,, \tag{A.6}$$

or equivalently,

$$\theta = 2\arctan\left(\sqrt{\frac{1+e}{1-e}}\,\tan\frac{E}{2}\right). \tag{A.7}$$

For nearly circular orbits ($e \ll 1$) a simpler series can be used:

$$\theta \approx E + 2e\sin E \approx M + 2e\sin M + \frac{5}{4}e^2\sin 2M + \ldots\,. \tag{A.8}$$

A.2. Some detailed analysis of V1371 Tau

Scenario Overview:

We observed a light curve ranging from 1.00 (out of eclipse) to 0.83 (during eclipse), indicating an eclipse depth of 17%. The question is: what is the contribution of a third component to the total observed flux?

Ideal Case: Three Identical Stars

If all three stars were identical, each contributing equally to the total flux:

Total flux = $3F$

During an eclipse of one star: flux drops by F

Depth = $\frac{F}{3F} = \frac{1}{3} = 33\%$

So, a 33% eclipse depth would indicate three equal stars.

Actual Observation: 17% primary Eclipse Depth

In our case, the primary eclipse depth is only 17%. This suggests the third star contributes significantly more flux than each eclipsing star.

Assuming the third component contributes approximately 33% of the total flux (i.e., 0.33), the eclipse depth is diluted by this contribution.

To find the true eclipse depth of the eclipsing stars alone, we remove the flux contribution of the third component from the light curve. The corrected eclipse depth ($D_{\text{corrected}}$) is given by:

$$D_{\text{corrected}} = 1 - \frac{F_{\text{ecl}} - F_3}{F_{\text{total}} - F_3}\,, \tag{A.9}$$

where:

$$\begin{aligned} F_{\text{total}} &= 1.00 \quad \text{(flux out of eclipse)} \\ F_{\text{ecl}} &= 0.83 \quad \text{(flux during eclipse)} \\ F_3 &= 0.33 \quad \text{(flux from third component)} \end{aligned}$$

Substituting values:

$$D_{\text{corrected}} = 1 - \frac{0.83 - 0.33}{1.00 - 0.33} = 1 - \frac{0.50}{0.67} = 1 - 0.75 = 0.25 = 25\%\,. \tag{A.10}$$

Therefore, the true eclipse depth of the two eclipsing stars, without dilution from the third star's light, is 25%, which is significantly deeper than the observed 17%.

The depth of a transit light curve is related to the fraction of stellar flux blocked by a transiting object, such as a planet or stellar companion. If the stellar flux outside the transit is normalized to 1, the transit depth is given by:

$$\delta = \frac{F_{\text{out}} - F_{\text{in}}}{F_{\text{out}}} \tag{A.11}$$

where:

- F_{out} is the out-of-transit flux (typically normalized to 1);
- F_{in} is the minimum in-transit flux;
- δ is the transit depth.

In this work, we consider a light curve with an initial depth of $\delta_0 = 0.25$ and aim to reduce it to a new depth of $\delta_1 = 0.17$.

Calculating the In-Transit Flux

Assuming $F_{\text{out}} = 1$, we obtain:

$$F_{\text{in},0} = 1 - \delta_0 = 1 - 0.25 = 0.75 \tag{A.12}$$

and

$$F_{\text{in},1} = 1 - \delta_1 = 1 - 0.17 = 0.83 \tag{A.13}$$

In other words, to achieve the desired depth, we need to increase the in-transit flux from 0.75 to 0.83.

Correcting the Light Curve

If we already have observational data for the light curve with depth $\delta_0 = 0.25$, we can correct the in-transit points using the following linear transformation:

$$F_{\text{corrected}} = 1 + (F_{\text{original}} - 1) \cdot \frac{F_{\text{in},1} - 1}{F_{\text{in},0} - 1} \tag{A.14}$$

Substituting the numerical values:

$$F_{\text{corrected}} = 1 + (F_{\text{original}} - 1) \cdot \frac{0.83 - 1}{0.75 - 1} = 1 + (F_{\text{original}} - 1) \cdot \frac{-0.17}{-0.25} = 1 + (F_{\text{original}} - 1) \cdot 0.68 \tag{A.15}$$

This correction factor of 0.68 ensures that the minimum flux is adjusted from 0.75 to 0.83.

Synthetic Light Curve Case

If the light curve is being generated from a model (e.g., using the `batman` code), the depth can be directly adjusted by changing the ratio of the transiting object's radius to the stellar radius:

$$\delta \approx \left(\frac{R_p}{R_*} \right)^2 \tag{A.16}$$

To obtain the radius ratio corresponding to $\delta_1 = 0.17$, we take the square root:

$$\frac{R_p}{R_*} = \sqrt{0.17} \approx 0.412 \tag{A.17}$$

Thus, to achieve the desired depth, the parameter R_p/R_* in the model should be adjusted to approximately 0.412.

Bayesian Fusion of Temperature Estimates

Using Bayes' Theorem and assuming that each measurement follows a Gaussian distribution, perform the Bayesian fusion of the following temperature estimates:

- First measurement: $\mu_1 = 27\,985$ K, $\quad \sigma_1 = 3\,533$ K
- Second measurement: $\mu_2 = 28\,000$ K, $\quad \sigma_2 = 3\,000$ K

The fused (posterior) mean and variance for two Gaussian distributions with known uncertainties are given by:

$$\mu_{\text{post}} = \frac{\mu_1/\sigma_1^2 + \mu_2/\sigma_2^2}{1/\sigma_1^2 + 1/\sigma_2^2}$$
$$\sigma^2_{\text{post}} = \left(\frac{1}{\sigma_1^2} + \frac{1}{\sigma_2^2}\right)^{-1}$$

Substituting the values:

$$\frac{1}{\sigma_1^2} = \frac{1}{3533^2} \approx 8.012 \times 10^{-8}$$
$$\frac{1}{\sigma_2^2} = \frac{1}{3000^2} = 1.111 \times 10^{-7}$$

Posterior Variance

$$\frac{1}{\sigma^2_{\text{post}}} = 8.012 \times 10^{-8} + 1.111 \times 10^{-7} = 1.912 \times 10^{-7}$$
$$\sigma^2_{\text{post}} = \frac{1}{1.912 \times 10^{-7}} \approx 5.23 \times 10^6$$
$$\sigma_{\text{post}} \approx \sqrt{5.23 \times 10^6} \approx 2\,286 \text{ K}$$

Posterior Mean

$$\mu_{\text{post}} = \frac{27\,985 \cdot 8.012 \times 10^{-8} + 28\,000 \cdot 1.111 \times 10^{-7}}{1.912 \times 10^{-7}}$$
$$\approx \frac{2.242 + 3.111}{1.912 \times 10^{-7}} \approx \frac{5.353}{1.912 \times 10^{-7}} \approx 27\,997 \text{ K}$$

Final Result

$$\boxed{T = 27\,997 \pm 2\,286 \text{ K}} \tag{A.18}$$

B Sample List of the Proposals Approved in TESS General Investigator program

Table B.1: Targets observed in TESS sectors 084 to 096 for program G07166.

TIC ID	RA (deg)	Dec (deg)	Magnitude	Exp. Time
Sector 084 targets observed (2 min: 18, 20 s: 3)				
444325059	358.4022	56.8199	8.14	120 s
153880067	340.7387	44.7217	8.57	120 s
154355871	342.5908	41.9534	5.79	120 s
155030422	345.4804	42.3260	3.75	20 s
252500679	344.2689	48.6840	5.22	20 s
252670277	346.7759	50.1924	6.47	120 s
25692574	352.4030	48.3809	8.01	120 s
177638673	359.6937	46.4132	6.52	120 s
240757326	11.1816	48.2843	4.42	20 s
324820890	330.4092	50.1680	9.15	120 s
326247844	331.5348	49.9024	9.61	120 s
429843636	323.0863	59.5725	7.58	120 s
431116093	335.0947	51.8610	7.12	120 s
377900979	348.8663	62.0790	8.89	120 s
411577031	328.8793	65.3208	6.16	120 s
434893323	346.0093	63.3969	7.23	120 s
322060937	324.2377	68.1853	8.17	120 s
387813185	315.4040	68.1633	6.77	120 s
Sector 085 targets observed (2 min: 11, 20 s: 2)				
186598770	45.0497	38.1316	6.12	120 s
444325059	358.4022	56.8199	8.14	120 s

240757326	11.1816	48.2843	4.42	20 s
410501448	25.9154	50.6886	4.16	20 s
368237682	358.0505	67.1687	9.53	120 s
377900979	348.8663	62.0790	8.89	120 s
434893323	346.0093	63.3969	7.23	120 s
331811163	6.4635	71.8071	6.94	120 s
322060937	324.2377	68.1853	8.17	120 s
387813185	315.4040	68.1633	6.77	120 s
411577031	328.8793	65.3208	6.16	120 s

Sector 086 targets observed (2 min: 9, 20 s: 4)

259463816	62.1656	47.7123	3.94	20 s
285937814	54.1227	48.1924	4.24	20 s
26432264	56.6703	32.2901	6.58	120 s
2940839	81.9683	34.7828	8.14	120 s
252414037	76.5351	58.9723	5.41	20 s
8300380	65.5036	54.5120	9.10	120 s
331811163	6.4635	71.8071	6.94	120 s
387813185	315.4040	68.1633	6.77	120 s
48022676	281.6797	52.9879	5.95	20 s

Sector 087 targets observed (2 min: 8, 20 s: 7)

24824031	97.2067	-7.0347	5.49	20 s
24824033	97.2044	-7.0331	4.70	20 s
71727949	91.0562	-6.7089	5.21	20 s
425224332	111.7873	8.2891	2.99	20 s
52982382	102.4602	-32.5084	3.55	20 s
140214221	84.9123	-34.0743	2.65	20 s
201373582	91.7653	-34.3120	5.85	20 s
29628522	97.1635	-32.3712	6.09	20 s

Sector 088 targets observed (2 min: 8, 20 s: 5)

146036695	123.3729	-35.8994	5.15	20 s
155573117	123.5154	-28.3239	10.62	120 s
405216722	114.1762	-13.0638	9.03	120 s
175523591	116.5438	-37.9336	6.00	20 s
174008063	113.4626	-36.3384	5.53	20 s
174664153	114.9916	-37.5795	6.04	120 s
20521049	116.5022	-35.7958	5.00	20 s
20286771	115.6557	-36.6584	6.03	120 s

Sector 089 targets observed (2 min: 5, 20 s: 3)

16942434	138.2717	-43.4369	6.69	120 s

21408009	142.2843	-46.0353	6.60	120 s
15059115	135.9110	-41.5885	6.51	120 s
15167827	138.3190	-44.1935	6.22	120 s
15657690	138.7640	-45.5951	6.37	20 s

Sector 090 targets observed (2 min: 6, 20 s: 2)

18849233	164.0137	-45.9465	4.70	120 s
19084891	165.5704	-46.8460	6.70	120 s
21340120	172.0491	-44.3478	4.98	20 s
21992717	173.2563	-45.3282	5.35	20 s
21398350	172.0283	-44.4562	7.35	120 s
21748846	173.0624	-44.8024	8.72	120 s

Sector 091 targets observed (2 min: 5, 20 s: 5)

25481306	187.9204	-48.2059	6.49	120 s
25672634	189.2187	-48.2645	6.37	120 s
24296752	188.0670	-47.1471	6.35	120 s
24451074	188.7561	-47.7624	6.16	120 s
25953431	190.4974	-48.4625	6.16	120 s
29134364	188.1900	-48.1695	6.15	20 s
24280309	187.9994	-47.1206	6.10	120 s
25485239	187.9710	-48.2190	6.09	20 s
24277946	187.9939	-47.1598	6.08	120 s

Sector 092 targets observed (2 min: 6, 20 s: 3)

27465744	208.8803	-43.8182	5.12	20 s
27650303	210.2421	-43.9925	5.09	20 s
28785781	210.0221	-44.8143	5.08	20 s
27747767	209.5208	-44.1212	5.05	20 s
28551279	210.0647	-44.5904	5.02	20 s
29394871	211.4641	-45.0568	4.97	20 s
31405093	208.8632	-44.2363	6.15	120 s

Sector 093 targets observed (2 min: 9, 20 s: 4)

25550309	223.8579	-40.2648	6.46	120 s
25705236	225.4386	-40.5237	6.38	120 s
28081522	232.4225	-42.5221	6.37	120 s
28774555	232.1049	-43.2694	6.18	120 s
28855572	232.4925	-43.3308	6.16	120 s
30847733	228.2391	-41.6996	6.11	20 s
29823401	233.1727	-43.8849	5.72	120 s

Sector 094 targets observed (2 min: 8, 20 s: 5)

32604969	242.9947	-38.6980	6.45	120 s

32714180	244.0022	-39.0797	6.27	120 s
31862078	245.2216	-39.6286	6.11	20 s
31856487	243.4737	-39.4276	5.69	20 s
31074742	241.8962	-38.8354	5.52	20 s
29735051	241.6930	-38.8487	5.47	120 s
29471882	242.1561	-39.4850	5.46	120 s
29659265	241.0735	-39.0510	5.20	20 s
Sector 095 targets observed (2 min: 8, 20 s: 6)				
34442099	262.7762	-35.9333	5.23	20 s
34442098	262.7762	-35.9334	5.17	20 s
35812339	270.1605	-34.5431	5.06	20 s
35284117	267.9736	-34.8468	4.94	20 s
35074158	269.4210	-35.1990	4.89	20 s
33326384	266.8128	-35.9893	4.85	120 s
32842361	262.2951	-34.7387	4.56	120 s
33236612	268.3063	-35.8162	4.35	20 s
33236571	268.2852	-35.7671	4.34	120 s
Sector 096 targets observed (2 min: 7, 20 s: 5)				
36550470	280.1744	-32.4407	5.53	120 s
36721203	282.0087	-32.3777	5.49	20 s
37073809	282.3740	-33.0159	5.48	20 s
36284239	280.0054	-32.1810	5.34	120 s
35283781	279.1074	-32.8565	5.32	120 s
36002235	281.0006	-32.1391	5.12	20 s
35812535	280.7560	-32.0972	4.99	120 s

C Individual Sample Description

In order to provide a comprehensive overview of the selected targets, this section presents a detailed description of the photometric and spectroscopic characteristics of each system in the sample. For every object, we include its observed light curve and representative optical spectrum, highlighting features relevant to the classification and analysis of Be stars in binary systems.

The photometric data allow for the identification of variability patterns commonly associated with binarity, such as eclipses, ellipsoidal modulation, or outbursts, as well as potential signatures of circumstellar disk activity typical of Be stars. In addition to the visual inspection of the light curves, a frequency analysis was performed using time-series photometry to investigate periodic and quasi-periodic signals. This analysis provides important insights into the dynamical behavior of the systems, enabling the detection of orbital periods, pulsations, or disk-related variability.

Meanwhile, the spectroscopic profiles, particularly focusing on the presence of Balmer line emission (notably Hα), help confirm the Be nature of the component(s) and provide evidence for dynamical interactions within the system.

The light curve, frequency analysis, and optical spectrum of each target are summarized individually, where visual diagnostics are accompanied by brief commentary on the notable characteristics of each system. This integrated approach ensures clarity and traceability in the classification process and supports the selection criteria adopted in the present work.

C.1. TIC 10176636

Labadie-Bartz et al. (2022) classified the system with the spectral type of B3IV and found two characteristic frequencies based on the TESS photometric variability, the first frequency of 0.84 days^{-1} and the second of 1.60 days^{-1}. On the other hand, Burssens et al. (2020) classified the system as SPB and found a frequency of 0.041 days^{-1}. Furthermore Bowman et al. (2020) pointed out that this object has a temperature of 41 300 K, luminosity of log L/L$_\odot$ = 2.54 and v sin i equal to 162 km s^{-1}. No spectrum was found in the BESS catalog.

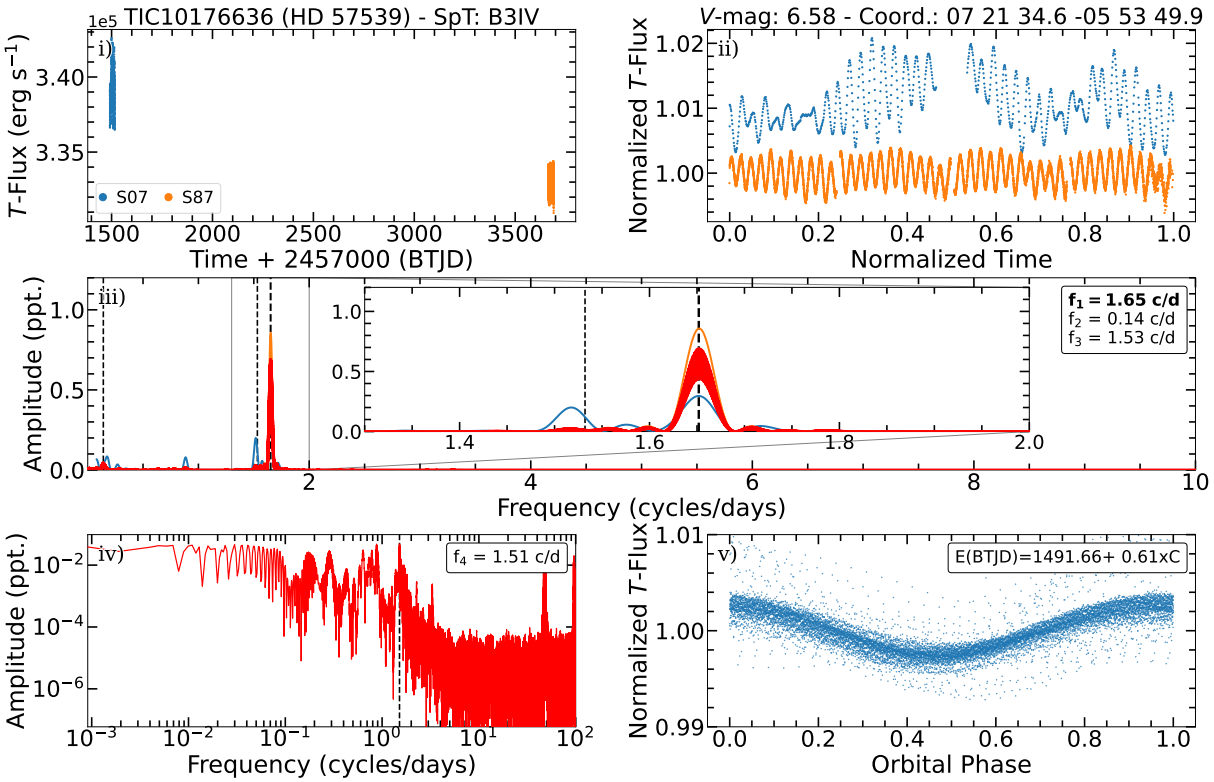

Figure C.1: Panels summarizing the photometric and frequency-domain analyses for the target TIC 10176636. (i) Raw T-Flux light curves from different sectors; (ii) normalized T-Flux light curves folded normalized time for each sector; (iii) Lomb-Scargle periodogram highlighting the three main frequencies f_1, f_2, and f_3, with a zoom-in inset; (iv) extended periodogram revealing a low-frequency component f_4; (v) orbital phase-folded light curve.

C.2. TIC 103994174

HD 189847 has been classified as B7Ve (Chojnowski et al., 2014). It is present in the companion star work of Kervella et al. (2019), but Guerrero et al. (2025a) conducted interferometric study and with Astrometric data from Gaia, found no binarity evidence of this target.

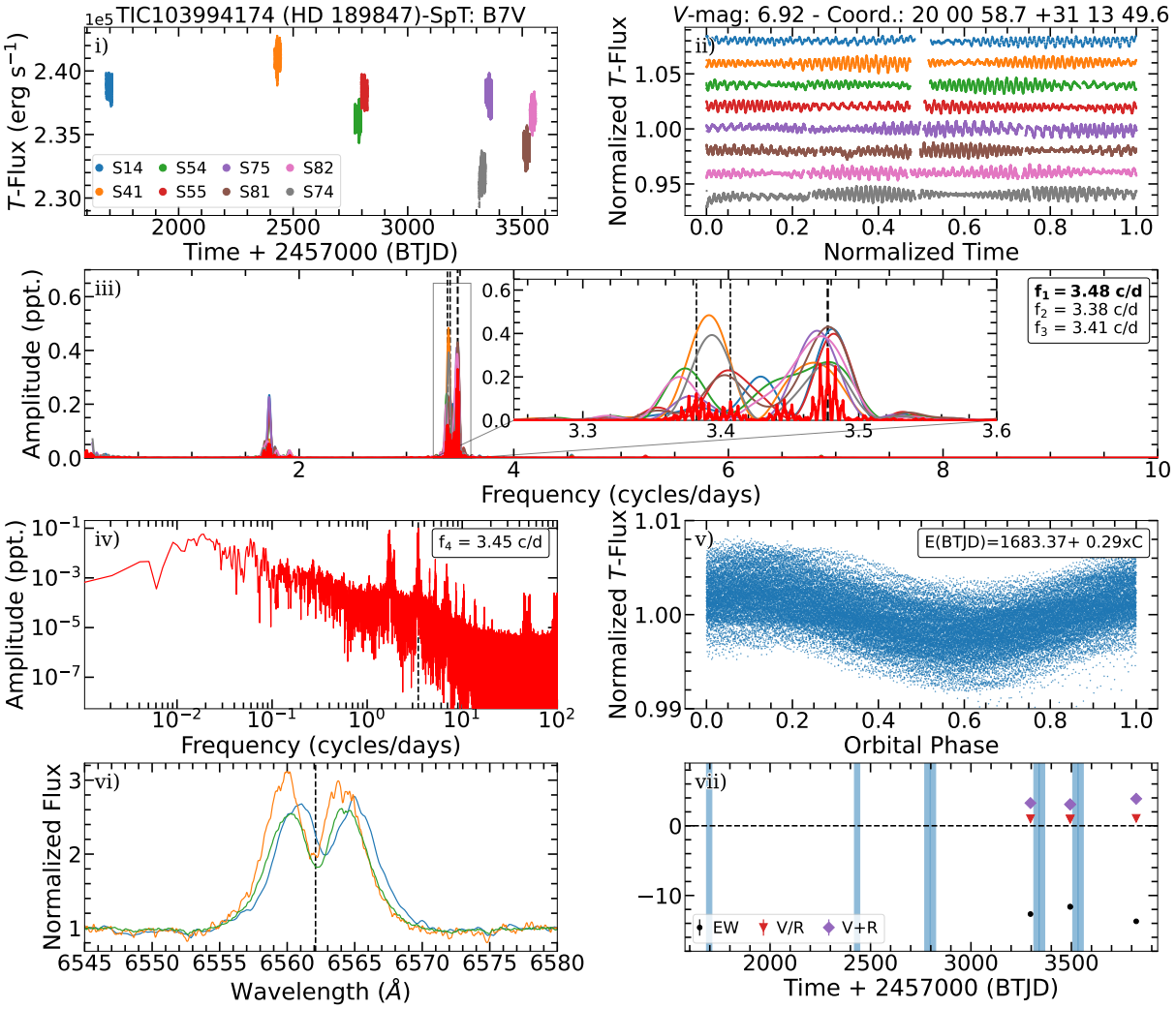

Figure C.2: Panels summarizing the photometric, spectroscopic, and frequency-domain analyses for the target TIC 103994174. (i) Raw T-Flux light curves from different sectors; (ii) normalized T-Flux light curves folded normalized time for each sector; (iii) Lomb-Scargle periodogram highlighting the three main frequencies f_1, f_2, and f_3, with a zoom-in inset; (iv) extended periodogram revealing a low-frequency component f_4; (v) orbital phase-folded light curve; (vi) optical spectrum centered on the Hα line (λ = 6562.8 Å); and (vii) temporal evolution of the equivalent width of the Hα line across available observations. Shaded regions in panel (vii) correspond to observation windows of sectors shown in panel (i).

C.3. TIC 11411724

HD 37903 has been classified as B1.5V. Labadie-Bartz et al. (2022) pointed out that this does not appear to be a classical Be star, being embedded in a strong reflection of the nebula NGC 2023 (Rozhkovskij and Kurchakov, 1968), and with characteristic photometric variability frequencies of 0.50 days^{-1}, 8.75 days^{-1} and between 10.00 and 11.50 days^{-1}. Souza et al. (2020) identified a possible binary pair with Speckle interferometry. No spectrum was found in the BESS catalog.

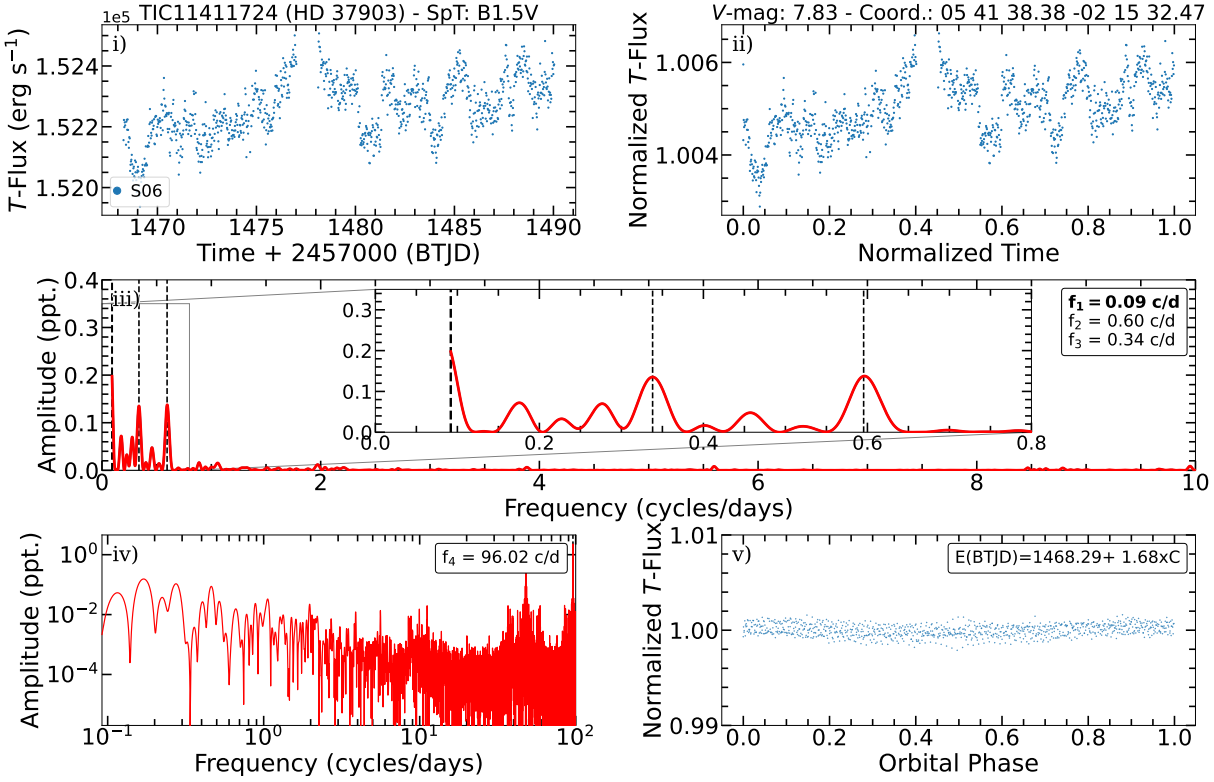

Figure C.3: Panels summarizing the photometric and frequency-domain analyses for the target TIC 10176636. (i) Raw T-Flux light curves from different sectors; (ii) normalized T-Flux light curves folded normalized time for each sector; (iii) Lomb-Scargle periodogram highlighting the three main frequencies f_1, f_2, and f_3, with a zoom-in inset; (iv) extended periodogram revealing a low-frequency component f_4; (v) orbital phase-folded light curve.

C.4. TIC 115091314

Merrill et al. (1932) was the first to study HD 168135, classifying it as B8e. Souza et al. (2020) identified a possible binary pair with Speckle interferometry. Furthermore, Halbedel (1996) determined $v \sin i$ equal to 260 km s^{-1}.

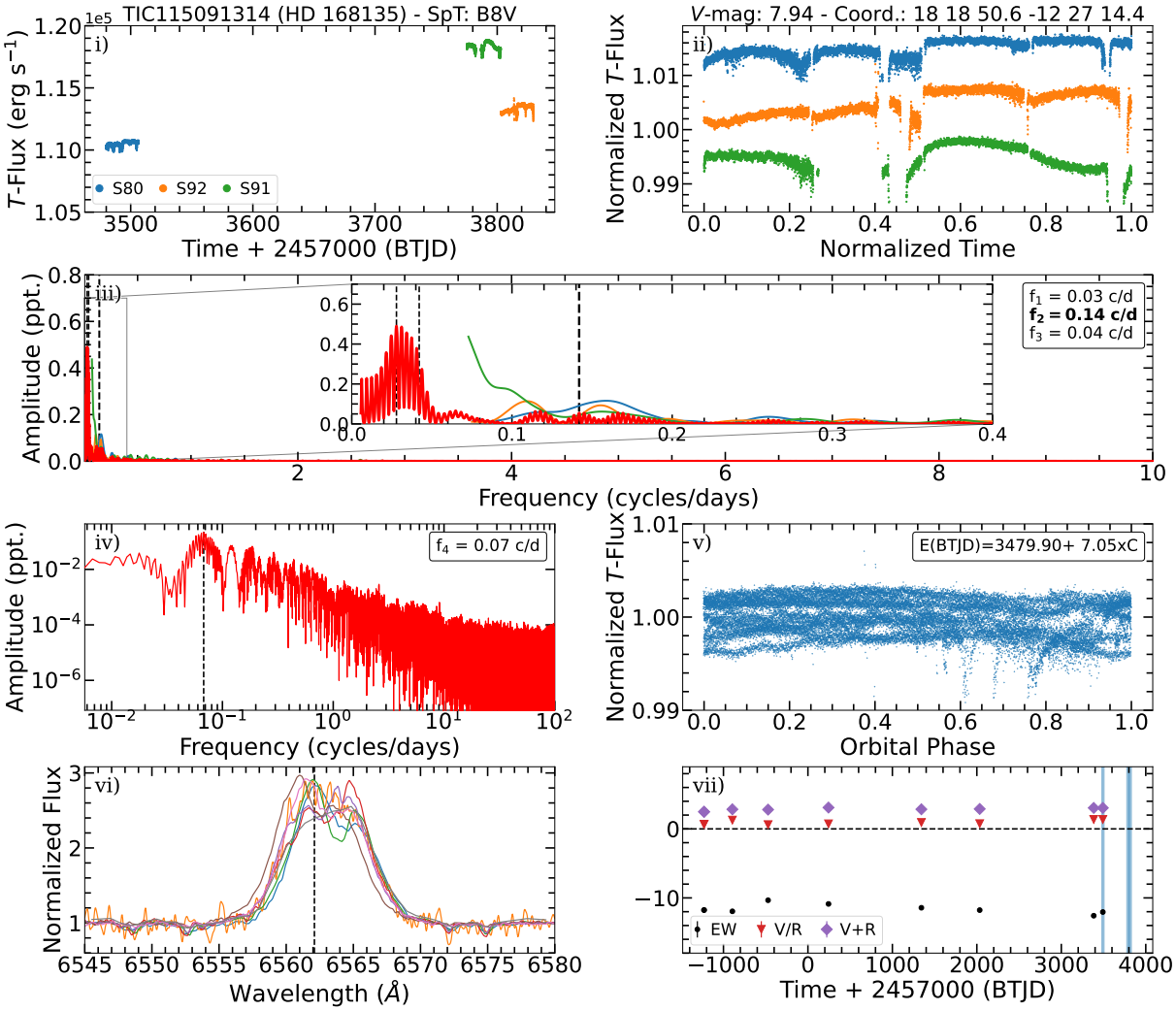

Figure C.4: Panels summarizing the photometric, spectroscopic, and frequency-domain analyses for the target TIC 115091314. (i) Raw T-Flux light curves from different sectors; (ii) normalized T-Flux light curves folded normalized time for each sector; (iii) Lomb-Scargle periodogram highlighting the three main frequencies f_1, f_2, and f_3, with a zoom-in inset; (iv) extended periodogram revealing a low-frequency component f_4; (v) orbital phase-folded light curve; (vi) optical spectrum centered on the Hα line (λ = 6562.8 Å); and (vii) temporal evolution of the equivalent width of the Hα line across available observations. Shaded regions in panel (vii) correspond to observation windows of sectors shown in panel (i).

C.5. TIC 117501818

HD 42529 was identified as a Be star by the Merrill and Burwell (1933) and Mendoza and Eugenio (1958) catalogs, and Banerjee et al. (2021) classified the system with the spectral type of B5V. Halbedel (1996) determined $v \sin i$ equal to 184 km s^{-1}.

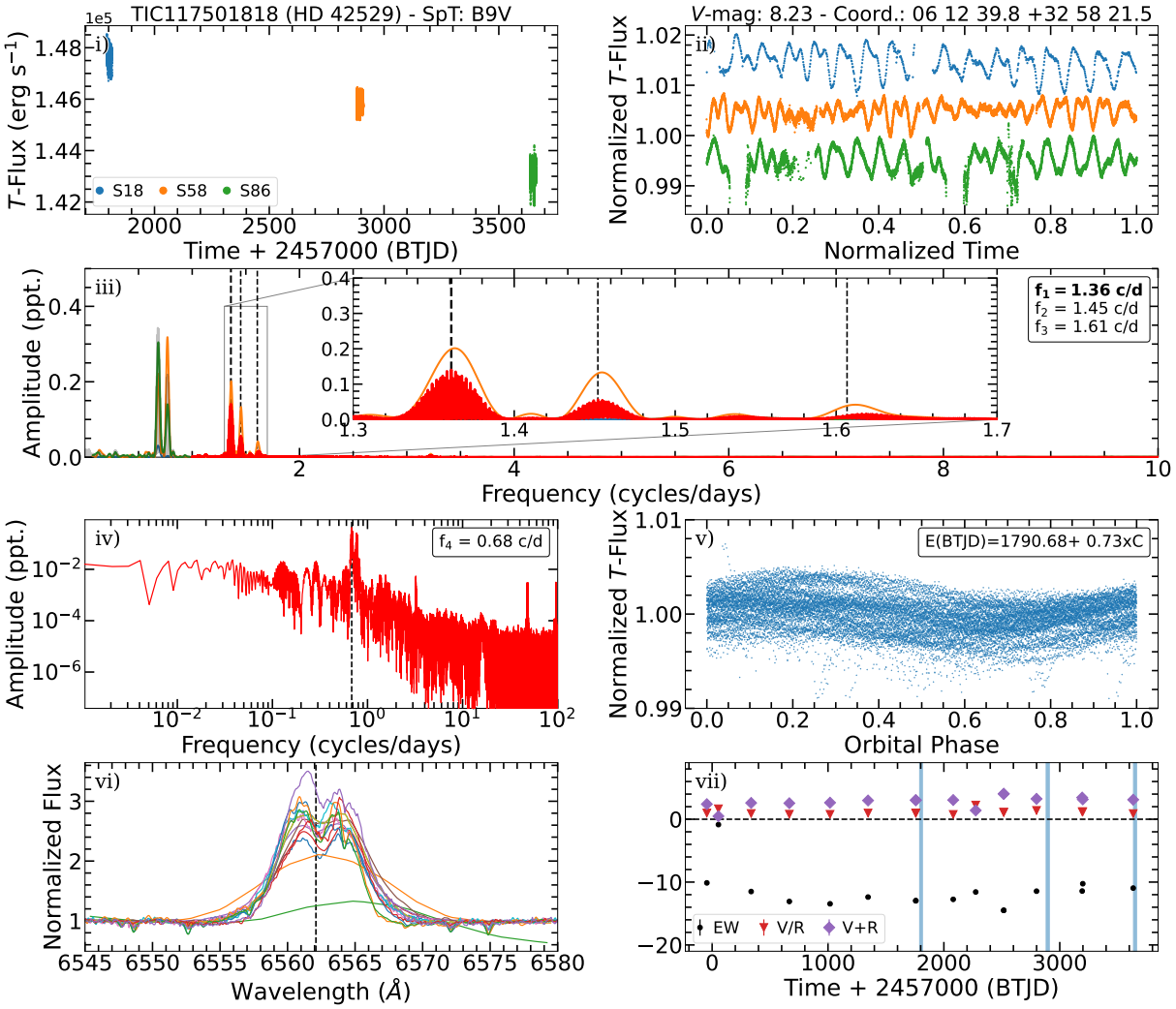

Figure C.5: Panels summarizing the photometric, spectroscopic, and frequency-domain analyses for the target TIC 117501818. (i) Raw T-Flux light curves from different sectors; (ii) normalized T-Flux light curves folded normalized time for each sector; (iii) Lomb-Scargle periodogram highlighting the three main frequencies f_1, f_2, and f_3, with a zoom-in inset; (iv) extended periodogram revealing a low-frequency component f_4; (v) orbital phase-folded light curve; (vi) optical spectrum centered on the Hα line (λ = 6562.8 Å); and (vii) temporal evolution of the equivalent width of the Hα line across available observations. Shaded regions in panel (vii) correspond to observation windows of sectors shown in panel (i).

C.6. TIC 118842700

Using spectroscopy data, Arcos et al. (2018) classified HD 167128 as B2V, with a temperature of 20,000 K and $v \sin i$ equal to 50 km s^{-1}. These measurements corroborate the results of Sigut and Ghafourian (2023a), which determined $v \sin i$ equal to 53 km s^{-1}. It is known that this object is not a single star, being more likely a binary pair, with a evolved and a Be star with mass ratio equal to 15 (Bodensteiner et al., 2020). Labadie-Bartz et al. (2022) points out the system as a low-frequency and low-variability system.

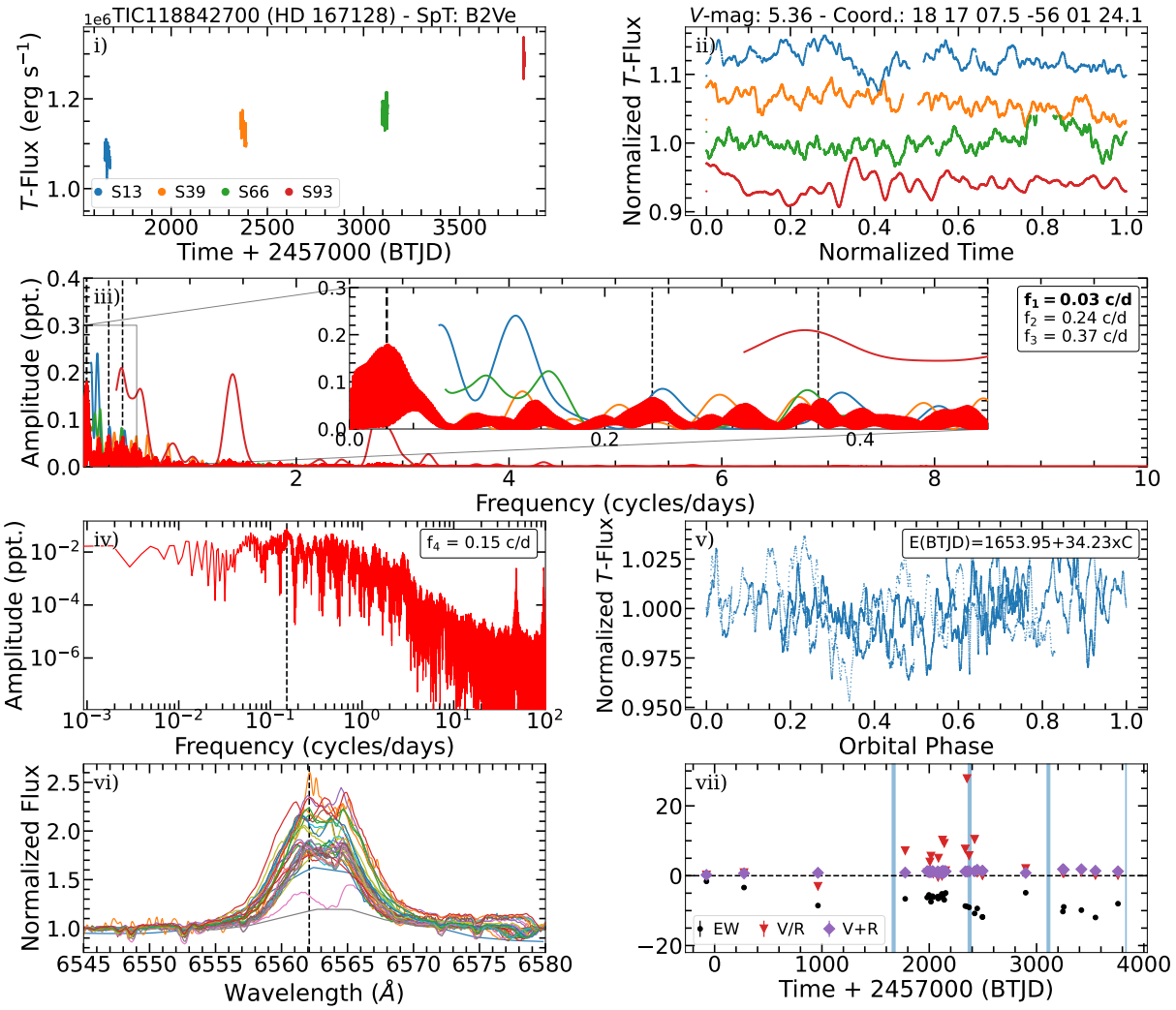

Figure C.6: Panels summarizing the photometric, spectroscopic, and frequency-domain analyses for the target TIC 118842700. (i) Raw T-Flux light curves from different sectors; (ii) normalized T-Flux light curves folded normalized time for each sector; (iii) Lomb-Scargle periodogram highlighting the three main frequencies f_1, f_2, and f_3, with a zoom-in inset; (iv) extended periodogram revealing a low-frequency component f_4; (v) orbital phase-folded light curve; (vi) optical spectrum centered on the Hα line (λ = 6562.8 Å); and (vii) temporal evolution of the equivalent width of the Hα line across available observations. Shaded regions in panel (vii) correspond to observation windows of sectors shown in panel (i).

C.7. TIC 124219174

HD 179405 was extensively studied by Gutiérrez-Soto et al. (2007b), who did not evaluate whether this is a multiple system, classifying it as B2IVe, and identified characteristic frequencies of ∼1.63 c/d, ∼2.78 c/d and ∼2.55 c/d when analyzing photometric data in 4 different filters, finding beat frequency characteristics. Subsequently, Chojnowski et al. (2017) identified that this is a binary system from radial velocity measurements.

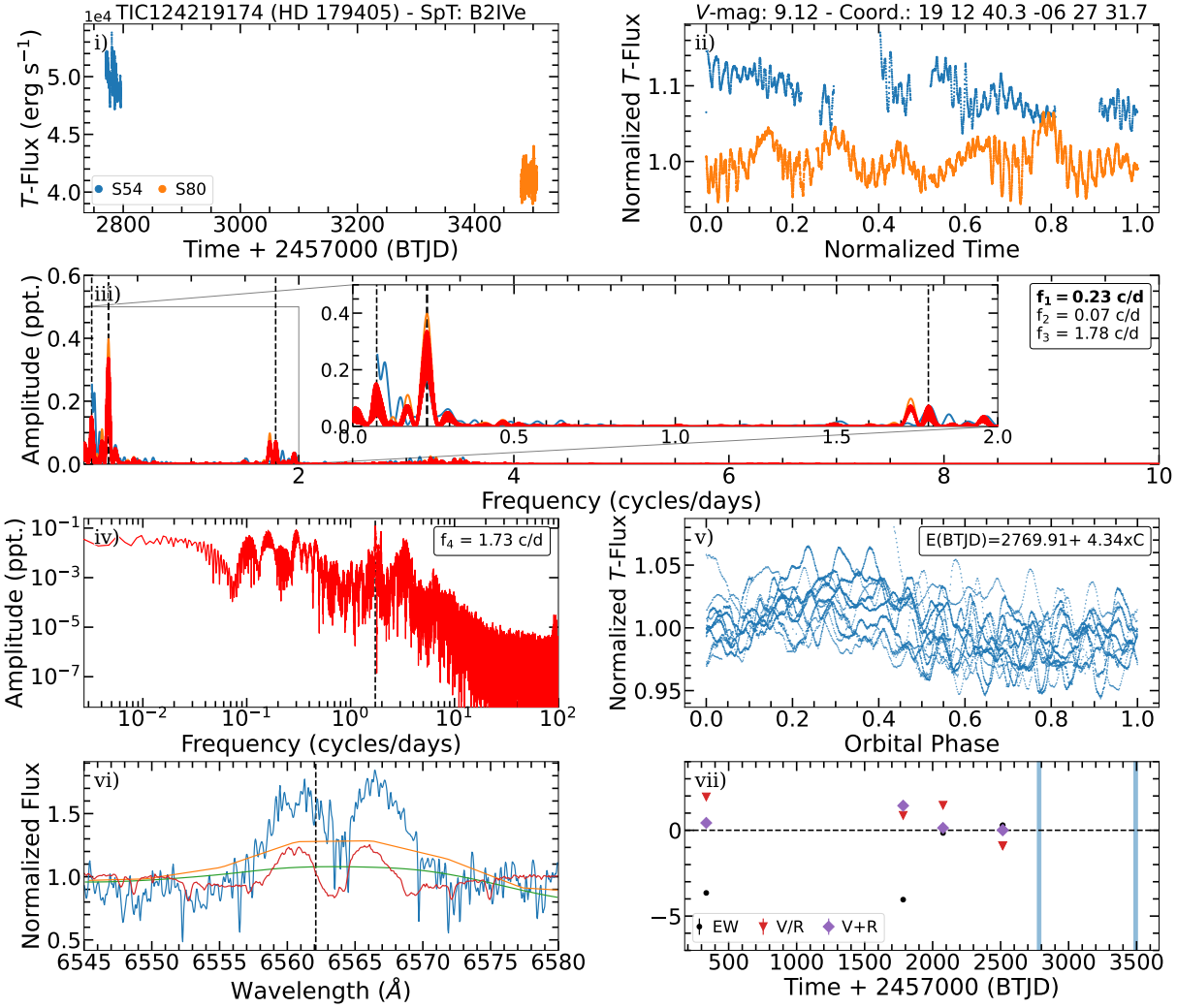

Figure C.7: Panels summarizing the photometric, spectroscopic, and frequency-domain analyses for the target TIC 124219174. (i) Raw T-Flux light curves from different sectors; (ii) normalized T-Flux light curves folded normalized time for each sector; (iii) Lomb-Scargle periodogram highlighting the three main frequencies f_1, f_2, and f_3, with a zoom-in inset; (iv) extended periodogram revealing a low-frequency component f_4; (v) orbital phase-folded light curve; (vi) optical spectrum centered on the Hα line (λ = 6562.8 Å); and (vii) temporal evolution of the equivalent width of the Hα line across available observations. Shaded regions in panel (vii) correspond to observation windows of sectors shown in panel (i).

C.8. TIC 124407255

Chojnowski et al. (2014) classified HD 51477 as B3Ve. Chojnowski et al. (2017) confirmed the Be nature of this star by identifying weak emission wings in its spectrum. No spectrum was found in the BESS catalog.

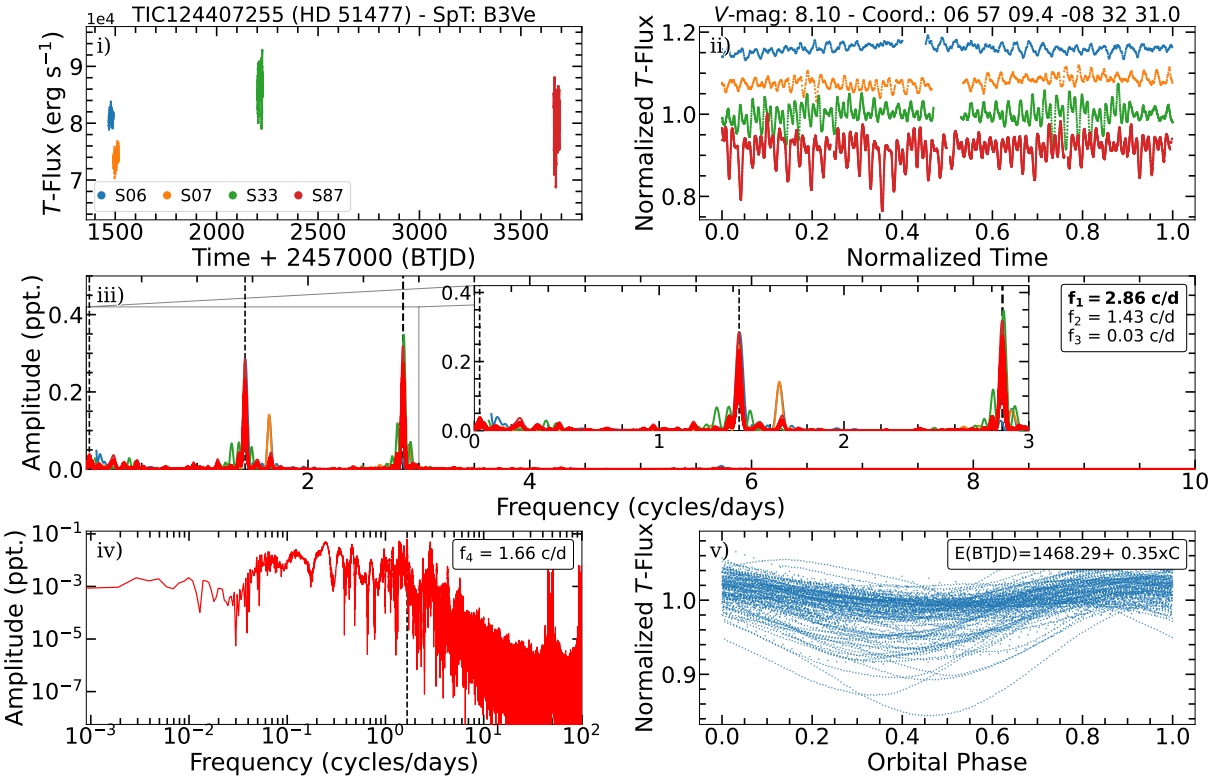

Figure C.8: Panels summarizing the photometric and frequency-domain analyses for the target TIC 124407255. (i) Raw T-Flux light curves from different sectors; (ii) normalized T-Flux light curves folded normalized time for each sector; (iii) Lomb-Scargle periodogram highlighting the three main frequencies f_1, f_2, and f_3, with a zoom-in inset; (iv) extended periodogram revealing a low-frequency component f_4; (v) orbital phase-folded light curve.

C.9. TIC 125755072

Eta Tauri (Alcyone) is the brightest object in the Pleiades open cluster, in the constellation Taurus, forming part of a quadruple system(?). It is classified as a B7III type system, with an inclination of ~45° and $v \sin i$ of 150 km s^{-1} (Sigut and Ghafourian, 2023a).

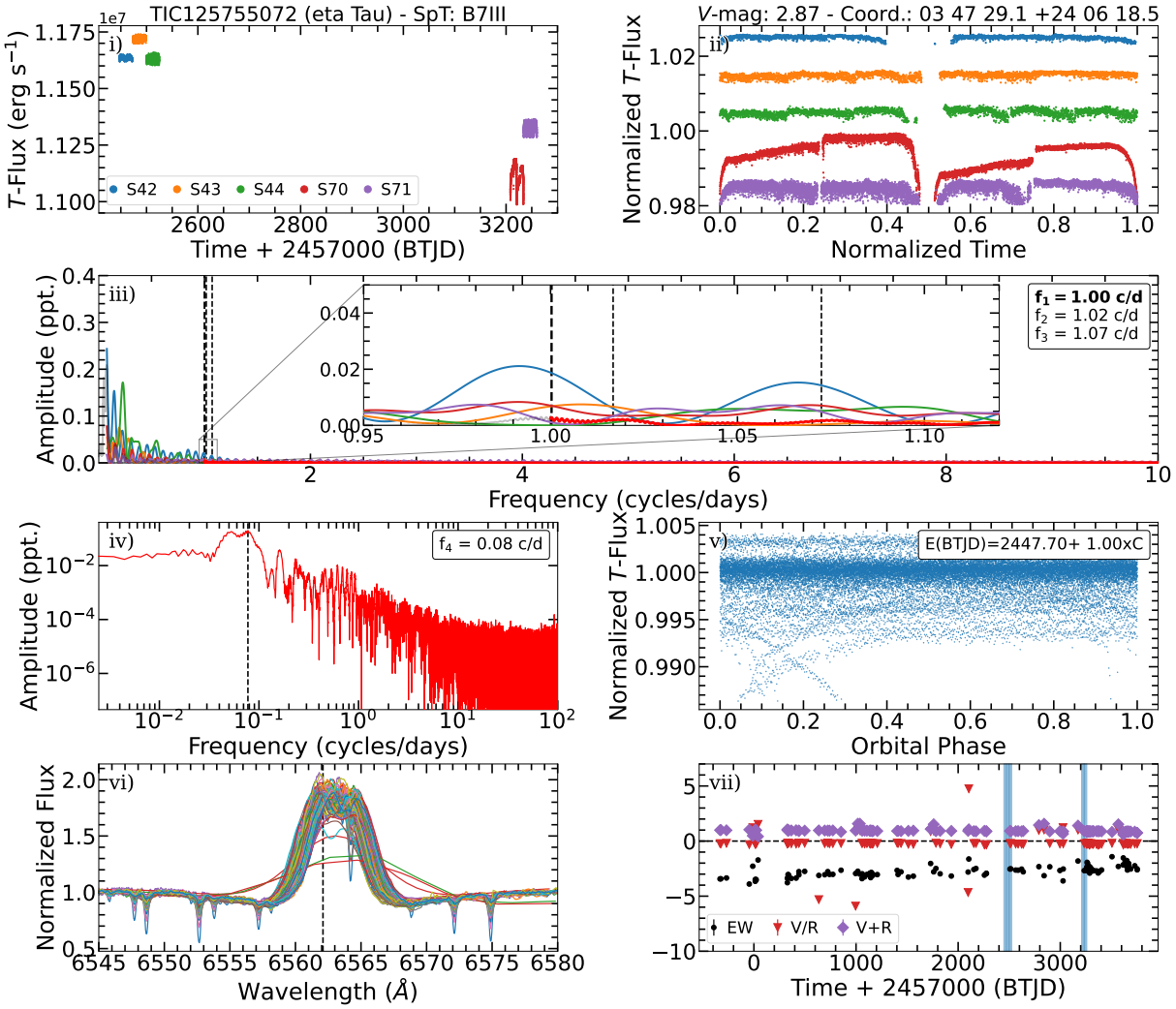

Figure C.9: Panels summarizing the photometric, spectroscopic, and frequency-domain analyses for the target TIC 125755072. (i) Raw T-Flux light curves from different sectors; (ii) normalized T-Flux light curves folded normalized time for each sector; (iii) Lomb-Scargle periodogram highlighting the three main frequencies f_1, f_2, and f_3, with a zoom-in inset; (iv) extended periodogram revealing a low-frequency component f_4; (v) orbital phase-folded light curve; (vi) optical spectrum centered on the Hα line (λ = 6562.8 Å); and (vii) temporal evolution of the equivalent width of the Hα line across available observations. Shaded regions in panel (vii) correspond to observation windows of sectors shown in panel (i).

C.10. TIC 126756648

Labadie-Bartz et al. (2018) present this system as B3Ve.

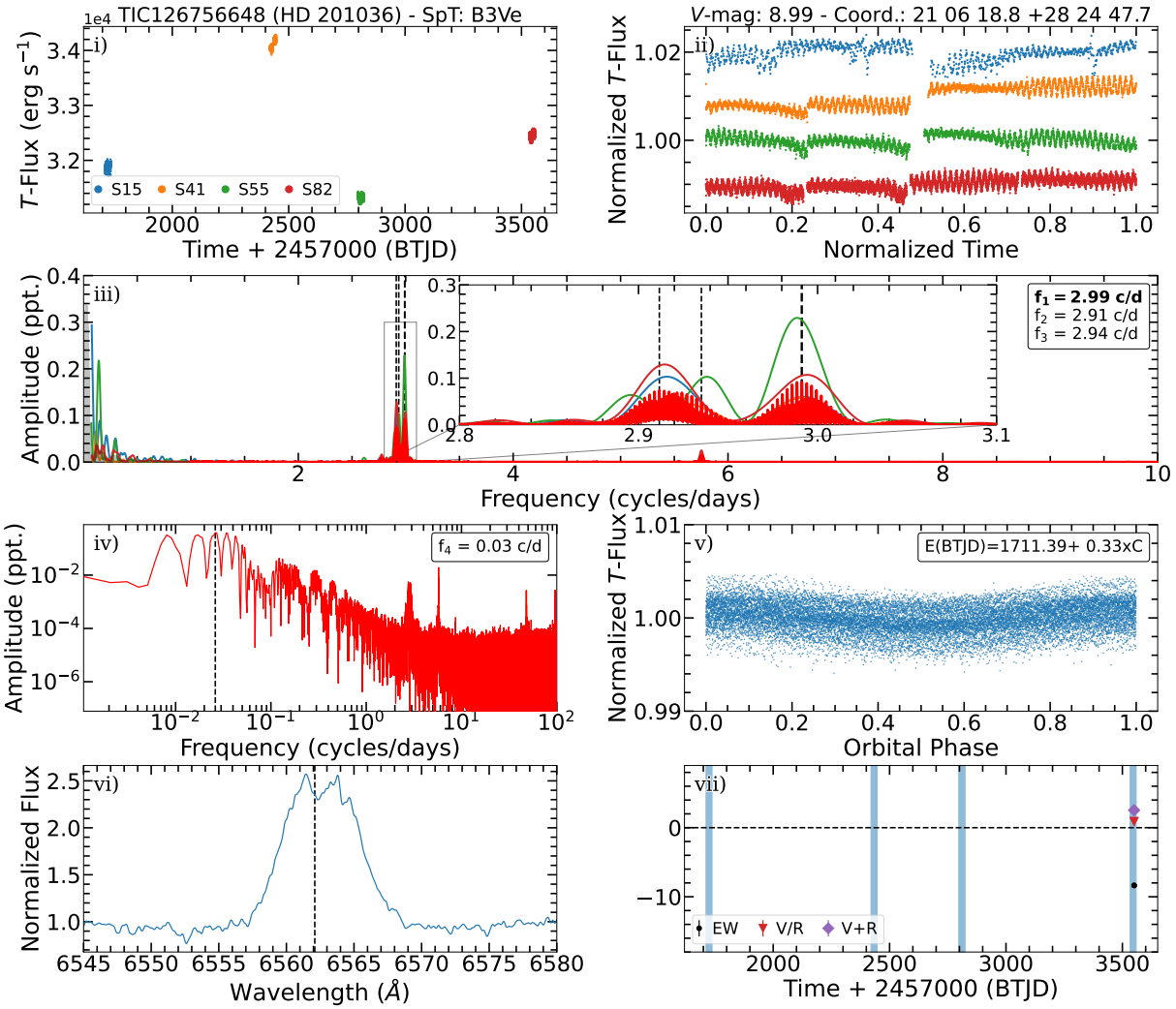

Figure C.10: Panels summarizing the photometric, spectroscopic, and frequency-domain analyses for the target TIC 126756648. (i) Raw T-Flux light curves from different sectors; (ii) normalized T-Flux light curves folded normalized time for each sector; (iii) Lomb-Scargle periodogram highlighting the three main frequencies f_1, f_2, and f_3, with a zoom-in inset; (iv) extended periodogram revealing a low-frequency component f_4; (v) orbital phase-folded light curve; (vi) optical spectrum centered on the Hα line (λ = 6562.8 Å); and (vii) temporal evolution of the equivalent width of the Hα line across available observations. Shaded regions in panel (vii) correspond to observation windows of sectors shown in panel (i).

C.11. TIC 12725034

Innes (1901) observed δ Sco during a lunar occultation in 1899, indicating for the first time its binary nature. After that, studies considered this object as a triple system, and it may even have a fourth hidden component. An extensive study was made by Tango et al. (2009), which confirmed previous results regarding the binary nature and the high eccentricity (~0.94) of this system. In addition, masses of 15 $M_\odot$ and 8 $M_\odot$ were obtained for the primary and secondary components, respectively, through a spectroscopic study.

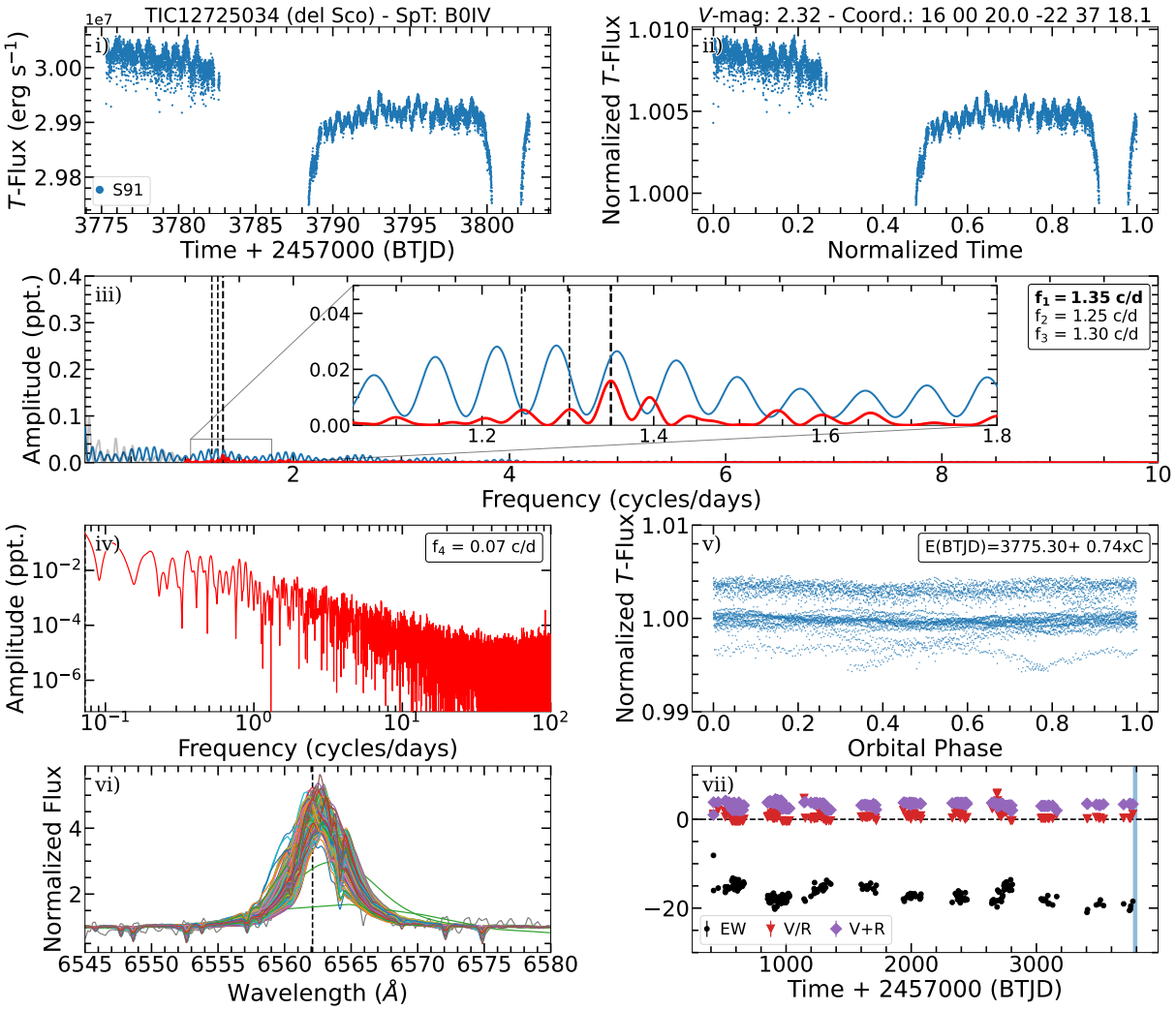

Figure C.11: Panels summarizing the photometric, spectroscopic, and frequency-domain analyses for the target TIC 12725034. (i) Raw T-Flux light curves from different sectors; (ii) normalized T-Flux light curves folded normalized time for each sector; (iii) Lomb-Scargle periodogram highlighting the three main frequencies f_1, f_2, and f_3, with a zoom-in inset; (iv) extended periodogram revealing a low-frequency component f_4; (v) orbital phase-folded light curve; (vi) optical spectrum centered on the Hα line (λ = 6562.8 Å); and (vii) temporal evolution of the equivalent width of the Hα line across available observations. Shaded regions in panel (vii) correspond to observation windows of sectors shown in panel (i).

C.12. TIC 127493611

o Pup is a B1IV object, a Be+sdO binary system with an orbital period of ∼29 d, and masses of ∼13 $M_\odot$ and ∼0.8 $M_\odot$ for the primary and secondary components, respectively (Koubský, P. et al., 2012). Labadie-Bartz et al. (2022) identified a clear frequency in their photometric data of 0.495 d^{-1}. Through spectral synthesis, Levenhagen et al. (2024a) inferred measurements of 27,500 K, log g equal to 3.2 cgs and $v \sin i$ of 326 km s^{-1} for the undeformed star.

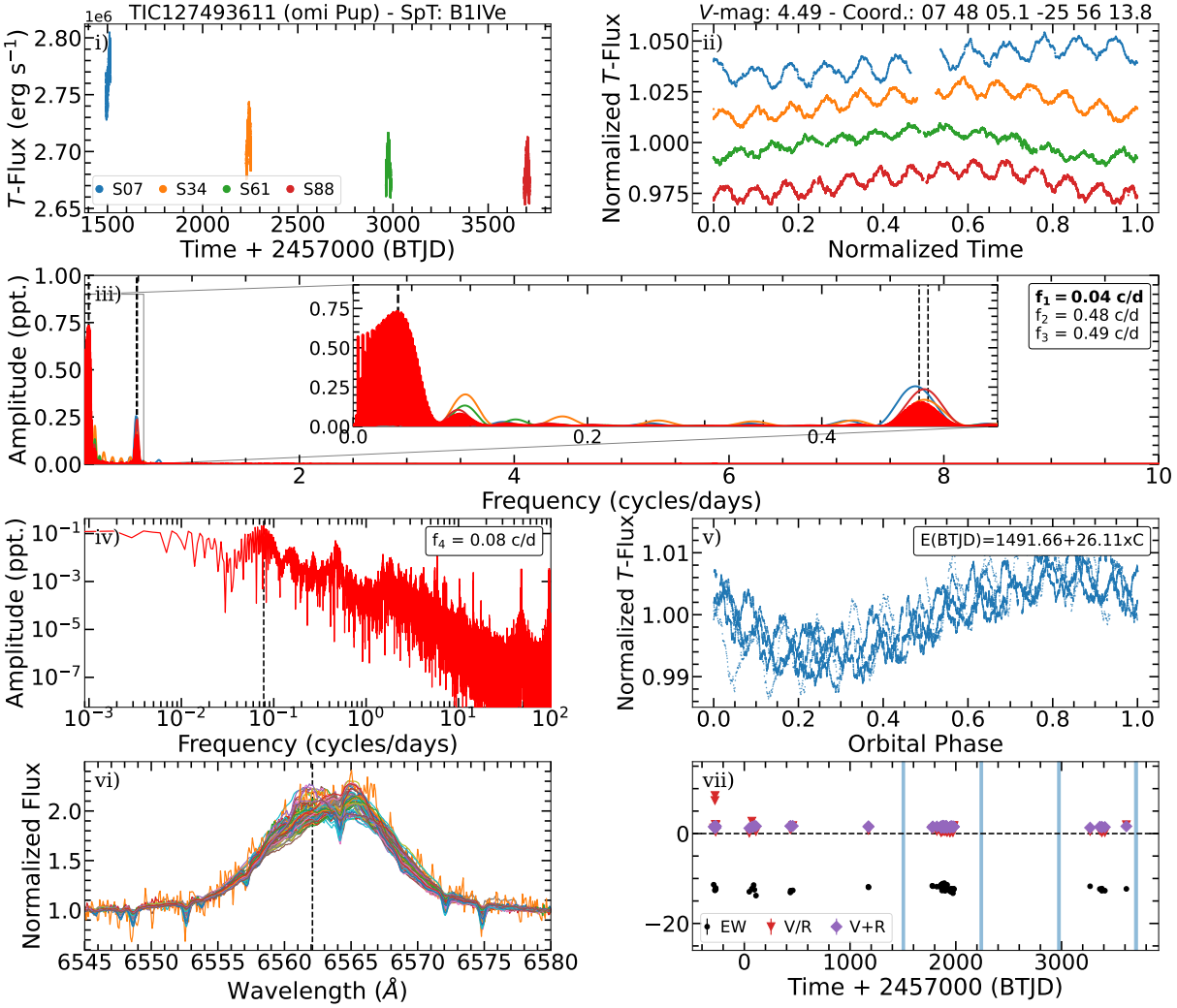

Figure C.12: Panels summarizing the photometric, spectroscopic, and frequency-domain analyses for the target TIC 127493611. (i) Raw T-Flux light curves from different sectors; (ii) normalized T-Flux light curves folded normalized time for each sector; (iii) Lomb-Scargle periodogram highlighting the three main frequencies f_1, f_2, and f_3, with a zoom-in inset; (iv) extended periodogram revealing a low-frequency component f_4; (v) orbital phase-folded light curve; (vi) optical spectrum centered on the Hα line (λ = 6562.8 Å); and (vii) temporal evolution of the equivalent width of the Hα line across available observations. Shaded regions in panel (vii) correspond to observation windows of sectors shown in panel (i).

C.13. TIC 128116539

η Cen had NRPs observed in its spectrum, where the l modes were estimated between 3 and 8, as well as the azimuth order m at 4±2 (Janot-Pacheco et al., 1991b; Levenhagen et al., 2003a). Using a spectroscopic analysis, Levenhagen and Leister (2006b) was able to determine the temperature of 20,500 K, log g 3.80 dex, v sin i of 310 km s^{-1} and the mass of 8.5 M$_\odot$, classifying this object with the spectral type of B2Ve. In agreement with this result, Levenhagen et al. (2024a) inferred measurements of 21,700 K, log g equal to 4.0 cgs and v sin i of 246 km s^{-1} for the undeformed star.

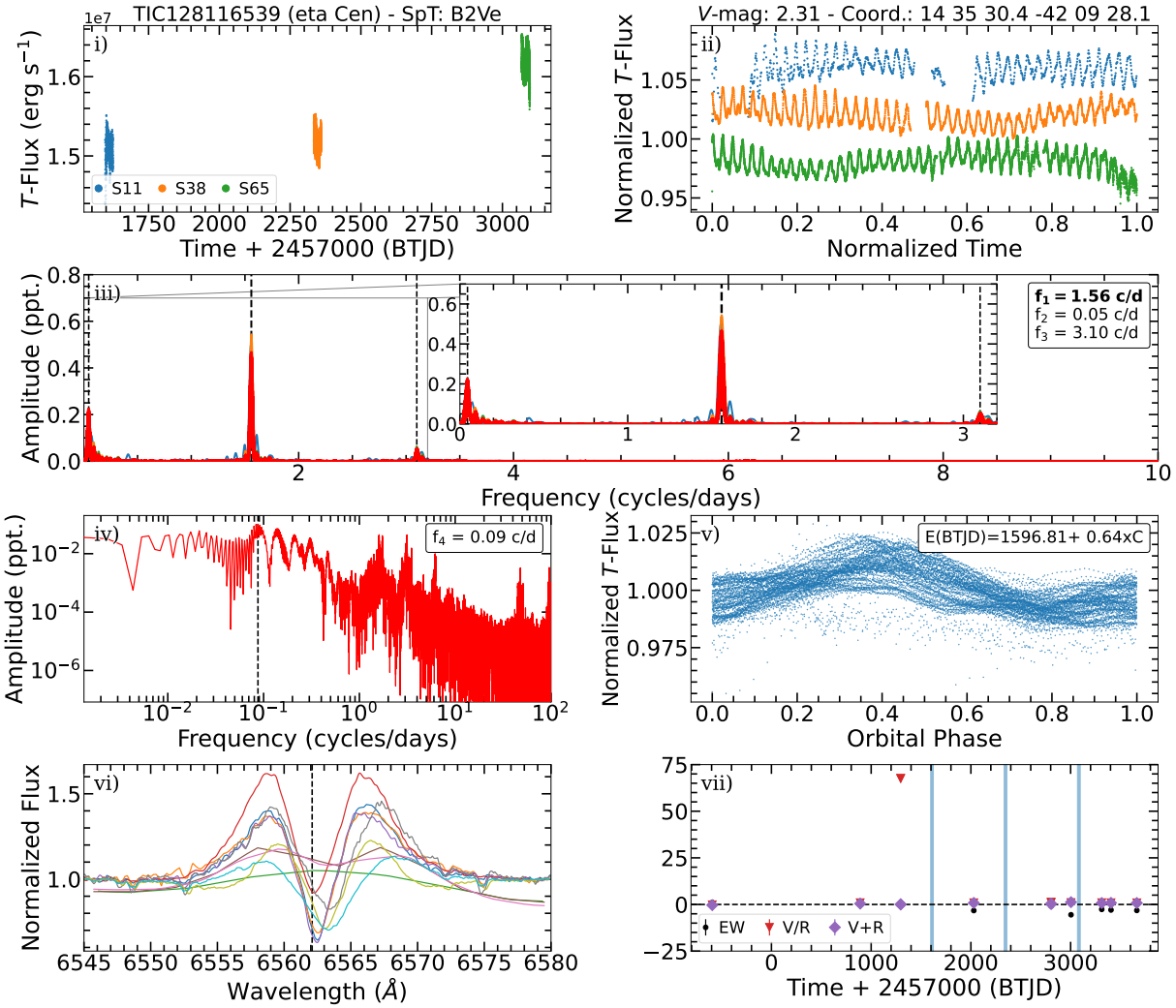

Figure C.13: Panels summarizing the photometric, spectroscopic, and frequency-domain analyses for the target TIC 128116539. (i) Raw T-Flux light curves from different sectors; (ii) normalized T-Flux light curves folded normalized time for each sector; (iii) Lomb-Scargle periodogram highlighting the three main frequencies f$_1$, f$_2$, and f$_3$, with a zoom-in inset; (iv) extended periodogram revealing a low-frequency component f$_4$; (v) orbital phase-folded light curve; (vi) optical spectrum centered on the Hα line (λ = 6562.8 Å); and (vii) temporal evolution of the equivalent width of the Hα line across available observations. Shaded regions in panel (vii) correspond to observation windows of sectors shown in panel (i).

C.14. TIC 136027289

HD 201522 was studied by Kervella et al. (2019) who characterized the physical presence of stellar and substellar companions through astrometry.

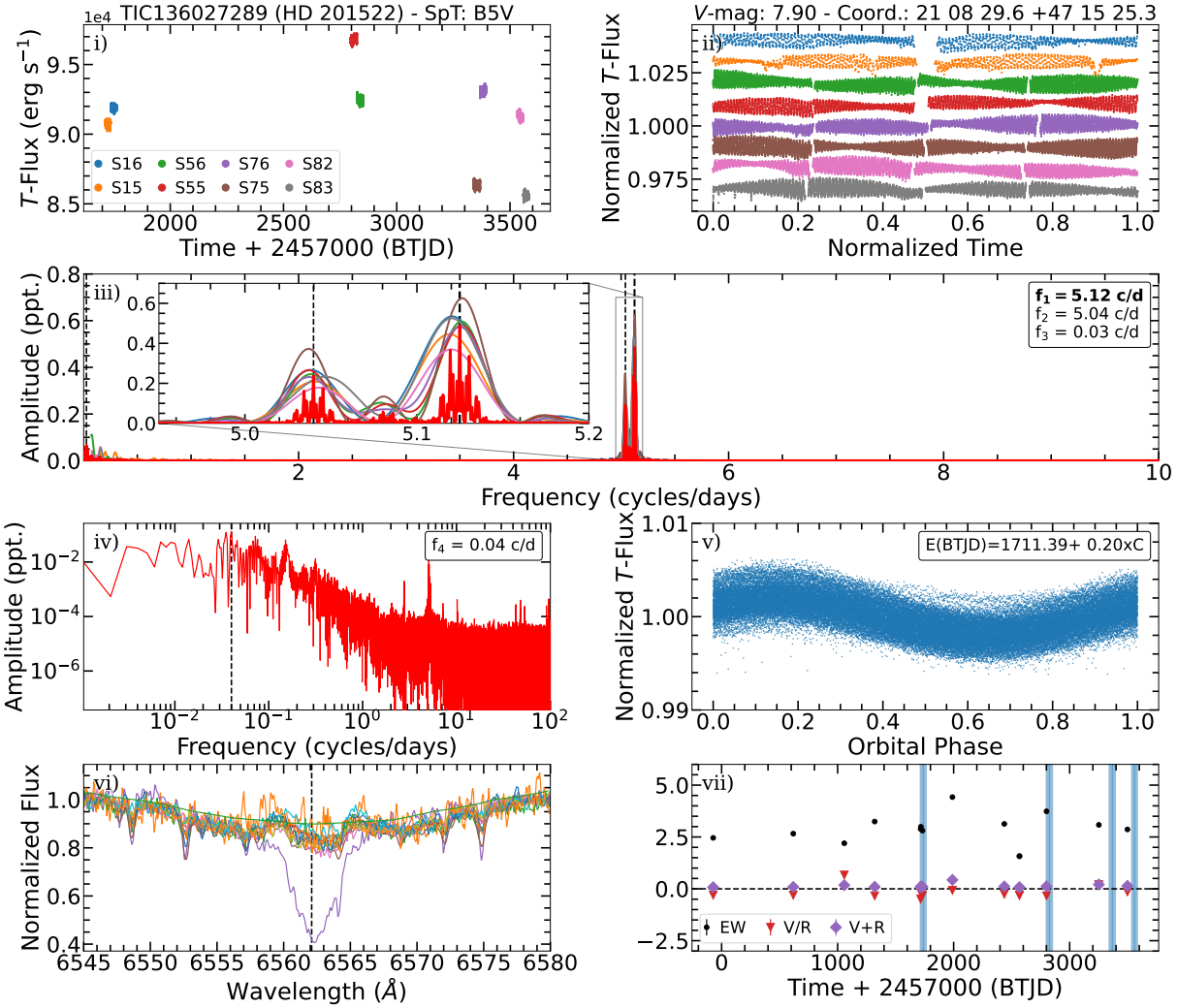

Figure C.14: Panels summarizing the photometric, spectroscopic, and frequency-domain analyses for the target TIC 136027289. (i) Raw T-Flux light curves from different sectors; (ii) normalized T-Flux light curves folded normalized time for each sector; (iii) Lomb-Scargle periodogram highlighting the three main frequencies f_1, f_2, and f_3, with a zoom-in inset; (iv) extended periodogram revealing a low-frequency component f_4; (v) orbital phase-folded light curve; (vi) optical spectrum centered on the Hα line (λ = 6562.8 Å); and (vii) temporal evolution of the equivalent width of the Hα line across available observations. Shaded regions in panel (vii) correspond to observation windows of sectors shown in panel (i).

C.15. TIC 136704900

HR 8107 (HD 201836) was identified as a Be star by Hirata et al. (1986), and is classified as a B5V star. Later studies revealed it to be a Be star with a nearby binary companion (Shokry et al., 2018), rather than part of a hierarchical multiple system in which the Be star would be an isolated component. The object also appears as an eclipsing binary with a period of 12.14569 days (IJspeert et al., 2021; Rivinius et al., 2025b).

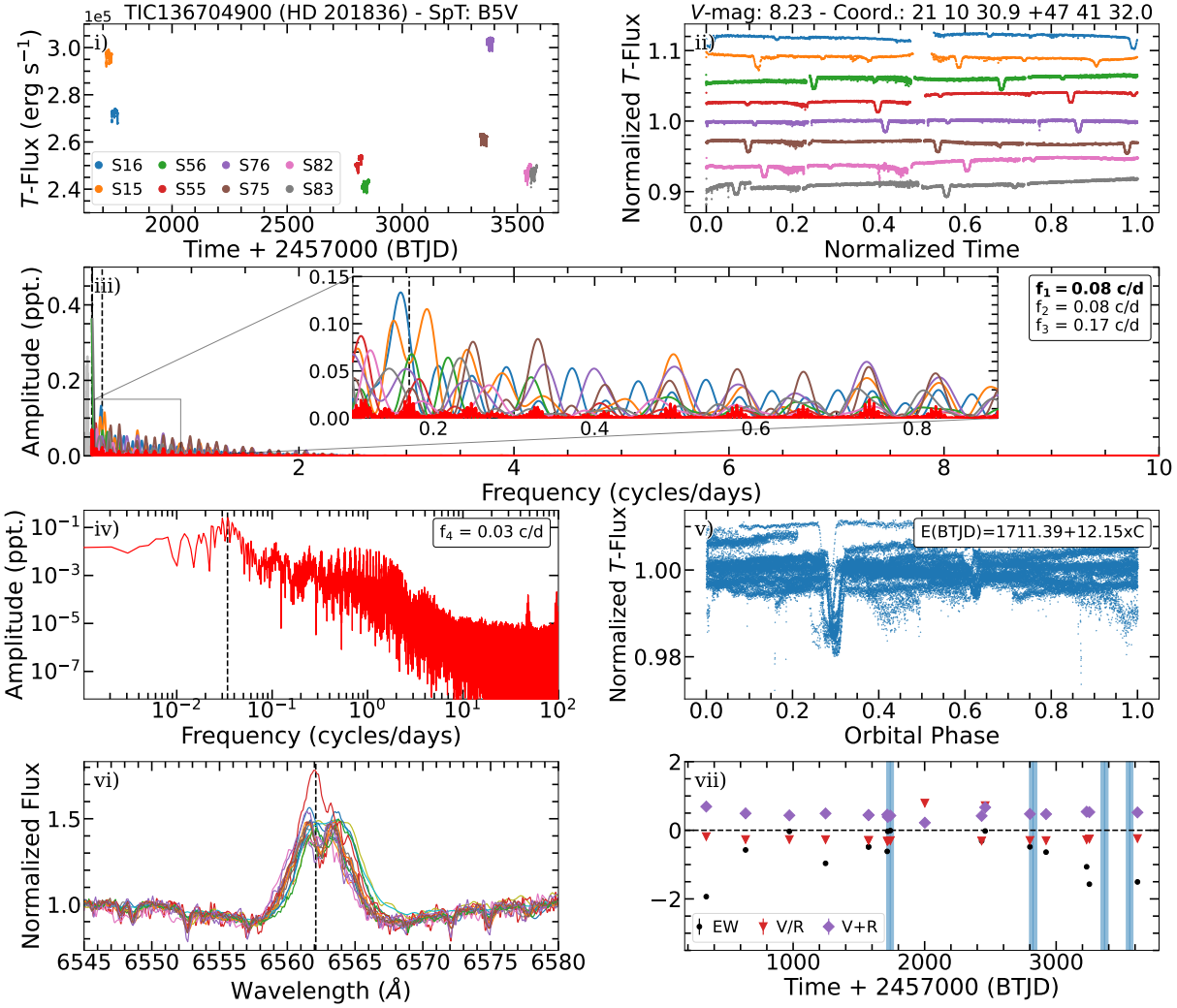

Figure C.15: Panels summarizing the photometric, spectroscopic, and frequency-domain analyses for the target TIC 136704900. (i) Raw T-Flux light curves from different sectors; (ii) normalized T-Flux light curves folded normalized time for each sector; (iii) Lomb-Scargle periodogram highlighting the three main frequencies f_1, f_2, and f_3, with a zoom-in inset; (iv) extended periodogram revealing a low-frequency component f_4; (v) orbital phase-folded light curve; (vi) optical spectrum centered on the Hα line (λ = 6562.8 Å); and (vii) temporal evolution of the equivalent width of the Hα line across available observations. Shaded regions in panel (vii) correspond to observation windows of sectors shown in panel (i).

C.16. TIC 140006471

HD 72067 is classified as a Be star with a $v \sin i$ measurement equal to 150 km s^{-1} (De Araujo and de Freitas Pacheco, 1990a). Nichols and Slavin (2004b) reported this object as a B2V star. It was first identified as a binary system by van den Bos (1929), and more recently by Souza et al. (2020) with Speckle interferometry.

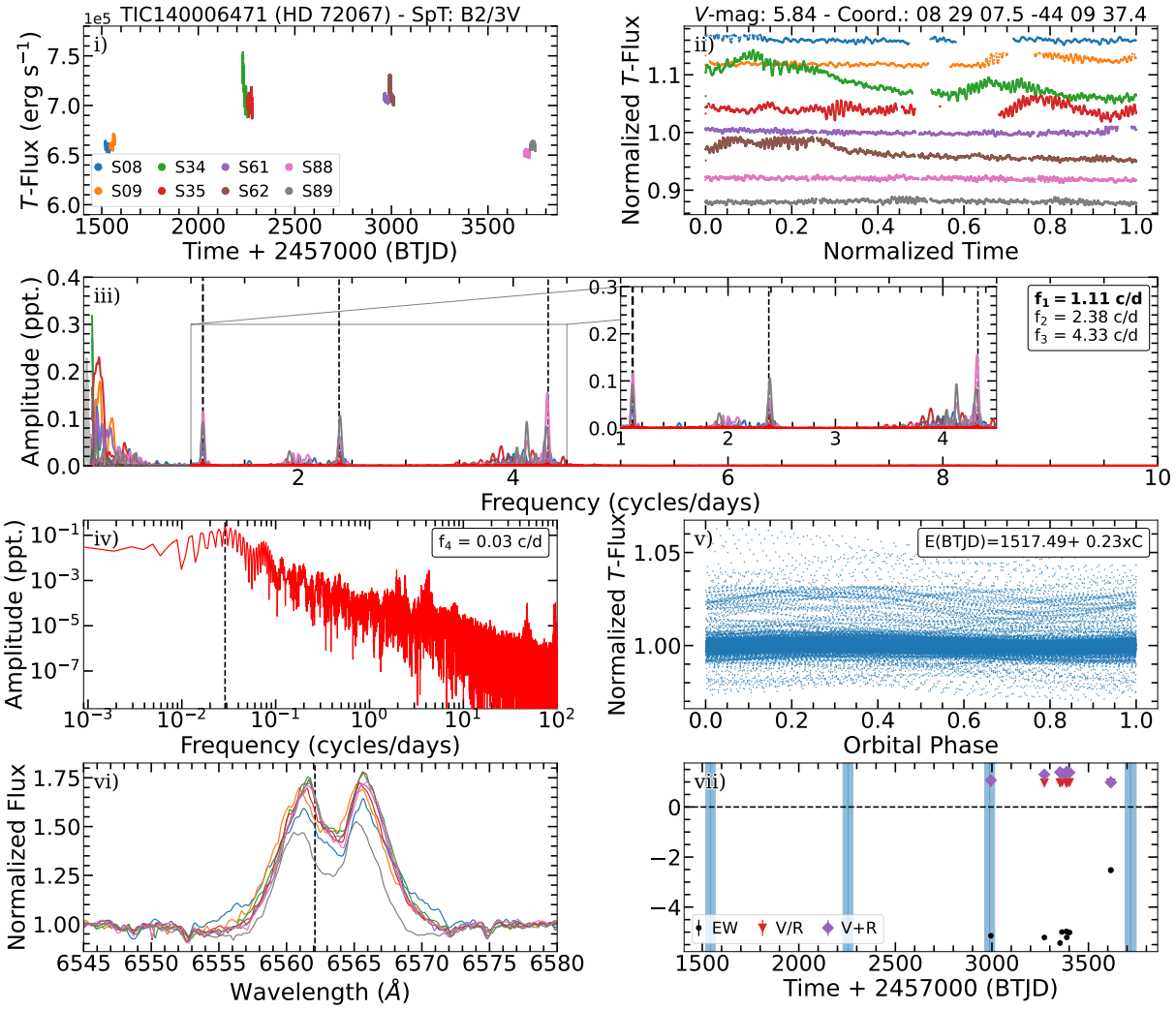

Figure C.16: Panels summarizing the photometric, spectroscopic, and frequency-domain analyses for the target TIC 140006471. (i) Raw T-Flux light curves from different sectors; (ii) normalized T-Flux light curves folded normalized time for each sector; (iii) Lomb-Scargle periodogram highlighting the three main frequencies f_1, f_2, and f_3, with a zoom-in inset; (iv) extended periodogram revealing a low-frequency component f_4; (v) orbital phase-folded light curve; (vi) optical spectrum centered on the Hα line (λ = 6562.8 Å); and (vii) temporal evolution of the equivalent width of the Hα line across available observations. Shaded regions in panel (vii) correspond to observation windows of sectors shown in panel (i).

C.17. TIC 140031673

HD 71510 was studied by Kervella et al. (2019) who characterized the physical presence of stellar and substellar companions through astrometry, and more recently by Souza et al. (2020) with Speckle interferometry. Has a temperature of ~19,500K (Kochanek, 2022a) and $v \sin i$ of 150 km s^{-1} (Solar et al., 2022a).

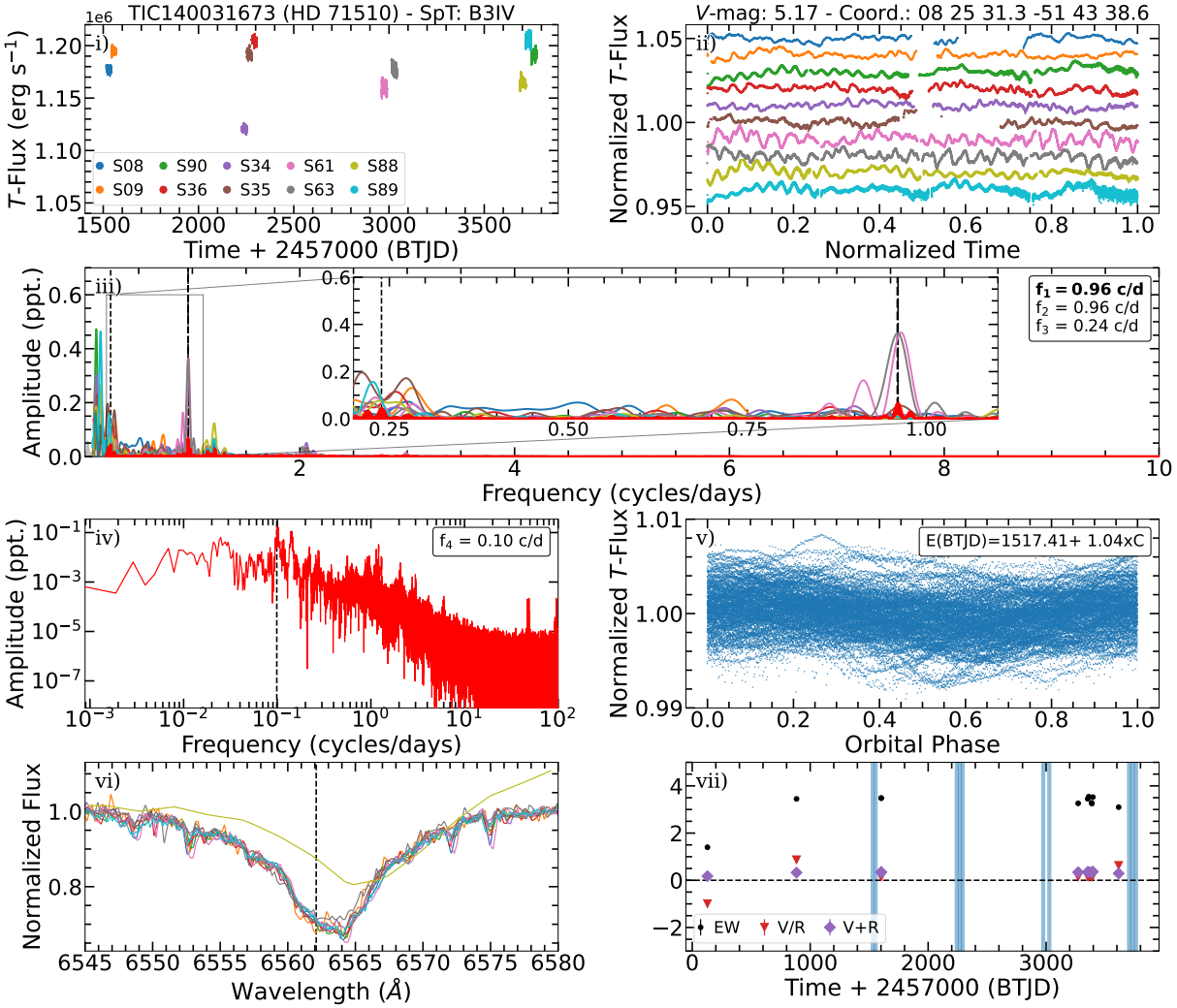

Figure C.17: Panels summarizing the photometric, spectroscopic, and frequency-domain analyses for the target TIC 140031673. (i) Raw T-Flux light curves from different sectors; (ii) normalized T-Flux light curves folded normalized time for each sector; (iii) Lomb-Scargle periodogram highlighting the three main frequencies f_1, f_2, and f_3, with a zoom-in inset; (iv) extended periodogram revealing a low-frequency component f_4; (v) orbital phase-folded light curve; (vi) optical spectrum centered on the Hα line (λ = 6562.8 Å); and (vii) temporal evolution of the equivalent width of the Hα line across available observations. Shaded regions in panel (vii) correspond to observation windows of sectors shown in panel (i).

C.18. TIC 140214221

Levenhagen et al. (2024a) presents a temperature of 12,500 K and $v \sin i$ of 170 km s^{-1} for α Col. Sigut and Ghafourian (2023a) classifies the system with the spectral type B9V and unlike the previous author, he points out $v \sin i$ of 199 km s^{-1}. Solar et al. (2022a) points out three rotation speeds 190 km s^{-1}, 181 km s^{-1} and 188 km s^{-1}.

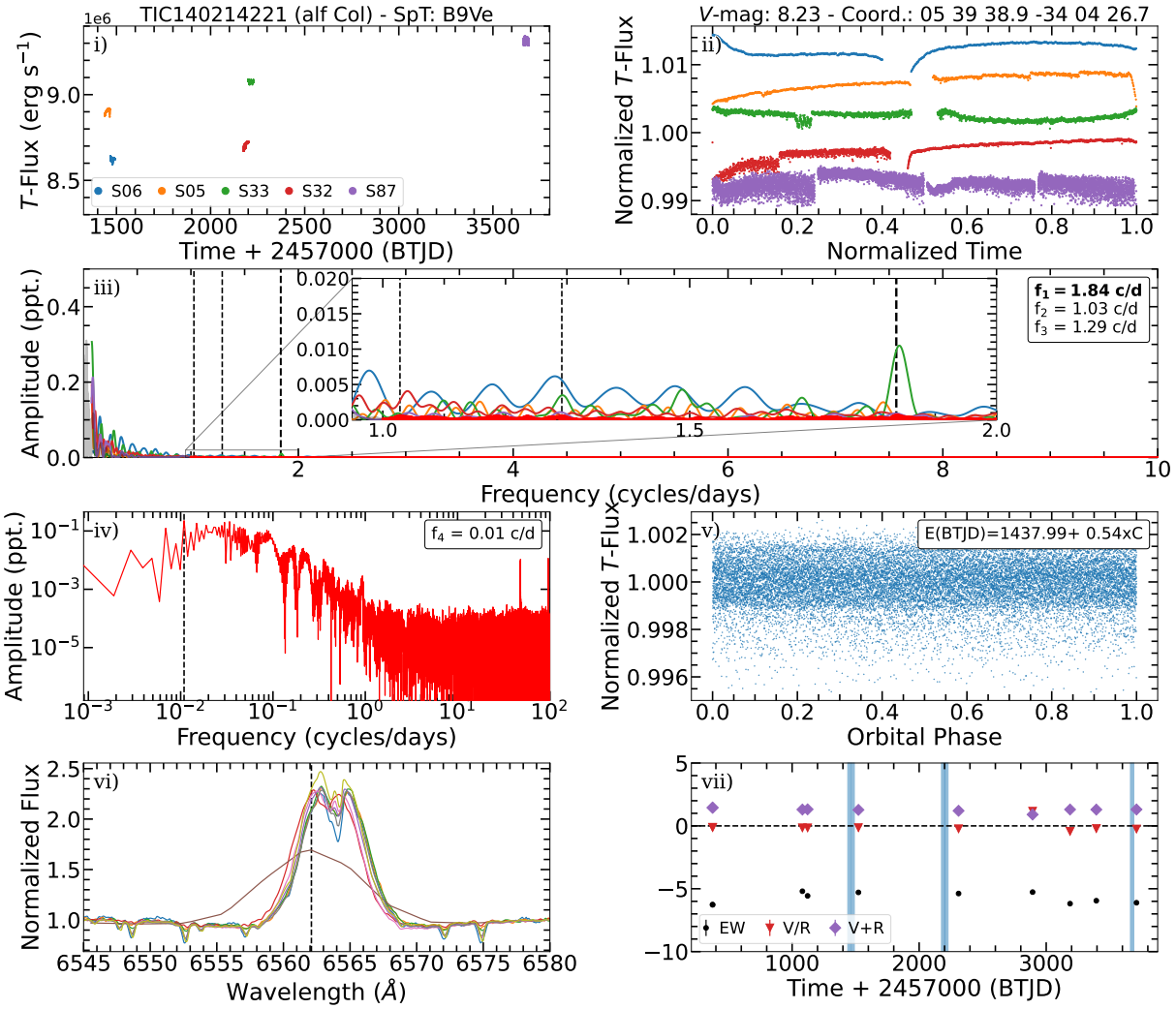

Figure C.18: Panels summarizing the photometric, spectroscopic, and frequency-domain analyses for the target TIC 140214221. (i) Raw T-Flux light curves from different sectors; (ii) normalized T-Flux light curves folded normalized time for each sector; (iii) Lomb-Scargle periodogram highlighting the three main frequencies f_1, f_2, and f_3, with a zoom-in inset; (iv) extended periodogram revealing a low-frequency component f_4; (v) orbital phase-folded light curve; (vi) optical spectrum centered on the Hα line (λ = 6562.8 Å); and (vii) temporal evolution of the equivalent width of the Hα line across available observations. Shaded regions in panel (vii) correspond to observation windows of sectors shown in panel (i).

C.19. TIC 14200511

HD 194335 was classified as a system of spectral type B2IIIe, being a binary system with an orbital period of 63.1 days (Klement et al., 2024c). Wang et al. (2023c) determined the masses of ~8.65 $M_\odot$ and ~1.62 $M_\odot$ for the primary and secondary components, respectively.

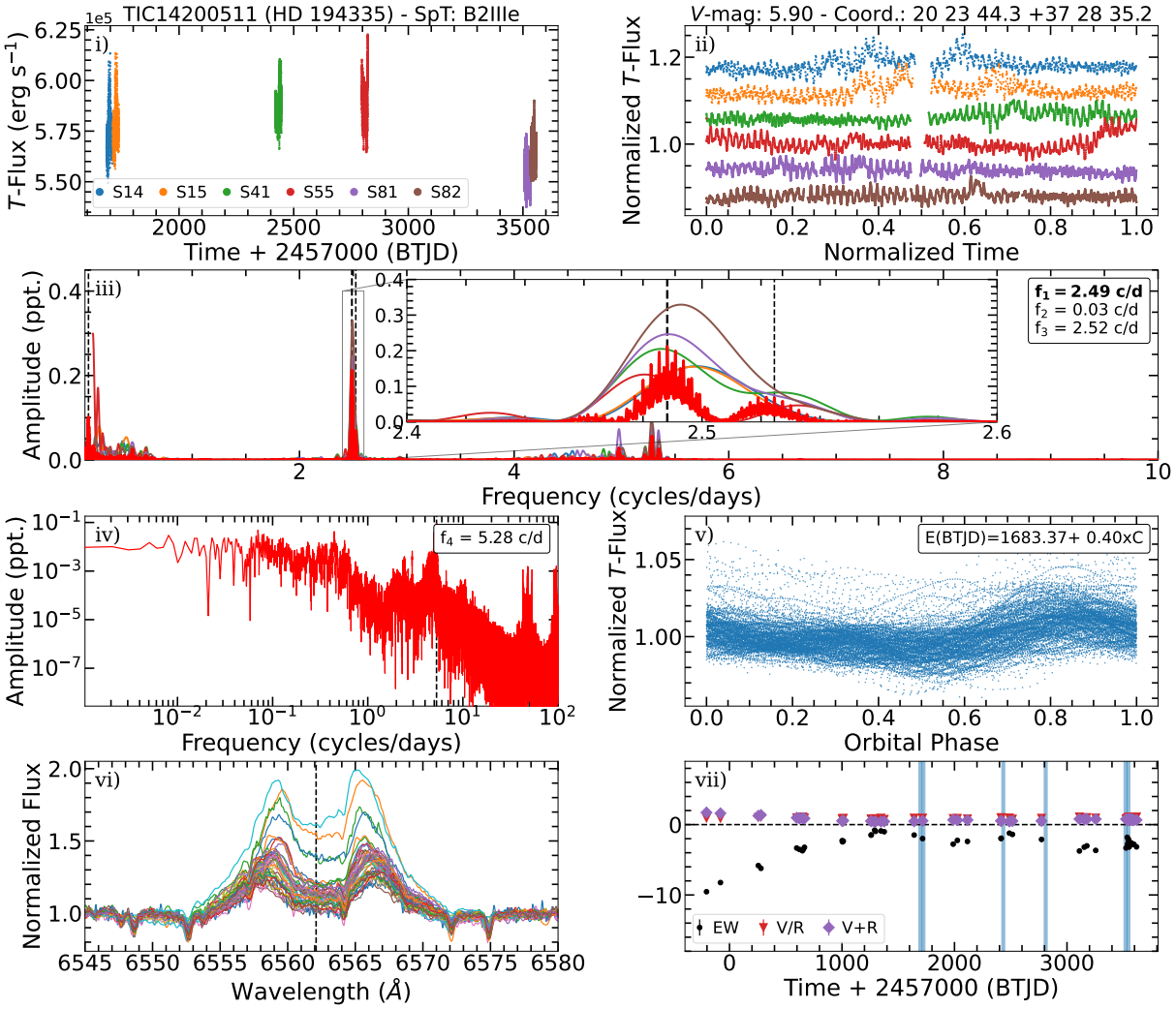

Figure C.19: Panels summarizing the photometric, spectroscopic, and frequency-domain analyses for the target TIC 14200511. (i) Raw T-Flux light curves from different sectors; (ii) normalized T-Flux light curves folded normalized time for each sector; (iii) Lomb-Scargle periodogram highlighting the three main frequencies f_1, f_2, and f_3, with a zoom-in inset; (iv) extended periodogram revealing a low-frequency component f_4; (v) orbital phase-folded light curve; (vi) optical spectrum centered on the Hα line (λ = 6562.8 Å); and (vii) temporal evolution of the equivalent width of the Hα line across available observations. Shaded regions in panel (vii) correspond to observation windows of sectors shown in panel (i).

C.20. TIC 144028101

μ Lup (HD 135734) was classified as a binary system of spectral type B7V + B8Ve. (Zwintz et al., 2024b). Levenhagen et al. (2024a) inferred measurements of 12,000 K, log g equal to 3.5 cgs and $v \sin i$ of 100 km s^{-1} for the undeformed star.

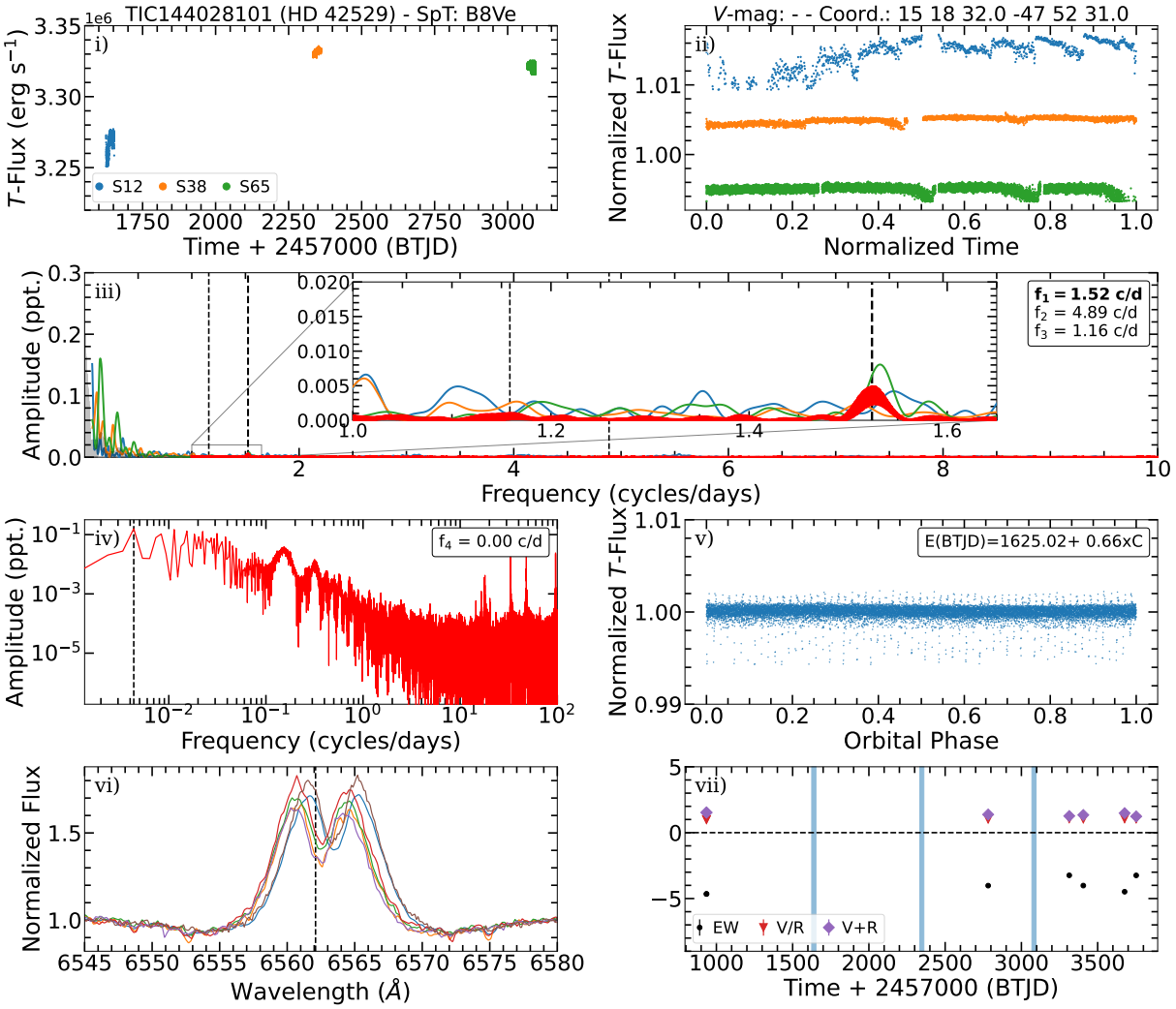

Figure C.20: Panels summarizing the photometric, spectroscopic, and frequency-domain analyses for the target TIC 144028101. (i) Raw T-Flux light curves from different sectors; (ii) normalized T-Flux light curves folded normalized time for each sector; (iii) Lomb-Scargle periodogram highlighting the three main frequencies f_1, f_2, and f_3, with a zoom-in inset; (iv) extended periodogram revealing a low-frequency component f_4; (v) orbital phase-folded light curve; (vi) optical spectrum centered on the Hα line (λ = 6562.8 Å); and (vii) temporal evolution of the equivalent width of the Hα line across available observations. Shaded regions in panel (vii) correspond to observation windows of sectors shown in panel (i).

C.21. TIC 146036695

r Pup (or MX Pup) is a binary system of the SB1 type, with an orbital period of ~5.15 days, and is classified as B1V spectral type and with $v \sin i$ equal to 149 (Carrier et al., 2002; Sigut and Ghafourian, 2023a). Levenhagen et al. (2024a) inferred measurements of 23,600 K, log g equal to 3.3 cgs and $v \sin i$ of 121 km s^{-1} for the undeformed star.

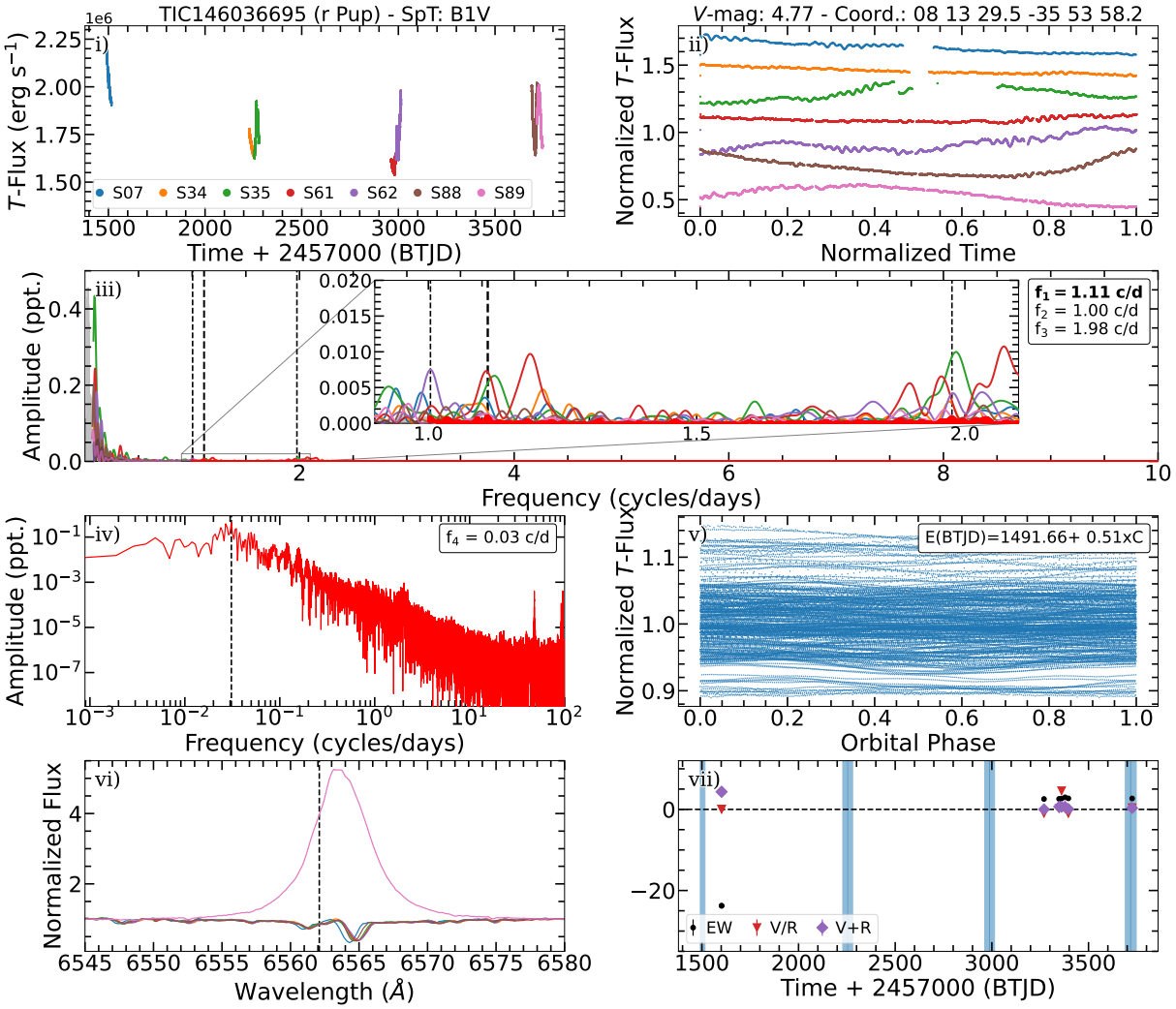

Figure C.21: Panels summarizing the photometric, spectroscopic, and frequency-domain analyses for the target TIC 146036695. (i) Raw T-Flux light curves from different sectors; (ii) normalized T-Flux light curves folded normalized time for each sector; (iii) Lomb-Scargle periodogram highlighting the three main frequencies f_1, f_2, and f_3, with a zoom-in inset; (iv) extended periodogram revealing a low-frequency component f_4; (v) orbital phase-folded light curve; (vi) optical spectrum centered on the Hα line (λ = 6562.8 Å); and (vii) temporal evolution of the equivalent width of the Hα line across available observations. Shaded regions in panel (vii) correspond to observation windows of sectors shown in panel (i).

C.22. TIC 14709809

RY Gem is an eclipsing binary system with an orbital period of 9.3 days, classified with the spectral types of A0V (9,200 K) and K0IV for the primary and secondary components respectively (Plavec and Dobias, 1987b). The physical parameters of the system can be found in the work of Malkov (2020b).

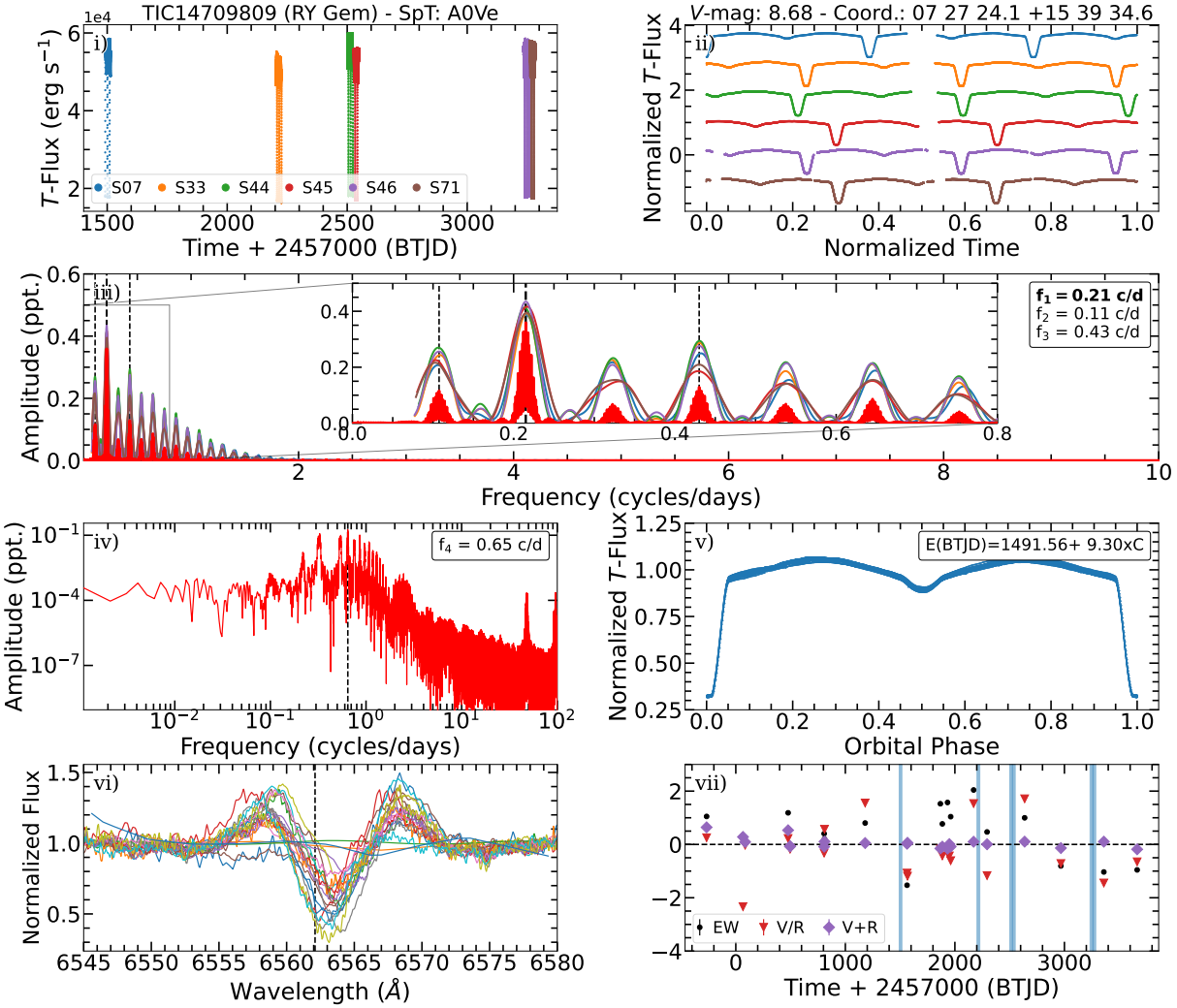

Figure C.22: Panels summarizing the photometric, spectroscopic, and frequency-domain analyses for the target TIC 14709809. (i) Raw T-Flux light curves from different sectors; (ii) normalized T-Flux light curves folded normalized time for each sector; (iii) Lomb-Scargle periodogram highlighting the three main frequencies f_1, f_2, and f_3, with a zoom-in inset; (iv) extended periodogram revealing a low-frequency component f_4; (v) orbital phase-folded light curve; (vi) optical spectrum centered on the Hα line (λ = 6562.8 Å); and (vii) temporal evolution of the equivalent width of the Hα line across available observations. Shaded regions in panel (vii) correspond to observation windows of sectors shown in panel (i).

C.23. TIC 148917425

Kappa Draconis (κ Dra, HD 109387) is a single-lined spectroscopic binary, with one of its stars being a classical Be star (Banerjee et al., 2021; Hutter et al., 2021). It is classified with spectral type B6III, with a temperature of 14,800 K, by Baines et al. (2017). It has an orbital period of ~62 days, and a detailed spectral analysis, with physical measurements of the system's components, can be found in the work of Klement et al. (2022)

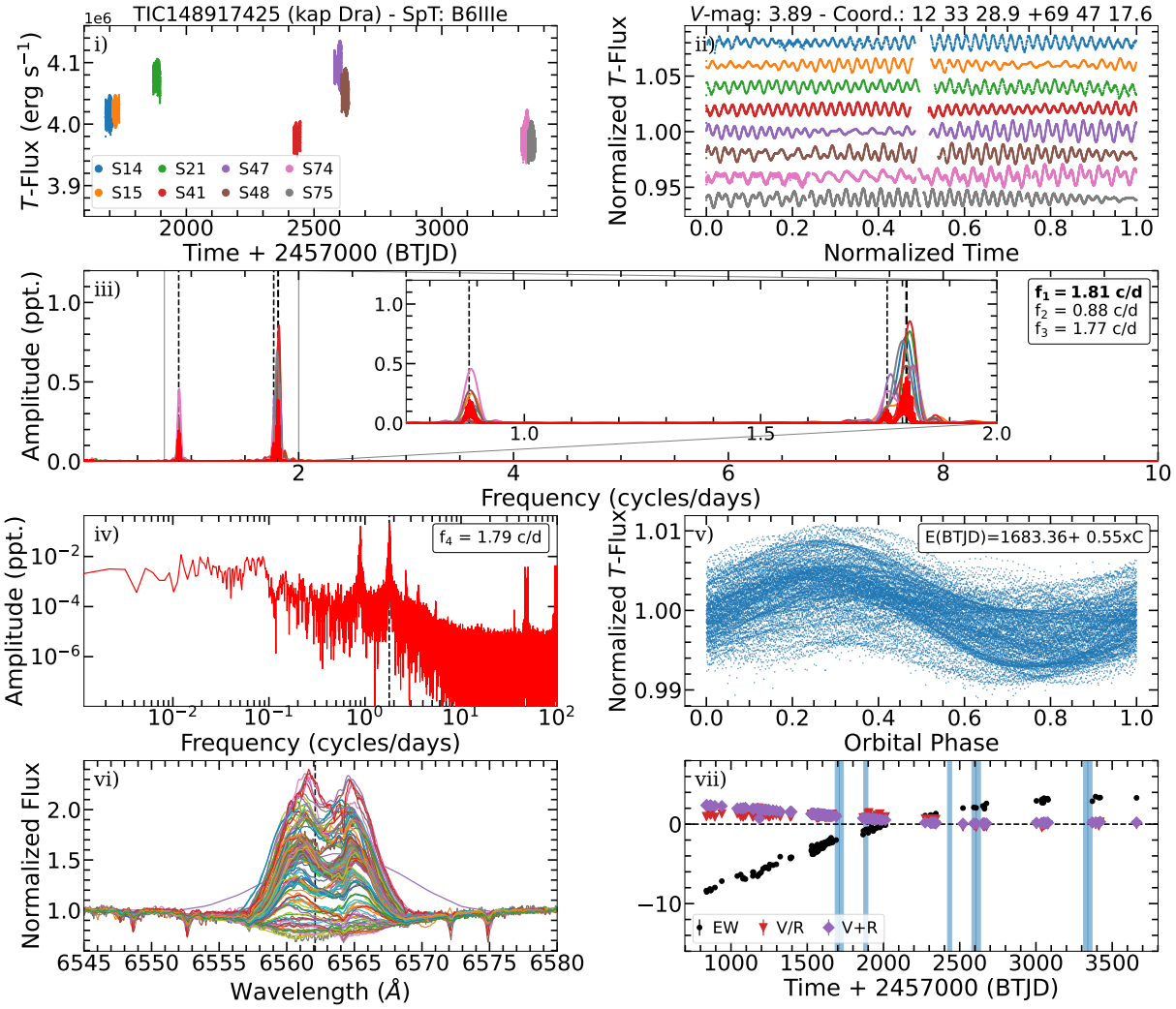

Figure C.23: Panels summarizing the photometric, spectroscopic, and frequency-domain analyses for the target TIC 148917425. (i) Raw T-Flux light curves from different sectors; (ii) normalized T-Flux light curves folded normalized time for each sector; (iii) Lomb-Scargle periodogram highlighting the three main frequencies f_1, f_2, and f_3, with a zoom-in inset; (iv) extended periodogram revealing a low-frequency component f_4; (v) orbital phase-folded light curve; (vi) optical spectrum centered on the Hα line (λ = 6562.8 Å); and (vii) temporal evolution of the equivalent width of the Hα line across available observations. Shaded regions in panel (vii) correspond to observation windows of sectors shown in panel (i).

C.24. TIC 151300497

Walborn (1973) categorized HD 155806 with a spectral type of 07.5V[n]e. Later Różański et al. (2022) specified the system with the ST O7.5V((f))z(e) and $v \sin i$ of 91 km s^{-1}. Its temperature was inferred to be 30,000 K and log g equal to 3.15 cgs. Labadie-Bartz et al. (2022) points out that it is not a classical Be star.

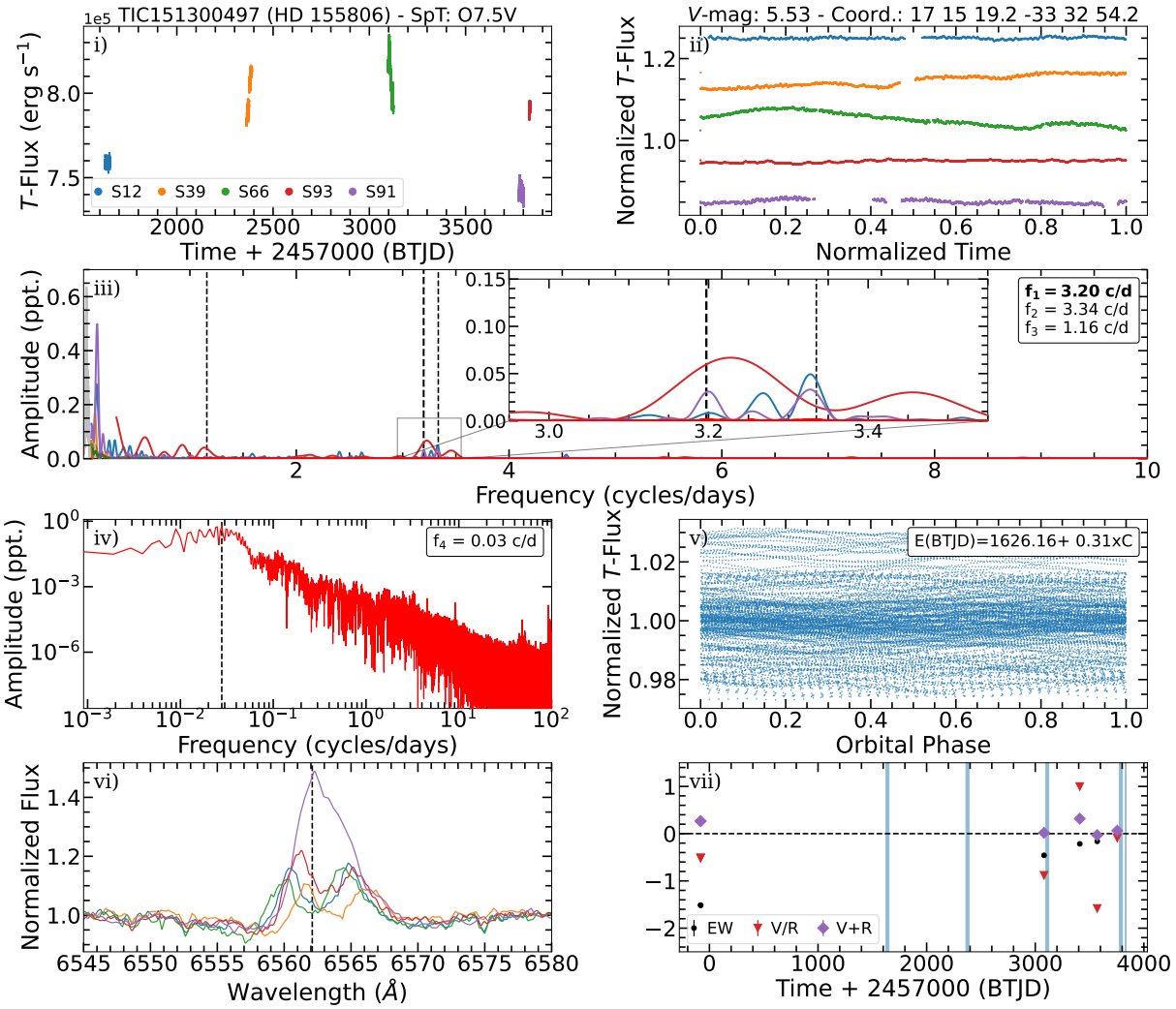

Figure C.24: Panels summarizing the photometric, spectroscopic, and frequency-domain analyses for the target TIC 151300497. (i) Raw T-Flux light curves from different sectors; (ii) normalized T-Flux light curves folded normalized time for each sector; (iii) Lomb-Scargle periodogram highlighting the three main frequencies f_1, f_2, and f_3, with a zoom-in inset; (iv) extended periodogram revealing a low-frequency component f_4; (v) orbital phase-folded light curve; (vi) optical spectrum centered on the Hα line (λ = 6562.8 Å); and (vii) temporal evolution of the equivalent width of the Hα line across available observations. Shaded regions in panel (vii) correspond to observation windows of sectors shown in panel (i).

C.25. TIC 151546818

V457 Sct (HD 174513) is an object of spectral type B1Ve, with $v \sin i$ of 180 km s^{-1}, 27,500 K and mass of ~19 $M_\odot$ (Neubauer, 1943; Levenhagen and Leister, 2004).

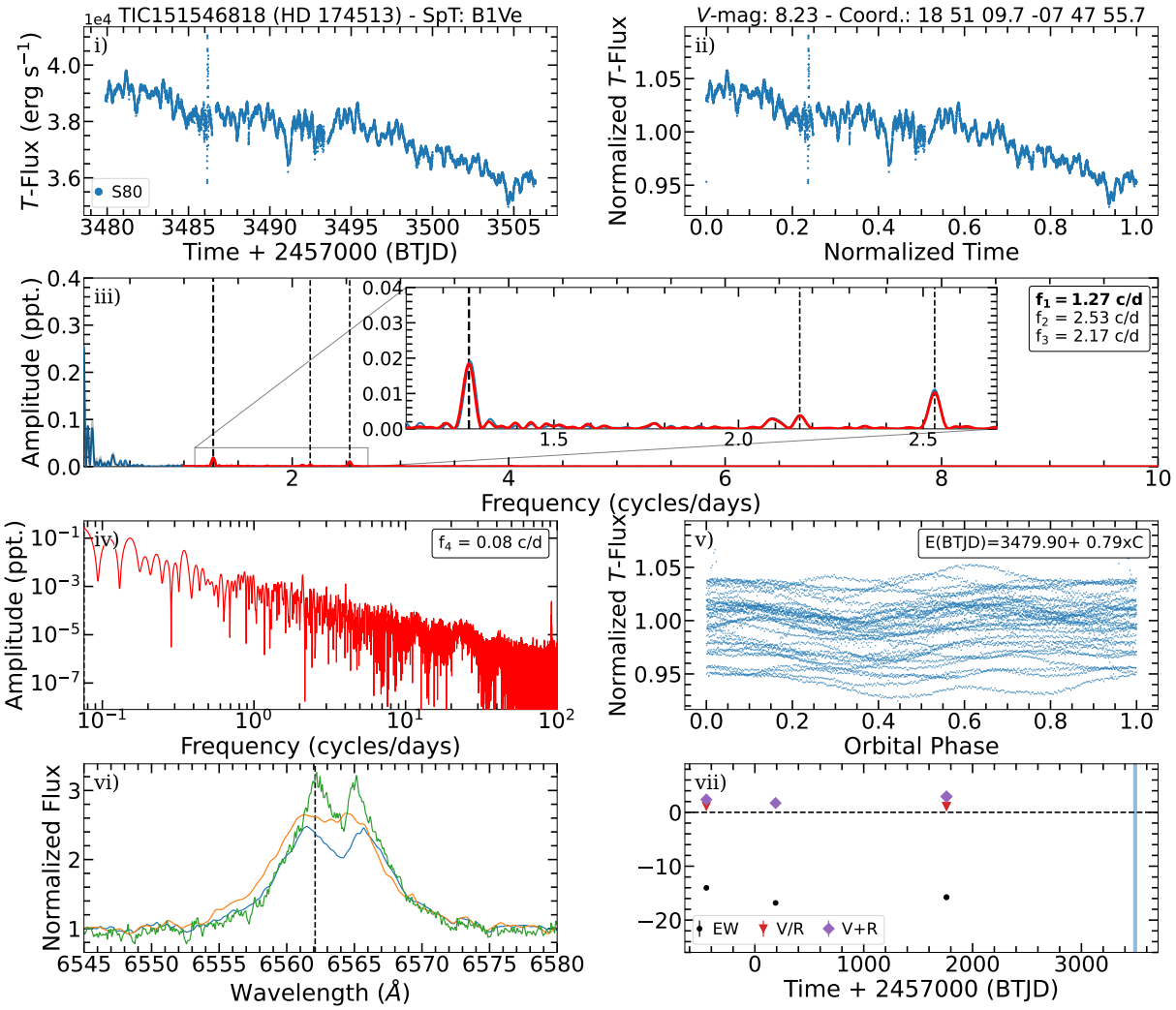

Figure C.25: Panels summarizing the photometric, spectroscopic, and frequency-domain analyses for the target TIC 151546818. (i) Raw *T*-Flux light curves from different sectors; (ii) normalized *T*-Flux light curves folded normalized time for each sector; (iii) Lomb-Scargle periodogram highlighting the three main frequencies f_1, f_2, and f_3, with a zoom-in inset; (iv) extended periodogram revealing a low-frequency component f_4; (v) orbital phase-folded light curve; (vi) optical spectrum centered on the Hα line (λ = 6562.8 Å); and (vii) temporal evolution of the equivalent width of the Hα line across available observations. Shaded regions in panel (vii) correspond to observation windows of sectors shown in panel (i).

C.26. TIC 152859121

Zeta Oph (ζ Ophiuchi, HD 14975) has a spectral type of O9.5V and $v \sin i$ of ~400 km s^{-1} (Howarth and Smith, 2001). Is a runaway detached binary (Neuhaeuser et al., 2020), pointing to an Oe-type star by Howarth et al. (2014), who identified characteristic pulsations as a combination of radial and non-radial pulsations with frequencies of 5.18, 2.96 and 2.67 d^{-1}. No evidence of emission lines was found in BeSS database.

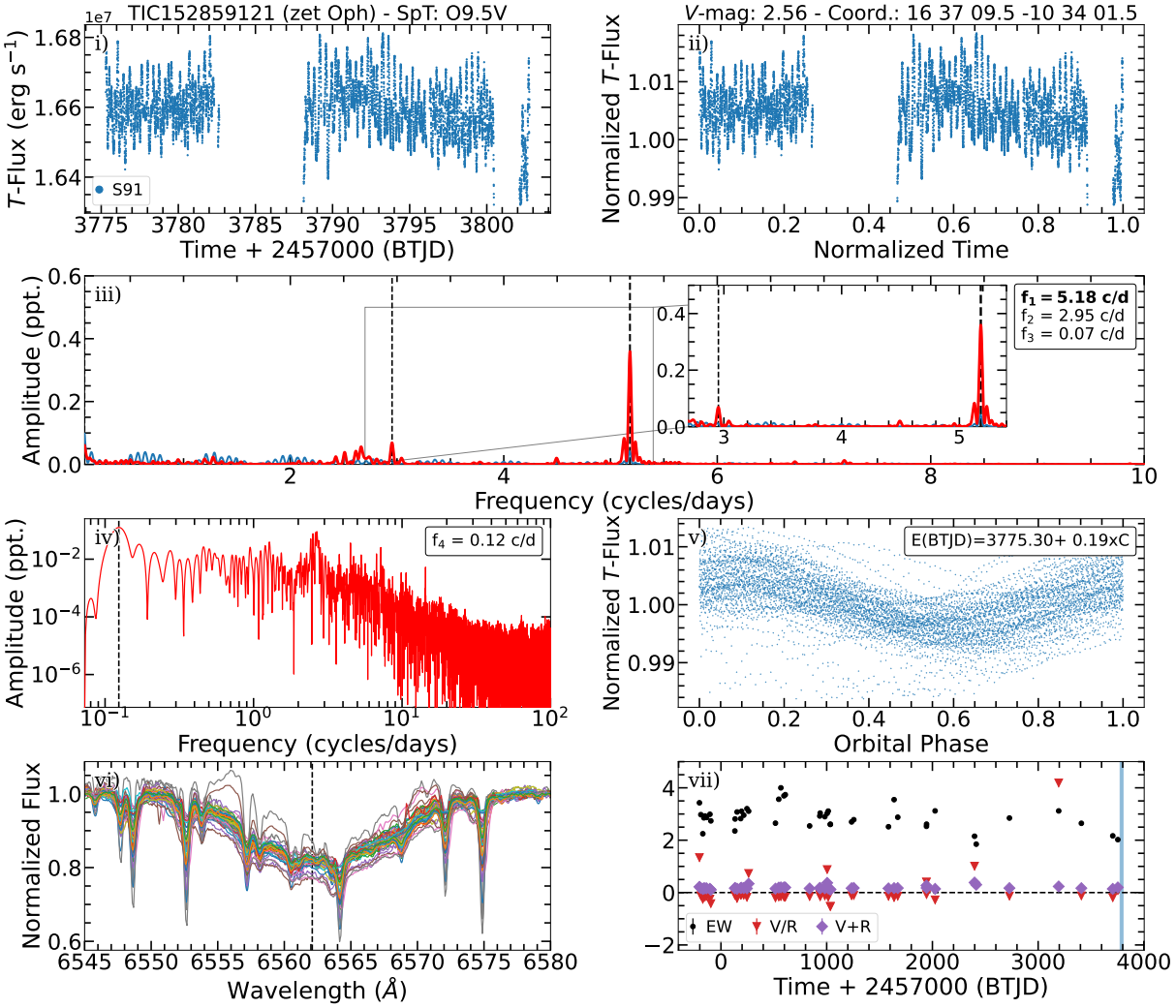

Figure C.26: Panels summarizing the photometric, spectroscopic, and frequency-domain analyses for the target TIC 152859121. (i) Raw T-Flux light curves from different sectors; (ii) normalized T-Flux light curves folded normalized time for each sector; (iii) Lomb-Scargle periodogram highlighting the three main frequencies f_1, f_2, and f_3, with a zoom-in inset; (iv) extended periodogram revealing a low-frequency component f_4; (v) orbital phase-folded light curve; (vi) optical spectrum centered on the Hα line (λ = 6562.8 Å); and (vii) temporal evolution of the equivalent width of the Hα line across available observations. Shaded regions in panel (vii) correspond to observation windows of sectors shown in panel (i).

C.27. TIC 153880067

MWC 656 (HD 215227) is a binary system with an orbital period of ~60 days that has FeII and HeII emission lines, and was initially identified as the first system composed of a black hole and a Be star (Casares et al., 2014). More recently, Janssens et al. (2023) inferred a mass ratio much lower than previously proposed, so that the idea that there is a black hole in the system is no longer supported, but rather another type of compact object.

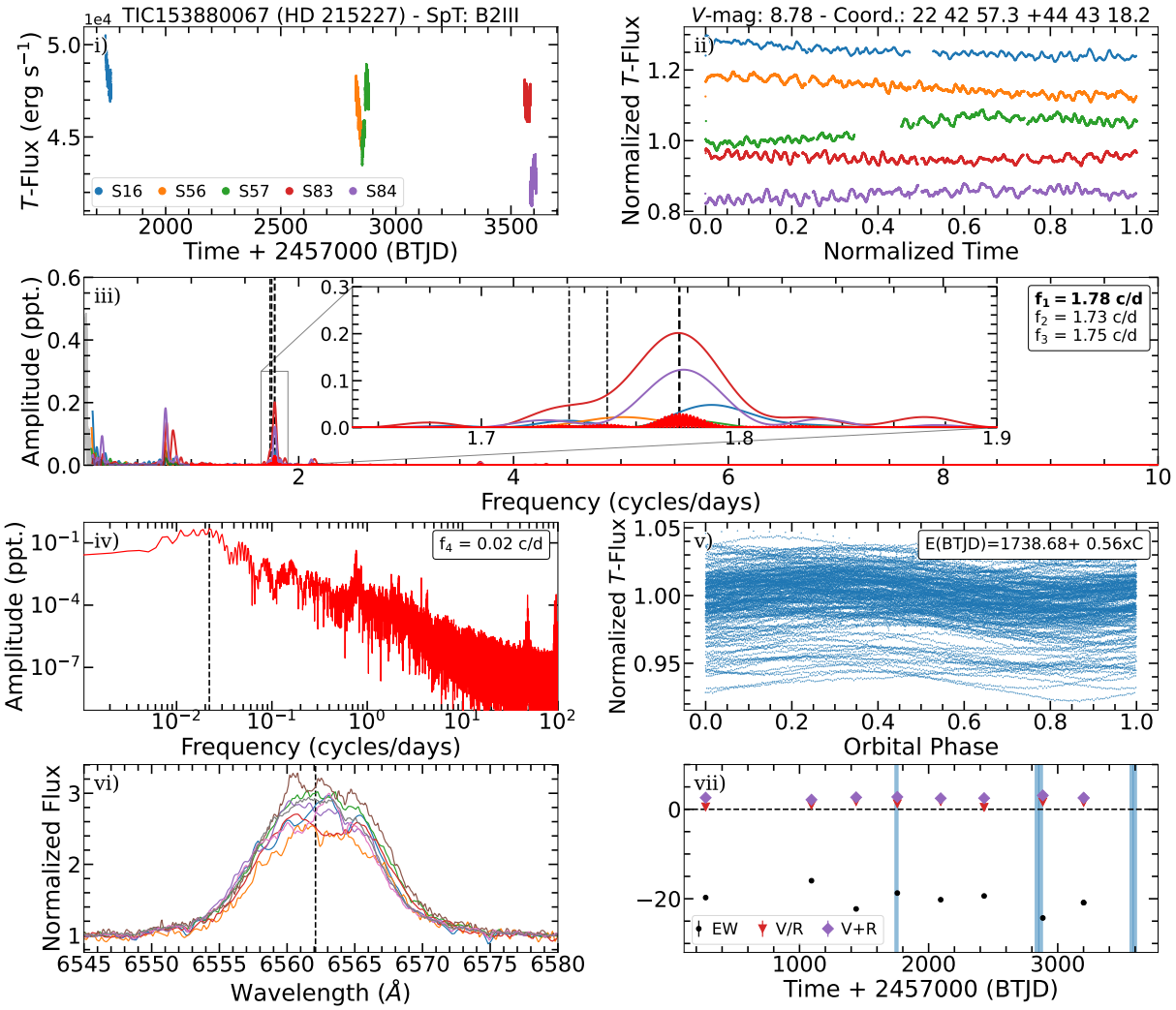

Figure C.27: Panels summarizing the photometric, spectroscopic, and frequency-domain analyses for the target TIC 153880067. (i) Raw T-Flux light curves from different sectors; (ii) normalized T-Flux light curves folded normalized time for each sector; (iii) Lomb-Scargle periodogram highlighting the three main frequencies f_1, f_2, and f_3, with a zoom-in inset; (iv) extended periodogram revealing a low-frequency component f_4; (v) orbital phase-folded light curve; (vi) optical spectrum centered on the Hα line (λ = 6562.8 Å); and (vii) temporal evolution of the equivalent width of the Hα line across available observations. Shaded regions in panel (vii) correspond to observation windows of sectors shown in panel (i).

C.28. TIC 154355871

14 Lac (HD 216200) is a binary system formed by a Be star of spectral type B3IVne, $v \sin i$ of 195 km s^{-1}, 17,600 K, mass of ~13 $M_\odot$ and orbital period of ~10 days (Negueruela et al., 2024; Catanzaro, 2013; Harmanec et al., 2015).

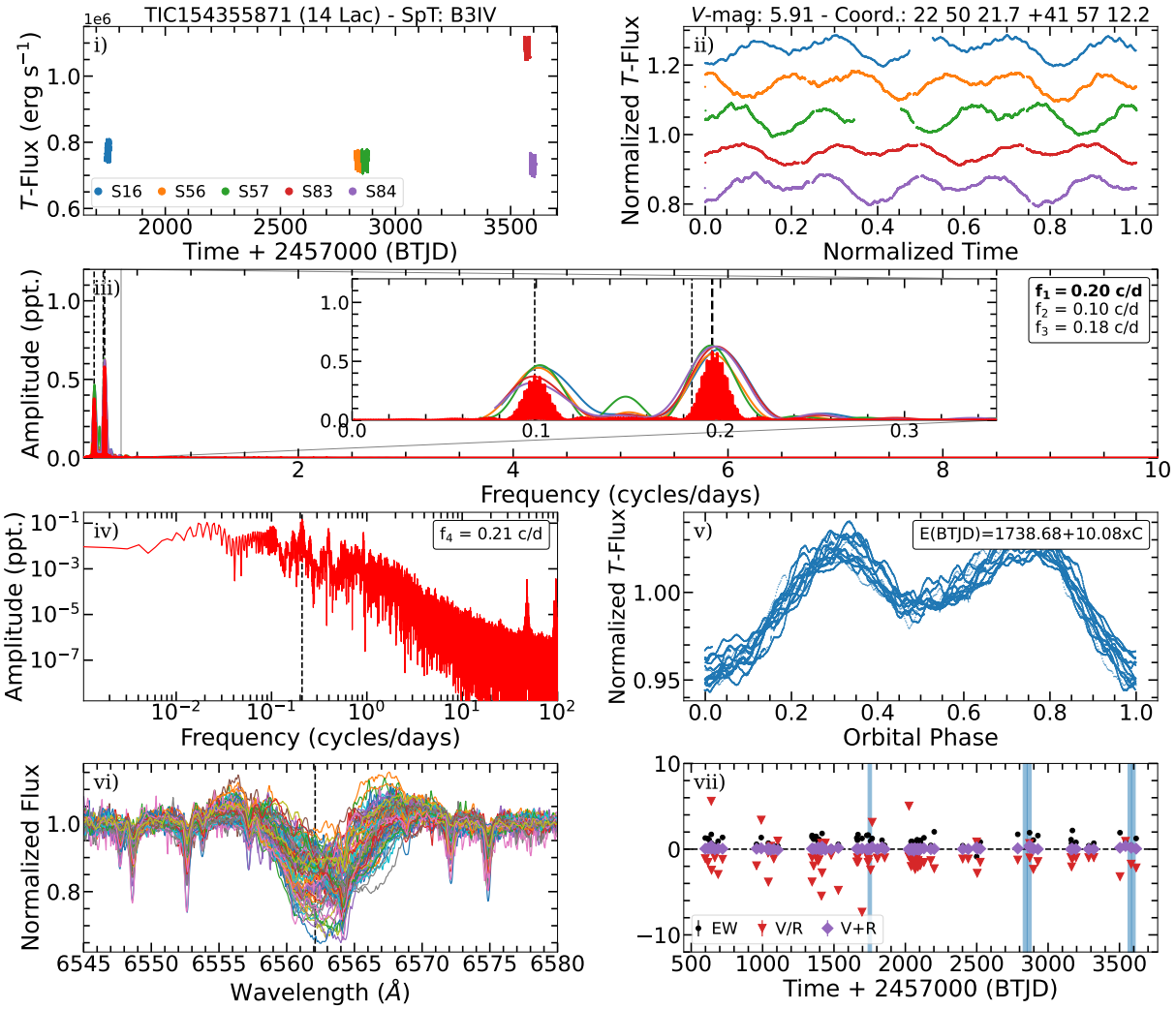

Figure C.28: Panels summarizing the photometric, spectroscopic, and frequency-domain analyses for the target TIC 154355871. (i) Raw T-Flux light curves from different sectors; (ii) normalized T-Flux light curves folded normalized time for each sector; (iii) Lomb-Scargle periodogram highlighting the three main frequencies f_1, f_2, and f_3, with a zoom-in inset; (iv) extended periodogram revealing a low-frequency component f_4; (v) orbital phase-folded light curve; (vi) optical spectrum centered on the Hα line (λ = 6562.8 Å); and (vii) temporal evolution of the equivalent width of the Hα line across available observations. Shaded regions in panel (vii) correspond to observation windows of sectors shown in panel (i).

C.29. TIC 155030422

omi And (HD 217675) is a hierarchical quadruple system with configuration AB or "2 + 2" that contains a Be star and spectral type of B6V (Zhuchkov et al., 2010; Mitrofanova et al., 2021). Sigut and Ghafourian (2023a) inferred $v \sin i$ of 301 km s^{-1}.

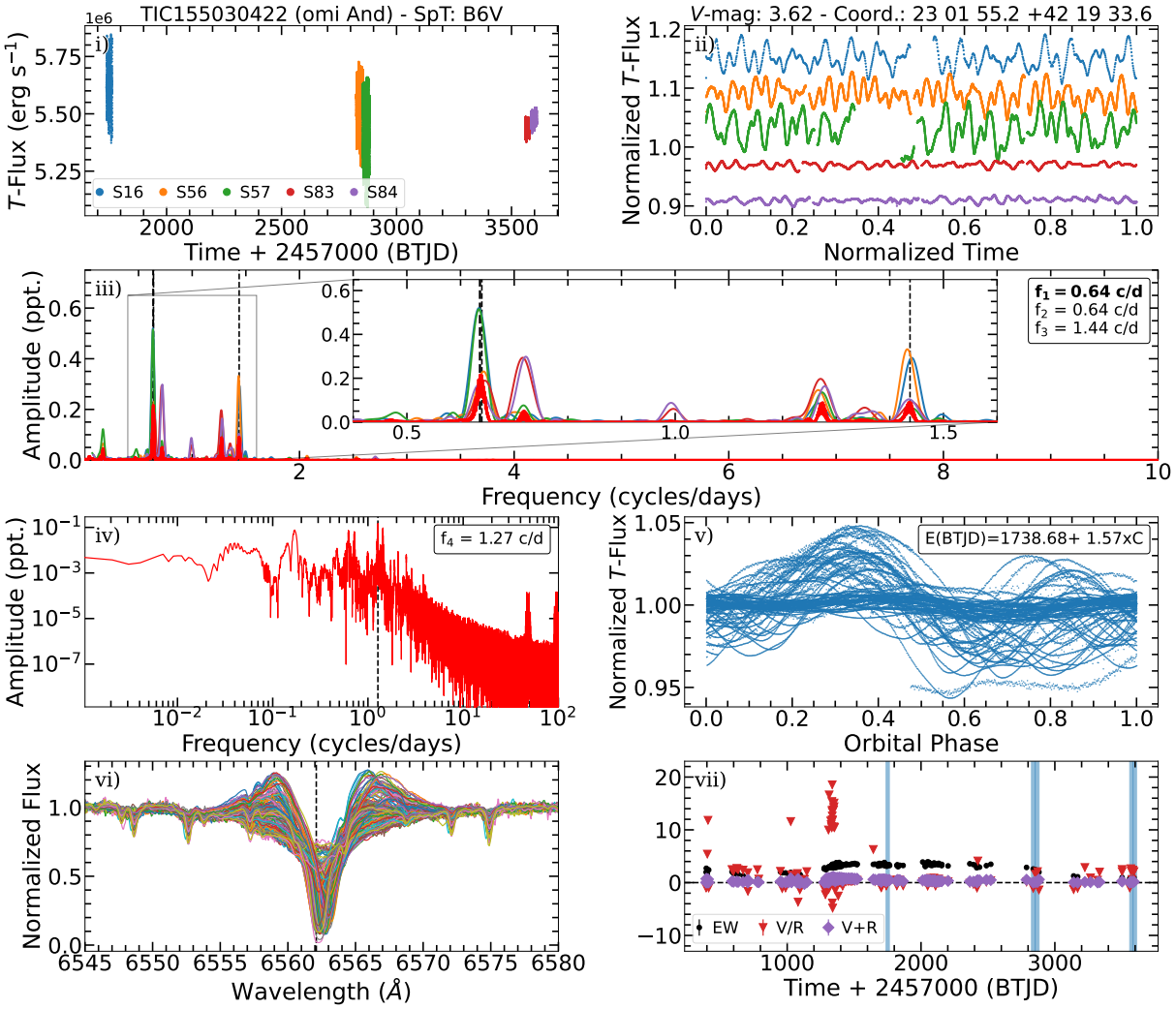

Figure C.29: Panels summarizing the photometric, spectroscopic, and frequency-domain analyses for the target TIC 155030422. (i) Raw T-Flux light curves from different sectors; (ii) normalized T-Flux light curves folded normalized time for each sector; (iii) Lomb-Scargle periodogram highlighting the three main frequencies f_1, f_2, and f_3, with a zoom-in inset; (iv) extended periodogram revealing a low-frequency component f_4; (v) orbital phase-folded light curve; (vi) optical spectrum centered on the Hα line (λ = 6562.8 Å); and (vii) temporal evolution of the equivalent width of the Hα line across available observations. Shaded regions in panel (vii) correspond to observation windows of sectors shown in panel (i).

C.30. TIC 155573117

CD-27 5181 has been classified as OB+e in Stephenson and Sanduleak (1971), but there is no concrete confirmation of its binary nature or the existence of a Be star. It may be either an eclipsing or ellipsoidal binary system, with the two strong signals being harmonically related at ~0.6 and ~1.2 days^{-1} (Labadie-Bartz et al., 2022). No BeSS spectrum is available.

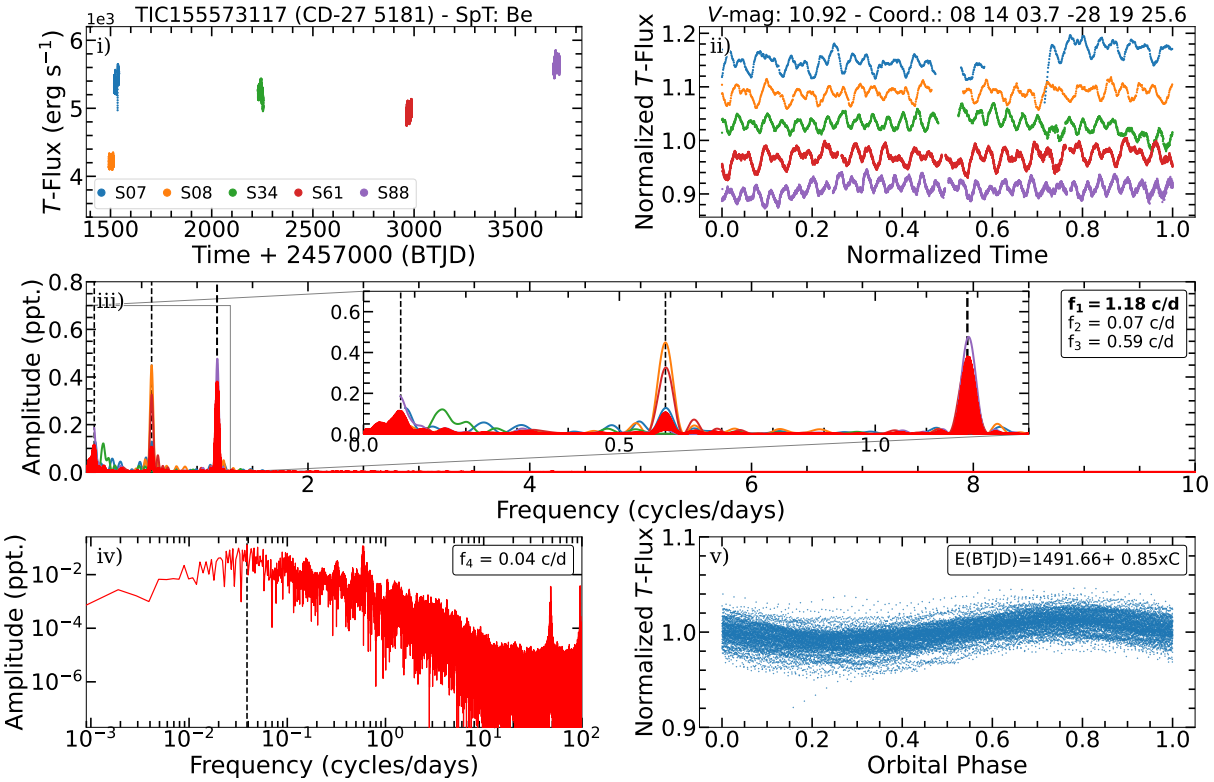

Figure C.30: Panels summarizing the photometric and frequency-domain analyses for the target TIC 155573117. (i) Raw T-Flux light curves from different sectors; (ii) normalized T-Flux light curves folded normalized time for each sector; (iii) Lomb-Scargle periodogram highlighting the three main frequencies f_1, f_2, and f_3, with a zoom-in inset; (iv) extended periodogram revealing a low-frequency component f_4; (v) orbital phase-folded light curve.

C.31. TIC 157420220

4 Herculis (HD 142926) is a binary system with an orbital period of ~46 days and spectral type B9Ve. The Be star is the primary component of the system with temperature of 12,500 K, log g of 4.0 csg and $v \sin i$ of 360 km s^{-1} (Kubát et al., 1998; Sigut and Ghafourian, 2023a; Klement et al., 2024b).

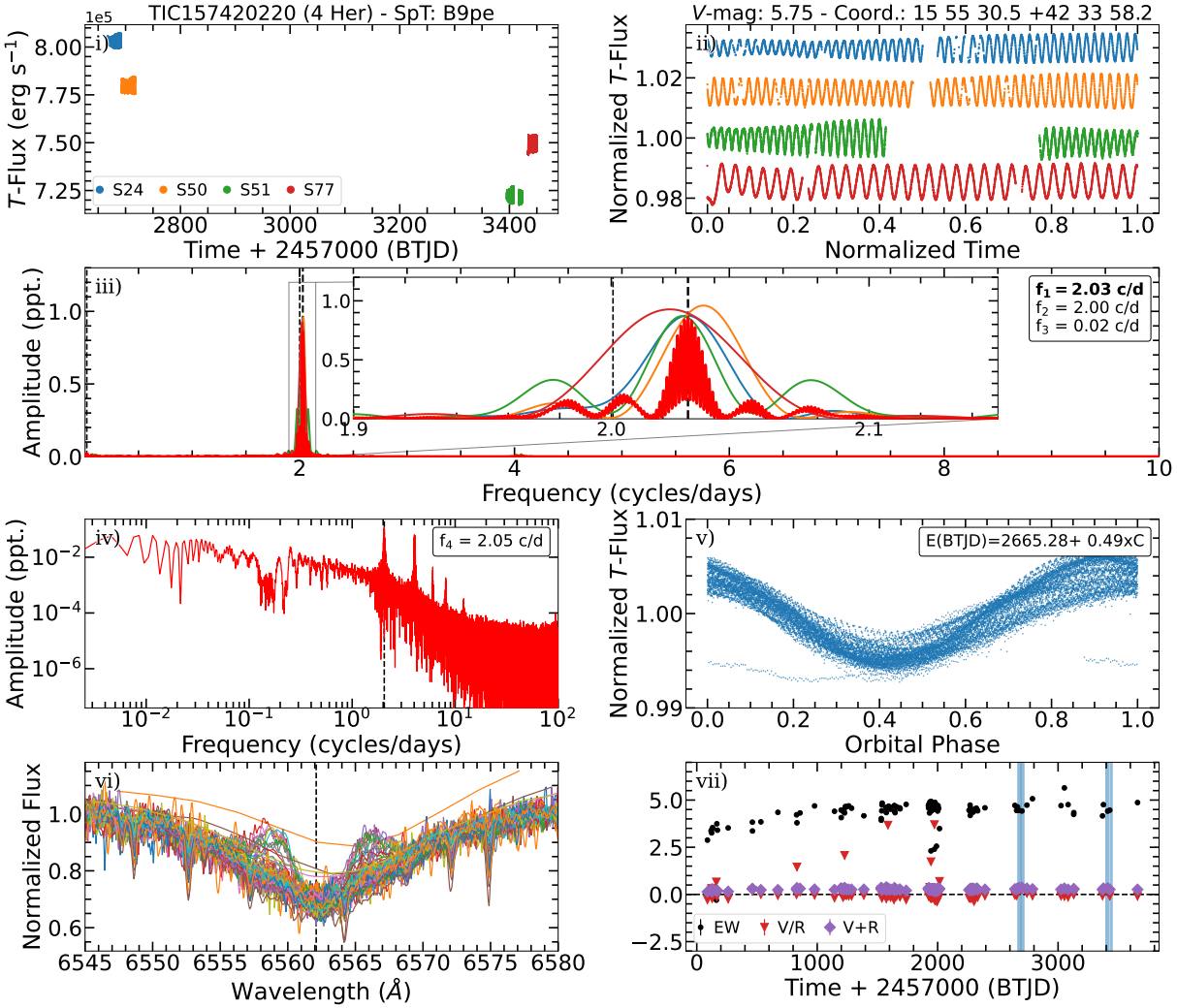

Figure C.31: Panels summarizing the photometric, spectroscopic, and frequency-domain analyses for the target TIC 157420220. (i) Raw T-Flux light curves from different sectors; (ii) normalized T-Flux light curves folded normalized time for each sector; (iii) Lomb-Scargle periodogram highlighting the three main frequencies f_1, f_2, and f_3, with a zoom-in inset; (iv) extended periodogram revealing a low-frequency component f_4; (v) orbital phase-folded light curve; (vi) optical spectrum centered on the Hα line (λ = 6562.8 Å); and (vii) temporal evolution of the equivalent width of the Hα line across available observations. Shaded regions in panel (vii) correspond to observation windows of sectors shown in panel (i).

C.32. TIC 159117671

HD 112028 (HR 4893) is a triple system (Jaschek and Andrillat, 1998).

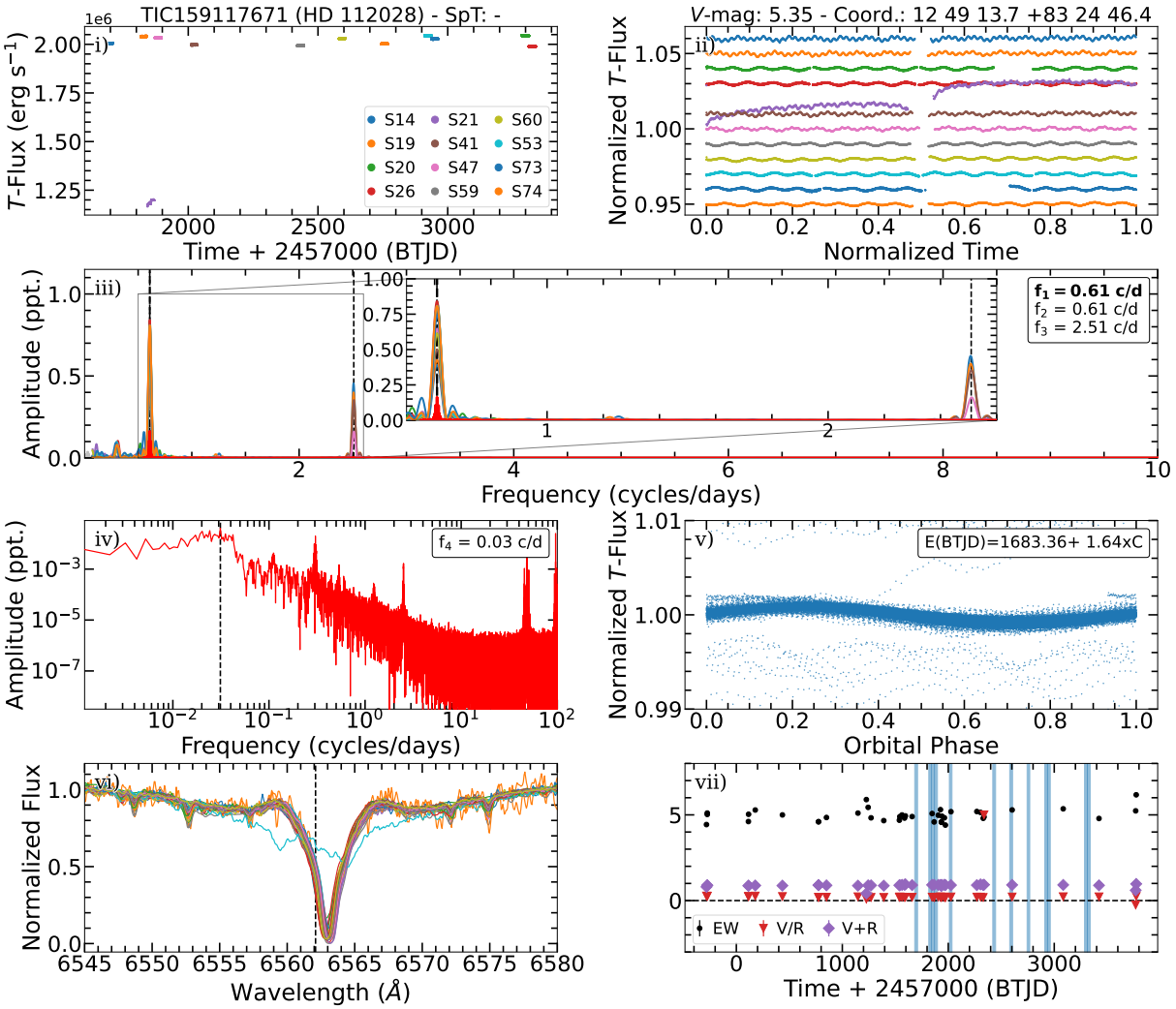

Figure C.32: Panels summarizing the photometric, spectroscopic, and frequency-domain analyses for the target TIC 159117671. (i) Raw T-Flux light curves from different sectors; (ii) normalized T-Flux light curves folded normalized time for each sector; (iii) Lomb-Scargle periodogram highlighting the three main frequencies f_1, f_2, and f_3, with a zoom-in inset; (iv) extended periodogram revealing a low-frequency component f_4; (v) orbital phase-folded light curve; (vi) optical spectrum centered on the Hα line (λ = 6562.8 Å); and (vii) temporal evolution of the equivalent width of the Hα line across available observations. Shaded regions in panel (vii) correspond to observation windows of sectors shown in panel (i).

C.33. TIC 16887256

θ CrB (HD 138749, HR 5778) is a binary system classified with the spectral type B6III, with $v \sin i$ of 320 km s^{-1} (Rivinius et al., 2006; Rhee et al., 2007). Its Be star presents a weak Hα emission and an orbital period of ~361 years (Klement et al., 2024b).

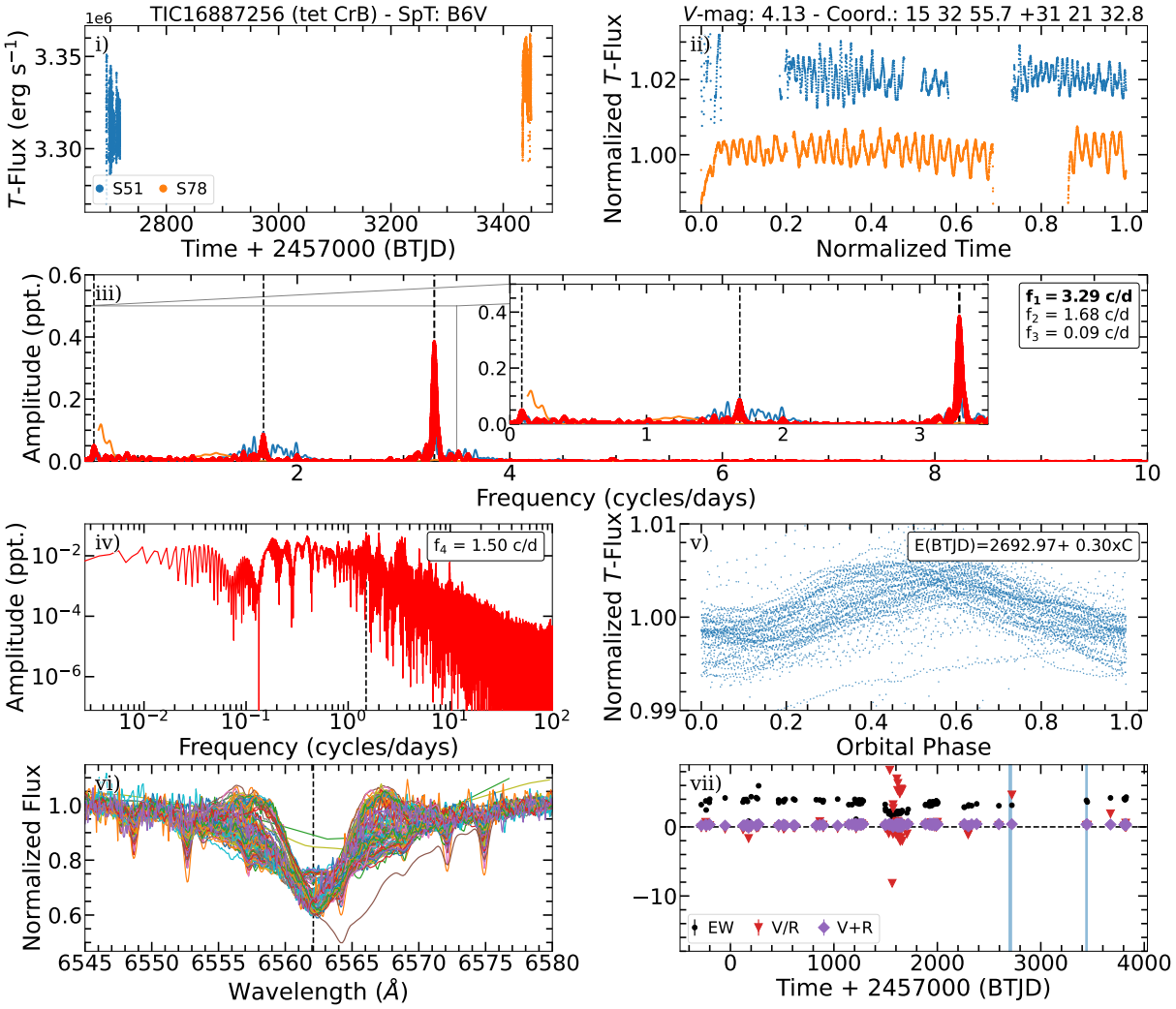

Figure C.33: Panels summarizing the photometric, spectroscopic, and frequency-domain analyses for the target TIC 16887256. (i) Raw T-Flux light curves from different sectors; (ii) normalized T-Flux light curves folded normalized time for each sector; (iii) Lomb-Scargle periodogram highlighting the three main frequencies f_1, f_2, and f_3, with a zoom-in inset; (iv) extended periodogram revealing a low-frequency component f_4; (v) orbital phase-folded light curve; (vi) optical spectrum centered on the Hα line (λ = 6562.8 Å); and (vii) temporal evolution of the equivalent width of the Hα line across available observations. Shaded regions in panel (vii) correspond to observation windows of sectors shown in panel (i).

C.34. TIC 171895762

V828 Ara (HD 153261, HR 6304) is a type B2IVe star with $v \sin i$ of 184 km s^{-1} (Yudin, 2001).

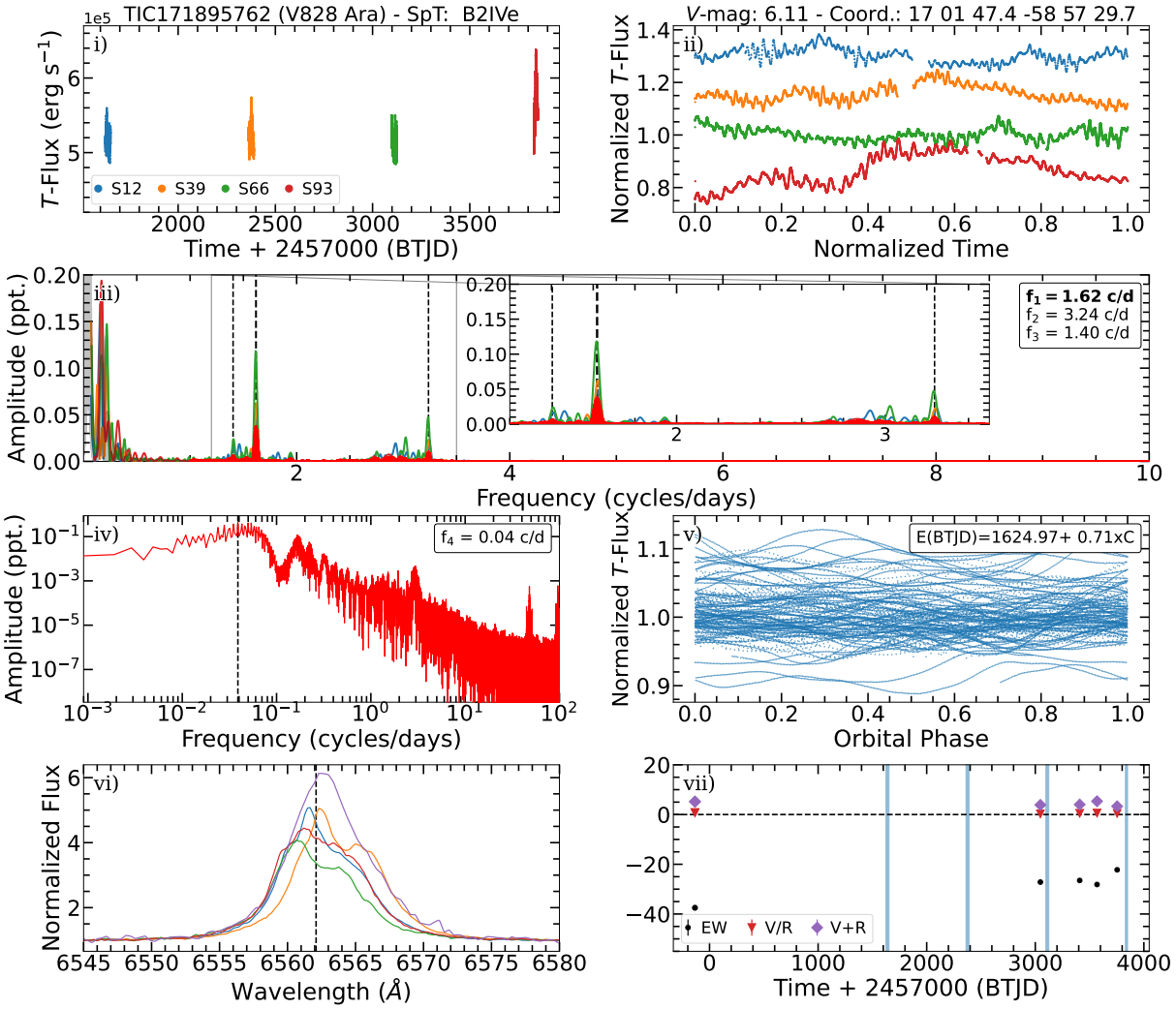

Figure C.34: Panels summarizing the photometric, spectroscopic, and frequency-domain analyses for the target TIC 171895762. (i) Raw T-Flux light curves from different sectors; (ii) normalized T-Flux light curves folded normalized time for each sector; (iii) Lomb-Scargle periodogram highlighting the three main frequencies f_1, f_2, and f_3, with a zoom-in inset; (iv) extended periodogram revealing a low-frequency component f_4; (v) orbital phase-folded light curve; (vi) optical spectrum centered on the Hα line (λ = 6562.8 Å); and (vii) temporal evolution of the equivalent width of the Hα line across available observations. Shaded regions in panel (vii) correspond to observation windows of sectors shown in panel (i).

C.35. TIC 174008063

z Pup (HD 60606, HR 2911) is a type B2Ve star with temperature of 19,600 K and $v \sin i$ of 285 km s^{-1} (Frémat et al., 2005).

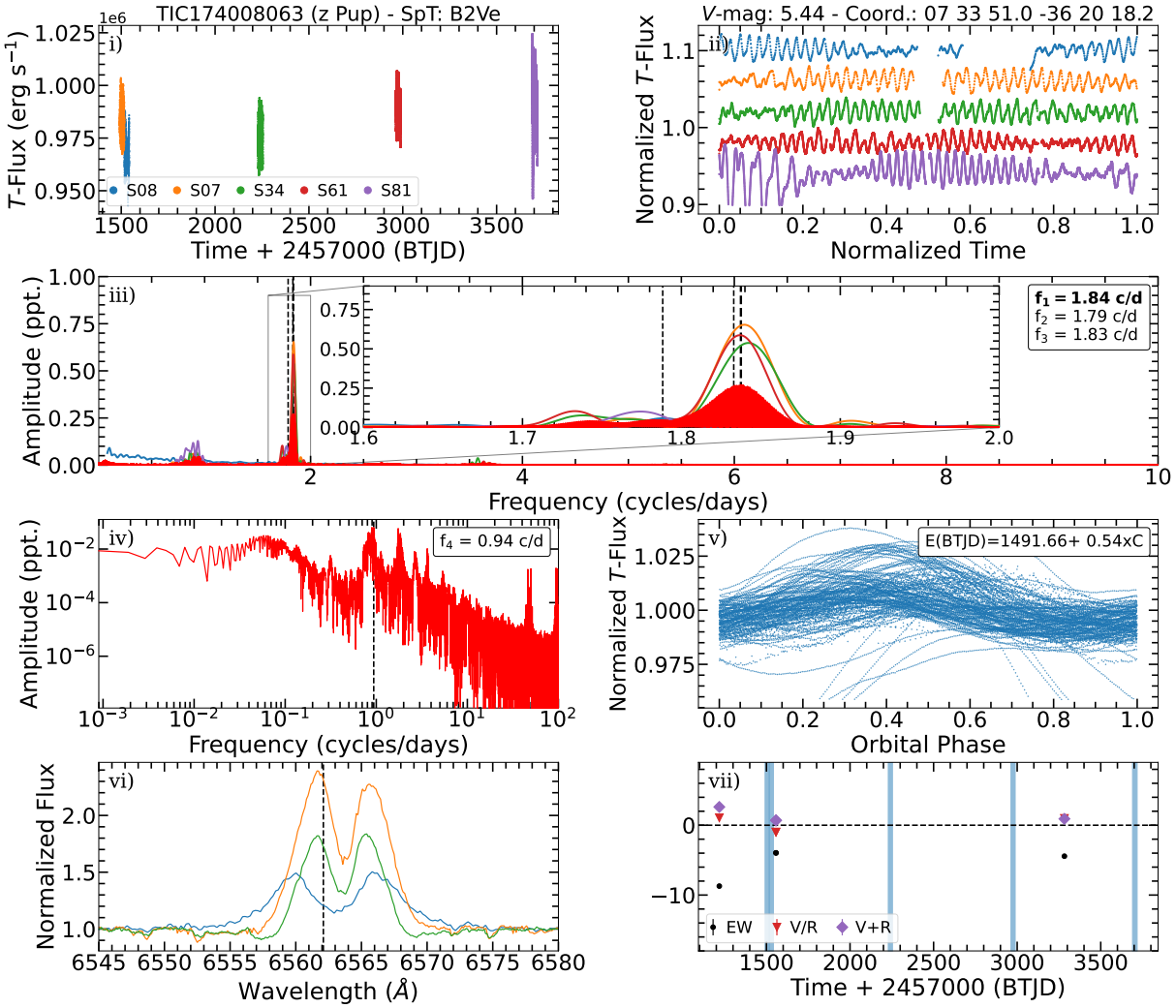

Figure C.35: Panels summarizing the photometric, spectroscopic, and frequency-domain analyses for the target TIC 174008063. (i) Raw T-Flux light curves from different sectors; (ii) normalized T-Flux light curves folded normalized time for each sector; (iii) Lomb-Scargle periodogram highlighting the three main frequencies f_1, f_2, and f_3, with a zoom-in inset; (iv) extended periodogram revealing a low-frequency component f_4; (v) orbital phase-folded light curve; (vi) optical spectrum centered on the Hα line (λ = 6562.8 Å); and (vii) temporal evolution of the equivalent width of the Hα line across available observations. Shaded regions in panel (vii) correspond to observation windows of sectors shown in panel (i).

C.36. TIC 174664153

No relevant information was found about this object.

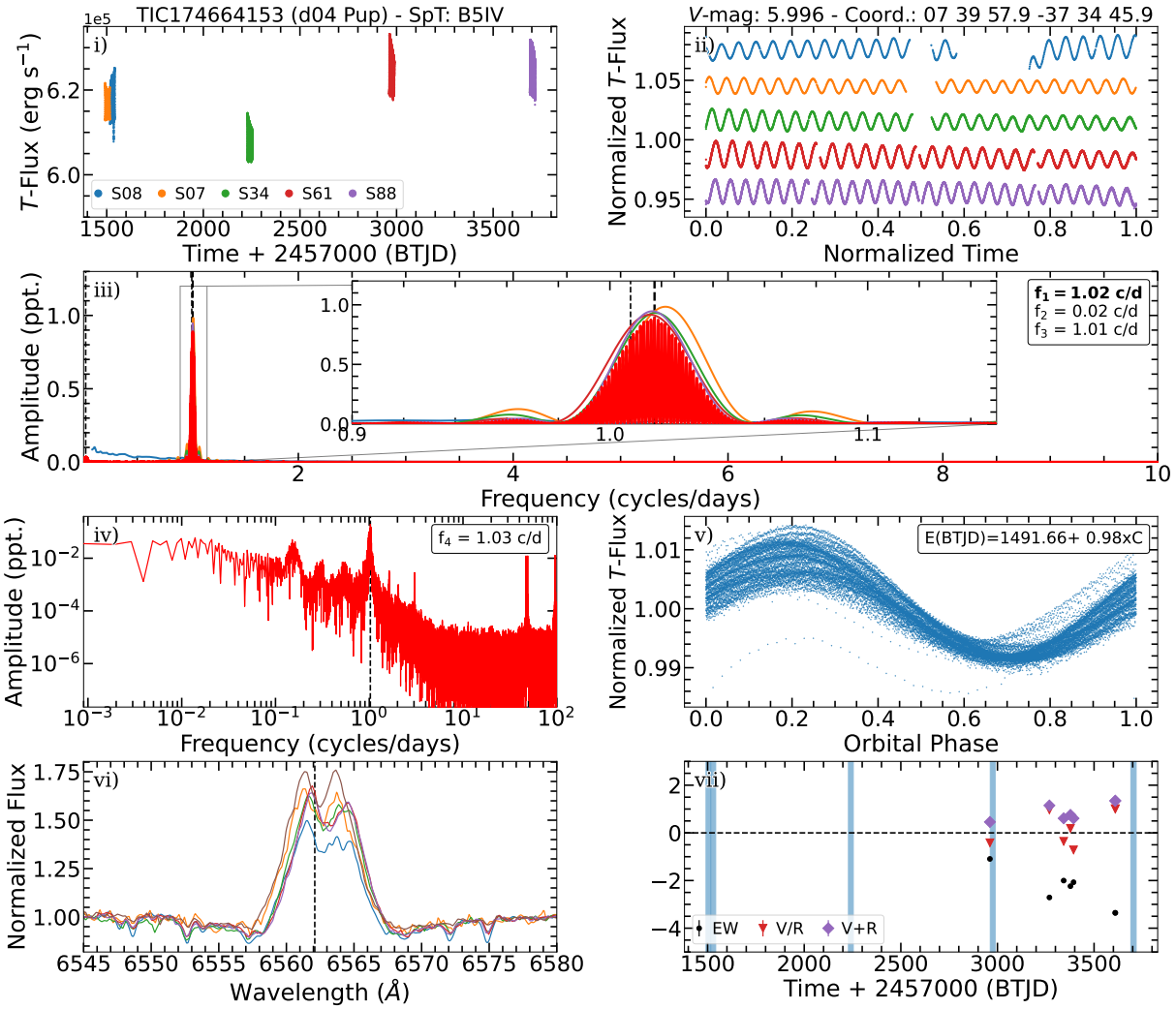

Figure C.36: Panels summarizing the photometric, spectroscopic, and frequency-domain analyses for the target TIC 174664153. (i) Raw T-Flux light curves from different sectors; (ii) normalized T-Flux light curves folded normalized time for each sector; (iii) Lomb-Scargle periodogram highlighting the three main frequencies f_1, f_2, and f_3, with a zoom-in inset; (iv) extended periodogram revealing a low-frequency component f_4; (v) orbital phase-folded light curve; (vi) optical spectrum centered on the Hα line (λ = 6562.8 Å); and (vii) temporal evolution of the equivalent width of the Hα line across available observations. Shaded regions in panel (vii) correspond to observation windows of sectors shown in panel (i).

C.37. TIC 175523591

HD 63215 (HIP 37915) has a temperature of 14.027 K (Silaj and Landstreet, 2014). It is present in the companion star work of Kervella et al. (2019).

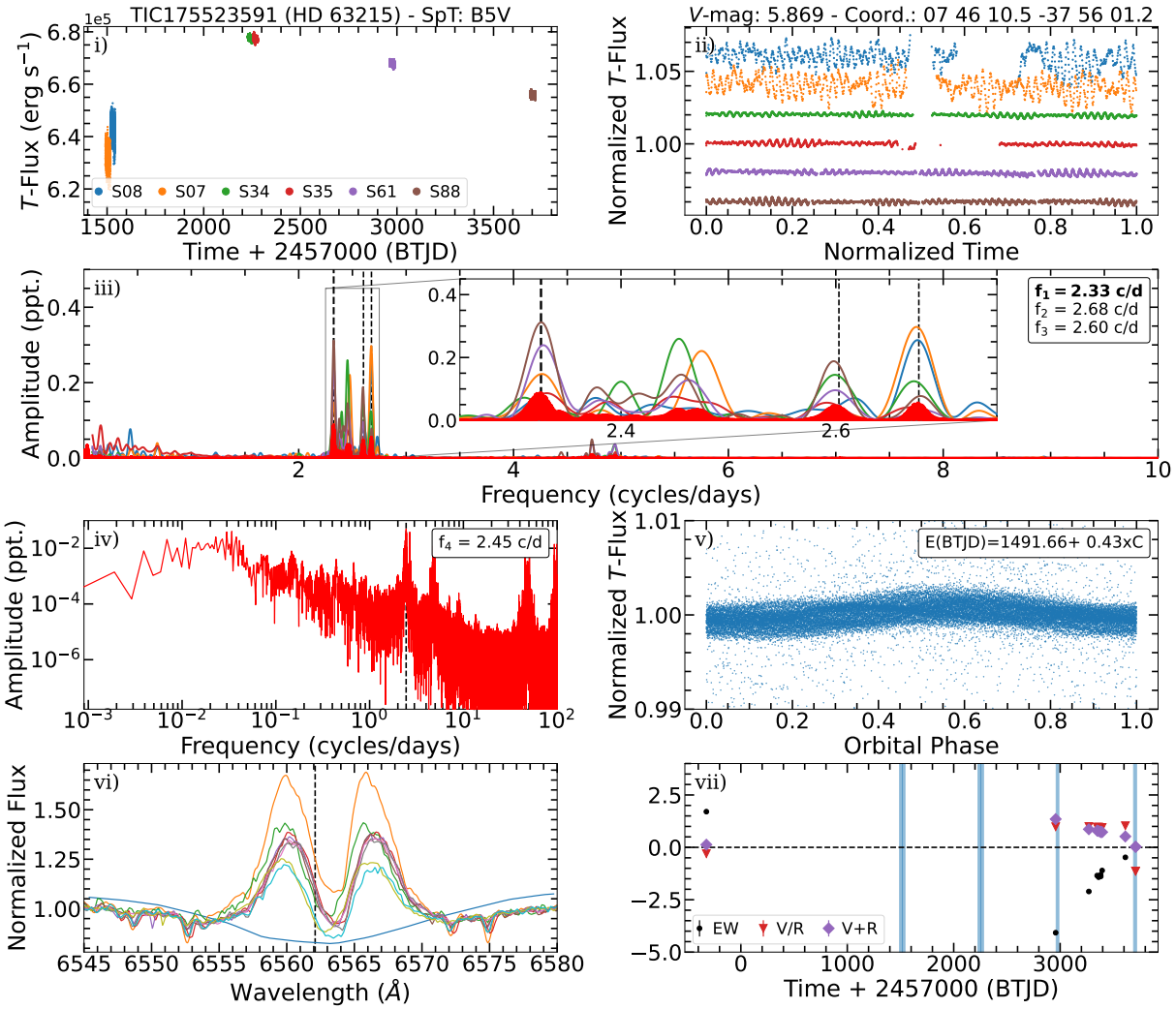

Figure C.37: Panels summarizing the photometric, spectroscopic, and frequency-domain analyses for the target TIC 175523591. (i) Raw T-Flux light curves from different sectors; (ii) normalized T-Flux light curves folded normalized time for each sector; (iii) Lomb-Scargle periodogram highlighting the three main frequencies f_1, f_2, and f_3, with a zoom-in inset; (iv) extended periodogram revealing a low-frequency component f_4; (v) orbital phase-folded light curve; (vi) optical spectrum centered on the Hα line (λ = 6562.8 Å); and (vii) temporal evolution of the equivalent width of the Hα line across available observations. Shaded regions in panel (vii) correspond to observation windows of sectors shown in panel (i).

C.38. TIC 181627638

HD 179343 was classified with spectral type Ae by Merrill and Burwell (1949), and was later updated to B9Vsh in the study of the Paschen region of the spectra of Be stars by Andrillat et al. (1994). Docobo et al. (2004) carried out studies on its multiplicity by measuring the angular separation via Speckle interferometry. Today, it is known that this object is a system with 7 stars, the primary component being a Be shell-type star (Vollmann, 2008; Souza et al., 2020).

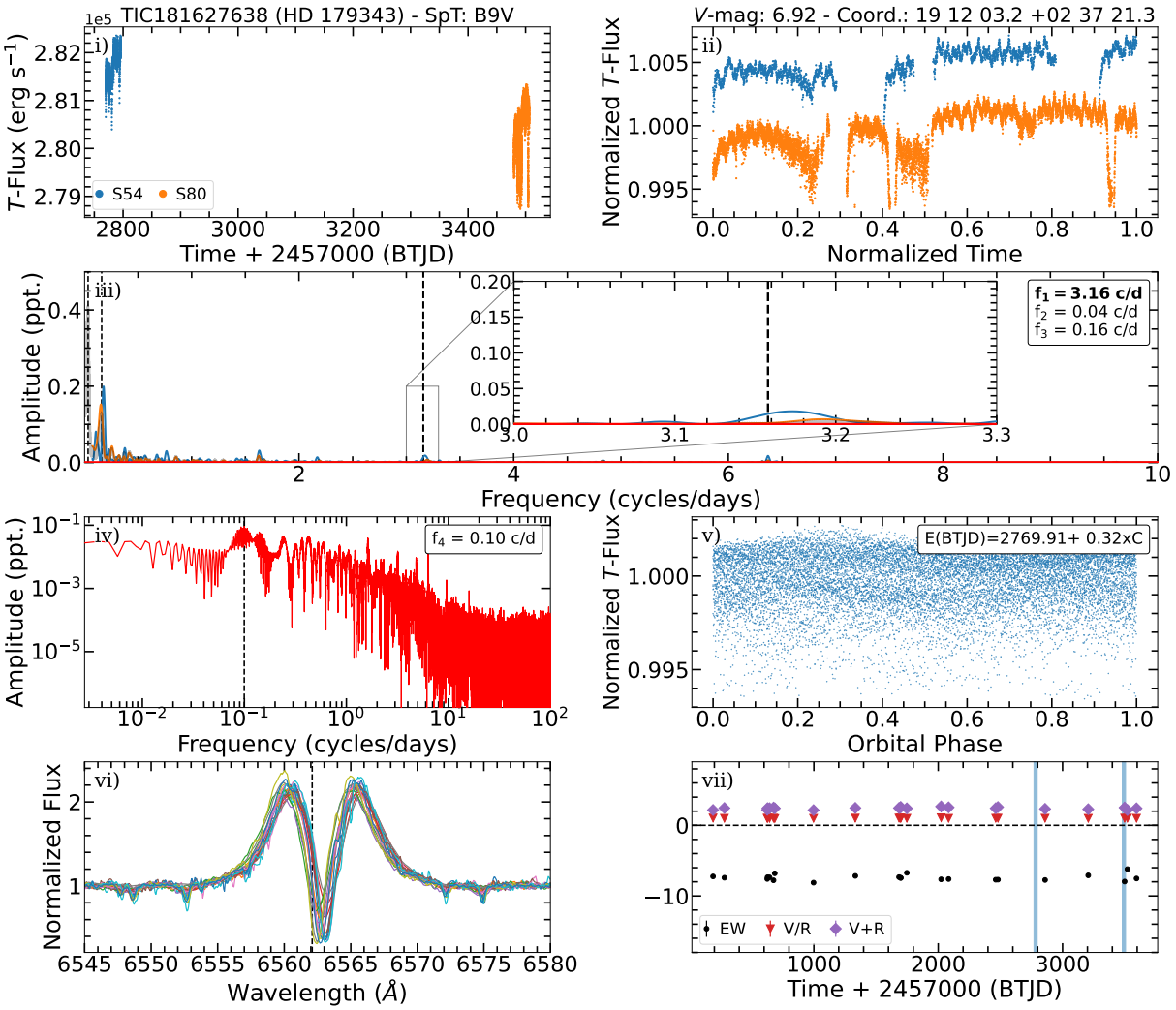

Figure C.38: Panels summarizing the photometric, spectroscopic, and frequency-domain analyses for the target TIC 181627638. (i) Raw T-Flux light curves from different sectors; (ii) normalized T-Flux light curves folded normalized time for each sector; (iii) Lomb-Scargle periodogram highlighting the three main frequencies f_1, f_2, and f_3, with a zoom-in inset; (iv) extended periodogram revealing a low-frequency component f_4; (v) orbital phase-folded light curve; (vi) optical spectrum centered on the Hα line (λ = 6562.8 Å); and (vii) temporal evolution of the equivalent width of the Hα line across available observations. Shaded regions in panel (vii) correspond to observation windows of sectors shown in panel (i).

C.39. TIC 186598770

HD 18552 has a spectral type of B8Vne and a $v \sin i$ of 288 km s^{-1} (Labadie-Bartz et al., 2017). It was studied by Kervella et al. (2019) who characterized the physical presence of stellar and substellar companions through astrometry and by Castañón Esteban et al. (2024) who calculated some physical properties of this object.

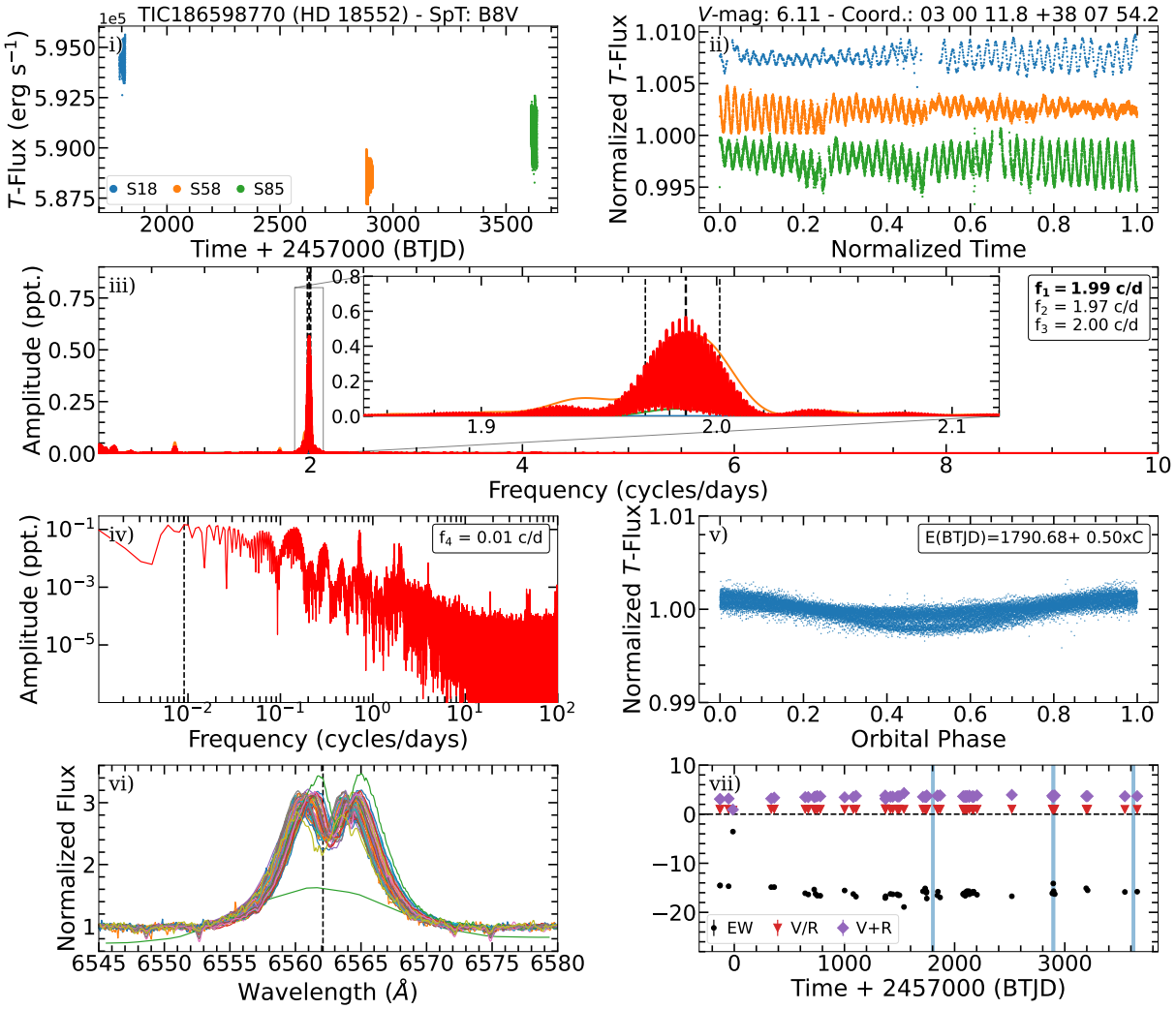

Figure C.39: Panels summarizing the photometric, spectroscopic, and frequency-domain analyses for the target TIC 186598770. (i) Raw T-Flux light curves from different sectors; (ii) normalized T-Flux light curves folded normalized time for each sector; (iii) Lomb-Scargle periodogram highlighting the three main frequencies f_1, f_2, and f_3, with a zoom-in inset; (iv) extended periodogram revealing a low-frequency component f_4; (v) orbital phase-folded light curve; (vi) optical spectrum centered on the Hα line (λ = 6562.8 Å); and (vii) temporal evolution of the equivalent width of the Hα line across available observations. Shaded regions in panel (vii) correspond to observation windows of sectors shown in panel (i).

C.40. TIC 187683138

HD 33656 is a star with spectral type B5Ve (Chojnowski et al., 2014) and it was studied by Kervella et al. (2019) who characterized the physical presence of stellar and substellar companions through astrometry. No spectrum was found in the BESS catalog.

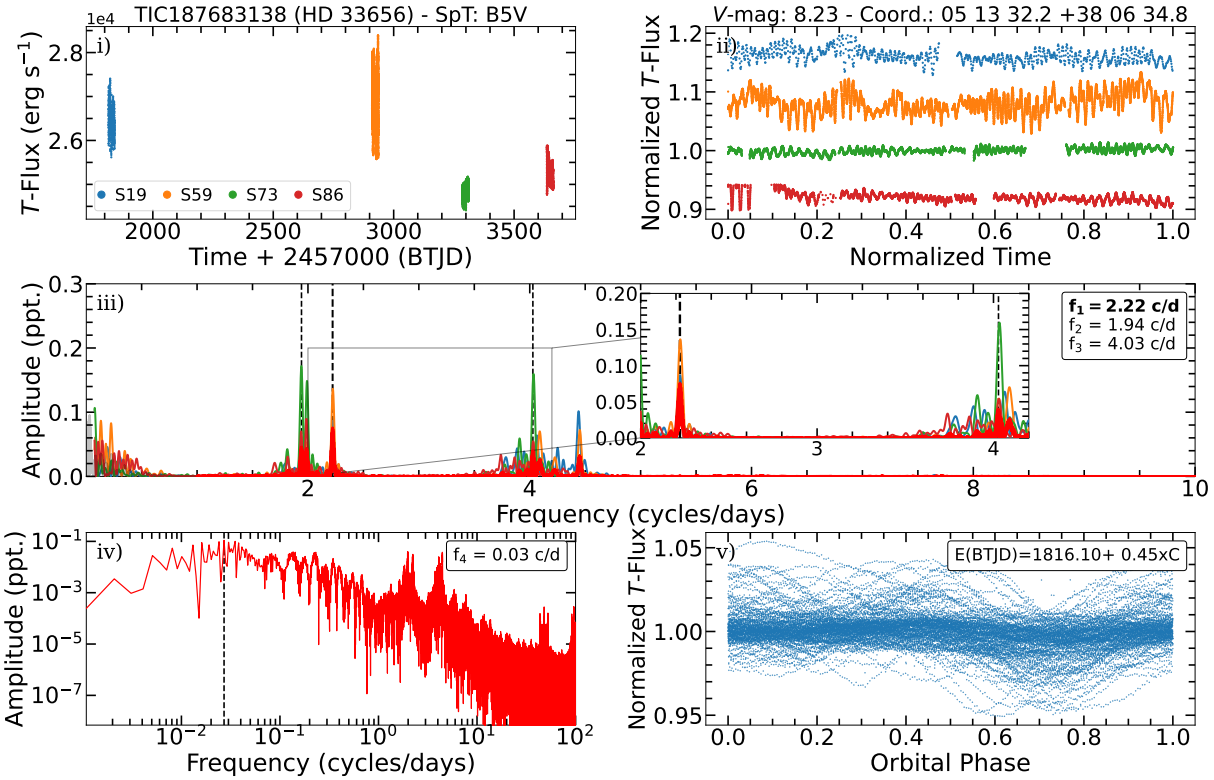

Figure C.40: Panels summarizing the photometric and frequency-domain analyses for the target TIC 187683138. (i) Raw T-Flux light curves from different sectors; (ii) normalized T-Flux light curves folded normalized time for each sector; (iii) Lomb-Scargle periodogram highlighting the three main frequencies f_1, f_2, and f_3, with a zoom-in inset; (iv) extended periodogram revealing a low-frequency component f_4; (v) orbital phase-folded light curve.

C.41. TIC 19704573

ζ Tau is a classical Be star with a circumstellar disk that presents a cyclic variation of the V/R ratio with a period of 1430 days (Štefl et al., 2009). Its star is part of a binary system with an orbital period of ~133 days and a mass ratio equal to 0.121 (Carciofi et al., 2009).

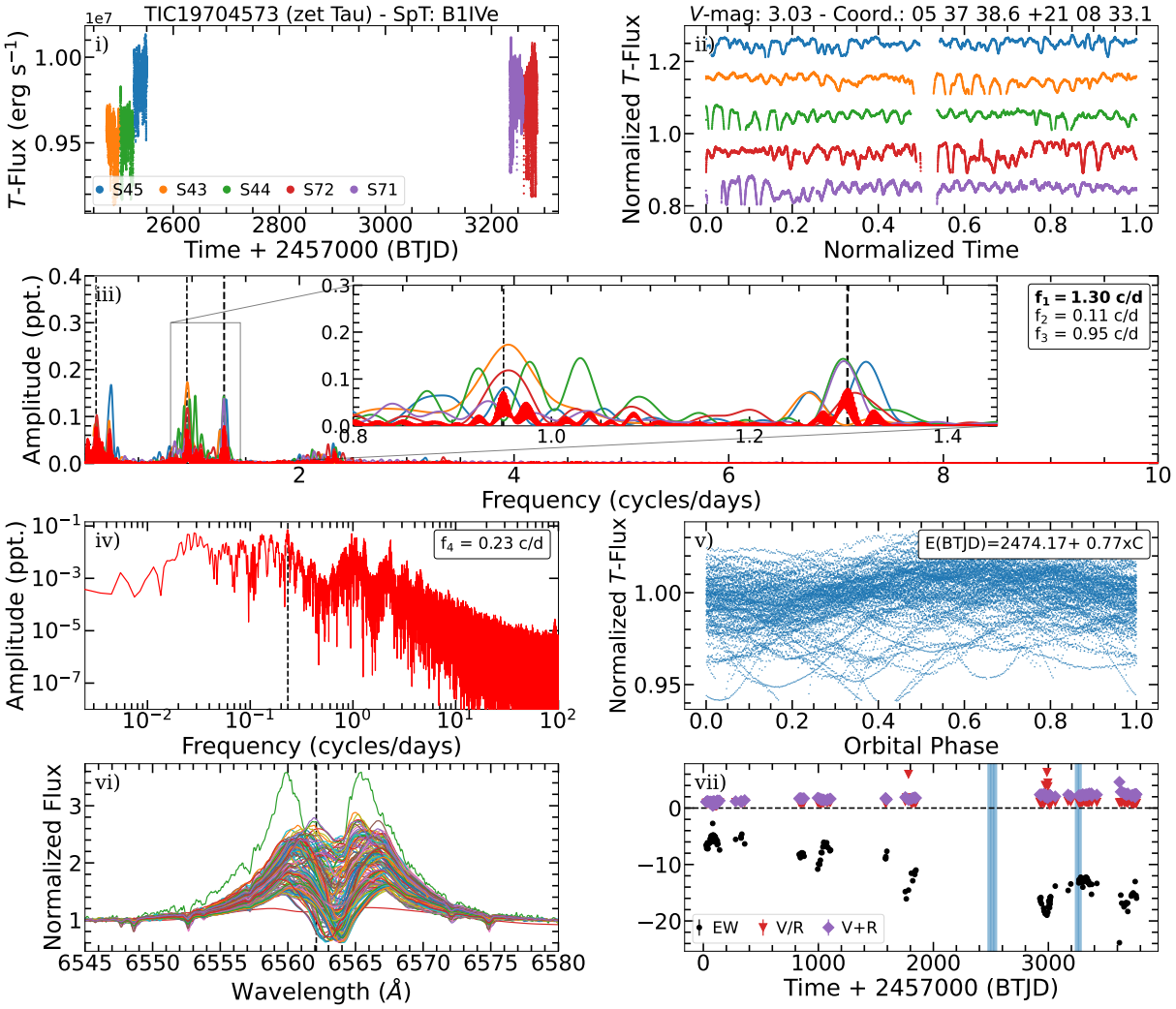

Figure C.41: Panels summarizing the photometric, spectroscopic, and frequency-domain analyses for the target TIC 19704573. (i) Raw T-Flux light curves from different sectors; (ii) normalized T-Flux light curves folded normalized time for each sector; (iii) Lomb-Scargle periodogram highlighting the three main frequencies f_1, f_2, and f_3, with a zoom-in inset; (iv) extended periodogram revealing a low-frequency component f_4; (v) orbital phase-folded light curve; (vi) optical spectrum centered on the Hα line (λ = 6562.8 Å); and (vii) temporal evolution of the equivalent width of the Hα line across available observations. Shaded regions in panel (vii) correspond to observation windows of sectors shown in panel (i).

C.42. TIC 200410503

HD 159845 is classified with the spectral type of B3III (Bailer-Jones et al., 2018) and was studied by Kervella et al. (2019) who characterized the physical presence of stellar and substellar companions through astrometry. No spectrum was found in the BESS catalog.

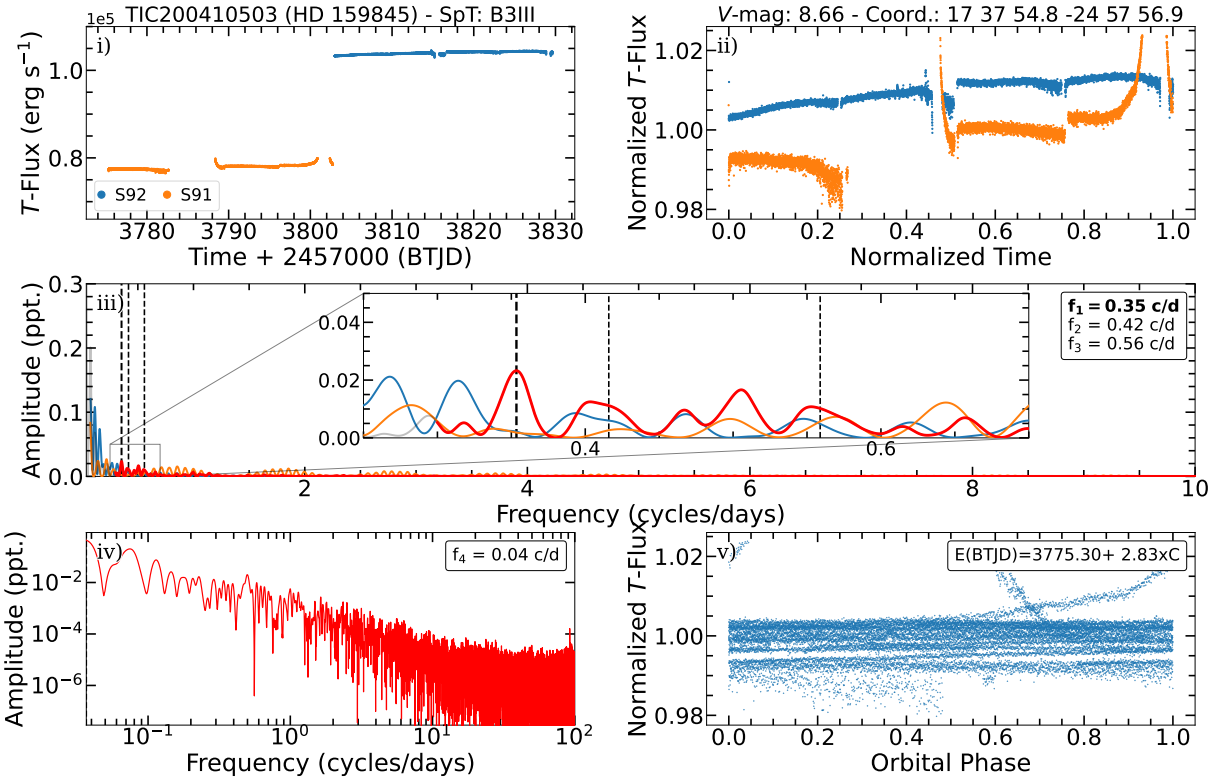

Figure C.42: Panels summarizing the photometric and frequency-domain analyses for the target TIC 200410503. (i) Raw T-Flux light curves from different sectors; (ii) normalized T-Flux light curves folded normalized time for each sector; (iii) Lomb-Scargle periodogram highlighting the three main frequencies f_1, f_2, and f_3, with a zoom-in inset; (iv) extended periodogram revealing a low-frequency component f_4; (v) orbital phase-folded light curve.

C.43. TIC 201373582

HD 42054 (HR 2170) is a Be star of type B5Ve (Oudmaijer and Parr, 2010) and was studied by Kervella et al. (2019) who characterized the physical presence of stellar and substellar companions through astrometry.

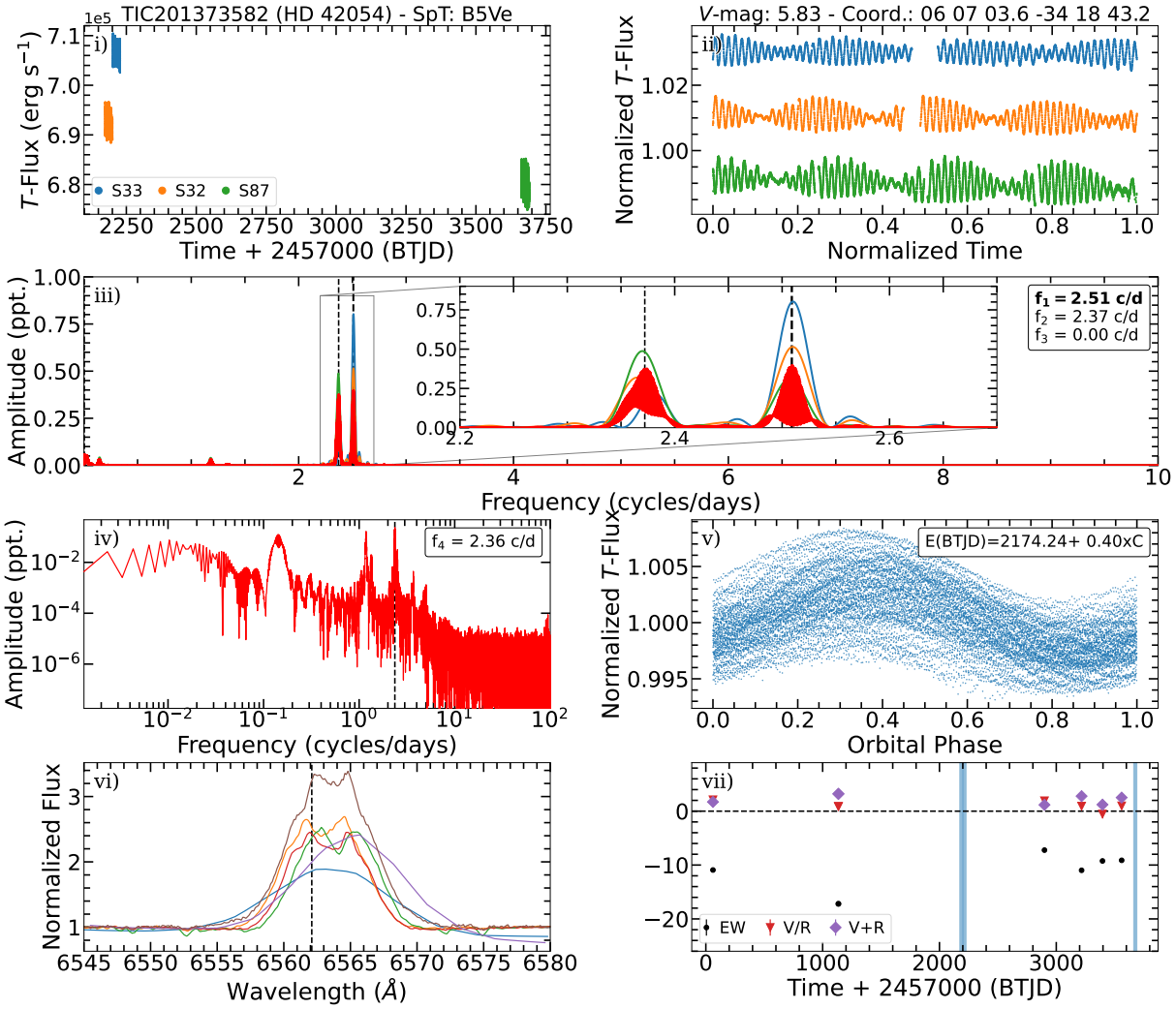

Figure C.43: Panels summarizing the photometric, spectroscopic, and frequency-domain analyses for the target TIC 201373582. (i) Raw T-Flux light curves from different sectors; (ii) normalized T-Flux light curves folded normalized time for each sector; (iii) Lomb-Scargle periodogram highlighting the three main frequencies f_1, f_2, and f_3, with a zoom-in inset; (iv) extended periodogram revealing a low-frequency component f_4; (v) orbital phase-folded light curve; (vi) optical spectrum centered on the Hα line (λ = 6562.8 Å); and (vii) temporal evolution of the equivalent width of the Hα line across available observations. Shaded regions in panel (vii) correspond to observation windows of sectors shown in panel (i).

C.44. TIC 202788979

HD 232214 is a Be star of type B8 (Chojnowski et al., 2014) and was studied by Kervella et al. (2019) who characterized the physical presence of stellar and substellar companions through astrometry. No spectrum was found in the BESS catalog.

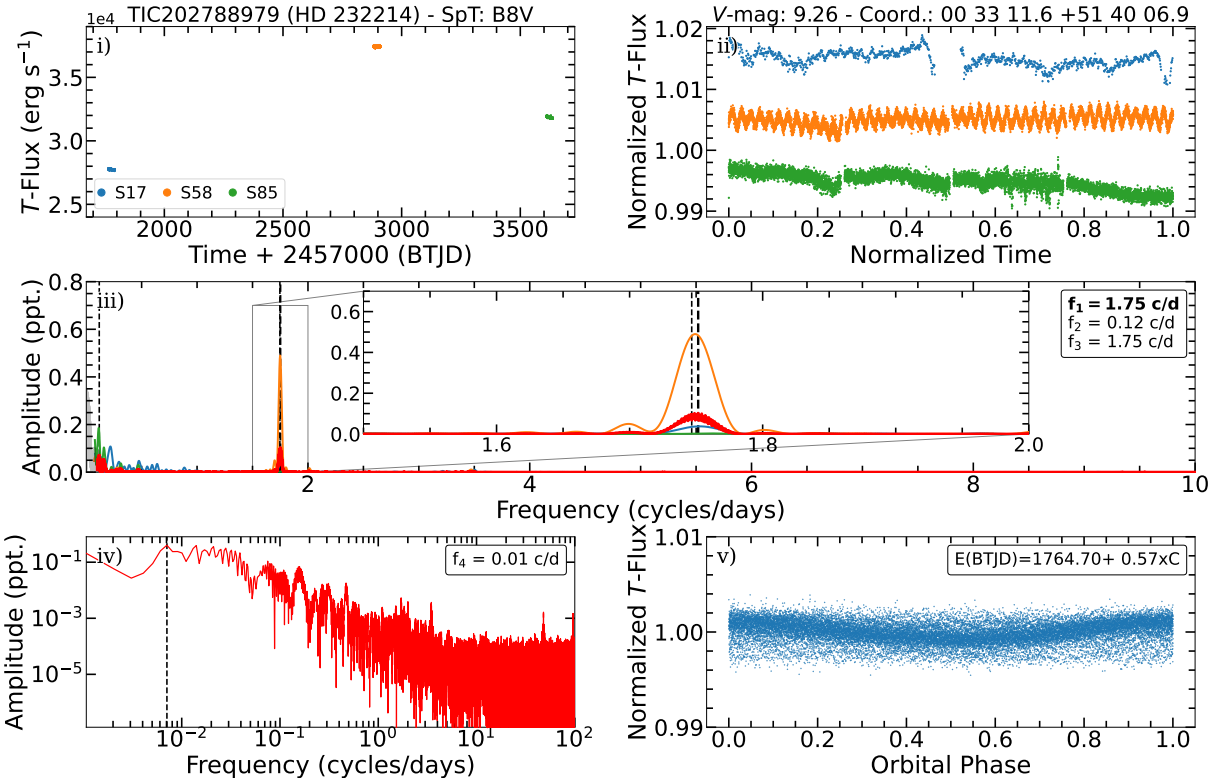

Figure C.44: Panels summarizing the photometric and frequency-domain analyses for the target TIC 202788979. (i) Raw T-Flux light curves from different sectors; (ii) normalized T-Flux light curves folded normalized time for each sector; (iii) Lomb-Scargle periodogram highlighting the three main frequencies f_1, f_2, and f_3, with a zoom-in inset; (iv) extended periodogram revealing a low-frequency component f_4; (v) orbital phase-folded light curve.

C.45. TIC 203468988

HD 161004 is a Be star of type B9IVe (Chojnowski et al., 2014) and was studied by Souza et al. (2020) who identified a possible triple system with Speckle interferometry. No spectrum was found in the BESS catalog.

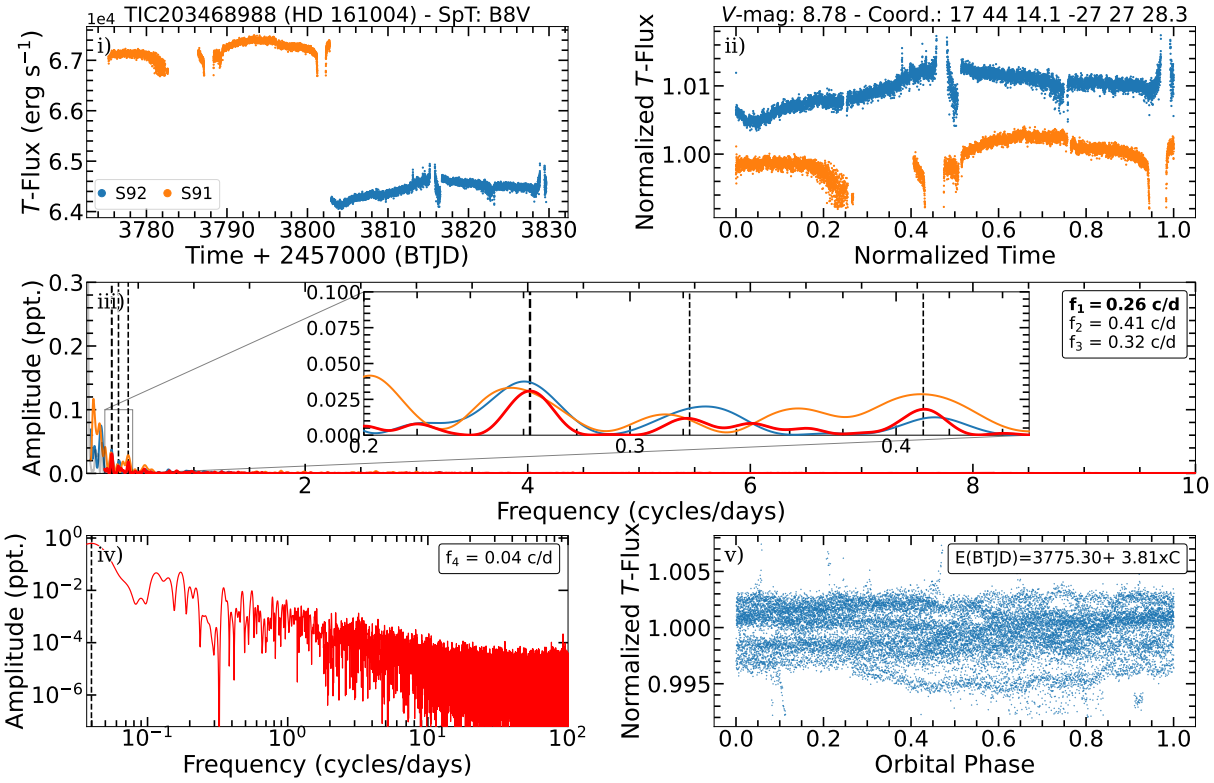

Figure C.45: Panels summarizing the photometric and frequency-domain analyses for the target TIC 203468988. (i) Raw T-Flux light curves from different sectors; (ii) normalized T-Flux light curves folded normalized time for each sector; (iii) Lomb-Scargle periodogram highlighting the three main frequencies f_1, f_2, and f_3, with a zoom-in inset; (iv) extended periodogram revealing a low-frequency component f_4; (v) orbital phase-folded light curve.

C.46. TIC 203500116

BD-08 4674 is classified with the spectral type of B8Ve (Chojnowski et al., 2014) and was studied by Kervella et al. (2019) who characterized the physical presence of stellar and substellar companions through astrometry. No spectrum was found in the BESS catalog.

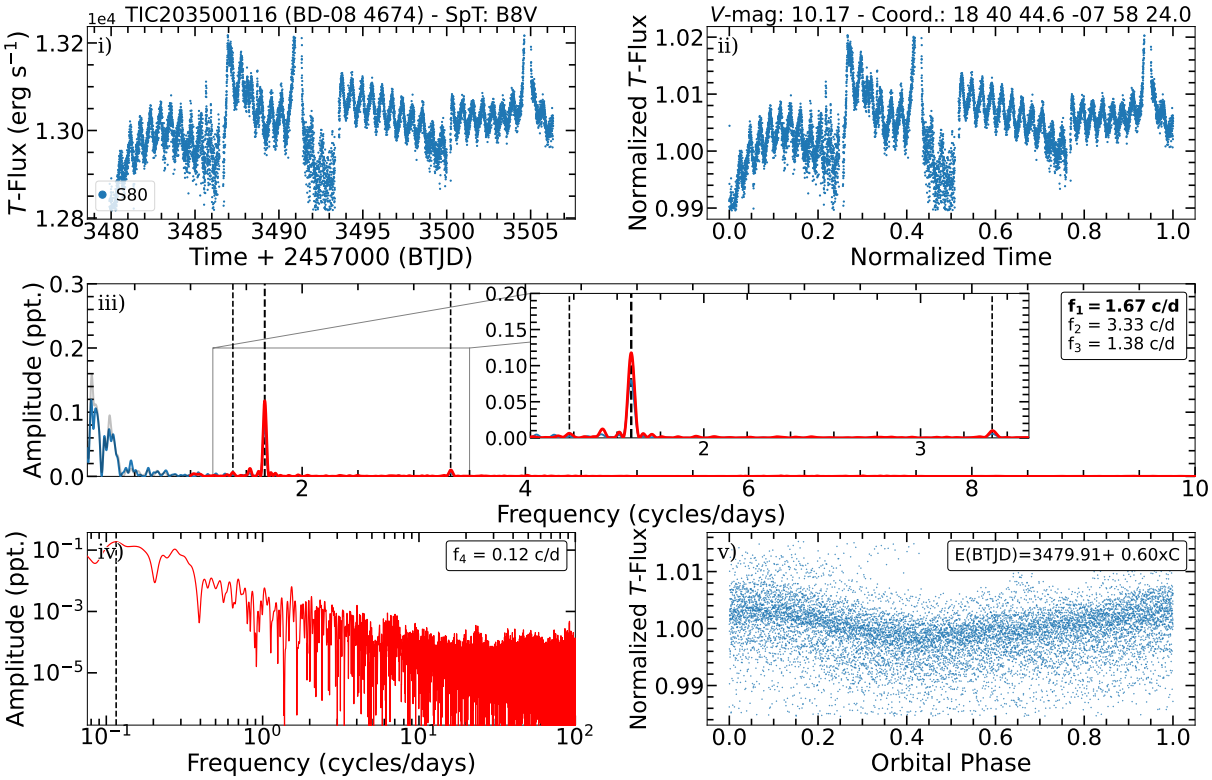

Figure C.46: Panels summarizing the photometric and frequency-domain analyses for the target TIC 203500116. (i) Raw T-Flux light curves from different sectors; (ii) normalized T-Flux light curves folded normalized time for each sector; (iii) Lomb-Scargle periodogram highlighting the three main frequencies f_1, f_2, and f_3, with a zoom-in inset; (iv) extended periodogram revealing a low-frequency component f_4; (v) orbital phase-folded light curve.

C.47. TIC 204191276

χ Oph (HIP 80569) is a binary system classified with spectral type B2V, mass of ~11 $M_\odot$, orbital period of ~139 days and $v \sin i$ of 149 km s^{-1} (Delorme et al., 2024; Wang et al., 2023b; Sigut and Ghafourian, 2023a).

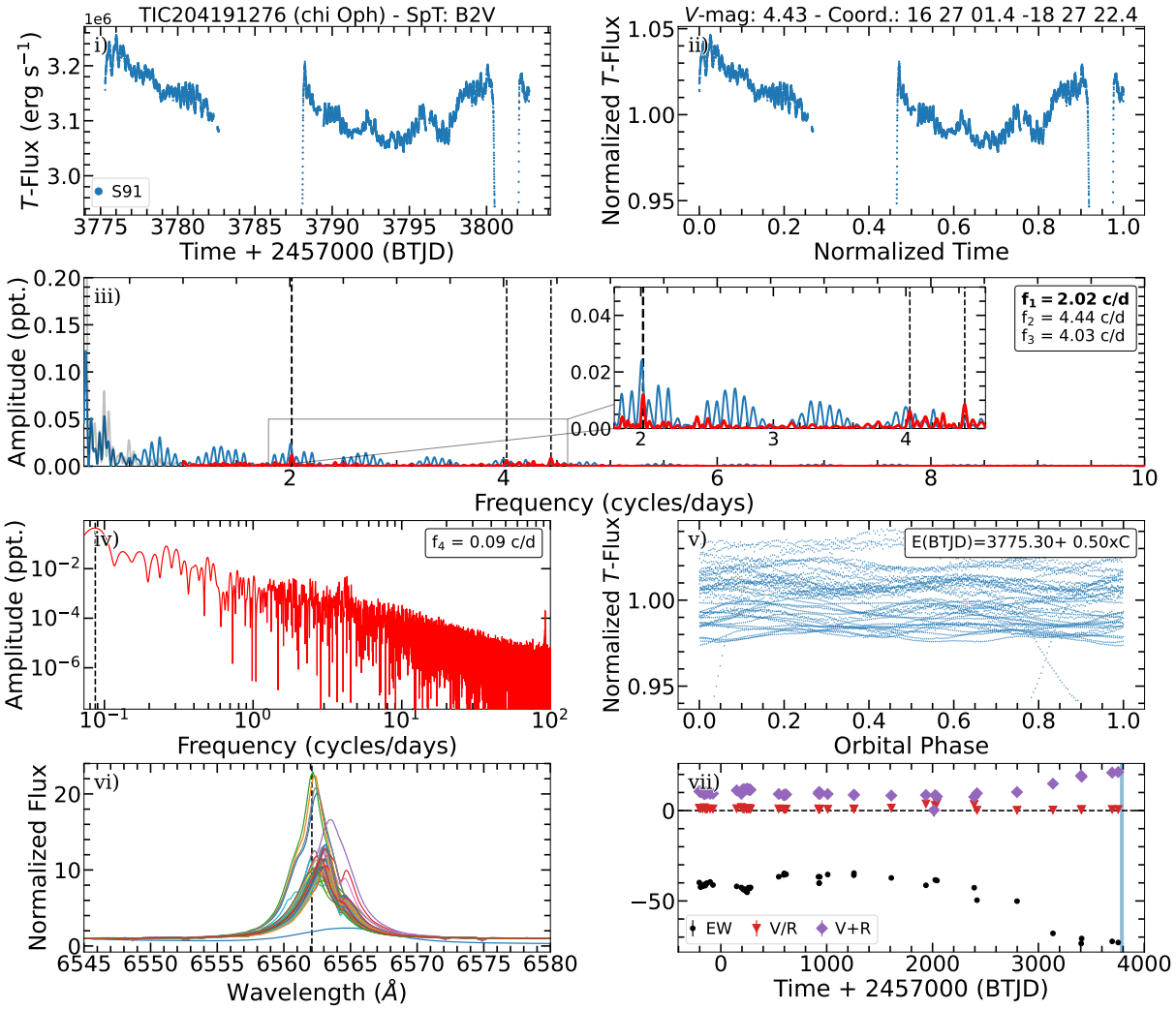

Figure C.47: Panels summarizing the photometric, spectroscopic, and frequency-domain analyses for the target TIC 204191276. (i) Raw T-Flux light curves from different sectors; (ii) normalized T-Flux light curves folded normalized time for each sector; (iii) Lomb-Scargle periodogram highlighting the three main frequencies f_1, f_2, and f_3, with a zoom-in inset; (iv) extended periodogram revealing a low-frequency component f_4; (v) orbital phase-folded light curve; (vi) optical spectrum centered on the Hα line (λ = 6562.8 Å); and (vii) temporal evolution of the equivalent width of the Hα line across available observations. Shaded regions in panel (vii) correspond to observation windows of sectors shown in panel (i).

C.48. TIC 209330890

HD 180126 is a binary system classified with spectral type B2IV, log g equal to 3.80 cgs, 1,500 K and $v \sin i$ of 243 km s^{-1} (Labadie-Bartz et al., 2018).

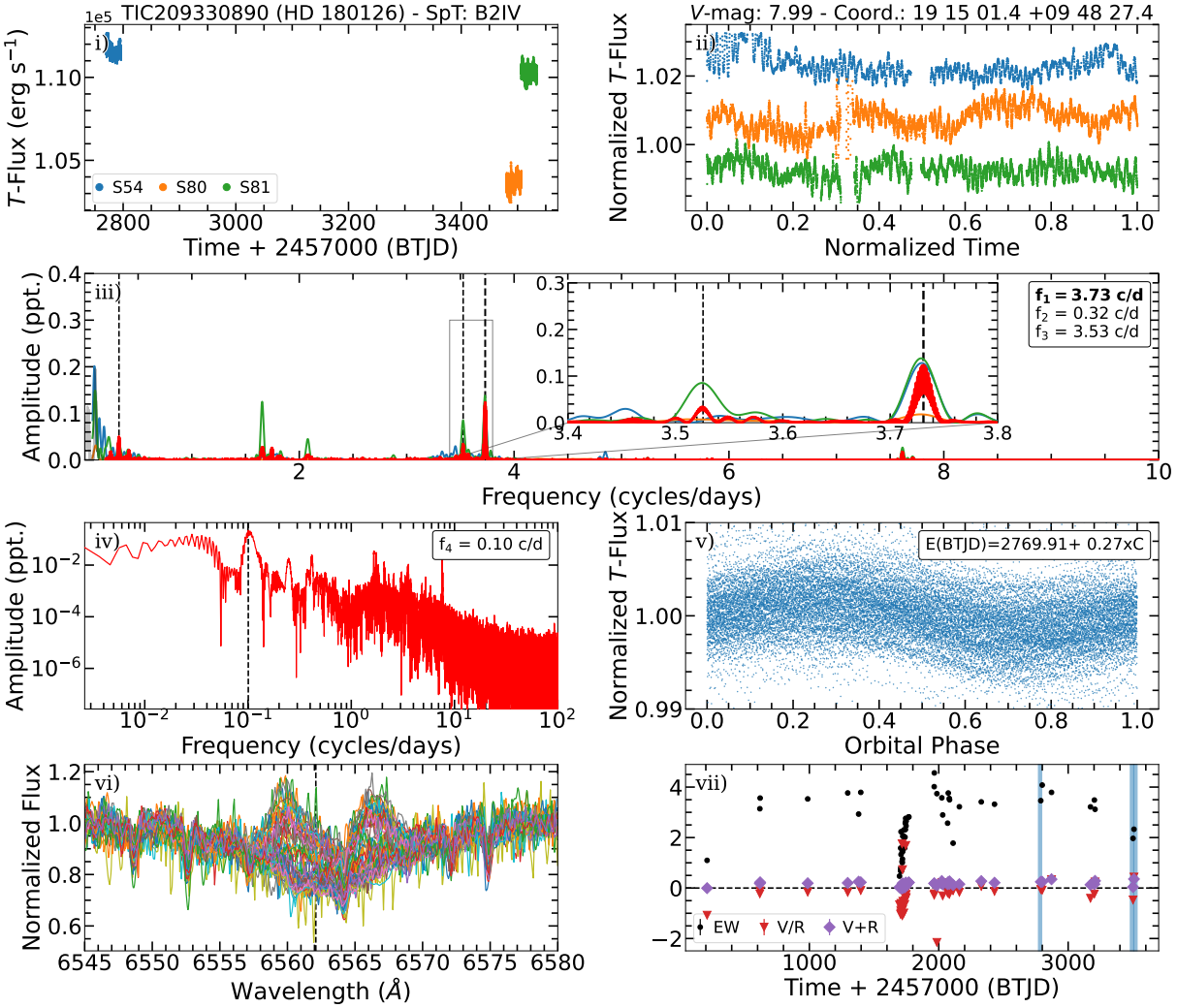

Figure C.48: Panels summarizing the photometric, spectroscopic, and frequency-domain analyses for the target TIC 209330890. (i) Raw T-Flux light curves from different sectors; (ii) normalized T-Flux light curves folded normalized time for each sector; (iii) Lomb-Scargle periodogram highlighting the three main frequencies f_1, f_2, and f_3, with a zoom-in inset; (iv) extended periodogram revealing a low-frequency component f_4; (v) orbital phase-folded light curve; (vi) optical spectrum centered on the Hα line (λ = 6562.8 Å); and (vii) temporal evolution of the equivalent width of the Hα line across available observations. Shaded regions in panel (vii) correspond to observation windows of sectors shown in panel (i).

C.49. TIC 213153401

HD 154538 is a binary system classified by Nazé and Robrade (2023) with spectral type B3V and luminosity 3.051 $L/L_{\odot}$.

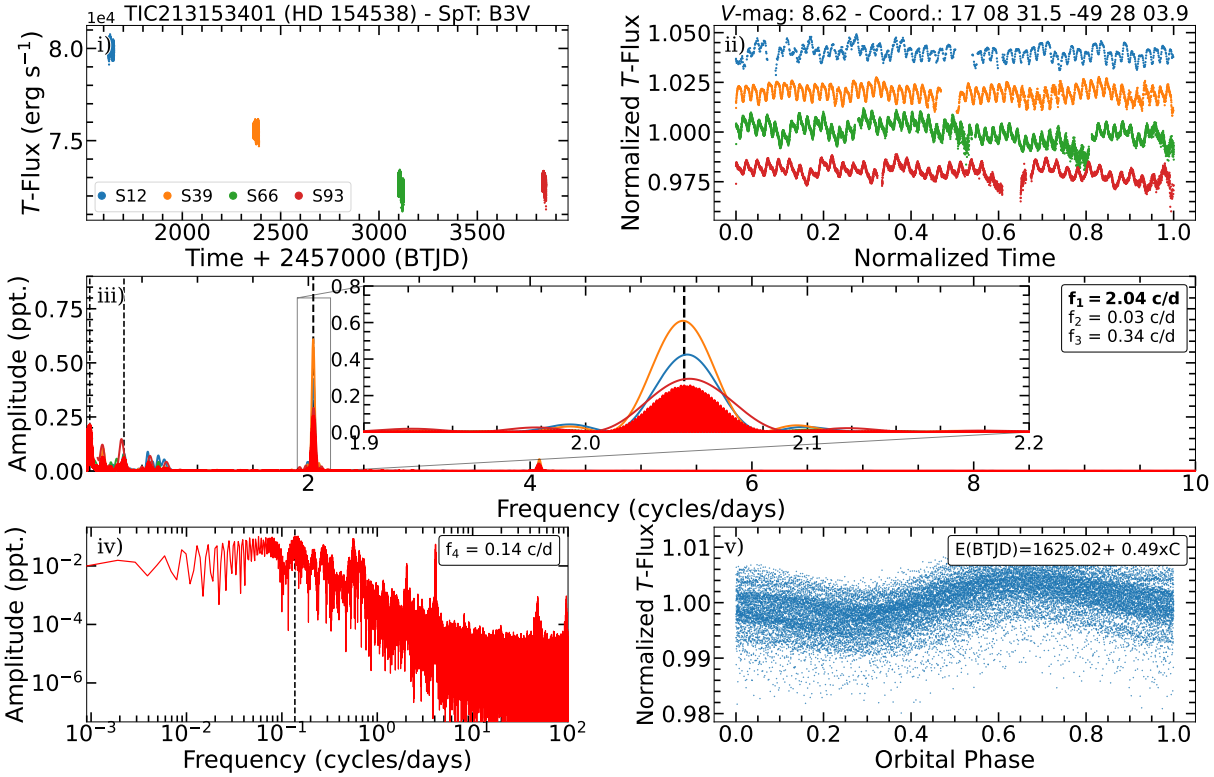

Figure C.49: Panels summarizing the photometric and frequency-domain analyses for the target TIC 213153401. (i) Raw T-Flux light curves from different sectors; (ii) normalized T-Flux light curves folded normalized time for each sector; (iii) Lomb-Scargle periodogram highlighting the three main frequencies f_1, f_2, and f_3, with a zoom-in inset; (iv) extended periodogram revealing a low-frequency component f_4; (v) orbital phase-folded light curve.

C.50. TIC 217667184

ι Ara (HD 157042) is a Be star with a temperature of 29,010 K, $v \sin i$ of 355 km s^{-1} and a mass of 12.7 $M_\odot$ (Zorec et al., 2016). It was identified as a binary system composed of Be+sdO by Wang et al. (2021) with an orbital period of ~176 days and a mass ratio of ~0.1 (Wang et al., 2023b).

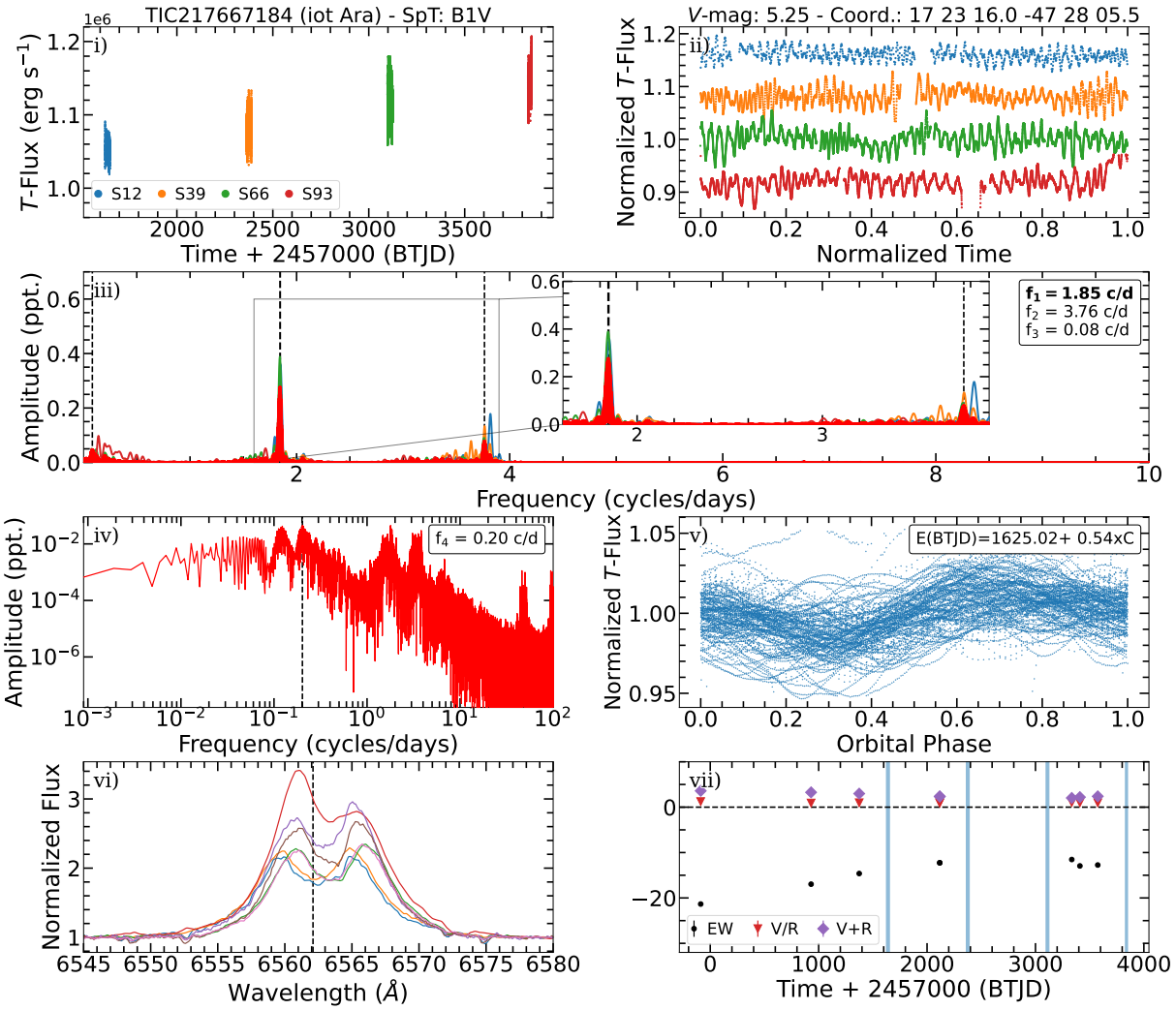

Figure C.50: Panels summarizing the photometric, spectroscopic, and frequency-domain analyses for the target TIC 217667184. (i) Raw T-Flux light curves from different sectors; (ii) normalized T-Flux light curves folded normalized time for each sector; (iii) Lomb-Scargle periodogram highlighting the three main frequencies f_1, f_2, and f_3, with a zoom-in inset; (iv) extended periodogram revealing a low-frequency component f_4; (v) orbital phase-folded light curve; (vi) optical spectrum centered on the Hα line (λ = 6562.8 Å); and (vii) temporal evolution of the equivalent width of the Hα line across available observations. Shaded regions in panel (vii) correspond to observation windows of sectors shown in panel (i).

C.51. TIC 228199255

Labadie-Bartz et al. (2018) presents this object as a Be star of type B8 and was studied by Kervella et al. (2019) who characterized the physical presence of stellar and substellar companions through astrometry. No spectrum was found in the BESS catalog.

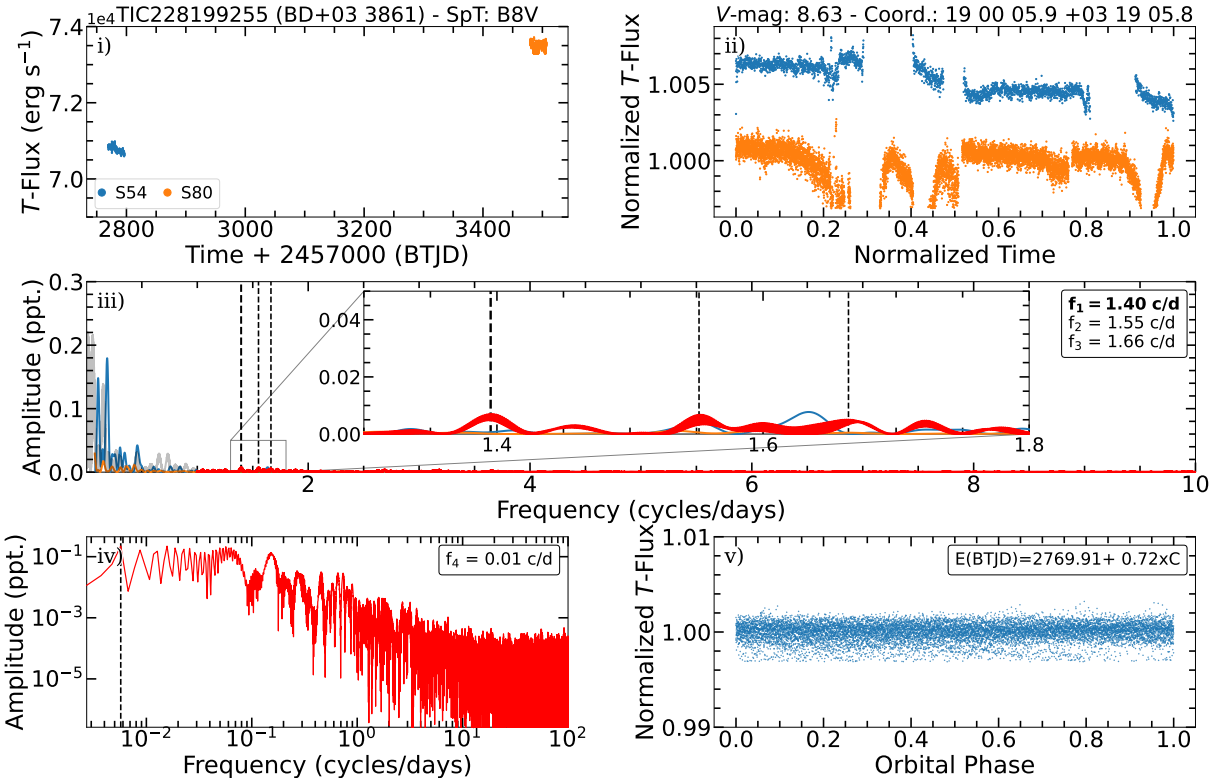

Figure C.51: Panels summarizing the photometric and frequency-domain analyses for the target TIC 228199255. (i) Raw *T*-Flux light curves from different sectors; (ii) normalized *T*-Flux light curves folded normalized time for each sector; (iii) Lomb-Scargle periodogram highlighting the three main frequencies f_1, f_2, and f_3, with a zoom-in inset; (iv) extended periodogram revealing a low-frequency component f_4; (v) orbital phase-folded light curve.

C.52. TIC 230981971

Achernar (α Eridani, HD 10144) has spectral type B3Vpe and is the brightest Be star in the sky (Jaschek et al., 1981; de Souza et al., 2003). The Be nature of Achernar was detected through hydrogen lines in the emission observed by Andrews and Breger (1966). Achernar is a binary system, and the companion of the Be star is an early A-type main-sequence star with an orbital period of ~7 years (Kervella and de Souza, 2007; Kervella et al., 2008, 2022).

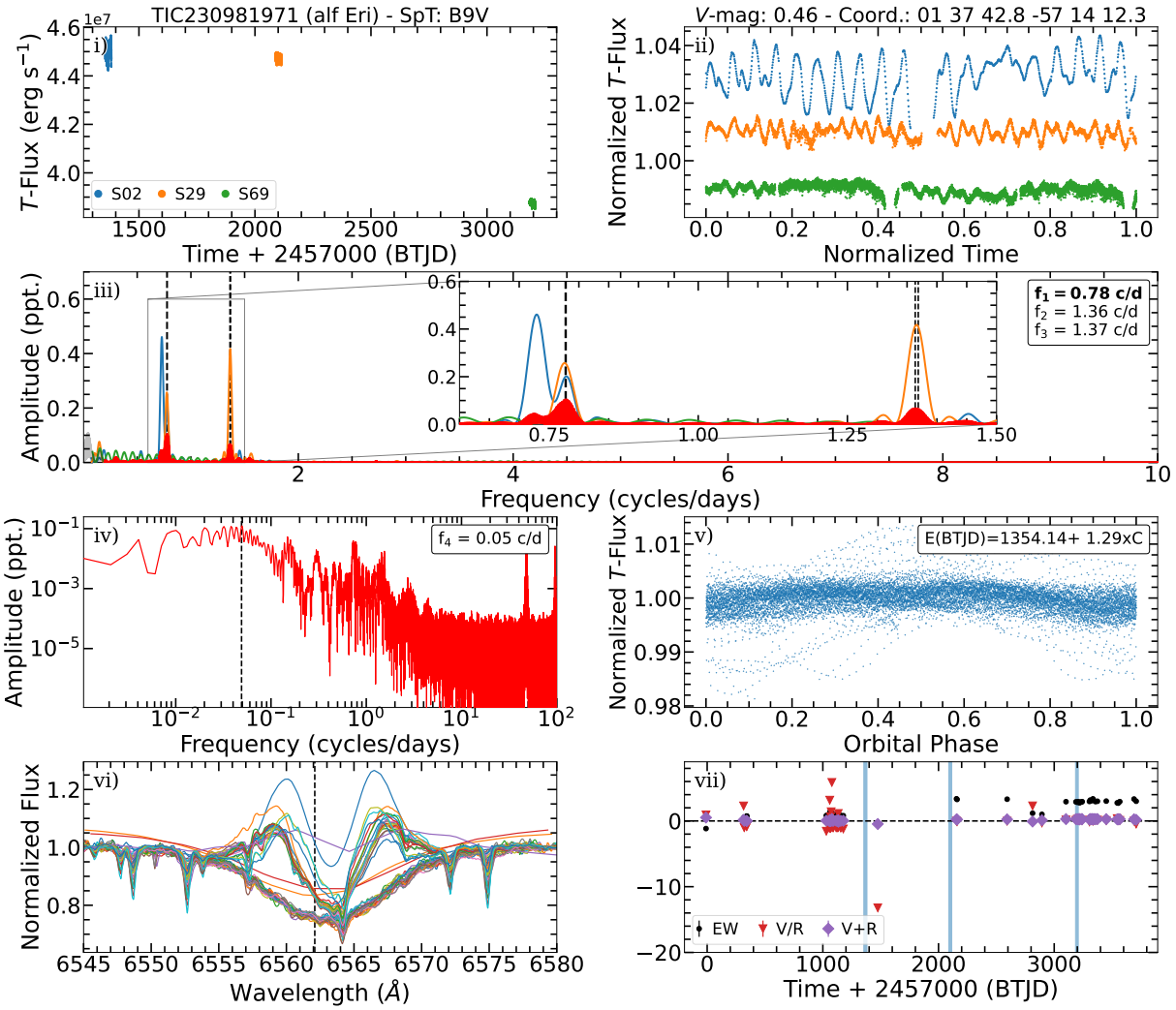

Figure C.52: Panels summarizing the photometric, spectroscopic, and frequency-domain analyses for the target TIC 230981971. (i) Raw T-Flux light curves from different sectors; (ii) normalized T-Flux light curves folded normalized time for each sector; (iii) Lomb-Scargle periodogram highlighting the three main frequencies f_1, f_2, and f_3, with a zoom-in inset; (iv) extended periodogram revealing a low-frequency component f_4; (v) orbital phase-folded light curve; (vi) optical spectrum centered on the Hα line (λ = 6562.8 Å); and (vii) temporal evolution of the equivalent width of the Hα line across available observations. Shaded regions in panel (vii) correspond to observation windows of sectors shown in panel (i).

C.53. TIC 231430254

HD 159032 is a binary system of spectral type B9IV Chojnowski et al. (2014). No spectrum was found in the BESS catalog.

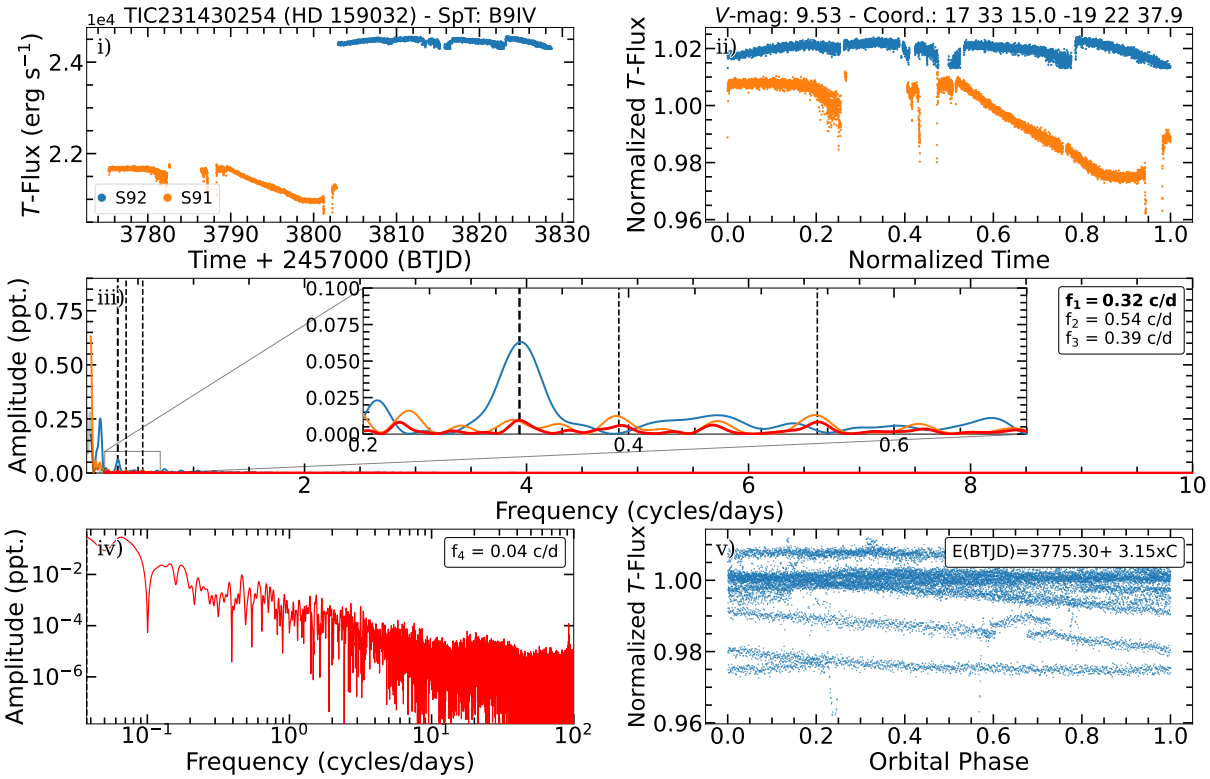

Figure C.53: Panels summarizing the photometric and frequency-domain analyses for the target TIC 231430254. (i) Raw T-Flux light curves from different sectors; (ii) normalized T-Flux light curves folded normalized time for each sector; (iii) Lomb-Scargle periodogram highlighting the three main frequencies f_1, f_2, and f_3, with a zoom-in inset; (iv) extended periodogram revealing a low-frequency component f_4; (v) orbital phase-folded light curve.

C.54. TIC 232166879

Schoettler et al. (2020) classifies the HD 41288 as a binary system with spectral type B5. No spectrum was found in the BESS catalog.

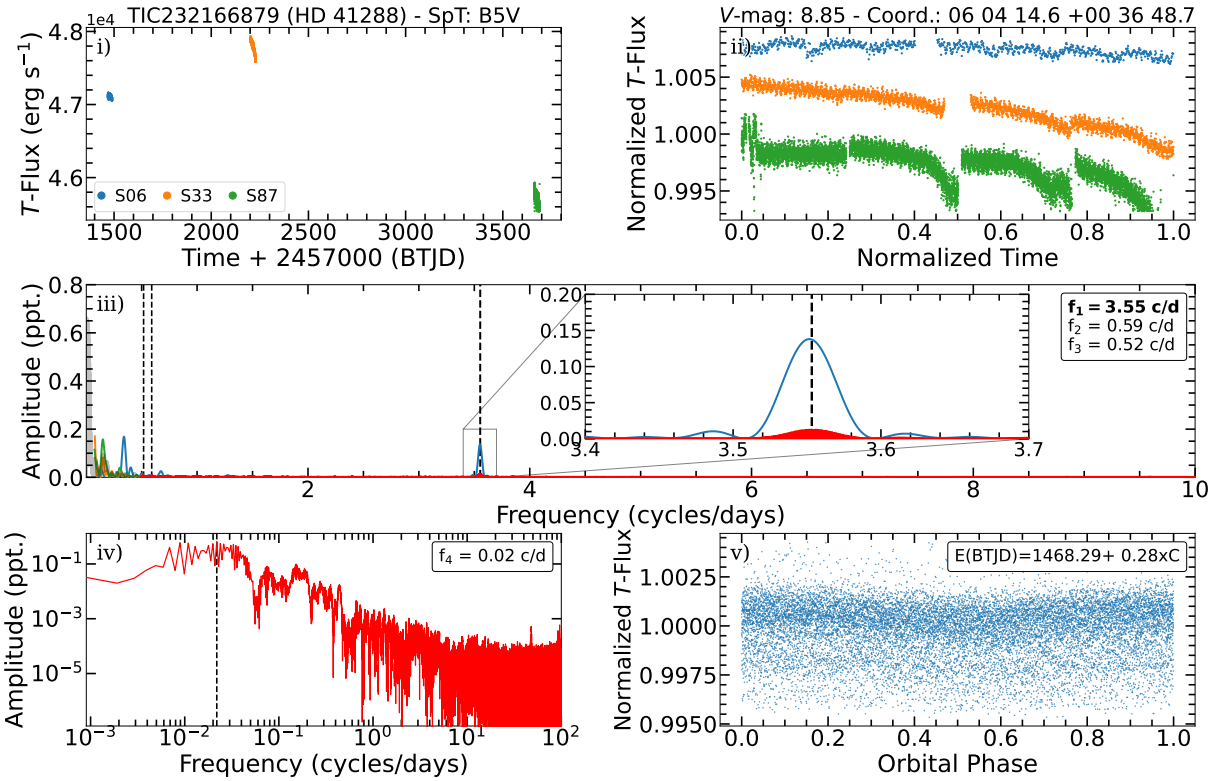

Figure C.54: Panels summarizing the photometric and frequency-domain analyses for the target TIC 232166879. (i) Raw T-Flux light curves from different sectors; (ii) normalized T-Flux light curves folded normalized time for each sector; (iii) Lomb-Scargle periodogram highlighting the three main frequencies f_1, f_2, and f_3, with a zoom-in inset; (iv) extended periodogram revealing a low-frequency component f_4; (v) orbital phase-folded light curve.

C.55. TIC 23459321

HD 55606 is a Be star with a temperature of 33,020 K, $v \sin i$ of 355 km s^{-1} and a mass of 29.4 $M_\odot$ (Zorec et al., 2016). It is a binary system composed of a Be + sdO star with an orbital period of ~94 days (Chojnowski et al., 2018).

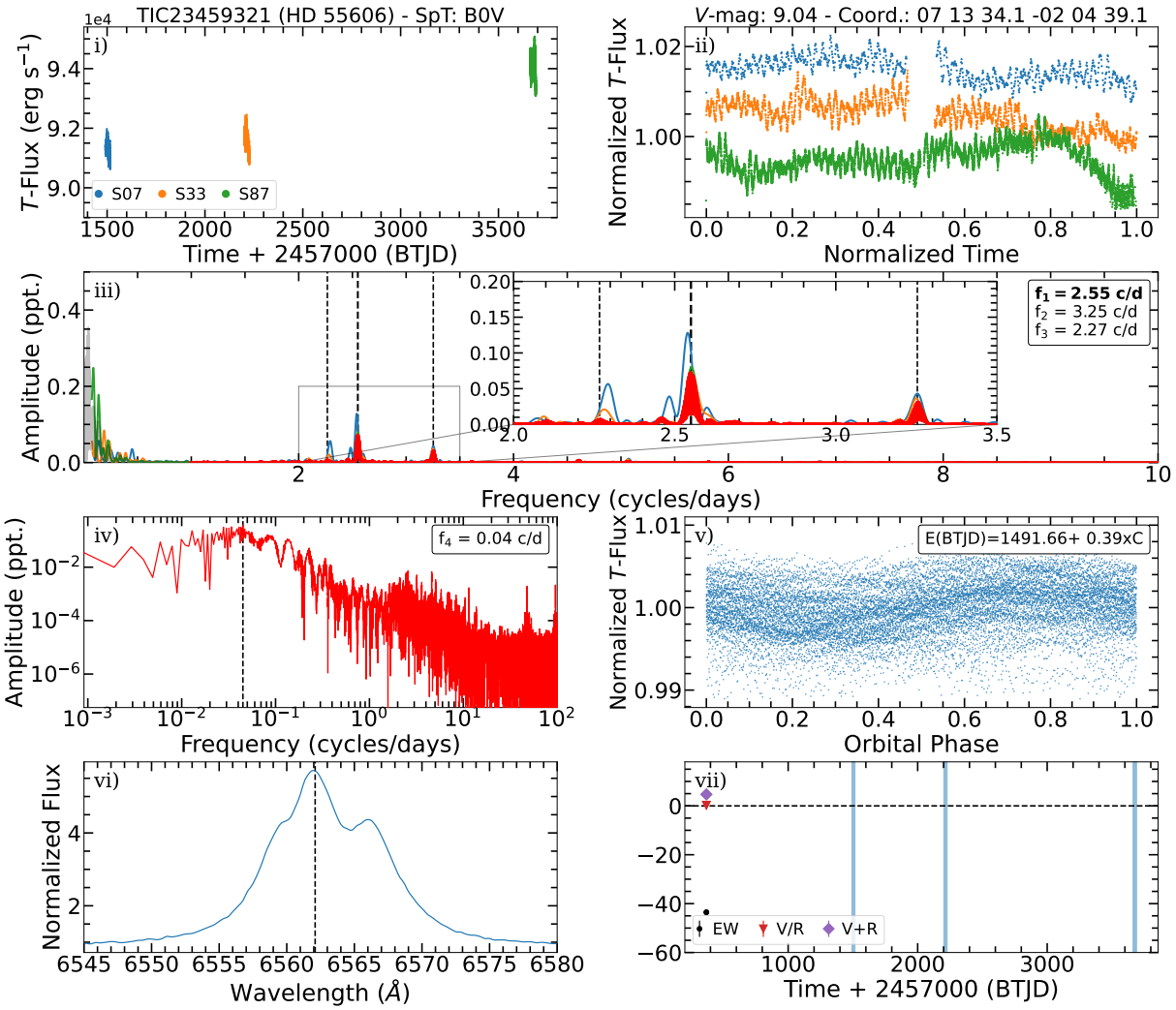

Figure C.55: Panels summarizing the photometric, spectroscopic, and frequency-domain analyses for the target TIC 23459321. (i) Raw T-Flux light curves from different sectors; (ii) normalized T-Flux light curves folded normalized time for each sector; (iii) Lomb-Scargle periodogram highlighting the three main frequencies f_1, f_2, and f_3, with a zoom-in inset; (iv) extended periodogram revealing a low-frequency component f_4; (v) orbital phase-folded light curve; (vi) optical spectrum centered on the Hα line (λ = 6562.8 Å); and (vii) temporal evolution of the equivalent width of the Hα line across available observations. Shaded regions in panel (vii) correspond to observation windows of sectors shown in panel (i).

C.56. TIC 237532447

HD 50087 was studied by Gutiérrez-Soto et al. (2007a) as a Be star and did not identify photometric variability in COROT precursor data. Kervella et al. (2019) studied this object and characterized the physical presence of stellar and substellar companions through astrometry. No spectrum was found in the BESS catalog.

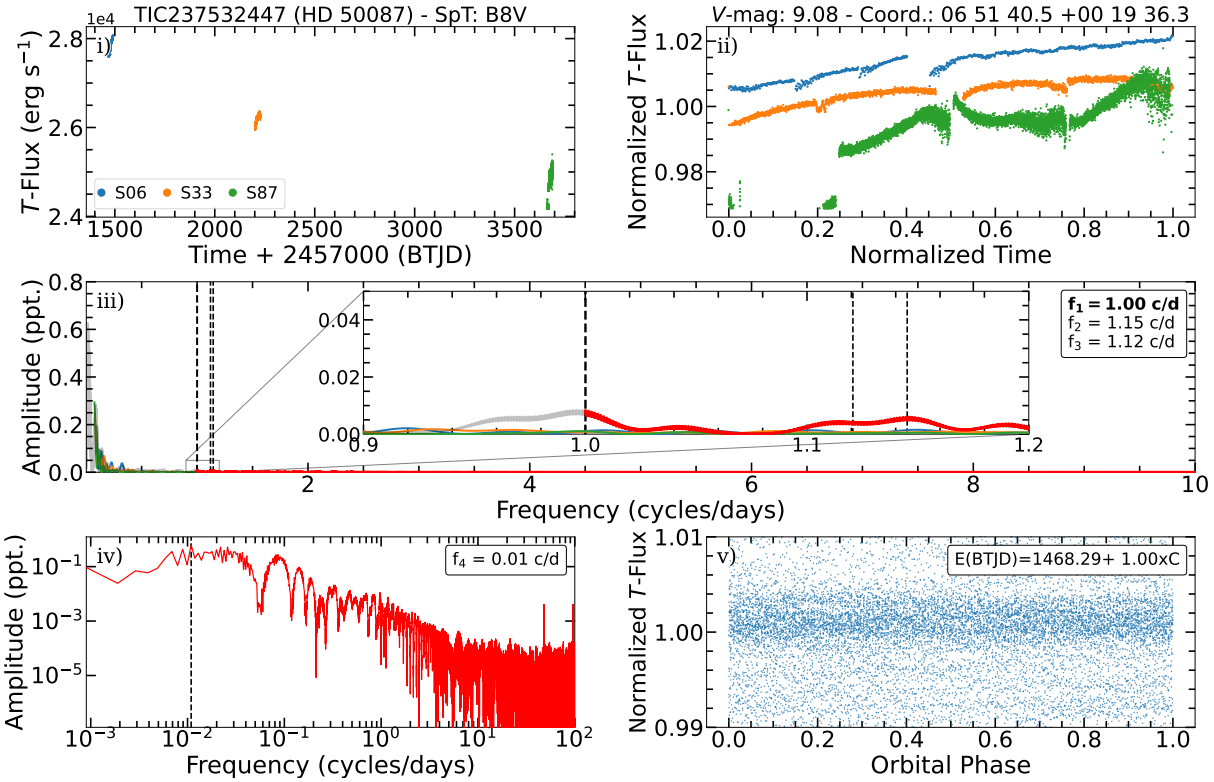

Figure C.56: Panels summarizing the photometric and frequency-domain analyses for the target TIC 237532447. (i) Raw T-Flux light curves from different sectors; (ii) normalized T-Flux light curves folded normalized time for each sector; (iii) Lomb-Scargle periodogram highlighting the three main frequencies f_1, f_2, and f_3, with a zoom-in inset; (iv) extended periodogram revealing a low-frequency component f_4; (v) orbital phase-folded light curve.

C.57. TIC 237840594

HD 51893 is classified as a Be star by (Chojnowski et al., 2015), and was identified as a double system more recently by Guerrero et al. (2025a). No spectrum was found in the BESS catalog.

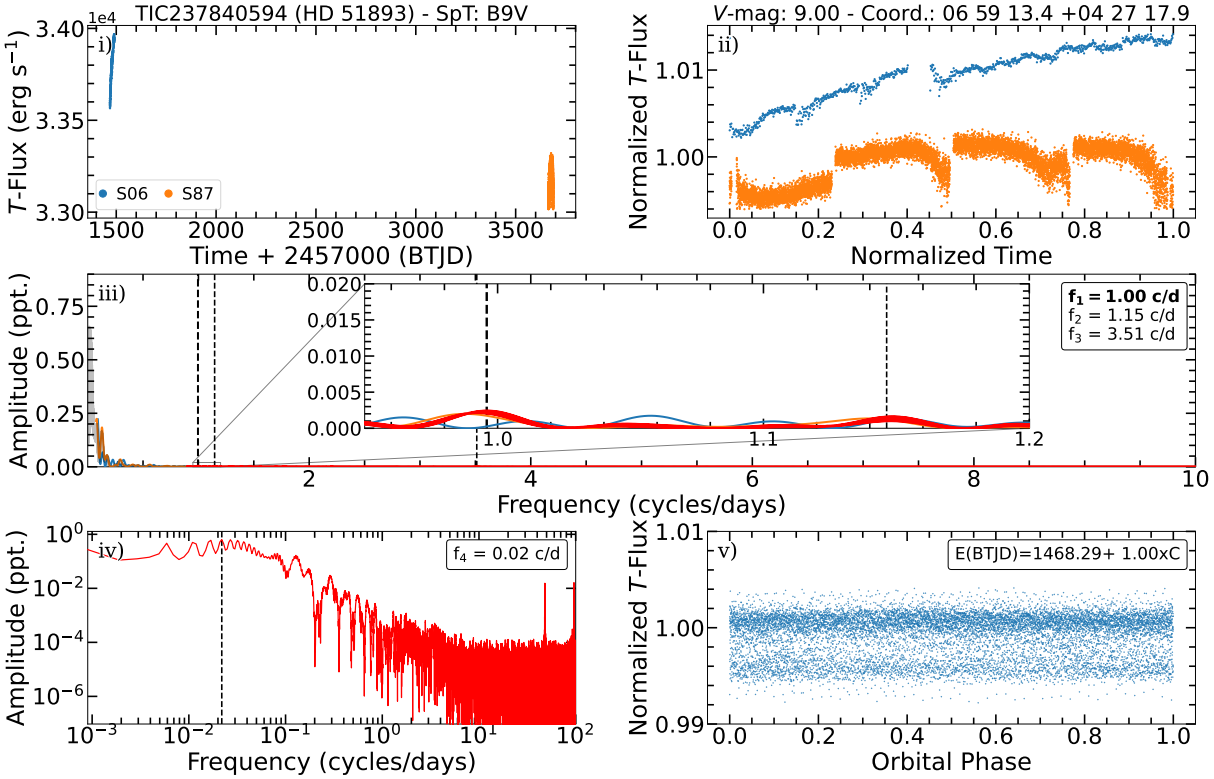

Figure C.57: Panels summarizing the photometric and frequency-domain analyses for the target TIC 237840594. (i) Raw T-Flux light curves from different sectors; (ii) normalized T-Flux light curves folded normalized time for each sector; (iii) Lomb-Scargle periodogram highlighting the three main frequencies f_1, f_2, and f_3, with a zoom-in inset; (iv) extended periodogram revealing a low-frequency component f_4; (v) orbital phase-folded light curve.

C.58. TIC 238771552

HD 18231 is spectroscopy binary classified as B8. No spectrum was found in the BESS catalog.

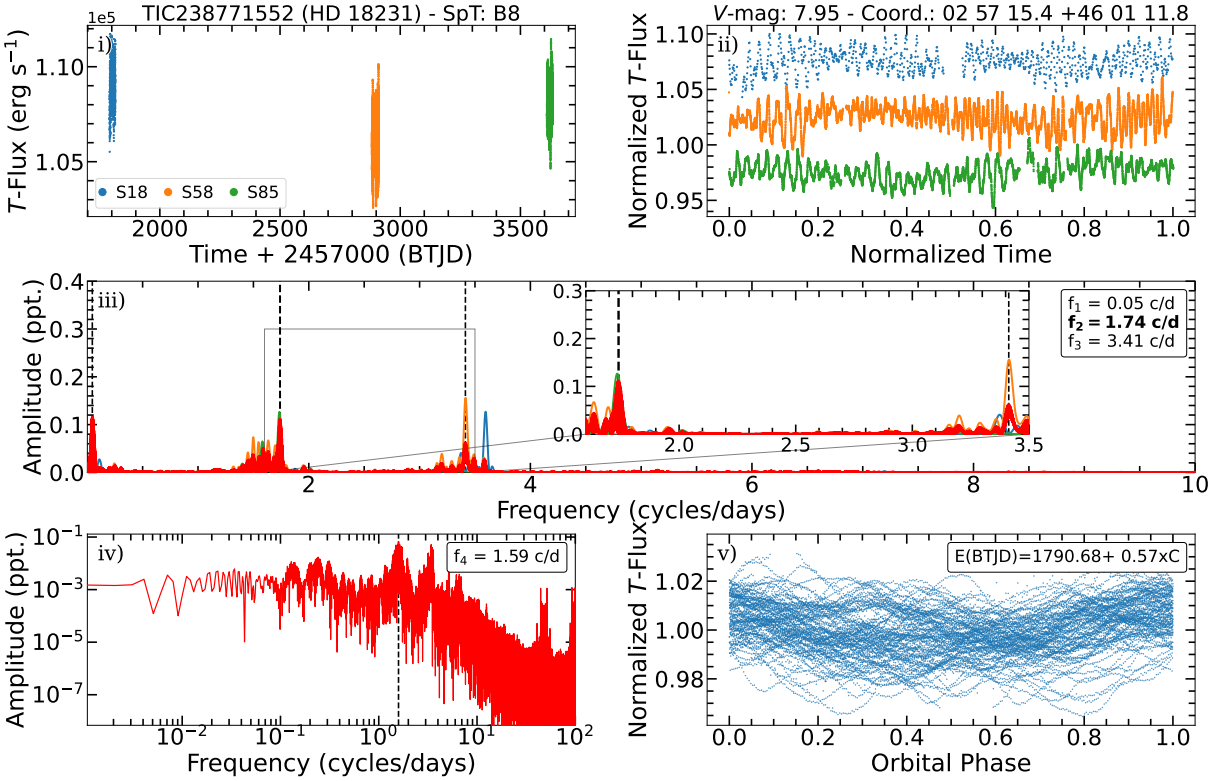

Figure C.58: Panels summarizing the photometric and frequency-domain analyses for the target TIC 238771552. (i) Raw T-Flux light curves from different sectors; (ii) normalized T-Flux light curves folded normalized time for each sector; (iii) Lomb-Scargle periodogram highlighting the three main frequencies f_1, f_2, and f_3, with a zoom-in inset; (iv) extended periodogram revealing a low-frequency component f_4; (v) orbital phase-folded light curve.

C.59. TIC 239103320

HD 37266 is a B8Ve type star (Chojnowski et al., 2014) and was studied by Kervella et al. (2019) who characterized the physical presence of stellar and substellar companions through astrometry. No spectrum was found in the BESS catalog.

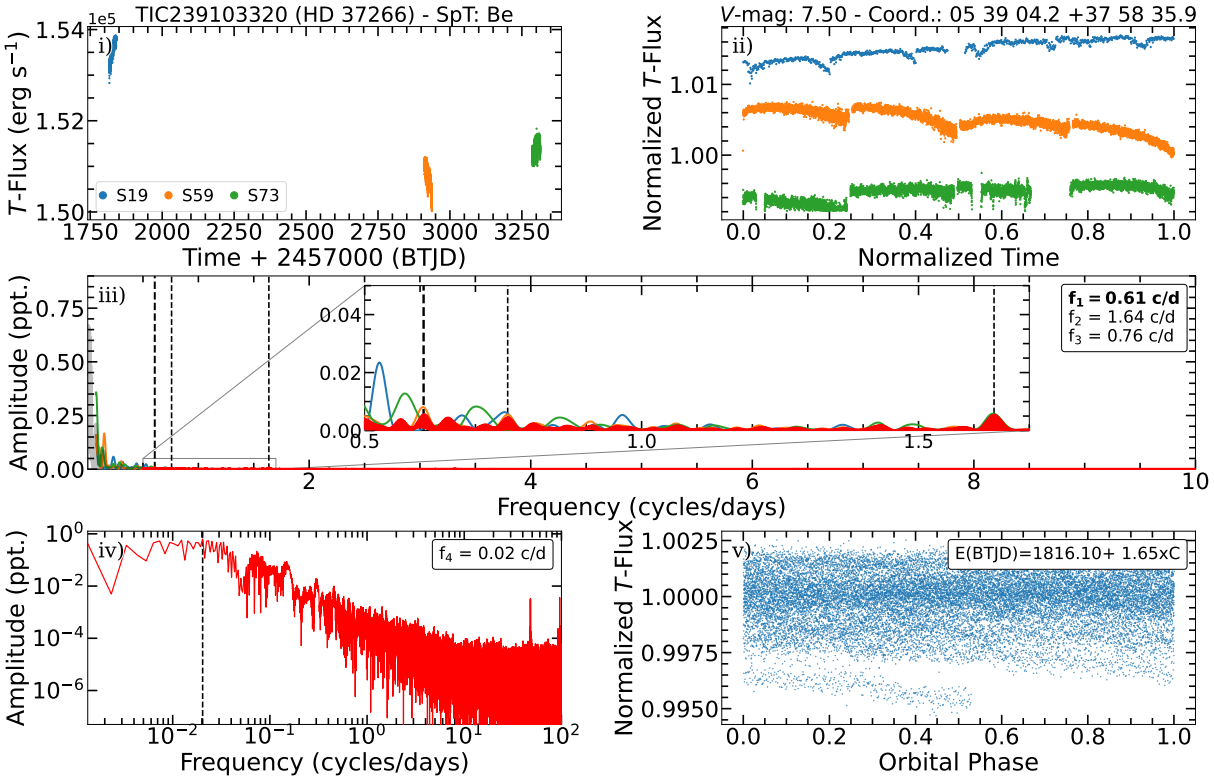

Figure C.59: Panels summarizing the photometric and frequency-domain analyses for the target TIC 239103320. (i) Raw T-Flux light curves from different sectors; (ii) normalized T-Flux light curves folded normalized time for each sector; (iii) Lomb-Scargle periodogram highlighting the three main frequencies f_1, f_2, and f_3, with a zoom-in inset; (iv) extended periodogram revealing a low-frequency component f_4; (v) orbital phase-folded light curve.

C.60. TIC 239408899

BD+43 3913 was reported as a Be star by Jaschek and Egret (1982). It has the spectral type of B1.5Vnnpe (Nazé et al., 2022) and is a binary pair (Wang et al., 2023b).

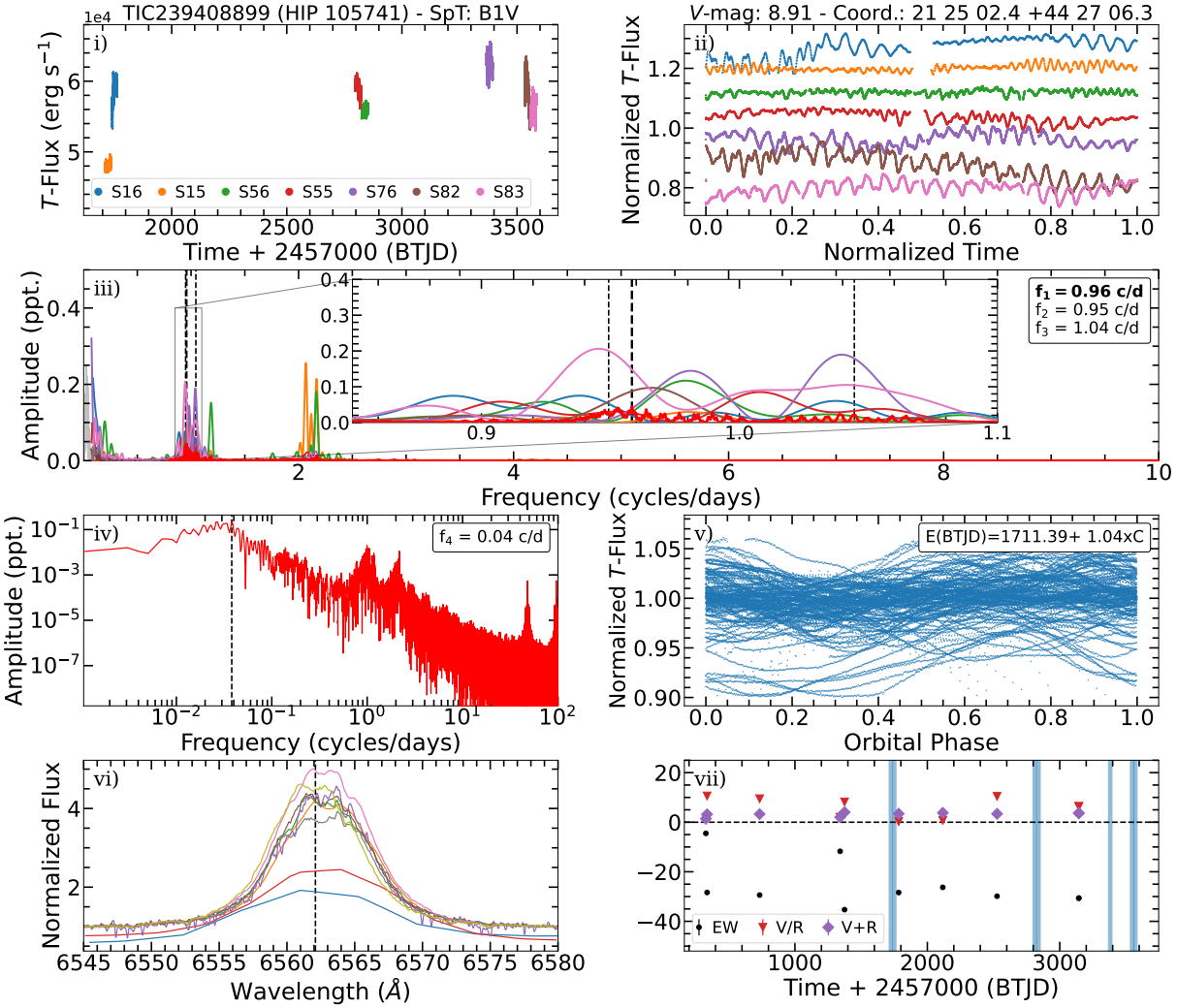

Figure C.60: Panels summarizing the photometric, spectroscopic, and frequency-domain analyses for the target TIC 239408899. (i) Raw T-Flux light curves from different sectors; (ii) normalized T-Flux light curves folded normalized time for each sector; (iii) Lomb-Scargle periodogram highlighting the three main frequencies f_1, f_2, and f_3, with a zoom-in inset; (iv) extended periodogram revealing a low-frequency component f_4; (v) orbital phase-folded light curve; (vi) optical spectrum centered on the Hα line (λ = 6562.8 Å); and (vii) temporal evolution of the equivalent width of the Hα line across available observations. Shaded regions in panel (vii) correspond to observation windows of sectors shown in panel (i).

C.61. TIC 239880242

HD 42529 is a star with spectral type B9Ve with a temperature of ~12,000 K (Labadie-Bartz et al., 2017; Shi et al., 2023a).

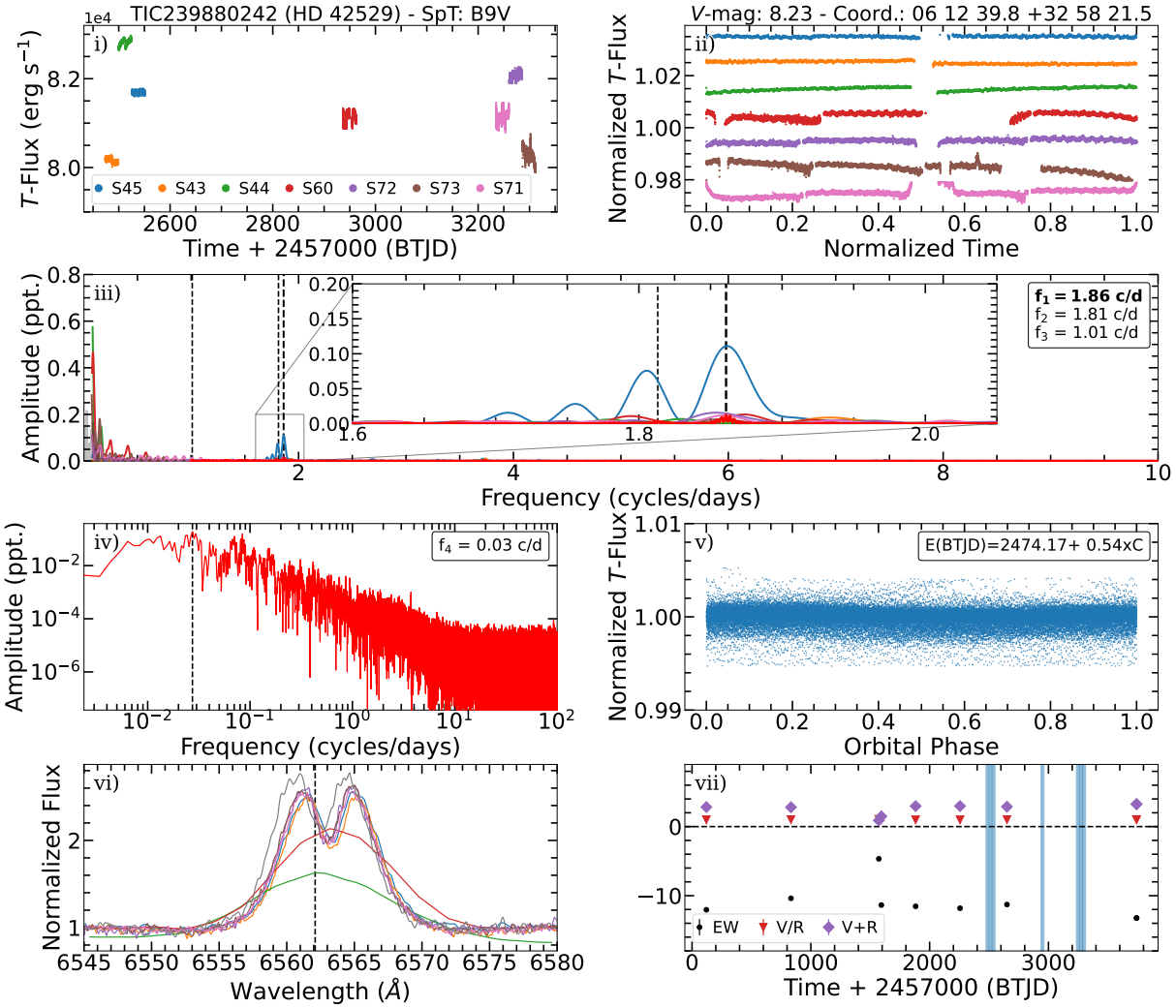

Figure C.61: Panels summarizing the photometric, spectroscopic, and frequency-domain analyses for the target TIC 239880242. (i) Raw T-Flux light curves from different sectors; (ii) normalized T-Flux light curves folded normalized time for each sector; (iii) Lomb-Scargle periodogram highlighting the three main frequencies f_1, f_2, and f_3, with a zoom-in inset; (iv) extended periodogram revealing a low-frequency component f_4; (v) orbital phase-folded light curve; (vi) optical spectrum centered on the Hα line (λ = 6562.8 Å); and (vii) temporal evolution of the equivalent width of the Hα line across available observations. Shaded regions in panel (vii) correspond to observation windows of sectors shown in panel (i).

C.62. TIC 239968973

HD 254168 is presented as a Be star of spectral type B5 by Chen et al. (2016). Labadie-Bartz et al. (2018) presented this object as a B7Ve and identified six outbursts in the APOGEE + KELT photometric data. Furthermore, was studied by Kervella et al. (2019) who characterized the physical presence of stellar and substellar companions through astrometry. No spectrum was found in the BESS catalog.

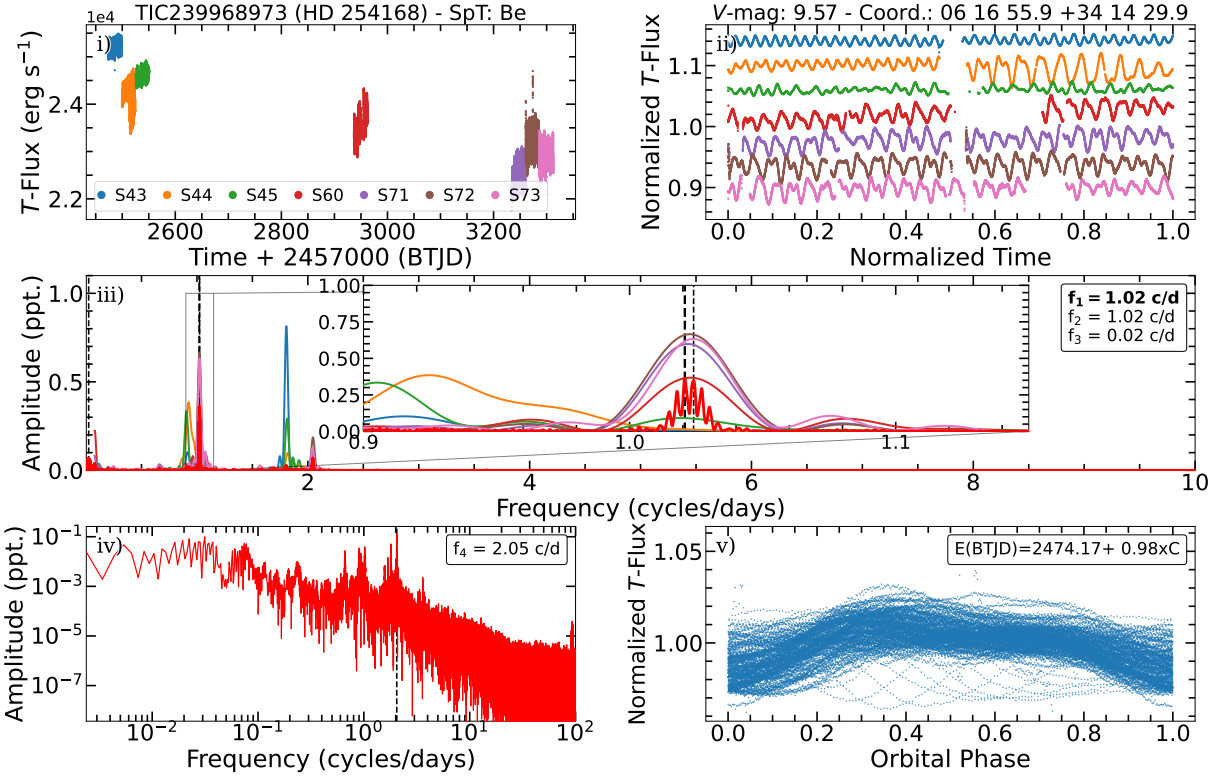

Figure C.62: Panels summarizing the photometric and frequency-domain analyses for the target TIC 239968973. (i) Raw T-Flux light curves from different sectors; (ii) normalized T-Flux light curves folded normalized time for each sector; (iii) Lomb-Scargle periodogram highlighting the three main frequencies f_1, f_2, and f_3, with a zoom-in inset; (iv) extended periodogram revealing a low-frequency component f_4; (v) orbital phase-folded light curve.

C.63. TIC 240003393

Labadie-Bartz et al. (2018) presented HD 43681 as a B8shell and no identified outbursts in the APOGEE + KELT photometric data. Furthermore, was studied by Kervella et al. (2019) who characterized the physical presence of stellar and substellar companions through astrometry.

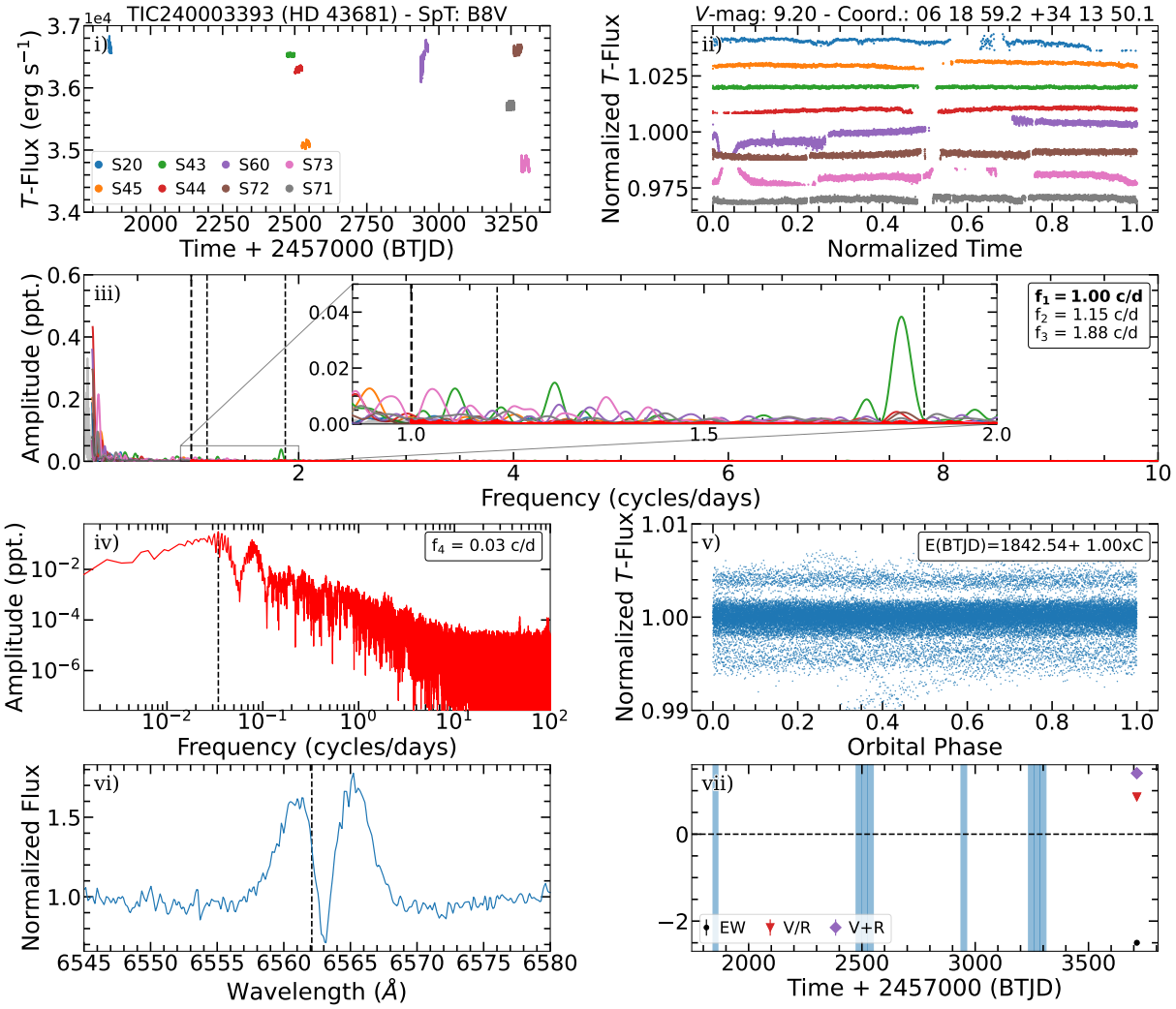

Figure C.63: Panels summarizing the photometric, spectroscopic, and frequency-domain analyses for the target TIC 240003393. (i) Raw T-Flux light curves from different sectors; (ii) normalized T-Flux light curves folded normalized time for each sector; (iii) Lomb-Scargle periodogram highlighting the three main frequencies f_1, f_2, and f_3, with a zoom-in inset; (iv) extended periodogram revealing a low-frequency component f_4; (v) orbital phase-folded light curve; (vi) optical spectrum centered on the Hα line (λ = 6562.8 Å); and (vii) temporal evolution of the equivalent width of the Hα line across available observations. Shaded regions in panel (vii) correspond to observation windows of sectors shown in panel (i).

C.64. TIC 240258004

V2162 Cyg (HD 204722, HIP 106079) is identified with the spectral type of B1.5 and is a candidate for a Be + sdOB binary system (Klement et al., 2024b).

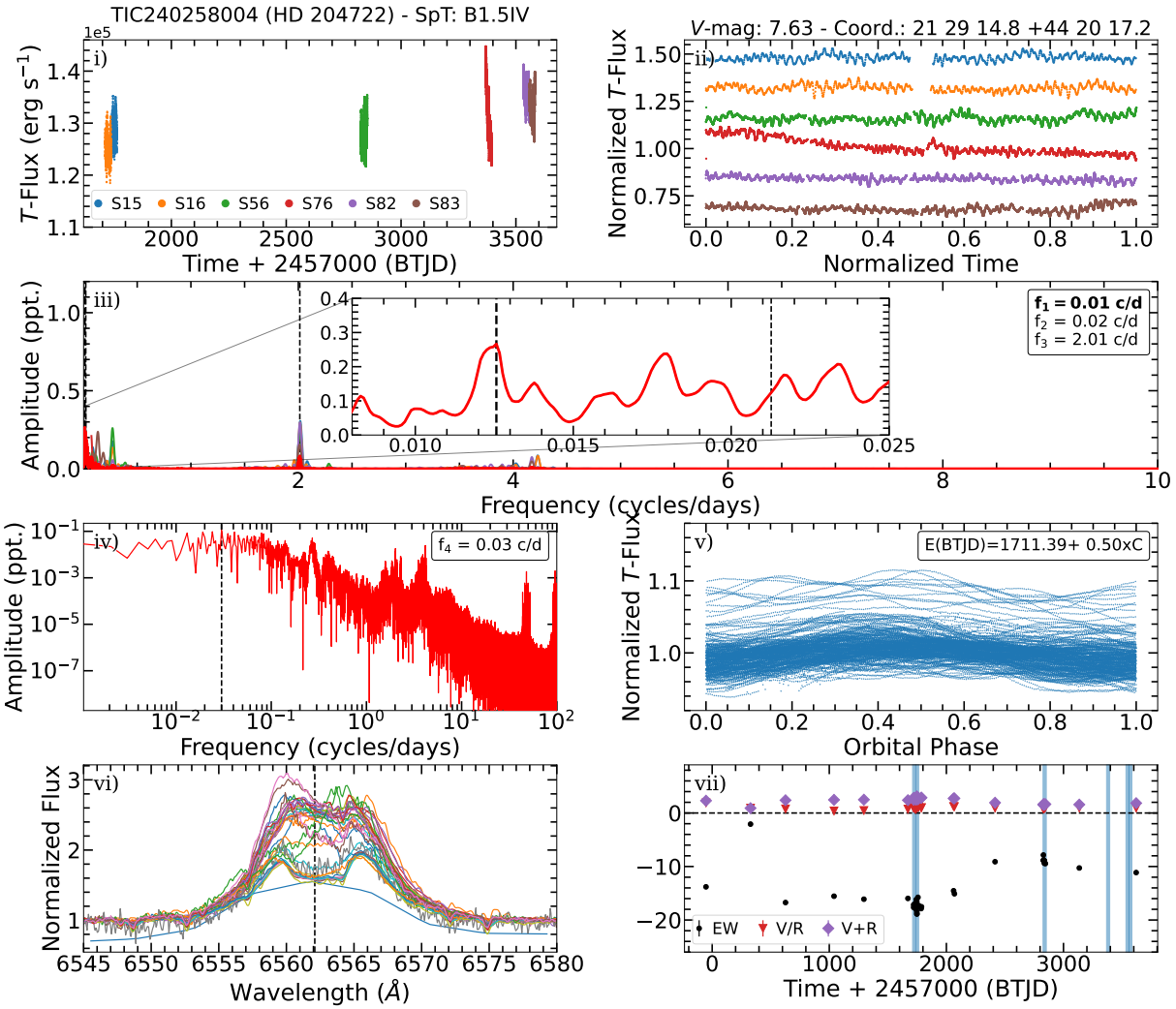

Figure C.64: Panels summarizing the photometric, spectroscopic, and frequency-domain analyses for the target TIC 240258004. (i) Raw T-Flux light curves from different sectors; (ii) normalized T-Flux light curves folded normalized time for each sector; (iii) Lomb-Scargle periodogram highlighting the three main frequencies f_1, f_2, and f_3, with a zoom-in inset; (iv) extended periodogram revealing a low-frequency component f_4; (v) orbital phase-folded light curve; (vi) optical spectrum centered on the Hα line (λ = 6562.8 Å); and (vii) temporal evolution of the equivalent width of the Hα line across available observations. Shaded regions in panel (vii) correspond to observation windows of sectors shown in panel (i).

C.65. TIC 240285395

V2163 Cyg (HD 204860) is a B5.5Ve type star (Chojnowski et al., 2014) and was studied by Kervella et al. (2019) who characterized the physical presence of stellar and substellar companions through astrometry.

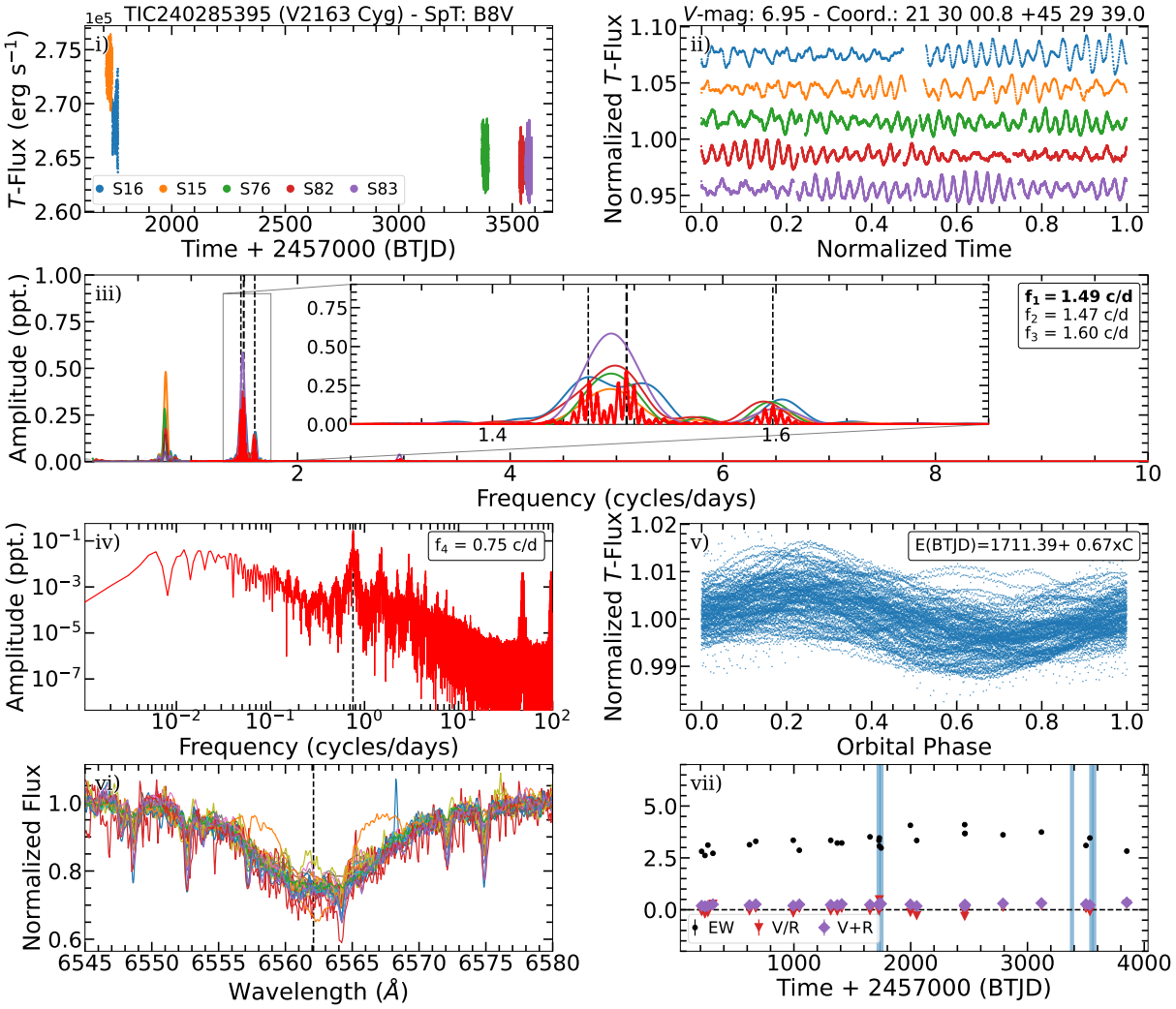

Figure C.65: Panels summarizing the photometric, spectroscopic, and frequency-domain analyses for the target TIC 240285395. (i) Raw T-Flux light curves from different sectors; (ii) normalized T-Flux light curves folded normalized time for each sector; (iii) Lomb-Scargle periodogram highlighting the three main frequencies f_1, f_2, and f_3, with a zoom-in inset; (iv) extended periodogram revealing a low-frequency component f_4; (v) orbital phase-folded light curve; (vi) optical spectrum centered on the Hα line (λ = 6562.8 Å); and (vii) temporal evolution of the equivalent width of the Hα line across available observations. Shaded regions in panel (vii) correspond to observation windows of sectors shown in panel (i).

C.66. TIC 240757326

o Cas (Omi Cas, HD 4180) is a Be star with a temperature of 17,400 K and *v* sin i of 215 (Zorec et al., 2016).

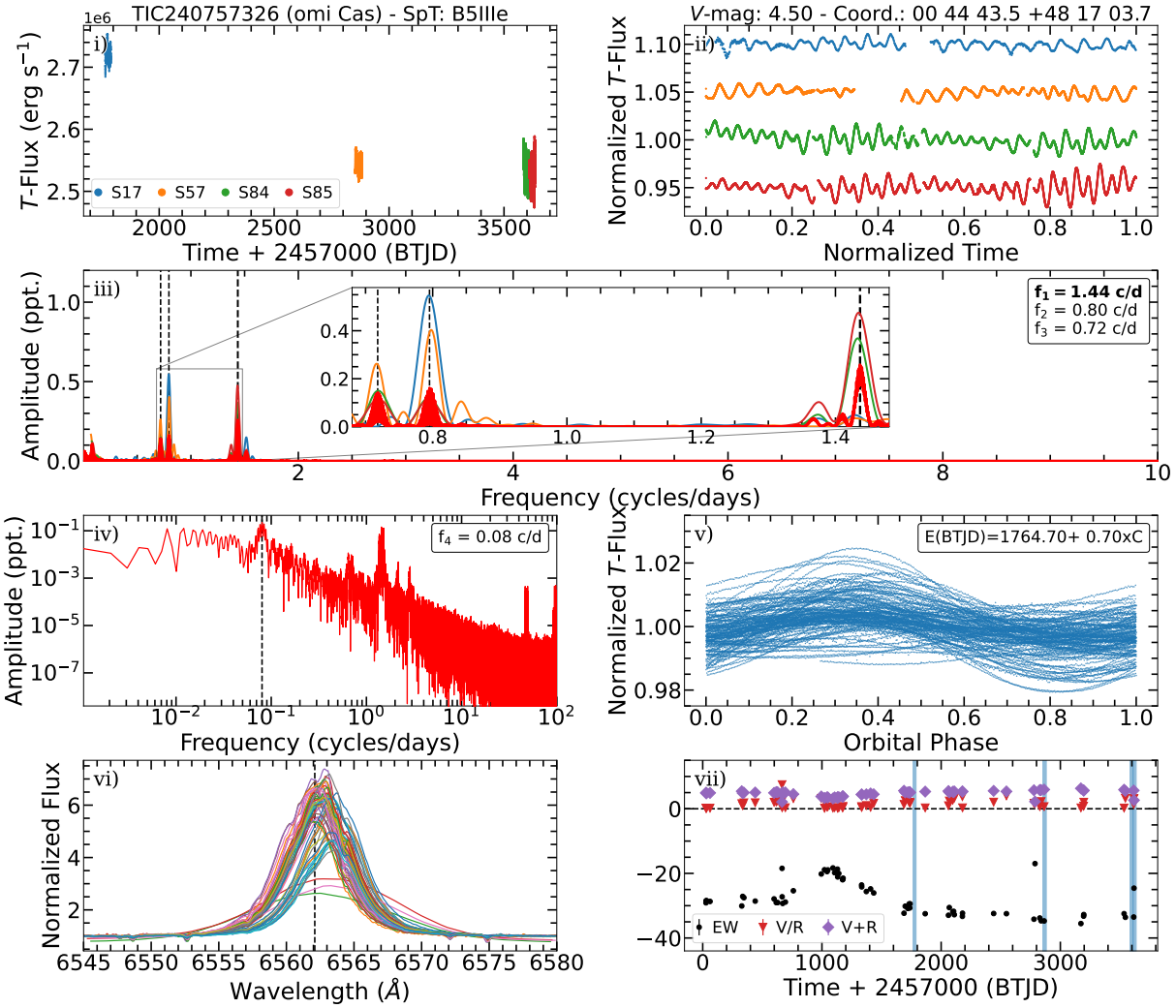

Figure C.66: Panels summarizing the photometric, spectroscopic, and frequency-domain analyses for the target TIC 240757326. (i) Raw T-Flux light curves from different sectors; (ii) normalized T-Flux light curves folded normalized time for each sector; (iii) Lomb-Scargle periodogram highlighting the three main frequencies f_1, f_2, and f_3, with a zoom-in inset; (iv) extended periodogram revealing a low-frequency component f_4; (v) orbital phase-folded light curve; (vi) optical spectrum centered on the Hα line (λ = 6562.8 Å); and (vii) temporal evolution of the equivalent width of the Hα line across available observations. Shaded regions in panel (vii) correspond to observation windows of sectors shown in panel (i).

C.67. TIC 243647020

μ Cen (HD 120324) is a Be star studied by Levenhagen et al. (2024a) who inferred measurements of 22,500 K, log g equal to 3.7 cgs and $v \sin i$ of 125 km s^{-1} for the undeformed star.

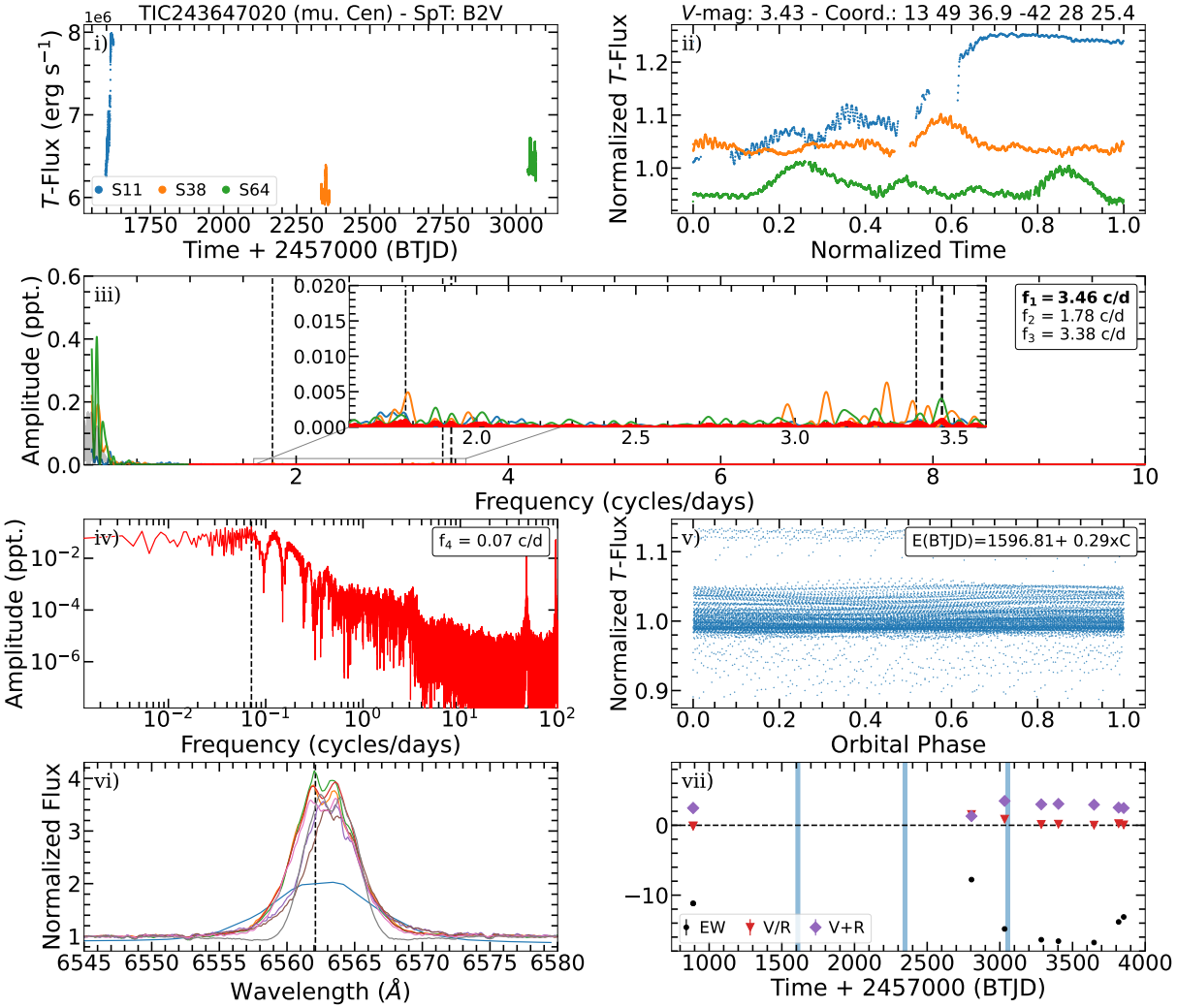

Figure C.67: Panels summarizing the photometric, spectroscopic, and frequency-domain analyses for the target TIC 243647020. (i) Raw T-Flux light curves from different sectors; (ii) normalized T-Flux light curves folded normalized time for each sector; (iii) Lomb-Scargle periodogram highlighting the three main frequencies f_1, f_2, and f_3, with a zoom-in inset; (iv) extended periodogram revealing a low-frequency component f_4; (v) orbital phase-folded light curve; (vi) optical spectrum centered on the Hα line (λ = 6562.8 Å); and (vii) temporal evolution of the equivalent width of the Hα line across available observations. Shaded regions in panel (vii) correspond to observation windows of sectors shown in panel (i).

C.68. TIC 24824031

β Monocerotis (HD 45725/45726/45727, HR 2356/2357/2358) is a triple system containing three Be's (Cowley and Gugula, 1973) stars. No spectrum was found in the BESS catalog.

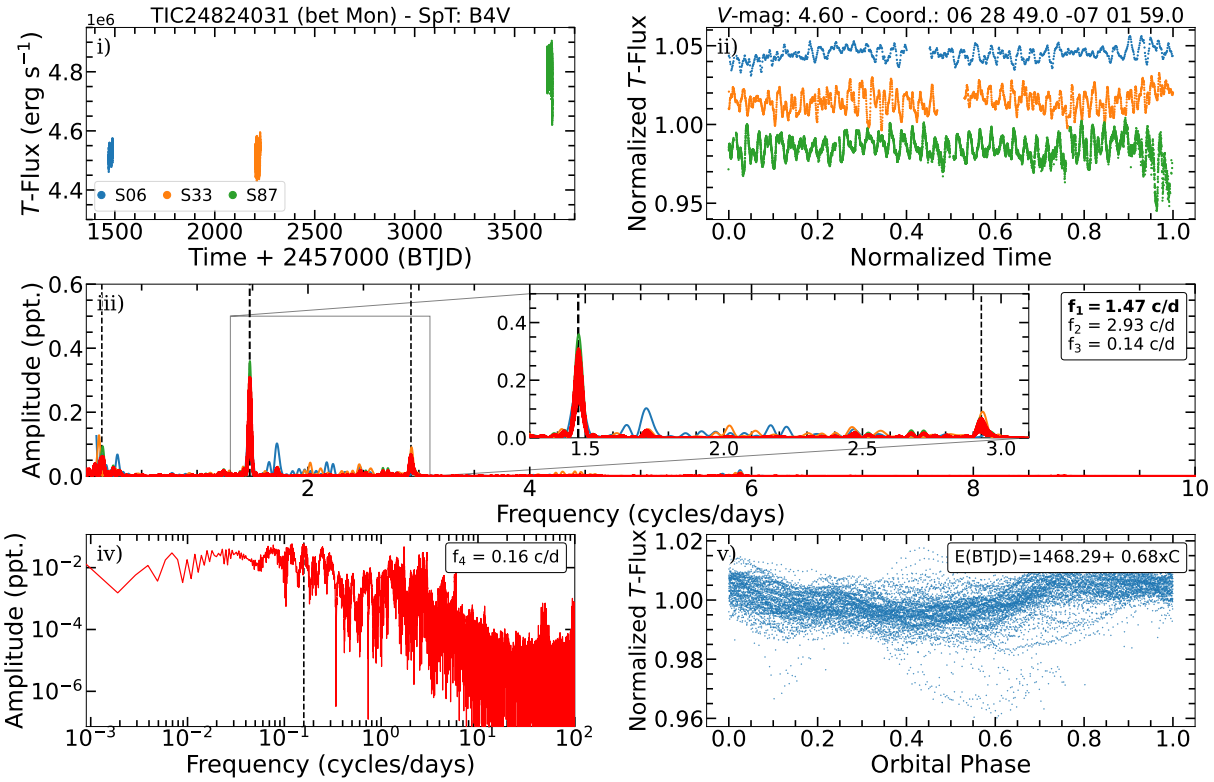

Figure C.68: Panels summarizing the photometric and frequency-domain analyses for the target TIC 24824031. (i) Raw T-Flux light curves from different sectors; (ii) normalized T-Flux light curves folded normalized time for each sector; (iii) Lomb-Scargle periodogram highlighting the three main frequencies f_1, f_2, and f_3, with a zoom-in inset; (iv) extended periodogram revealing a low-frequency component f_4; (v) orbital phase-folded light curve.

C.69. TIC 250936039

HD 15113 ... No spectrum was found in the BESS catalog.

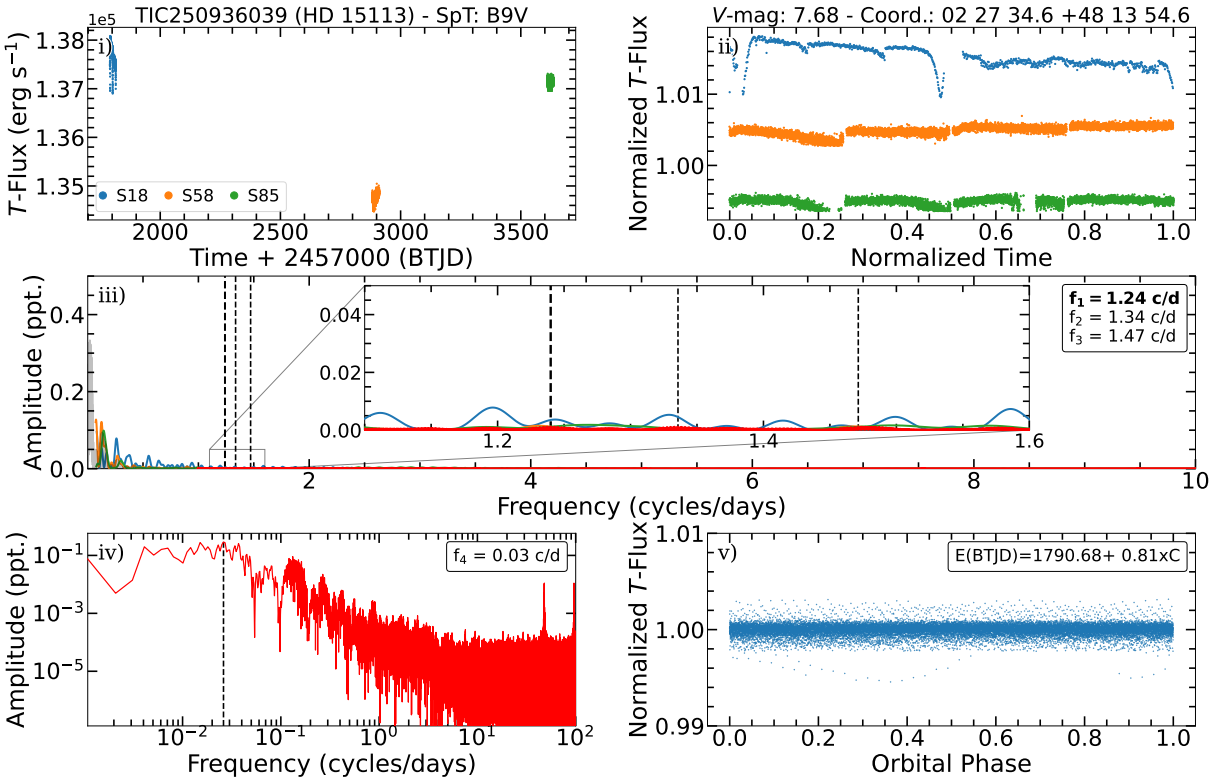

Figure C.69: Panels summarizing the photometric and frequency-domain analyses for the target TIC 250936039. (i) Raw *T*-Flux light curves from different sectors; (ii) normalized *T*-Flux light curves folded normalized time for each sector; (iii) Lomb-Scargle periodogram highlighting the three main frequencies f_1, f_2, and f_3, with a zoom-in inset; (iv) extended periodogram revealing a low-frequency component f_4; (v) orbital phase-folded light curve.

C.70. TIC 252414037

11 Cam (HD 32343) is a B3Ve star with a temperature of 18,130 K, $v \sin i$ of 105 km s^{-1} and a mass of 6.0 $M_\odot$ (Zorec et al., 2016).

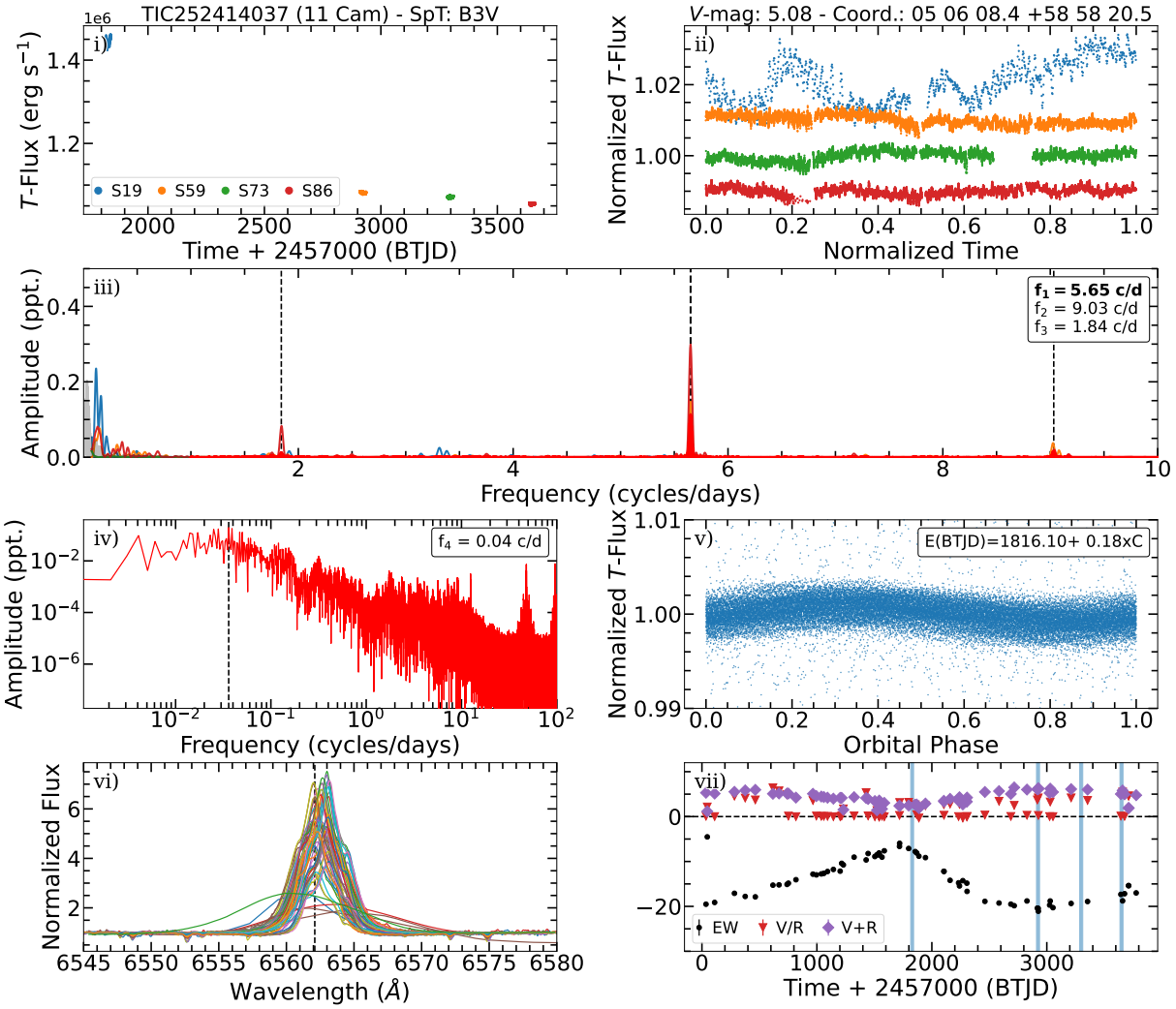

Figure C.70: Panels summarizing the photometric, spectroscopic, and frequency-domain analyses for the target TIC 252414037. (i) Raw T-Flux light curves from different sectors; (ii) normalized T-Flux light curves folded normalized time for each sector; (iii) Lomb-Scargle periodogram highlighting the three main frequencies f_1, f_2, and f_3, with a zoom-in inset; (iv) extended periodogram revealing a low-frequency component f_4; (v) orbital phase-folded light curve; (vi) optical spectrum centered on the Hα line (λ = 6562.8 Å); and (vii) temporal evolution of the equivalent width of the Hα line across available observations. Shaded regions in panel (vii) correspond to observation windows of sectors shown in panel (i).

C.71. TIC 252500679

HD 217050 is a Be star with a temperature of 22,050 K, $v \sin i$ of 358 km s^{-1} and a mass of 8.8 $M_\odot$ (Zorec et al., 2016).

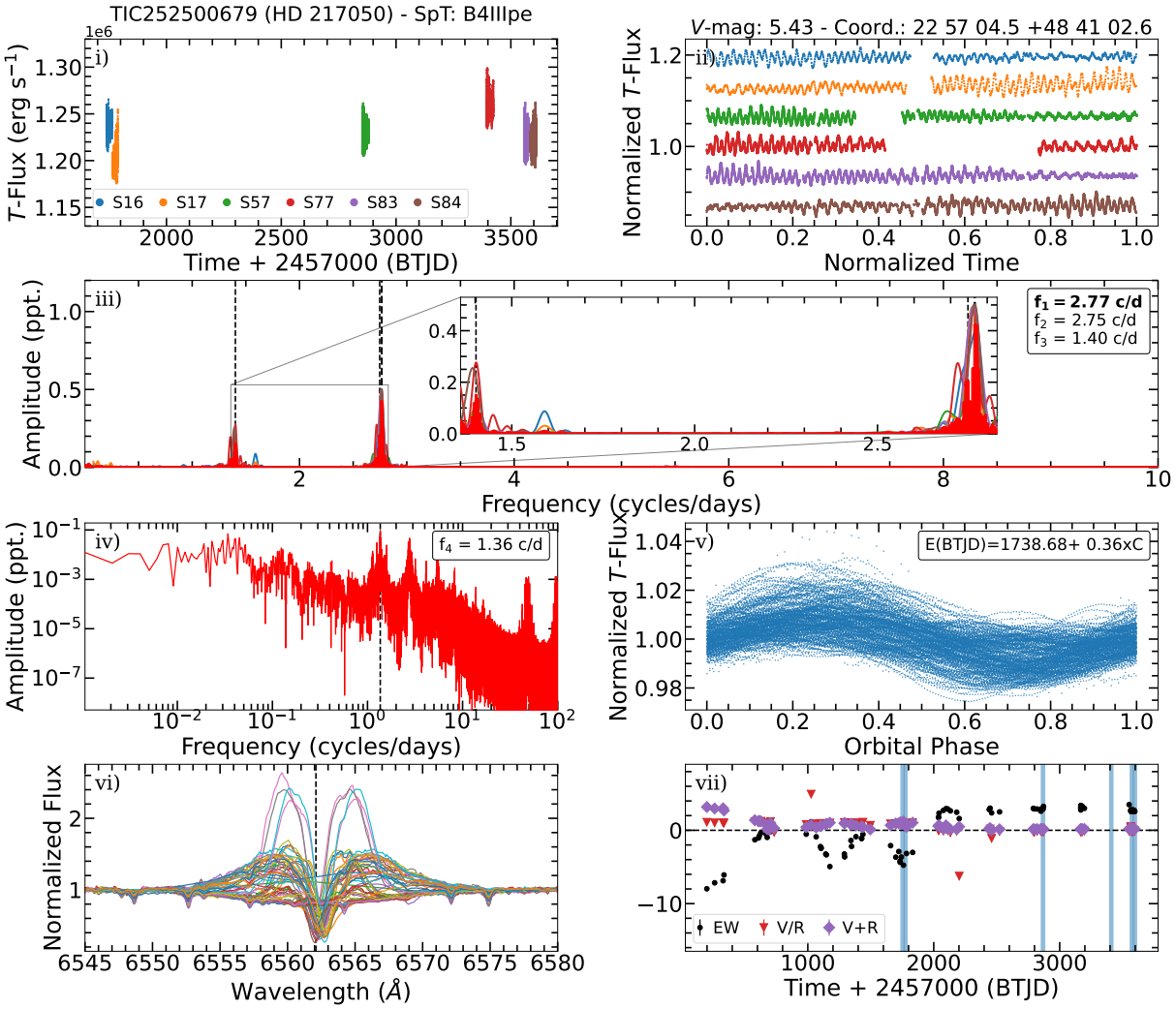

Figure C.71: Panels summarizing the photometric, spectroscopic, and frequency-domain analyses for the target TIC 252500679. (i) Raw *T*-Flux light curves from different sectors; (ii) normalized *T*-Flux light curves folded normalized time for each sector; (iii) Lomb-Scargle periodogram highlighting the three main frequencies f_1, f_2, and f_3, with a zoom-in inset; (iv) extended periodogram revealing a low-frequency component f_4; (v) orbital phase-folded light curve; (vi) optical spectrum centered on the Hα line (λ = 6562.8 Å); and (vii) temporal evolution of the equivalent width of the Hα line across available observations. Shaded regions in panel (vii) correspond to observation windows of sectors shown in panel (i).

C.72. TIC 252670277

KX And (HD 218393) is a binary system with spectral type B3pe + G8II (Bodensteiner et al., 2020). It is an interacting system with matter transfer and emission of bipolar jets (Ziegenbalg, 2024). It should not be a classical Be star.

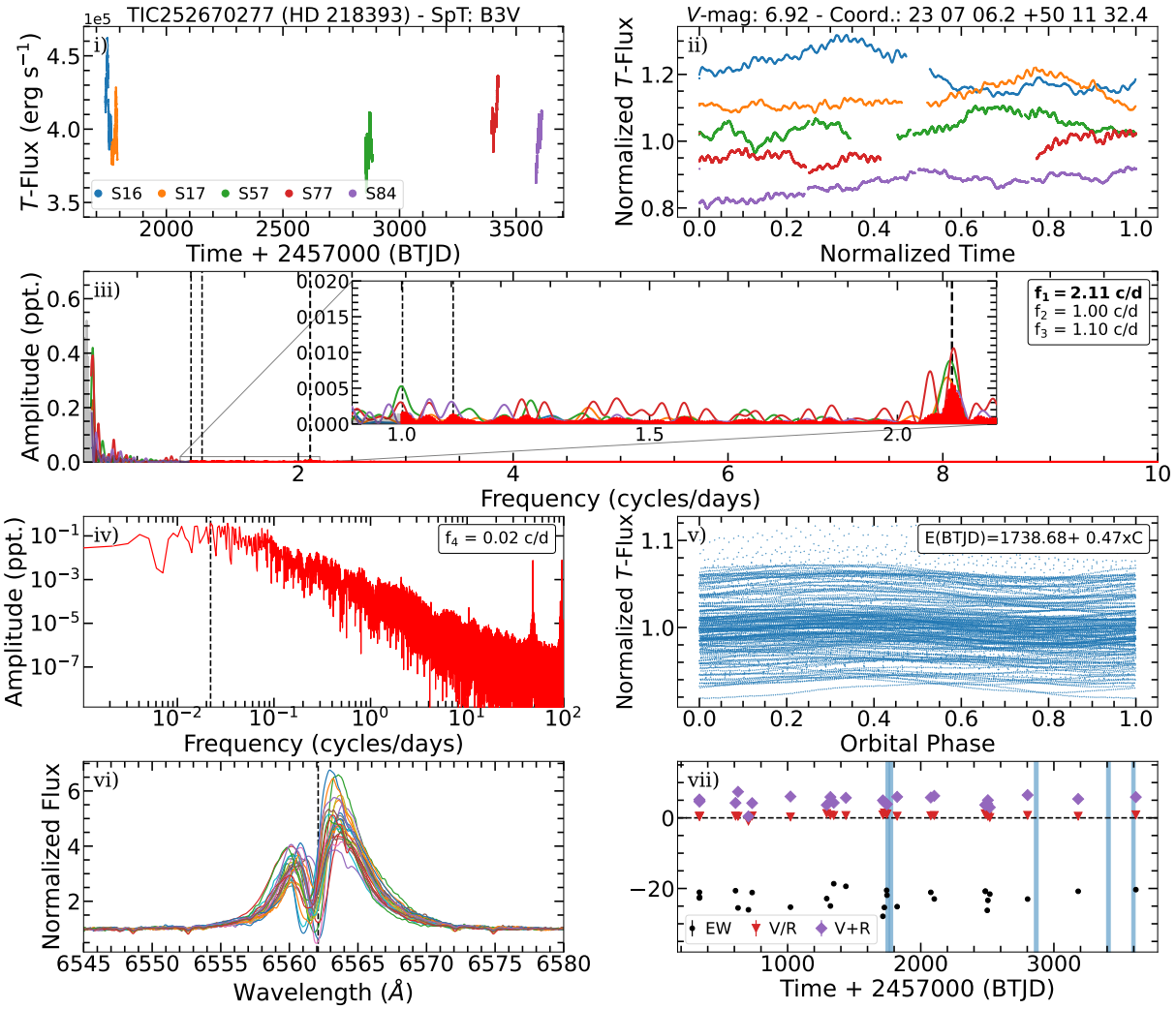

Figure C.72: Panels summarizing the photometric, spectroscopic, and frequency-domain analyses for the target TIC 252670277. (i) Raw T-Flux light curves from different sectors; (ii) normalized T-Flux light curves folded normalized time for each sector; (iii) Lomb-Scargle periodogram highlighting the three main frequencies f_1, f_2, and f_3, with a zoom-in inset; (iv) extended periodogram revealing a low-frequency component f_4; (v) orbital phase-folded light curve; (vi) optical spectrum centered on the Hα line (λ = 6562.8 Å); and (vii) temporal evolution of the equivalent width of the Hα line across available observations. Shaded regions in panel (vii) correspond to observation windows of sectors shown in panel (i).

C.73. TIC 253212775

Alfonso-Garzón et al. (2012) presented this V495 Cen (CD-55 4911) as an eclipsing binary system. It is an interacting system consisting of an evolved F-type giant that is transferring matter to an early B-type dwarf star (Rosales Guzmán et al., 2018; Rosales et al., 2019; Bodensteiner et al., 2020).

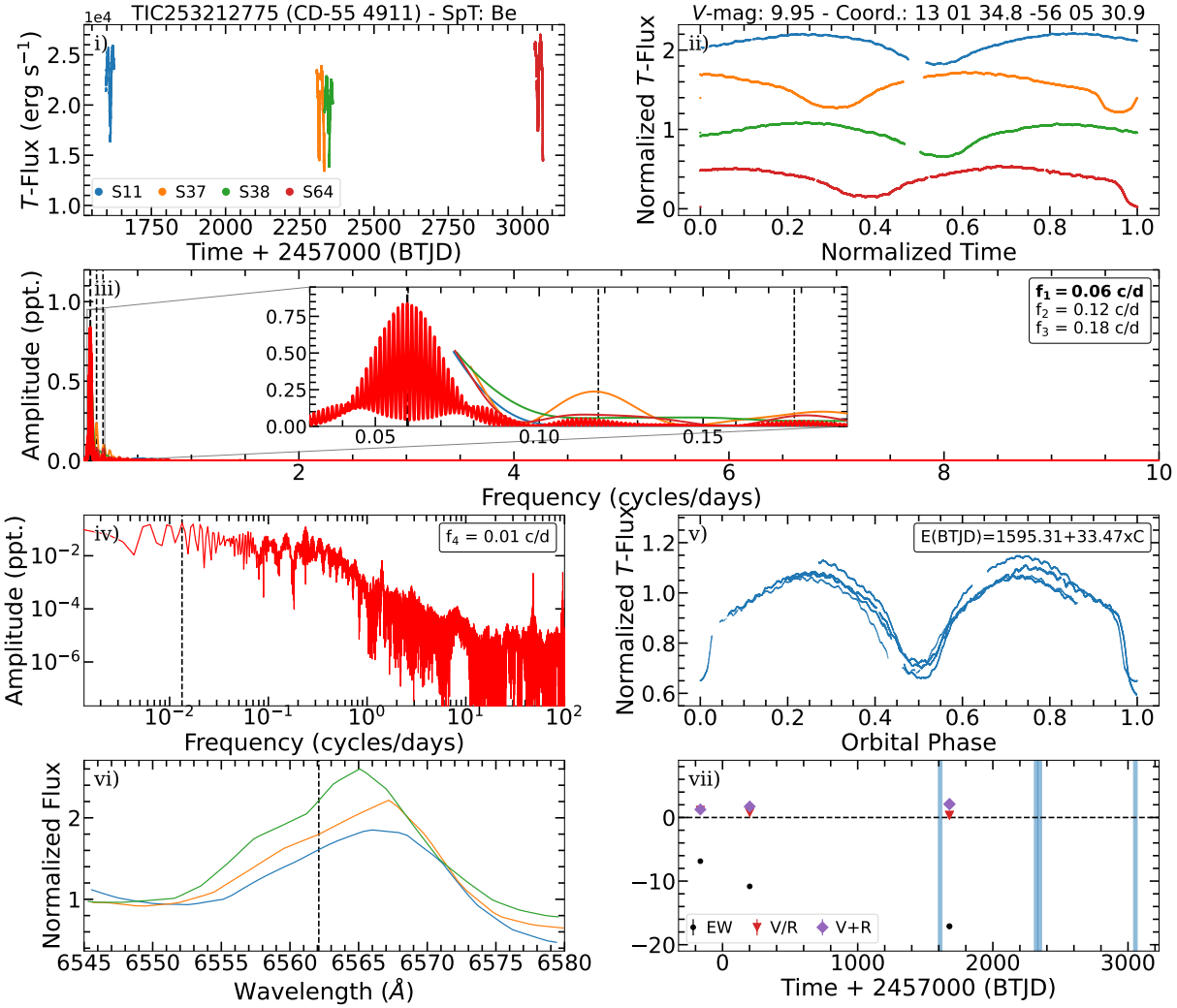

Figure C.73: Panels summarizing the photometric, spectroscopic, and frequency-domain analyses for the target TIC 253212775. (i) Raw T-Flux light curves from different sectors; (ii) normalized T-Flux light curves folded normalized time for each sector; (iii) Lomb-Scargle periodogram highlighting the three main frequencies f_1, f_2, and f_3, with a zoom-in inset; (iv) extended periodogram revealing a low-frequency component f_4; (v) orbital phase-folded light curve; (vi) optical spectrum centered on the Hα line (λ = 6562.8 Å); and (vii) temporal evolution of the equivalent width of the Hα line across available observations. Shaded regions in panel (vii) correspond to observation windows of sectors shown in panel (i).

C.74. TIC 253380837

Labadie-Bartz et al. (2022) presented this object (HD 113573) of spectral type B4Ve as an eclipsing binary system from TESS photometric data.

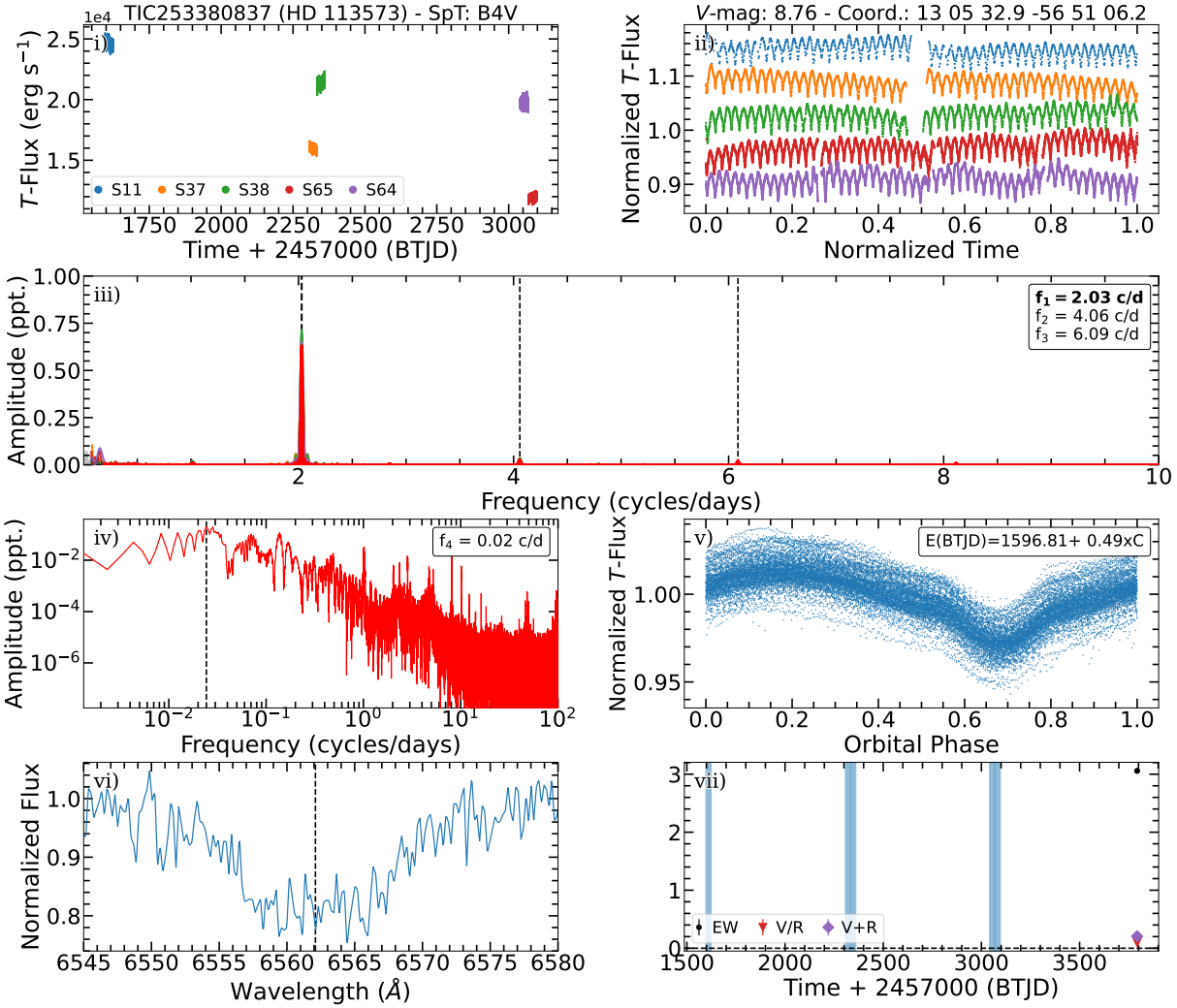

Figure C.74: Panels summarizing the photometric, spectroscopic, and frequency-domain analyses for the target TIC 253380837. (i) Raw T-Flux light curves from different sectors; (ii) normalized T-Flux light curves folded normalized time for each sector; (iii) Lomb-Scargle periodogram highlighting the three main frequencies f_1, f_2, and f_3, with a zoom-in inset; (iv) extended periodogram revealing a low-frequency component f_4; (v) orbital phase-folded light curve; (vi) optical spectrum centered on the Hα line (λ = 6562.8 Å); and (vii) temporal evolution of the equivalent width of the Hα line across available observations. Shaded regions in panel (vii) correspond to observation windows of sectors shown in panel (i).

C.75. TIC 25692574

HD 221188 was studied by Kervella et al. (2019) who characterized the physical presence of stellar and substellar companions through astrometry. No spectrum was found in the BESS catalog.

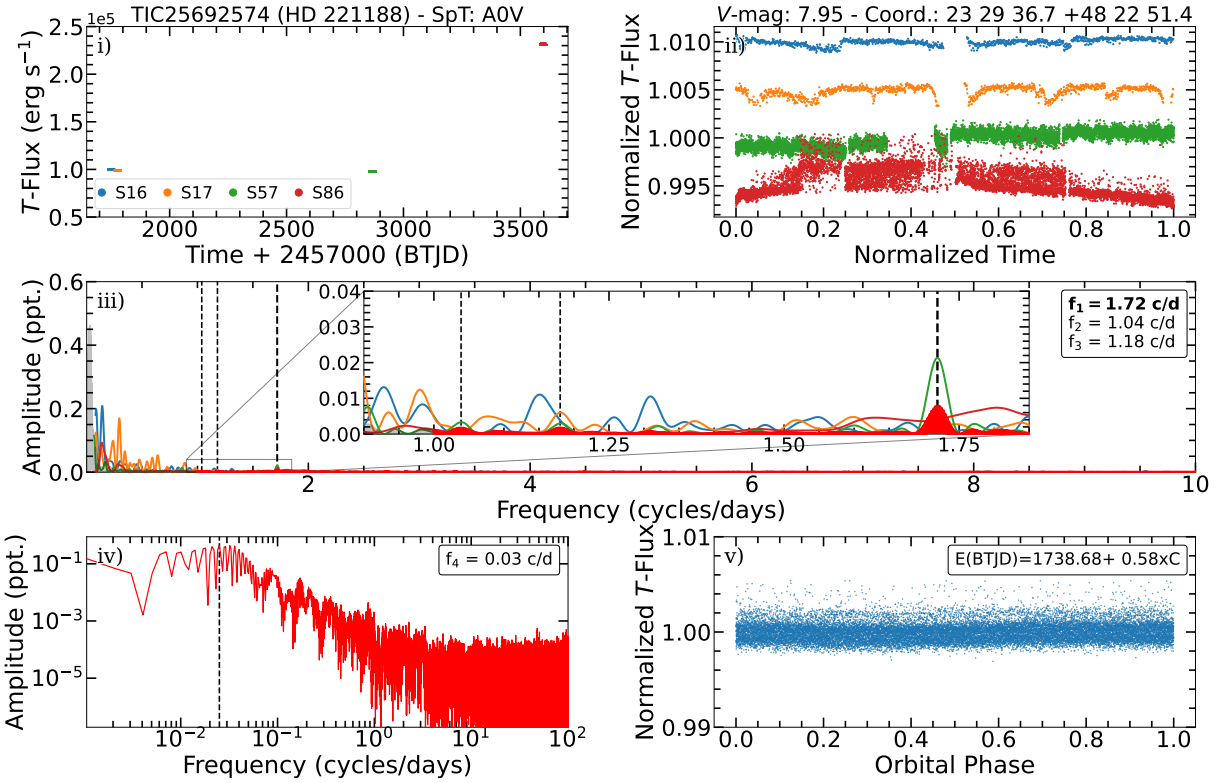

Figure C.75: Panels summarizing the photometric and frequency-domain analyses for the target TIC 25692574. (i) Raw T-Flux light curves from different sectors; (ii) normalized T-Flux light curves folded normalized time for each sector; (iii) Lomb-Scargle periodogram highlighting the three main frequencies f_1, f_2, and f_3, with a zoom-in inset; (iv) extended periodogram revealing a low-frequency component f_4; (v) orbital phase-folded light curve.

C.76. TIC 258704817

CO Cir (HD 129954) has the spectral type of B2.5Ve (Labadie-Bartz et al., 2022) and was studied by Kervella et al. (2019) who characterized the physical presence of stellar and substellar companions through astrometry.

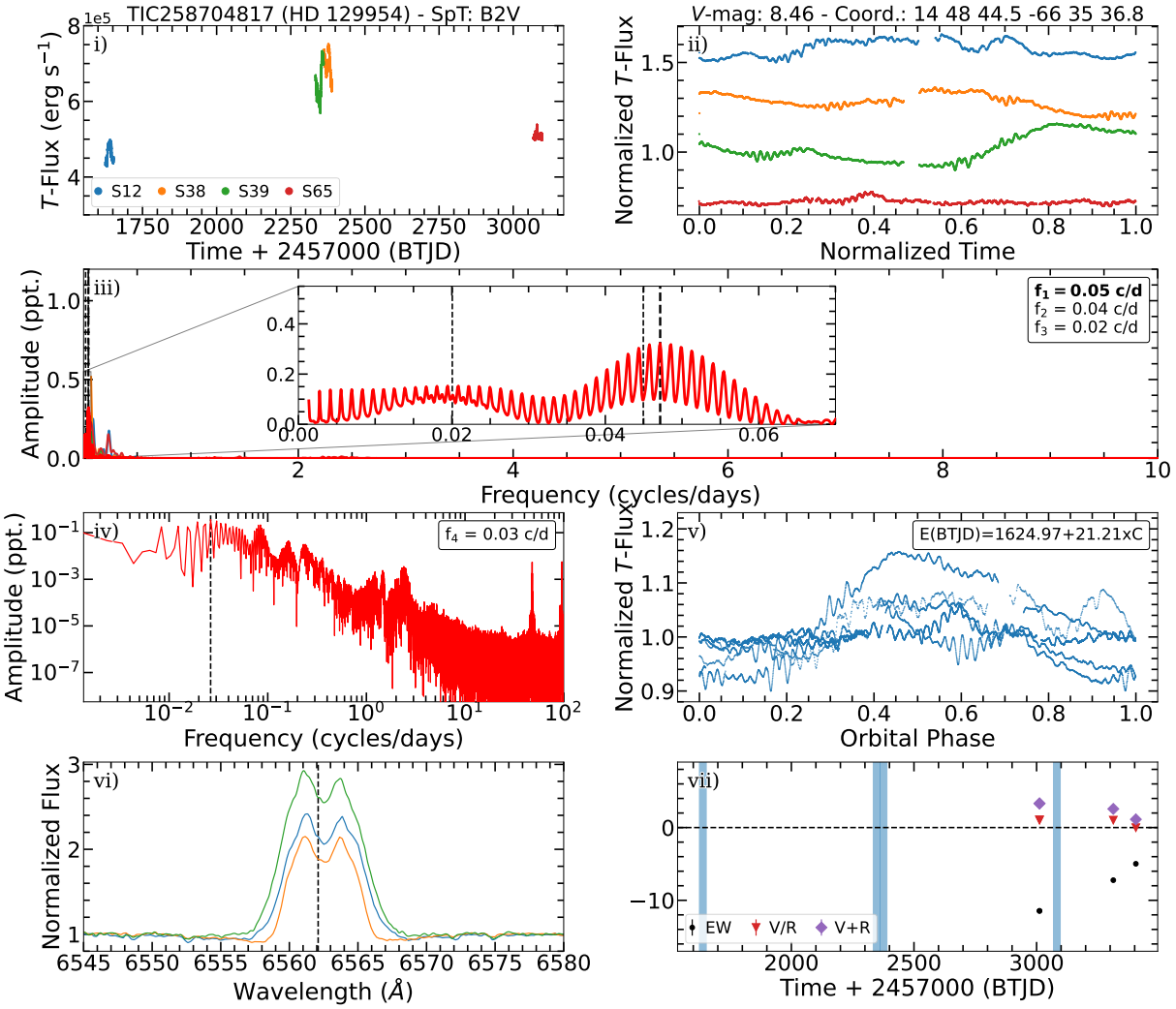

Figure C.76: Panels summarizing the photometric, spectroscopic, and frequency-domain analyses for the target TIC 258704817. (i) Raw T-Flux light curves from different sectors; (ii) normalized T-Flux light curves folded normalized time for each sector; (iii) Lomb-Scargle periodogram highlighting the three main frequencies f_1, f_2, and f_3, with a zoom-in inset; (iv) extended periodogram revealing a low-frequency component f_4; (v) orbital phase-folded light curve; (vi) optical spectrum centered on the Hα line (λ = 6562.8 Å); and (vii) temporal evolution of the equivalent width of the Hα line across available observations. Shaded regions in panel (vii) correspond to observation windows of sectors shown in panel (i).

C.77. TIC 259463816

48 Per (c Per, HD 25940) is a Be star with a temperature of 19,410 K, $v \sin i$ of 219 km s^{-1} and a mass of 7.2 $M_\odot$ (Zorec et al., 2016). It is possibly a spectroscopic binary with a period of ~17 days (Klement et al., 2024b).

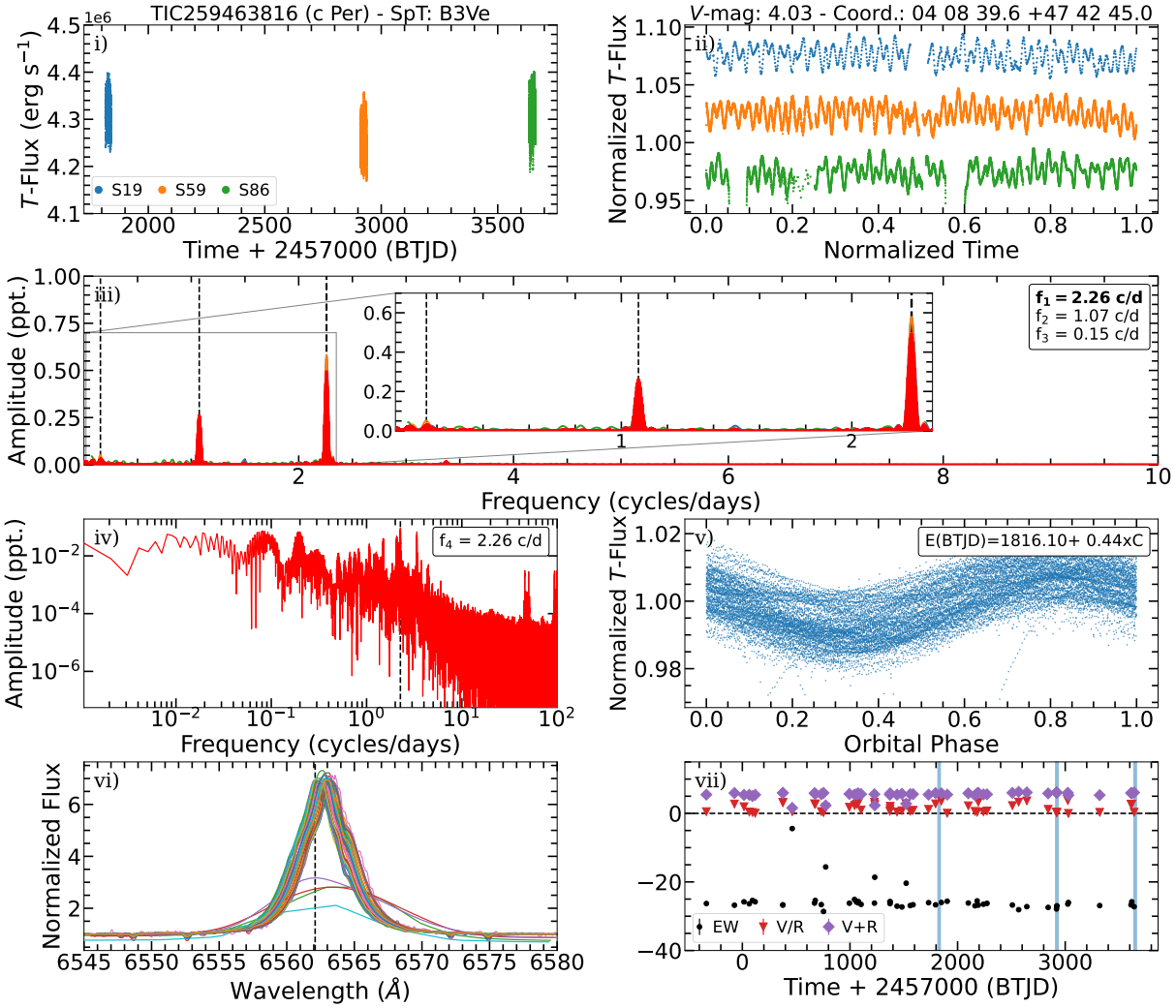

Figure C.77: Panels summarizing the photometric, spectroscopic, and frequency-domain analyses for the target TIC 259463816. (i) Raw T-Flux light curves from different sectors; (ii) normalized T-Flux light curves folded normalized time for each sector; (iii) Lomb-Scargle periodogram highlighting the three main frequencies f_1, f_2, and f_3, with a zoom-in inset; (iv) extended periodogram revealing a low-frequency component f_4; (v) orbital phase-folded light curve; (vi) optical spectrum centered on the Hα line (λ = 6562.8 Å); and (vii) temporal evolution of the equivalent width of the Hα line across available observations. Shaded regions in panel (vii) correspond to observation windows of sectors shown in panel (i).

C.78. TIC 261993378

lam Cru (HD 112078) is a Be star with a temperature of 20,010 K, $v \sin i$ of 324 km s^{-1} and a mass of 5.8 $M_\odot$ (Zorec et al., 2016) and was studied by Kervella et al. (2019) who characterized the physical presence of stellar and substellar companions through astrometry.

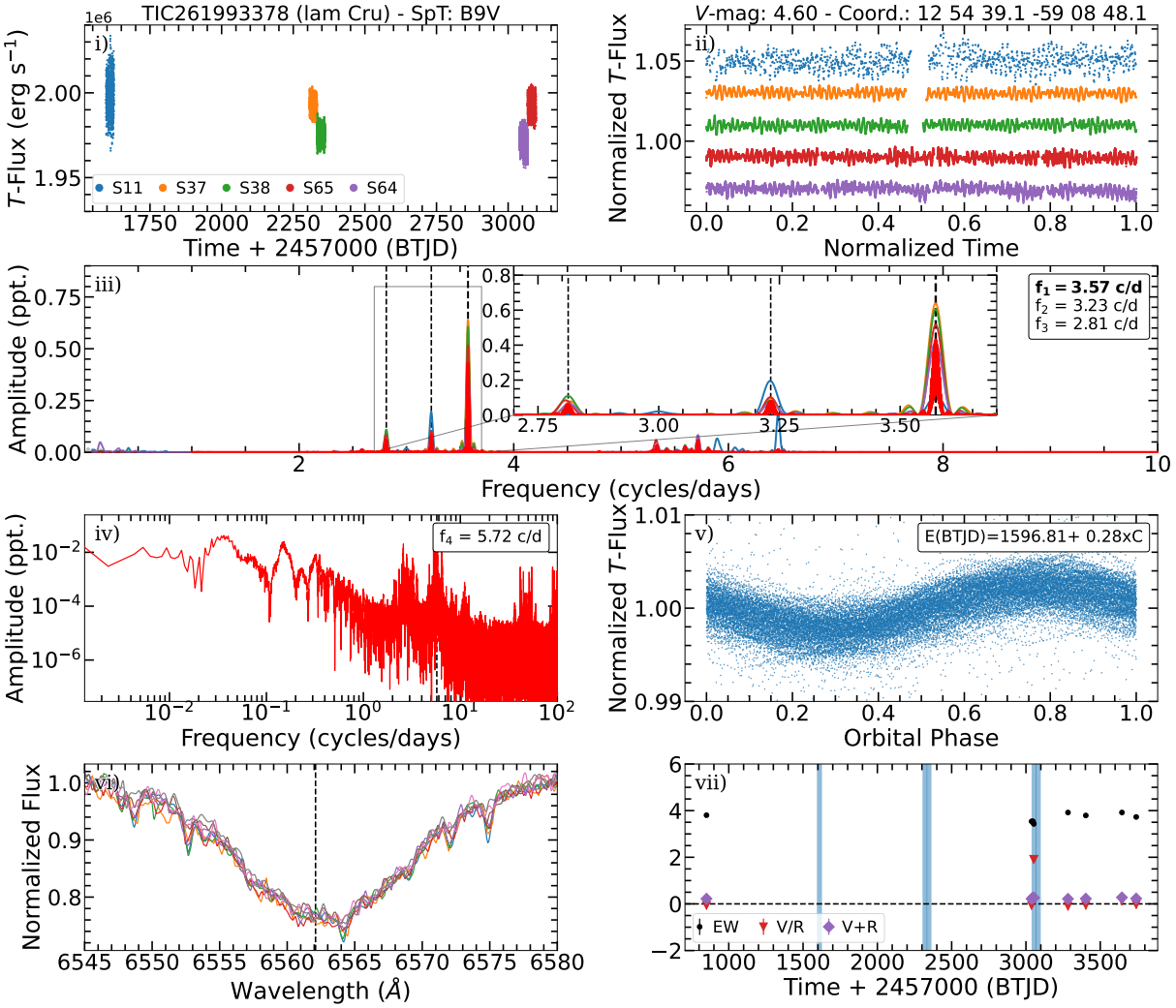

Figure C.78: Panels summarizing the photometric, spectroscopic, and frequency-domain analyses for the target TIC 261993378. (i) Raw T-Flux light curves from different sectors; (ii) normalized T-Flux light curves folded normalized time for each sector; (iii) Lomb-Scargle periodogram highlighting the three main frequencies f_1, f_2, and f_3, with a zoom-in inset; (iv) extended periodogram revealing a low-frequency component f_4; (v) orbital phase-folded light curve; (vi) optical spectrum centered on the Hα line (λ = 6562.8 Å); and (vii) temporal evolution of the equivalent width of the Hα line across available observations. Shaded regions in panel (vii) correspond to observation windows of sectors shown in panel (i).

C.79. TIC 262169297

HD 33357 is shown with the spectral type of B1:V:ne in the catalog of Morgan et al. (1955) and as an eclipsing binary system in the catalog of Gaia Collaboration et al. (2023).

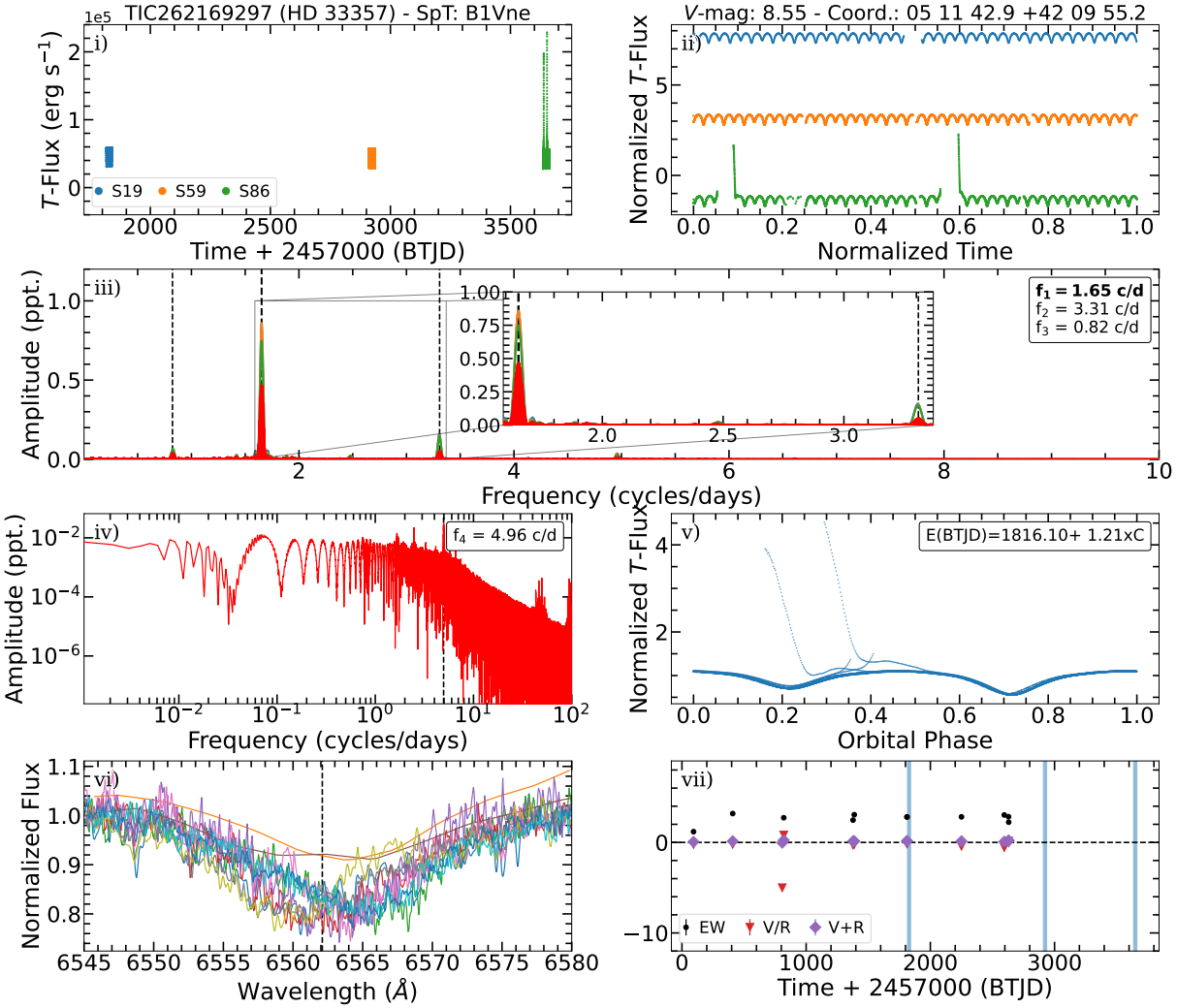

Figure C.79: Panels summarizing the photometric, spectroscopic, and frequency-domain analyses for the target TIC 262169297. (i) Raw T-Flux light curves from different sectors; (ii) normalized T-Flux light curves folded normalized time for each sector; (iii) Lomb-Scargle periodogram highlighting the three main frequencies f_1, f_2, and f_3, with a zoom-in inset; (iv) extended periodogram revealing a low-frequency component f_4; (v) orbital phase-folded light curve; (vi) optical spectrum centered on the Hα line (λ = 6562.8 Å); and (vii) temporal evolution of the equivalent width of the Hα line across available observations. Shaded regions in panel (vii) correspond to observation windows of sectors shown in panel (i).

C.80. TIC 26432264

HD 23478 was studied by Sikora et al. (2015) as a magnetic B-type star that presents Ha emission lines, being a non-classical Be star with a mass of 6.1 $M_\odot$ and a temperature of 20,000 K. No spectrum was found in the BESS catalog.

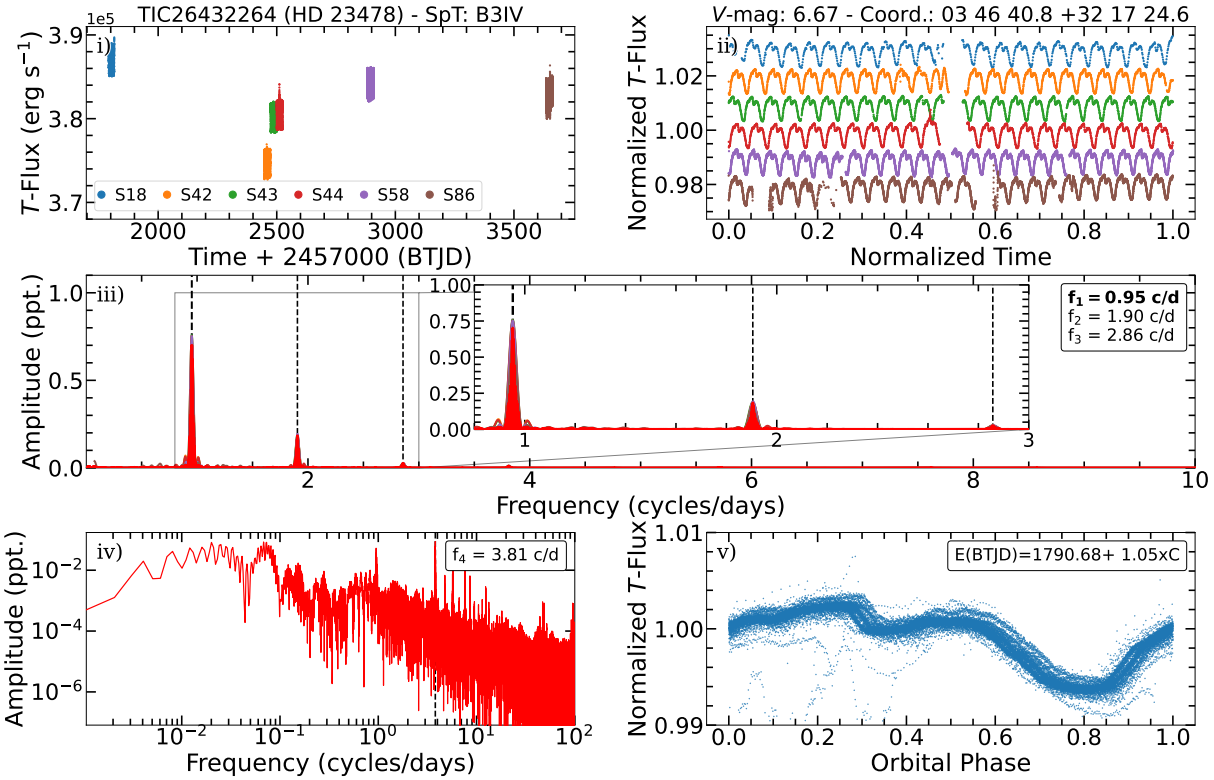

Figure C.80: Panels summarizing the photometric and frequency-domain analyses for the target TIC 26432264. (i) Raw T-Flux light curves from different sectors; (ii) normalized T-Flux light curves folded normalized time for each sector; (iii) Lomb-Scargle periodogram highlighting the three main frequencies f_1, f_2, and f_3, with a zoom-in inset; (iv) extended periodogram revealing a low-frequency component f_4; (v) orbital phase-folded light curve.

C.81. TIC 264459943

psi01 Ori (HD 35439, spectral type of B1Ve) is a Be star with a temperature of 26,830 K, $v \sin i$ of 284 km s^{-1} and a mass of 12.8 $M_\odot$ (Zorec et al., 2016) and was studied by Kervella et al. (2019) who characterized the physical presence of stellar and substellar companions through astrometry.

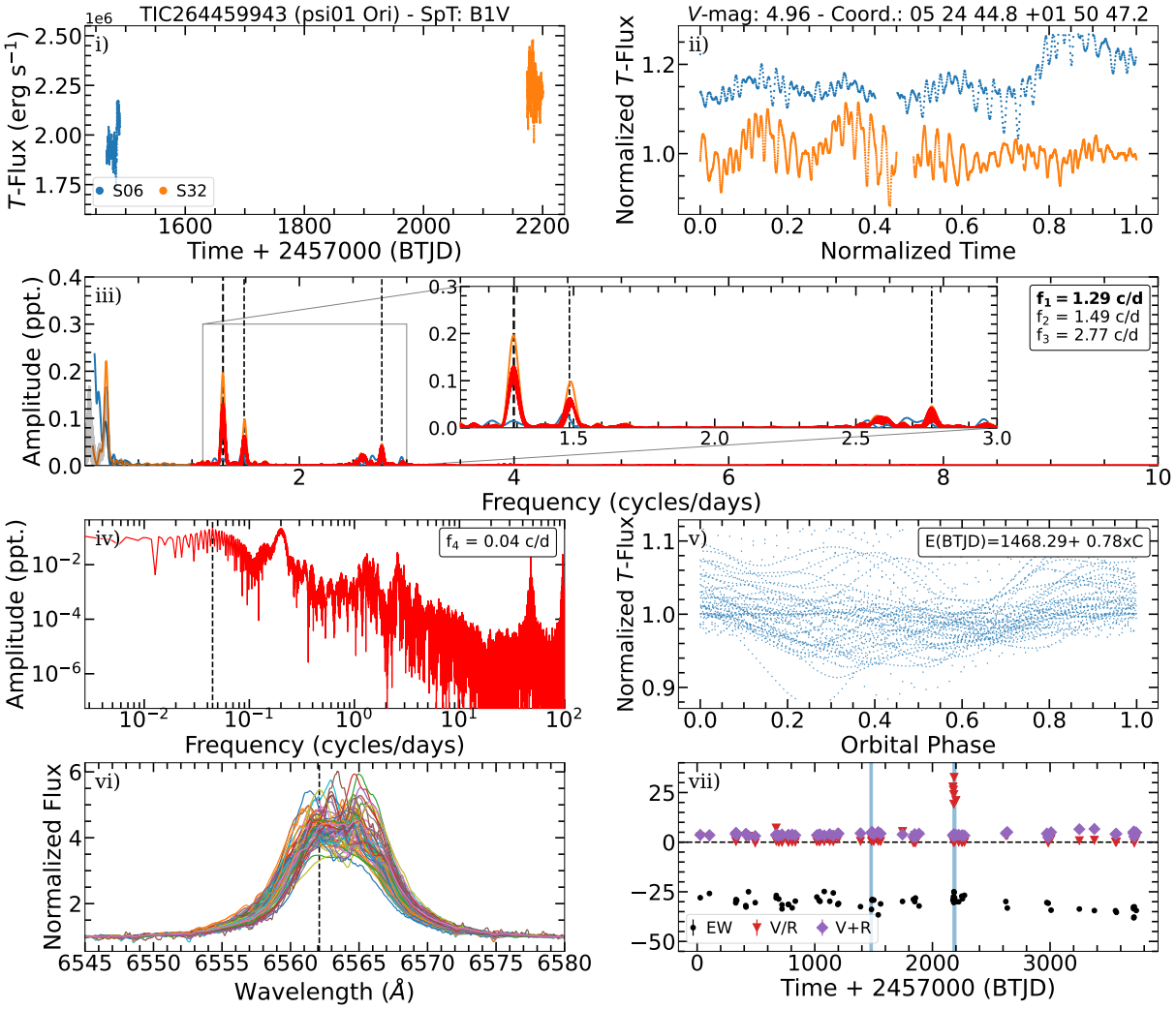

Figure C.81: Panels summarizing the photometric, spectroscopic, and frequency-domain analyses for the target TIC 264459943. (i) Raw T-Flux light curves from different sectors; (ii) normalized T-Flux light curves folded normalized time for each sector; (iii) Lomb-Scargle periodogram highlighting the three main frequencies f_1, f_2, and f_3, with a zoom-in inset; (iv) extended periodogram revealing a low-frequency component f_4; (v) orbital phase-folded light curve; (vi) optical spectrum centered on the Hα line (λ = 6562.8 Å); and (vii) temporal evolution of the equivalent width of the Hα line across available observations. Shaded regions in panel (vii) correspond to observation windows of sectors shown in panel (i).

C.82. TIC 264631173

V1372 Ori (HD 36012 or MWC 757, and spectral type of B2Vne) is a Be star with a temperature of 19,870 K, $v \sin i$ of 195 km s^{-1} and a mass of 6.1 $M_\odot$ (Zorec et al., 2016) and was studied by Kervella et al. (2019) who characterized the physical presence of stellar and substellar companions through astrometry.

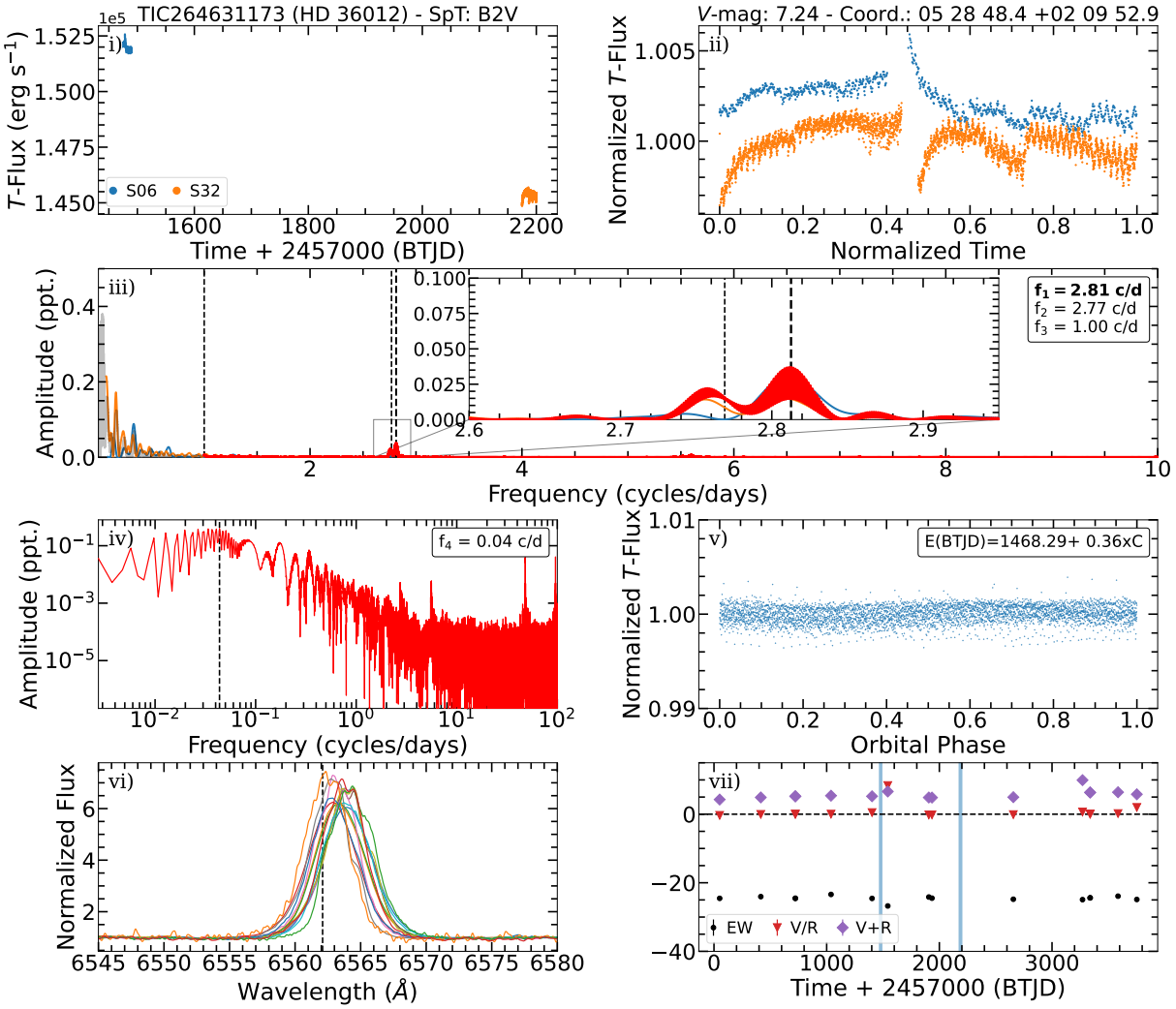

Figure C.82: Panels summarizing the photometric, spectroscopic, and frequency-domain analyses for the target TIC 264631173. (i) Raw T-Flux light curves from different sectors; (ii) normalized T-Flux light curves folded normalized time for each sector; (iii) Lomb-Scargle periodogram highlighting the three main frequencies f_1, f_2, and f_3, with a zoom-in inset; (iv) extended periodogram revealing a low-frequency component f_4; (v) orbital phase-folded light curve; (vi) optical spectrum centered on the Hα line (λ = 6562.8 Å); and (vii) temporal evolution of the equivalent width of the Hα line across available observations. Shaded regions in panel (vii) correspond to observation windows of sectors shown in panel (i).

C.83. TIC 265911941

π Aquarii (HD 212571, MWC 388) is a classical Be star of spectral type B1 III–IVe, with an estimated mass of $11 \pm 1.5\,M_\odot$, effective temperature of approximately 24 000 K, projected rotational velocity $v \sin i \approx 271\,\mathrm{km\,s^{-1}}$, and an equatorial radius of about $5.8\,R_\odot$. It is part of a binary system with an orbital period of 84.1 days, hosting a companion of approximately $2\,M_\odot$ orbiting with an inclination between 50° and 75°. Recent studies (Bjorkman et al., 2002b) suggest that the companion may be a white dwarf, whose interaction with the circumstellar disk leads to γ Cas-like X-ray activity and periodic variations in the emission line profiles, particularly Hα.

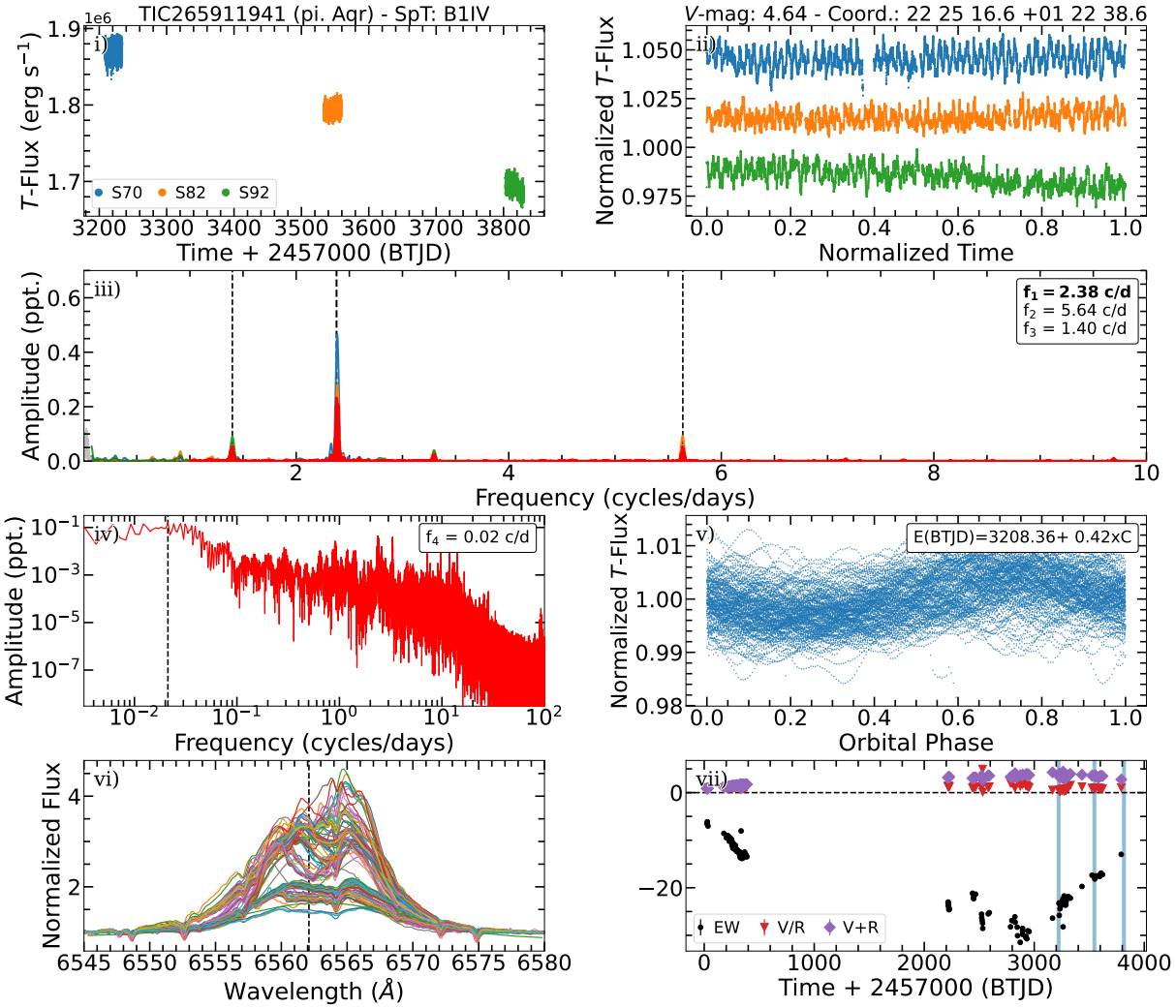

Figure C.83: Panels summarizing the photometric, spectroscopic, and frequency-domain analyses for the target TIC 265911941. (i) Raw T-Flux light curves from different sectors; (ii) normalized T-Flux light curves folded normalized time for each sector; (iii) Lomb-Scargle periodogram highlighting the three main frequencies f_1, f_2, and f_3, with a zoom-in inset; (iv) extended periodogram revealing a low-frequency component f_4; (v) orbital phase-folded light curve; (vi) optical spectrum centered on the Hα line (λ = 6562.8 Å); and (vii) temporal evolution of the equivalent width of the Hα line across available observations. Shaded regions in panel (vii) correspond to observation windows of sectors shown in panel (i).

C.84. TIC 266498398

HD 25348 (BD+20 2465, SAO 75348) is a classical Be star of spectral type B3Vne, located in the constellation Cancer. It has an effective temperature of approximately 17,000 K, a mass around 6.5 $M_\odot$, a radius of about 4.5 $R_\odot$, and a projected rotational velocity $v \sin i \approx 300\,\mathrm{km\,s^{-1}}$. The star exhibits emission lines, particularly Hα, originating from a circumstellar equatorial disk. No confirmed stellar companion has been identified, although the presence of the disk suggests interaction with circumstellar material (Merrill, 1925).

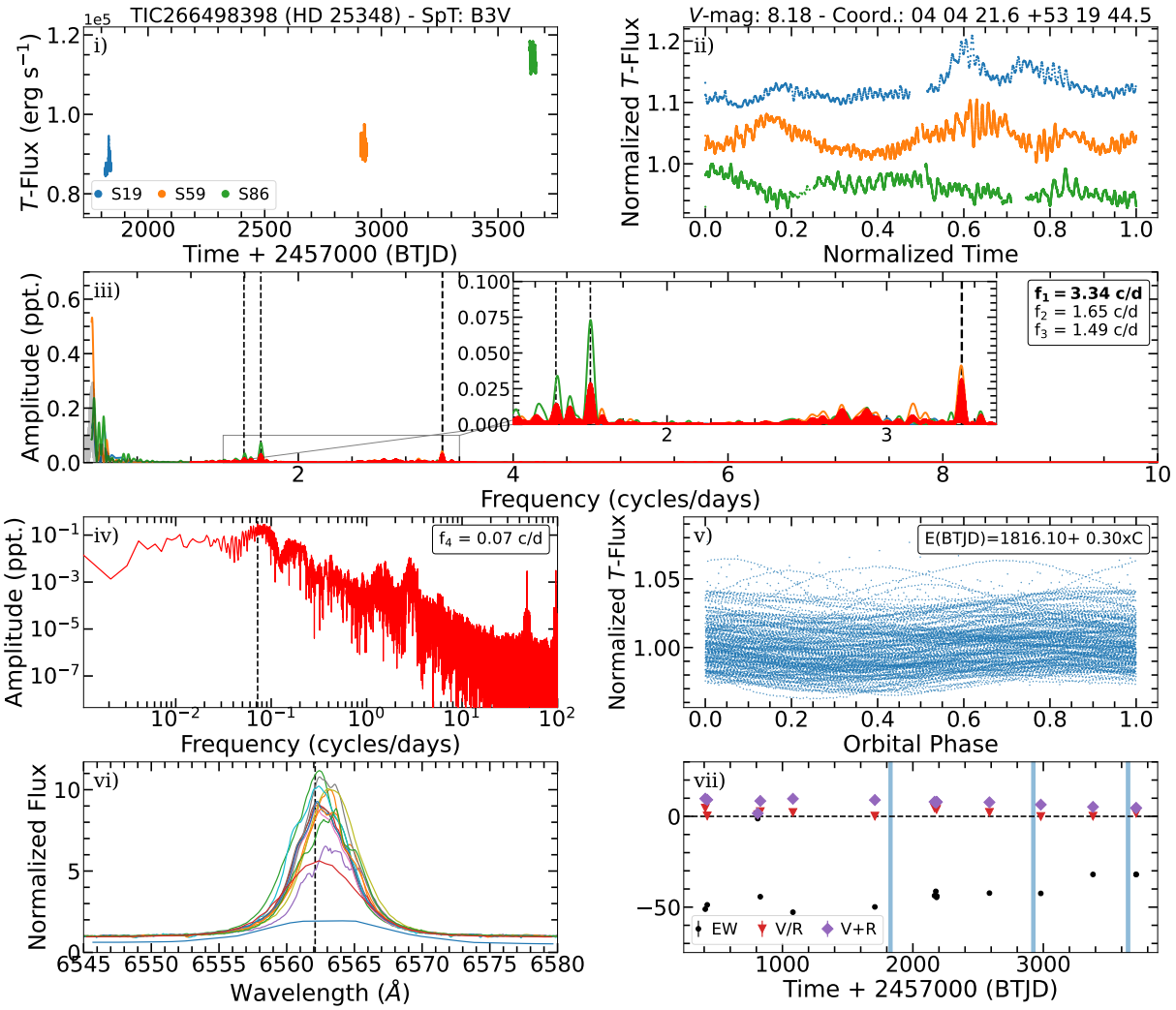

Figure C.84: Panels summarizing the photometric, spectroscopic, and frequency-domain analyses for the target TIC 266498398. (i) Raw T-Flux light curves from different sectors; (ii) normalized T-Flux light curves folded normalized time for each sector; (iii) Lomb-Scargle periodogram highlighting the three main frequencies f_1, f_2, and f_3, with a zoom-in inset; (iv) extended periodogram revealing a low-frequency component f_4; (v) orbital phase-folded light curve; (vi) optical spectrum centered on the Hα line (λ = 6562.8 Å); and (vii) temporal evolution of the equivalent width of the Hα line across available observations. Shaded regions in panel (vii) correspond to observation windows of sectors shown in panel (i).

C.85. TIC 27043894

HD 32811 is a classical Be star of spectral type B8Vne located in the constellation Taurus. It exhibits emission lines typical of Be stars, indicating the presence of a circumstellar disk formed by rapid rotation. Speckle interferometry observations have been conducted to identify possible stellar companions, though no definitive companion has been confirmed (Guerrero et al., 2025b).

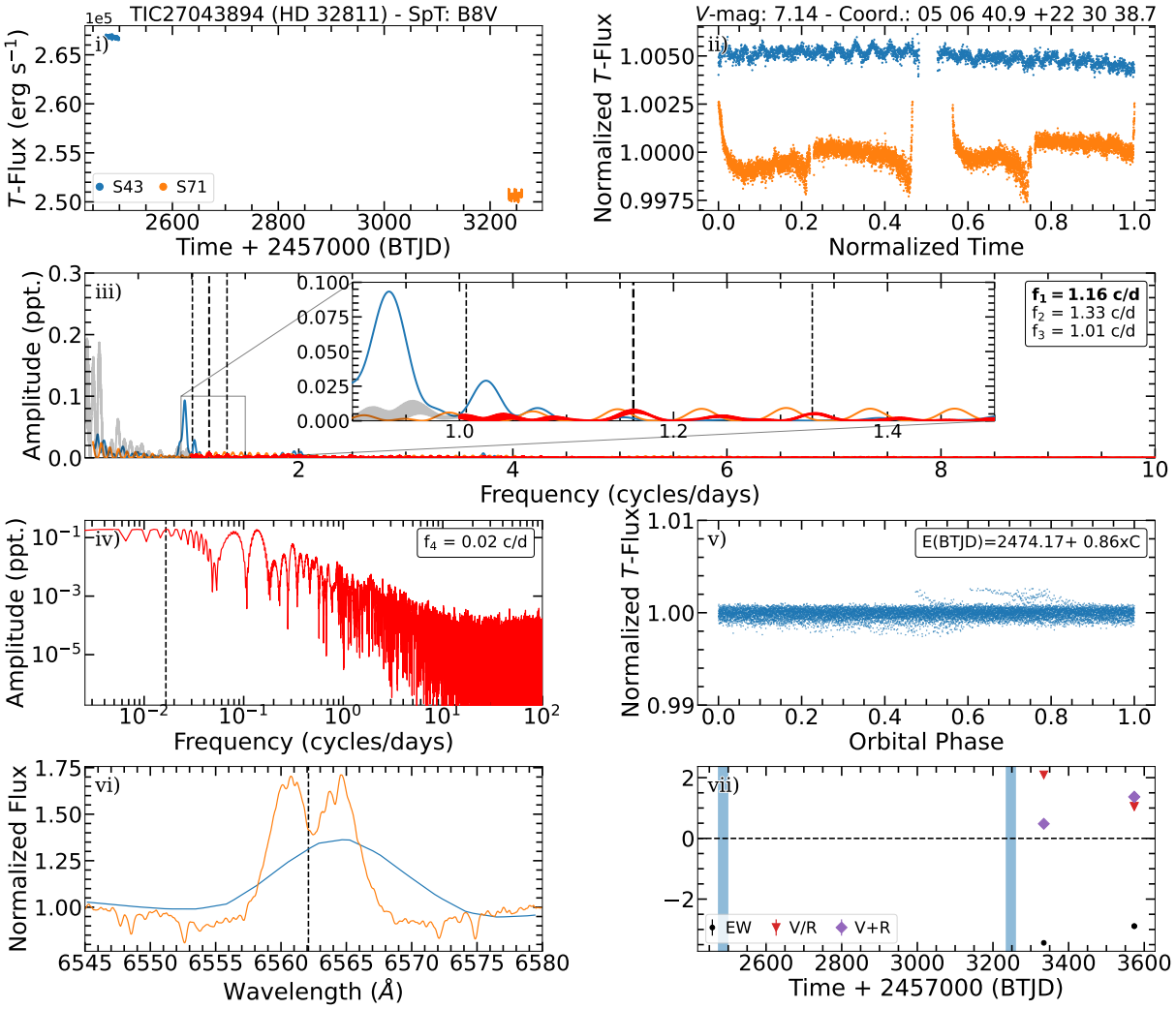

Figure C.85: Panels summarizing the photometric, spectroscopic, and frequency-domain analyses for the target TIC 27043894. (i) Raw T-Flux light curves from different sectors; (ii) normalized T-Flux light curves folded normalized time for each sector; (iii) Lomb-Scargle periodogram highlighting the three main frequencies f_1, f_2, and f_3, with a zoom-in inset; (iv) extended periodogram revealing a low-frequency component f_4; (v) orbital phase-folded light curve; (vi) optical spectrum centered on the Hα line (λ = 6562.8 Å); and (vii) temporal evolution of the equivalent width of the Hα line across available observations. Shaded regions in panel (vii) correspond to observation windows of sectors shown in panel (i).

C.86. TIC 27141005

105 Tauri (HD 32991) is a classical Be star of spectral type B2Ve located in the constellation Taurus. It exhibits typical emission lines associated with a circumstellar decretion disk caused by rapid rotation. The star has an estimated effective temperature of about 21,000 K and a mass near 8.6 $M_\odot$. Recent interferometric observations from the CHARA Array program on the multiplicity of classical Be stars have not detected any stellar companions around HD 32991, suggesting it may be a single star or a binary with an undetectable companion (García et al., 2024).

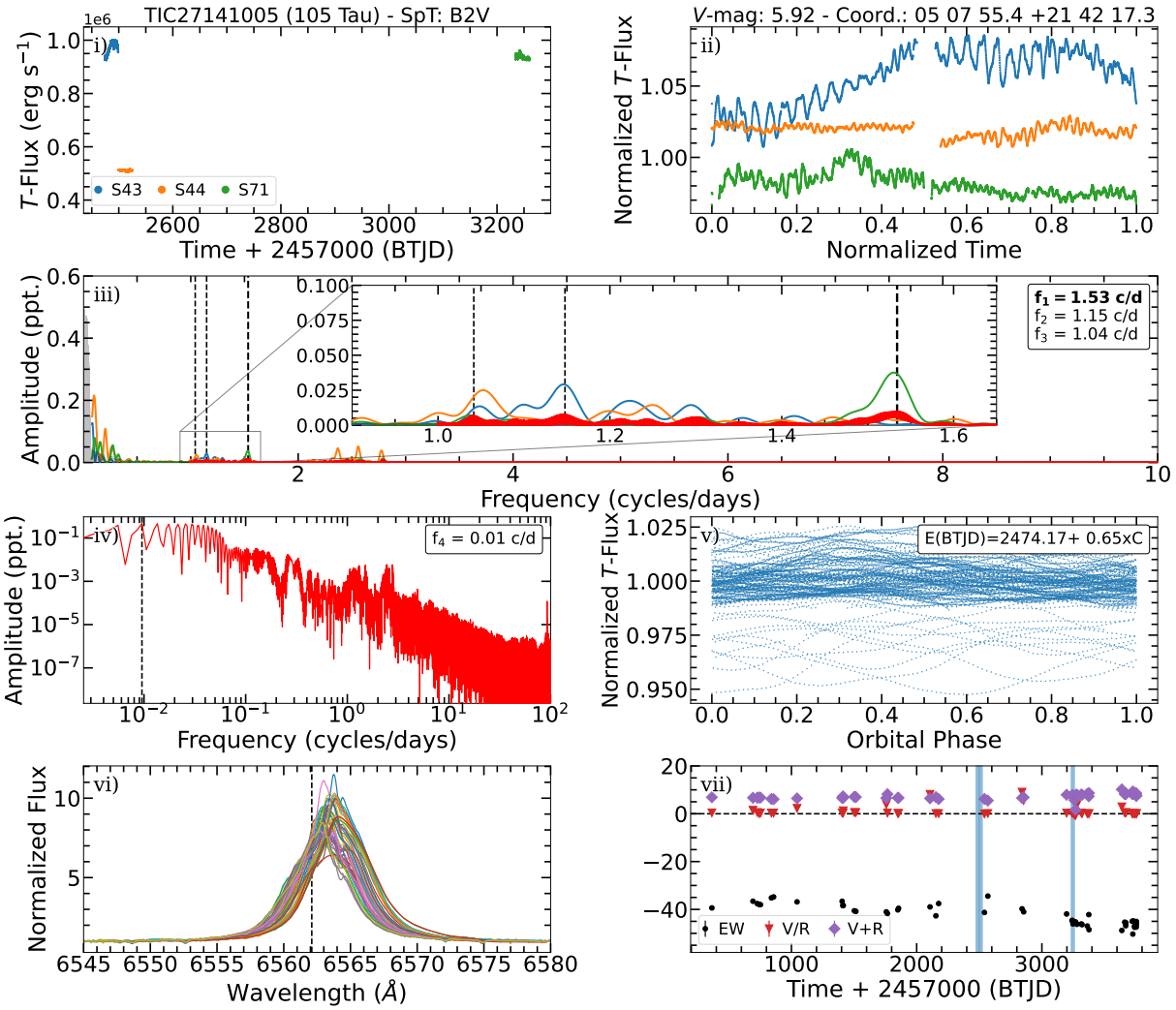

Figure C.86: Panels summarizing the photometric, spectroscopic, and frequency-domain analyses for the target TIC 27141005. (i) Raw T-Flux light curves from different sectors; (ii) normalized T-Flux light curves folded normalized time for each sector; (iii) Lomb-Scargle periodogram highlighting the three main frequencies f_1, f_2, and f_3, with a zoom-in inset; (iv) extended periodogram revealing a low-frequency component f_4; (v) orbital phase-folded light curve; (vi) optical spectrum centered on the Hα line (λ = 6562.8 Å); and (vii) temporal evolution of the equivalent width of the Hα line across available observations. Shaded regions in panel (vii) correspond to observation windows of sectors shown in panel (i).

C.87. TIC 271959772

HD 186485 (TIC 271959772, spectral type B8V) is a main-sequence B-type star with an effective temperature of approximately 12,000 K and a mass around 3.2 $M_\odot$ (Pecaut and Mamajek, 2013). Unlike classical Be stars, it does not exhibit emission lines or a circumstellar disk. This star was investigated by Kervella et al. (2019) in their study of nearby stars using Gaia DR2 astrometry to detect stellar and substellar companions; however, no significant companions were found for HD 186485.

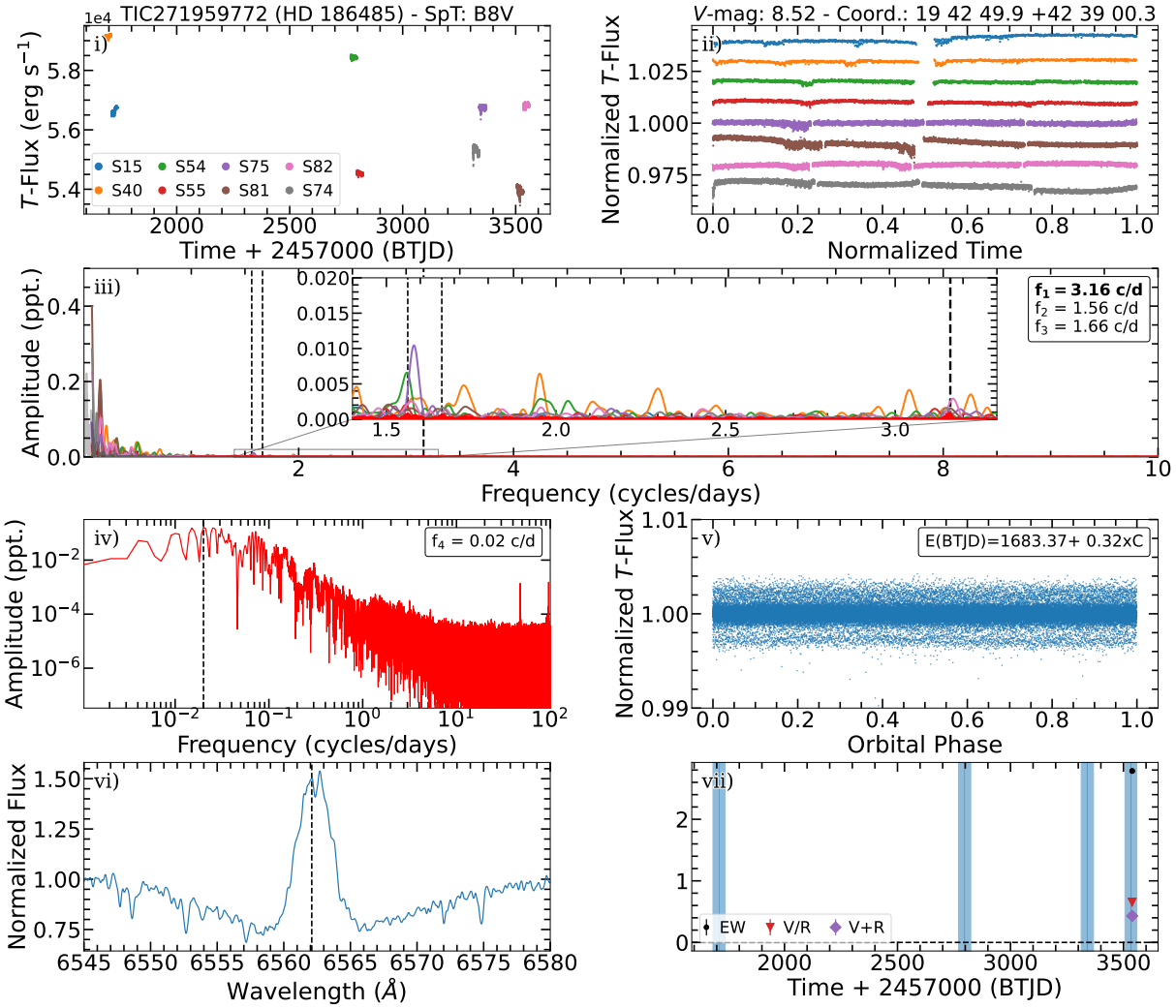

Figure C.87: Panels summarizing the photometric, spectroscopic, and frequency-domain analyses for the target TIC 271959772. (i) Raw T-Flux light curves from different sectors; (ii) normalized T-Flux light curves folded normalized time for each sector; (iii) Lomb-Scargle periodogram highlighting the three main frequencies f_1, f_2, and f_3, with a zoom-in inset; (iv) extended periodogram revealing a low-frequency component f_4; (v) orbital phase-folded light curve; (vi) optical spectrum centered on the Hα line (λ = 6562.8 Å); and (vii) temporal evolution of the equivalent width of the Hα line across available observations. Shaded regions in panel (vii) correspond to observation windows of sectors shown in panel (i).

C.88. TIC 279192753

HD 34123 (TIC 279192753, spectral type B6III) is a B-type giant star with an estimated effective temperature around 14,000 K and a mass approximately 5.5 $M_\odot$ (Gray and Corbally, 2009; Pecaut and Mamajek, 2013). It does not show emission lines characteristic of Be stars. Astrometric studies, such as Kervella et al. (2019), have not found evidence of stellar or substellar companions around this star.

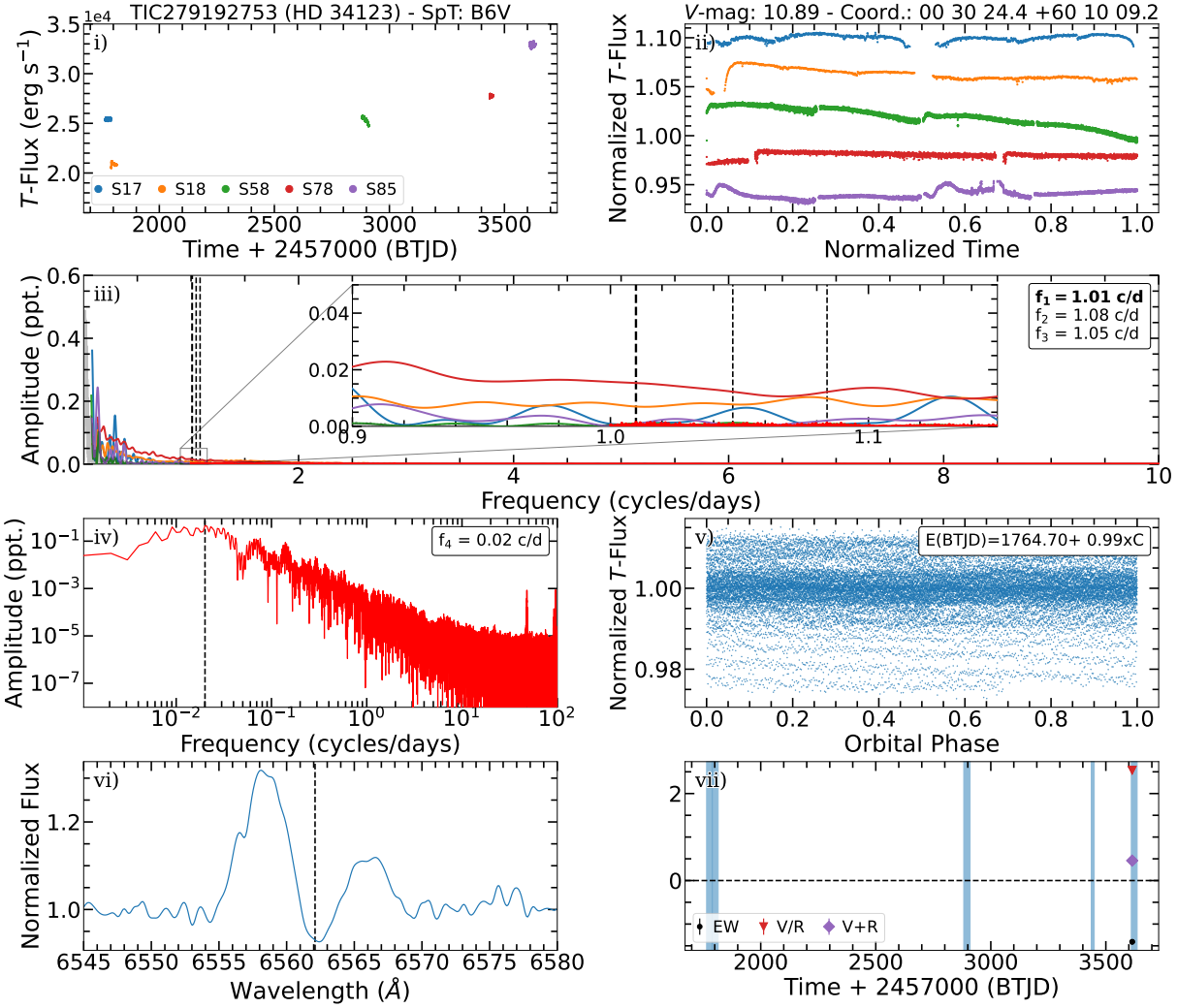

Figure C.88: Panels summarizing the photometric, spectroscopic, and frequency-domain analyses for the target TIC 279192753. (i) Raw T-Flux light curves from different sectors; (ii) normalized T-Flux light curves folded normalized time for each sector; (iii) Lomb-Scargle periodogram highlighting the three main frequencies f_1, f_2, and f_3, with a zoom-in inset; (iv) extended periodogram revealing a low-frequency component f_4; (v) orbital phase-folded light curve; (vi) optical spectrum centered on the Hα line (λ = 6562.8 Å); and (vii) temporal evolution of the equivalent width of the Hα line across available observations. Shaded regions in panel (vii) correspond to observation windows of sectors shown in panel (i).

C.89. TIC 281047621

ome Ori (HD 37490) is a Be star of type B3V with no signs of binarity.

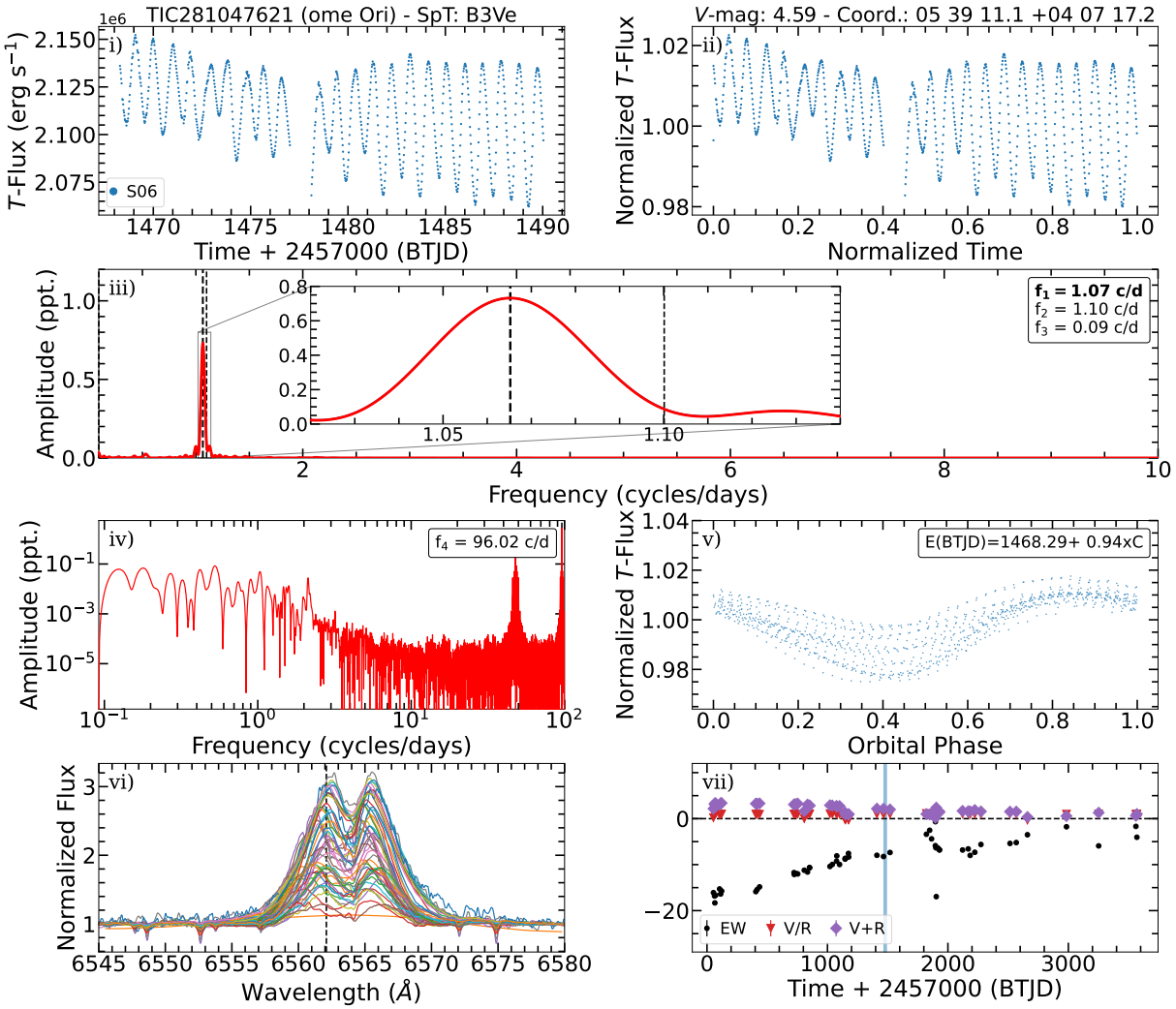

Figure C.89: Panels summarizing the photometric, spectroscopic, and frequency-domain analyses for the target TIC 281047621. (i) Raw T-Flux light curves from different sectors; (ii) normalized T-Flux light curves folded normalized time for each sector; (iii) Lomb-Scargle periodogram highlighting the three main frequencies f_1, f_2, and f_3, with a zoom-in inset; (iv) extended periodogram revealing a low-frequency component f_4; (v) orbital phase-folded light curve; (vi) optical spectrum centered on the Hα line (λ = 6562.8 Å); and (vii) temporal evolution of the equivalent width of the Hα line across available observations. Shaded regions in panel (vii) correspond to observation windows of sectors shown in panel (i).

C.90. TIC 281717549

HD 49787 is a Be star of type B1V with no signs of binarity.

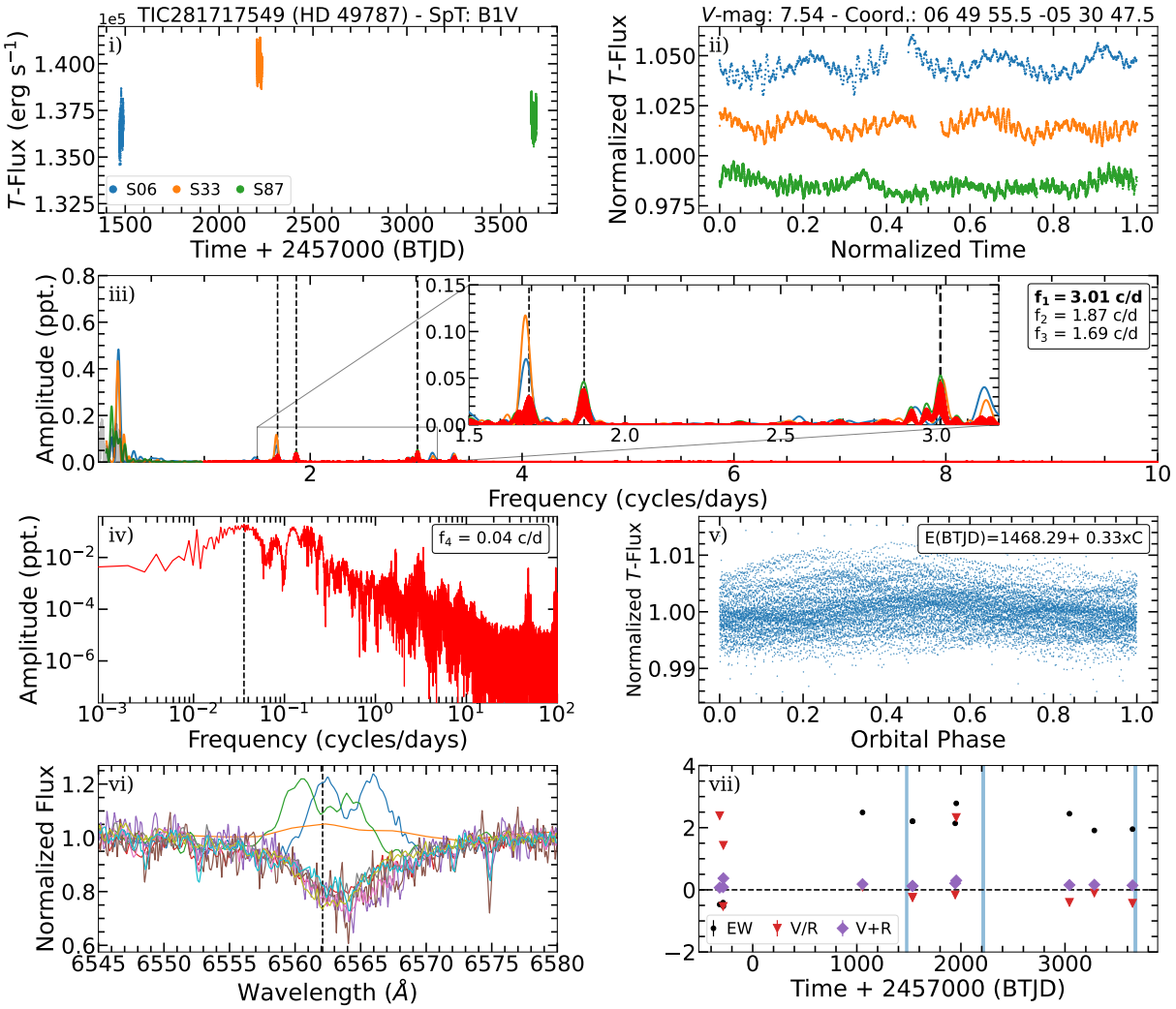

Figure C.90: Panels summarizing the photometric, spectroscopic, and frequency-domain analyses for the target TIC 281717549. (i) Raw T-Flux light curves from different sectors; (ii) normalized T-Flux light curves folded normalized time for each sector; (iii) Lomb-Scargle periodogram highlighting the three main frequencies f_1, f_2, and f_3, with a zoom-in inset; (iv) extended periodogram revealing a low-frequency component f_4; (v) orbital phase-folded light curve; (vi) optical spectrum centered on the Hα line (λ = 6562.8 Å); and (vii) temporal evolution of the equivalent width of the Hα line across available observations. Shaded regions in panel (vii) correspond to observation windows of sectors shown in panel (i).

C.91. TIC 283206453

HD 51193 is a Be star of type B1V with no signs of binarity.

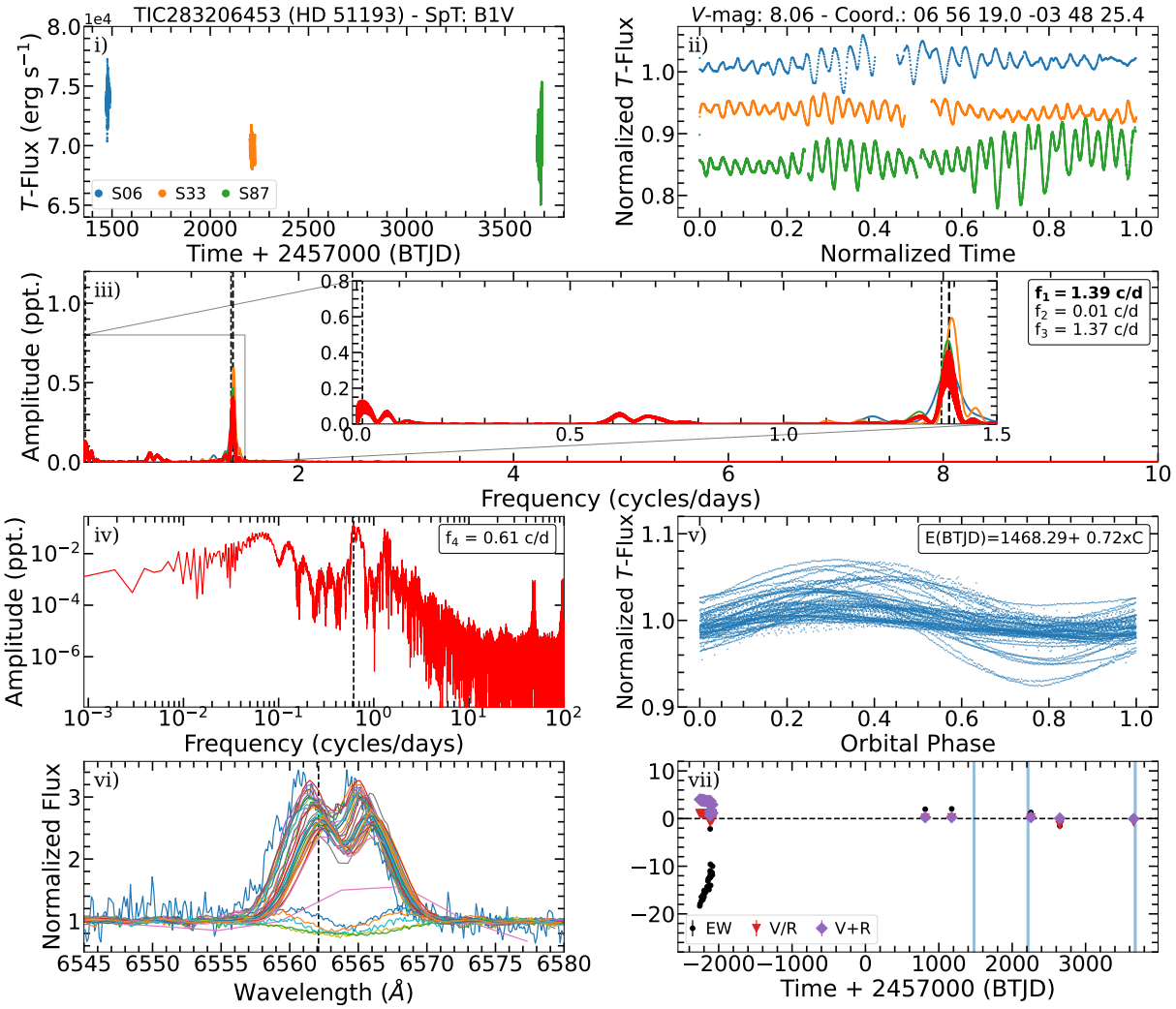

Figure C.91: Panels summarizing the photometric, spectroscopic, and frequency-domain analyses for the target TIC 283206453. (i) Raw T-Flux light curves from different sectors; (ii) normalized T-Flux light curves folded normalized time for each sector; (iii) Lomb-Scargle periodogram highlighting the three main frequencies f_1, f_2, and f_3, with a zoom-in inset; (iv) extended periodogram revealing a low-frequency component f_4; (v) orbital phase-folded light curve; (vi) optical spectrum centered on the Hα line (λ = 6562.8 Å); and (vii) temporal evolution of the equivalent width of the Hα line across available observations. Shaded regions in panel (vii) correspond to observation windows of sectors shown in panel (i).

C.92. TIC 28569279

β Lyr (HD 174638) has a Be star, being an eclipsing and spectroscopic binary system.

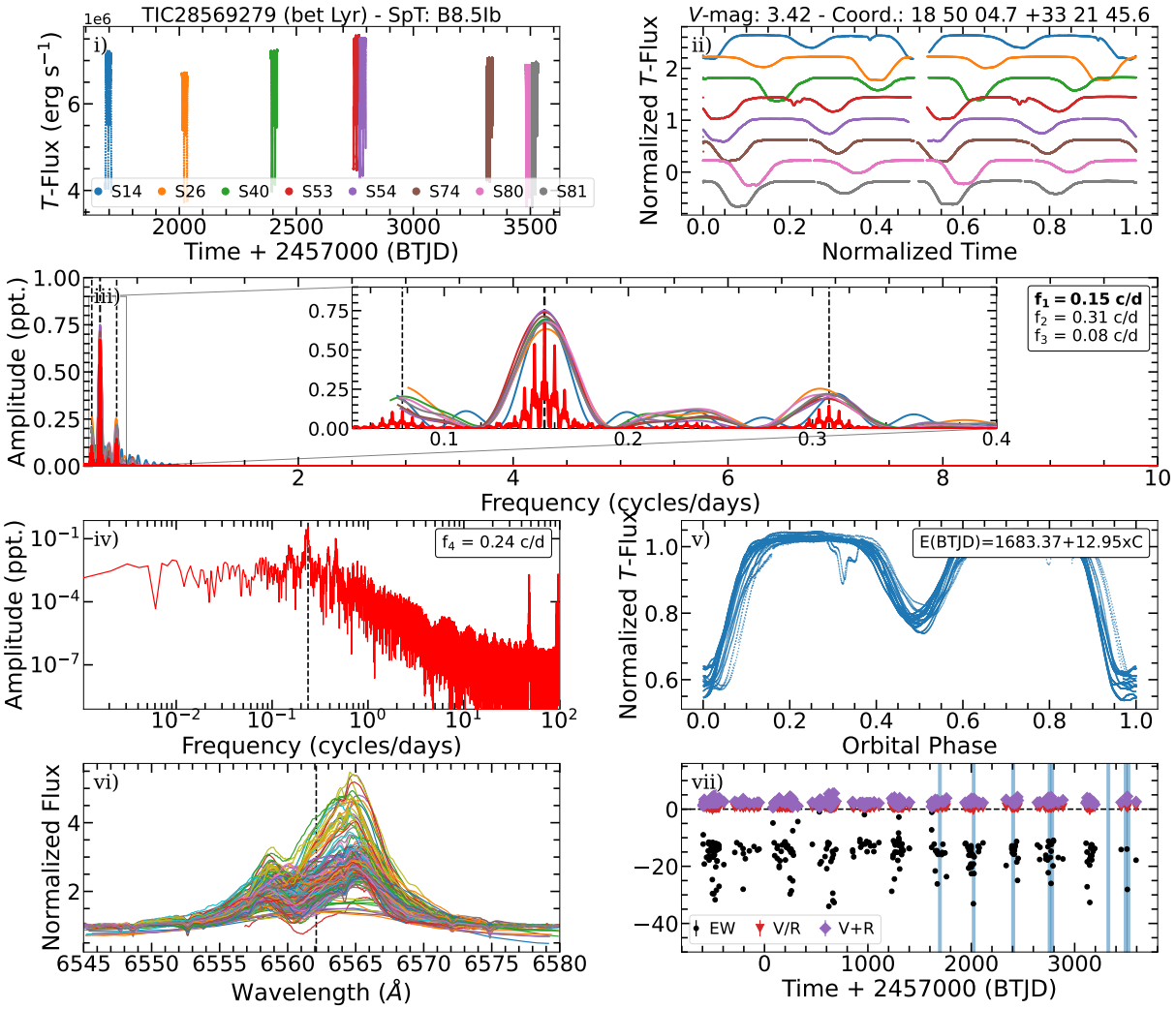

Figure C.92: Panels summarizing the photometric, spectroscopic, and frequency-domain analyses for the target TIC 28569279. (i) Raw T-Flux light curves from different sectors; (ii) normalized T-Flux light curves folded normalized time for each sector; (iii) Lomb-Scargle periodogram highlighting the three main frequencies f_1, f_2, and f_3, with a zoom-in inset; (iv) extended periodogram revealing a low-frequency component f_4; (v) orbital phase-folded light curve; (vi) optical spectrum centered on the Hα line (λ = 6562.8 Å); and (vii) temporal evolution of the equivalent width of the Hα line across available observations. Shaded regions in panel (vii) correspond to observation windows of sectors shown in panel (i).

C.93. TIC 285937814

ψ Per (HD 22192) is a Be star with no signs of binary.

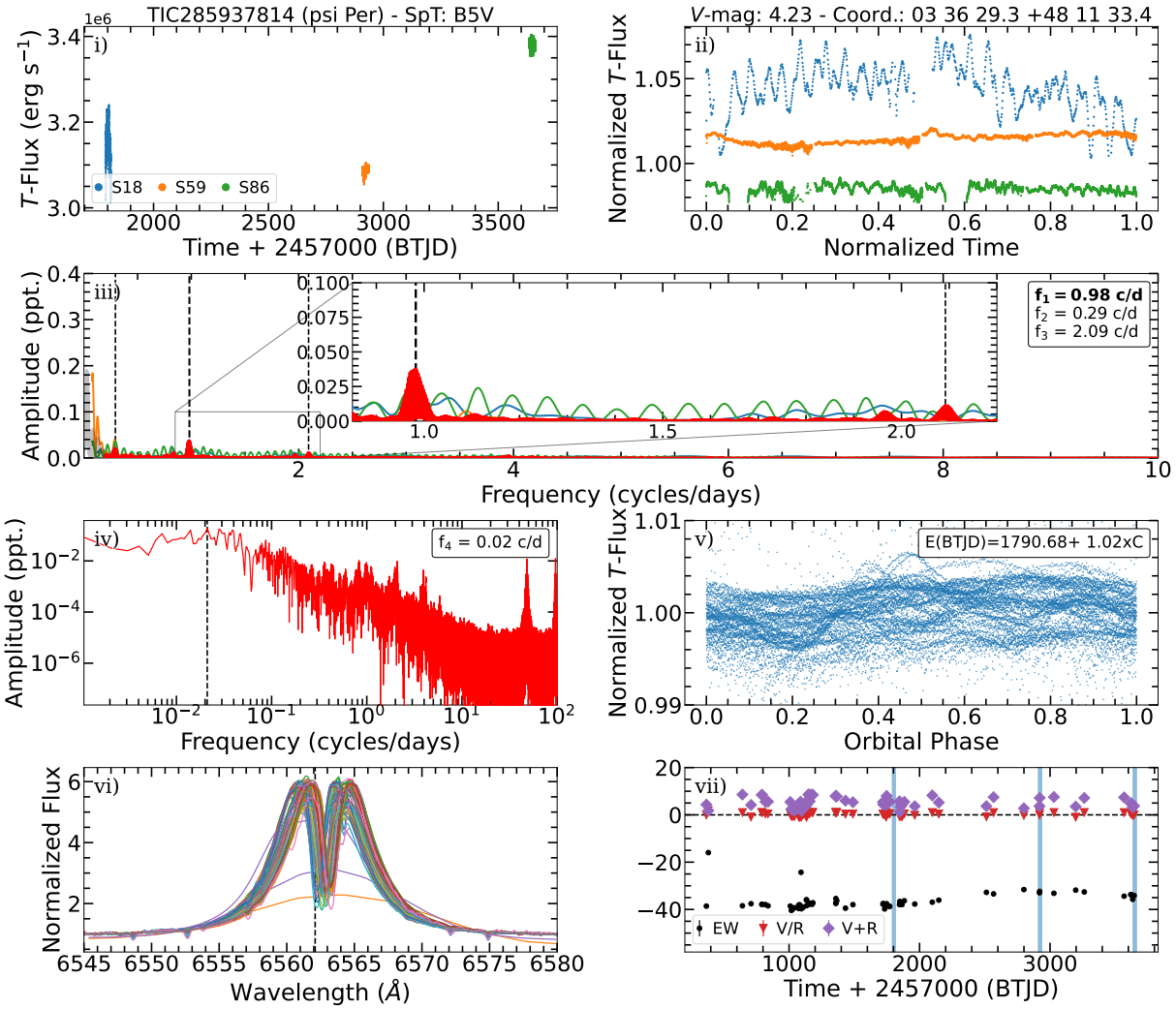

Figure C.93: Panels summarizing the photometric, spectroscopic, and frequency-domain analyses for the target TIC 285937814. (i) Raw T-Flux light curves from different sectors; (ii) normalized T-Flux light curves folded normalized time for each sector; (iii) Lomb-Scargle periodogram highlighting the three main frequencies f_1, f_2, and f_3, with a zoom-in inset; (iv) extended periodogram revealing a low-frequency component f_4; (v) orbital phase-folded light curve; (vi) optical spectrum centered on the Hα line (λ = 6562.8 Å); and (vii) temporal evolution of the equivalent width of the Hα line across available observations. Shaded regions in panel (vii) correspond to observation windows of sectors shown in panel (i).

C.94. TIC 2940839

IU Aur (HD 35652) is a candidate triple system, but with no signs of a Be star in its system (Borkovits et al., 2025).

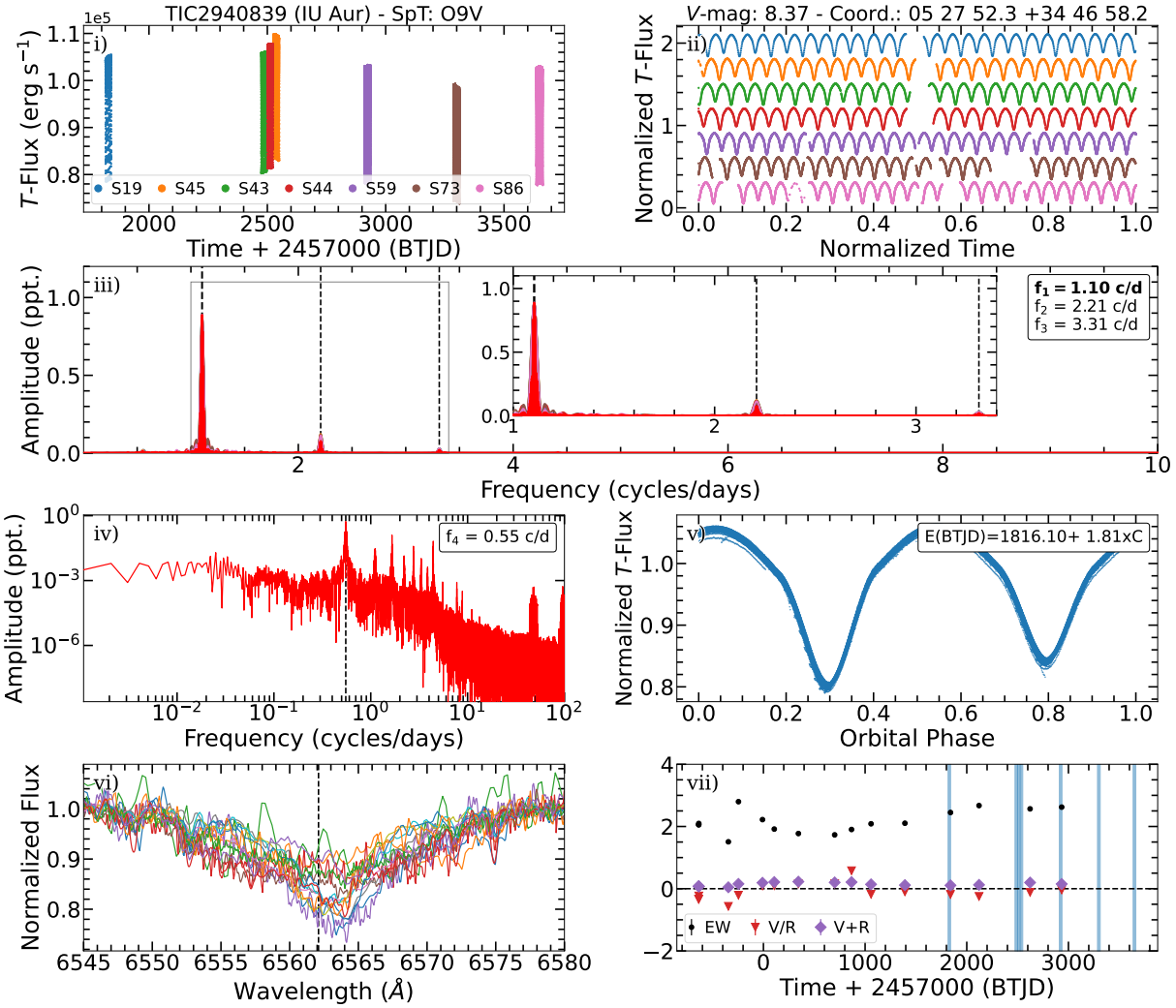

Figure C.94: Panels summarizing the photometric, spectroscopic, and frequency-domain analyses for the target TIC 2940839. (i) Raw T-Flux light curves from different sectors; (ii) normalized T-Flux light curves folded normalized time for each sector; (iii) Lomb-Scargle periodogram highlighting the three main frequencies f_1, f_2, and f_3, with a zoom-in inset; (iv) extended periodogram revealing a low-frequency component f_4; (v) orbital phase-folded light curve; (vi) optical spectrum centered on the Hα line (λ = 6562.8 Å); and (vii) temporal evolution of the equivalent width of the Hα line across available observations. Shaded regions in panel (vii) correspond to observation windows of sectors shown in panel (i).

C.95. TIC 294355648

f01 Ori (HD 42545) is a Be star, but with no signs of binarity.

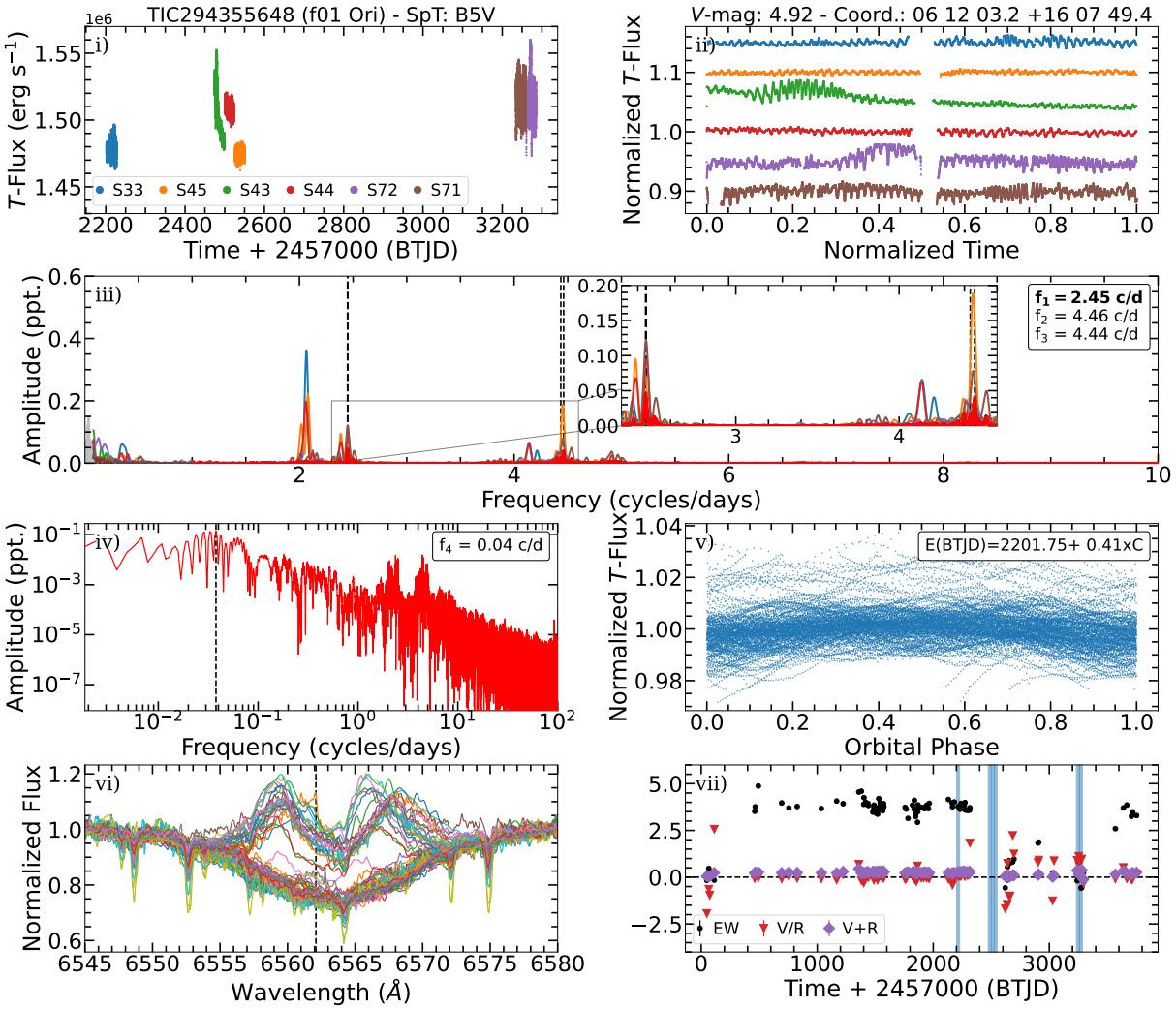

Figure C.95: Panels summarizing the photometric, spectroscopic, and frequency-domain analyses for the target TIC 294355648. (i) Raw T-Flux light curves from different sectors; (ii) normalized T-Flux light curves folded normalized time for each sector; (iii) Lomb-Scargle periodogram highlighting the three main frequencies f_1, f_2, and f_3, with a zoom-in inset; (iv) extended periodogram revealing a low-frequency component f_4; (v) orbital phase-folded light curve; (vi) optical spectrum centered on the Hα line (λ = 6562.8 Å); and (vii) temporal evolution of the equivalent width of the Hα line across available observations. Shaded regions in panel (vii) correspond to observation windows of sectors shown in panel (i).

C.96. TIC 29628522

HD 45871 is a Be star, where astrometric studies, such as Kervella et al. (2019), have found evidence of stellar or substellar companions around this star.

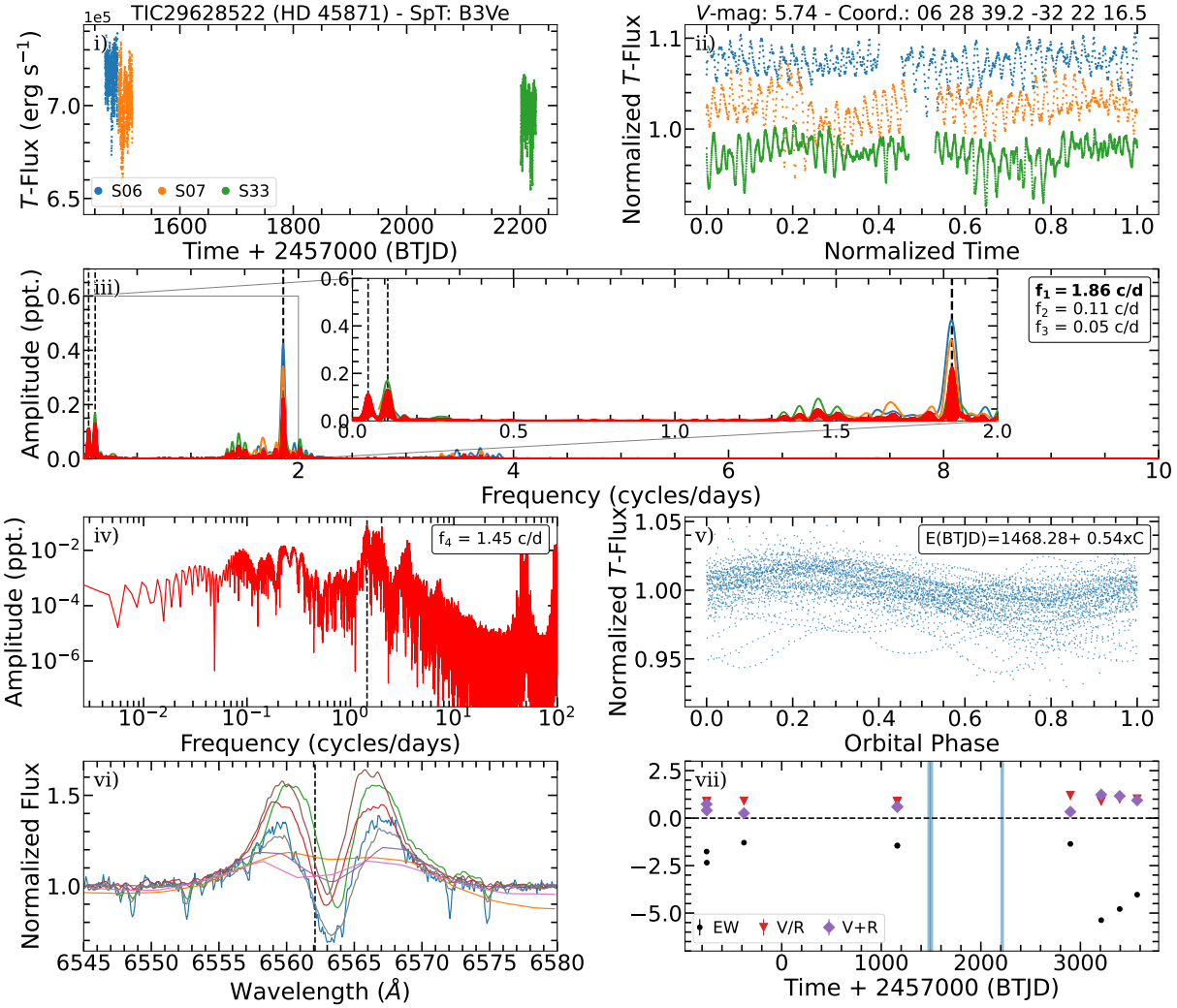

Figure C.96: Panels summarizing the photometric, spectroscopic, and frequency-domain analyses for the target TIC 29628522. (i) Raw T-Flux light curves from different sectors; (ii) normalized T-Flux light curves folded normalized time for each sector; (iii) Lomb-Scargle periodogram highlighting the three main frequencies f_1, f_2, and f_3, with a zoom-in inset; (iv) extended periodogram revealing a low-frequency component f_4; (v) orbital phase-folded light curve; (vi) optical spectrum centered on the Hα line (λ = 6562.8 Å); and (vii) temporal evolution of the equivalent width of the Hα line across available observations. Shaded regions in panel (vii) correspond to observation windows of sectors shown in panel (i).

C.97. TIC 296969980

tet Cir (HD 131492) is a Be star, but with no signs of binarity.

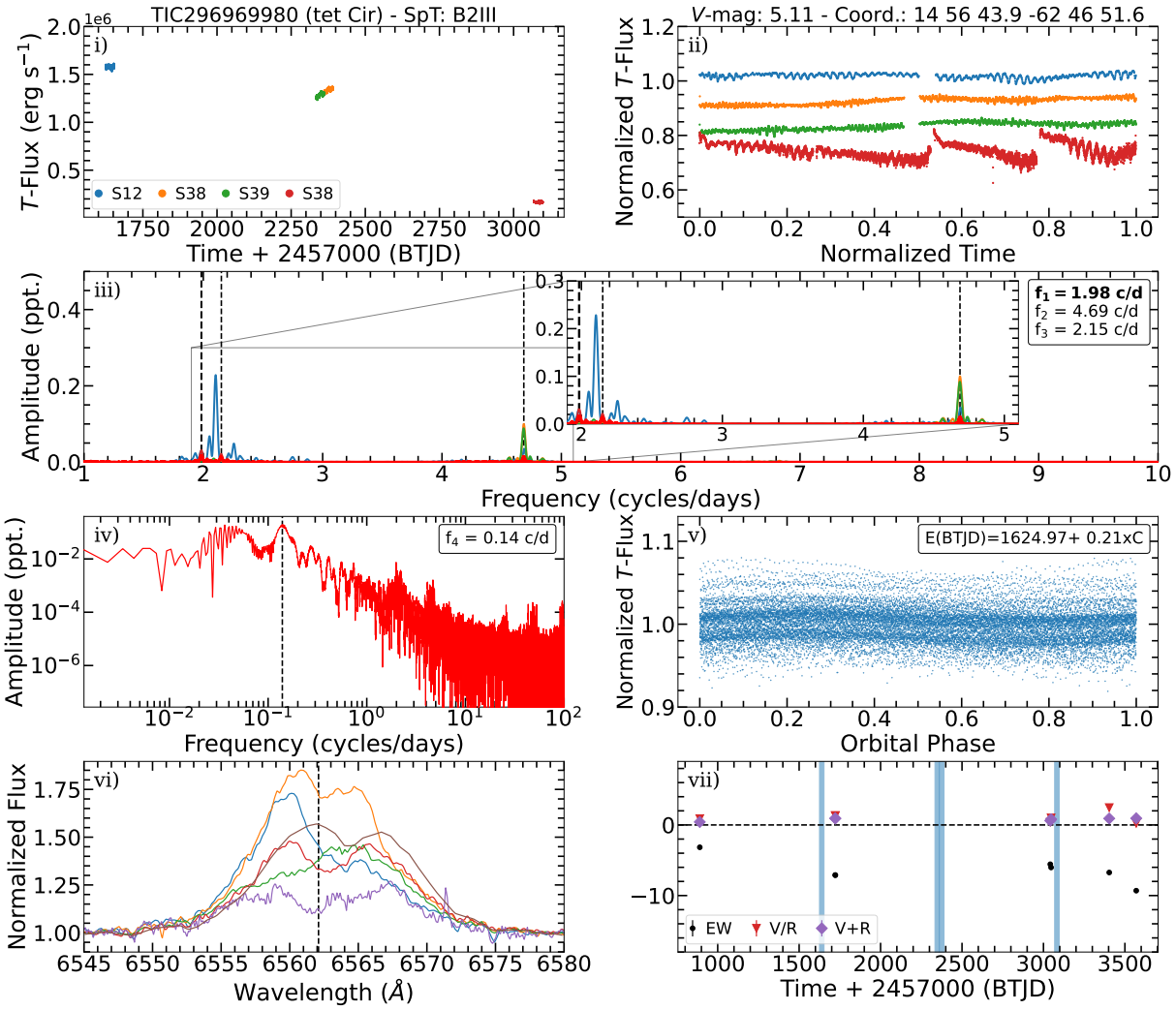

Figure C.97: Panels summarizing the photometric, spectroscopic, and frequency-domain analyses for the target TIC 296969980. (i) Raw T-Flux light curves from different sectors; (ii) normalized T-Flux light curves folded normalized time for each sector; (iii) Lomb-Scargle periodogram highlighting the three main frequencies f_1, f_2, and f_3, with a zoom-in inset; (iv) extended periodogram revealing a low-frequency component f_4; (v) orbital phase-folded light curve; (vi) optical spectrum centered on the Hα line (λ = 6562.8 Å); and (vii) temporal evolution of the equivalent width of the Hα line across available observations. Shaded regions in panel (vii) correspond to observation windows of sectors shown in panel (i).

C.98. TIC 304114338

60 Cyg is a Be+sdOB binary Rivinius et al. (2025b).

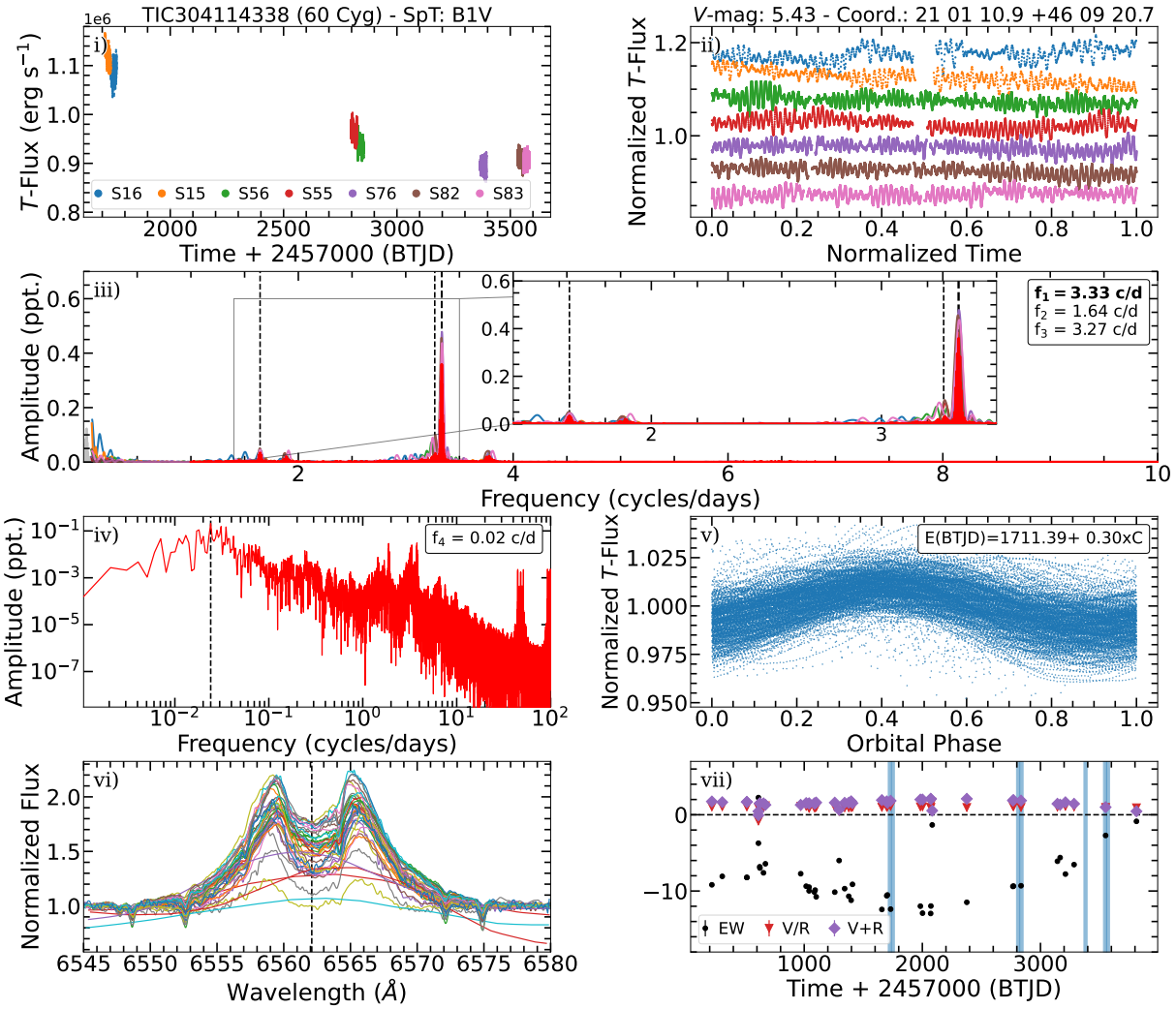

Figure C.98: Panels summarizing the photometric, spectroscopic, and frequency-domain analyses for the target TIC 304114338. (i) Raw T-Flux light curves from different sectors; (ii) normalized T-Flux light curves folded normalized time for each sector; (iii) Lomb-Scargle periodogram highlighting the three main frequencies f_1, f_2, and f_3, with a zoom-in inset; (iv) extended periodogram revealing a low-frequency component f_4; (v) orbital phase-folded light curve; (vi) optical spectrum centered on the Hα line (λ = 6562.8 Å); and (vii) temporal evolution of the equivalent width of the Hα line across available observations. Shaded regions in panel (vii) correspond to observation windows of sectors shown in panel (i).

C.99. TIC 30562668

Labadie-Bartz et al. (2022) classified HD 76838 as a non-classical Be star, with a pulsating β Cepheid composing its system.

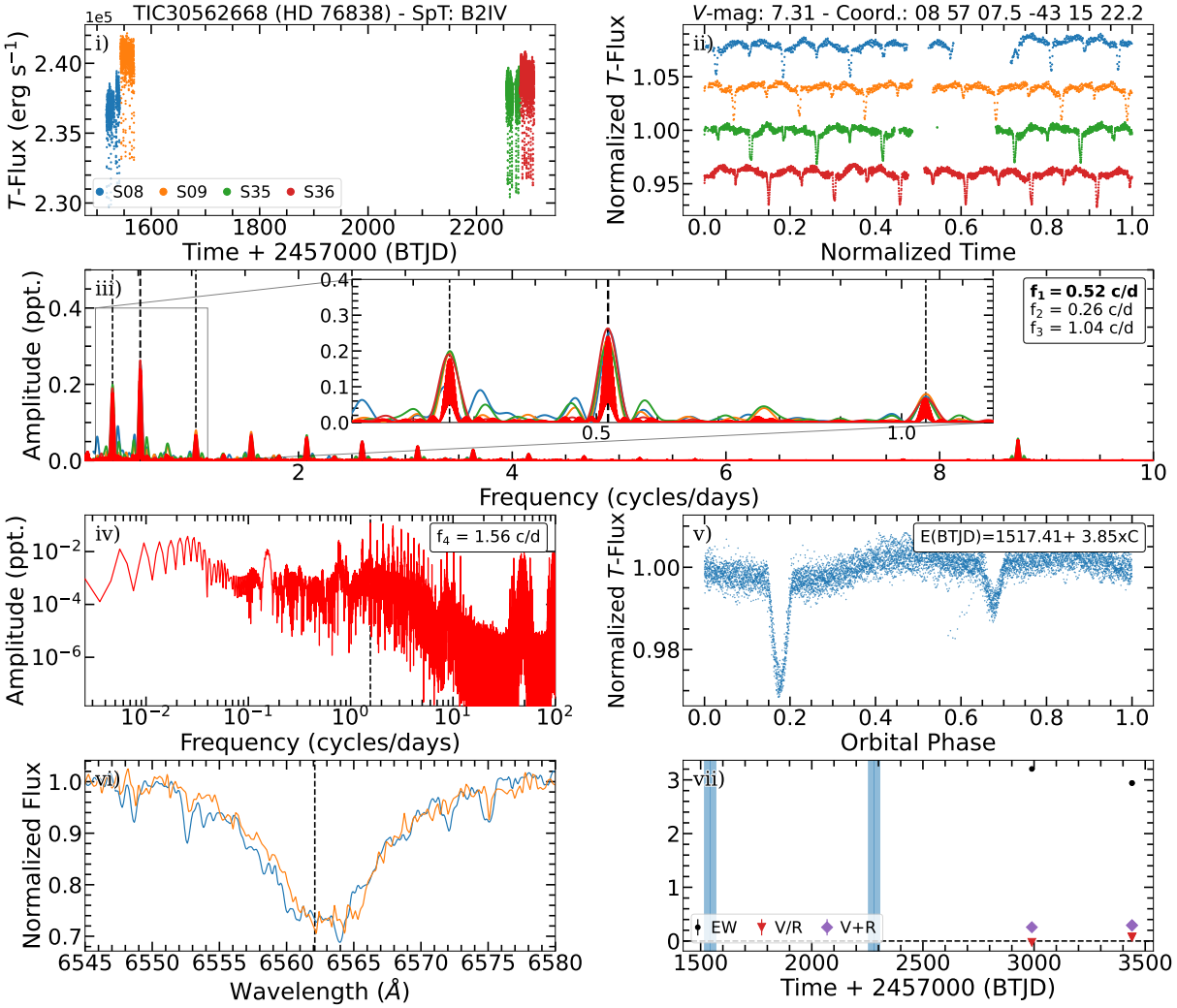

Figure C.99: Panels summarizing the photometric, spectroscopic, and frequency-domain analyses for the target TIC 30562668. (i) Raw T-Flux light curves from different sectors; (ii) normalized T-Flux light curves folded normalized time for each sector; (iii) Lomb-Scargle periodogram highlighting the three main frequencies f_1, f_2, and f_3, with a zoom-in inset; (iv) extended periodogram revealing a low-frequency component f_4; (v) orbital phase-folded light curve; (vi) optical spectrum centered on the Hα line (λ = 6562.8 Å); and (vii) temporal evolution of the equivalent width (EW) of the Hα line across available observations. Shaded regions in panel (vii) correspond to observation windows of sectors shown in panel (i).

C.100. TIC 310852121

bet Psc (HD 217891) is a Be star, but with no signs of binarity.

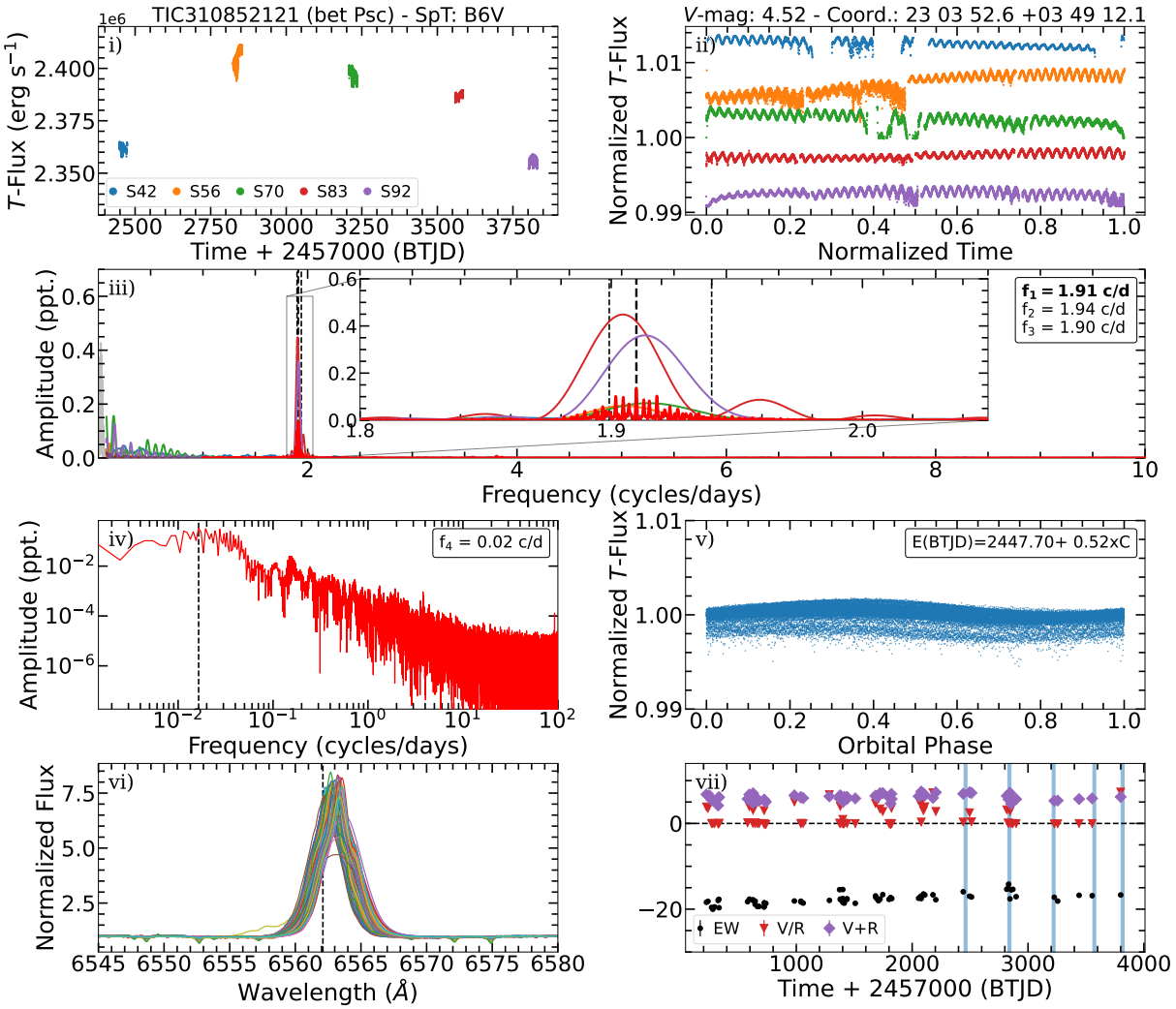

Figure C.100: Panels summarizing the photometric, spectroscopic, and frequency-domain analyses for the target TIC 310852121. (i) Raw T-Flux light curves from different sectors; (ii) normalized T-Flux light curves folded normalized time for each sector; (iii) Lomb-Scargle periodogram highlighting the three main frequencies f_1, f_2, and f_3, with a zoom-in inset; (iv) extended periodogram revealing a low-frequency component f_4; (v) orbital phase-folded light curve; (vi) optical spectrum centered on the Hα line (λ = 6562.8 Å); and (vii) temporal evolution of the equivalent width of the Hα line across available observations. Shaded regions in panel (vii) correspond to observation windows of sectors shown in panel (i).

C.101. TIC 311282109

Despite being presented as a Be star by Guerrero et al. (2025a), HD 37838 no evidence was found to classify this system as a Be star or binary system. No spectrum was found in the BESS catalog.

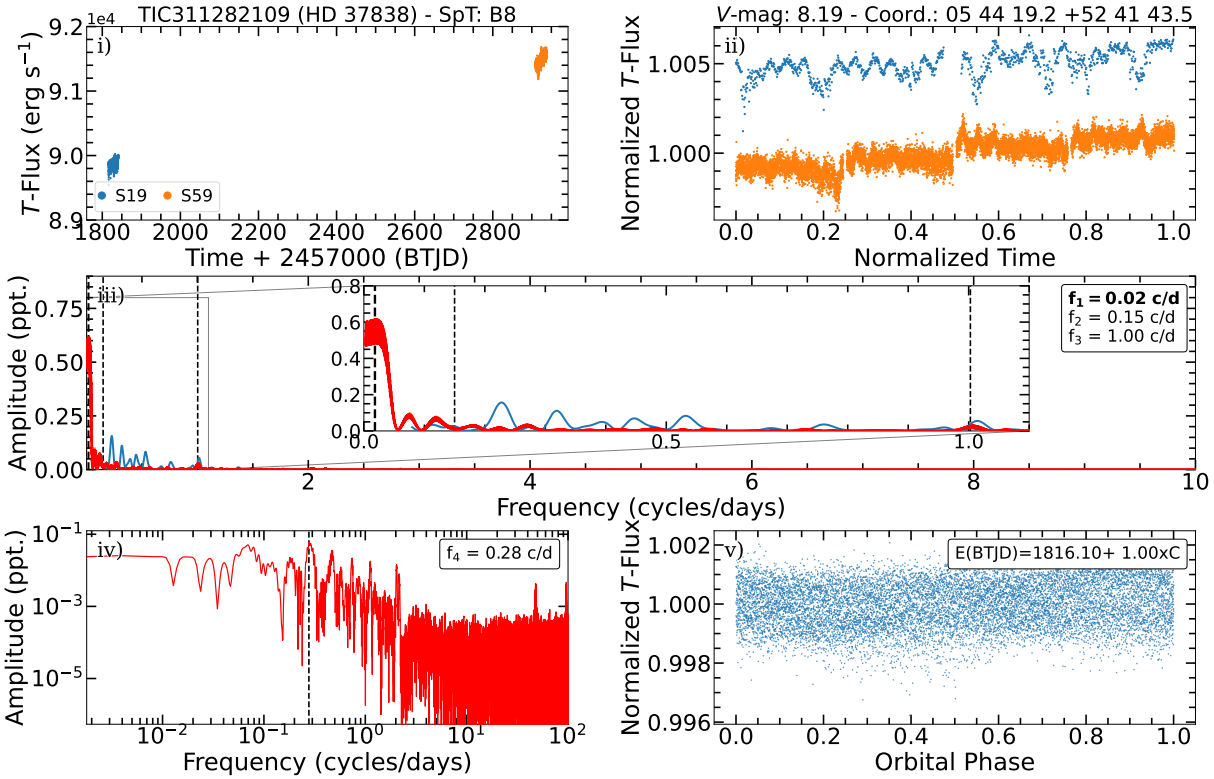

Figure C.101: Panels summarizing the photometric and frequency-domain analyses for the target TIC 311282109. (i) Raw T-Flux light curves from different sectors; (ii) normalized T-Flux light curves folded normalized time for each sector; (iii) Lomb-Scargle periodogram highlighting the three main frequencies f_1, f_2, and f_3, with a zoom-in inset; (iv) extended periodogram revealing a low-frequency component f_4; (v) orbital phase-folded light curve.

C.102. TIC 312730071

HD 40254 is a Be star, but with no signs of binarity.

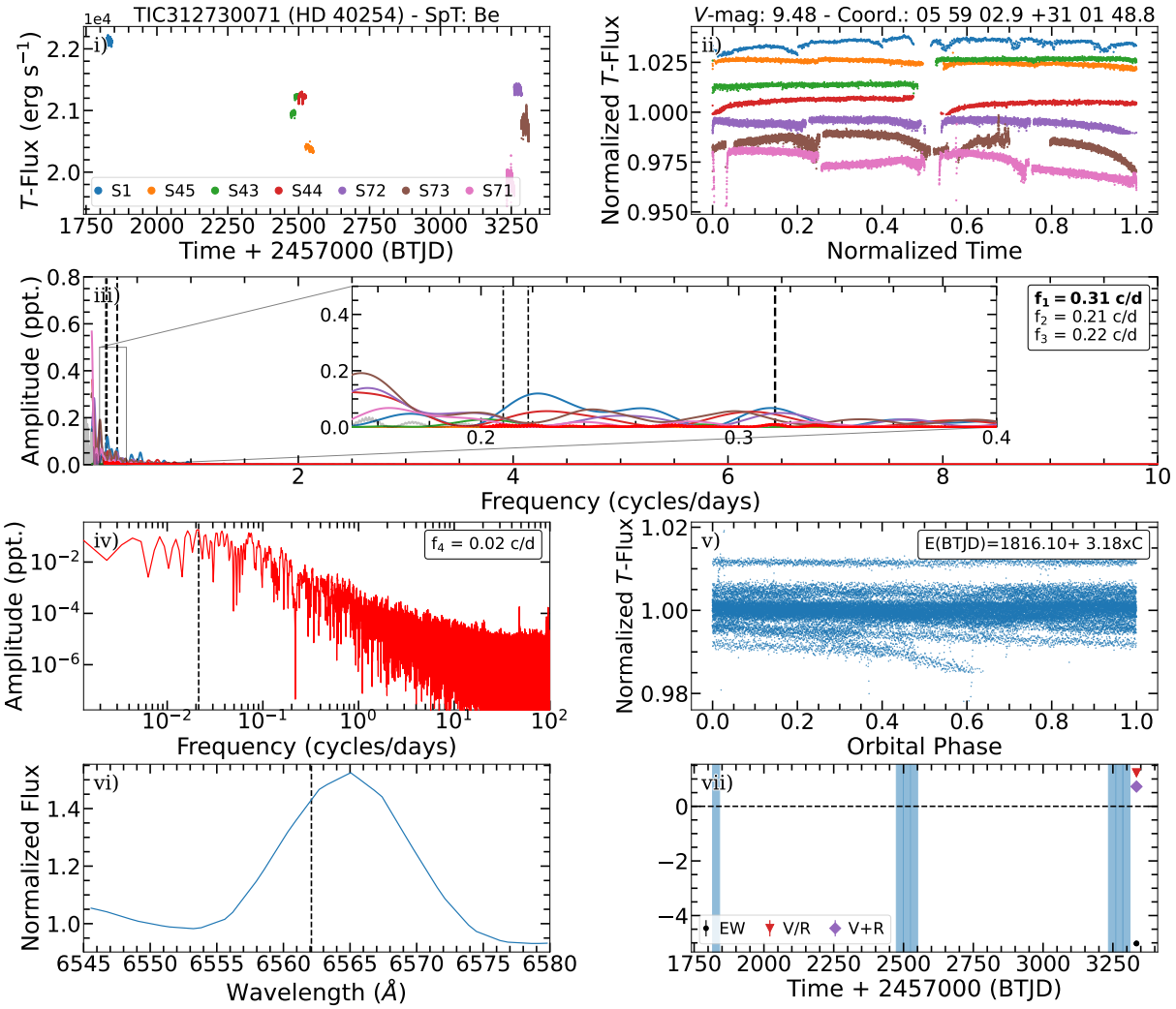

Figure C.102: Panels summarizing the photometric, spectroscopic, and frequency-domain analyses for the target TIC 312730071. (i) Raw T-Flux light curves from different sectors; (ii) normalized T-Flux light curves folded normalized time for each sector; (iii) Lomb-Scargle periodogram highlighting the three main frequencies f_1, f_2, and f_3, with a zoom-in inset; (iv) extended periodogram revealing a low-frequency component f_4; (v) orbital phase-folded light curve; (vi) optical spectrum centered on the Hα line (λ = 6562.8 Å); and (vii) temporal evolution of the equivalent width of the Hα line across available observations. Shaded regions in panel (vii) correspond to observation windows of sectors shown in panel (i).

C.103. TIC 317958778

omi Aqr (HD 209409) is a Be star, but with no signs of binarity.

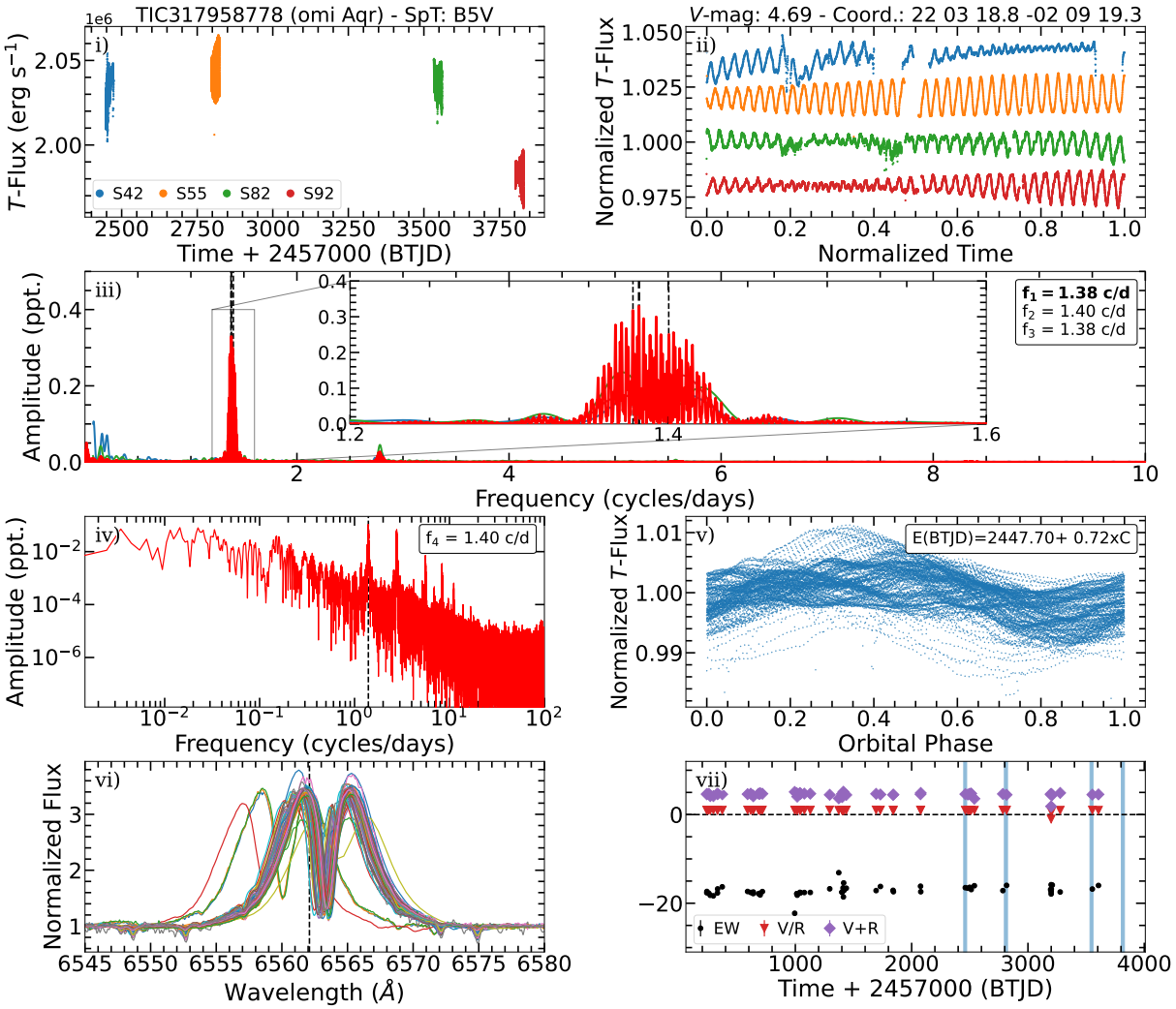

Figure C.103: Panels summarizing the photometric, spectroscopic, and frequency-domain analyses for the target TIC 317958778. (i) Raw T-Flux light curves from different sectors; (ii) normalized T-Flux light curves folded normalized time for each sector; (iii) Lomb-Scargle periodogram highlighting the three main frequencies f_1, f_2, and f_3, with a zoom-in inset; (iv) extended periodogram revealing a low-frequency component f_4; (v) orbital phase-folded light curve; (vi) optical spectrum centered on the Hα line (λ = 6562.8 Å); and (vii) temporal evolution of the equivalent width of the Hα line across available observations. Shaded regions in panel (vii) correspond to observation windows of sectors shown in panel (i).

C.104. TIC 322060937

HD 206135 is a Be star, but with no signs of binarity. No spectrum was found in the BESS catalog.

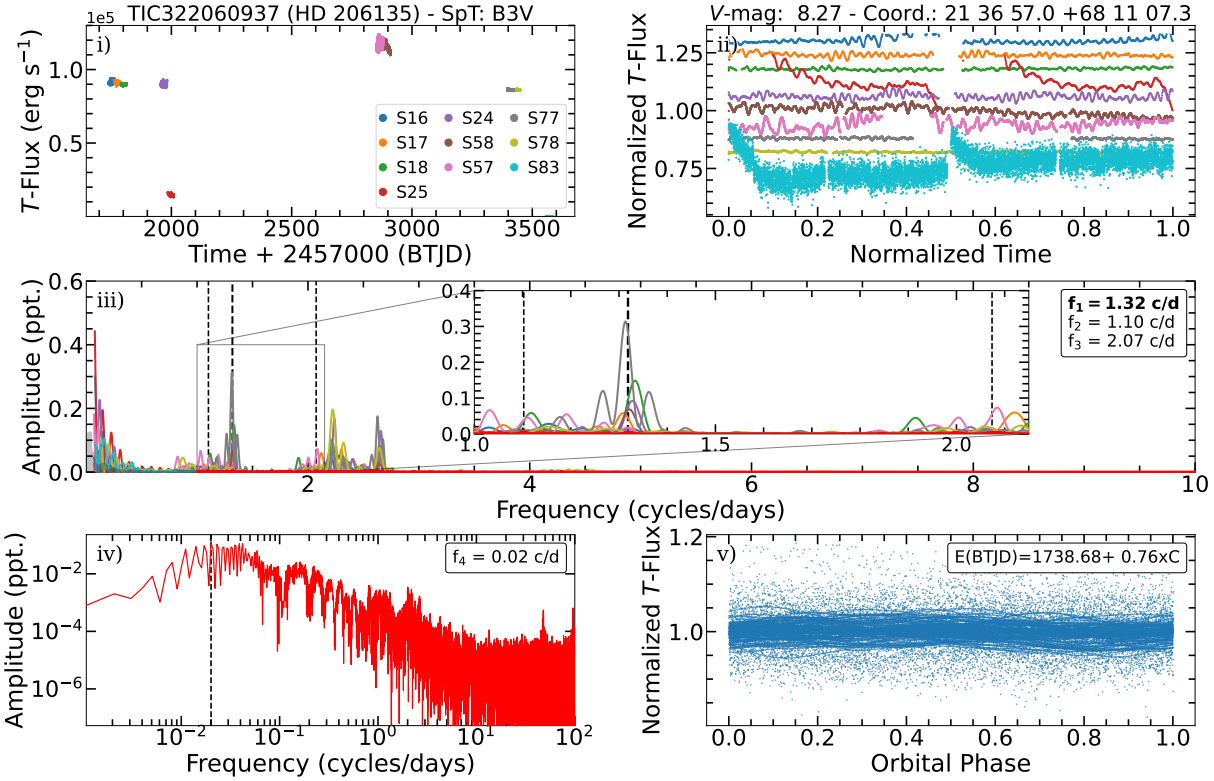

Figure C.104: Panels summarizing the photometric and frequency-domain analyses for the target TIC 322060937. (i) Raw T-Flux light curves from different sectors; (ii) normalized T-Flux light curves folded normalized time for each sector; (iii) Lomb-Scargle periodogram highlighting the three main frequencies f_1, f_2, and f_3, with a zoom-in inset; (iv) extended periodogram revealing a low-frequency component f_4; (v) orbital phase-folded light curve.

C.105. TIC 322104948

HD 306989 was studied by Labadie-Bartz et al. (2022) who pointed out that this object should not be a classical Be star.

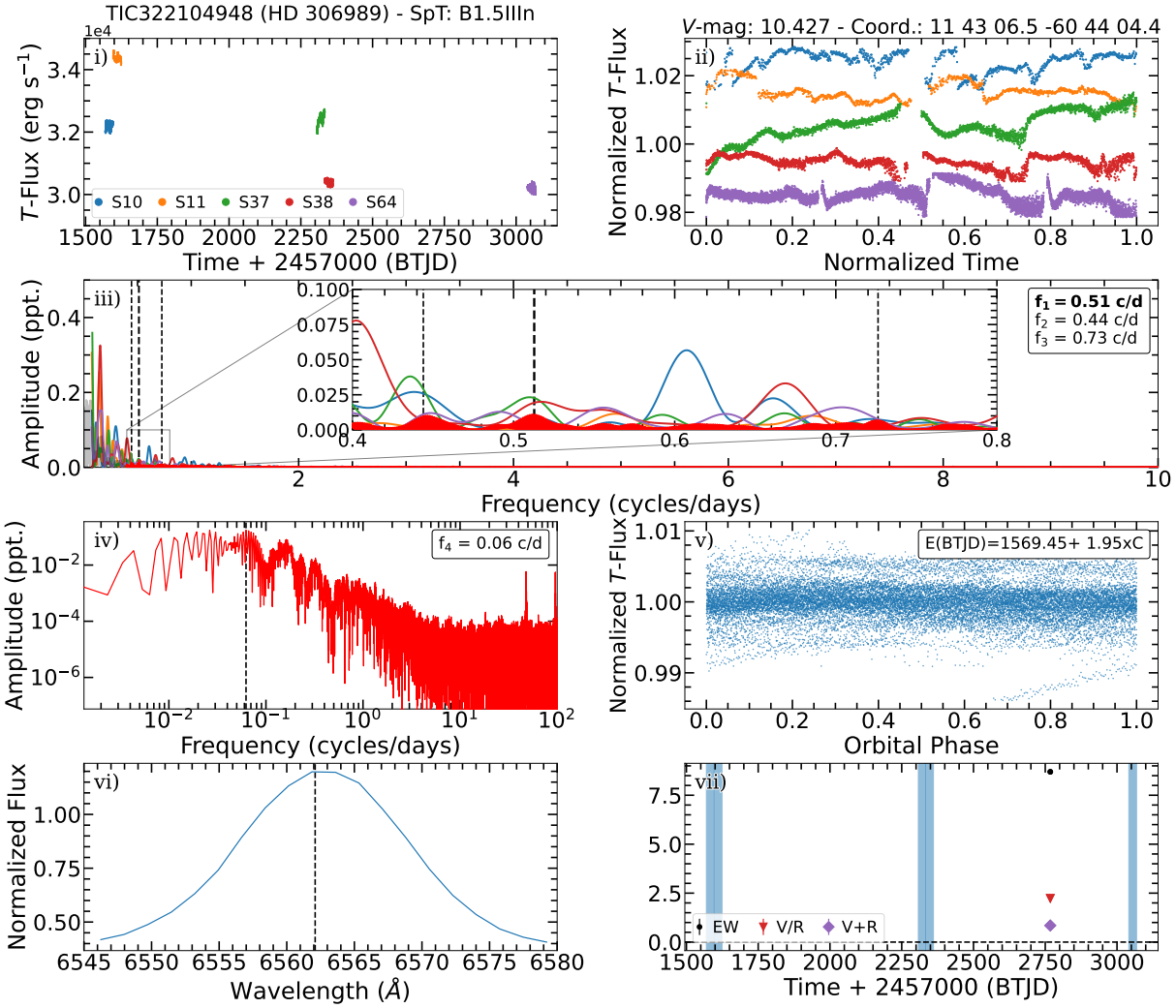

Figure C.105: Panels summarizing the photometric, spectroscopic, and frequency-domain analyses for the target TIC 322104948. (i) Raw T-Flux light curves from different sectors; (ii) normalized T-Flux light curves folded normalized time for each sector; (iii) Lomb-Scargle periodogram highlighting the three main frequencies f_1, f_2, and f_3, with a zoom-in inset; (iv) extended periodogram revealing a low-frequency component f_4; (v) orbital phase-folded light curve; (vi) optical spectrum centered on the Hα line (λ = 6562.8 Å); and (vii) temporal evolution of the equivalent width of the Hα line across available observations. Shaded regions in panel (vii) correspond to observation windows of sectors shown in panel (i).

C.106. TIC 323348984

HD 37330 has been identified as a Be star of type B5–B7 Vne (Warren Jr and Hesser, 1978). There are indications that it is a single-line spectroscopic binary and possibly has hidden companions, suggested by proper motion anomalies detected with Hipparcos and Gaia DR2 data (Kounkel et al., 2019; Kervella et al., 2019).

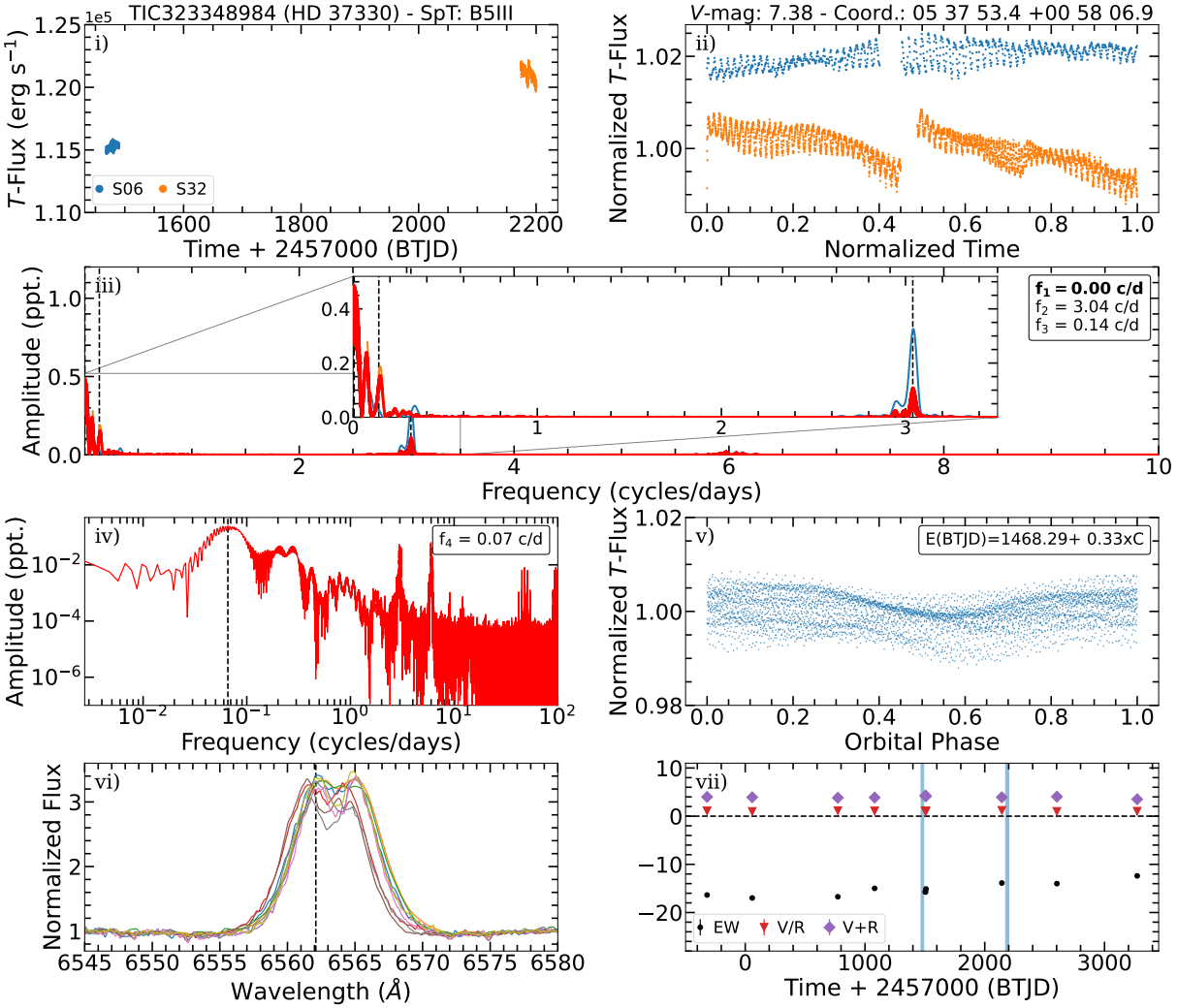

Figure C.106: Panels summarizing the photometric, spectroscopic, and frequency-domain analyses for the target TIC 323348984. (i) Raw T-Flux light curves from different sectors; (ii) normalized T-Flux light curves folded normalized time for each sector; (iii) Lomb-Scargle periodogram highlighting the three main frequencies f_1, f_2, and f_3, with a zoom-in inset; (iv) extended periodogram revealing a low-frequency component f_4; (v) orbital phase-folded light curve; (vi) optical spectrum centered on the Hα line (λ = 6562.8 Å); and (vii) temporal evolution of the equivalent width of the Hα line across available observations. Shaded regions in panel (vii) correspond to observation windows of sectors shown in panel (i).

C.107. TIC 324252945

HD 121195 is a Be star, but with no signs of binarity. No spectrum was found in the BESS catalog.

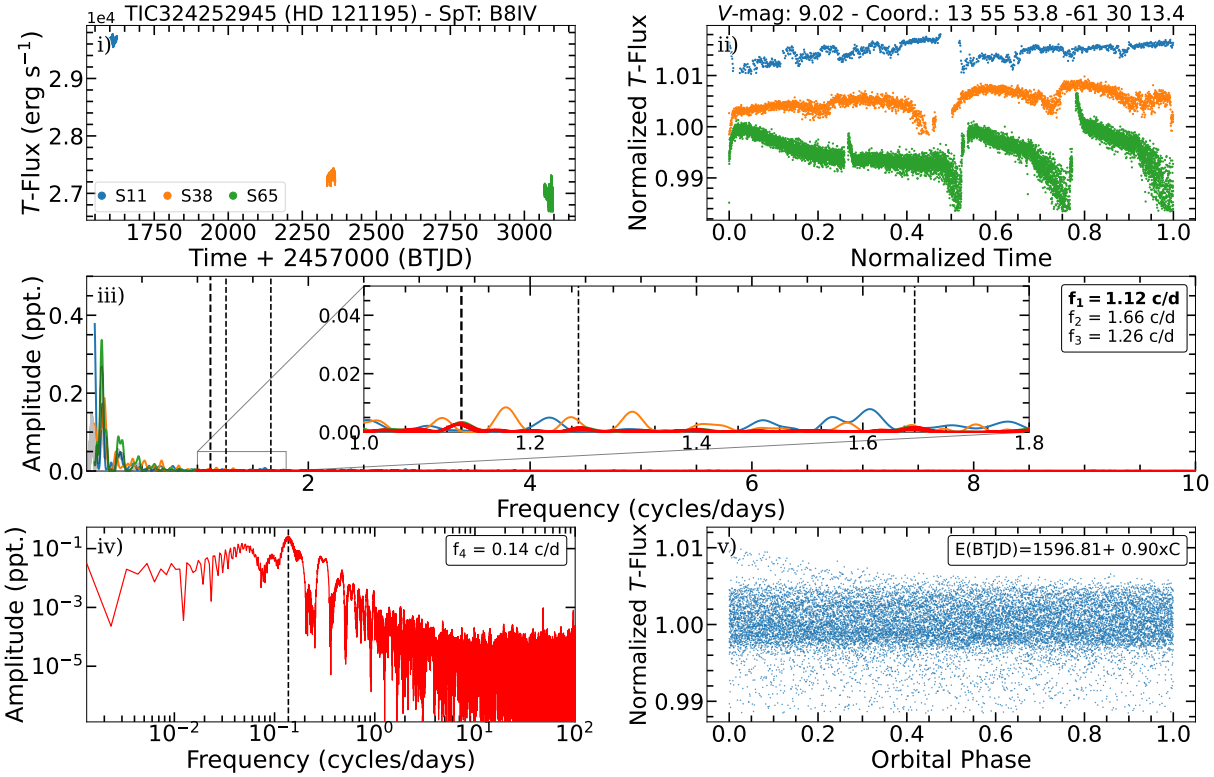

Figure C.107: Panels summarizing the photometric and frequency-domain analyses for the target TIC 324252945. (i) Raw T-Flux light curves from different sectors; (ii) normalized T-Flux light curves folded normalized time for each sector; (iii) Lomb-Scargle periodogram highlighting the three main frequencies f_1, f_2, and f_3, with a zoom-in inset; (iv) extended periodogram revealing a low-frequency component f_4; (v) orbital phase-folded light curve.

C.108. TIC 324820890

BD+49 3718 is a binary system with X-ray emissions. It does not appear to have a classical Be star.

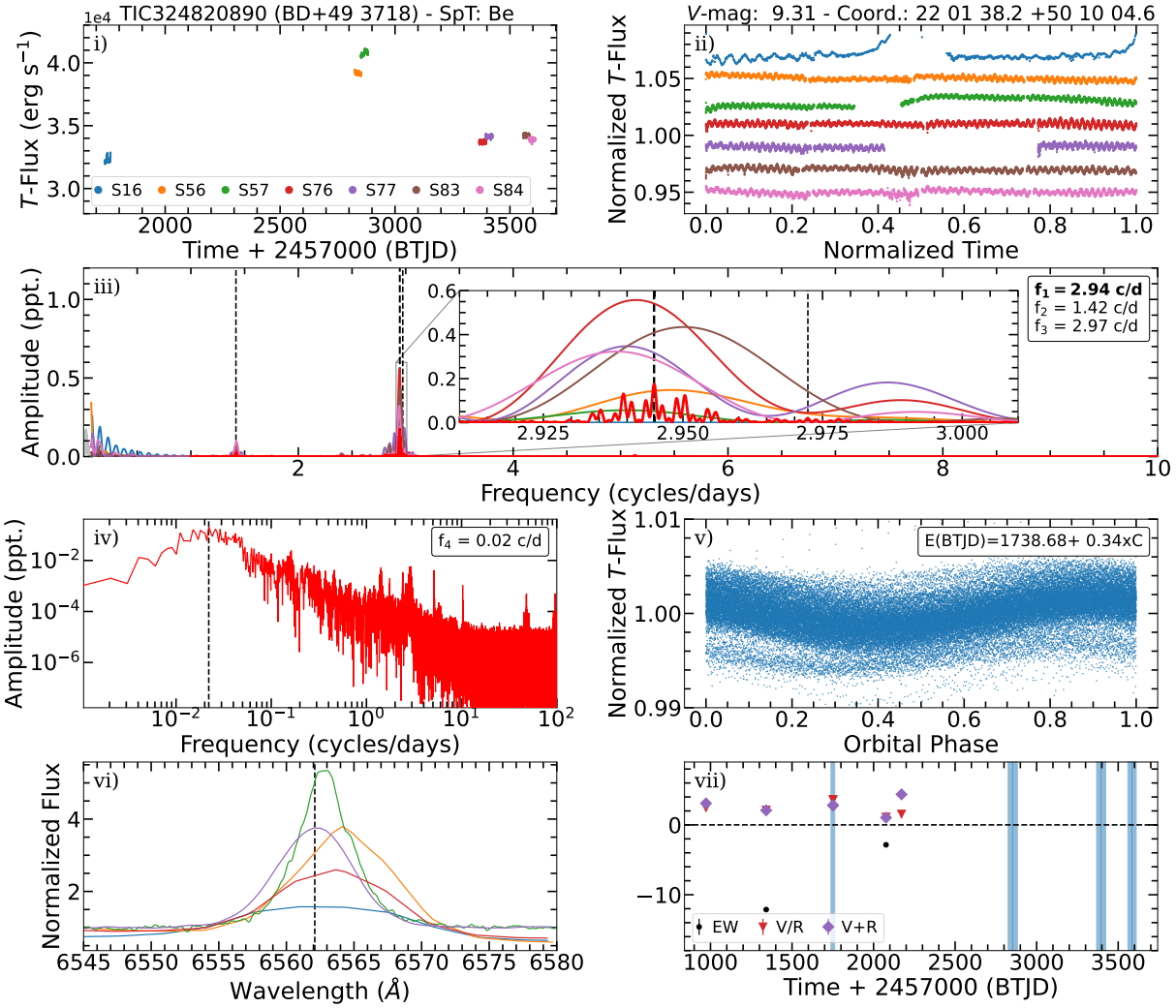

Figure C.108: Panels summarizing the photometric, spectroscopic, and frequency-domain analyses for the target TIC 324820890. (i) Raw T-Flux light curves from different sectors; (ii) normalized T-Flux light curves folded normalized time for each sector; (iii) Lomb-Scargle periodogram highlighting the three main frequencies f_1, f_2, and f_3, with a zoom-in inset; (iv) extended periodogram revealing a low-frequency component f_4; (v) orbital phase-folded light curve; (vi) optical spectrum centered on the Hα line (λ = 6562.8 Å); and (vii) temporal evolution of the equivalent width of the Hα line across available observations. Shaded regions in panel (vii) correspond to observation windows of sectors shown in panel (i).

C.109. TIC 326247844

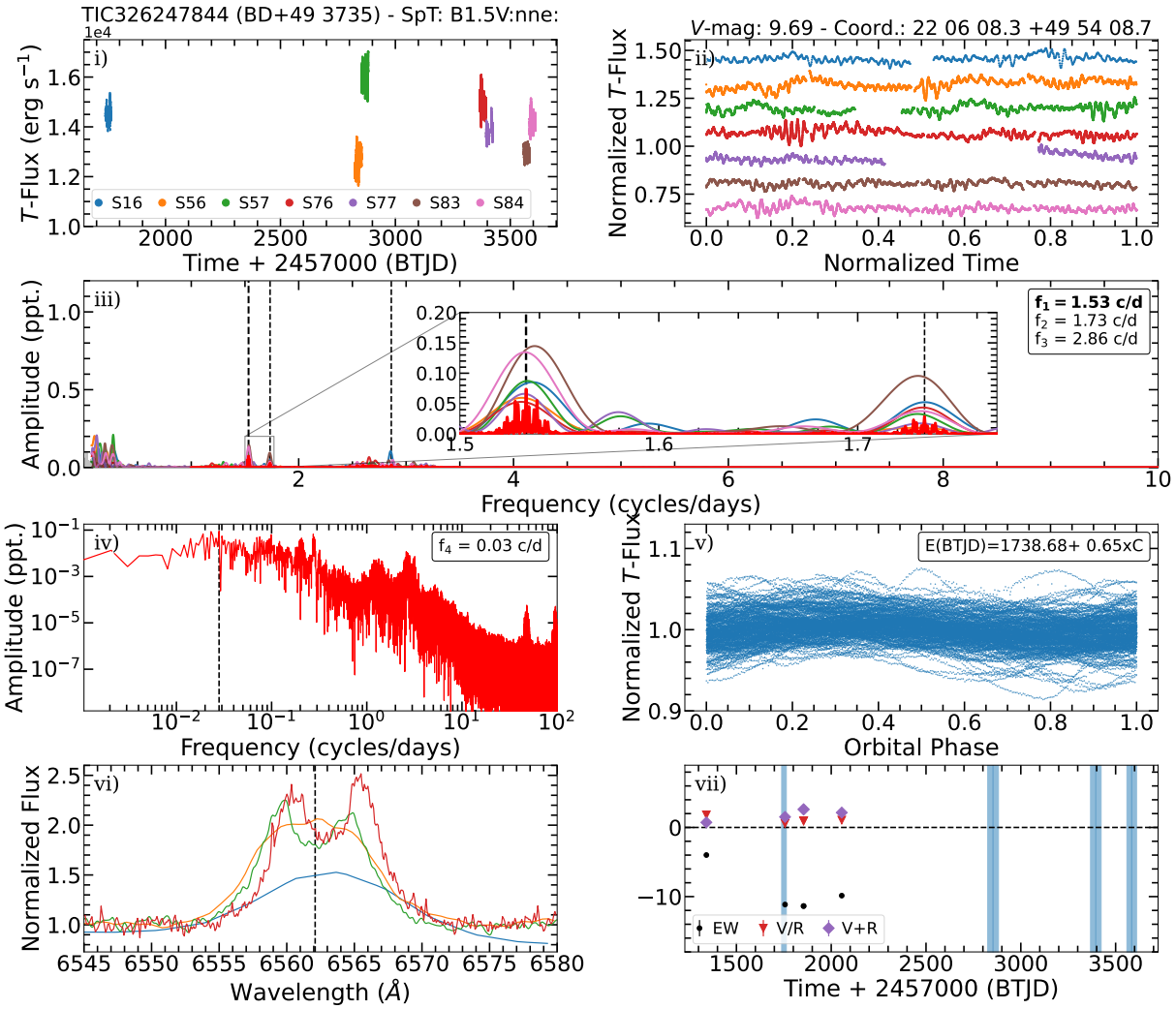

Figure C.109: Panels summarizing the photometric, spectroscopic, and frequency-domain analyses for the target TIC 326247844. (i) Raw T-Flux light curves from different sectors; (ii) normalized T-Flux light curves folded normalized time for each sector; (iii) Lomb-Scargle periodogram highlighting the three main frequencies f_1, f_2, and f_3, with a zoom-in inset; (iv) extended periodogram revealing a low-frequency component f_4; (v) orbital phase-folded light curve; (vi) optical spectrum centered on the Hα line (λ = 6562.8 Å); and (vii) temporal evolution of the equivalent width of the Hα line across available observations. Shaded regions in panel (vii) correspond to observation windows of sectors shown in panel (i).

C.110. TIC 326999260

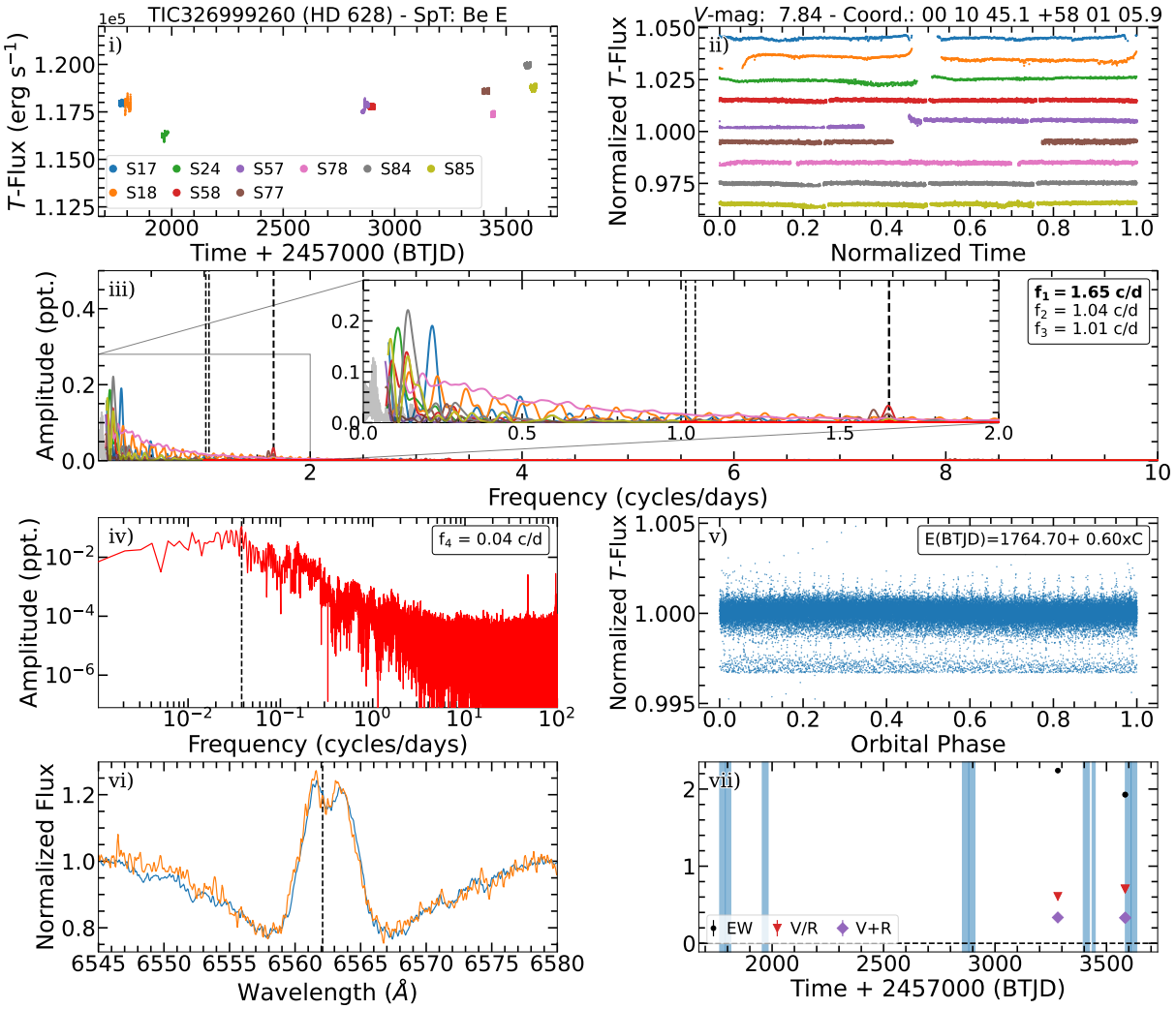

Figure C.110: Panels summarizing the photometric, spectroscopic, and frequency-domain analyses for the target TIC 326999260. (i) Raw T-Flux light curves from different sectors; (ii) normalized T-Flux light curves folded normalized time for each sector; (iii) Lomb-Scargle periodogram highlighting the three main frequencies f_1, f_2, and f_3, with a zoom-in inset; (iv) extended periodogram revealing a low-frequency component f_4; (v) orbital phase-folded light curve; (vi) optical spectrum centered on the Hα line (λ = 6562.8 Å); and (vii) temporal evolution of the equivalent width of the Hα line across available observations. Shaded regions in panel (vii) correspond to observation windows of sectors shown in panel (i).

C.111. TIC 32882261

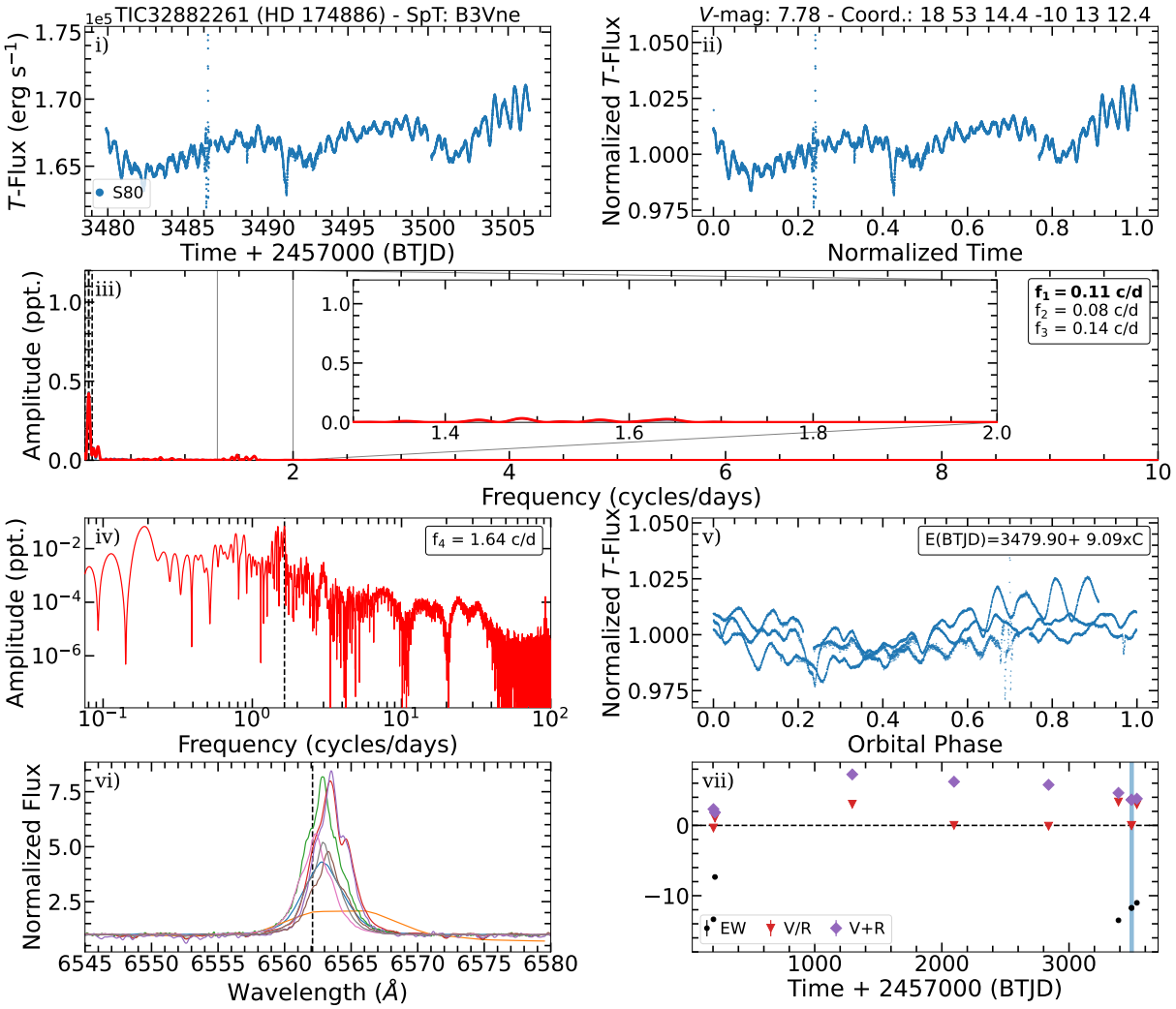

Figure C.111: Panels summarizing the photometric, spectroscopic, and frequency-domain analyses for the target TIC 32882261. (i) Raw T-Flux light curves from different sectors; (ii) normalized T-Flux light curves folded normalized time for each sector; (iii) Lomb-Scargle periodogram highlighting the three main frequencies f_1, f_2, and f_3, with a zoom-in inset; (iv) extended periodogram revealing a low-frequency component f_4; (v) orbital phase-folded light curve; (vi) optical spectrum centered on the Hα line (λ = 6562.8 Å); and (vii) temporal evolution of the equivalent width of the Hα line across available observations. Shaded regions in panel (vii) correspond to observation windows of sectors shown in panel (i).

C.112. TIC 329947655

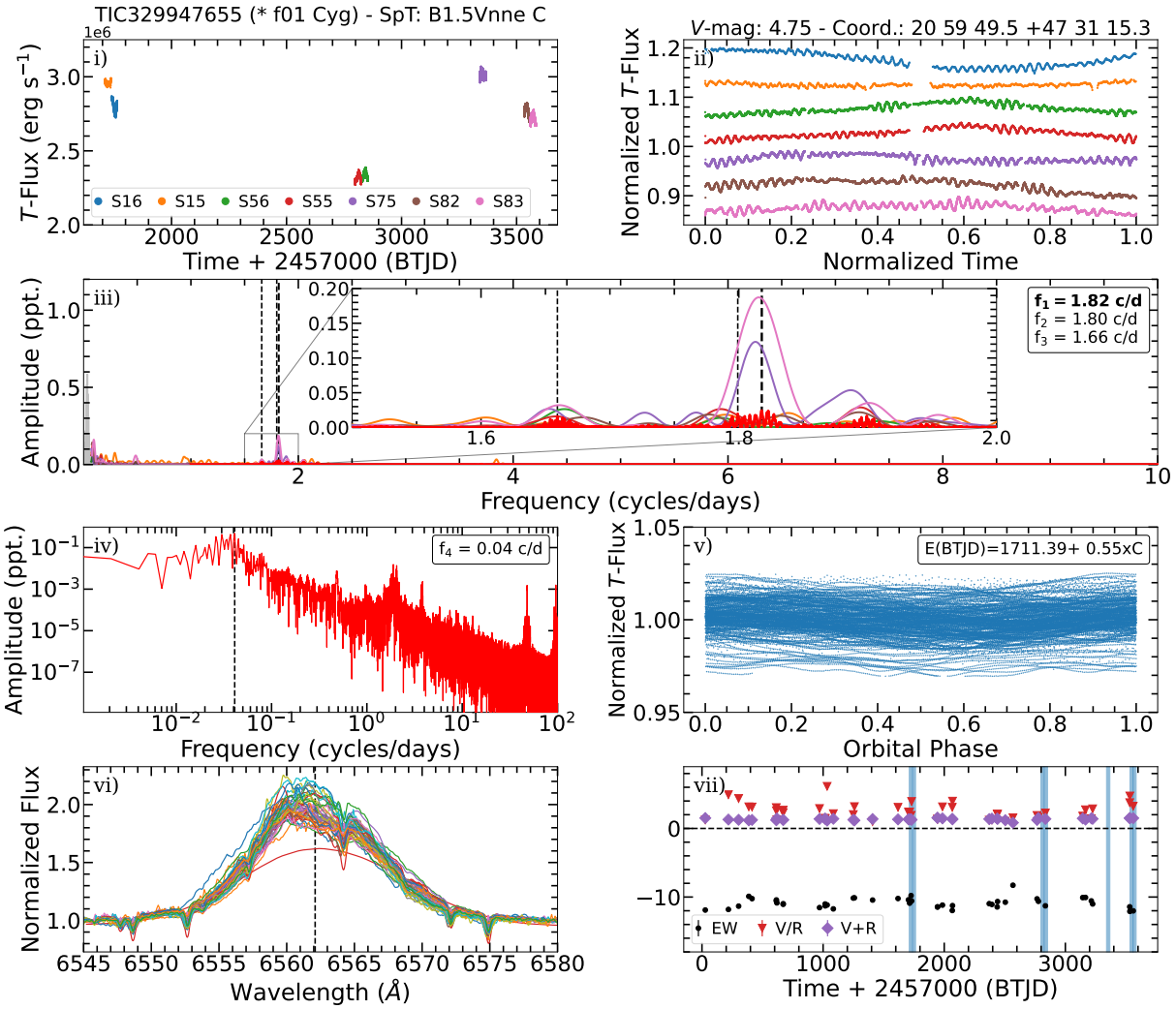

Figure C.112: Panels summarizing the photometric, spectroscopic, and frequency-domain analyses for the target TIC 329947655. (i) Raw T-Flux light curves from different sectors; (ii) normalized T-Flux light curves folded normalized time for each sector; (iii) Lomb-Scargle periodogram highlighting the three main frequencies f_1, f_2, and f_3, with a zoom-in inset; (iv) extended periodogram revealing a low-frequency component f_4; (v) orbital phase-folded light curve; (vi) optical spectrum centered on the Hα line (λ = 6562.8 Å); and (vii) temporal evolution of the equivalent width of the Hα line across available observations. Shaded regions in panel (vii) correspond to observation windows of sectors shown in panel (i).

C.113. TIC 331811163

No spectrum was found in the BESS catalog.

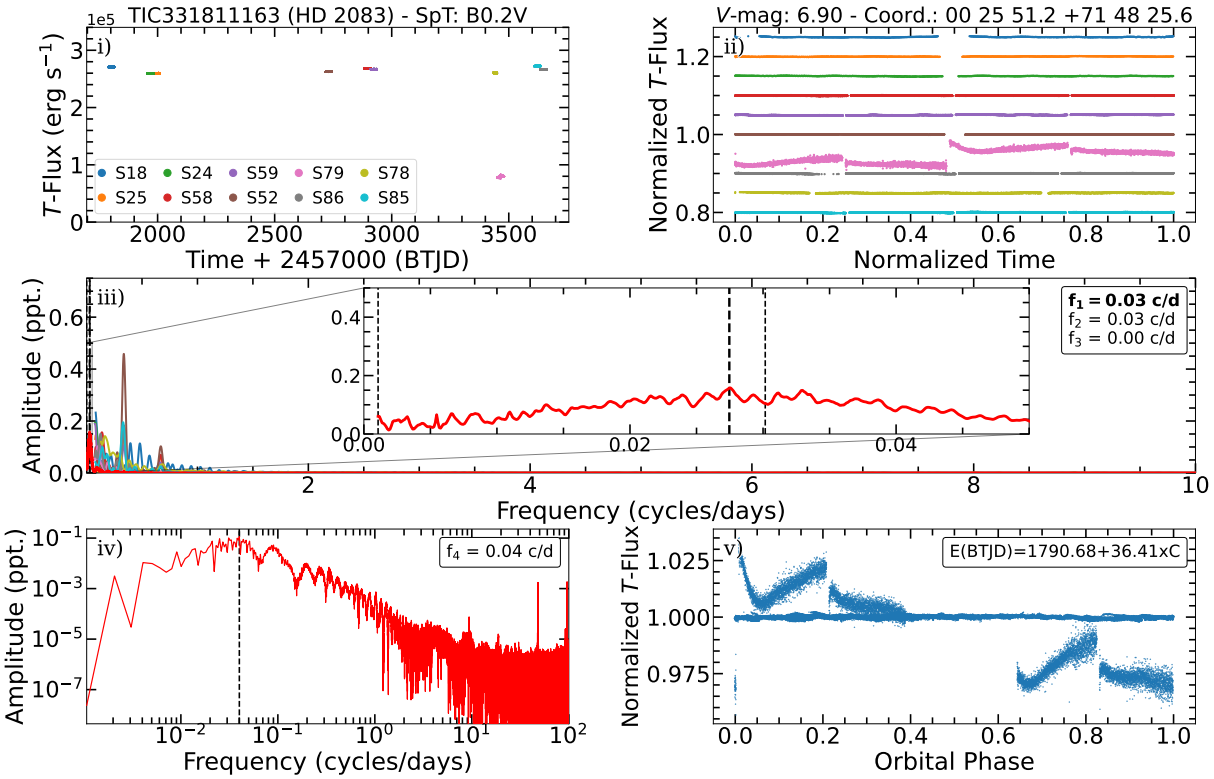

Figure C.113: Panels summarizing the photometric and frequency-domain analyses for the target TIC 331811163. (i) Raw T-Flux light curves from different sectors; (ii) normalized T-Flux light curves folded normalized time for each sector; (iii) Lomb-Scargle periodogram highlighting the three main frequencies f_1, f_2, and f_3, with a zoom-in inset; (iv) extended periodogram revealing a low-frequency component f_4; (v) orbital phase-folded light curve.

C.114. TIC 333670784

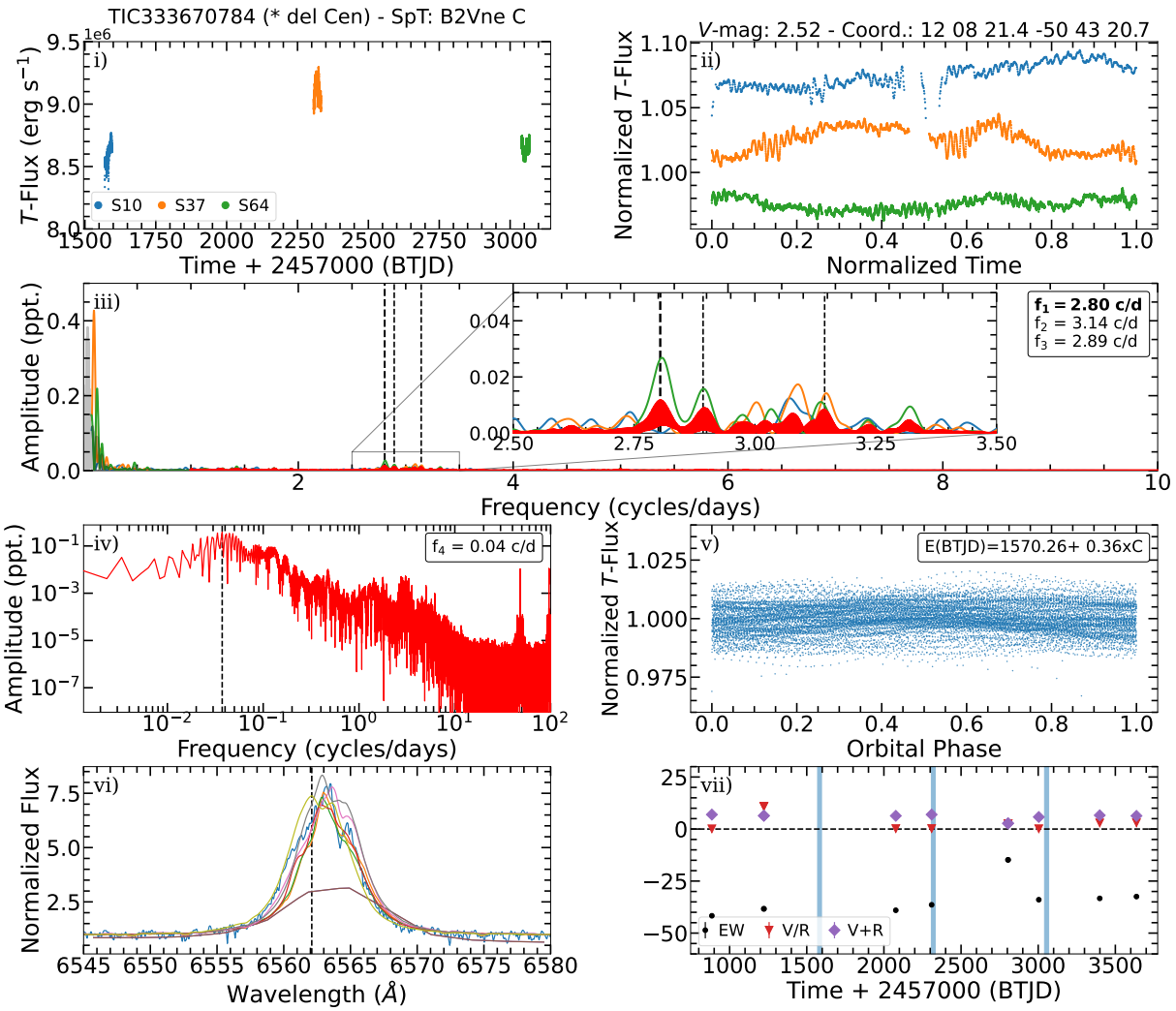

Figure C.114: Panels summarizing the photometric, spectroscopic, and frequency-domain analyses for the target TIC 333670784. (i) Raw T-Flux light curves from different sectors; (ii) normalized T-Flux light curves folded normalized time for each sector; (iii) Lomb-Scargle periodogram highlighting the three main frequencies f_1, f_2, and f_3, with a zoom-in inset; (iv) extended periodogram revealing a low-frequency component f_4; (v) orbital phase-folded light curve; (vi) optical spectrum centered on the Hα line (λ = 6562.8 Å); and (vii) temporal evolution of the equivalent width of the Hα line across available observations. Shaded regions in panel (vii) correspond to observation windows of sectors shown in panel (i).

C.115. TIC 33993533

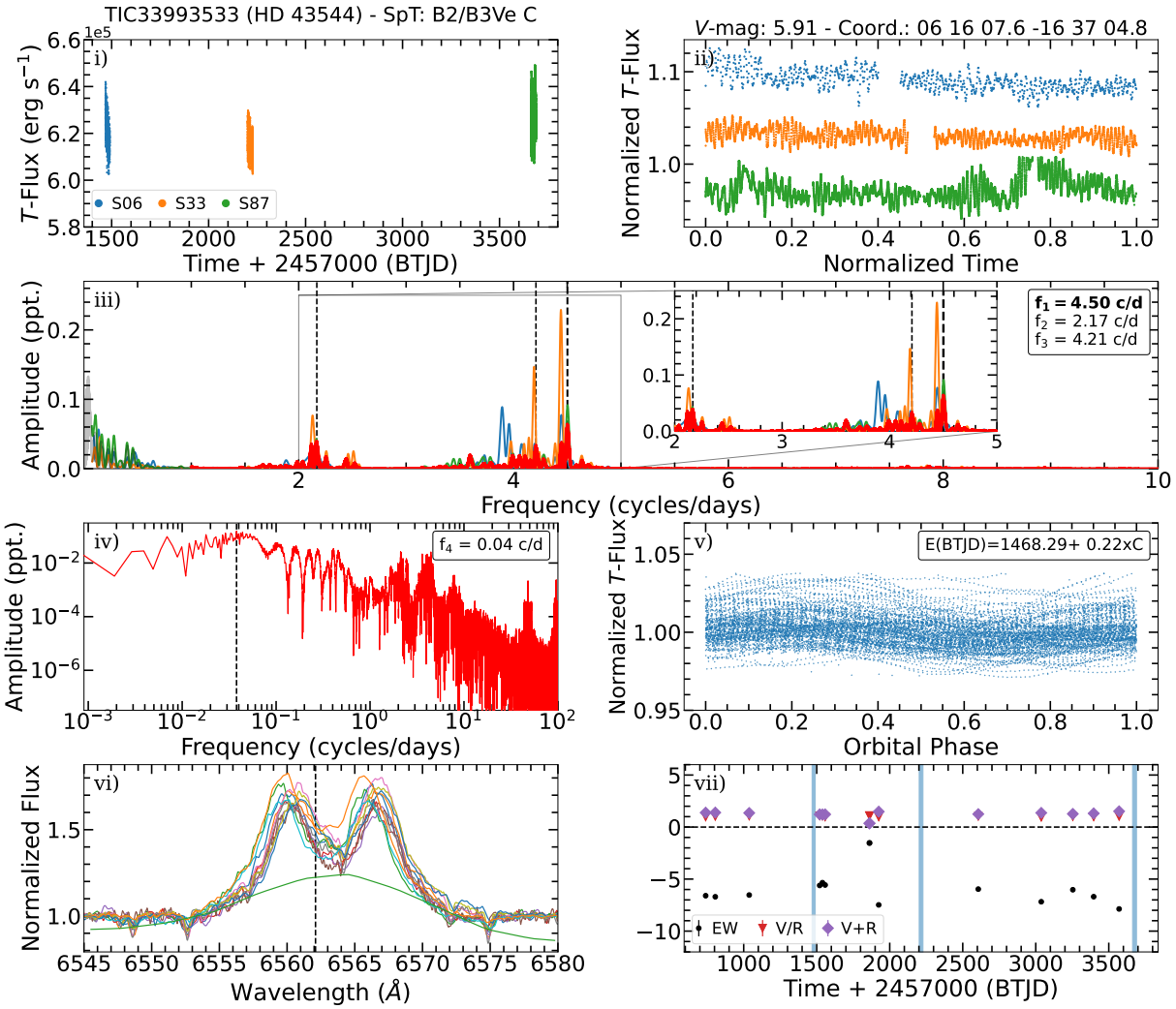

Figure C.115: Panels summarizing the photometric, spectroscopic, and frequency-domain analyses for the target TIC 33993533. (i) Raw T-Flux light curves from different sectors; (ii) normalized T-Flux light curves folded normalized time for each sector; (iii) Lomb-Scargle periodogram highlighting the three main frequencies f_1, f_2, and f_3, with a zoom-in inset; (iv) extended periodogram revealing a low-frequency component f_4; (v) orbital phase-folded light curve; (vi) optical spectrum centered on the Hα line (λ = 6562.8 Å); and (vii) temporal evolution of the equivalent width of the Hα line across available observations. Shaded regions in panel (vii) correspond to observation windows of sectors shown in panel (i).

C.116. TIC 343908909

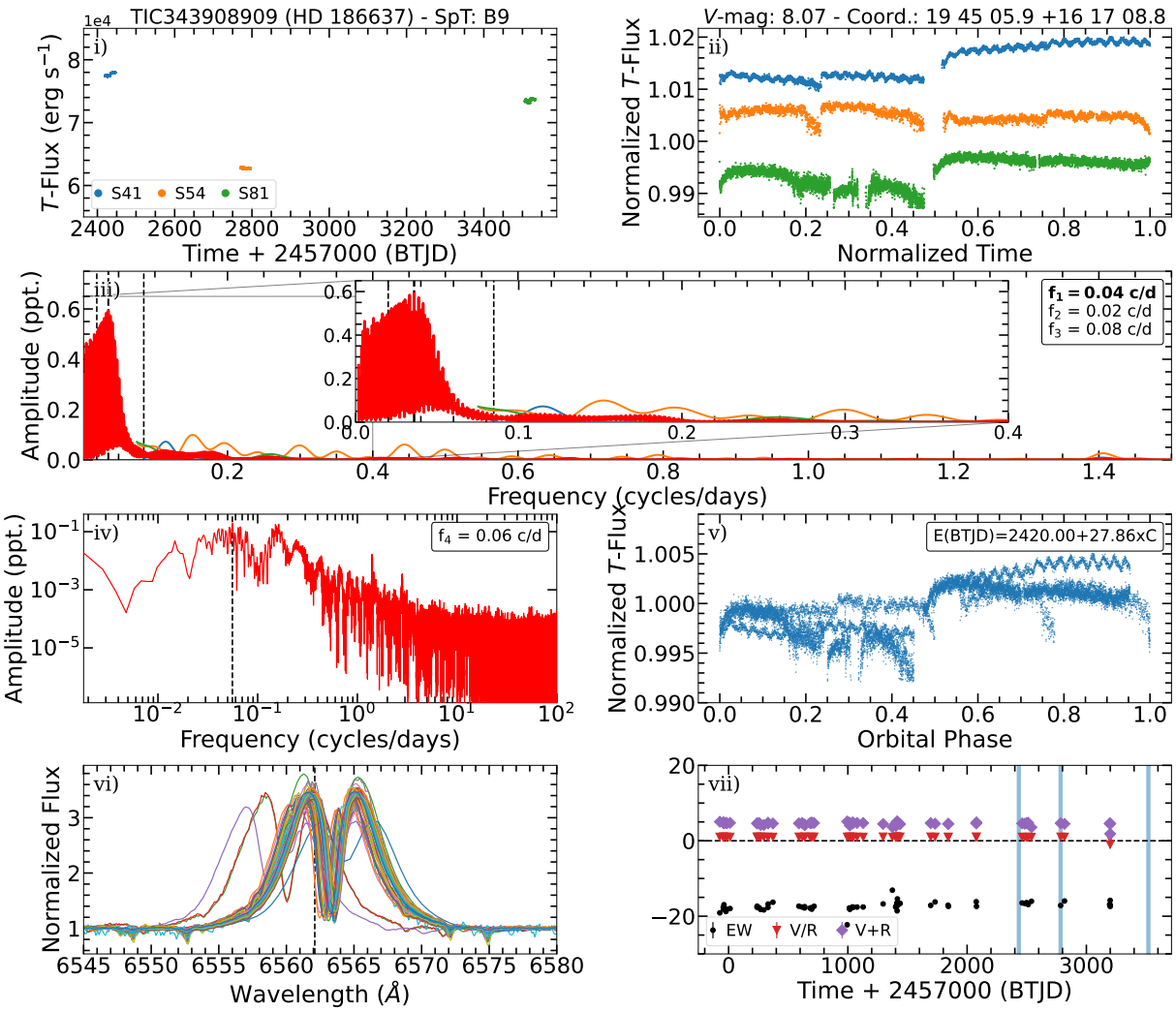

Figure C.116: Panels summarizing the photometric, spectroscopic, and frequency-domain analyses for the target TIC 343908909. (i) Raw T-Flux light curves from different sectors; (ii) normalized T-Flux light curves folded normalized time for each sector; (iii) Lomb-Scargle periodogram highlighting the three main frequencies f_1, f_2, and f_3, with a zoom-in inset; (iv) extended periodogram revealing a low-frequency component f_4; (v) orbital phase-folded light curve; (vi) optical spectrum centered on the Hα line (λ = 6562.8 Å); and (vii) temporal evolution of the equivalent width of the Hα line across available observations. Shaded regions in panel (vii) correspond to observation windows of sectors shown in panel (i).

C.117. TIC 354462452

No spectrum was found in the BESS catalog.

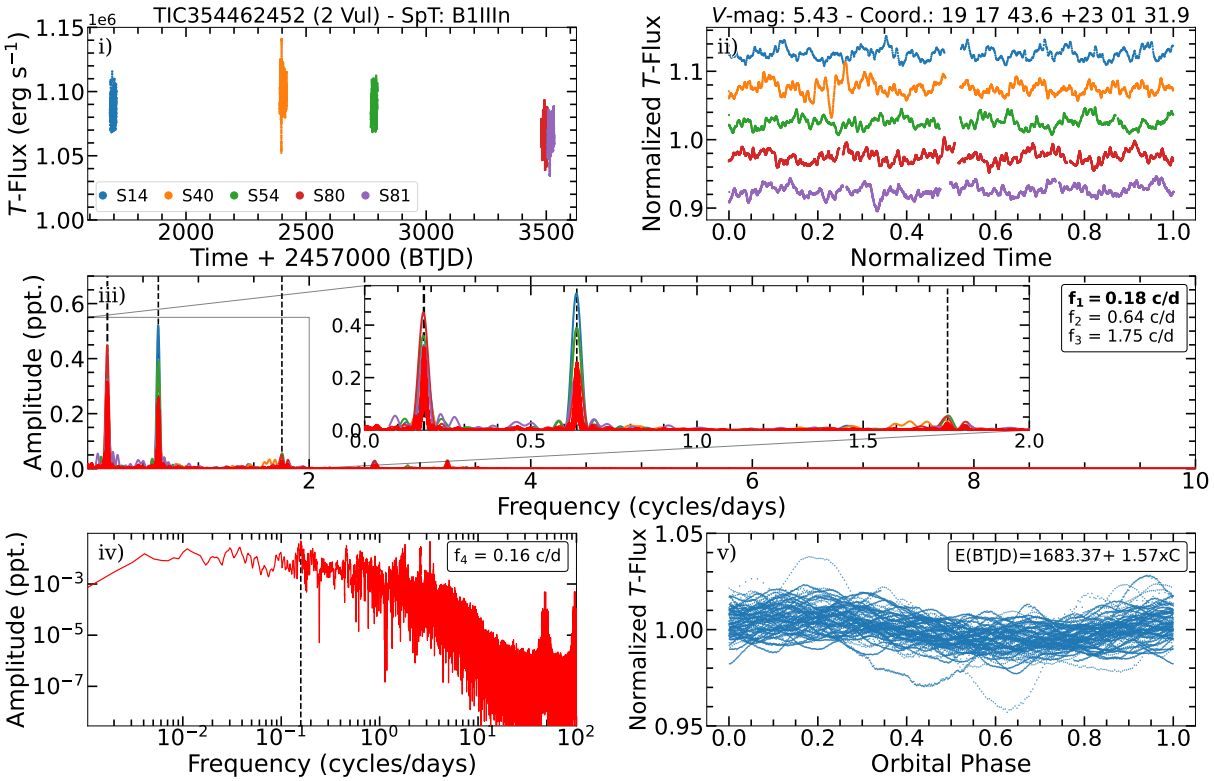

Figure C.117: Panels summarizing the photometric and frequency-domain analyses for the target TIC 354462452. (i) Raw T-Flux light curves from different sectors; (ii) normalized T-Flux light curves folded normalized time for each sector; (iii) Lomb-Scargle periodogram highlighting the three main frequencies f_1, f_2, and f_3, with a zoom-in inset; (iv) extended periodogram revealing a low-frequency component f_4; (v) orbital phase-folded light curve.

C.118. TIC 354770601

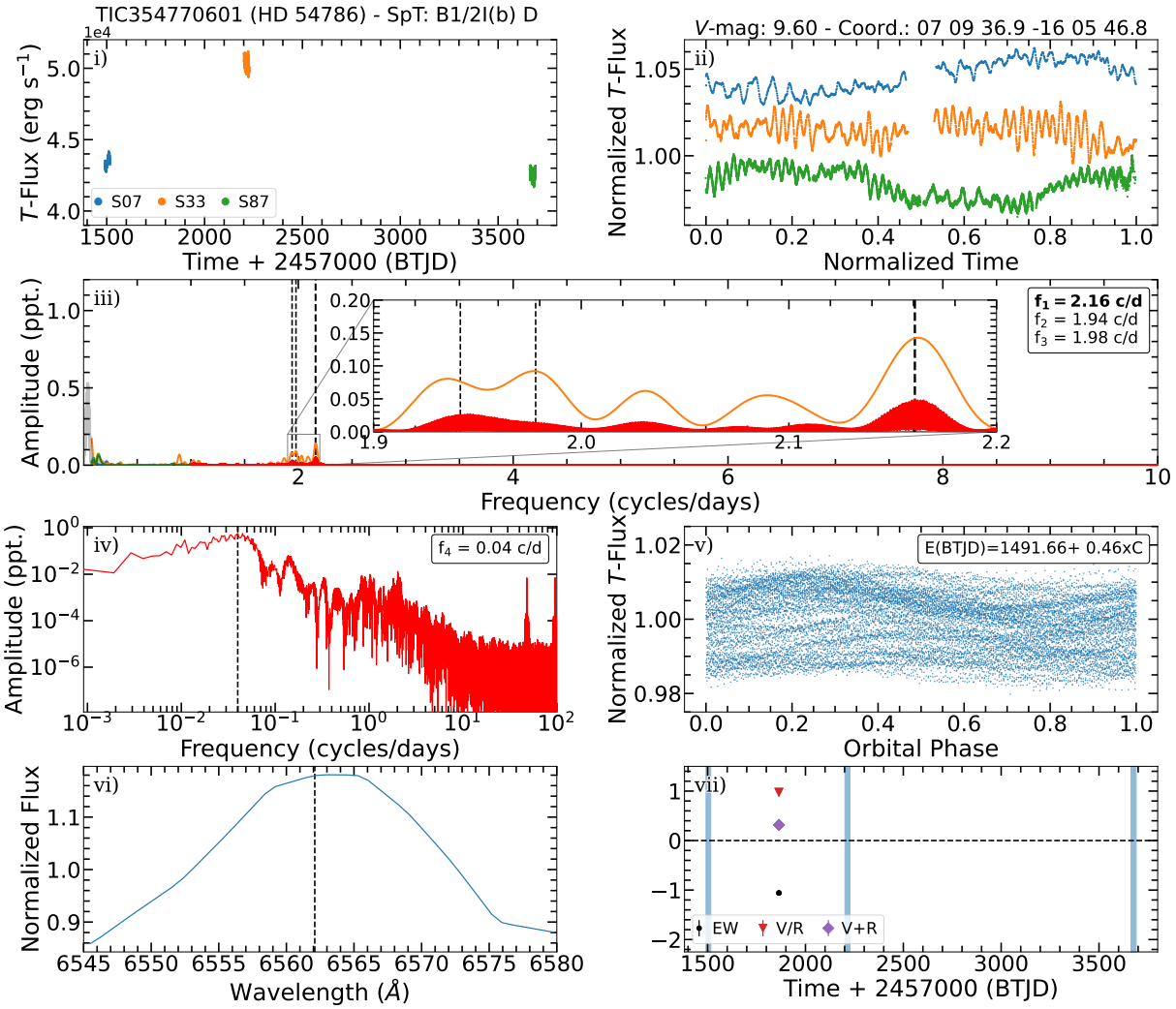

Figure C.118: Panels summarizing the photometric, spectroscopic, and frequency-domain analyses for the target TIC 354770601. (i) Raw T-Flux light curves from different sectors; (ii) normalized T-Flux light curves folded normalized time for each sector; (iii) Lomb-Scargle periodogram highlighting the three main frequencies f_1, f_2, and f_3, with a zoom-in inset; (iv) extended periodogram revealing a low-frequency component f_4; (v) orbital phase-folded light curve; (vi) optical spectrum centered on the Hα line (λ = 6562.8 Å); and (vii) temporal evolution of the equivalent width of the Hα line across available observations. Shaded regions in panel (vii) correspond to observation windows of sectors shown in panel (i).

C.119. TIC 355653322

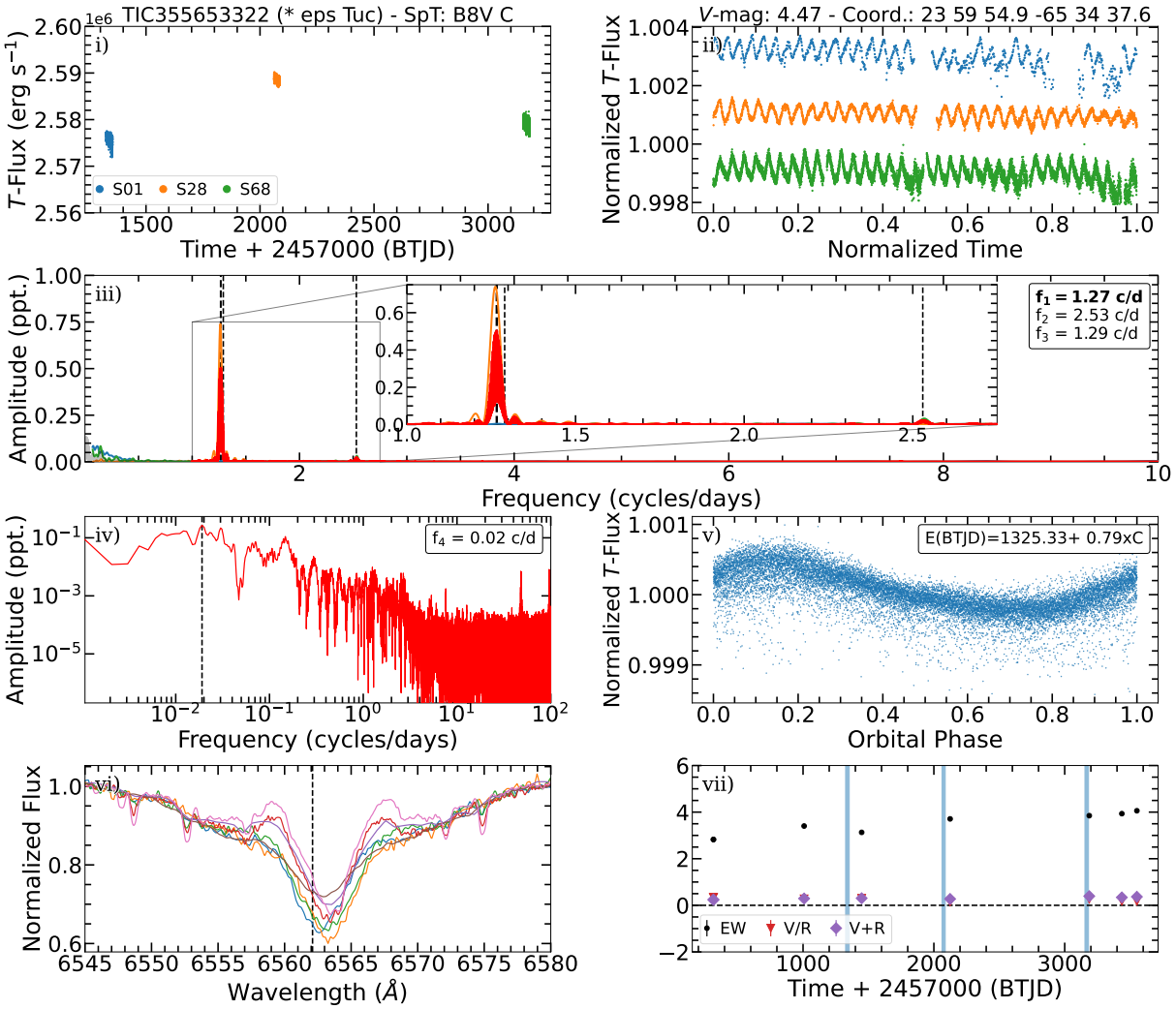

Figure C.119: Panels summarizing the photometric, spectroscopic, and frequency-domain analyses for the target TIC 355653322. (i) Raw T-Flux light curves from different sectors; (ii) normalized T-Flux light curves folded normalized time for each sector; (iii) Lomb-Scargle periodogram highlighting the three main frequencies f_1, f_2, and f_3, with a zoom-in inset; (iv) extended periodogram revealing a low-frequency component f_4; (v) orbital phase-folded light curve; (vi) optical spectrum centered on the Hα line (λ = 6562.8 Å); and (vii) temporal evolution of the equivalent width of the Hα line across available observations. Shaded regions in panel (vii) correspond to observation windows of sectors shown in panel (i).

C.120. TIC 356239023

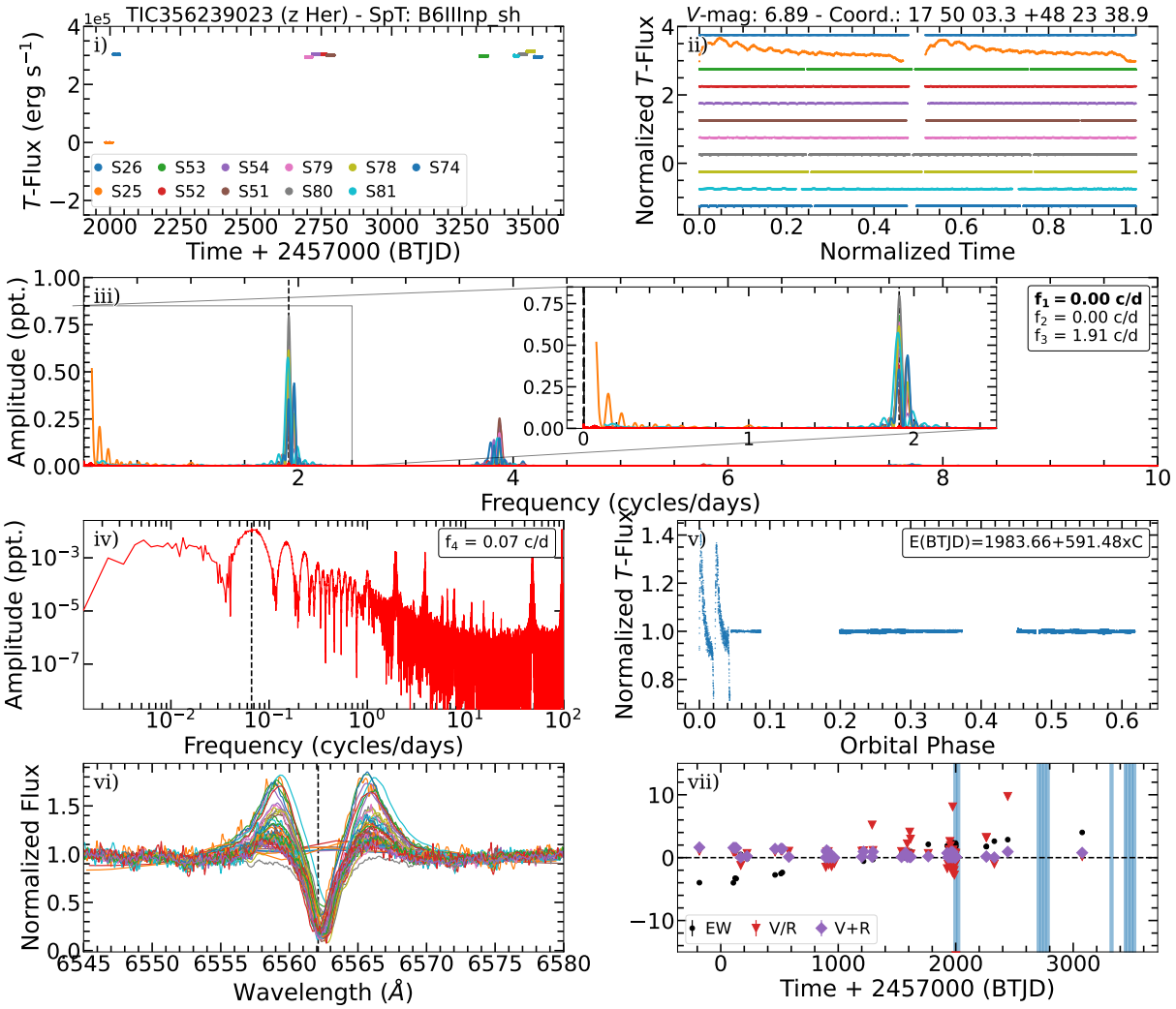

Figure C.120: Panels summarizing the photometric, spectroscopic, and frequency-domain analyses for the target TIC 356239023. (i) Raw T-Flux light curves from different sectors; (ii) normalized T-Flux light curves folded normalized time for each sector; (iii) Lomb-Scargle periodogram highlighting the three main frequencies f_1, f_2, and f_3, with a zoom-in inset; (iv) extended periodogram revealing a low-frequency component f_4; (v) orbital phase-folded light curve; (vi) optical spectrum centered on the Hα line (λ = 6562.8 Å); and (vii) temporal evolution of the equivalent width of the Hα line across available observations. Shaded regions in panel (vii) correspond to observation windows of sectors shown in panel (i).

C.121. TIC 358499972

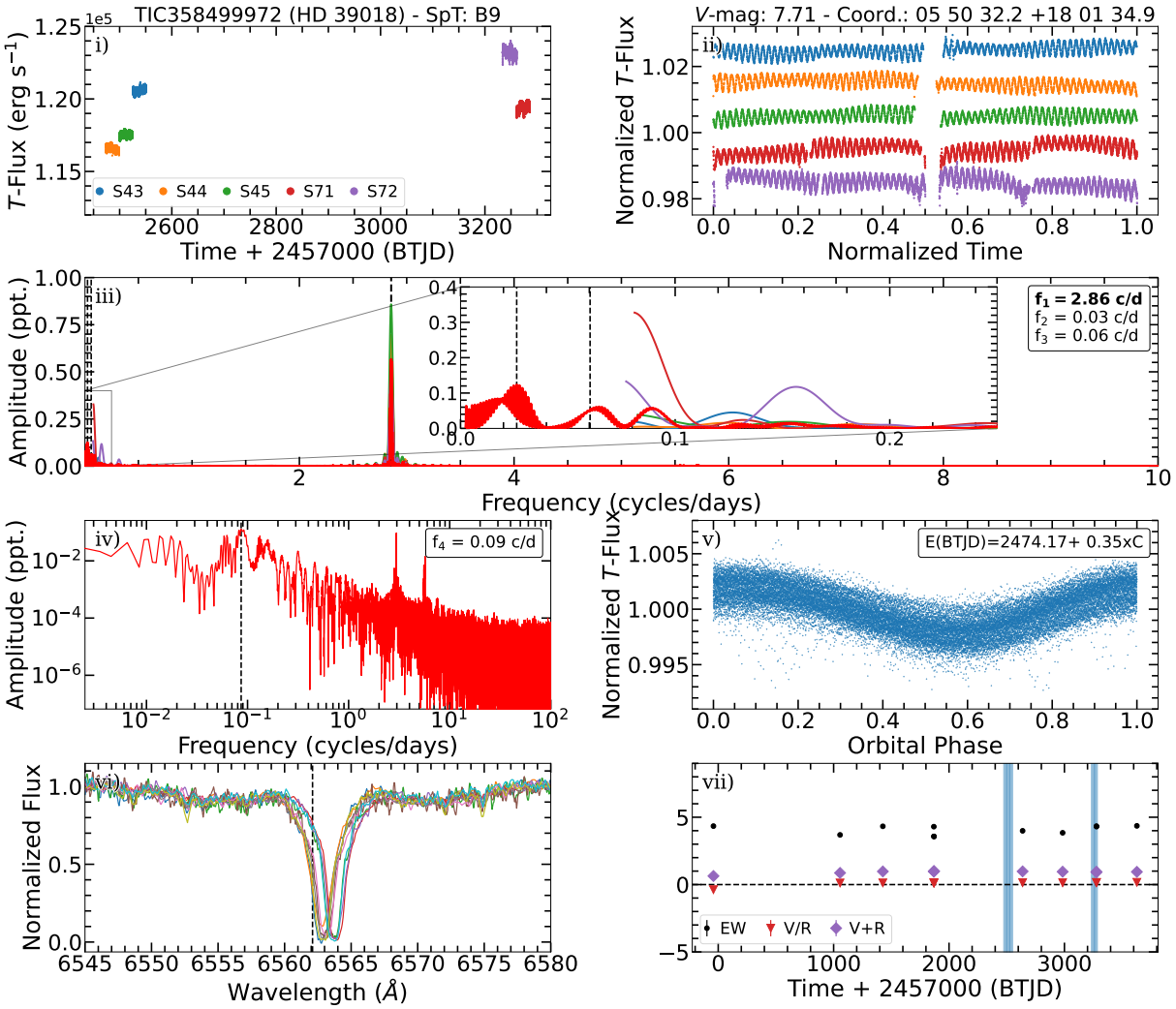

Figure C.121: Panels summarizing the photometric, spectroscopic, and frequency-domain analyses for the target TIC 358499972. (i) Raw T-Flux light curves from different sectors; (ii) normalized T-Flux light curves folded normalized time for each sector; (iii) Lomb-Scargle periodogram highlighting the three main frequencies f_1, f_2, and f_3, with a zoom-in inset; (iv) extended periodogram revealing a low-frequency component f_4; (v) orbital phase-folded light curve; (vi) optical spectrum centered on the Hα line (λ = 6562.8 Å); and (vii) temporal evolution of the equivalent width of the Hα line across available observations. Shaded regions in panel (vii) correspond to observation windows of sectors shown in panel (i).

C.122. TIC 364398342

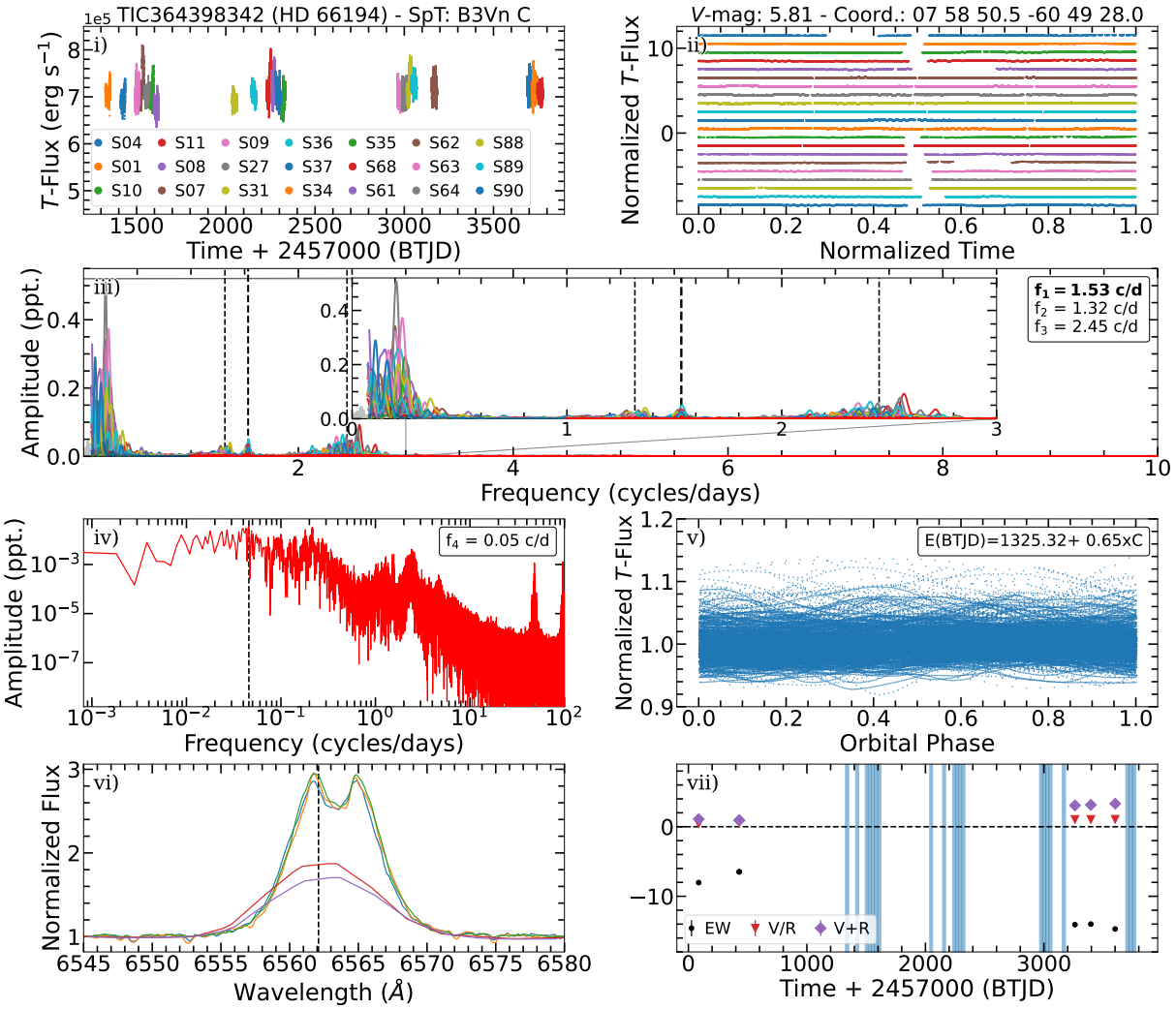

Figure C.122: Panels summarizing the photometric, spectroscopic, and frequency-domain analyses for the target TIC 364398342. (i) Raw T-Flux light curves from different sectors; (ii) normalized T-Flux light curves folded normalized time for each sector; (iii) Lomb-Scargle periodogram highlighting the three main frequencies f_1, f_2, and f_3, with a zoom-in inset; (iv) extended periodogram revealing a low-frequency component f_4; (v) orbital phase-folded light curve; (vi) optical spectrum centered on the Hα line (λ = 6562.8 Å); and (vii) temporal evolution of the equivalent width of the Hα line across available observations. Shaded regions in panel (vii) correspond to observation windows of sectors shown in panel (i).

C.123. TIC 364921141

No spectrum was found in the BESS catalog.

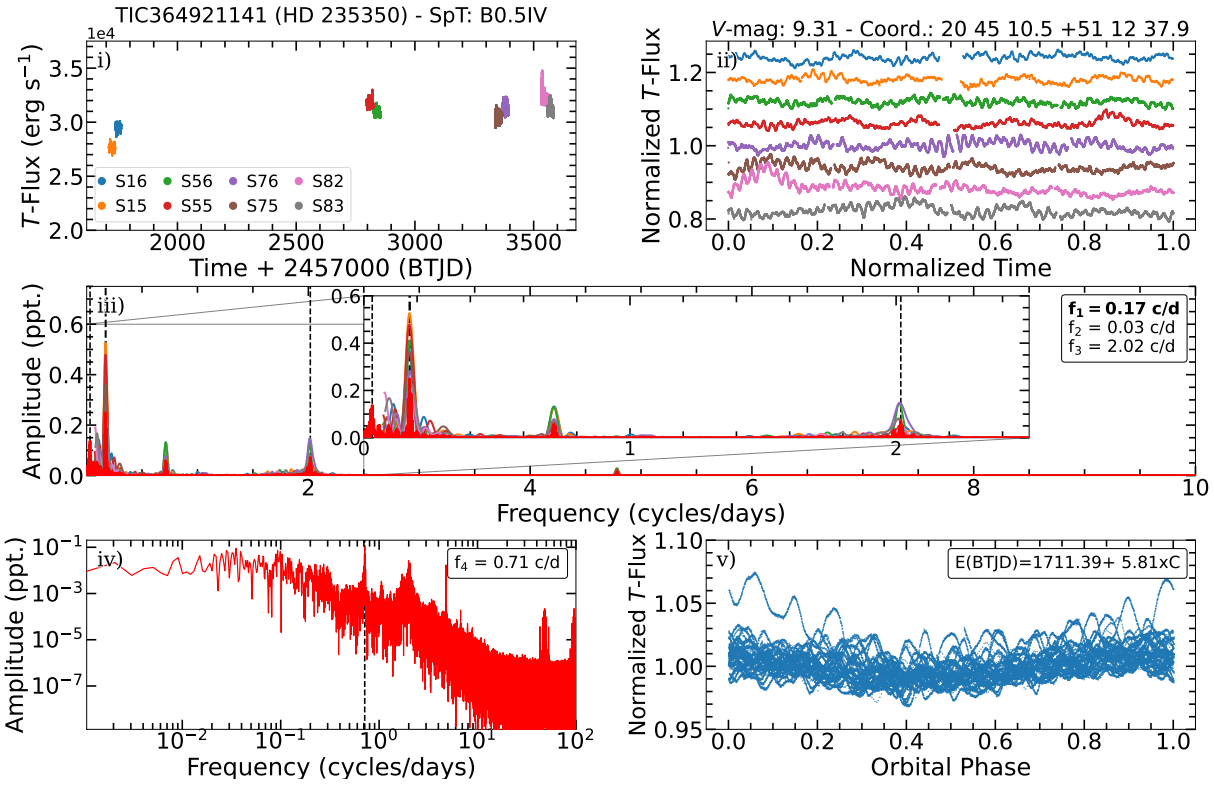

Figure C.123: Panels summarizing the photometric and frequency-domain analyses for the target TIC 364921141. (i) Raw T-Flux light curves from different sectors; (ii) normalized T-Flux light curves folded normalized time for each sector; (iii) Lomb-Scargle periodogram highlighting the three main frequencies f_1, f_2, and f_3, with a zoom-in inset; (iv) extended periodogram revealing a low-frequency component f_4; (v) orbital phase-folded light curve.

C.124. TIC 368237682

No spectrum was found in the BESS catalog.

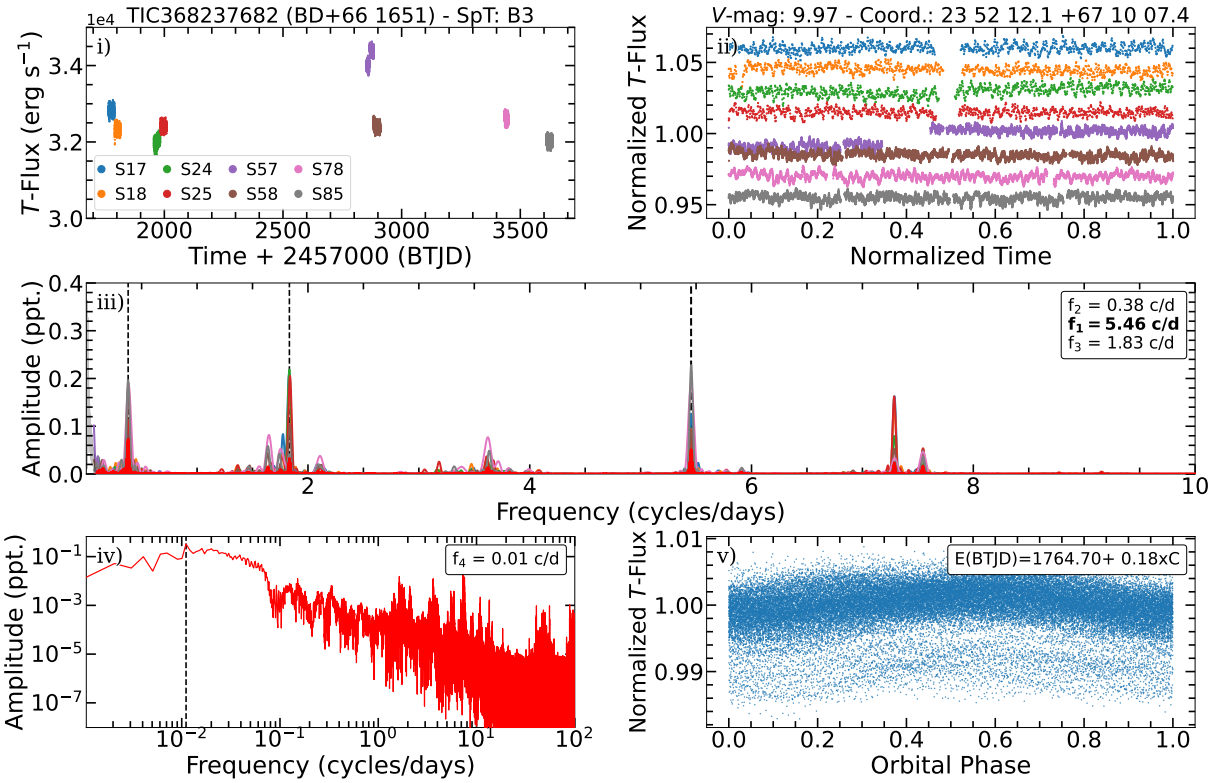

Figure C.124: Panels summarizing the photometric and frequency-domain analyses for the target TIC 368237682. (i) Raw T-Flux light curves from different sectors; (ii) normalized T-Flux light curves folded normalized time for each sector; (iii) Lomb-Scargle periodogram highlighting the three main frequencies f_1, f_2, and f_3, with a zoom-in inset; (iv) extended periodogram revealing a low-frequency component f_4; (v) orbital phase-folded light curve.

C.125. TIC 368799545

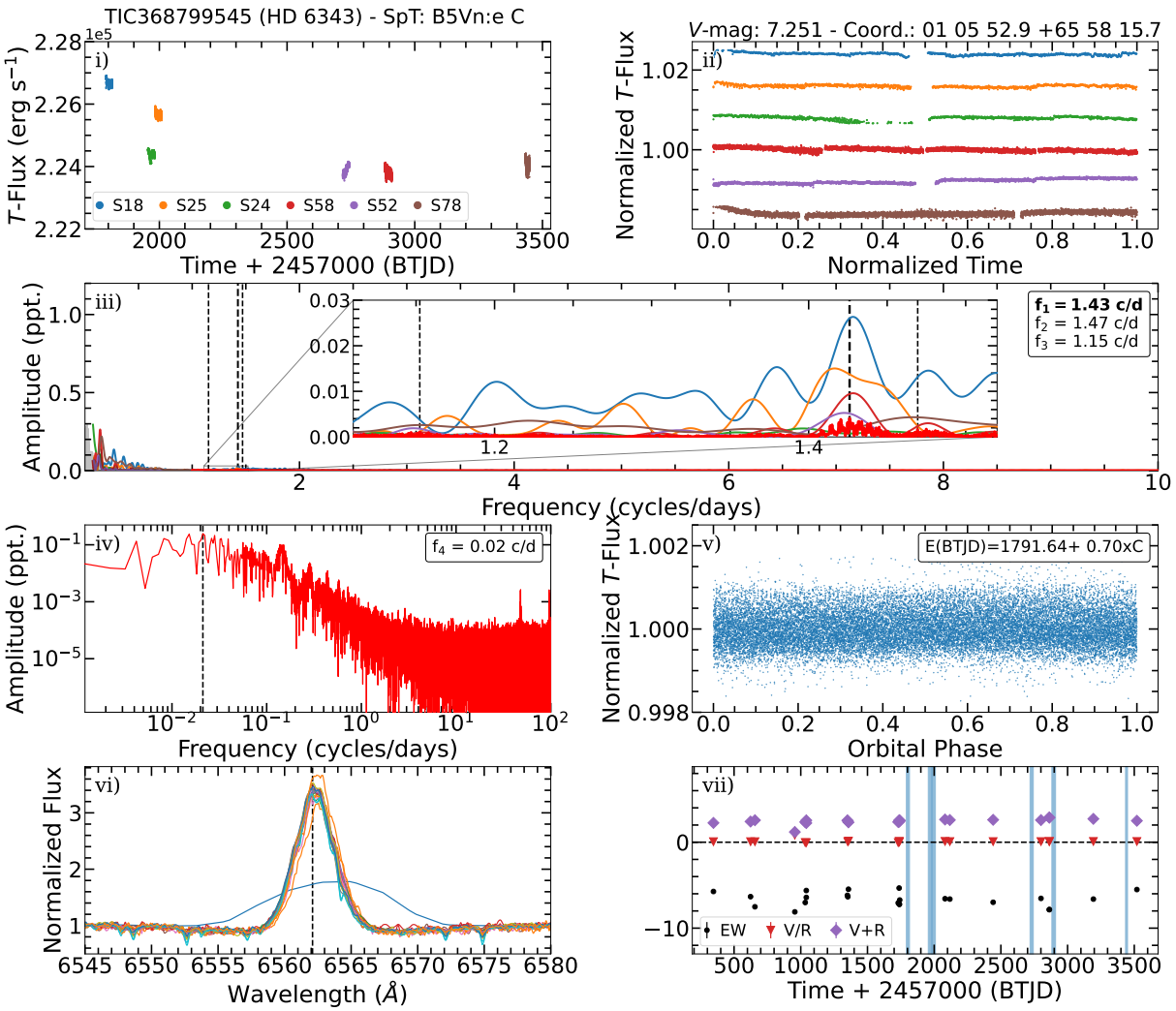

Figure C.125: Panels summarizing the photometric, spectroscopic, and frequency-domain analyses for the target TIC 368799545. (i) Raw T-Flux light curves from different sectors; (ii) normalized T-Flux light curves folded normalized time for each sector; (iii) Lomb-Scargle periodogram highlighting the three main frequencies f_1, f_2, and f_3, with a zoom-in inset; (iv) extended periodogram revealing a low-frequency component f_4; (v) orbital phase-folded light curve; (vi) optical spectrum centered on the Hα line (λ = 6562.8 Å); and (vii) temporal evolution of the equivalent width of the Hα line across available observations. Shaded regions in panel (vii) correspond to observation windows of sectors shown in panel (i).

C.126. TIC 370042412

7 Vul (HR 7409) has a low-mass companion orbiting with P=69.3d (Vennes et al., 2011), strongly suspected Be+sdOB binary (Rivinius et al., 2025b).

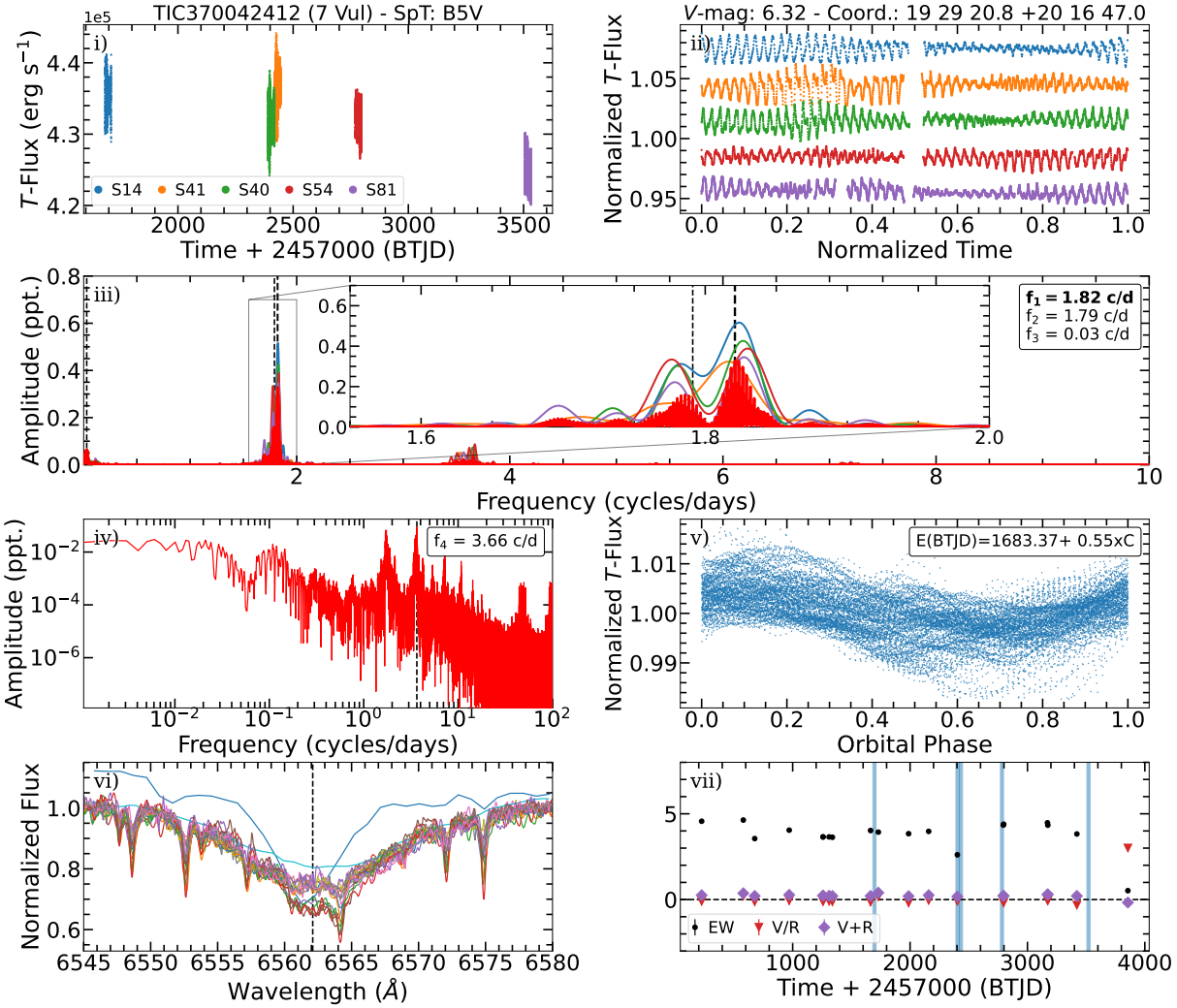

Figure C.126: Panels summarizing the photometric, spectroscopic, and frequency-domain analyses for the target TIC 370042412. (i) Raw T-Flux light curves from different sectors; (ii) normalized T-Flux light curves folded normalized time for each sector; (iii) Lomb-Scargle periodogram highlighting the three main frequencies f_1, f_2, and f_3, with a zoom-in inset; (iv) extended periodogram revealing a low-frequency component f_4; (v) orbital phase-folded light curve; (vi) optical spectrum centered on the Hα line (λ = 6562.8 Å); and (vii) temporal evolution of the equivalent width of the Hα line across available observations. Shaded regions in panel (vii) correspond to observation windows of sectors shown in panel (i).

C.127. TIC 370259865

HD 170783 is classified as a Be star, but with no signs of binarity.

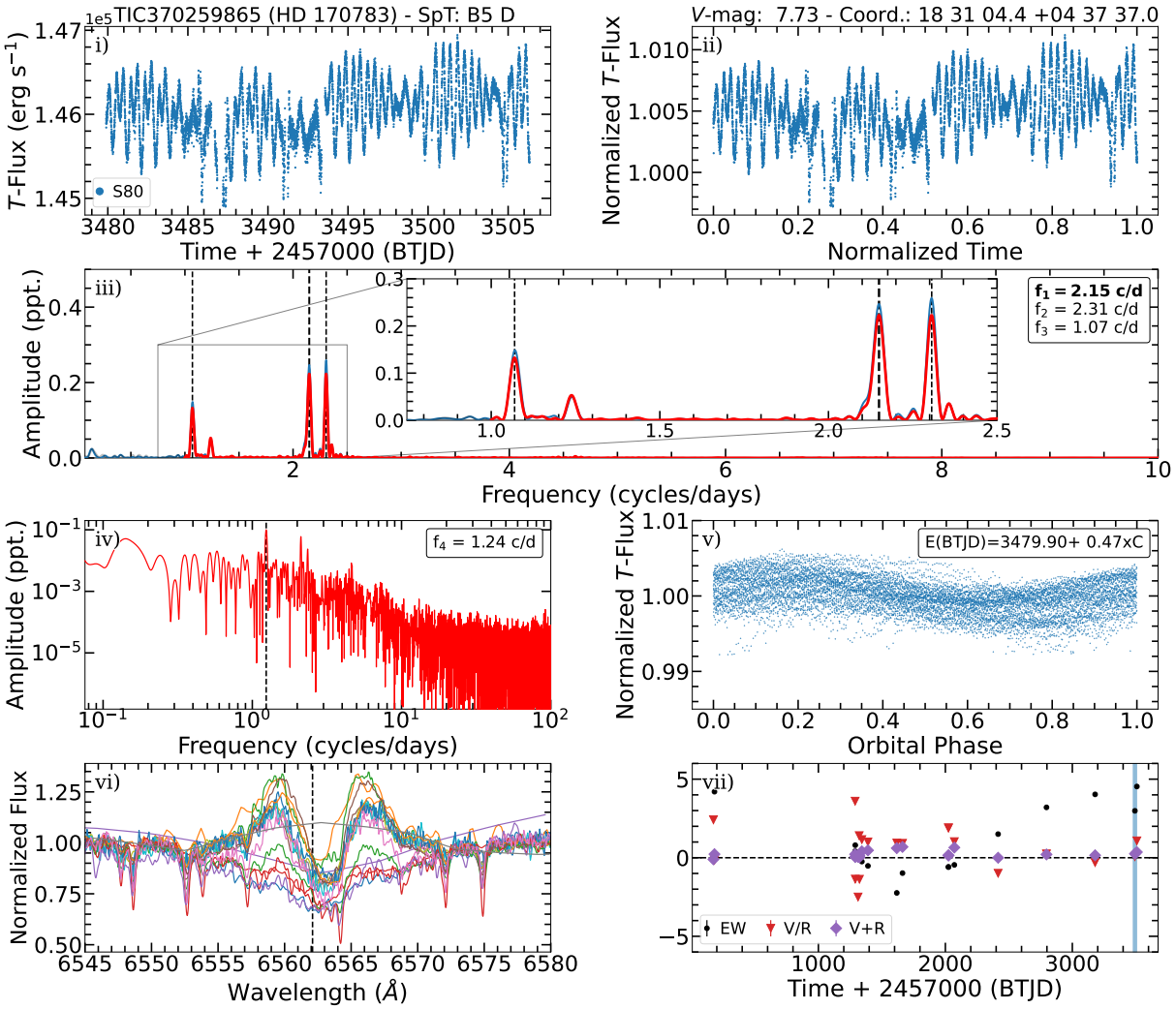

Figure C.127: Panels summarizing the photometric, spectroscopic, and frequency-domain analyses for the target TIC 370259865. (i) Raw T-Flux light curves from different sectors; (ii) normalized T-Flux light curves folded normalized time for each sector; (iii) Lomb-Scargle periodogram highlighting the three main frequencies f_1, f_2, and f_3, with a zoom-in inset; (iv) extended periodogram revealing a low-frequency component f_4; (v) orbital phase-folded light curve; (vi) optical spectrum centered on the Hα line (λ = 6562.8 Å); and (vii) temporal evolution of the equivalent width of the Hα line across available observations. Shaded regions in panel (vii) correspond to observation windows of sectors shown in panel (i).

C.128. TIC 377900979

V808 Cas (BD+61 2408) is an eclipsing binary system studied by Kervella et al. (2019); Bodensteiner et al. (2020), classified as a Be star, but which does not present Balmer series emission lines in the BeSS spectra.

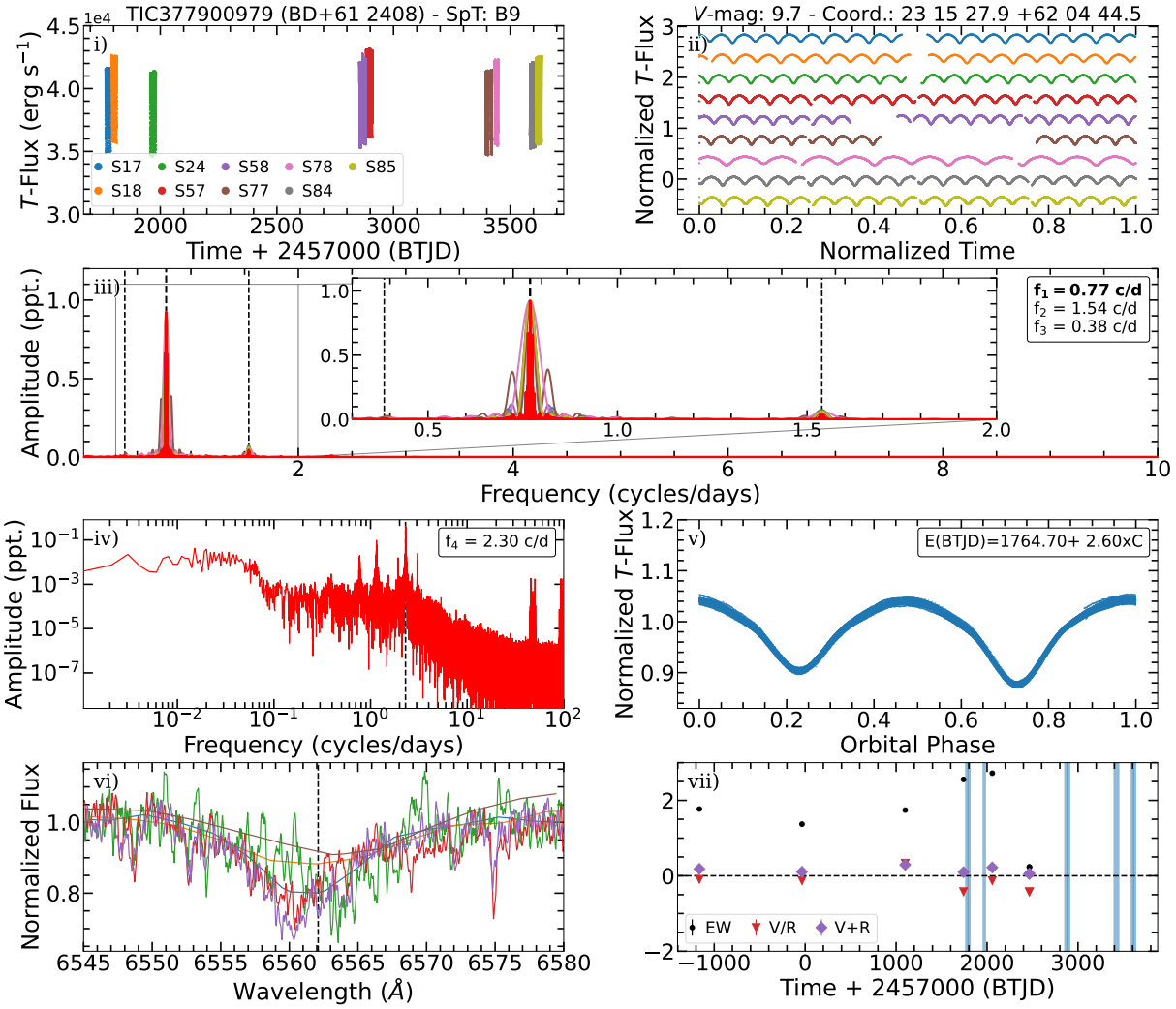

Figure C.128: Panels summarizing the photometric, spectroscopic, and frequency-domain analyses for the target TIC 377900979. (i) Raw T-Flux light curves from different sectors; (ii) normalized T-Flux light curves folded normalized time for each sector; (iii) Lomb-Scargle periodogram highlighting the three main frequencies f_1, f_2, and f_3, with a zoom-in inset; (iv) extended periodogram revealing a low-frequency component f_4; (v) orbital phase-folded light curve; (vi) optical spectrum centered on the Hα line (λ = 6562.8 Å); and (vii) temporal evolution of the equivalent width of the Hα line across available observations. Shaded regions in panel (vii) correspond to observation windows of sectors shown in panel (i).

C.129. TIC 377967736

HD 219523 is classified as a Be star (Chojnowski et al., 2015), being identified as belonging to a multiple system (Kervella and de Souza, 2007; Guerrero et al., 2025a).

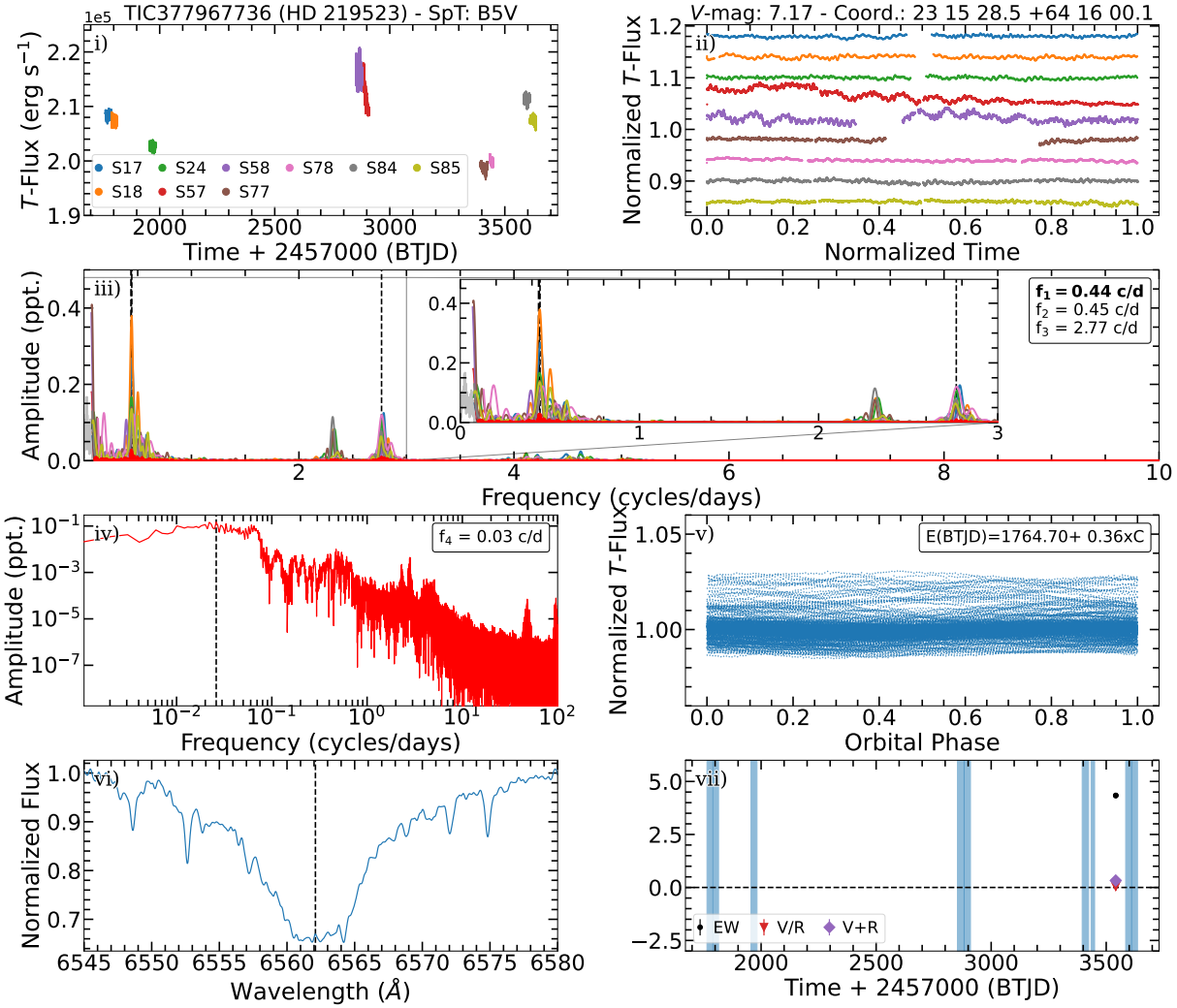

Figure C.129: Panels summarizing the photometric, spectroscopic, and frequency-domain analyses for the target TIC 377967736. (i) Raw T-Flux light curves from different sectors; (ii) normalized T-Flux light curves folded normalized time for each sector; (iii) Lomb-Scargle periodogram highlighting the three main frequencies f_1, f_2, and f_3, with a zoom-in inset; (iv) extended periodogram revealing a low-frequency component f_4; (v) orbital phase-folded light curve; (vi) optical spectrum centered on the Hα line (λ = 6562.8 Å); and (vii) temporal evolution of the equivalent width of the Hα line across available observations. Shaded regions in panel (vii) correspond to observation windows of sectors shown in panel (i).

C.130. TIC 385509348

17 Tau (HD 23302) is classified as a Be star, but has no signs of binarity.

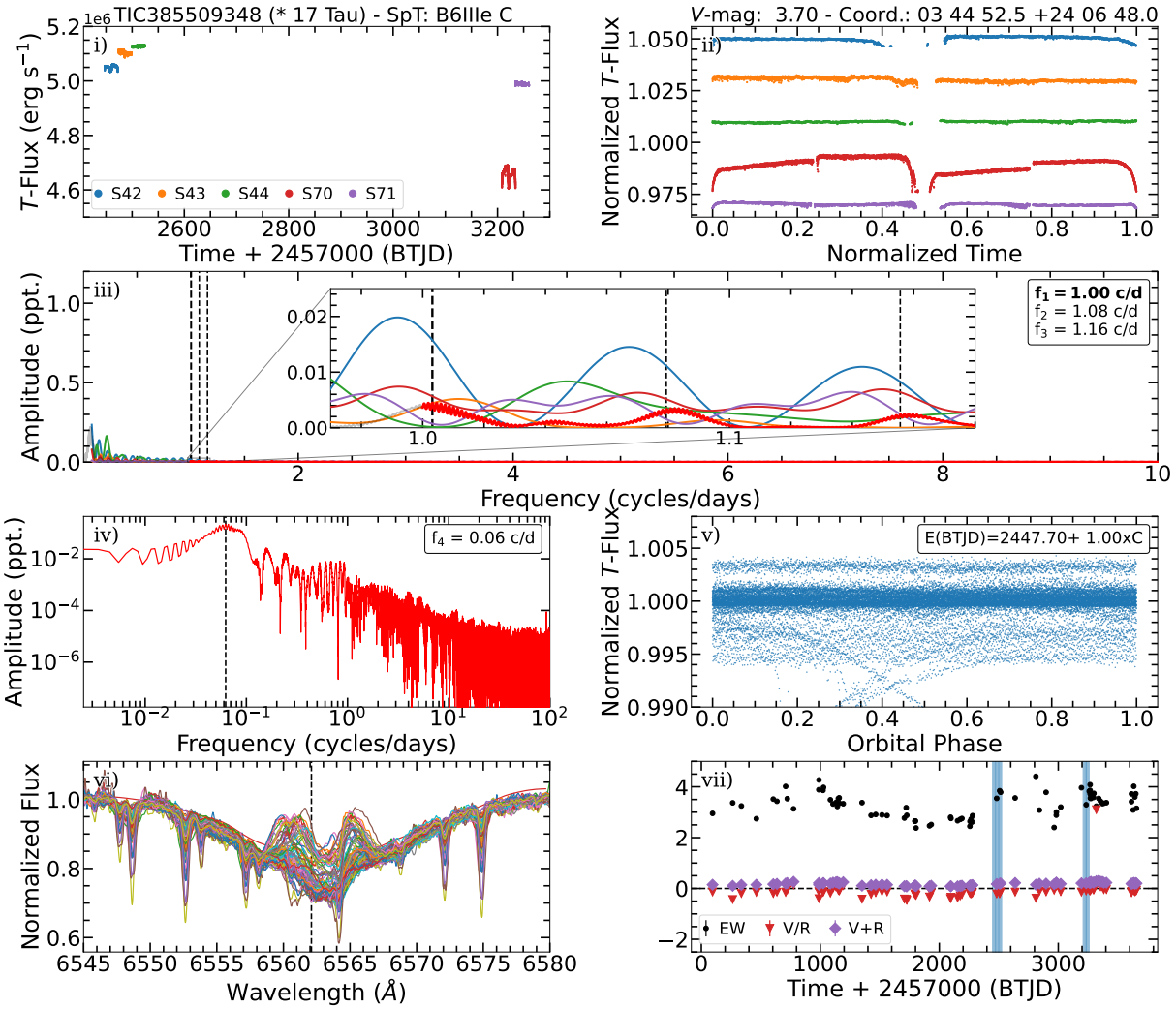

Figure C.130: Panels summarizing the photometric, spectroscopic, and frequency-domain analyses for the target TIC 385509348. (i) Raw T-Flux light curves from different sectors; (ii) normalized T-Flux light curves folded normalized time for each sector; (iii) Lomb-Scargle periodogram highlighting the three main frequencies f_1, f_2, and f_3, with a zoom-in inset; (iv) extended periodogram revealing a low-frequency component f_4; (v) orbital phase-folded light curve; (vi) optical spectrum centered on the Hα line (λ = 6562.8 Å); and (vii) temporal evolution of the equivalent width of the Hα line across available observations. Shaded regions in panel (vii) correspond to observation windows of sectors shown in panel (i).

C.131. TIC 387813185

HD 200775 appears to be a Herbig Be Star transition object presenting one of the highest emission intensities in the sample. It was studied by Kervella et al. (2019), classified as non-binary.

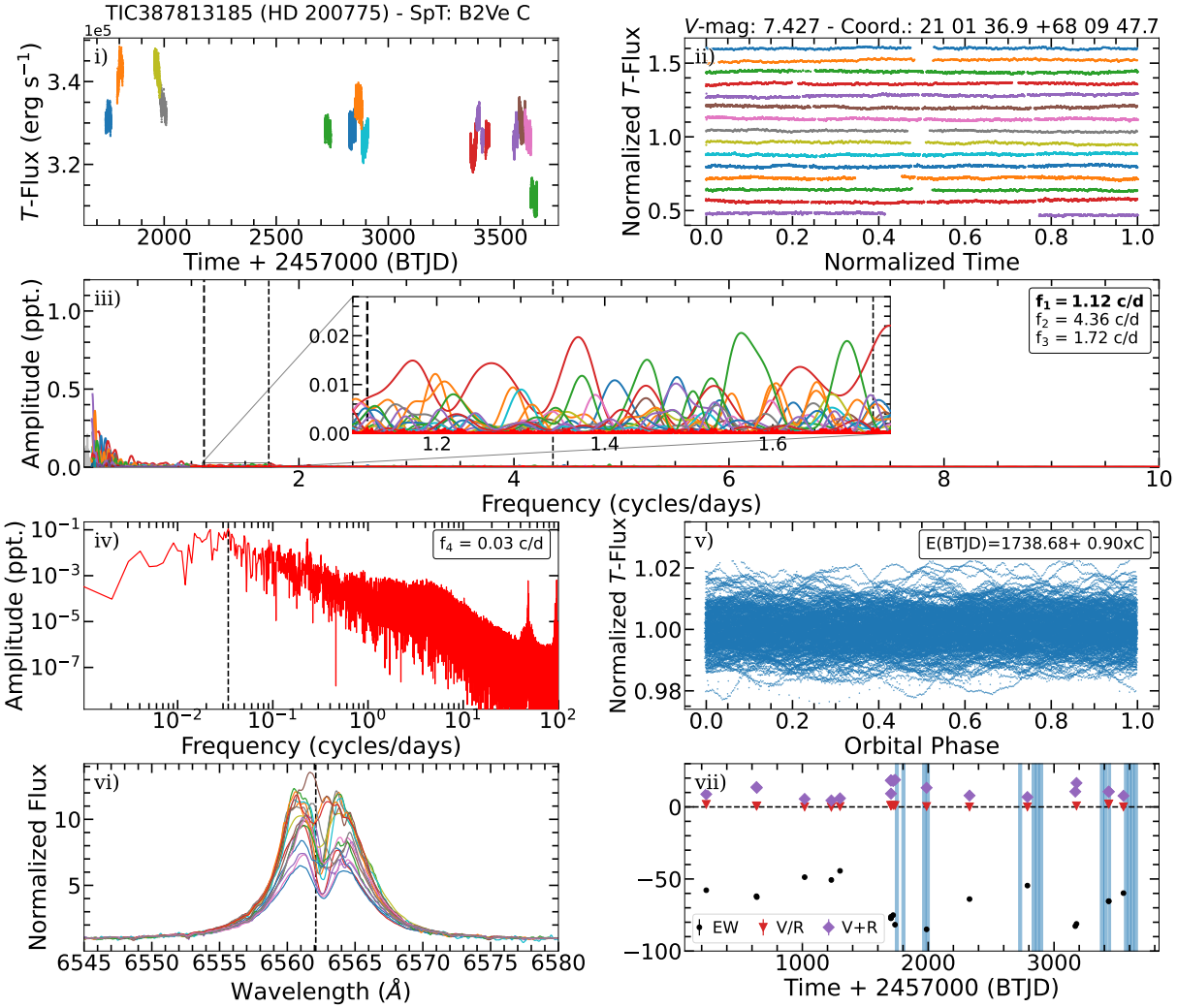

Figure C.131: Panels summarizing the photometric, spectroscopic, and frequency-domain analyses for the target TIC 387813185. (i) Raw T-Flux light curves from different sectors; (ii) normalized T-Flux light curves folded normalized time for each sector; (iii) Lomb-Scargle periodogram highlighting the three main frequencies f_1, f_2, and f_3, with a zoom-in inset; (iv) extended periodogram revealing a low-frequency component f_4; (v) orbital phase-folded light curve; (vi) optical spectrum centered on the Hα line (λ = 6562.8 Å); and (vii) temporal evolution of the equivalent width of the Hα line across available observations. Shaded regions in panel (vii) correspond to observation windows of sectors shown in panel (i).

C.132. TIC 394728064

HD 93237 is a eclipsing binary and was classified as a Be star, but no spectrum in the BeSS catalog confirms such a nature. This object was also studied by Labadie-Bartz et al. (2022), and indicated that its Be nature remains unclear.

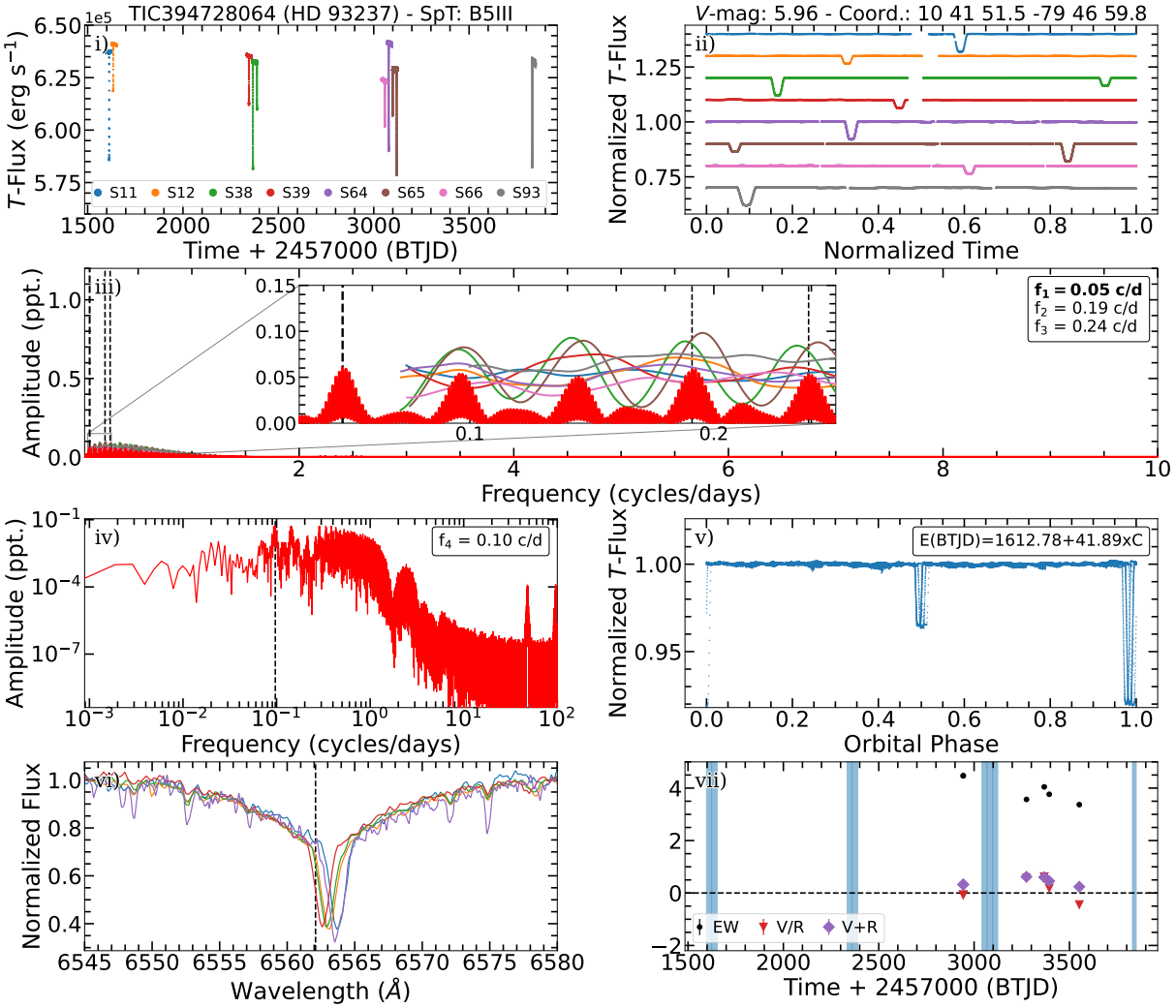

Figure C.132: Panels summarizing the photometric, spectroscopic, and frequency-domain analyses for the target TIC 394728064. (i) Raw T-Flux light curves from different sectors; (ii) normalized T-Flux light curves folded normalized time for each sector; (iii) Lomb-Scargle periodogram highlighting the three main frequencies f_1, f_2, and f_3, with a zoom-in inset; (iv) extended periodogram revealing a low-frequency component f_4; (v) orbital phase-folded light curve; (vi) optical spectrum centered on the Hα line (λ = 6562.8 Å); and (vii) temporal evolution of the equivalent width of the Hα line across available observations. Shaded regions in panel (vii) correspond to observation windows of sectors shown in panel (i).

C.133. TIC 399626383

RX Cas is classified as a semi-detached emission-line binary (Harmanec et al., 2015). No spectrum was found in the BESS catalog.

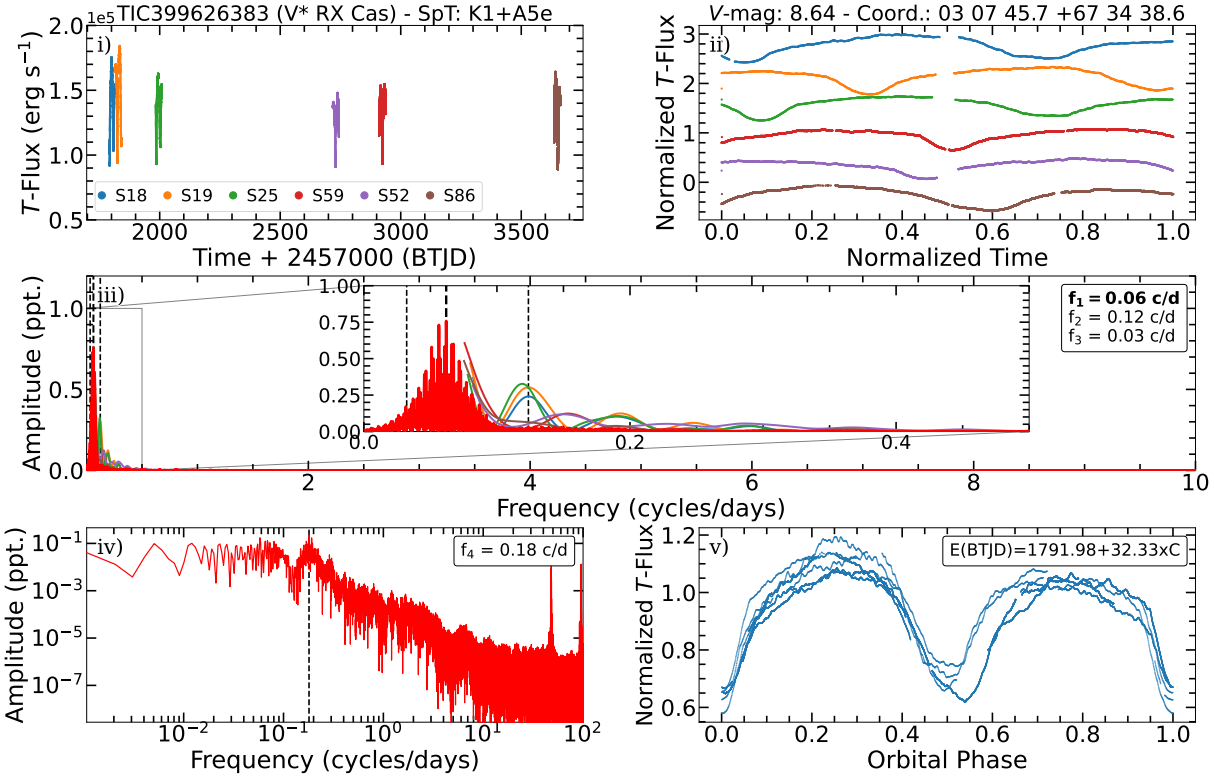

Figure C.133: Panels summarizing the photometric and frequency-domain analyses for the target TIC 399626383. (i) Raw T-Flux light curves from different sectors; (ii) normalized T-Flux light curves folded normalized time for each sector; (iii) Lomb-Scargle periodogram highlighting the three main frequencies f_1, f_2, and f_3, with a zoom-in inset; (iv) extended periodogram revealing a low-frequency component f_4; (v) orbital phase-folded light curve.

C.134. TIC 402978131

HD 5679 is classified as a spectroscopic binary, but with no sign of a Be star in the system. No spectrum was found in the BESS catalog.

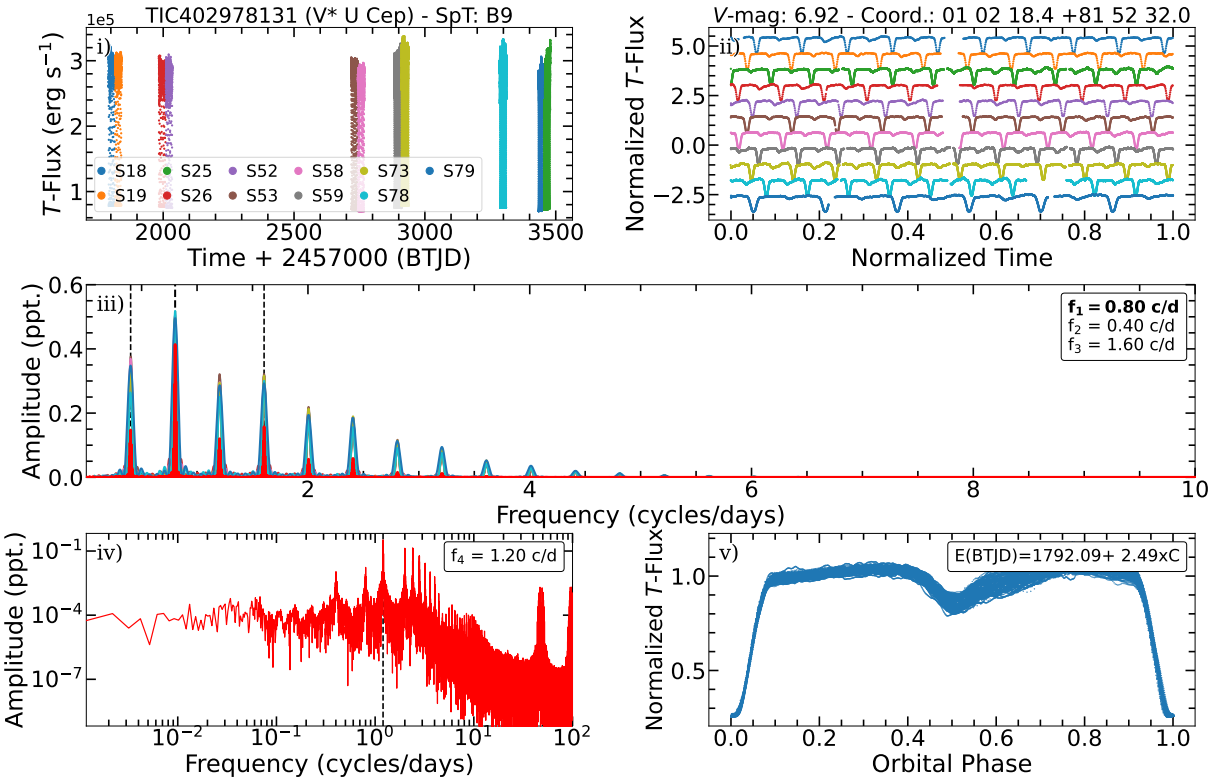

Figure C.134: Panels summarizing the photometric and frequency-domain analyses for the target TIC 402978131. (i) Raw T-Flux light curves from different sectors; (ii) normalized T-Flux light curves folded normalized time for each sector; (iii) Lomb-Scargle periodogram highlighting the three main frequencies f_1, f_2, and f_3, with a zoom-in inset; (iv) extended periodogram revealing a low-frequency component f_4; (v) orbital phase-folded light curve.

C.135. TIC 404619905

66 Oph is classified as a Be star and is well studied by Marr et al. (2021). Unfortunately and curiously, the spectra in the BeSS catalog have not shown emission lines for approximately 1 decade.

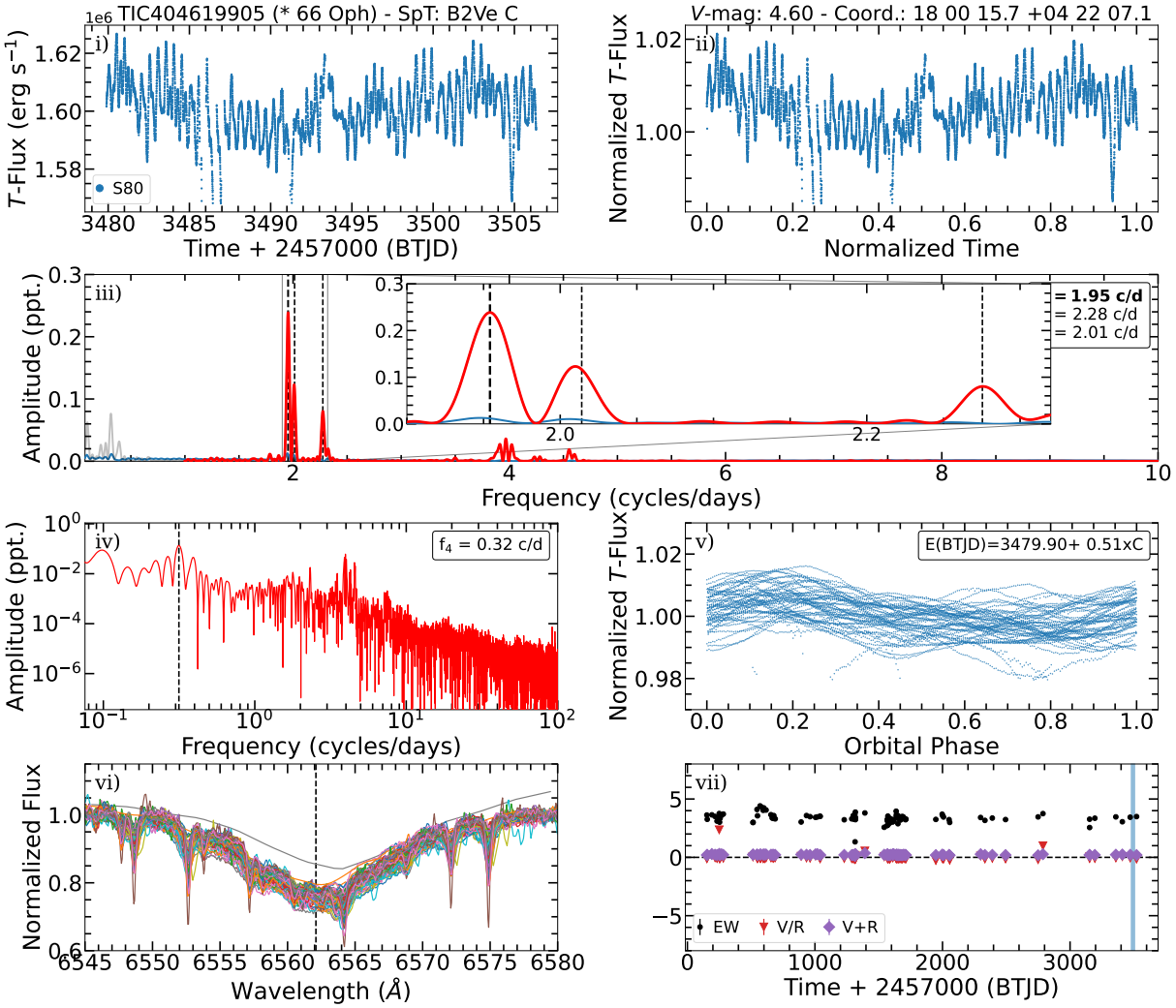

Figure C.135: Panels summarizing the photometric, spectroscopic, and frequency-domain analyses for the target TIC 404619905. (i) Raw T-Flux light curves from different sectors; (ii) normalized T-Flux light curves folded normalized time for each sector; (iii) Lomb-Scargle periodogram highlighting the three main frequencies f_1, f_2, and f_3, with a zoom-in inset; (iv) extended periodogram revealing a low-frequency component f_4; (v) orbital phase-folded light curve; (vi) optical spectrum centered on the Hα line (λ = 6562.8 Å); and (vii) temporal evolution of the equivalent width of the Hα line across available observations. Shaded regions in panel (vii) correspond to observation windows of sectors shown in panel (i).

C.136. TIC 405216722

HD 60993 is classified as a Be star, but in the study conducted with interferometry by Souza et al. (2020) no signs of a stellar companion were found. No spectrum was found in the BESS catalog.

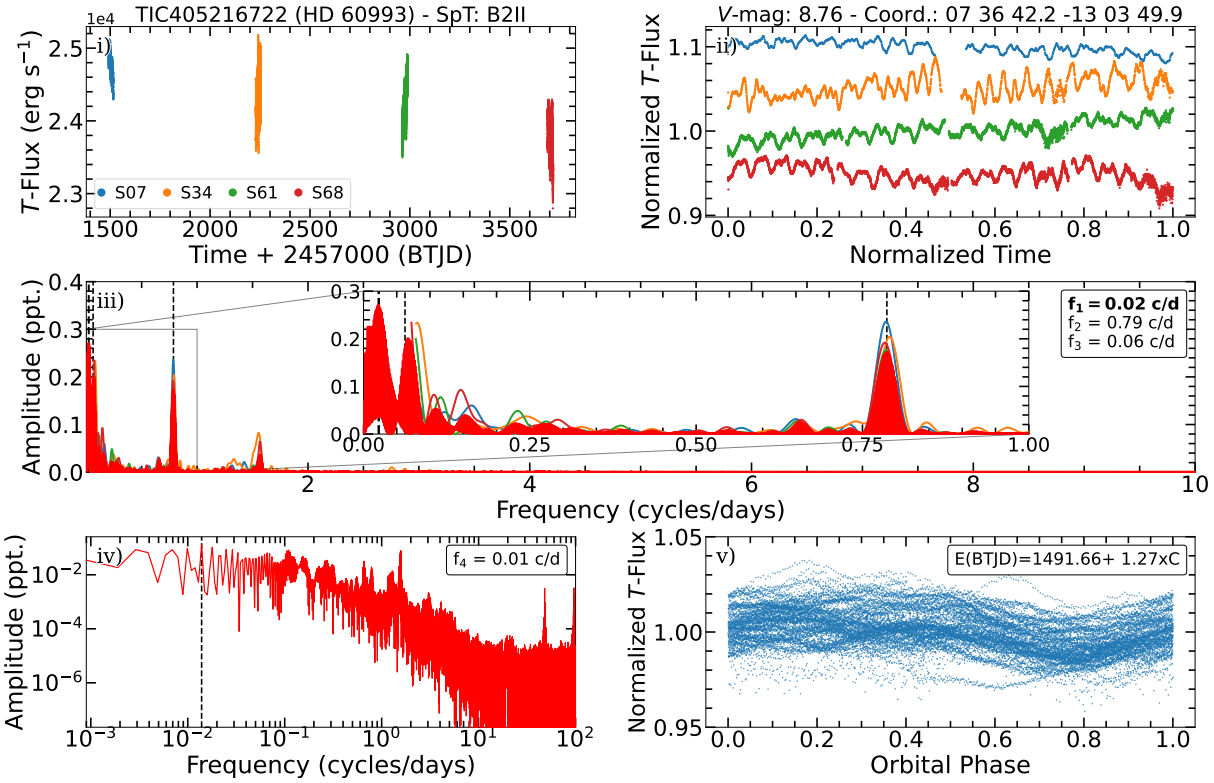

Figure C.136: Panels summarizing the photometric and frequency-domain analyses for the target TIC 405216722. (i) Raw T-Flux light curves from different sectors; (ii) normalized T-Flux light curves folded normalized time for each sector; (iii) Lomb-Scargle periodogram highlighting the three main frequencies f_1, f_2, and f_3, with a zoom-in inset; (iv) extended periodogram revealing a low-frequency component f_4; (v) orbital phase-folded light curve.

C.137. TIC 410193513

RW Pet (HD 276247) is an eclipsing binary and spectroscopy, with a Be star (Labadie-Bartz et al., 2017).

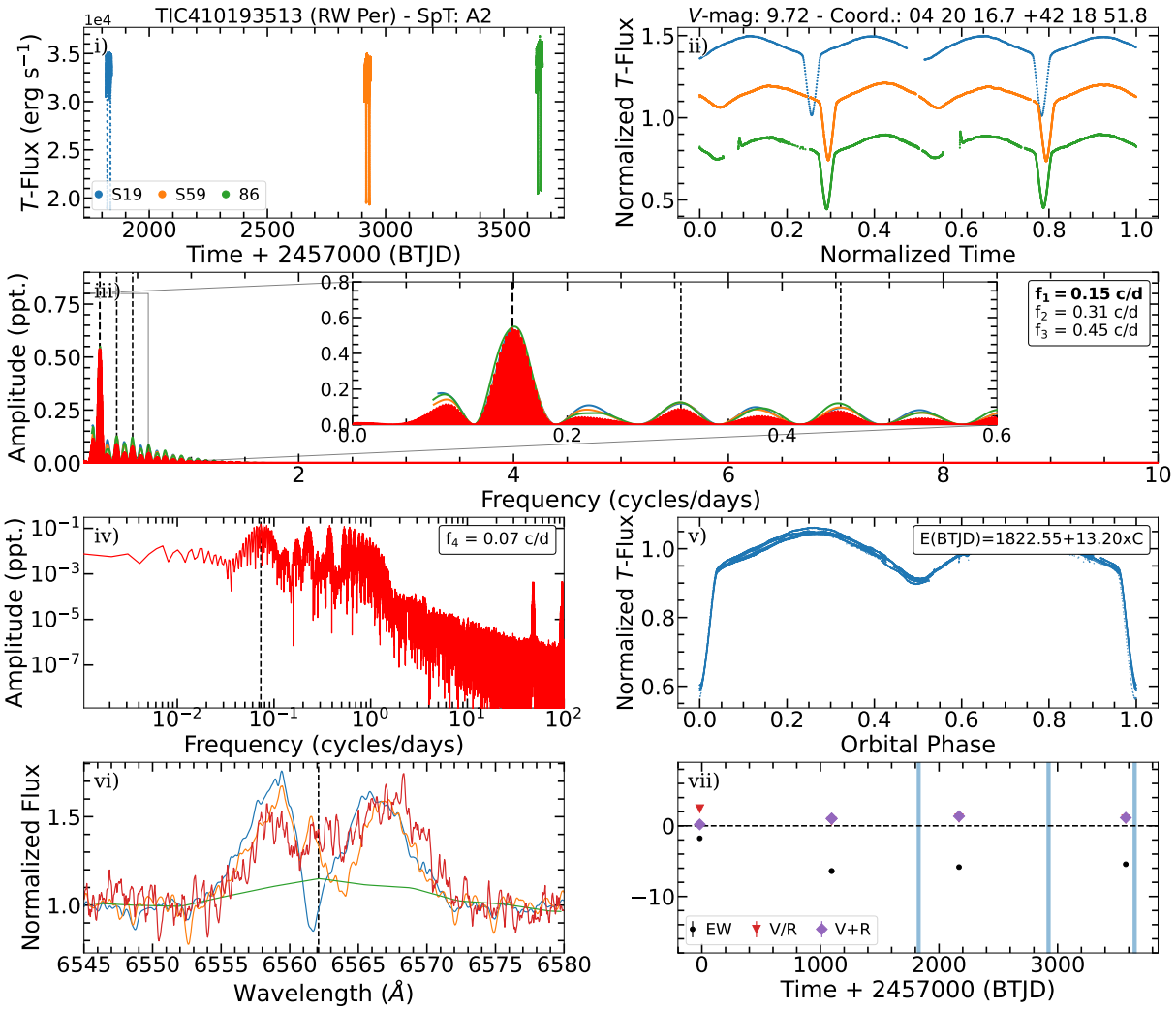

Figure C.137: Panels summarizing the photometric, spectroscopic, and frequency-domain analyses for the target TIC 410193513. (i) Raw T-Flux light curves from different sectors; (ii) normalized T-Flux light curves folded normalized time for each sector; (iii) Lomb-Scargle periodogram highlighting the three main frequencies f_1, f_2, and f_3, with a zoom-in inset; (iv) extended periodogram revealing a low-frequency component f_4; (v) orbital phase-folded light curve; (vi) optical spectrum centered on the Hα line (λ = 6562.8 Å); and (vii) temporal evolution of the equivalent width (EW) of the Hα line across available observations. Shaded regions in panel (vii) correspond to observation windows of sectors shown in panel (i).

C.138. TIC 410627159

48 Lib (HD 142983) is a B5-type Be star that shows no signs of binarity.

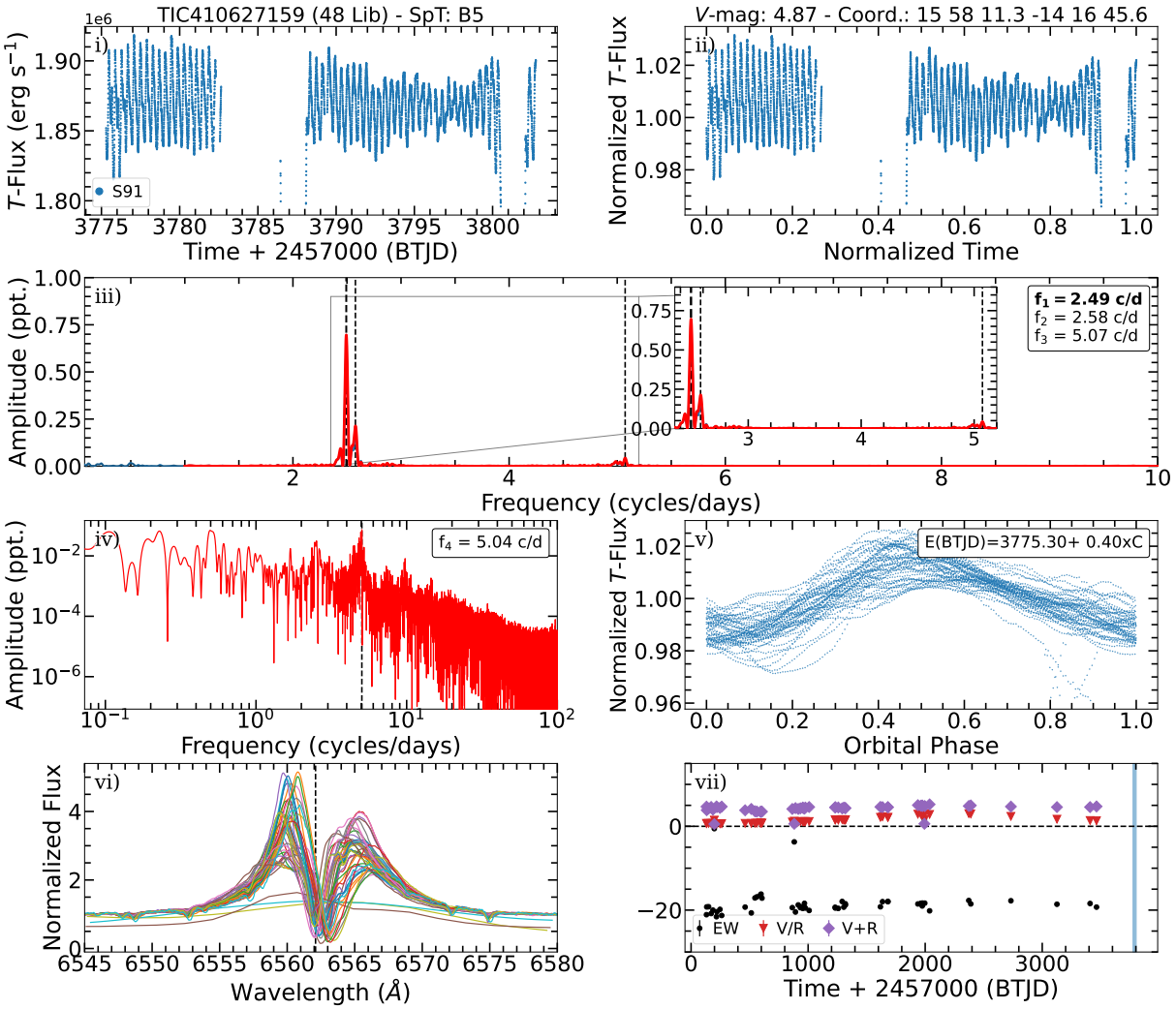

Figure C.138: Panels summarizing the photometric, spectroscopic, and frequency-domain analyses for the target TIC 410627159. (i) Raw T-Flux light curves from different sectors; (ii) normalized T-Flux light curves folded normalized time for each sector; (iii) Lomb-Scargle periodogram highlighting the three main frequencies f_1, f_2, and f_3, with a zoom-in inset; (iv) extended periodogram revealing a low-frequency component f_4; (v) orbital phase-folded light curve; (vi) optical spectrum centered on the Hα line (λ = 6562.8 Å); and (vii) temporal evolution of the equivalent width of the Hα line across available observations. Shaded regions in panel (vii) correspond to observation windows of sectors shown in panel (i).

C.139. TIC 411577031

HD 208682 was classified as a B2Ve star by (Slettebak, 1982) and as a binary by (Kervella et al., 2019).

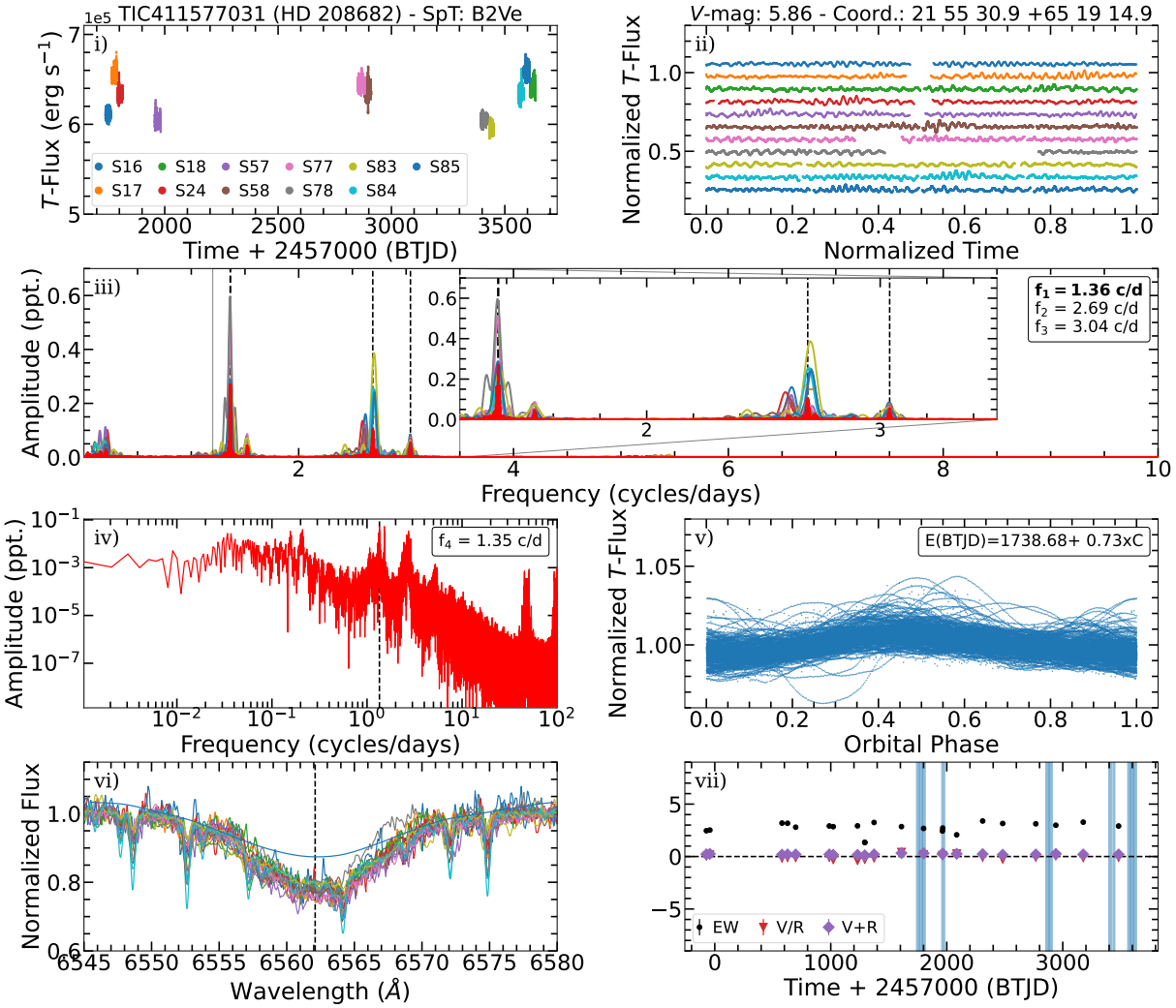

Figure C.139: Panels summarizing the photometric, spectroscopic, and frequency-domain analyses for the target TIC 411577031. (i) Raw T-Flux light curves from different sectors; (ii) normalized T-Flux light curves folded normalized time for each sector; (iii) Lomb-Scargle periodogram highlighting the three main frequencies f_1, f_2, and f_3, with a zoom-in inset; (iv) extended periodogram revealing a low-frequency component f_4; (v) orbital phase-folded light curve; (vi) optical spectrum centered on the Hα line (λ = 6562.8 Å); and (vii) temporal evolution of the equivalent width of the Hα line across available observations. Shaded regions in panel (vii) correspond to observation windows of sectors shown in panel (i).

C.140. TIC 412724758

Rivinius et al. (2003) pointed out that α Ara (HD 158427) may be a binary system with an orbital period greater than 71 d.

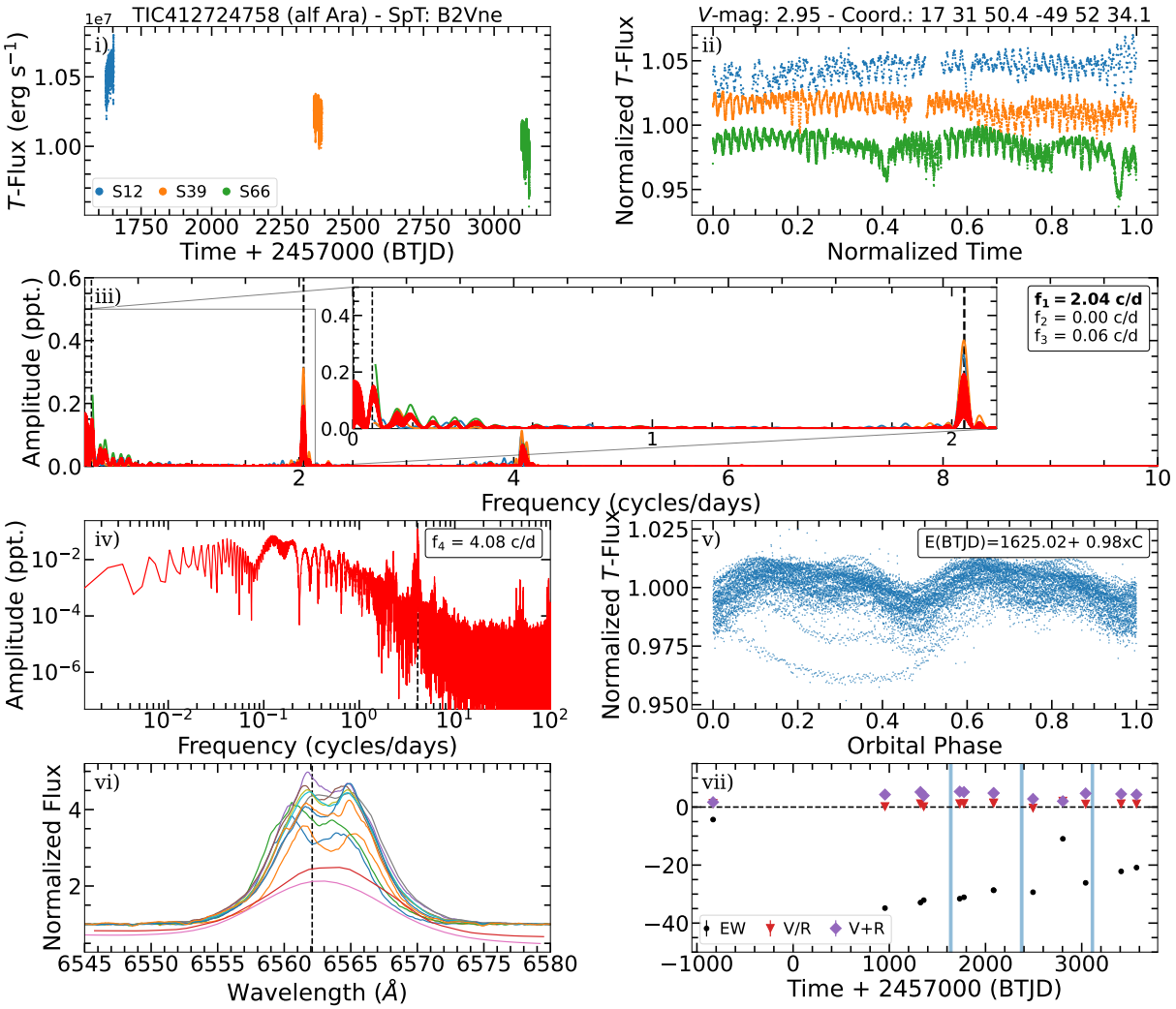

Figure C.140: Panels summarizing the photometric, spectroscopic, and frequency-domain analyses for the target TIC 412724758. (i) Raw T-Flux light curves from different sectors; (ii) normalized T-Flux light curves folded normalized time for each sector; (iii) Lomb-Scargle periodogram highlighting the three main frequencies f_1, f_2, and f_3, with a zoom-in inset; (iv) extended periodogram revealing a low-frequency component f_4; (v) orbital phase-folded light curve; (vi) optical spectrum centered on the Hα line (λ = 6562.8 Å); and (vii) temporal evolution of the equivalent width of the Hα line across available observations. Shaded regions in panel (vii) correspond to observation windows of sectors shown in panel (i).

C.141. TIC 4154938

HD 35079 was identified as binary Be in the work of Guerrero et al. (2025a) and by Kervella et al. (2019). No spectrum was found in the BESS catalog.

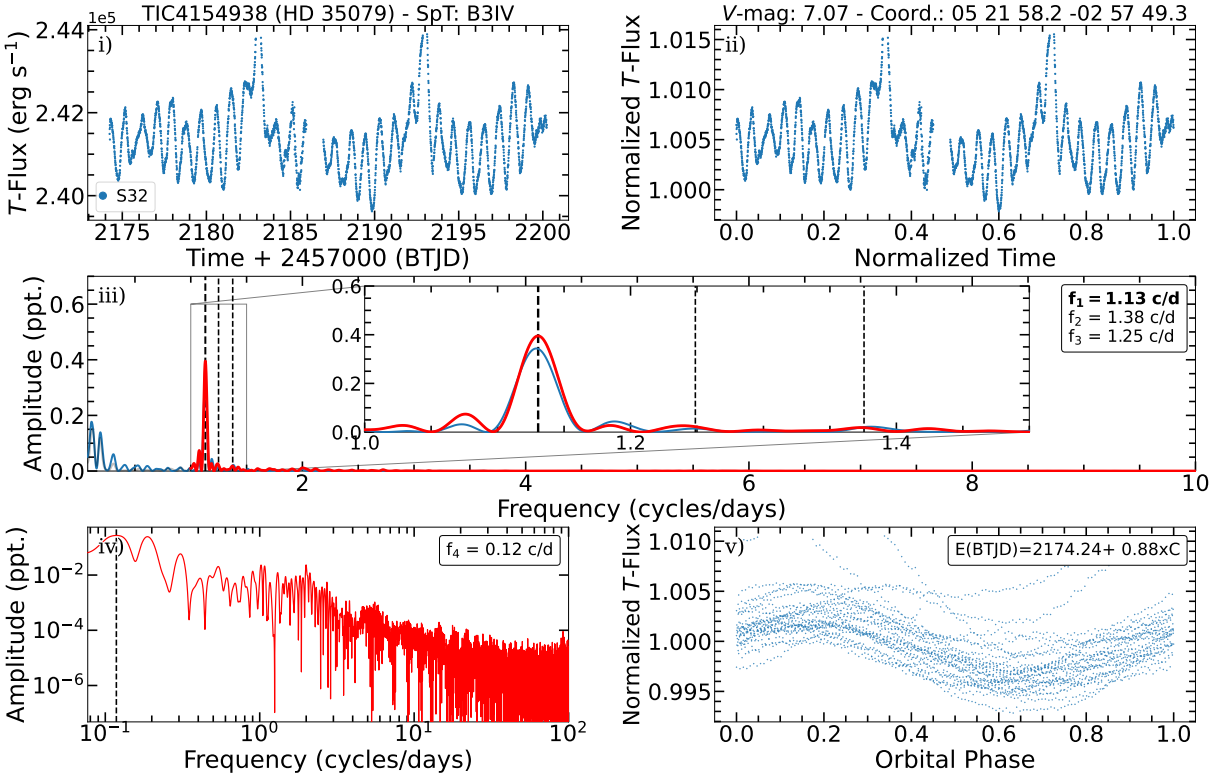

Figure C.141: Panels summarizing the photometric and frequency-domain analyses for the target TIC 4154938. (i) Raw T-Flux light curves from different sectors; (ii) normalized T-Flux light curves folded normalized time for each sector; (iii) Lomb-Scargle periodogram highlighting the three main frequencies f_1, f_2, and f_3, with a zoom-in inset; (iv) extended periodogram revealing a low-frequency component f_4; (v) orbital phase-folded light curve.

C.142. TIC 42360166

V1624 Cyg (28 Cyg) has spectral type B2, being a possible Be+Sdo binary system.

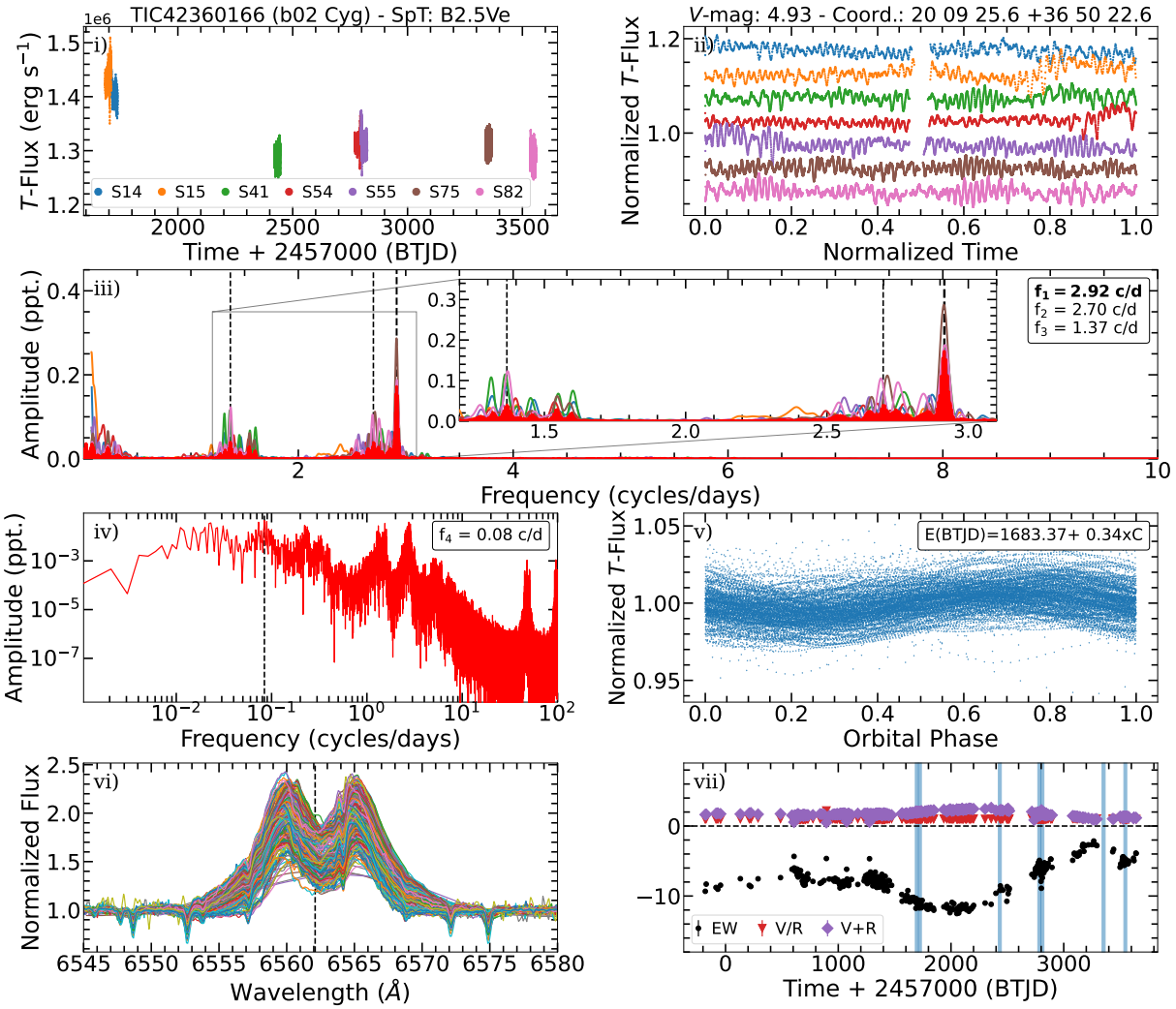

Figure C.142: Panels summarizing the photometric, spectroscopic, and frequency-domain analyses for the target TIC 42360166. (i) Raw T-Flux light curves from different sectors; (ii) normalized T-Flux light curves folded normalized time for each sector; (iii) Lomb-Scargle periodogram highlighting the three main frequencies f_1, f_2, and f_3, with a zoom-in inset; (iv) extended periodogram revealing a low-frequency component f_4; (v) orbital phase-folded light curve; (vi) optical spectrum centered on the Hα line (λ = 6562.8 Å); and (vii) temporal evolution of the equivalent width of the Hα line across available observations. Shaded regions in panel (vii) correspond to observation windows of sectors shown in panel (i).

C.143. TIC 424566072

HD 17520 is classified as a multiple system, but there is no evidence of it having a Be star. No spectrum was found in the BESS catalog.

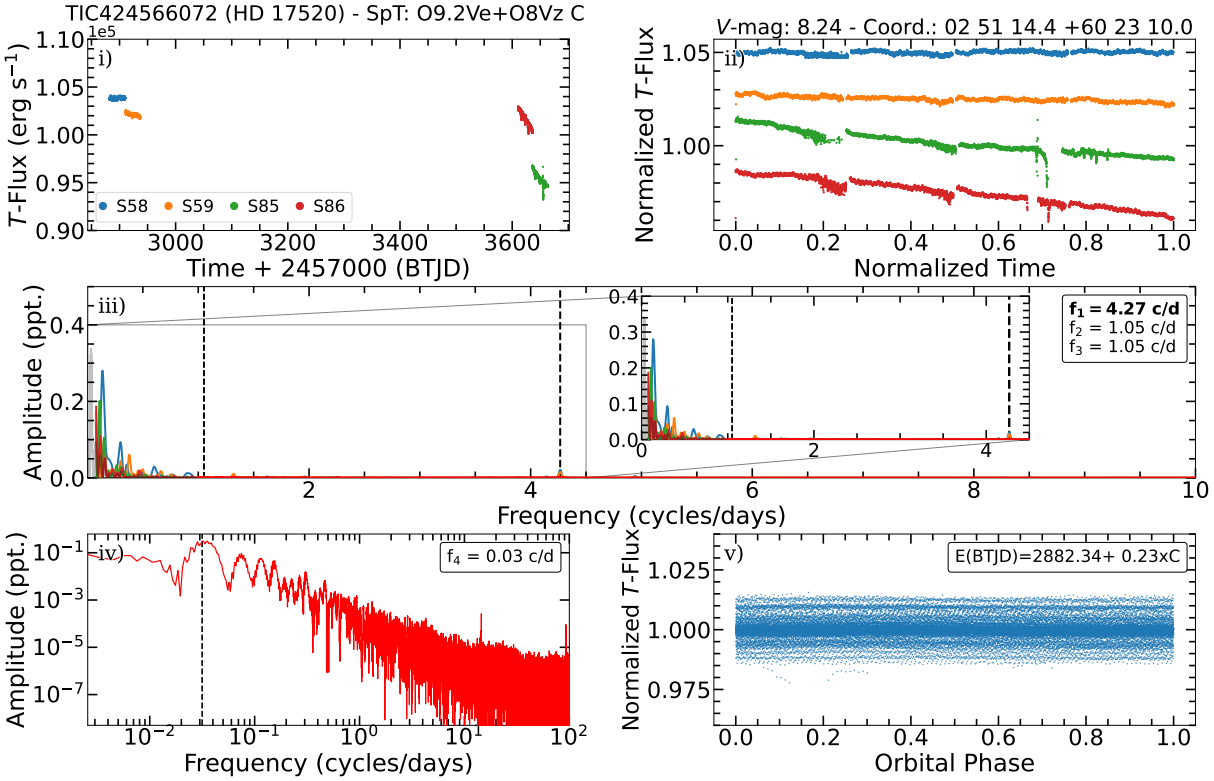

Figure C.143: Panels summarizing the photometric and frequency-domain analyses for the target TIC 424566072. (i) Raw T-Flux light curves from different sectors; (ii) normalized T-Flux light curves folded normalized time for each sector; (iii) Lomb-Scargle periodogram highlighting the three main frequencies f_1, f_2, and f_3, with a zoom-in inset; (iv) extended periodogram revealing a low-frequency component f_4; (v) orbital phase-folded light curve.

C.144. TIC 425224332

β CMi (HD 58715) was well studied by Klement et al. (2015), identifying it as a binary system that has a Be star, in addition to presenting its physical and orbital characteristics.

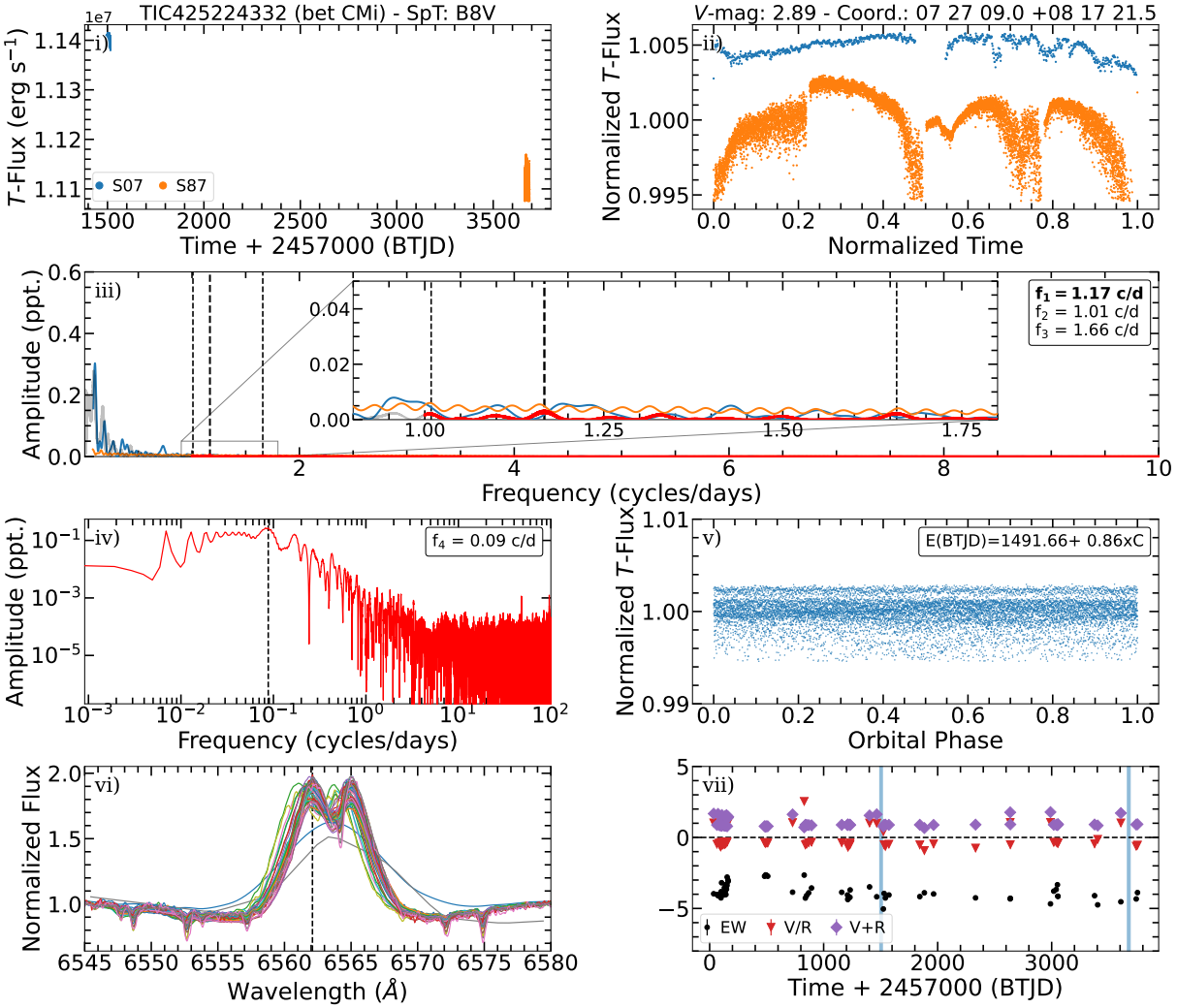

Figure C.144: Panels summarizing the photometric, spectroscopic, and frequency-domain analyses for the target TIC 425224332. (i) Raw T-Flux light curves from different sectors; (ii) normalized T-Flux light curves folded normalized time for each sector; (iii) Lomb-Scargle periodogram highlighting the three main frequencies f_1, f_2, and f_3, with a zoom-in inset; (iv) extended periodogram revealing a low-frequency component f_4; (v) orbital phase-folded light curve; (vi) optical spectrum centered on the Hα line (λ = 6562.8 Å); and (vii) temporal evolution of the equivalent width of the Hα line across available observations. Shaded regions in panel (vii) correspond to observation windows of sectors shown in panel (i).

C.145. TIC 427396133

HD 37115 is a Be star of type B7, and as detailed by Guerrero et al. (2025a), there is no reliability in the binarity of this system.

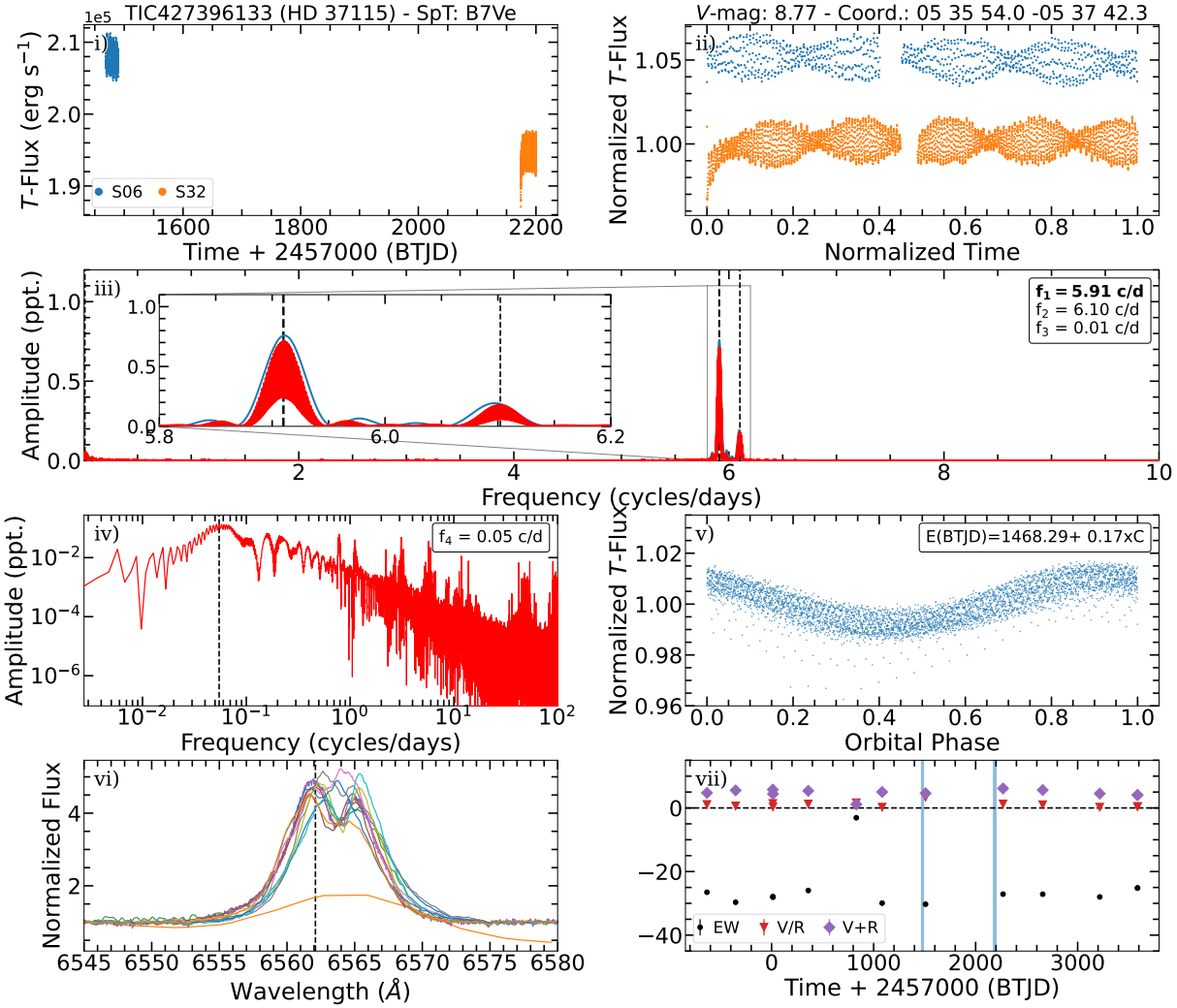

Figure C.145: Panels summarizing the photometric, spectroscopic, and frequency-domain analyses for the target TIC 427396133. (i) Raw T-Flux light curves from different sectors; (ii) normalized T-Flux light curves folded normalized time for each sector; (iii) Lomb-Scargle periodogram highlighting the three main frequencies f_1, f_2, and f_3, with a zoom-in inset; (iv) extended periodogram revealing a low-frequency component f_4; (v) orbital phase-folded light curve; (vi) optical spectrum centered on the Hα line (λ = 6562.8 Å); and (vii) temporal evolution of the equivalent width of the Hα line across available observations. Shaded regions in panel (vii) correspond to observation windows of sectors shown in panel (i).

C.146. TIC 429843636

HD 205329 has a Be star, and as detailed by Guerrero et al. (2025a), there is reliability in the binarity of this system, possibly being a triple system. No spectrum was found in the BeSS catalog.

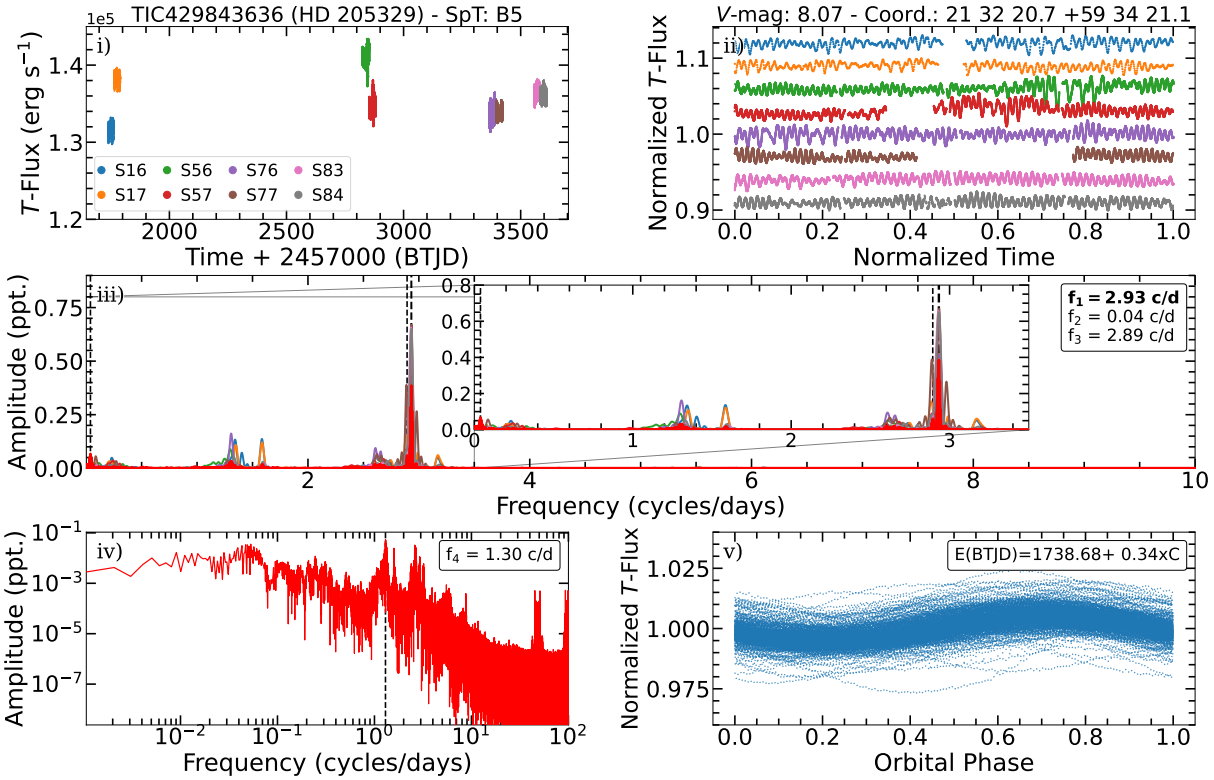

Figure C.146: Panels summarizing the photometric and frequency-domain analyses for the target TIC 429843636. (i) Raw T-Flux light curves from different sectors; (ii) normalized T-Flux light curves folded normalized time for each sector; (iii) Lomb-Scargle periodogram highlighting the three main frequencies f_1, f_2, and f_3, with a zoom-in inset; (iv) extended periodogram revealing a low-frequency component f_4; (v) orbital phase-folded light curve.

C.147. TIC 429863539

HD 43703 is a Be star of type B1, but without reliable signs of binarity.

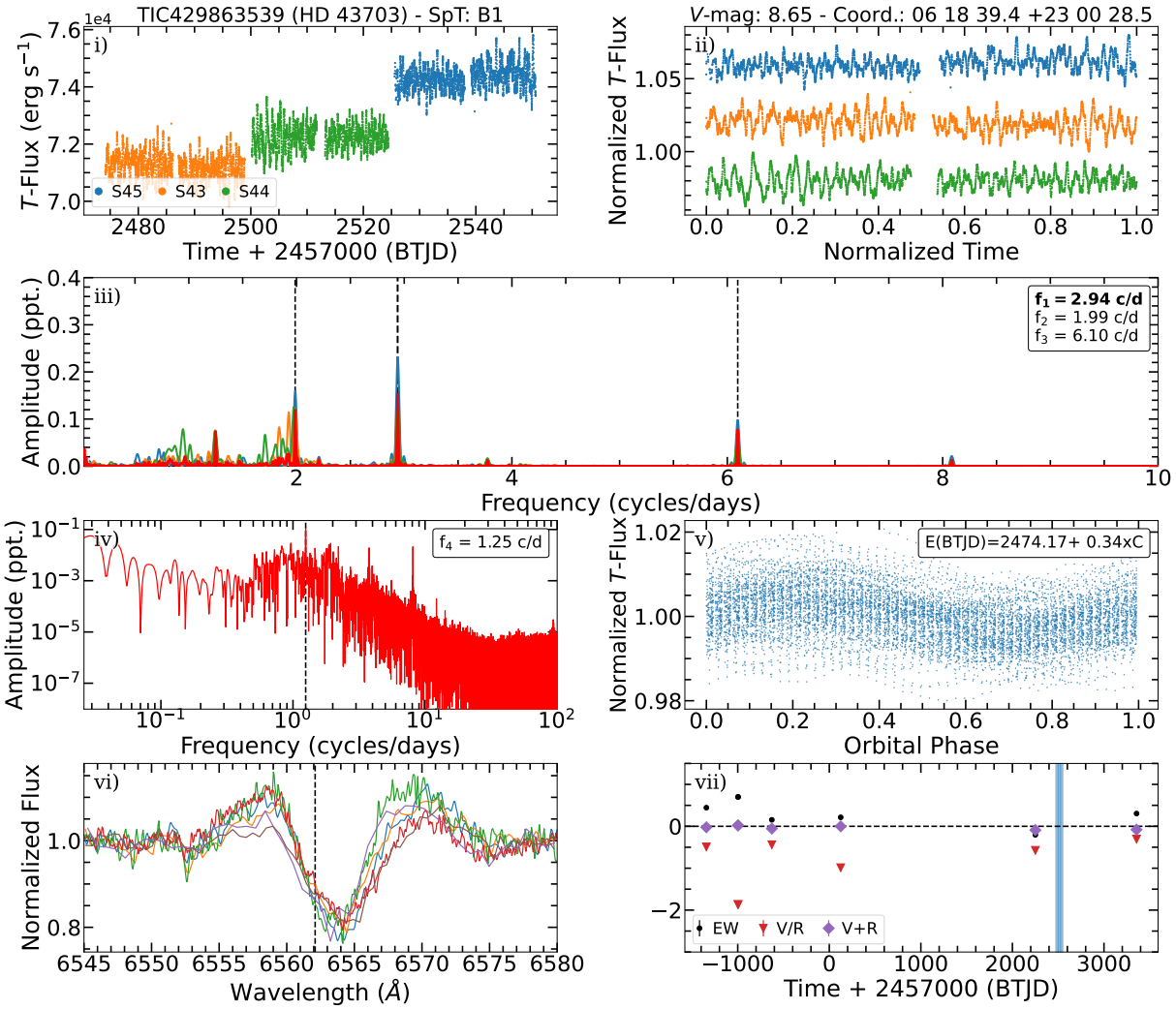

Figure C.147: Panels summarizing the photometric, spectroscopic, and frequency-domain analyses for the target TIC 429863539. (i) Raw T-Flux light curves from different sectors; (ii) normalized T-Flux light curves folded normalized time for each sector; (iii) Lomb-Scargle periodogram highlighting the three main frequencies f_1, f_2, and f_3, with a zoom-in inset; (iv) extended periodogram revealing a low-frequency component f_4; (v) orbital phase-folded light curve; (vi) optical spectrum centered on the Hα line (λ = 6562.8 Å); and (vii) temporal evolution of the equivalent width of the Hα line across available observations. Shaded regions in panel (vii) correspond to observation windows of sectors shown in panel (i).

C.148. TIC 431116093

HD 212044 is a Be star of type B2, but without reliable signs of binarity.

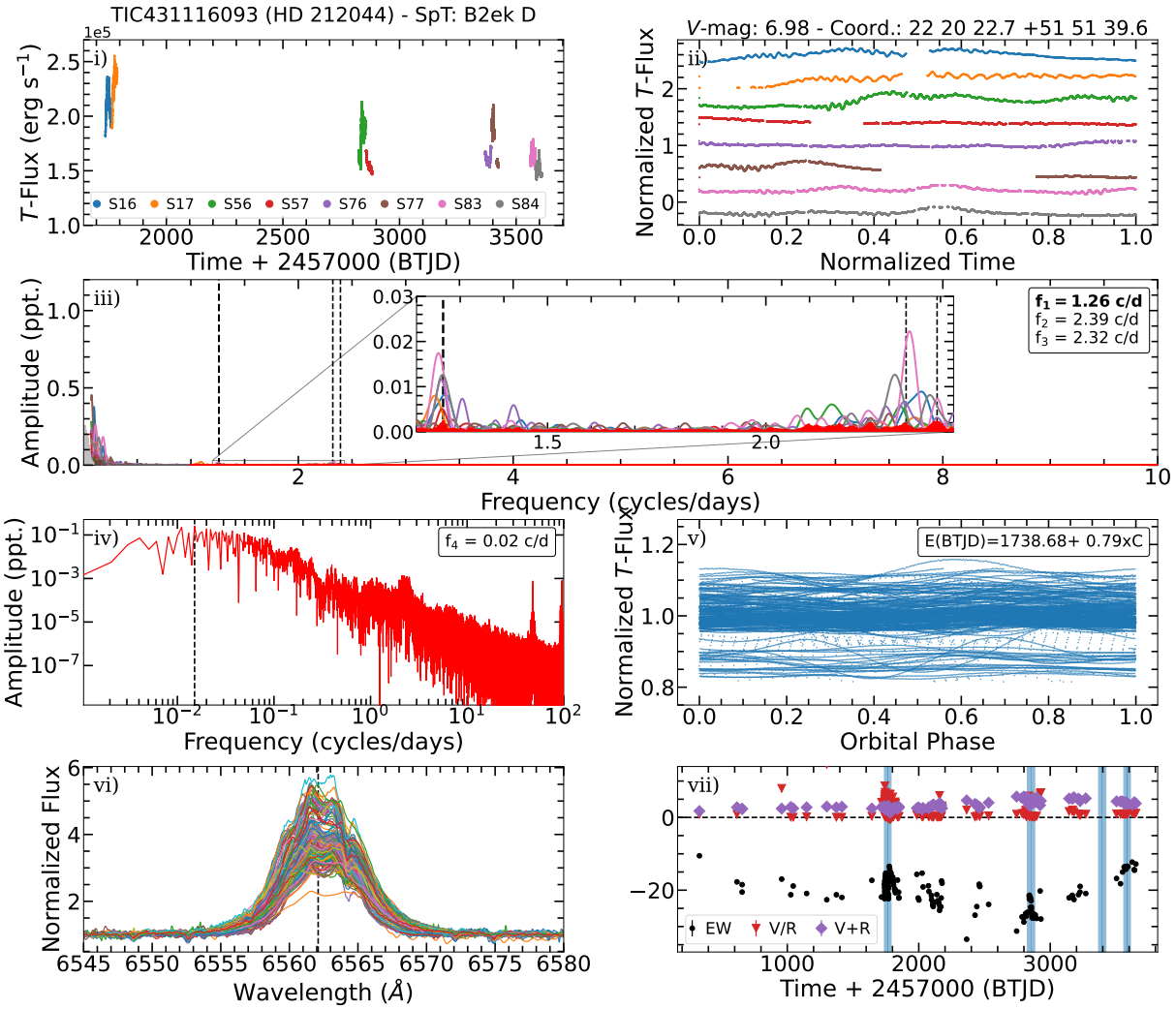

Figure C.148: Panels summarizing the photometric, spectroscopic, and frequency-domain analyses for the target TIC 431116093. (i) Raw T-Flux light curves from different sectors; (ii) normalized T-Flux light curves folded normalized time for each sector; (iii) Lomb-Scargle periodogram highlighting the three main frequencies f_1, f_2, and f_3, with a zoom-in inset; (iv) extended periodogram revealing a low-frequency component f_4; (v) orbital phase-folded light curve; (vi) optical spectrum centered on the Hα line (λ = 6562.8 Å); and (vii) temporal evolution of the equivalent width of the Hα line across available observations. Shaded regions in panel (vii) correspond to observation windows of sectors shown in panel (i).

C.149. TIC 434893323

HD 218066 is an eclipsing binary system classified in the literature with spectral type B1.5Vn and as a pulsating β-Cephei (Southworth and Bowman, 2022).

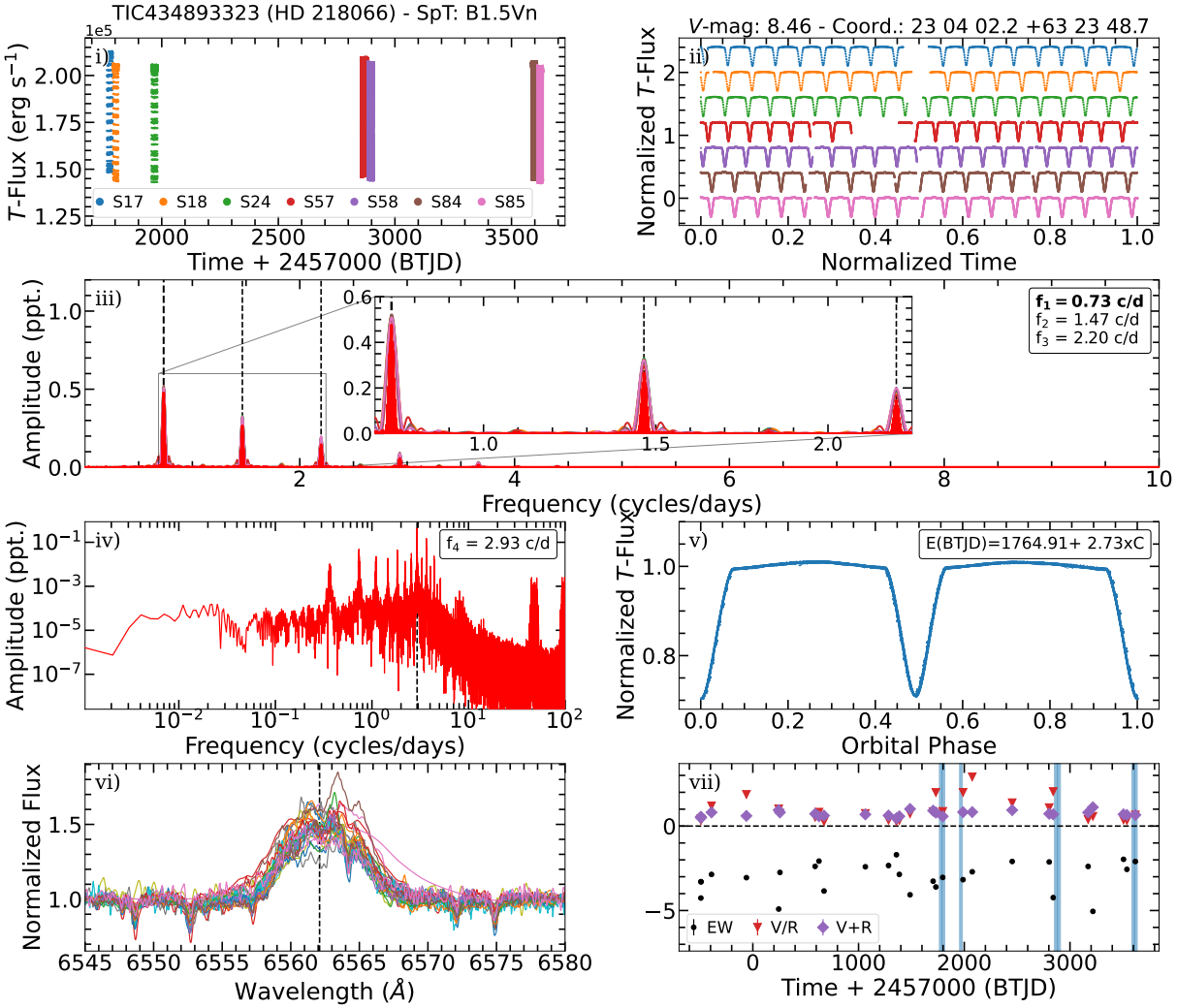

Figure C.149: Panels summarizing the photometric, spectroscopic, and frequency-domain analyses for the target TIC 434893323. (i) Raw T-Flux light curves from different sectors; (ii) normalized T-Flux light curves folded normalized time for each sector; (iii) Lomb-Scargle periodogram highlighting the three main frequencies f_1, f_2, and f_3, with a zoom-in inset; (iv) extended periodogram revealing a low-frequency component f_4; (v) orbital phase-folded light curve; (vi) optical spectrum centered on the Hα line (λ = 6562.8 Å); and (vii) temporal evolution of the equivalent width of the Hα line across available observations. Shaded regions in panel (vii) correspond to observation windows of sectors shown in panel (i).

C.150. TIC 441027987

ϵ Cap is classified as a Be star of spectral type B3. It is presented by Kervella et al. (2019) as a binary system.

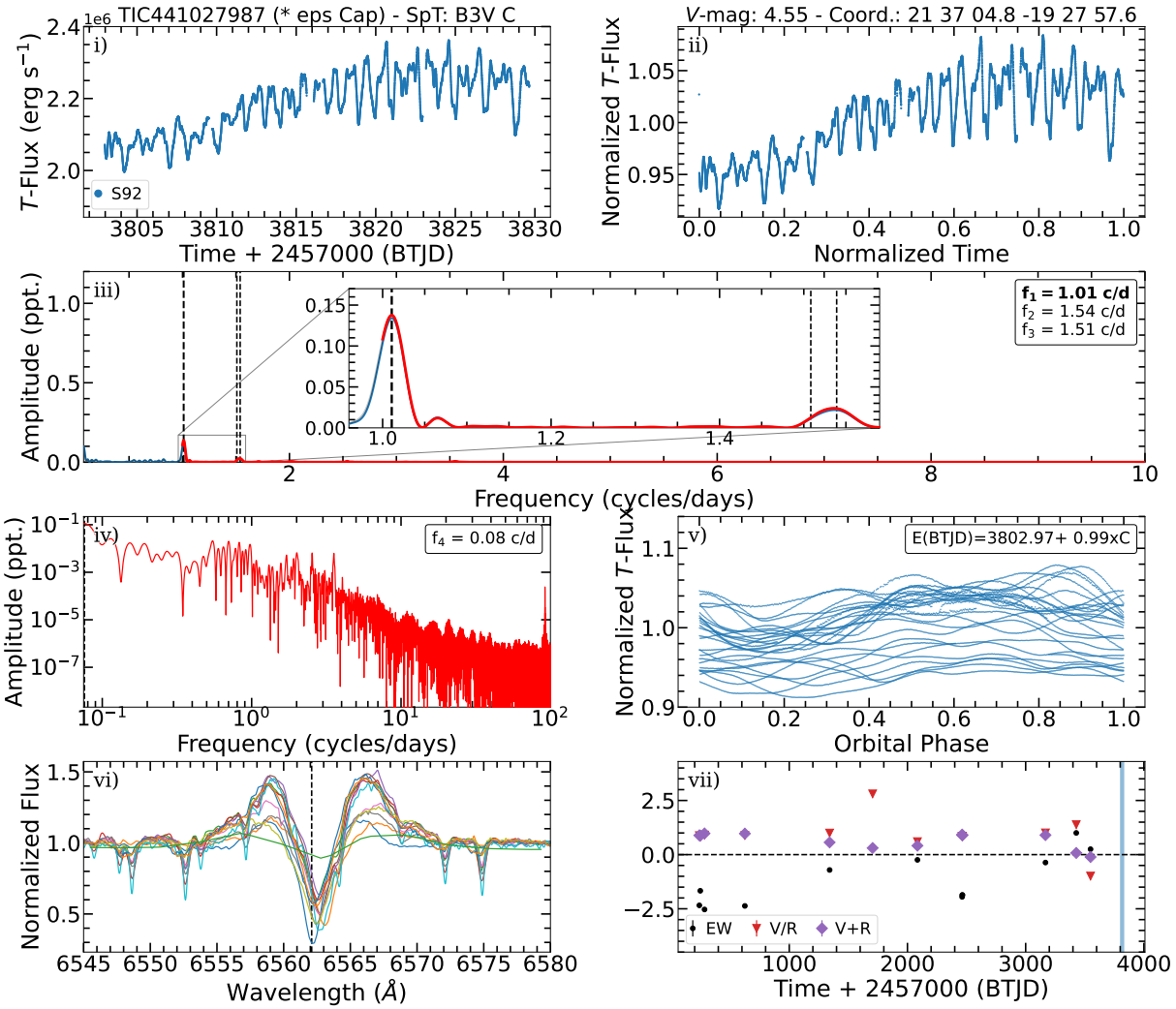

Figure C.150: Panels summarizing the photometric, spectroscopic, and frequency-domain analyses for the target TIC 441027987. (i) Raw T-Flux light curves from different sectors; (ii) normalized T-Flux light curves folded normalized time for each sector; (iii) Lomb-Scargle periodogram highlighting the three main frequencies f_1, f_2, and f_3, with a zoom-in inset; (iv) extended periodogram revealing a low-frequency component f_4; (v) orbital phase-folded light curve; (vi) optical spectrum centered on the Hα line (λ = 6562.8 Å); and (vii) temporal evolution of the equivalent width of the Hα line across available observations. Shaded regions in panel (vii) correspond to observation windows of sectors shown in panel (i).

C.151. TIC 442240473

HD 84511 is an eclipsing binary system without a Be star Labadie-Bartz et al. (2022).

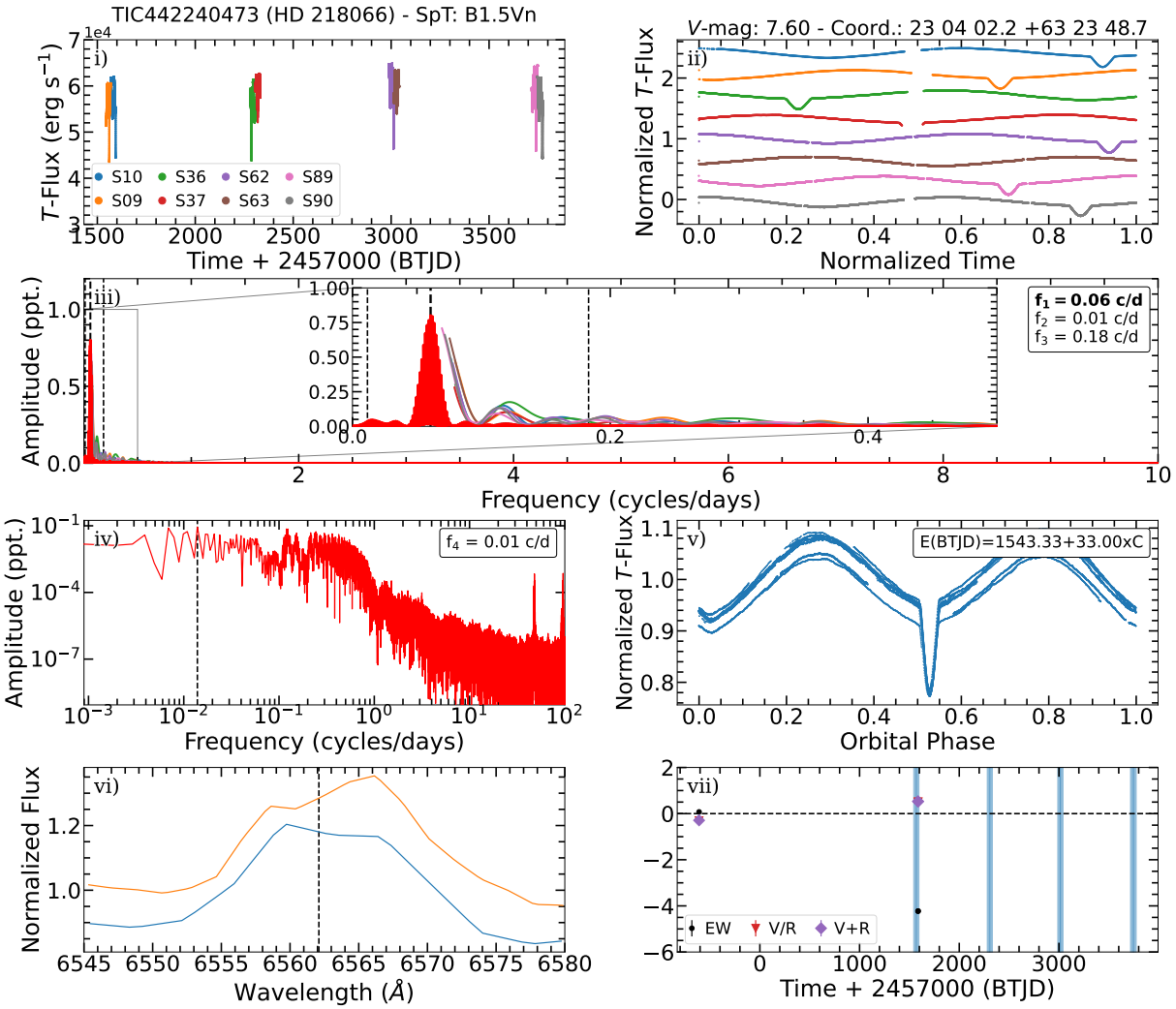

Figure C.151: Panels summarizing the photometric, spectroscopic, and frequency-domain analyses for the target TIC 442240473. (i) Raw T-Flux light curves from different sectors; (ii) normalized T-Flux light curves folded normalized time for each sector; (iii) Lomb-Scargle periodogram highlighting the three main frequencies f_1, f_2, and f_3, with a zoom-in inset; (iv) extended periodogram revealing a low-frequency component f_4; (v) orbital phase-folded light curve; (vi) optical spectrum centered on the Hα line (λ = 6562.8 Å); and (vii) temporal evolution of the equivalent width of the Hα line across available observations. Shaded regions in panel (vii) correspond to observation windows of sectors shown in panel (i).

C.152. TIC 444325059

HD 223924 is classified as a Be star, but with no signs of binarity. No spectrum was found in the BESS catalog.

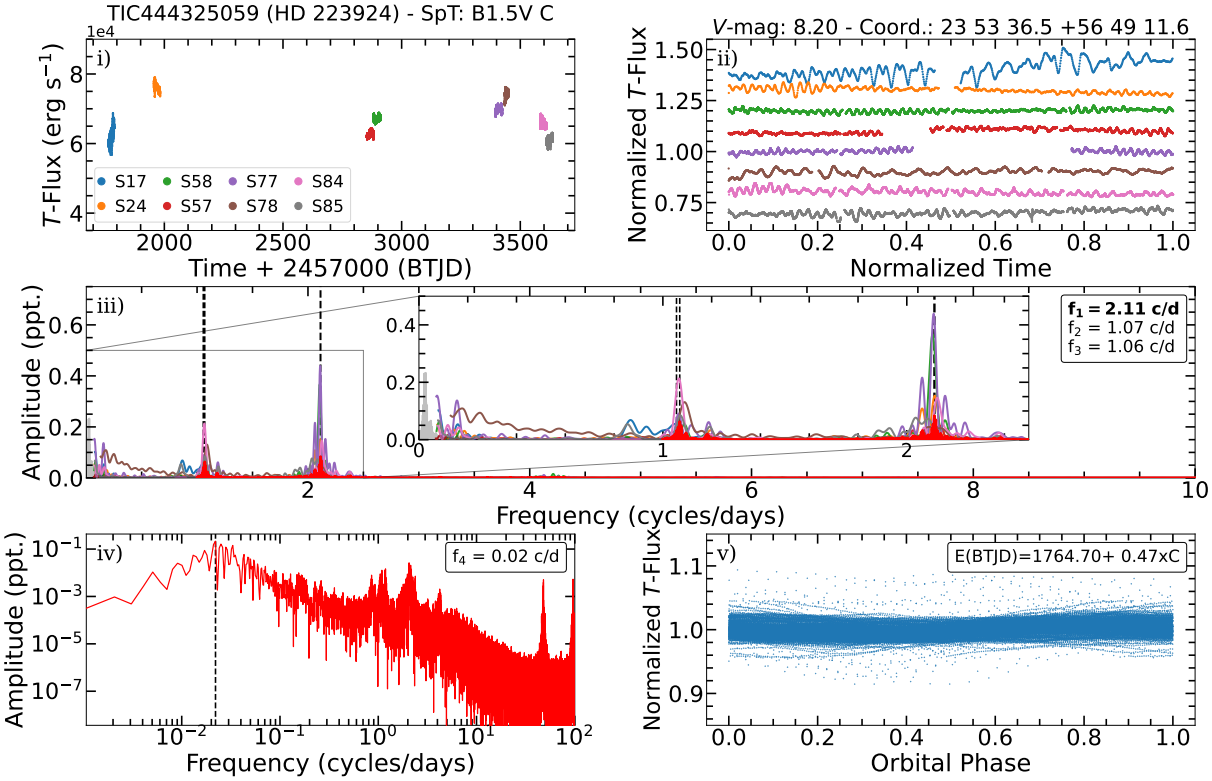

Figure C.152: Panels summarizing the photometric and frequency-domain analyses for the target TIC 444325059. (i) Raw T-Flux light curves from different sectors; (ii) normalized T-Flux light curves folded normalized time for each sector; (iii) Lomb-Scargle periodogram highlighting the three main frequencies f_1, f_2, and f_3, with a zoom-in inset; (iv) extended periodogram revealing a low-frequency component f_4; (v) orbital phase-folded light curve.

C.153. TIC 455463415

HD 135160 is an eclipsing binary system without a Be star, however, the BeSS spectra do not show characteristic emission lines in Hα.

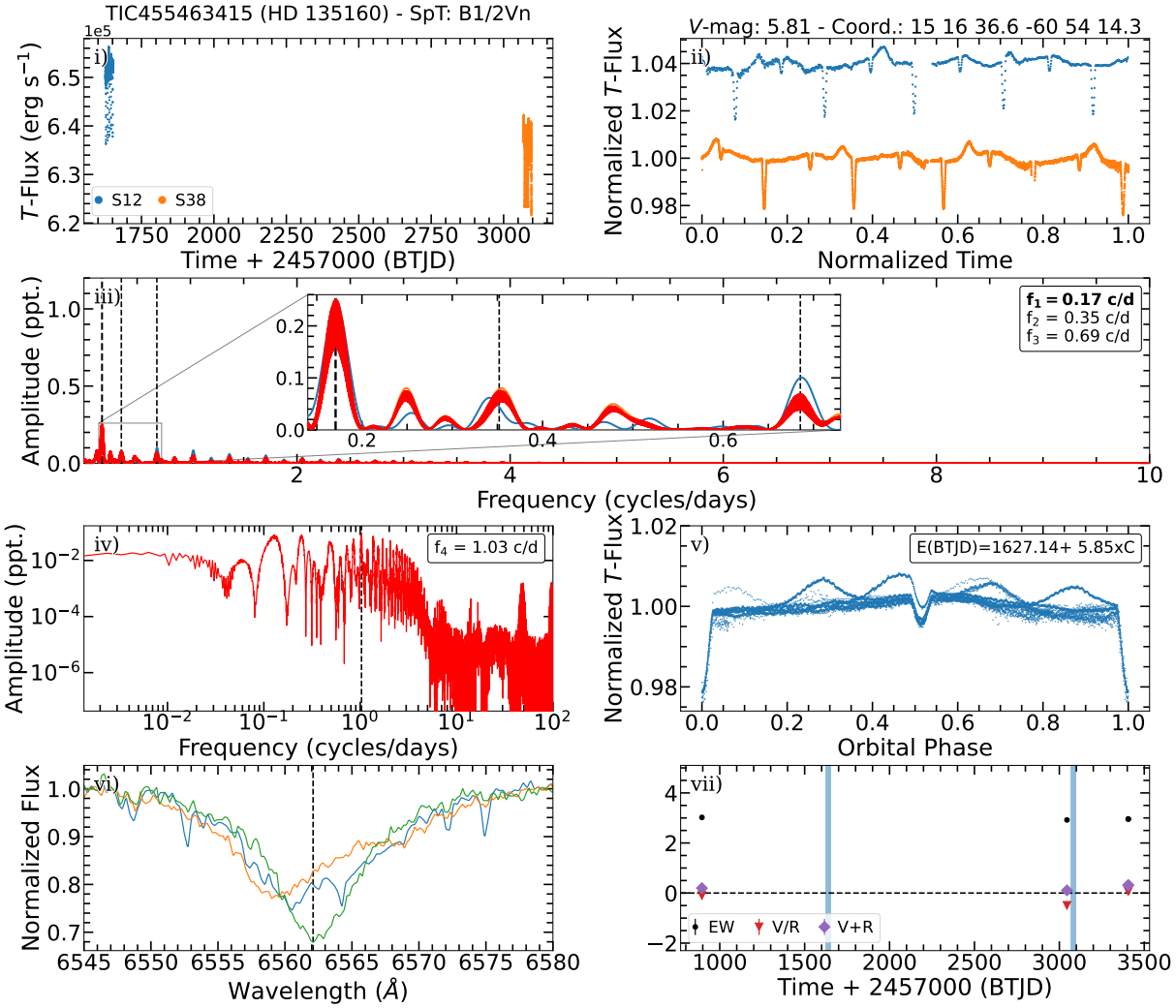

Figure C.153: Panels summarizing the photometric, spectroscopic, and frequency-domain analyses for the target TIC 455463415. (i) Raw T-Flux light curves from different sectors; (ii) normalized T-Flux light curves folded normalized time for each sector; (iii) Lomb-Scargle periodogram highlighting the three main frequencies f_1, f_2, and f_3, with a zoom-in inset; (iv) extended periodogram revealing a low-frequency component f_4; (v) orbital phase-folded light curve; (vi) optical spectrum centered on the Hα line (λ = 6562.8 Å); and (vii) temporal evolution of the equivalent width of the Hα line across available observations. Shaded regions in panel (vii) correspond to observation windows of sectors shown in panel (i).

C.154. TIC 460532958

p Car (HD 91465) is a Be star with no signs of binary.

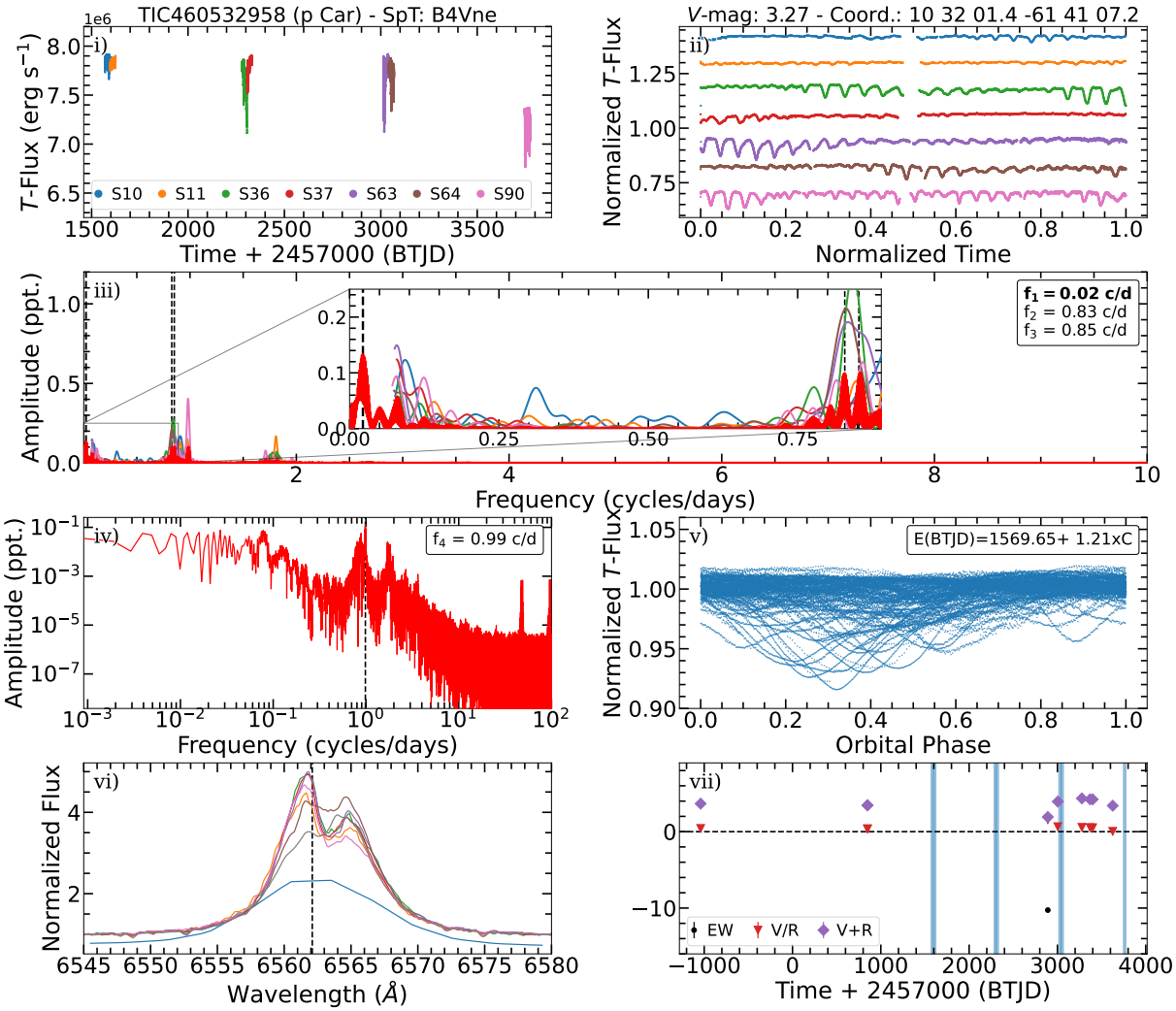

Figure C.154: Panels summarizing the photometric, spectroscopic, and frequency-domain analyses for the target TIC 460532958. (i) Raw T-Flux light curves from different sectors; (ii) normalized T-Flux light curves folded normalized time for each sector; (iii) Lomb-Scargle periodogram highlighting the three main frequencies f_1, f_2, and f_3, with a zoom-in inset; (iv) extended periodogram revealing a low-frequency component f_4; (v) orbital phase-folded light curve; (vi) optical spectrum centered on the Hα line (λ = 6562.8 Å); and (vii) temporal evolution of the equivalent width of the Hα line across available observations. Shaded regions in panel (vii) correspond to observation windows of sectors shown in panel (i).

C.155. TIC 46247269

LR Gem (HD 43078), despite being a clear eclipsing binary system, has not been studied in detail. Its classification is uncertain, with some being identified as either a beta Cepheid variable or a blue supergiant. There are no spectra in the BeSS catalog, nor any evidence of a Be star among the stars in its system.

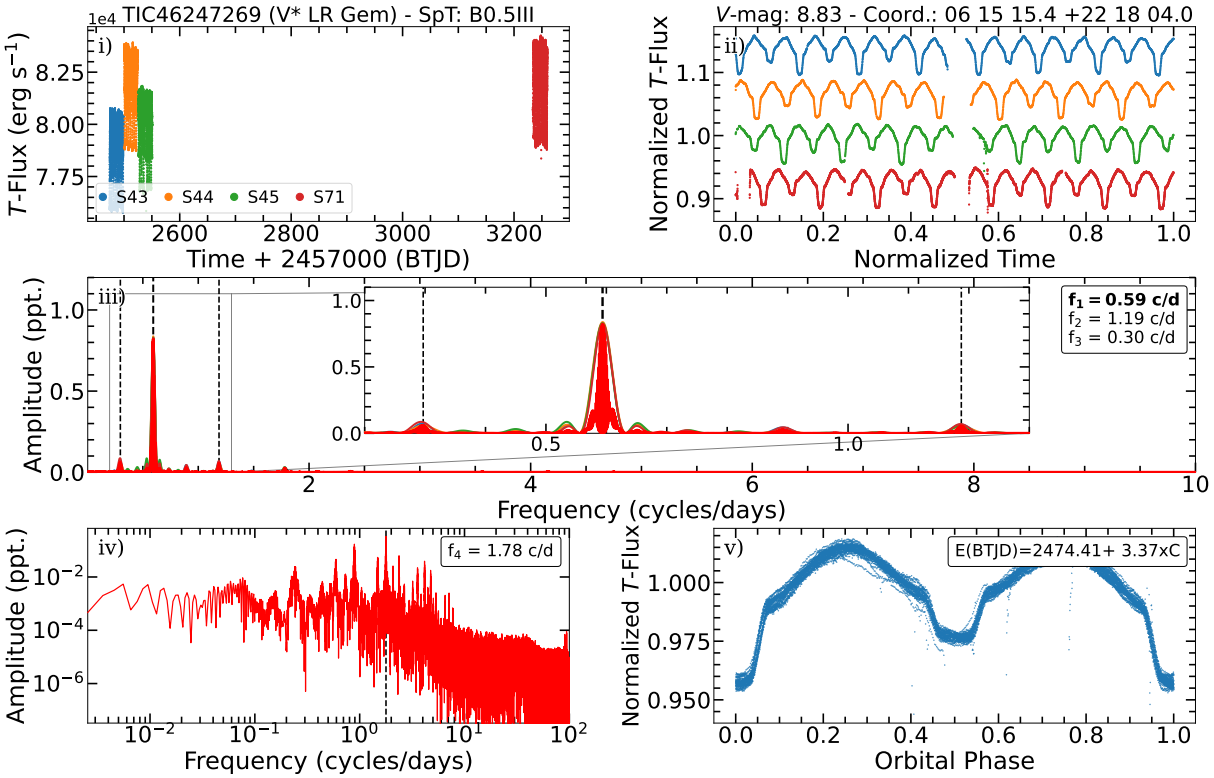

Figure C.155: Panels summarizing the photometric and frequency-domain analyses for the target TIC 46247269. (i) Raw T-Flux light curves from different sectors; (ii) normalized T-Flux light curves folded normalized time for each sector; (iii) Lomb-Scargle periodogram highlighting the three main frequencies f_1, f_2, and f_3, with a zoom-in inset; (iv) extended periodogram revealing a low-frequency component f_4; (v) orbital phase-folded light curve.

C.156. TIC 51288359

HD 151083 was classified as a Be star by Balona and Ozuyar (2021). Its light curve shows eclipse-like variations with a period of 1.80 days, superposed pulsations, and low-frequency stochastic variability. While a short-period EB would be incompatible with a classical Be star, a blended EB+Be system remains possible, though no BeSS spectra are available for confirmation.

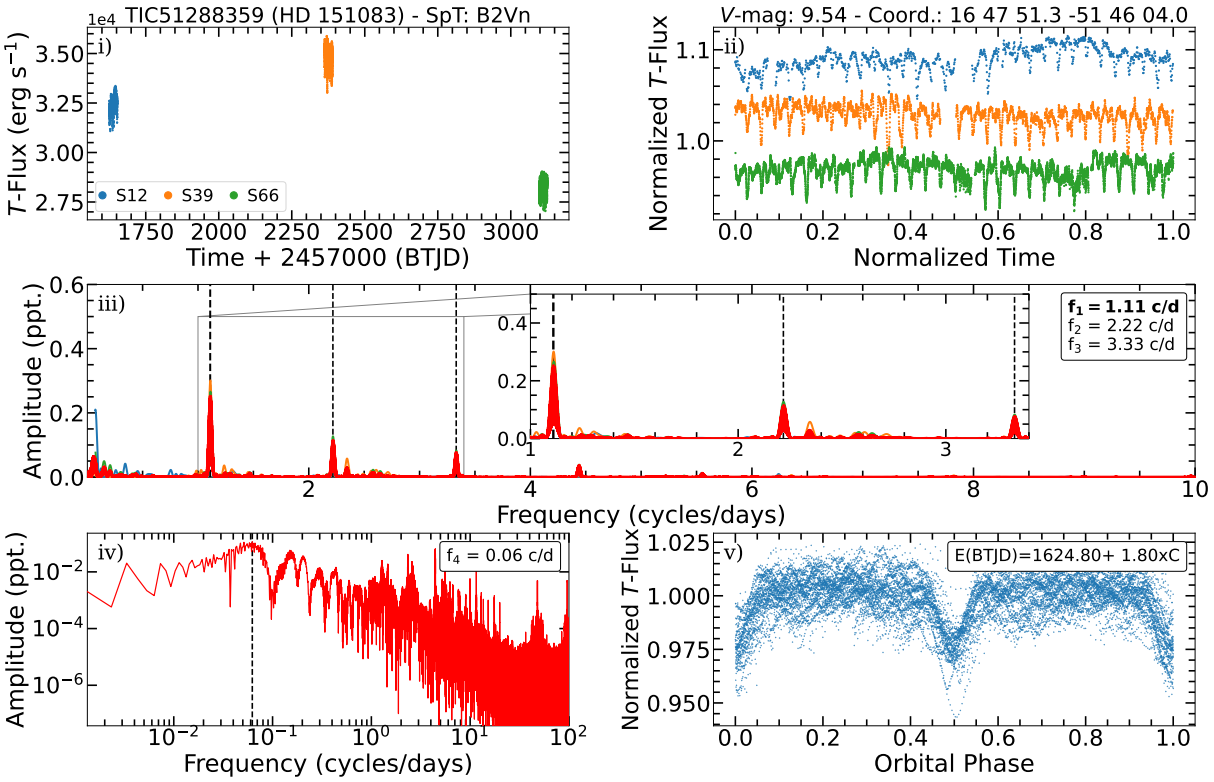

Figure C.156: Panels summarizing the photometric and frequency-domain analyses for the target TIC 51288359. (i) Raw T-Flux light curves from different sectors; (ii) normalized T-Flux light curves folded normalized time for each sector; (iii) Lomb-Scargle periodogram highlighting the three main frequencies f_1, f_2, and f_3, with a zoom-in inset; (iv) extended periodogram revealing a low-frequency component f_4; (v) orbital phase-folded light curve.

C.157. TIC 709917565

bet Mon A (HD 45725) is classified as a Be star, but has no evidence of binarity, and its light is mixed with neighboring stars.

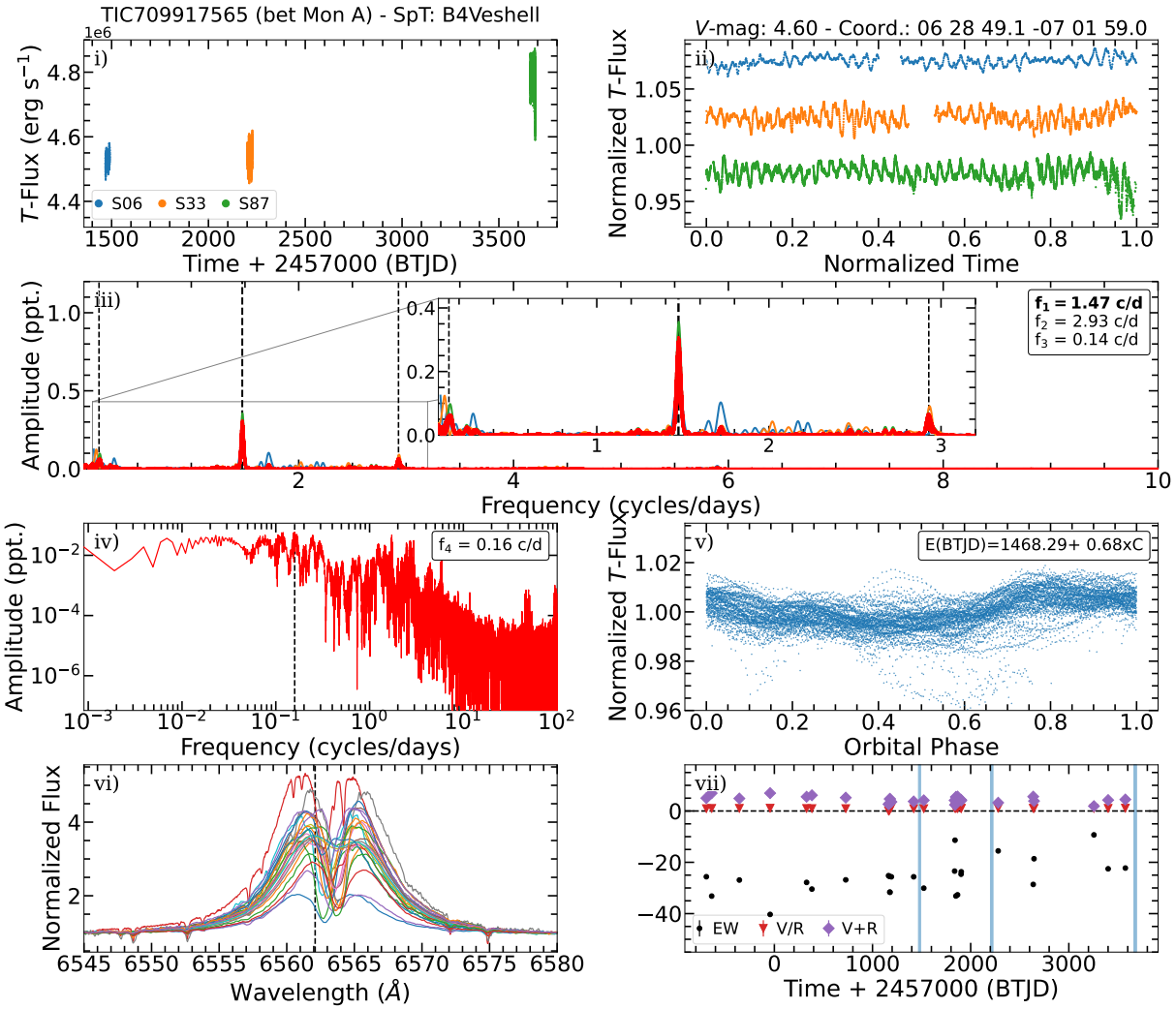

Figure C.157: Panels summarizing the photometric, spectroscopic, and frequency-domain analyses for the target TIC 709917565. (i) Raw T-Flux light curves from different sectors; (ii) normalized T-Flux light curves folded normalized time for each sector; (iii) Lomb-Scargle periodogram highlighting the three main frequencies f_1, f_2, and f_3, with a zoom-in inset; (iv) extended periodogram revealing a low-frequency component f_4; (v) orbital phase-folded light curve; (vi) optical spectrum centered on the Hα line (λ = 6562.8 Å); and (vii) temporal evolution of the equivalent width of the Hα line across available observations. Shaded regions in panel (vii) correspond to observation windows of sectors shown in panel (i).

C.158. TIC 90296023

HD 72754 display BeSS spectra with very strong, narrow, single-peaked Hα emission feature. Nevertheless, BeSS lists the star as a shell object. A Beta Lyrae-type eclipsing binary with mass transfer, showing strong Hα emission (E/C ~ 8–10). Not a classical Be star (Labadie-Bartz et al., 2022).

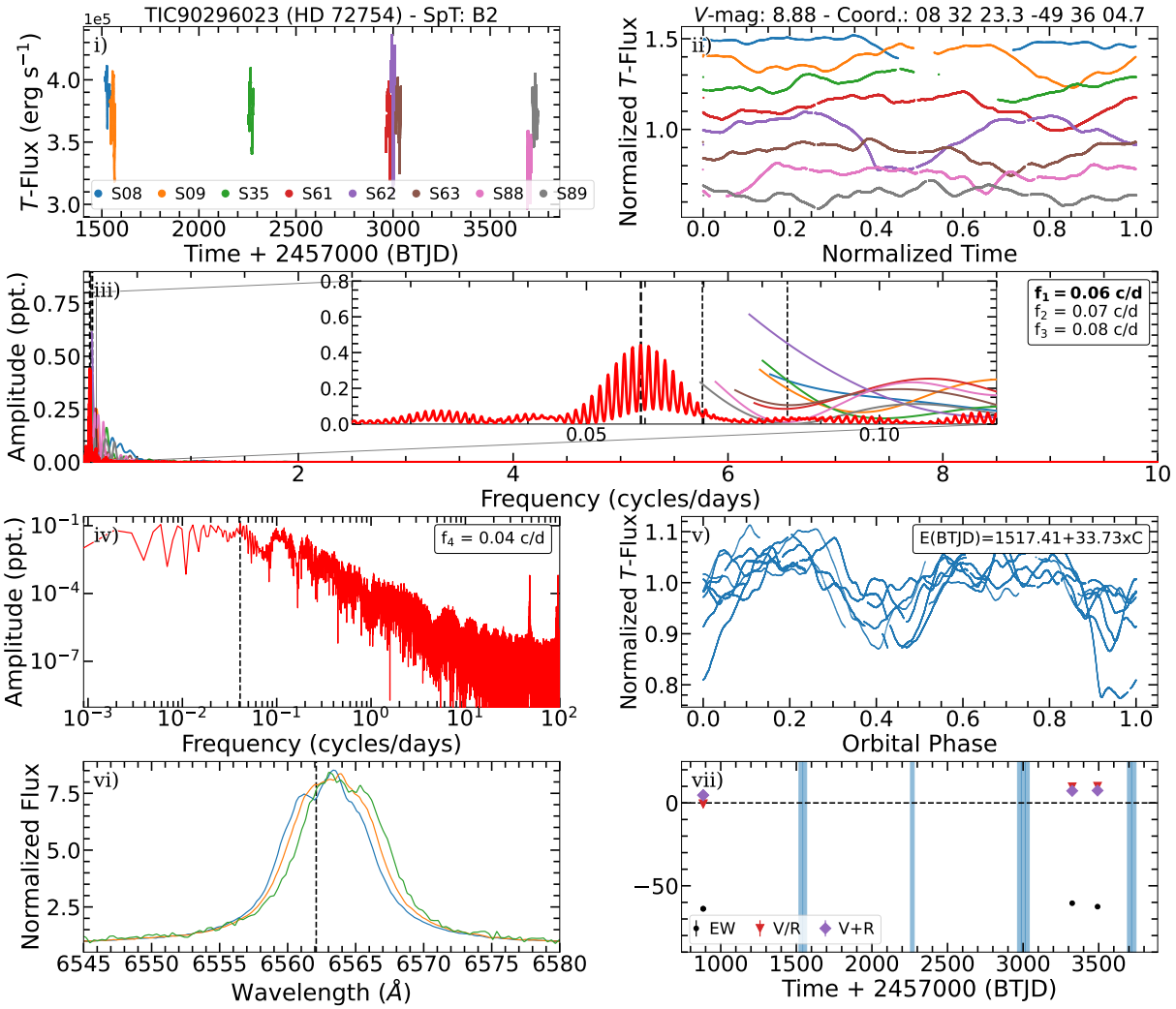

Figure C.158: Panels summarizing the photometric, spectroscopic, and frequency-domain analyses for the target TIC 90296023. (i) Raw T-Flux light curves from different sectors; (ii) normalized T-Flux light curves folded normalized time for each sector; (iii) Lomb-Scargle periodogram highlighting the three main frequencies f_1, f_2, and f_3, with a zoom-in inset; (iv) extended periodogram revealing a low-frequency component f_4; (v) orbital phase-folded light curve; (vi) optical spectrum centered on the Hα line (λ = 6562.8 Å); and (vii) temporal evolution of the equivalent width (EW) of the Hα line across available observations. Shaded regions in panel (vii) correspond to observation windows of sectors shown in panel (i).

Bibliography

Abt, H. A. (1984). The frequency of binary stars. *ApJ*, 285:247–257. [pg: 1]

Abt, H. A. and Cardona, O. (1984). Be stars in binaries. *Astrophysical Journal, Part 1 (ISSN 0004-637X), vol. 285, Oct. 1, 1984, p. 190-194.*, 285:190–194. [pg: 53, 106]

Aerts, C. (2021). Probing the interior physics of stars through asteroseismology. *Reviews of Modern Physics*, 93(1):015001. [pg: 24]

Aerts, C., Christensen-Dalsgaard, J., Kurtz, D. W., Aerts, C., Christensen-Dalsgaard, J., and Kurtz, D. (2010). *Introducing Asteroseismology*. Springer. [pg: 29, 30]

Aghakhanloo, M., Murphy, J. W., Smith, N., Parejko, J., Díaz-Rodríguez, M., Drout, M. R., Groh, J. H., Guzman, J., and Stassun, K. G. (2020). Inferring the parallax of westerlund 1 from gaia dr2. *Monthly Notices of the Royal Astronomical Society*, 492(2):2497–2509. [pg: 16]

Alfonso-Garzón, J., Domingo, A., Mas-Hesse, J., and Giménez, A. (2012). The first integral-omc catalogue of optically variable sources. *Astronomy & Astrophysics*, 548:A79. [pg: 202]

Almeida, L. A., Sana, H., de Mink, S. E., Tramper, F., Soszyński, I., Langer, N., Barbá, R. H., Cantiello, M., Damineli, A., de Koter, A., Garcia, M., Gräfener, G., Herrero, A., Howarth, I., Maíz Apellániz, J., Norman, C., Ramírez-Agudelo, O. H., and Vink, J. S. (2015). Discovery of the Massive Overcontact Binary VFTS352: Evidence for Enhanced Internal Mixing. *ApJ*, 812(2):102. [pg: 101]

Andrews, P. J. and Breger, M. (1966). Hydrogen emission in Achernar. *The Observatory*, 86:108–109. [pg: 181]

Andrillat, Y., Jaschek, M., and Jaschek, C. (1994). A study of be stars in the wavelength region around paschen 7. *Astronomy and Astrophysics Suppl., Vol. 103, p. 135-155 (1994)*, 103:135–155. [pg: 167]

Antoniou, V. and Zezas, A. (2016). Star formation history and X-ray binary populations: the case of the Large Magellanic Cloud. *Monthly Notices of the Royal Astronomical Society*, 459(1):528–553. [pg: 2]

Arcos, C., Kanaan, S., Chávez, J., Vanzi, L., Araya, I., and Curé, M. (2018). Stellar parameters and h α line profile variability of be stars in the besos survey. *Monthly Notices of the Royal Astronomical Society*, 474(4):5287–5299. [pg: 135]

Baade, D., Pigulski, A., Rivinius, T., Wang, L., Martayan, C., Handler, G., Panoglou, D., Carciofi, A. C., Kuschnig, R., Mehner, A., et al. (2018). Short-term variability and mass loss in be stars-iv. two groups of closely spaced, approximately equidistant frequencies in three decades of space photometry of ν puppis (b7-8 iiie). *Astronomy & Astrophysics*, 620:A145. [pg: 53, 88]

Baade, D. e. a. (2016). Outbursts and disk formation in the be star μ centauri. *Astronomy & Astrophysics*, 588:A56. [pg: 66, 70]

Bailer-Jones, C., Rybizki, J., Fouesneau, M., Mantelet, G., and Andrae, R. (2018). Estimating distance from parallaxes. iv. distances to 1.33 billion stars in gaia data release 2. *The Astronomical Journal*, 156(2):58. [pg: 171]

Baines, E. K., Armstrong, J. T., Schmitt, H. R., Zavala, R., Benson, J. A., Hutter, D. J., Tycner, C., and van Belle, G. T. (2017). Fundamental parameters of 87 stars from the navy precision optical interferometer. *The Astronomical Journal*, 155(1):30. [pg: 152]

Balona, L. A. and Ozuyar, D. (2021). Pulsating b-type stars observed by tess. *Monthly Notices of the Royal Astronomical Society*, 508(2):1701–1714. [pg: 285]

Banerjee, G., Mathew, B., Paul, K., Subramaniam, A., Bhattacharyya, S., and Anusha, R. (2021). Optical spectroscopy of galactic field classical be stars. *Monthly Notices of the Royal Astronomical Society*, 500(3):3926–3943. [pg: 134, 152]

Bjorkman, K. S., Miroshnichenko, A. S., McDavid, D., and Pogrosheva, T. M. (2002a). A study of π aquarii during a quasi-normal star phase: refined fundamental parameters and evidence for binarity. *The Astrophysical Journal*, 573(2):812. [pg: 52]

Bjorkman, K. S., Miroshnichenko, A. S., McDavid, D., and Pogrosheva, T. M. (2002b). Variability of the hα emission line in the be star π aquarii. *The Astrophysical Journal*, 573:812–818. [pg: 212]

Bodensteiner, J., Shenar, T., Mahy, L., Fabry, M., Marchant, P., Abdul-Masih, M., Banyard, G., Bowman, D., Dsilva, K., Frost, A., et al. (2020). Is hr 6819 a triple system containing a black hole?-an alternative explanation. *Astronomy & Astrophysics*, 641:A43. [pg: 135, 201, 202]

Bodensteiner, J., Shenar, T., and Sana, H. (2020). Investigating the lack of main-sequence companions to massive Be stars. *A&A*, 641:A42. [pg: 257]

Bodensteiner, J., Shenar, T., Sana, H., Britavskiy, N., Crowther, P. A., Langer, N., Lennon, D. J., Mahy, L., Patrick, L. R., Villaseñor, J. I., Abdul-Masih, M., Bowman, D. M., de Koter, A., de Mink, S. E., Deshmukh, K., Fabry, M., Gilkis, A., Götberg, Y., Holgado, G., Izzard, R. G., Janssens, S., Kalari, V. M., Keszthelyi, Z., Kubát, J., Mandel, I., Maravelias, G., Oskinova, L. M., Pauli, D., Ramachandran, V., Rocha, D. F., Renzo, M., Sander, A. A. C., Schneider, F. R. N., Schootemeijer, A., Sen, K., Stoop, M., Toonen, S., van Loon, J. Th., Valli, R., Vigna-Gómez, A., Vink, J. S., Wang, C., and Xu, X.-T. (2025). Binarity at low metallicity (bloem) - multiplicity properties of oe and be stars. *A&A*, 698:A38. [pg: 2]

Böhm-Vitense, E. (1981). The effective temperature scale. *ARA&A*, 19:295–318. [pg: 99]

Borkovits, T., Rappaport, S., Mitnyan, T., Bíró, I., Csányi, I., Forgács-Dajka, E., Forró, A., Hajdu, T., Seli, B., Sztakovics, J., et al. (2025). Then and now: A new look at the eclipse timing variations of hierarchical triple star candidates in the primordial kepler field, revisited by tess. *Astronomy & Astrophysics*, 695:A209. [pg: 96, 223]

Bowman, D., Burssens, S., Simón-Díaz, S., Edelmann, P., Rogers, T., Horst, L., Röpke, F., and Aerts, C. (2020). Photometric detection of internal gravity waves in upper main-sequence stars-ii. combined tess photometry and high-resolution spectroscopy. *Astronomy & Astrophysics*, 640:A36. [pg: 130]

Brasseur, C. E., Phillip, C., Fleming, S. W., Mullally, S. E., and White, R. L. (2019). Astrocut: Tools for creating cutouts of tess images. *Astrophysics Source Code Library*, page ascl:1905.007. [pg: 67]

Brown, A. G. A. e. a. (2018). Gaia data release 2: Summary of the contents and survey properties. *Astronomy & Astrophysics*, 616:A1. [pg: 64]

Burssens, S., Bowman, D. M., Aerts, C., Pedersen, M. G., Moravveji, E., and Buysschaert, B. (2019). New β cep pulsators discovered with k2 space photometry. *MNRAS*, 489(1):1304–1320. [pg: 77]

Burssens, S., Simón-Díaz, S., Bowman, D., Holgado, G., Michielsen, M., De Burgos, A., Castro, N., Barbá, R., and Aerts, C. (2020). Variability of ob stars from tess southern sectors 1–13 and high-resolution iacob and own spectroscopy. *Astronomy & Astrophysics*, 639:A81. [pg: 66, 130]

Carciofi, A. C., Bjorkman, J. E., Otero, S. A., Okazaki, A. T., Štefl, S., Rivinius, T., Baade, D., and Haubois, X. (2011). The first determination of the viscosity parameter in the circumstellar disk of a be star. *The Astrophysical Journal Letters*, 744(1):L15. [pg: 53]

Carciofi, A. C., Okazaki, A., Le Bouquin, J.-B., Štefl, S., Rivinius, T., Baade, D., Bjorkman, J., and Hummel, C. (2009). Cyclic variability of the circumstellar disk of the be star ζ tauri-ii. testing the 2d global disk oscillation model. *Astronomy & Astrophysics*, 504(3):915–927. [pg: 170]

Cardelli, J. A., Clayton, G. C., and Mathis, J. S. (1989). The relationship between infrared, optical, and ultraviolet extinction. *The Astrophysical Journal*, 345:245–256. [pg: 13, 65, 95]

Carrier, F., Burki, G., and Burnet, M. (2002). Search for duplicity in periodic variable be stars. *Astronomy & Astrophysics*, 385(2):488–502. [pg: 150]

Casares, J., Negueruela, I., Ribó, M., Ribas, I., Paredes, J. M., Herrero, A., and Simón-Díaz, S. (2014). A be-type star with a black-hole companion. *Nature*, 505(7483):378–381. [pg: 156]

Castañón Esteban, A., Steele, I. A., and Jermak, H. E. (2024). A study of be stars in the time domain–i. spectral data and polarimetry. *Monthly Notices of the Royal Astronomical Society*, 529(2):1555–1570. [pg: 168]

Catanzaro, G. (2013). Spectroscopic atlas of hα and hβ in a sample of northern be stars. *Astronomy & Astrophysics*, 550:A79. [pg: 157]

Chandrasekhar, S. (1950). *Radiative Transfer*. Dover Publications. [pg: 55]

Chen, P., Liu, J., and Shan, H. (2016). A new approach to the infrared photometric study of be stars. *Monthly Notices of the Royal Astronomical Society*, 463(2):1162–1172. [pg: 191]

Chojnowski, S. D., Labadie-Bartz, J., Rivinius, T., Gies, D., Panoglou, D., Fernandes, M. B., Wisniewski, J. P., Whelan, D. G., Mennickent, R. E., McMillan, R., et al. (2018). The remarkable be+ sdob binary hd 55606. i. orbital and stellar parameters. *The Astrophysical Journal*, 865(1):76. [pg: 184]

Chojnowski, S. D., Whelan, D. G., Wisniewski, J. P., Majewski, S. R., Hall, M., Shetrone, M., Beaton, R., Burton, A., Damke, G., Eikenberry, S., et al. (2014). High-resolution h-band spectroscopy of be stars with sdss-iii/apogee. i. new be stars, line identifications, and line profiles. *The Astronomical Journal*, 149(1):7. [pg: 131, 137, 169, 173, 174, 175, 182, 188, 194]

Chojnowski, S. D., Whelan, D. G., Wisniewski, J. P., Majewski, S. R., Hall, M., Shetrone, M., Beaton, R., Burton, A., Damke, G., Eikenberry, S., Hasselquist, S., Holtzman, J. A., Mészáros, S., Nidever, D., Schneider, D. P., Wilson, J., Zasowski, G., Bizyaev, D., Brewington, H., Brinkmann, J., Ebelke, G., Frinchaboy, P. M., Kinemuchi, K., Malanushenko, E., Malanushenko, V., Marchante, M., Oravetz, D., Pan, K., and Simmons, A. (2015). High-Resolution H-Band Spectroscopy of Be Stars With SDSS-III/Apogee: I. New Be Stars, Line Identifications, and Line Profiles. *AJ*, 149(1):7. [pg: 186, 258]

Chojnowski, S. D., Wisniewski, J. P., Whelan, D. G., Labadie-Bartz, J., Fernandes, M. B., Lin, C.-C., Majewski, S. R., Stringfellow, G. S., Mennickent, R. E., Roman-Lopes, A., et al. (2017). High-resolution h-band spectroscopy of be stars with sdss-iii/apogee. ii. line profile and radial velocity variability. *The Astronomical Journal*, 153(4):174. [pg: 136, 137]

Claret, A. and Bloemen, S. (2011). Gravity and limb-darkening coefficients for the kepler, corot, spitzer, uvby, ubvrijhk, and sloan photometric systems. *Astronomy & Astrophysics*, 529:A75. [pg: 75, 102]

Clemens, J. C., Crain, J. A., and Anderson, R. (2004). The Goodman spectrograph. In *Ground-based Instrumentation for Astronomy*, volume 5492, pages 331–340. [pg: 71]

Collaboration, G. (2021). Gaia data release 3: Summary of the contents and survey properties. *Astronomy & Astrophysics*, 649:A1. [pg: 2, 64]

Collaboration, L., Cardoso, D., Hedges, C., et al. (2018). Lightkurve: Kepler and tess time series analysis in python. *Astrophysics Source Code Library (ascl: 1812.013)*. [pg: 67, 97]

Collins, G. W. (1987). The use of terms and definitions in the study of be stars. In *International Astronomical Union Colloquium*, volume 92, pages 3–21. Cambridge University Press. [pg: 20]

Cowley, A. and Gugula, E. (1973). Cyclic variations of the be star beta 1 monocerotis. *Astronomy and Astrophysics, Vol. 22, p. 203-208*, 22:203–208. [pg: 197]

Crain, J. A., Clemens, J. C., and Bayliss, M. (2004). The goodman spectrograph control system. In *Proc. SPIE*, volume 5496, pages 455–462. [pg: 71]

Cranmer, S. R. (2005). A statistical study of threshold rotation rates for the formation of disks around be stars. *The Astrophysical Journal*, 634(1):585. [pg: 27]

Cranmer, S. R. (2009). A pulsational mechanism for producing keplerian disks around be stars. *The Astrophysical Journal*, 701(1):396. [pg: 31]

Damineli, A., Almeida, L. A., Blum, R. D., Damineli, D. S., Navarete, F., Rubinho, M. S., and Teodoro, M. (2016). Extinction law in the range 0.4–4.8 μm and the 8620 å dib towards the stellar cluster westerlund 1. *Monthly Notices of the Royal Astronomical Society*, 463(3):2653–2666. [pg: 13]

De Araujo, F. and de Freitas Pacheco, J. (1990a). Asymmetric winds in be stars. *Astrophysics and space science*, 163:49–58. [pg: 145]

De Araujo, F. X. and de Freitas Pacheco, J. A. (1990b). v sin i measurements of be stars. *Astronomy and Astrophysics*. [pg: 58]

De Mink, S., Langer, N., Izzard, R., Sana, H., and de Koter, A. (2013). The rotation rates of massive stars: the role of binary interaction through tides, mass transfer, and mergers. *The Astrophysical Journal*, 764(2):166. [pg: 52]

De Mink, S., Sana, H., Langer, N., Izzard, R., and Schneider, F. (2014). The incidence of stellar mergers and mass gainers among massive stars. *The Astrophysical Journal*, 782(1):7. [pg: 52]

de Mink, S. E., Cantiello, M., Langer, N., Pols, O. R., Brott, I., and Yoon, S. C. (2009). Rotational mixing in massive binaries. Detached short-period systems. *A&A*, 497(1):243–253. [pg: 109]

de Mink, S. E. et al. (2014). The incidence of stellar mergers and mass gainers among massive stars. *ApJ*, 782:7. [pg: 1]

de Souza, A. D., Kervella, P., Jankov, S., Abe, L., Vakili, F., Di Folco, E., and Paresce, F. (2003). The spinning-top be star achernar from vlti-vinci. *Astronomy & Astrophysics*, 407(3):L47–L50. [pg: 181]

De Wit, W., Lamers, H., Marquette, J., and Beaulieu, J. (2006). The remarkable light and colour variability of small magellanic cloud be stars. *Astronomy & Astrophysics*, 456(3):1027–1035. [pg: 20]

Degroote, P., Aerts, C., Ollivier, M., Miglio, A., Debosscher, J., Cuypers, J., Briquet, M., Montalbán, J., Thoul, A., Noels, A., et al. (2009). Corot's view of newly discovered b-star pulsators: results for 358 candidate b pulsators from the initial run's exoplanet field data. *A&A*, 506(1):471–489. [pg: 77]

Delorme, P., Chomez, A., Squicciarini, V., Janson, M., Flasseur, O., Schib, O., Gratton, R., Lagrange, A.-M., Langlois, M., Mayer, L., et al. (2024). Population of giant planets around b stars from the first part of the beast survey. *Astronomy & Astrophysics*, 692:A263. [pg: 176]

Desnoux, V. and Buil, C. (2005). Spectroscopic monitoring of be type stars. In *The Society for Astronomical Sciences 24th Annual Symposium on Telescope Science, held May 24-26, 2005. Published by Society for Astronomical Sciences, 2005., p. 129*, volume 24, page 129. [pg: 59]

Dickel, J. R. and McKinley, R. R. (1969). 610.5 mhz contour maps of the supernova remnants hb 9, simeis 147, and ic 443. *ApJ*, 155:67. [pg: 96]

Dinçel, B., Neuhäuser, R., Yerli, S. K., Ankay, A. ş., Tetzlaff, N., Torres, G., and Mugrauer, M. (2015). Discovery of an ob runaway star inside snr s147. *MNRAS*, 448(4):3196–3205. [pg: 98, 104]

Docobo, J., Andrade, M., Ling, J., Prieto, C., Tamazian, V., Balega, Y. Y., Blanco, J., Maximov, A., Lahulla, J., and Alvarez, C. (2004). Binary star speckle interferometry: Measurements and orbits. *The Astronomical Journal*, 127(2):1181. [pg: 167]

Duchêne, G. and Kraus, A. (2013). Stellar multiplicity. *Annual Review of Astronomy and Astrophysics*, 51(1):269–310. [pg: 1, 33, 96]

Dziembowski, W. (1982). Nonlinear mode coupling in oscillating stars. i – second order theory of the coherent mode coupling. *Acta Astronomica*, 32:147–171. [pg: 79]

Eggleton, P. P. (1983). Aproximations to the radii of Roche lobes. *ApJ*, 268:368–369. [pg: 48]

Eker, Z., Soydugan, F., Bilir, S., Bakış, V., Aliçavuş, F., Özer, S., Aslan, G., Alpsoy, M., and Köse, Y. (2020). Empirical bolometric correction coefficients for nearby main-sequence stars in the gaia era. *Monthly Notices of the Royal Astronomical Society*, 496(3):3887–3905. [pg: 84, 99]

Ekström, S., Georgy, C., Eggenberger, P., Meynet, G., Mowlavi, N., Wyttenbach, A., Granada, A., Decressin, T., Hirschi, R., Frischknecht, U., Charbonnel, C., and Maeder, A. (2012a). Grids of stellar models with rotation. I. Models from 0.8 to 120 $M_{\odot}$ at solar metallicity (Z = 0.014). *A&A*, 537:A146. [pg: 2]

Ekström, S., Georgy, C., Eggenberger, P., Meynet, G., Mowlavi, N., Wyttenbach, A., Granada, A., Decressin, T., Hirschi, R., Frischknecht, U., et al. (2012b). Grids of stellar models with rotation-i. models from 0.8 to 120 m at solar metallicity (z= 0.014). *A&A*, 537:A146. [pg: 109, 110]

El-Badry, K. and Burdge, K. B. (2022). NGC 1850 BH1 is another stripped-star binary masquerading as a black hole. *Monthly Notices of the Royal Astronomical Society*, 511(1):24–29. [pg: 2]

Emilio, M., Andrade, L., Janot-Pacheco, E., Baglin, A., Gutiérrez-Soto, J., Suárez, J. C., de Batz, B., Diago, P., Fabregat, J., Floquet, M., et al. (2010). Photometric variability of the be star corot-id 102761769. *A&A*, 522:A43. [pg: 110]

et al., G. C. (2023). Gaia data release 3: Summary of the content and survey properties. *Astronomy and Astrophysics*, 674:A1. [pg: 64]

Evans, C. J. e. a. (2021). The gaia mission and its contribution to the study of binary stars. *Astronomy & Astrophysics Review*, 29(2):1–23. [pg: 64]

Fekel Jr, F. C. (1981). The properties of close multiple stars. *AJ, Part 1, vol. 246, June 15, 1981, p. 879-898.*, 246:879–898. [pg: 96]

Ferrand, G. and Safi-Harb, S. (2012). A census of high-energy observations of galactic supernova remnants. *Advances in Space Research*, 49(9):1313–1319. [pg: 96]

Foreman-Mackey, D., Hogg, D. W., Lang, D., and Goodman, J. (2013). emcee: the mcmc hammer. *Publications of the Astronomical Society of the Pacific*, 125(925):306. [pg: 3, 71, 75, 98]

Frémat, Y., Zorec, J., Hubert, A.-M., and Floquet, M. (2005). Effects of gravitational darkening on the determination of fundamental parameters in fast-rotating b-type stars. *Astronomy & Astrophysics*, 440(1):305–320. [pg: 164]

Gaia Collaboration, Eyer, L., Rimoldini, L., Audard, M., et al. (2023). Gaia data release 3: Summary of the variability processing and analysis. *Astronomy & Astrophysics*, 674:A1. [pg: 208]

García, S. M., Monnier, J. D., Che, X., et al. (2024). The chara array interferometric program on the multiplicity of classical be stars: New detections and orbits of stripped subdwarf companions. *The Astrophysical Journal*, XYZ(ABC):123–145. [pg: 215]

Gardner, T., Monnier, J. D., Fekel, F. C., Schaefer, G., Johnson, K. J. C., Le Bouquin, J.-B., Kraus, S., Anugu, N., Setterholm, B. R., Labdon, A., et al. (2020). Armada. i. triple companions detected in b-type binaries α del and ν gem. *Astron. J.*, 161(1):40. [pg: 96]

Glebocki, R. and Gnacinski, P. (2005). Vizier online data catalog: catalog of stellar rotational velocities (glebocki+ 2005). *VizieR online data catalog*, pages III–244. [pg: 26]

Goldreich, P. and Nicholson, P. D. (1989). Tidal friction in early-type stars. *Astrophysical Journal, Part 1 (ISSN 0004-637X), vol. 342, July 15, 1989, p. 1079-1084.*, 342:1079–1084. [pg: 51]

Gontcharov, G. A. (2022). Astrometric solutions for binary stars in gaia dr3. *Astrophysical Journal*, 907(1):20. [pg: 64]

Gray, D. F. (2005). *The Observation and Analysis of Stellar Photospheres*. Cambridge University Press, Cambridge, UK, 3rd edition. [pg: 99]

Gray, R. O. and Corbally, C. J. (2009). *Stellar Spectral Classification*. Princeton University Press, Princeton, NJ. [pg: 217]

Green, G. M., Schlafly, E. F., Zucker, C., Speagle, J. S., and Finkbeiner, D. P. (2019). A 3d dust map based on gaia, pan-starrs 1, and 2mass. *The Astrophysical Journal*, 887(1):93. [pg: 65]

Guerrero, C., Souza, T., Fernandes, M. B., and Jurado, A. G. (2025a). Identification of possible stellar companions via speckle interferometry in a sample of be stars ii. *The Astronomical Journal*, 169(5):251. [pg: 131, 186, 230, 258, 270, 274, 275]

Guerrero, C. A., Souza, T. B., Borges Fernandes, M., and Guajardo Jurado, A. D. (2025b). Identification of possible stellar companions via speckle interferometry in a sample of be stars ii. *The Astronomical Journal*, 160(6):1–15. [pg: 214]

Gutiérrez-Soto, J., Fabregat, J., Suso, J., Lanzara, M., Garrido, R., Hubert, A.-M., and Floquet, M. (2007a). A photometric study of be stars located in the seismology fields of corot. *Astronomy & Astrophysics*, 476(2):927–933. [pg: 185]

Gutiérrez-Soto, J., Fabregat, J., Suso, J., Suárez, J. C., Moya, A., Garrido, R., Hubert, A.-M., Floquet, M., Neiner, C., and Frémat, Y. (2007b). Multiperiodic pulsations in the be stars nw serpentis and v1446 aquilae. *Astronomy & Astrophysics*, 472(2):565–570. [pg: 136]

Gvaramadze, V. (2006). Supernova remnant s 147 and its associated neutron star (s). *Astronomy & Astrophysics*, 454(1):239–246. [pg: 96, 104]

Hadrava, P. (1995). Orbital elements of multiple spectroscopic stars. *Astron. Astrophys. Suppl. Ser.*, 114:393. [pg: 98]

Halbedel, E. M. (1996). Rotational velocity determinations for 164 be and b stars. *Publications of the Astronomical Society of the Pacific*, 108(728):833. [pg: 133, 134]

Harmanec, P., Koubskỳ, P., Nemravová, J., Royer, F., Briot, D., North, P., Lampens, P., Frémat, Y., Yang, S., Božić, H., et al. (2015). Properties and nature of be stars-30. reliable physical properties of a semi-detached b9. 5e+ g8iii binary br cmi= hd 61273 compared to those of other well studied semi-detached emission-line binaries. *Astronomy & astrophysics*, 573:A107. [pg: 157, 262]

Harrison, K. M. (2011). *Astronomical spectroscopy for amateurs*. Springer Science & Business Media. [pg: 22]

Hastings, B., Langer, N., Wang, C., Schootemeijer, A., and Milone, A. P. (2021). Stringent upper limit on Be star fractions produced by binary interaction. *A&A*, 653:A144. [pg: 2]

Herbig, G. H. and Spalding Jr, J. F. (1955). Axial rotation and line broadening in stars of spectral types f0-k5. *Astrophysical Journal, vol. 121, p. 118*, 121:118. [pg: 24]

Herrero, A., Kudritzki, R. P., Vilchez, J. M., Kunze, D., Butler, K., and Haser, S. (1992). The mass and helium discrepancy in massive young stars. In Heber, U. and Jeffery, C. S., editors, *The Atmospheres of Early-Type Stars*, pages 21–23, Berlin, Heidelberg. Springer Berlin Heidelberg. [pg: 109]

Hertzsprung, E. (1908). Über die Sterne der Unterabteilungenc undac nach der Spektralklassifikation von Antonia C. Maury. [pg: 14]

Hilditch, R. W. (2001). *An introduction to close binary stars*. Cambridge University Press. [pg: 49]

Hirata, R., Kogure, M., Nakajima, K., Sato, T., Slettebak, S., and McCluskey, H. F. (1986). On the nature of some emission-line stars. i - a spectroscopic study of 24 be stars. *Publications of the Astronomical Society of Japan*, 38:509–526. [pg: 144]

Howarth, I. D., Goss, K., Stevens, I., Chaplin, W., and Elsworth, Y. (2014). Amplitude variability in satellite photometry of the non-radially pulsating o9. 5 v star ζ oph. *Monthly Notices of the Royal Astronomical Society*, 440(2):1674–1679. [pg: 155]

Howarth, I. D. and Smith, K. C. (2001). Rotational mixing in early-type main-sequence stars. *Monthly Notices of the Royal Astronomical Society*, 327(2):353–368. [pg: 155]

Hubeny, I. and Lanz, T. (2011). Synspec: General spectrum synthesis program. *Astrophysics Source Code Library*, pages ascl–1109. [pg: 98]

Hummel, W. and Vrancken, M. (2000). V/r variations and density waves in the disks of be stars. *A&A*, 359:1075–1082. [pg: 59]

Hut, P. (1981). Tidal evolution in close binary systems. *Astronomy and Astrophysics, vol. 99, no. 1, June 1981, p. 126-140.*, 99:126–140. [pg: 51]

Hutter, D., Tycner, C., Zavala, R., Benson, J., Hummel, C., and Zirm, H. (2021). Surveying the bright stars by optical interferometry. iii. a magnitude-limited multiplicity survey of classical be stars. *The Astrophysical Journal Supplement Series*, 257(2):69. [pg: 152]

IJspeert, L., Pablo, H., Bowman, D. M., Ramiaramanantsoa, T., Johnston, C., Mennickent, R. E., and Neiner, C. (2021). A tess view of be stars: detection of outbursts, pulsations, and eclipses. *Astronomy & Astrophysics*, 652:A56. [pg: 144]

Innes, R. (1901). Anomalous occultations of stars by the moon. *Monthly Notices of the Royal Astronomical Society, Vol. 61, p. 414*, 61:414. [pg: 140]

Janot-Pacheco, E. et al. (1991a). Non-radial pulsations in η cen. *Astronomy and Astrophysics*. [pg: 58]

Janot-Pacheco, E., Leister, N. V., Hubert, A., Floquet, M., and Hubert, H. (1991b). Rapid spectroscopic variability in be stars. *Information Bulletin on Variable Stars, No. 3651,# 1.*, 3651. [pg: 142]

Janssens, S., Shenar, T., Degenaar, N., Bodensteiner, J., Sana, H., Audenaert, J., and Frost, A. (2023). Mwc 656 is unlikely to contain a black hole. *Astronomy & Astrophysics*, 677:L9. [pg: 156]

Jaschek, C. and Andrillat, Y. (1998). Ae and a type shell stars. *Astronomy and Astrophysics Supplement Series*, 130(3):507–512. [pg: 161]

Jaschek, M. and Egret, D. (1982). A catalogue of be stars. In *Symposium-International Astronomical Union*, volume 98, pages 261–263. Cambridge University Press. [pg: 189]

Jaschek, M., Slettebak, A., and Jaschek, C. (1981). Be star terminology. *Be star newsletter*, 4:9–11. [pg: 20, 181]

Jayasinghe, T. e. a. (2020). The asas-sn catalog of variable stars v: The be stars. *MNRAS*, 493(4):4045–4070. [pg: 66]

Kallrath, J. (2022). Fifty years of eclipsing binary analysis with the wilson–devinney model. *Galaxies*, 10(1):17. [pg: 72]

Kervella, P., Arenou, F., Mignard, F., and Thévenin, F. (2019). Stellar and substellar companions of nearby stars from gaia dr2-binarity from proper motion anomaly. *Astronomy & Astrophysics*, 623:A72. [pg: 58, 64, 131, 143, 146, 166, 168, 169, 171, 172, 173, 175, 180, 185, 188, 191, 192, 194, 204, 205, 207, 210, 211, 216, 217, 225, 235, 257, 260, 268, 270, 279]

Kervella, P., Borgniet, S., de Souza, A. D., Mérand, A., Gallenne, A., Rivinius, T., Lacour, S., Carciofi, A., Faes, D. M., Le Bouquin, J.-B., et al. (2022). The binary system of the spinning-top be star achernar. *Astronomy & Astrophysics*, 667:A111. [pg: 181]

Kervella, P. and de Souza, A. D. (2007). The environment of the fast rotating star achernar-high-resolution thermal infrared imaging with visir in burst mode. *Astronomy & Astrophysics*, 474(3):L49–L52. [pg: 181, 258]

Kervella, P., de Souza, A. D., and Bendjoya, P. (2008). The close-in companion of the fast rotating be star achernar. *Astronomy & Astrophysics*, 484(1):L13–L16. [pg: 181]

Kippenhahn, R., Weigert, A., and Weiss, A. (1990). *Stellar structure and evolution*, volume 192. Springer. [pg: 17]

Klement, R., Baade, D., Rivinius, T., Gies, D. R., Wang, L., Labadie-Bartz, J., dos Santos, P. T., Monnier, J. D., Carciofi, A. C., Mérand, A., et al. (2022). Dynamical masses of the primary be star and secondary sdb star in the single-lined binary κ dra (b6 iiie). *The Astrophysical Journal*, 940(1):86. [pg: 152]

Klement, R., Carciofi, A. C., Rivinius, T., Panoglou, D., Vieira, R., Bjorkman, J., Štefl, S., Tycner, C., Faes, D., Korčáková, D., et al. (2015). Multitechnique testing of the viscous decretion disk model-i. the stable and tenuous disk of the late-type be star β cmi. *Astronomy & Astrophysics*, 584:A85. [pg: 273]

Klement, R. et al. (2024a). Orbital properties of binary be stars. *Astronomy and Astrophysics*. Submitted. [pg: 58]

Klement, R., Hadrava, P., Rivinius, T., Baade, D., Cabezas, M., Heida, M., Schaefer, G. H., Gardner, T., Gies, D. R., Anugu, N., et al. (2021). ν Gem: a hierarchical triple system with an outer Be star. *Astrophys. J.*, 916(1):24. [pg: 96]

Klement, R., Rivinius, T., Gies, D. R., Baade, D., Mérand, A., Monnier, J. D., Schaefer, G. H., Lanthermann, C., Anugu, N., Kraus, S., et al. (2024b). The chara array interferometric program on the multiplicity of classical be stars: new detections and orbits of stripped subdwarf companions. *The Astrophysical Journal*, 962(1):70. [pg: 160, 162, 193, 206]

Klement, R., Rivinius, T., Gies, D. R., Baade, D., Mérand, A., Monnier, J. D., Schaefer, G. H., Lanthermann, C., Anugu, N., Kraus, S., and Gardner, T. (2024c). The chara array interferometric program on the multiplicity of classical be stars: New detections and orbits of stripped subdwarf companions. *The Astrophysical Journal*, 962(1):70. [pg: 148]

Klement, R. e. a. (2015). Disk truncation and precession in the be binary ζ tauri. *Astronomy and Astrophysics*, 584:A85. [pg: 70]

Klement, R. e. a. (2019). The be star 60 cygni: Orbit, disk structure, and v/r variability. *A&A*, 627:A57. [pg: 88]

Kochanek, C. (2022a). The progenitor of the vela pulsar. *Monthly Notices of the Royal Astronomical Society*, 511(3):3428–3439. [pg: 146]

Kochanek, C. S. (2022b). Fundamental stellar parameters from photometry. *Astrophysical Journal*. [pg: 58]

Kopal, Z. (1959a). *Close Binary Systems*. Chapman and Hall, London. [pg: 46]

Kopal, Z. (1959b). *Close Binary Systems*. Chapman & Hall. [pg: 72]

Koubský, P., Harmanec, P., Yang, S., et al. (2006). Spectroscopic investigation of be stars. xx. ves 203 = hd 81357: an interacting be binary. *A&A*, 459:849–859. [pg: 59, 66]

Koubský, P., Kotková, L., Votruba, V., Slechta, M., and Dvoraková, S. (2012). o puppis: another be+sdo binary? *A&A*, 545:A121. [pg: 141]

Kounkel, M., Covey, K., Moe, M., Kratter, K. M., Suárez, G., Stassun, K. G., Román-Zúñiga, C., Hernandez, J., Kim, J. S., Ramírez, K. P., et al. (2019). Close companions around young stars. *The Astronomical Journal*, 157(5):196. [pg: 235]

Kramer, M., Lyne, A. G., Hobbs, G., Löhmer, O., Carr, P., Jordan, C., and Wolszczan, A. (2003). The proper motion, age, and initial spin period of PSR J0538+2817 in S147. *Astrophys. J.*, 593(1):L31. [pg: 96]

Kubát, J., Koubskỳ, P., Harmanec, P., Hubert, A., and Hadrava, P. (1998). Wind and jets in the be star 4 herculis. In *Cyclical Variability in Stellar Winds: Proceedings of the ESO Workshop Held at Garching, Germany, 14–17 October 1997*, pages 139–139. Springer. [pg: 160]

Kurtz, D. W., Shibahashi, H., Murphy, S. J., Bedding, T. R., and Bowman, D. M. (2015). A unifying explanation of complex frequency spectra of gamma dor, spb and be stars: combination frequencies and highly non-sinusoidal light curves. *Monthly Notices of the Royal Astronomical Society*, 450:3015–3024. [pg: 79]

Labadie-Bartz, J., Carciofi, A. C., de Amorim, T. H., Rubio, A., Figueiredo, A. L., dos Santos, P. T., and Thomson-Paressant, K. (2022). Classifying be star variability with tess. i. the southern ecliptic. *The Astronomical Journal*, 163(5):226. [pg: 77, 78, 86, 114, 130, 132, 135, 141, 153, 159, 203, 205, 228, 234, 261, 280, 287]

Labadie-Bartz, J., Chojnowski, S. D., Whelan, D. G., Pepper, J., McSwain, M. V., Fernandes, M. B., Wisniewski, J. P., Stringfellow, G. S., Carciofi, A. C., Siverd, R. J., et al. (2018). Outbursts and disk variability in be stars. *The Astronomical Journal*, 155(2):53. [pg: 139, 177, 180, 191, 192]

Labadie-Bartz, J., Pepper, J., McSwain, M. V., Bjorkman, J., Bjorkman, K., Lund, M. B., Rodriguez, J. E., Stassun, K. G., Stevens, D. J., James, D. J., et al. (2017). Photometric variability of the be star population. *The Astronomical Journal*, 153(6):252. [pg: 2, 23, 59, 66, 67, 111, 168, 190, 266]

Labadie-Bartz, J. e. a. (2018). Short-cadence kepler photometry of be stars: pulsations and outbursts. *AJ*, 156(252). [pg: 66]

Landin, N., Mendes, L., and Vaz, L. (2009). Combined effects of tidal and rotational distortions on the equilibrium configuration of low-mass, pre-main sequence stars. *Astronomy & Astrophysics*, 494(1):209–227. [pg: 50]

Langer, N. (2012). Presupernova evolution of massive single and binary stars. *ARA&A*, 50:107–164. [pg: 1]

Lanz, T. and Hubeny, I. (2007). A grid of NLTE line-blanketed model atmospheres of early B-type stars. *ApJS*, 169(1):83. [pg: 98]

Lee, U., Saio, H., and Osaki, Y. (1991). Viscous excretion discs around be stars. *Monthly Notices of the Royal Astronomical Society*, 250(2):432–437. [pg: 53]

Levenhagen, R., Leister, N. V., Zorec, J., Janot-Pacheco, E., Hubert, A., and Floquet, M. (2003a). Nrps and circumstellar activity in hd 127972. *Astronomy & Astrophysics*, 400(2):599–612. [pg: 142]

Levenhagen, R. S., Curé, M., Arcos, C., Diaz, M. P., Araya, I., Amôres, E. B., Turis-Gallo, D., and Concha, D. (2024a). Zpektr: A code for spectral synthesis of fast-rotating stars. *Astronomy & Astrophysics*, 685:A57. [pg: 141, 142, 147, 149, 150, 196]

Levenhagen, R. S. et al. (2003b). Spectroscopic study of η cen. *Astronomy and Astrophysics*. [pg: 58]

Levenhagen, R. S. et al. (2024b). Physical parameters of be stars in gaia era. *Astronomy and Astrophysics*. [pg: 58, 59]

Levenhagen, R. S. and Leister, N. V. (2004). Physical parameters of southern b-and be-type stars. *The Astronomical Journal*, 127(2):1176. [pg: 154]

Levenhagen, R. S. and Leister, N. V. (2006a). Fundamental parameters of be stars. *Monthly Notices of the Royal Astronomical Society*. [pg: 58]

Levenhagen, R. S. and Leister, N. V. (2006b). Spectroscopic analysis of southern b and be stars. *Monthly Notices of the Royal Astronomical Society*, 371(1):252–262. [pg: 142]

Li, G., Guo, Z., Fuller, J., Bedding, T. R., Murphy, S. J., Colman, I. L., and Hey, D. R. (2020). The effect of tides on near-core rotation: analysis of 35 kepler γ doradus stars in eclipsing and spectroscopic binaries. *Monthly Notices of the Royal Astronomical Society*, 497(4):4363–4375. [pg: 51]

Lucy, L. B. (1967). Gravity-darkening for stars with convective envelopes. *Zeitschrift für Astrophysik, Vol. 65, p. 89*, 65:89. [pg: 11]

Maeder, A. and Meynet, G. (2000). The evolution of rotating stars. *Annual Review of Astronomy and Astrophysics*, 38(1):143–190. [pg: 24]

Mahy, L., Rauw, G., De Becker, M., Eenens, P., and Flores, C. (2013). A spectroscopic investigation of the o-type star population in four cygnus ob associations-i. determination of the binary fraction. *Astronomy & Astrophysics*, 550:A27. [pg: 51]

Malkov, O. Y. (2020a). Physical parameters of close binaries. *Astronomy Reports*. [pg: 59]

Malkov, O. Y. (2020b). Semidetached double-lined eclipsing binaries: Stellar parameters and rare classes. *Monthly Notices of the Royal Astronomical Society*, 491(4):5489–5497. [pg: 151]

Marchant, P. et al. (2024). Constraining massive binary evolution with post-interaction systems. *A&A*. in press. [pg: 1]

Marr, K. C., Jones, C. E., Carciofi, A. C., Rubio, A. C., Mota, B. C., Ghoreyshi, M. R., Hatfield, D. W., and Rímulo, L. R. (2021). The be star 66 ophiuchi: 60 years of disk evolution. *The Astrophysical Journal*, 912(1):76. [pg: 264]

Martayan, C., Baade, D., and Fabregat, J. (2010a). A slitless spectroscopic survey for hα emission-line objects in smc clusters. *Astronomy & Astrophysics*, 509:A11. [pg: 21]

Martayan, C., Frémat, Y., Hubert, A.-M., Floquet, M., Zorec, J., and Neiner, C. (2007). Effects of metallicity, star-formation conditions, and evolution in b and be stars-ii. small magellanic cloud, field of ngc 330. *Astronomy & Astrophysics*, 462(2):683–694. [pg: 53]

Martayan, C., Rivinius, T., Baade, D., Hubert, A.-M., and Zorec, J. (2010b). Review about populations of Be stars: stellar evolution of extreme stars. Review about Be stars populations at the IAUS272. [pg: 20]

Martinez, A., Orsaria, M., González Felipe, R., and Lopez Fune, E. (2008). Materia extraña en el universo. *Revista mexicana de física E*, 54. [pg: 47]

Maíz Apellániz, J., Trigueros Páez, E., Negueruela, I., Barbá, R. H., Simón-Díaz, S., Lorenzo, J., Sota, A., Gamen, R. C., Fariña, C., Salas, J., Caballero, J. A., Morrell, N. I., Pellerin, A., Alfaro, E. J., Herrero, A., Arias, J. I., and Marco, A. (2019). Monos: Multiplicity of northern o-type spectroscopic systems - i. project description and spectral classifications and visual multiplicity of previously known objects. *A&A*, 626:A20. [pg: 96]

McSwain, M. V. and Gies, D. R. (2005). The evolutionary status of be stars: results from a photometric study of southern open clusters. *The Astrophysical Journal Supplement Series*, 161(1):118. [pg: 53]

Meilland, A., Millour, F., Kanaan, S., Stee, P., Petrov, R., Hofmann, K.-H., Natta, A., and Perraut, K. (2012). First spectro-interferometric survey of be stars-i. observations and constraints on the disk geometry and kinematics. *Astronomy & Astrophysics*, 538:A110. [pg: 53]

Mendoza, V. and Eugenio, E. (1958). A spectroscopic and photometric study of the be stars. *Astrophysical Journal, vol. 128, p. 207*, 128:207. [pg: 104, 134]

Mennickent, R., Kołaczkowski, Z., Djurasevic, G., Niemczura, E., Diaz, M., Curé, M., Araya, I., and Peters, G. (2012). A cyclic bipolar wind in the interacting binary v 393 scorpii. *Monthly Notices of the Royal Astronomical Society*, 427(1):607–624. [pg: 52]

Merrill, P. W. (1925). The discovery of emission lines in the spectra of early-type stars. *Astrophysical Journal*, 61:24–39. [pg: 213]

Merrill, P. W. (1929). The spectrum of bd+ 11 4673. *Astrophysical Journal, 69, 330-378 (1929)*, 69. [pg: 20]

Merrill, P. W. and Burwell, C. G. (1933). Catalogue and bibliography of stars of classes b and a whose spectra have bright hydrogen lines. *Astrophysical Journal, vol. 78, p. 87*, 78:87. [pg: 19, 134]

Merrill, P. W. and Burwell, C. G. (1943). Supplement to the mount wilson catalogue and bibliography of stars of classes b and a whose spectra have bright hydrogen lines. *Astrophysical Journal, vol. 98, p. 153*, 98:153. [pg: 19, 98, 105]

Merrill, P. W. and Burwell, C. G. (1949). Second supplement to the mount wilson catalogue and bibliography of stars of classes b and a whose spectra have bright hydrogen lines. *Astrophysical Journal, vol. 110, p. 387*, 110:387. [pg: 19, 167]

Merrill, P. W. and Burwell, C. G. (1950). Additional stars whose spectra have a bright h alpha line. *Astrophysical Journal, vol. 112, p. 72*, 112:72. [pg: 19]

Merrill, P. W., Humason, M. L., and Burwell, C. G. (1932). Discovery and observations of stars of class be: Second paper. *Astrophysical Journal, vol. 76, p. 156*, 76:156. [pg: 133]

Miglio, A., Montalbán, J., and Dupret, M.-A. (2007). Revised instability domains of SPB and β Cephei stars. *Communications in Asteroseismology*, 151:48–56. [pg: 109]

Milne, E. (1921). Radiative equilibrium in the outer layers of a star. *Monthly Notices of the Royal Astronomical Society, Vol. 81, p. 361-375*, 81:361–375. [pg: 10]

Minkowski, R. (1958). Cygnus loop and some related nebulosities. *Symposium - International Astronomical Union*, 8:1048–1052. [pg: 96]

Mitrofanova, A., Dyachenko, V., Beskakotov, A., Balega, Y., Maksimov, A., and Rastegaev, D. (2021). Speckle interferometry of nearby multiple stars. ii. 2007–2020 positional measurements and orbits of sixteen objects. *The Astronomical Journal*, 162(4):156. [pg: 158]

Moe, M. and Di Stefano, R. (2017a). Mind your ps and qs: The interrelation between period and mass-ratio distributions of binary stars. *ApJS*, 230:15. [pg: 1]

Moe, M. and Di Stefano, R. (2017b). Mind your ps and qs: the interrelation between period (p) and mass-ratio (q) distributions of binary stars. *The Astrophysical Journal Supplement Series*, 230(2):15. [pg: 96]

Morgan, W. W., Code, A. D., and Whitford, A. E. (1955). Studies in Galactic STRUCTURE.II.LUMINOSITY Classification for 1270 Blue Giant Stars. *ApJS*, 2:41. [pg: 208]

Mourard, D., Monnier, J. D., Meilland, A., et al. (2015). Investigating the geometry and kinematics of the be star δ sco during its 2011 periastron passage. *A&A*, 577:A51. [pg: 59]

Munitz, M. K. and Payne-Gaposchkin, C. (1957). Theories of the universe. *Physics Today*, 10(8):22. [pg: 16]

Naoz, S. (2016). The eccentric kozai-lidov effect and its applications. *Annual Review of Astronomy and Astrophysics*, 54(1):441–489. [pg: 112]

Nazé, Y., Rauw, G., Czesla, S., Smith, M. A., and Robrade, J. (2022). Velocity monitoring of γ cas stars reveals their binarity status. *Monthly Notices of the Royal Astronomical Society*, 510(2):2286–2304. [pg: 189]

Nazé, Y. and Robrade, J. (2023). Srg/erosita survey of be stars. *Monthly Notices of the Royal Astronomical Society*, 525(3):4186–4201. [pg: 178]

Negueruela, I., Simón-Díaz, S., de Burgos, A., Casasbuenas, A., and Beck, P. G. (2024). The iacob project-xii. new grid of northern standards for the spectral classification of b-type stars. *Astronomy & Astrophysics*, 690:A176. [pg: 157]

Negueruela, I., Steele, I. A., and Bernabeu, G. (2004). On the class of oe stars'. *Astronomische Nachrichten: Astronomical Notes*, 325(9):749–760. [pg: 20]

Neiner, C., de Batz, B., Cochard, F., Floquet, M., Mekkas, A., and Desnoux, V. (2011). The Be Star Spectra (BeSS) Database. *AJ*, 142(5):149. [pg: 2, 69]

Neiner, C. e. a. (2018). Ten years of bess database: achievements and perspectives. *Contributions of the Astronomical Observatory Skalnaté Pleso*, 48:150–158. [pg: 69, 70]

Neubauer, F. (1943). Twenty new class be stars. *Publications of the Astronomical Society of the Pacific*, 55(323):99. [pg: 154]

Neuhaeuser, R., Gießler, F., and Hambaryan, V. V. (2020). A nearby recent supernova that ejected the runaway star ζ oph, the pulsar psr b1706- 16, and 60fe found on earth. *Monthly Notices of the Royal Astronomical Society*, 498(1):899–917. [pg: 155]

Nichols, J. S. and Slavin, J. D. (2004a). Classification of hd 72067. *Astrophysical Journal*. [pg: 58]

Nichols, J. S. and Slavin, J. D. (2004b). Shocked clouds in the vela supernova remnant. *The Astrophysical Journal*, 610(1):285. [pg: 145]

Okazaki, A. and Negueruela, I. (2001a). A natural explanation for periodic x-ray outbursts in be/x-ray binaries. *Astronomy & Astrophysics*, 377(1):161–174. [pg: 52]

Okazaki, A. T. and Negueruela, I. (2001b). A natural explanation for periodic x-ray outbursts in be/x-ray binaries. *A&A*, 377:161–174. [pg: 59, 67]

Oudmaijer, R. D. and Parr, A. M. (2010). The binary fraction and mass ratio of be and b stars: a comparative very large telescope/naco study. *Monthly Notices of the Royal Astronomical Society*, 405(4):2439–2446. [pg: 51, 172]

Packet, W. (1981). On the spin-up of the mass accreting component in a close binary system. *A&A*, 102(1):17–19. [pg: 1]

Paczynski, B. (1971). Evolutionary processes in close binary systems. *Annual Review of Astronomy and Astrophysics, vol. 9, p. 183*, 9:183. [pg: 47]

Paczyński, B. (1967). Evolutionary processes in close binary systems. *Acta Astron.*, 17:287. [pg: 1]

Panoglou, D., Carciofi, A. C., Vieira, R. G., Cyr, I. H., Jones, C. E., Okazaki, A. T., and Rivinius, T. (2016). Be discs in binary systems–i. coplanar orbits. *Monthly Notices of the Royal Astronomical Society*, 461(3):2616–2629. [pg: 52]

Panoglou, D. e. a. (2018). Binary interactions and disk structure in be stars. *MNRAS*, 473(3):3039–3056. [pg: 66]

Pecaut, M. J. and Mamajek, E. E. (2013). Intrinsic colors, temperatures, and bolometric corrections of pre-main-sequence stars. *The Astrophysical Journal Supplement Series*, 208(1):9. [pg: 216, 217]

Plavec, M. and Dobias, J. (1987a). Ry gem: an eclipsing binary system. *Bulletin of the Astronomical Institutes of Czechoslovakia*. [pg: 59]

Plavec, M. J. and Dobias, J. J. (1987b). The moderately interacting algol binary rs cephei. *Astronomical Journal (ISSN 0004-6256), vol. 93, Jan. 1987, p. 171-182.*, 93:171–182. [pg: 151]

Pols, O., Cote, J., Waters, L., and Heise, J. (1991). The formation of be stars through close binary evolution. *Astronomy and Astrophysics (ISSN 0004-6361), vol. 241, no. 2, Jan. 1991, p. 419-438.*, 241:419–438. [pg: 52]

Pols, O. R., Cote, J., Waters, L. B. F. M., and Heise, J. (1991). The formation of Be stars through close binary evolution. *A&A*, 241:419. [pg: 1]

Porter, J. M. and Rivinius, T. (2003a). Classical be stars. *Publications of the Astronomical Society of the Pacific*, 115:1153–1170. [pg: 1]

Porter, J. M. and Rivinius, T. (2003b). Classical be stars. *Publications of the Astronomical Society of the Pacific*, 115(812):1153. [pg: 20]

Prasow-Émond, M., Hlavacek-Larrondo, J., Fogarty, K., Artigau, É., Mawet, D., Gandhi, P., Steiner, J., Rameau, J., Lafrenière, D., Fabian, A., et al. (2024). The first high-contrast images of near high-mass x-ray binaries with keck/nirc2. *The Astrophysical Journal*, 967(1):8. [pg: 82]

Prša, A. e. a. (2022). The tess eclipsing binary catalog. i. *Astrophysical Journal Supplement Series*, 258(1):16. [pg: 67]

Ramsay, G., Hakala, P., and Charles, P. A. (2022). A tess search for donor-star pulsations in high-mass x-ray binaries. *MNRAS*, 516(1):1219–1236. [pg: 66]

Reig, P. (2011). Be/x-ray binaries. *Astrophysics and Space Science*, 332:1–29. [pg: 52]

Rhee, J. H., Song, I., Zuckerman, B., and McElwain, M. (2007). Characterization of dusty debris disks: the iras and hipparcos catalogs. *The Astrophysical Journal*, 660(2):1556. [pg: 162]

Ricker, G. R. e. a. (2015). Transiting exoplanet survey satellite (tess). *Journal of Astronomical Telescopes, Instruments, and Systems*, 1(1):014003. [pg: 66]

Rivinius, T., Baade, D., and Štefl, S. (2003). Non-radially pulsating be stars. *Astronomy & Astrophysics*, 411(2):229–247. [pg: 269]

Rivinius, T., Carciofi, A. C., and Martayan, C. (2013). Classical be stars. rapidly rotating b stars with viscous keplerian decretion disks. *A&ARv*, 21:69. [pg: 1, 2, 18, 20, 52, 59, 66, 67, 70, 79, 88, 114]

Rivinius, T., Klement, R., Chojnowski, S., Baade, D., Abdul-Masih, M., Przybilla, N., Fló, J. G., Heathcote, B., Hadrava, P., Gies, D., et al. (2025a). Newborn be star systems observed shortly after mass transfer. *A&A*, 694:A172. [pg: 96, 98, 104, 107, 115]

Rivinius, T., Klement, R., Chojnowski, S., Baade, D., Abdul-Masih, M., Przybilla, N., Fló, J. G., Heathcote, B., Hadrava, P., Gies, D., et al. (2025b). Newborn be star systems observed shortly after mass transfer. *Astronomy & Astrophysics*, 694:A172. [pg: 144, 227, 255]

Rivinius, T., Štefl, S., and Baade, D. (2006). Bright be-shell stars. *Astronomy & Astrophysics*, 459(1):137–145. [pg: 162]

Rocha, D. F., Almeida, L. A., Damineli, A., Navarete, F., Abdul-Masih, M., and Mace, G. N. (2022). Distance and age of the massive stellar cluster westerlund 1–ii. the eclipsing binary w36. *MNRAS*, 517(3):3749–3762. [pg: 100, 101, 109]

Rosales, J., Mennickent, R., Schleicher, D., and Senhadji, A. (2019). Evolutionary process of the interacting binary v495 centauri. *Monthly Notices of the Royal Astronomical Society*, 483(1):862–872. [pg: 202]

Rosales Guzmán, J., Mennickent, R., Djurašević, G., Araya, I., and Curé, M. (2018). Spectroscopic and photometric study of the eclipsing interacting binary v495 centauri. *Monthly Notices of the Royal Astronomical Society*, 476(3):3039–3050. [pg: 202]

Rosen, A. L., Offner, S. S., Sadavoy, S. I., Bhandare, A., Vázquez-Semadeni, E., and Ginsburg, A. (2020). Zooming in on individual star formation: low-and high-mass stars. *Space Science Reviews*, 216(4):62. [pg: 18]

Różański, T., Niemczura, E., Lemiesz, J., Posiłek, N., and Różański, P. (2022). Suppnet: Neural network for stellar spectrum normalisation. *Astronomy & Astrophysics*, 659:A199. [pg: 153]

Rozhkovskij, D. A. and Kurchakov, A. V. (1968). Catalogue of reflection nebulae. *Trudy Astrofizicheskogo Instituta Alma-Ata*, 11:3–42. [pg: 132]

Russell, H. N. (1914). Relations Between the Spectra and Other Characteristics of the Stars. *Popular Astronomy*, 22:275–294. [pg: 14]

Sallmen, S. and Welsh, B. (2004). Intermediate-velocity gas observed towards the shajn 147 snr. *Astronomy & Astrophysics*, 426(2):555–565. [pg: 98]

Sana, H. (2014). Binary interaction dominates the evolution of massive stars. *IAUS*, 297:174–183. [pg: 1]

Sana, H., de Mink, S. E., de Koter, A., et al. (2012). Binary interaction dominates the evolution of massive stars. *Science*, 337(6093):444–446. [pg: 1, 5, 33, 51]

Scargle, J. D. (1982). Studies in astronomical time series analysis. ii-statistical aspects of spectral analysis of unevenly spaced data. *ApJ*, 263:835–853. [pg: 66]

Schild, R. and Romanishin, W. (1976). A study of be stars in clusters. In *Symposium-International Astronomical Union*, volume 70, pages 31–32. Cambridge University Press. [pg: 21]

Schneider, F. R. N., Ohlmann, S. T., Podsiadlowski, P., Röpke, F. K., Balbus, S. A., Pakmor, R., and Springel, V. (2019). Stellar mergers as the origin of magnetic massive stars. *nature*, 574(7777):211–214. [pg: 1]

Schoettler, C., De Bruijne, J., Vaher, E., and Parker, R. J. (2020). Runaway and walkaway stars from the onc with gaia dr2. *Monthly Notices of the Royal Astronomical Society*, 495(3):3104–3123. [pg: 183]

Schootemeijer, A., Lennon, D. J., Garcia, M., Langer, N., Hastings, B., and Schürmann, C. (2022). A census of OBe stars in nearby metal-poor dwarf galaxies reveals a high fraction of extreme rotators. *A&A*, 667:A100. [pg: 2]

Secchi, A. (1866). Schreiben des herrn prof. secchi, directors der sternwarte des collegio romano, an den herausgeber. *Astronomische Nachrichten, volume 68, p. 63*, 68:63. [pg: 18]

Sen, K., Langer, N., Pauli, D., Gräfener, G., Schootemeijer, A., Sana, H., Shenar, T., Mahy, L., and Wang, C. (2023). Reverse Algols and hydrogen-rich Wolf-Rayet stars from very massive binaries. *A&A*, 672:A198. [pg: 1]

Serenelli, A., Weiss, A., Aerts, C., Angelou, G. C., Baroch, D., Bastian, N., Beck, P. G., Bergemann, M., Bestenlehner, J. M., Czekala, I., et al. (2021). Weighing stars from birth to death: mass determination methods across the hrd. *The Astronomy and Astrophysics Review*, 29(1):4. [pg: 24]

Shenar, T., Bodensteiner, J., Abdul-Masih, M., Fabry, M., Mahy, L., Marchant, P., Banyard, G., Bowman, D., Dsilva, K., Hawcroft, C., et al. (2020). The "hidden" companion in lb-1 unveiled by spectral disentangling. *A&A*, 639:L6. [pg: 98]

Shenar, T., Sana, H., Mahy, L., El-Badry, K., Marchant, P., Langer, N., Hawcroft, C., Fabry, M., Sen, K., Almeida, L. A., et al. (2022). An x-ray-quiet black hole born with a negligible kick in a massive binary within the large magellanic cloud. *Nature Astronomy*, 6(9):1085–1092. [pg: 100]

Shenar, T., Wade, G. A., Marchant, P., Bagnulo, S., Bodensteiner, J., Bowman, D. M., Gilkis, A., Langer, N., Nicolas-Chené, A., Oskinova, L., Van Reeth, T., Sana, H., St-Louis, N., de Oliveira, A. S., Todt, H., and Toonen, S. (2023). A massive helium star with a sufficiently strong magnetic field to form a magnetar. *Science*, 381(6659):761–765. [pg: 1]

Shi, X.-d., Qian, S.-b., Zhu, L.-y., Liu, L., Li, L.-j., and Zang, L. (2023a). Observational properties of 155 o-and b-type massive pulsating stars. *The Astrophysical Journal Supplement Series*, 265(2):33. [pg: 190]

Shi, Y. et al. (2023b). Binary be stars and disk interactions. *Monthly Notices of the Royal Astronomical Society*. [pg: 59]

Shokry, A., Mennickent, R. E., Baade, D., Otero, S., Carciofi, M. A., and de Souza, A. D. (2018). Photometric and spectroscopic study of be stars with warm companions. *Monthly Notices of the Royal Astronomical Society*, 480(1):111–123. [pg: 144]

Sigut, T. and Ghafourian, N. R. (2023a). Comparing be star inclination angles determined from hα fitting and gravitational darkening. *The Astrophysical Journal*, 948(1):34. [pg: 135, 138, 147, 150, 158, 160, 176]

Sigut, T. A. A. and Ghafourian, N. (2023b). Spectral types and disk interaction in be stars. *Monthly Notices of the Royal Astronomical Society*. [pg: 58]

Sikora, J., Wade, G., Bohlender, D., Neiner, C., Oksala, M., Shultz, M., Cohen, D. H., Ud-Doula, A., Grunhut, J., Monin, D., et al. (2015). Confirming hd 23478 as a new magnetic b star hosting an hα-bright centrifugal magnetosphere. *Monthly Notices of the Royal Astronomical Society*, 451(2):1928–1938. [pg: 209]

Silaj, J. and Landstreet, J. (2014). Accurate age determinations of several nearby open clusters containing magnetic ap stars. *Astronomy & Astrophysics*, 566:A132. [pg: 166]

Silk, J. and Wallerstein, G. (1973). High-velocity gas in supernova remnants. ii. shajn 147. *ApJ*, 181:799–804. [pg: 96, 98]

Simón-Díaz, S. and Herrero, A. (2014). The iacob project-i. rotational velocities in northern galactic o-and early b-type stars revisited. the impact of other sources of line-broadening. *Astronomy & Astrophysics*, 562:A135. [pg: 98]

Slettebak, A. (1982). Spectral types and rotational velocities of the brighter be stars and af type shell stars. *Astrophysical Journal Supplement Series, vol. 50, Sept. 1982, p. 55-83.*, 50:55–83. [pg: 268]

Slettebak, A. (2012). *Be and shell stars*, volume 70. Springer Science & Business Media. [pg: 20]

Smalley, B. (2005). Teff and log g determinations. *Memorie della Società Astronomica Italiana Supplement, v. 8, p. 130 (2005)*, 8:130. [pg: 7]

Solar, M., Arcos, C., Curé, M., Levenhagen, R. S., and Araya, I. (2022a). Automatic algorithm to obtain v sin i values via fourier transform in the besos database. *Monthly Notices of the Royal Astronomical Society*, 511(3):4404–4416. [pg: 146, 147]

Solar, M. et al. (2022b). v sin i measurements from spectral modeling. *Astronomy and Astrophysics*. [pg: 58]

Southworth, J. and Bowman, D. M. (2022). High-mass pulsators in eclipsing binaries observed using tess. *MNRAS*, 513(3):3191–3209. [pg: 66, 67, 278]

Souza, T., Guerrero, C., and Fernandes, M. B. (2020). Identification of possible stellar companions via speckle interferometry in a sample of be stars. *The Astronomical Journal*, 159(4):132. [pg: 58, 132, 133, 145, 146, 167, 174, 265]

Štefl, S., Rivinius, T., Carciofi, A. C., Le Bouquin, J.-B., Baade, D., Bjorkman, K., Hesselbach, E., Hummel, C., Okazaki, A., Pollmann, E., et al. (2009). Cyclic variability of the circumstellar disk of the be star ζ tauri-i. long-term monitoring observations. *Astronomy & Astrophysics*, 504(3):929–944. [pg: 170]

Stephenson, C. B. and Sanduleak, N. (1971). Luminous stars in the southern milky way. *Publications of the Warner & Swasey Observatory*, 1:1. [pg: 159]

Sterne, T. E. (1940). The effects of eccentricity on the light changes of eclipsing variables. *Proceedings of the National Academy of Sciences*, 26(1):36–40. [pg: 72]

Struve, O. (1931). On the origin of bright lines in spectra of stars of class b. *Astrophysical Journal, vol. 73, p. 94*, 73:94. [pg: 19, 25]

Takata, M., Ouazzani, R.-M., Saio, H., Christophe, S., Ballot, J., Antoci, V., Salmon, S., and Hijikawa, K. (2020). A diagnostic diagram for γ doradus variables and slowly pulsating b-type stars. *A&A*, 635:A106. [pg: 111]

Tango, W., Davis, J., Jacob, A., Mendez, A., North, J., O'Byrne, J., Seneta, E., and Tuthill, P. (2009). A new determination of the orbit and masses of the be binary system δ scorpii. *Monthly Notices of the Royal Astronomical Society*, 396(2):842–848. [pg: 140]

Tassoul, J.-L. (1987). On synchronization in early-type binaries. *Astrophysical Journal, Part 1 (ISSN 0004-637X), vol. 322, Nov. 15, 1987, p. 856-861.*, 322:856–861. [pg: 50]

Tobin, J. J., Looney, L. W., Li, Z.-Y., Chandler, C. J., Dunham, M. M., Segura-Cox, D., Sadavoy, S. I., Melis, C., Harris, R. J., Kratter, K., et al. (2016). The vla nascent disk and multiplicity survey of perseus protostars (vandam). ii. multiplicity of protostars in the perseus molecular cloud. *The Astrophysical Journal*, 818(1):73. [pg: 33]

Tokovinin, A. (2014). From binaries to multiples. i. data on f and g dwarfs within 67 pc of the sun. *The Astronomical Journal*, 147(4):86. [pg: 96]

Townsend, R. H. D., Owocki, S. P., and Howarth, I. D. (2004). Be-star rotation: how close to critical? *MNRAS*, 350(1):189–195. [pg: 2, 25, 54]

Tutukov, A. and Fedorova, A. (2007). Formation and evolution of ae and be stars. *Astronomy reports*, 51:847–862. [pg: 20]

van de Hulst, H. C. (1946). The solid particles in interstellar space. *Recherches Astronomiques de l'observatoire d'Utrecht*, 11:2–i. [pg: 13]

van den Bos, W. H. (1929). Measures of Double Stars-10th Series. *Circular of the Union Observatory Johannesburg*, 80:59–102. [pg: 58, 145]

Van Hamme, W. (1993). New limb-darkening coefficients for modeling binary star light curves. *AJ*, 106:2096–2117. [pg: 75, 102]

Vennes, S., Kawka, A., Jonić, S., Pirković, I., Iliev, L., Kubát, J., Šlechta, M., Németh, P., and Kraus, M. (2011). On the nature of the be star hr 7409 (7 vul). *Monthly Notices of the Royal Astronomical Society*, 413(4):2760–2766. [pg: 255]

Vink, J. S., Davies, B., Harries, T. J., Oudmaijer, R. D., and Walborn, N. R. (2009). On the presence and absence of disks around O-type stars. *A&A*, 505(2):743–753. [pg: 2]

Vollmann, W. (2008). Double star astrometry with a simple ccd camera. *Journal of Double Star Observations, Fall*. [pg: 167]

Von Zeipel, H. (1924). The radiative equilibrium of a rotating system of gaseous masses. *Monthly Notices of the Royal Astronomical Society, Vol. 84, p. 665-683*, 84:665–683. [pg: 11]

Walborn, N. R. (1973). The space distribution of the o stars in the solar neighborhood. *Astronomical Journal, Vol. 78, p. 1067-1073, 1143-1144*, 78:1067–1073. [pg: 153]

Wang, C., Bodensteiner, J., Xu, X.-T., de Mink, S. E., Langer, N., Laplace, E., Vigna-Gómez, A., Justham, S., Klencki, J., Olejak, A., Valli, R., and Schootemeijer, A. (2024). Stripped helium-star and compact object binaries in coeval populations – predictions based on detailed binary evolution models. [pg: 2]

Wang, C., Langer, N., Schootemeijer, A., Castro, N., Adscheid, S., Marchant, P., and Hastings, B. (2020). Effects of Close Binary Evolution on the Main-sequence Morphology of Young Star Clusters. *ApJ*, 888(1):L12. [pg: 1]

Wang, L. et al. (2023a). Mass determinations in be binaries. *Astrophysical Journal*. [pg: 58]

Wang, L., Gies, D. R., Peters, G. J., Götberg, Y., Chojnowski, S. D., Lester, K. V., and Howell, S. B. (2021). The detection and characterization of be+ sdo binaries from hst/stis fuv spectroscopy. *The Astronomical Journal*, 161(5):248. [pg: 179]

Wang, L., Gies, D. R., Peters, G. J., and Han, Z. (2023b). The orbital and physical properties of five southern be+ sdo binary systems. *The Astronomical Journal*, 165(5):203. [pg: 176, 179, 189]

Wang, L., Gies, D. R., Peters, G. J., and Han, Z. (2023c). The orbital and physical properties of five southern be+sdo binary systems. *The Astronomical Journal*, 165(5):203. [pg: 148]

Warren Jr, W. H. and Hesser, J. E. (1978). A photometric study of the orion ob 1 association. iii-subgroup analyses. *Astrophysical Journal Supplement Series, vol. 36, Apr. 1978, p. 497-572.*, 36:497–572. [pg: 235]

Wheelwright, H. E., Oudmaijer, R. D., and de Wit, W. J. (2012). Probing the companions of massive young stellar objects with near-infrared interferometry. *MNRAS*, 423:L11–L15. [pg: 59]

Wilson, R. E. and Devinney, E. J. (1971). Realization of accurate close-binary light curves: application to mr cygni. *Astrophysical Journal, vol. 166, p. 605*, 166:605. [pg: 72]

Yudin, R. (2001). Statistical analysis of intrinsic polarization, ir excess and projected rotational velocity distributions of classical be stars. *Astronomy & Astrophysics*, 368(3):912–931. [pg: 163]

Zahn, J.-P. (1977). Tidal friction in close binary stars. *Astronomy and Astrophysics, vol. 57, no. 3, May 1977, p. 383-394.*, 57:383–394. [pg: 51]

Zari, E., Hashemi, H., Brown, A. G. A., Jardine, K., and de Zeeuw, P. T. (2018). 3d maps of young stars in the solar neighbourhood with gaia dr2. *Astronomy & Astrophysics*, 620:A172. [pg: 94]

Zechmeister, M. and Kürster, M. (2009). The generalised lomb-scargle periodogram-a new formalism for the floating-mean and keplerian periodograms. *Astronomy & Astrophysics*, 496(2):577–584. [pg: 66]

Zhuchkov, R. Y., Malogolovets, E., Kiyaeva, O., Orlov, V., Bikmaev, I., Balega, Y. Y., and Safina, D. (2010). Physical parameters and dynamical properties of the multiple star o and. *Astronomy reports*, 54:1134–1149. [pg: 158]

Ziegenbalg, S. (2024). Detection of 19 lt-yr long bipolar jets from interacting binary kx and. *Research Notes of the AAS*, 8(11):289. [pg: 201]

Zorec, J. (2004). Rotation and properties of be stars. In *Symposium-International Astronomical Union*, volume 215, pages 73–82. Cambridge University Press. [pg: 25]

Zorec, J. and Briot, D. (1997). Critical study of the frequency of be stars taking into account their outstanding characteristics. *Astronomy and Astrophysics, v. 318, p. 443-460*, 318:443–460. [pg: 20, 21, 25, 52, 53]

Zorec, J., Frémat, Y., de Souza, A. D., Royer, F., Cidale, L., Hubert, A.-M., Semaan, T., Martayan, C., Cochetti, Y. R., Arias, M. L., et al. (2016). Critical study of the distribution of rotational velocities of be stars-i. deconvolution methods, effects due to gravity darkening, macroturbulence, and binarity. *Astronomy & Astrophysics*, 595:A132. [pg: 53, 54, 93, 107, 115, 179, 184, 195, 199, 200, 206, 207, 210, 211]

Zwintz, K. et al. (2024a). Binary classification of hd 135734. *Astronomy and Astrophysics*. In press. [pg: 59]

Zwintz, K., Pigulski, A., Kuschnig, R., Wade, G., Doherty, G., Earl, M., Lovekin, C., Müllner, M., Piché-Perrier, S., Steindl, T., et al. (2024b). Catalogue of brite-constellation targets-i. fields 1 to 14 (november 2013–april 2016). *Astronomy & Astrophysics*, 683:A49. [pg: 149]